PolyPublie
Polytechnique Montréal

POLYTECHNIQUE MONTRÉAL
UNIVERSITÉ D'INGÉNIERIE

Titre: Title:	Towards a New Tectonic Model for the Western Grenville Province: Insight from Structural, Geochemical and Geochronological Data from the Highway 117 Transect, Quebec, Canada
Auteur: Author:	Christopher William Lambert
Date:	2022
Type:	Mémoire ou thèse / Dissertation or Thesis
Référence: Citation:	Lambert, C. W. (2022). Towards a New Tectonic Model for the Western Grenville Province: Insight from Structural, Geochemical and Geochronological Data from the Highway 117 Transect, Quebec, Canada [Ph.D. thesis, Polytechnique Montréal]. PolyPublie. https://publications.polymtl.ca/10759/

Document en libre accès dans PolyPublie
Open Access document in PolyPublie

URL de PolyPublie: PolyPublie URL:	https://publications.polymtl.ca/10759/
Directeurs de recherche: Advisors:	Félix Gervais
Programme: Program:	Génie minéral

Ce fichier a été téléchargé à partir de PolyPublie, le dépôt institutionnel de Polytechnique Montréal
This file has been downloaded from PolyPublie, the institutional repository of Polytechnique Montréal

https://publications.polymtl.ca

POLYTECHNIQUE MONTRÉAL

affiliée à l'Université de Montréal

Towards a new tectonic model for the western Grenville Province: Insight from structural, geochemical and geochronological data from the highway 117 transect, Quebec, Canada

CHRISTOPHER WILLIAM LAMBERT

Département des génies civil, géologique et des mines

Thèse présentée en vue de l'obtention du diplôme de *Philosophiæ Doctor*

Génie minéral

Novembre 2022

© Christopher William Lambert, 2022.

POLYTECHNIQUE MONTRÉAL

affiliée à l'Université de Montréal

Cette thèse intitulée:

Towards a new tectonic model for the western Grenville Province: Insight from structural, geochemical and geochronological data from the highway 117 transect, Quebec, Canada

présentée par **Christopher William LAMBERT**

en vue de l'obtention du diplôme de *Philosophiæ Doctor*

a été dûment acceptée par le jury d'examen constitué de :

Marc LEGAULT, président

Félix GERVAIS, membre et directeur de recherche

Kyle LARSON, membre

Jean BÉDARD, membre externe

DEDICATION

This thesis is dedicated to my wife and family - who believed in me even when I did not.

ACKNOWLEDGEMENTS

I would like to extend my sincere gratitude to all the people who supported me and contributed in any way to the work presented herein. First and foremost, I would like to thank my supervisor, Félix Gervais, for his guidance and endless patience, especially through the challenges I faced in the final year. I have benefited tremendously from our discussions and your thoughtful comments and revisions of the works herein. Thank you for taking a chance on me.

My sincere gratitude also goes to the Ministère de l'Énergie et des Ressources naturelles du Québec (MERNQ), for financial and logistical support, especially the efforts of Abdelali Moukhsil, who was always willing to share insight and discuss Grenvillian geology with me. Thank you to Fabien Solgandi, my liaison at MERNQ, who made sure my thin sections were made and geochemical samples analyzed at the respective laboratories.

I would also like to extend my gratitude to Jim Crowley and his team at the Boise State University Geochronology Laboratory, not only for organizing and conducting analyses, but for his endless patience, recommendations and thoughtful insights into many of the challenges I encountered in the geochronology section of the work. My sincere appreciation also goes to Kyle Larson at UBC Okanagan, who was happy to share recommendations during the project proposal and valuable insight while visiting in the field. To Jean Bédard at the Geological Survey of Canada, who was happy to offer advice and answer the many, and probably naïve, geochemistry related questions that arose during this research. Comments and suggestions by both Kyle and Jean, along with Marc Legault, who were the reviewers of the thesis, were also greatly appreciated.

Then to Christie Rowe at McGill university, for introducing me to 'Streetcar2Subduction', which was the inspiration for our 'virtual chapter' (chapter 2). Christie's passion for geology is unmatched and infectious, and I am truly grateful to her for always including me in field trips and post-graduate social events.

Although reviews of the article (chapter 4) were not known at the time of submission, I appreciate efforts of the anonymous reviewers of the article as well as the time and effort taken by the reviewers of this thesis.

Thank you to my friends and colleagues at Polytechnique Montréal and McGill. Specifically, Anne-Laure Bonnet, for translating various texts into French. To Myriam Roy for being an excellent field assistant/translator. To Gaëlle Labat and Charles Kavanagh-Lepage in the Poly-

Grenville research group, for welcoming my wife and I into a foreign country, the countless geology (and social) discussions, and for the continued support through the PhD process. Charles especially, who was a great field companion and sounding board for ideas and concepts presented herein. His willingness to review and assist with any section of the work and his efforts in keeping my moral high through the trying times, are all greatly appreciated. To Moses Angombe, for his wiliness to share insightful tips and techniques, but most of all, his encouragement and friendship over the last few years.

I would also like to extend my gratitude to my Canadian “family”, Christine, Brain and Ursula for welcoming my wife into your homes and extended family.

Finally, I would like to thank my family, especially my wife, who despite her own adversities, provided a source of hope and encouragement during these most dire times. Without their endless support and patience, completing this arduous process would not have been possible.

RÉSUMÉ

Les orogènes continentaux de collision sont des systèmes tectoniques dynamiques qui ont joué un rôle essentiel dans le remodelage de la croûte terrestre. Les processus de déformation et d'exhumation qui ont été actifs au cours de leur évolution sont au centre de débats d'actualité. L'orogène Méso-Néoprotérozoïque de Grenville, partiellement préservé sous la forme de la Province de Grenville au Canada, ne fait pas exception et présente un intérêt particulier, car il expose les différents niveaux structuraux d'un orogène et s'est développé au cours d'une période entre les régimes tectoniques anciens (par exemple, le Précambrien) et modernes (par exemple, le Phanérozoïque). Sur la base de compilations de données à l'échelle de l'orogène et de modèles numériques 2-D, il a été largement considéré comme un grand orogène chaud de longue durée (« LHO ») qui a évolué à travers diverses phases d'écoulement ductile (écoulement en chenal ou nappes ductiles) jusqu'à l'effondrement orogénique pendant la phase initiale d'Ottawan (environ 1090-1020 Ma), déformant la croûte inférieure moyenne de la Ceinture allochtone (AB), qui est composée de roches péri-cratoniques et exotiques accrétées sur la Laurentie. Puis, au cours de la phase ultérieure de Rigolet (environ 1005-980 Ma), la Ceinture parautochtone (PB), qui comprend le socle laurentien et ses séquences de couverture, aurait été remaniée soit dans un prisme orogénique ou par un mode d'écoulement ductile. Ces modèles conceptuels, en particulier ceux proposés pour l'évolution au cours de la phase de Rigolet, doivent encore être testés en détail, ce qui passe par la collecte de données sur le terrain et des analyses modernes.

Afin d'approfondir la compréhension de l'événement grenvillien, et plus particulièrement de la déformation du PB durant la phase de Rigolet, cette étude se concentre sur le transect généralement peu étudié de la route 117 à travers la province de Grenville dans l'ouest du Québec. Dans les trois chapitres principaux de cette étude, des données structurales (chapitre 2), géochimiques (chapitre 3) et géochronologiques (chapitres 2 & 4), basées sur des données terrain mais acquise par des techniques analytiques de pointe, sont présentées afin de caractériser l'architecture structurale préservée le long de ce transect et de proposer un nouveau modèle tectonique pour la déformation du PB durant la phase de Rigolet. De plus, une grande partie des données est présentée dans une nouvelle visite auto-guidée dans « Google Earth » afin de s'intégrer dans une nouvelle ère de publications virtuelles et interactives.

L'architecture le long du transect expose divers (sous-)domaines allochtones et parautochtones. et a été précédemment définie sur la base de données limitées provenant d'études régionales avant les

développements récents de la tectonique grenvillienne et nécessite donc des réinterprétations. Les nouvelles données structurales et géochronologiques présentées dans cette étude à travers les domaines parautochtone (c'est-à-dire la zone de chevauchement du front du Grenville (GFTZ) ; les Terranes du Réservoir Dozois (RDT) et de la Vérendrye (VT)) et allochtone (c'est-à-dire les Terranes de Renzy (RT) et du Lac Dumoine (LDT)) définissent le premier ensemble complet de données le long du transect, en particulier entre la GFTZ et l'ensemble de roche ayant échappée à l'Orogénie grenvillienne appelée couverture orogénique. L'interprétation structurale (chapitre 2) du RDT et du VT révèle que les gneiss sont des tectonites S>>L et qu'il existe au moins 3 événements de déformation (Sn-1 ; Sn ; Sn+1). La gneissosité omniprésente dans le RDT et le VT (Sn) est syn-migmatitique, a un faible pendage (<30^{o}C) qui montre une variation significative de directions le long du transect pour définir une série de sous-domaines structuraux. L'abondance de grains de quartz non allongés dans les leucosomes de Sn du RDT et du VT est interprétée comme évidence d'une déformation en présence de fusion partielle. Bien que les indicateurs cinématiques dans les gneiss RDT à faible pendage montrent une direction de transport dominante vers le SW, parallèle au grain structural de l'orogène, ils ont une distribution bimodale (NE-SW et NW-SE) qui suggère que la déformation était probablement triclinique.

Les résultats de la géochronologie U-Pb sur zircon (chapitres 2 et 4) provenant des leucosomes felsiques et des veines d'injection syn- à tardi-déformation à travers les différents niveaux structuraux contribuent également à la caractérisation du transect. D'une part, les dates obtenues sur les cœurs de zircon hérités correspondent systématiquement aux âges attendus pour les gneiss hôtes, ce qui appuie la subdivision tectonique proposée pour la région étudiée. D'autre part, les âges de cristallisation $^{207}Pb/^{206}Pb$ entre 1020 ± 13 Ma et 968 ± 10 Ma fournissent la première preuve que les gneiss dans le RDT et le VT ont été déformés pendant la phase Rigolet alors que la roche hôte était partiellement fondue. Les résultats contraignent l'âge du chevauchement vers le NO, qui se manifeste généralement par la rotation de boudins mafiques de dimension métrique dans la zone de cisaillement Teddy, et par des plis en fourreau asymétriques dans le VT à 1002-1008 Ma. Par contraste, l'âge de 1040 ± 9 Ma d'un dyke granitique tardif à la déformation en décrochement dextre le long de la zone de cisaillement controversée de Baskatong démontre que la déformation ductile dans le LDT s'est déroulé pendant la phase Ottawan, ce qui appuie l'hypothèse que ce domaine fait partie de L'AB

Les grains de zircon provenant des échantillons révèlent systématiquement des morphologies complexes. Ils sont généralement caractérisés par des noyaux hérités et des successions de zones de textures distinctes qui partagent pour la plupart des caractéristiques d'éléments traces et donnent des âges moyens pondérés $^{207}Pb/^{206}Pb$ grenvilliens qui se chevauchent. Certains spécimens étaient physiquement liés au leucosome dans leur gneiss hôte et, d'après la différence entre les populations grenvilliennes les plus anciennes (1020 ± 6 Ma) et les plus jeunes (968 ± 4) dans ces échantillons (erreurs d'étalonnage externes exclues), la déformation de Rigolet s'est probablement produite sur une période prolongée d'au moins 30 Ma. La plupart du leucosome granitique et des intrusions dans le RDT et le VT sont interprétés comme le produit de multiples événements de fusion à présence d'eau pendant cette période en raison de: i) les morphologies complexes des zircons; ii) les caractéristiques physiques des migmatites dans le RDT et le VT, particulièrement leurs limites diffuses avec leur roches hôtes; iii) la présence de hornblende péritectique qui implique l'addition d'eau lors de la fusion; iv) les températures du thermomètre Ti-in-zircon (625-778ºC) qui sont à la limite inférieure pour la fusion par biotite-déshydratation des roches Bt-Qtz-Pl (< 800ºC).

L'une des principales hypothèses issues des observations de terrain était plusieurs ensembles de roches dispersés dans les gneiss parautochthones (RDT et VT) pourraient faire partie de la RT Mésoprotérozoïque allochtone, en raison de leurs similitudes lithologiques, structurales et métamorphiques. Une nouvelle cartographie le long du transect (chapitre 2) a révélé que les gneiss du PB s'étendaieent structurellement au-dessus et au-dessous des composants de la RT (sensu stricto), ce qui implique que les composants de la RT et les équivalents de la RT sont complètement enveloppés dans le PB.

Pour vérifier cette hypothèse, une partie de cette étude (chapitre 2) examine les signatures en éléments traces immobiles de vingt-cinq affleurements et boudins mafiques recueillis dans les gneiss migmatitiques de la RDT et du VT. Les résultats révèlent que ces corps mafiques définissent trois groupes géochimiques, à savoir les basaltes « komatiitiques » (groupe U1) et les andésites et basaltes tholéiitiques (groupes U2 et U3). Les groupes U2 et U3 se distinguent par la présence de grands creux négatifs en Ta-Nb dans le premier groupe et d'anomalies nulles en Ti dans le second. En s'appuyant sur des méthodes préétablies et novatrices, les signatures d'éléments traces immobiles des trois groupes sont comparées à des suites mafiques connues pour avoir des affinités magmatiques avec la province contiguë du Supérieur (c'est-à-dire autochtone) ou avec des terranes interprétés comme faisant partie de l'AB. Les suites autochtones considérées ici comprennent les

métavolcaniques mafiques archéennes de la ceinture de roches vertes de l'Abitibi et plusieurs suites mafiques protérozoïques (environ 2470-1140 Ma) (Senneterre, Matachewan, Sudbury et Abitibi). Les métagabbros coronitiques et les suites mafiques de la RT sont considérés comme des suites de référence uniques à l'AB en Ontario et dans la région étudiée respectivement et devraient donc surplomber structurellement le PB.

Afin d'identifier à quelles suites connues appartiennent les groupes U1-3, les caractéristiques suivantes ont été comparées : (1) les profils normalisés des éléments immobiles N-MORB ; (2) les différences dans leurs anomalies HFSE (par ex. Ta, Nb, Ti) ; (3) les diagrammes de rapport d'éléments incompatibles, définis par l'enrichissement en éléments de terres rares (ETR) légères $(La/Sm)_{CN}$ et lourdes $((Gd/Yb)_{CN}$ et $(Tb/Yb)_{CN)}$ par rapport à la pente globale des ETR en REE_{CN} $(La/Yb)_{CN}$. Les résultats des comparaisons d'éléments traces immobiles indiquent une affiliation claire à l'AB pour la plupart des corps mafiques enveloppés dans les gneiss de la RDT et de la VT, en particulier aux suites de la RT, ce qui confirme nos observations de terrain et implique qu'une partie de l'AB inférieur a dû être démembrée et incorporée dans le PB pendant la déformation de Rigolet. Ces résultats suggèrent que la délimitation des domaines tectoniques et de leurs frontières dans la province de Grenville, comme le « Allochthon Boundary Thrust », n'est pas simple et que les méthodes antérieures d'identification des différents niveaux structuraux basées sur la corrélation de leurs suites mafiques respectives dans les LHO doivent être considérées avec prudence.

En intégrant toutes les données, cette étude présente une nouvelle coupe géologique transversale pour une longueur de 140 km du transect et propose un nouveau modèle pour la déformation du PB pendant la phase de Rigolet. La déformation pervasive en présence de fusion partielle pendant au moins 30 Ma suggère que les gneiss migmatitiques des RDT et VT constituaient un chenal de faible viscosité s'étant écoulé de façon ductile « channel flow » pendant la phase Rigolet. De plus, les résultats des études structurales (chapitre 2) et géochimiques (chapitre 3), suggèrent que les RT représentent des composants allochtones enveloppés dans des gneiss parautochtones. D'après les résultats de la géochronologie et les preuves de terrain présentées dans cette étude (chapitre 4), les dykes felsiques ont bréchifié les composants mafiques de la RT coïncidant avec la déformation dans le PB, ce qui a pu conduire à leur démembrement et à leur incorporation dans la chenal parautochtone sous forme de radeaux mafiques de taille métriques à kilométriques.

Les résultats de cette étude sont en contradiction avec les modèles conceptuels proposés pour l'évolution de la Province de Grenville occidentale qui considèrent que le PB a été affecté par l'effondrement gravitationnel du noyau orogénique ou a évolué sous forme de prisme orogénique pendant la phase de Rigolet. Au contraire, le modèle tectonique proposé dans cette étude est comparable à des modèles plus récents préconisant un écoulement ductile au sein du PB dans l'est du Québec durant cette phase de l'orogenèse grenvillienne Ceci suggère que le Rigolet était une phase orogénique majeure impliquant une fusion et un écoulement prolongés de la croûte profonde. Ces résultats ont donc des implications importantes concernant l'évolution tectonique de l'orogenèse grenvillienne ainsi que des implications possibles pour l'évolution du socle tectonique dans d'autres LHO.

ABSTRACT

Continental collisional orogens are dynamic tectonic systems that played vital roles in remolding the Earth's crust and the deformation and exhumation processes that were active during their evolution are the focus of topical debates. The Meso-Neoproterozoic Grenville Orogen, partially preserved as the Grenville Province in Canada, is no exception and is of particular interest as it exposes various structural levels of an orogen and straddles ancient (e.g. Precambrian) and modern (e.g. Phanerozoic) tectonic regimes. Based on orogen-wide data compilations and 2-D numerical models, it has largely been considered a large, hot long-duration orogen (LHO) that evolved through various phases of ductile flow (channel flow or ductile nappes) to orogenic collapse during the initial Ottawan (ca. 1090-1020 Ma) phase, deforming the mid-lower crust of the Allochthonous Belt (AB), which is composed of peri-cratonic and exotic rocks accreted to Laurentia. Then, during the later Rigolet phase (ca. 1005-980 Ma) the Parautochthonous Belt (PB), comprising the Laurentian basement and cover sequences, was reworked by foreland-ward thick-skinned thrusting or a mode of ductile flow. These largely conceptual models, especially those proposed for the evolution during the Rigolet phase, still require detailed testing, which is routed in field-based data collection and modern analyses.

To further the understanding of the Grenvillian event, specifically deformation of the PB during the Rigolet phase, this study focuses on the generally understudied highway 117 transect through the Grenville Province in western Quebec. In the three core chapters of this study, field-based structural (chapter 2), geochemical (chapter 3) and modern geochronological data (chapters 2 & 4) are presented in order to characterize the tectonic architecture preserved along this transect and propose a new tectonic model for deformation in the PB during the Rigolet phase. Furthermore, a large part of the data is presented in a novel, self-guided tour in Google Earth to integrate into a new era of virtual and interactive publications.

The architecture along the transect exposes various allochthonous and parautochthonous (sub)domains and was previously defined based on limited data from regional studies before recent developments in Grenvillian tectonics and thus, require re-interpretations. New structural and geochronological data presented in this study through the parautochthonous (i.e. Grenville Front Thrust Zone (GFTZ); Reservoir Dozois (RDT) and Vérendrye (VT) terranes) and allochthonous (i.e. Renzy (RT) and Lac Dumoine (LDT) terranes) domains defines the first comprehensive dataset along the length the transect, particularly between the GFTZ and the orogenic lid to the

orogen. The structural interpretation (chapter 2) of the RDT and VT reveals that the gneisses are S>>L tectonites and there are at least 3 deformation fabrics (S_{n-1}; S_n; S_{n+1}). The pervasive gneissosity in both the RDT and VT (S_n) is a syn-migmatitic amphibolite grade fabric that is mostly shallow dipping (<30°C) but shows significant variation along the transect to define a series of structural subdomains. Abundant undeformed quartz grains in the S_n leucosomes are interpreted to record suprasolidus conditions, implying the RDT and VT define a panel of rocks that were deformed while still partially molten. Although kinematic indicators in the shallow dipping RDT gneisses show a dominant transport direction was to the SW, parallel to the length of orogen, they have a bimodal distribution (NE-SW and NW-SE) which suggests that tectonism in these PB domains was probably triclinic.

U-Pb zircon geochronology results (chapters 2 & 4) from syn- to late-deformational felsic leucosomes and injection veins through the various structural levels further aids in the characterization of the transect. Whereas the inherited dates systematically matched the ages expected for the host gneisses to support the tectonic subdivision of the study area, the $^{207}Pb/^{206}Pb$ weighted mean crystallization ages provide the first proof that the gneisses within the RDT and VT were deformed in the presence of melt during the Rigolet phase between 1020 ± 13 Ma and 968 ± 10 Ma and that the LDT forms part of the AB, deformed during the Ottawan phase (>1040 Ma). The results also provide the first constraints on the minimum age of NW-directed tectonism in the study area, commonly manifested as the rotation of meter-decameter sized mafic boudins within the newly recognized Teddy Bear Shear Zone (1002 ± 16 Ma) and asymmetrical sheath folds in the VT (1008 ± 12 Ma). New ages of 1040 ± 9 Ma also date dextral shearing along the contentious Baskatong Shear Zone for the first time, whereas any sinistral shearing that was previously inferred along the same zone must have occurred before 1016 ± 9 Ma.

Zircon grains from the samples ubiquitously reveal complex morphologies, defined by inherited cores and successions of texturally distinct zones that mostly share trace element characteristics and yield overlapping Grenvillian $^{207}Pb/^{206}Pb$ weighted mean ages. Some samples were physically linked with leucosome in their host gneiss and based on the difference between the oldest (1020 ± 6 Ma) and youngest (968 ± 4) Grenvillian populations in these samples (external calibration errors excluded), Rigolet deformation likely occurred over a protracted period of at least 30 Ma. Based on i) the complex zircon morphologies; ii) the physical characteristics of the migmatites in the RDT and VT, particularly their diffuse boundaries and the presence of large peritectic hornblende; iii)

combined with Ti-in-zircon temperatures (625-778^{o}C) that are at the lower limit for biotite-dehydration melting of Bt-Qtz-Pl rocks (< 800^{o}C); most of the granitic leucosome and intrusions in the RDT and VT are interpreted as product of multiple water-present melting events during this time.

One of the key hypotheses driving this study was that several newly identified outcrops that are dispersed within the 'sea' parautochthonous (RDT and VT) gneisses may be part of the allochthonous Mesoproterozoic RT, based on their lithological, structural and metamorphic similarities. New mapping along the transect (chapter 2) reveals that the PB gneisses extend structurally above and below the RT (*sensu stricto*) components, which implies the RT components and the RT-equivalents are completely enveloped within the PB.

To test this hypothesis, part of this study (chapter 2) examines the immobile trace element signatures of twenty-five deformed and retrogressed mafic outcrops and boudins collected within the migmatitic gneisses of the RDT and VT. Results reveal that these mafic bodies define three geochemical groups, namely 'komatiitic' basalts (group U1) and tholeiitic andesites and basalts (groups U2 and U3). Groups U2 and U3 are distinguished based on the presence of large negative Ta-Nb troughs in the former group and nil-flat Ti anomalies in the latter. Building on pre-established and innovative methods, the immobile trace element signatures of the three groups are compared to mafic suites known to have magmatic affinities to either the contiguous Superior Province (i.e. autochthonous) or terranes interpreted to be part of the AB. Autochthonous suites considered herein, include Archean mafic metavolcanics from the Abitibi Greenstone Belt and several Proterozoic (ca. 2470-1140 Ma) mafic suites (Senneterre, Matachewan, Sudbury and Abitibi). The ca. 1160 Ma Algonquin-type coronitic metagabbro's and mafic suites of the RT are considered as reference suites unique to the AB in Ontario and the study region respectively and should therefore, structurally overly the PB.

In order to identify the most likely correlates of groups U1-3, the following characteristics were compared: (1) the N-MORB normalized immobile-element spider profiles; (2) differences in their HFSE (e.g. Ta, Nb, Ti) anomalies; (3) incompatible element ratio-ratio diagrams, defined by LREE enrichment $(La/Sm)_{CN}$ versus the overall REE_{CN} slope $(La/Yb)_{CN}$ and proxies for the depth of source melting inferred from $(Gd/Yb)_{CN}$ and $(Tb/Yb)_{CN}$. The results of the immobile trace element comparisons point to a clear AB affiliation for most mafic bodies enveloped within the RDT and

VT gneisses, especially to suites of the RT, which confirms the field observations and implies that part of the lower AB must have been dismembered and incorporated into the PB during Rigolet deformation. These findings suggests that the delineation of tectonic domains and their boundaries in the Grenville Province, such as the Allochthon Boundary Thrust, is not straightforward and that antecedent methods of identifying different structural levels based on the correlation of their respective mafic suites within LHOs should be considered with caution.

By integrating all the data, this study presents a new geological cross section for a 140 km length of the transect and proposes a new model for deformation of the PB during the Rigolet phase. Based on evidence for melt-present deformation for at least 30 Ma and evidence for suprasolidus deformation, this study proposes that the migmatitic RDT and VT gneisses in the PB represented melt-weakened panel in the PB that may have facilitated heterogenous ductile (channel) flow during the Rigolet phase. Furthermore, the results of the structural (chapter 2) and geochemical (chapter 3) investigations, suggest that the RT represent allochthonous components enveloped within parautochthonous gneisses. Based on geochronology results and field evidence presented in this study (chapter 4), felsic dykes brecciated mafic components of the RT coeval to deformation in the PB, which may have led to their dismemberment and incorporation into the parautochthonous channel as kilometer-decameter-sized mafic rafts.

The findings of this study are inconsistent with the conceptual models proposed for the evolution of the western Grenville Province that consider the PB was affected by gravitational collapse of the orogenic core or evolved as fold-and thrust belts along the orogen flanks during the Rigolet phase. Instead the tectonic model proposed in this study is comparable to more recent models advocating ductile flow within the PB in eastern Quebec during this phase of the Grenvillian orogeny, which suggests that the Rigolet was a major orogenic phase involving protracted melting and flow of the deep crust. These results thus have significant implications regarding the tectonic evolution of the Grenvillian Orogeny as well as implications for the evolution of the tectonic basement in other LHOs.

TABLE OF CONTENTS

DEDICATION iii
ACKNOWLEDGEMENTS iv
RÉSUMÉ vi
ABSTRACT xi
TABLE OF CONTENTS xv
LIST OF TABLES xviii
LIST OF FIGURES xx
LIST OF SYMBOLS AND ABBREVIATIONS xxxv
LIST OF APPENDICES xxxvi
Chapter 1 INTRODUCTION 1
1.1 Overview and scope of study 1
1.1.1 Study area 8
1.2 Regional geology 8
1.2.1 Tectonic setting 8
1.2.2 Pre-Grenvillian evolution 8
1.2.3 Tectonic subdivision of the Grenville Province 9
1.2.4 Evolution of the Grenville Orogen 10
1.2.5 Geology along Hw117 19
1.3 Thesis objectives 27
1.4 Methodology 34
1.4.1 Background, outcrop exposure and accessibility 34
1.4.2 Pre-field preparation and field mapping information and techniques 35
1.4.3 Geochemistry considerations 37
1.4.4 U-Pb zircon dating considerations 38
1.5 Structure of thesis and co-author statement 39
1.5.1 Structure of thesis 39
1.5.2 Co-author statement 42
1.5.3 Other contributions by author 42
Chapter 2 TRANSECT OF A LARGE HOT OROGEN: A NOVEL VIRTUAL TOUR THROUGH THE GRENVILLE PROVINCE OF WESTERN QUEBEC: GEOCHRONOLOGY AND STRUCTURAL CONTRIBUTIONS 44
2.1 Introduction 44
2.2 Geochronology 46
2.2.1 Sample CL6144: Syeno-granite intrusion in subvertical LDT gneisses (virtual stop no. 16) 46
2.2.2 Sample CL8025 granitic dyke along the SE margin of BSZ (virtual stop no. 17) 48
2.3 A new geological cross section for the Hw117 transect 52

2.3.1 Structures in the Grenville Front Thrust Zone (GFTZ).....52
2.3.2 Structure across the Dorval Detachment (DD) 53
2.3.3 Structures in the Reservoir Dozois Terrane (RDT).....57
2.3.4 Structures in the Vérendrye Terrane (VT) 62
2.3.5 Structures in the Renzy Terrane (RT) 65
2.3.6 Structures of the Lac Dumoine Terrane (LDT) and Central Metasedimentary Belt (including the Baskatong and Cayamant shear zones).....68
2.4 Synopsis of the structural characterization along Hw117.....70
Chapter 3 UNRAVELLING THE TECTONIC ARCHITECTURE OF THE GRENVILLE PROVINCE ALONG HW117: INSIGHTS FROM THE GEOCHEMICAL CORRELATION OF MAFIC SUITES.....73
3.1 Introduction.....73
3.2 Methodology 76
3.2.1 Unknown mafic samples in this study: sample collection and analyses 76
3.2.2 Screening out metasedimentary and cumulate rocks 76
3.2.3 Major and trace element mobility 77
3.2.4 Reference suites: data sources and screening.....80
3.2.5 Strategy of investigation and comparison to reference suites 81
3.3 Unknown mafic samples collected along Highway 117 83
3.3.1 Sample descriptions and field-based subdivision.....83
3.3.2 Geochemical classification.....88
3.4 Reference Suites.....97
3.4.1 Mafic suites with an autochthonous affinity 99
3.4.2 Mafic suites with an allochthonous affinity 103
3.5 Comparing unknown samples and reference suites 106
3.5.1 Comparison to reference suites with an autochthonous affinity 106
3.5.2 Comparison to reference suites with an allochthonous affinity 110
3.6 Discussion 111
3.6.1 Allochthonous affinity for most samples in the RDT and VT 111
3.6.2 Tectonic setting of the protoliths.....112
3.6.3 The tectonic architecture for the Grenville Orogen in western Quebec and geodynamic implications.....116
3.7 Conclusions 118
Chapter 4 ARTICLE 1: PROTRACTED MELT-PRESENT DEFORMATION DURING THE RIGOLET PHASE OF THE GRENVILLIAN OROGENY. INSIGHTS FROM

GEOCHRONOLOGY ALONG THE HIGHWAY 117 TRANSECT THROUGH THE GRENVILLE PROVINCE IN WESTERN QUEBEC, CANADA 120
4.1 Abstract 120
4.2 Introduction 120
4.3 Geological context 125
4.3.1 Geological subdivision along the highway 117 transect 125
4.4 Methodology 133
4.4.1 Methodology LA-ICP-MS preparation and analytical procedure 133
4.4.2 Presentation of ages and calibration of errors 133
4.4.3 Ti-in-zircon thermometry 136
4.4.4 Classification of multiple zircon zones 136
4.5 Geochronology results 137
4.5.1 Sample CL6070: inter-boudin granitic leucosome in the RDT 137
4.5.2 Sample CL6098: diatexites and pegmatites intruding Renzy-type gneisses 141
4.5.3 Sample CL6106: tonalitic-trondhjemitic intrusion in the Teddy Bear Shear Zone 146
4.5.4 Sample CL6112 granitic dykes intruding the Renzy Terrane 150
4.5.5 Sample CL6127: Granitic dyke in RDT gneisses 155
4.5.6 Sample CL6135: granitic injection in the VT 159
4.6 Discussion 162
4.6.1 Petrogenesis of felsic igneous rocks 162
4.6.2 Tectonic implications 166
4.7 Conclusions 170
Chapter 5 CONCLUSION (AND RECOMMENDATIONS) 172
5.1 Summary and conclusions 172
5.1.1 Towards a new model for deformation of the PB in western Quebec 172
5.2 Recommendations and future work 182
5.2.1 The ABT problem 182
5.2.2 General questions raised and recommendations for future work 184
REFERENCES 189
APPENDICES 227

LIST OF TABLES

Table 1.1. Summary of the key characteristics used to distinguish between the different tectonic models (taken from Gervais and Brown, 2011). 4
Table 2.1. List of abbreviations and descriptions of structures depicted on the cross section and discussed in this chapter. 56
Table 3.1. Field and geochemical grouping for each sample analysed in this study. 82
Table 3.2. Summary of the geochemical characteristics used to define geochemical groups U1-3 in this study 92
Table 3.3. Summary of reference suites considered in this study. 98
Table 4.1. Metadata for LA-ICP-MS U-(Th-)Pb analyses of samples analysed in this study. 135
Table 4.2. Summary table of the geochronology and Ti-in-zircon thermometry results from this study. 140
Table A.1. Summary of geochronology analyses for sample CL6144 from stop 16, v-chapter 2. 227
Table A.2. Summary of geochronology analyses for sample CL8025 from stop 17, v-chapter 2. 229
Table B.1. Geochemistry of unknown mafic samples analyzed in this study....243
Table B.2 Quantitative geochemical comparison of unknown mafic samples analyzed herein, to reference suites. 257
Table D. 1. (Above left and right) Metadata for LA-ICP-MS U-(Th-)Pb analyses and (below) summary of standard materials and analytical errors for each sample. 278
Table D. 2. Summary of geochronology analyses for sample CL6070. 279
Table D. 3. Summary of geochronology analyses for sample CL6098. 280
Table D.4. Summary of geochronology analyses for sample CL6106. 282
Table D.5. Summary of geochronology analyses for sample CL6112. 284
Table D.6. Summary of geochronology analyses for sample CL6127. 286
Table D.7. Summary of geochronology analyses for sample CL6135. 288
Table D.8. Comparison of $^{207}Pb/^{206}Pb$ vs $^{206}Pb/^{238}U$ weighted mean ages and individual dates for each population in the zircons from the various samples. 290

Table D.9. Ti-in-zircon temperatures (°C) calculated for each population over a range of pressures using the geothermometer of Hofmann *et al.* (2014). The aSiO2 = 1 and the aTiO2 = 0.5 following Schiller and Finger (2019). Results reported in the text are 3rd quartile estimates following recommendations of Tomkins *et al.* (2007).....291

LIST OF FIGURES

Figure 1.1. Schematic diagram summarising the tectonic processes considered to be active during orogenesis (Taken from Jannin *et al.*, 2018). (A). Orogenic wedge model (after Platt, 1986; Jamieson and Beaumont, 2013). (B) Model showing various forms of ductile flow (i.e. channel flow and hot nappes) typically considered active in long-hot-duration orogens (LHOs; after Beaumont *et al.*, 2006; Jamieson and Beaumont, 2013; Larson and Cottle, 2014). (C) Gravitational collapse model (after Rey *et al.*, 2001; Tirel *et al.*, 2008). 2

Figure 1.2. (A) Location of the Grenville Province (inset; modified after Martignole, *et al.*, (2000)), subdivision of the Grenville Province and location of the study area (red box). (B) Schematic illustration of the tectonic architecture of the Grenville Province with proposed timing and direction of movement across the primary tectono-metamorphic boundaries during the respective phases of the Grenvillian Orogeny according to Rivers (2008). Note the different timing of deformation in western and central segments and the difference between out-of-sequence and in-sequence thrusting above and below the Allochthon Boundary Thrust (ABT). Figure modified from Rivers (2015). 7

Figure 1.3. Schematic crustal-scale cross sections of the Grenville Province that were redrawn from results of the LITHOPROBE-seismic data. Study area is indicated by the black box and represented by cross-section C. Colors reflect tectonic subdivision and metamorphism from Fig. 1.2. GFTZ = Grenville Front Thrust Zone. DD = Dorval Detachment. From Rivers (2015), modified after Ludden and Hynes (2000).....11

Figure 1.4. Schematic evolution of the Grenville Orogen. The proposed model shows an evolution in mode of deformation from (A) a form of ductile flow to (B) orogenic collapse and (C) renewed reworking in the Parautochthonous Belt, where the (X) mid and (Y) lower crust of the Laurentian margin are rapidly buried then thrusted in the foreland orogenic wedge. Abbreviations: ABT(D) = Allochthon Boundary Thrust (Detachment); GF = Grenville Front; Mz = Mazinaw terrane; a = allochthonous; p = parautochthonous. From Rivers (2008). 13

Figure 1.5. Schematic model for the tectonic evolution of the Grenville Province in the central Grenville Province, specifically the development of a parautochthonous channel during the Rigolet phase. (A1-A2) Cross section of the western transect through their study area that accounts for the possible influence of the stiff Tétépisca anorthositic pluton during the

development of the channel. (B1-B4) Cross section that shows the progressive development of the parautochthonous channel in the eastern section. Without the influence of the Tétépisca pluton, the model in B1 shows the development of a ductile fabric (Da1) in the Allochthonous Belt (AB) during the Ottawan phase whereas the model in B2 shows the development of a ductile fabric (Da2) in the parautochthonous belt (PB) during the Rigolet phase. In B3 the intrusion of felsic dykes, generated in the PB, into the overlying AB, facilitated strain weakening and the development of a Rigolet fabric in the AB, which may then have promoted the development of a ductile channel that incorporates part of the lower AB during the Rigolet phase in B4 . ABT = Allochthon Boundary Thrust; TSZ = Thachic shear zone. From Jannin *et al.*, (2018) 17

Figure 1.6. GO-2 numerical model stopped at 82.5 Ma convergence and compared against the Montreal-Val d'Or cross section. (A) Cross section interpreted from the LITHOPROBE seismic survey (Martignole, *et al.*, 2000). Colors correspond to the division of the Grenville Province shown in Fig. 1.2. (B) Model result that shows ductile nappes (blocks E-D) stacked against an indenter (block F), whereas the core is defined by moderate dipping thrust sheets. (C-D) Models overlain by cross section outline. Abbreviations: Dorval Detachment (DD); Grenville Front Thrust Zone (GFTZ); Lac Dumoine Terrane (LDT); Mont Laurier Terrane (MLT); Morin Terrane (MT); Reservoir Cabonga Terrane (RCT); Reservoir Dozois Terrane (RDT); Superior Province (SuP). From Jamieson *et al.* (2007). 18

Figure 1.7. Location and subdivision of the study area along the Hw117 transect, focused between Val-d'Or and Grand Remous in western Quebec. Location of existing geochronology data sets are also shown. Map compiled from field work conducted as part of this study, integrated with previous interpretations (e.g. Indares and Martignole, 1990; Martignole and Pouget, 1994; Martignole, 1995; Guo and Dickin, 1996; Montreuil and Constantin, 2010; Dickin *et al.*, 2014; Lambert *et al.*, 2018, 2019). Published U-Pb zircon and monazite ages data derived from Childe *et al.* (1993); Martignole and Friedman (1998); Martignole and Martelat (2005) and from the MERN SIGEOM online database. Baskatong Shear Zone = BSZ. 20

Figure 2.1. Subdivision of the Grenville Province along part of the Hw117 (white line) geo-traverse and location of the cross section (yellow line A-A'-B) that is presented later in this chapter (Fig. 2.5). Note the map also shows the virtual stop locations. References used for map creation are the same as in Fig. 1.7. 45

Figure 2.2. Photos and graphics summarising the field relationships and results of LA-ICP-MS geochronology from a late dyke in the BSZ (stop 16; v-chapter 2). (A) Steep dipping gneisses of the BSZ. (B) Late-tectonic pink granitic dyke that cuts the steep gneissic fabric sampled for geochronology. (C) Examples of zircon grain morphology and ablation spot locations. (D) Chondrite normalized REE spidergram and (E-F) bivariate trace element diagrams used to aid in the distinction of the various zircon zones. (G) Kernel density histogram of spot dates within the sample. (H). Tera-Wasserberg plot of the Grenvillian zircon populations. (I) Weighted mean $^{207}Pb/^{206}Pb$ ages of the Grenvillian zones. The uncertainty of the ages is reported without (in parentheses) and with the propagation of external calibration errors. 48

Figure 2.3. Field photos of syn-late tectonic granitic dykes and concordant stringers that intrude the BSZ (stop 17; v-chapter 2). (A) A thick (ca 30 cm) granitic dyke sampled for geochronology, crosscuts the gneissosity but also contain aligned quartz ribbons in the dyke (inset). (B) Multiple winged porphyroclasts define kinematic indicators within the granitic veins and indicate a dextral strike-slip shear component. (C) Examples of a granitic dyke that connects to cogenetic, foliation parallel veins with kinematic indicators indicating a dextral sense of shear. Note the cuspate-lobate boundaries on the dykes which indicate that they were subjected to deformation after intruding the gneisses. 50

Figure 2.4. Graphics summarising the results of LA-ICP-MS geochronology for sample CL8025 (stop 17; v-chapter 2). (A) Examples of zircon grain morphology and ablation spot locations. (B) Chondrite normalized REE spidergram and (C-D) bivariate trace element diagrams used to aid in the distinction of the various zircon zones. (E) Kernel density histogram of spot dates within the sample. (F). Tera-Wasserberg plot of the Grenvillian zircon populations. (G) Graphic for a weighted mean $^{207}Pb/^{206}Pb$ ages of the Grenvillian zones. The uncertainty of the ages is reported without (in parentheses) and with the propagation of external calibration errors. 51

Figure 2.5. Geological cross section along line A-B (see Fig. 2.1), focusing on structural elements between the Dorval Detachment and the Baskatong Shear Zone along the Hw117 transect. Stereoplots depict planar and linear fabrics measured along the transect and summarize their trends in the different tectonic domains from NW to SE. Rose diagrams present the direction of ductile tectonic transport inferred from micro-to decameter-scale kinematic indicators. In the rose diagrams, the direction of transport (‘rose petals’) considers the movement of the

upper/top of the rock packages relative to N (0°), irrespective of normal, thrust, or strike slip type tectonics. The points on the rose diagram act as linear features and provide an indication of the plunge angle that correspond to the respective directions and can be used as a rough indicator of down dip (steep lineation = thrust/normal sense) or strike slip (shallow) type tectonics. Schematic diagrams at select locations along the transect are also presented to aid in the visualization of various structural elements such as fold geometries and the relationship between the fabrics. Unit colors are the same as in Fig. 2.1. The location of the field stops, geochronology samples and figures discussed herein, are also annotated on the cross section. Note that the number sign (#) is used in the text to refer to specific stereoplots and schematic diagrams in the text. 54

Figure 2.6. Legend to the cross-section in Fig. 2.5. Includes stereoplots summarizing tectonic fabrics collected across the RDT and RT. 55

Figure 2.7. An impressive outcrop ca. 50m north of stop 11 shows a subhorizontal gneissosity that 'flows' around mafic boudins within the Vérendrye Terrane. Notice how the gneisses pinch tightly into the neck of the metagabbro, which may be used as a meter-scale analogue for the interpretation of the fabrics where RDT gneisses pinched into the inter-limb region of the Renzy Terrane on a kilometer-scale (#15 in Fig. 2.5). In addition, here granitic injections extend from the VT gneisses at the inter-boudin neck, into the metagabbro where they started to brecciate the mafic body, similar to the relationships observed at stop 14 (Fig. 2.8). 64

Figure 2.8. Outcrop photos from stop 14. (A) An annotated interpretation of the contact between the parautochthonous Lac Rolland and allochthonous Renzy Terrane units in the footwall and hanging wall of what is possibly the ABT. Note how the granitic dykes intrude and partially brecciate the mafic Renzy unit. (B-C). Folded leucosome in the Lac Rolland gneiss (B) forms a connected network of syn-deformational granite that coalesces, pools and intrudes the metagabbro boudin of the Renzy Terrane (C). The location of the sample collected for geochronology is indicated by ‘X’. (D) Oblique view of the proposed ABT, separating gneisses from the Parautochthonous Belt (bottom) and Renzy Terrane units in the footwall and hanging wall respectively. (E) Mylonite units at the contact of volcano-sedimentary units of the Renzy Terrane (top right) and the parautochthonous Lac Rolland gneisses (bottom left), which are interpreted to represent the ABT. 67

Figure 3.1. The 1st order tectonic architecture of the western Grenville Province and the distribution or orientation of the various mafic suites discussed in this study. Dashed box indicates the study region and location of Fig. 3.2. Red boxes indicate the previous areas of study by La Flèche *et al.*, (2005; LF) and Martignole and Martelat (2005; MM). Abbreviations: Allochthonous Boundary Thrust (ABT); Ontario (ON); Quebec (QC); Southern Volcanic Zone (SVZ). Compiled after Fahrig and West (1986); Wheeler *et al.* (1996); Ketchum and Davidson (2000); Rivers, (2008) and Montreuil and Constantin (2010). Data sources presented in Table 3.3. 74

Figure 3.2. Location of the study area and distribution of mafic samples collected in this study. A description of the various segments is presented in section 1.2.5. See text for detailed discussion of the subdivision of the unknown samples according to field-based and geochemical characteristics (section 3.3). Abbreviations: Allochthonous Boundary Thrust (ABT); Baskatong Shear Zone (BSZ); Cadgecrib Shear Corridor (CSZ); Grenville Front Thrust Zone (GFTZ); Lac Perche Terrane (LPT); Shear Zone (SZ); Vérendrye Terrane (VT). Map modified after Martignole and Pouget (1994); Montreuil and Constantin (2010); Lambert *et al.* (2019) and the SIGEOM database (2020). 75

Figure 3.3. Examples of field outcrops from which mafic samples analysed in this study were collected. (A-C) Examples of RDT-2 type outcrops within the Reservoir Dozois Terrane. (D-E) Examples of VT-type outcrops from the Vérendrye Terrane. (F-G) Examples of RT-type outcrops from the RT (*sensu stricto*). (H). Example of the RDT-1 type subdivision, defined by decameter-scale outcrops within the RDT but have lithological and structural characteristics rather similar to outcrops within the RT. (A) Rotated garnet-bearing gabbroic boudin in tonalitic gneisses and locality of sample #36 (geochemical group U3). (B) Gabbroic and amphibolite rafts in diatexites and locality of sample #59 (geochemical group U2). (C) Sigmoidal garnet-bearing gabbroic boudin in migmatitic granodiorite gneisses and locality of samples #30 & #38 (geochemical groups U2). (D) Rounded amphibolitic boudin within migmatitic granite to granodiorite gneisses and locality of sample #98 (geochemical group U3). (E) Transposed succession of garnet-bearing mafic and intermediate gneisses and locality of sample #95 (geochemical group U2). (F) Interleaved garnet-rich felsic to mafic gneisses (metavolcanics), typical of the RT. (G) Deformed garnetiferous granulites and sample locality of sample #64 (RT control sample). (H) Concordant folded mafic layers in a

mixed package of garnet-bearing felsic to intermediate gneisses, typical of the RT. Locality of samples #39 (geochemical group U2) & #55 (geochemical group U3). 84

Figure 3.4. Photomicrograph examples of the principal mineral assemblages observed across all mafic samples collected within this study. (A) Hbl-Pl-Cpx-Grt±Opx±Bt dominated assemblages with porphyroblastic textures. (B) Hbl-Pl-Cpx-Grt±Opx±Bt dominated assemblages with granoblastic to nematoblastic textures. (C) Clinopyroxene free Hbl-Pl-Grt±Bt assemblages. (D) Garnet free Cpx-Pl-Opx-Bt±Hbl assemblages with relict, cumulate clinopyroxenes and orthopyroxenes. (E) Amphibolites with Hbl-Pl±Bt dominated assemblages. See text for detailed descriptions. All sections in plane polarized light. Mineral abbreviations after Whitney and Evans (2010). 86

Figure 3.5. Geochemical rock classification schemes for all the mafic suites discussed in this study according to the trace-element TAS proxy diagram (see A,C,E) of Winchester and Floyd, (1977; modified by Pearce, 1996) and the Al_2O_3-($FeO+Fe_2O_3+TiO_2$)-Mg cation diagram (see B,D,F) after Jensen (1976). (A, B) Mafic samples collected during this study .Symbology represents both their field-based subdivision and geochemical classification, with each geochemical group annotated with the prefixes U1, U2 and U3. Reference suites include: (C,D) komatiites, komatiitic basalts and tholeiitic basalts from the Southern Volcanic Zone and Chibougamau areas of the Abitibi Greenstone Belt in the Superior Province; (E, F) Paleo-Mesoproterozoic mafic dyke suites that part of the autochthonous Archean crust of Laurentia (i.e. Superior Province) and mafic suites considered unique to the Allochthonous Belt in the Grenville Province, such as the Algonquin metagabbro suite and mafic suites of the Renzy Terrane. Note that some reference suites do contain entries classified as calc-alkaline basalts on the Jensen diagram (not shown here; see Fig. B.8), which were excluded from further comparisons as none of the unknown samples collected in this study have a similar calc-alkaline classification. Abbreviations: Allochthonous Belt (AB), Calc-alkaline (CA), Southern Volcanic Zone (SVZ), Tholeiitic or tholeiite (TH), Verendrye Terrane (VT). Data sources are discussed in the literature and presented in Table 3.3. 89

Figure 3.6. MgO vs select major and trace elements for the unknown samples collected in this study. Symbology as in Fig. 3.5. Colored lines in (A) and (D) represent the elemental trend lines that were used to correlate unknown samples to reference suites with either an autochthonous (Abitibi, Sudbury, Senneterre dyke suites) or allochthonous (Algonquin

coronitic metagabbro) affinity in the previous studies around the Georgian Bay area of Ontario (Ketchum and Davidson, 2000) and the Grenville Front Thrust Zone of western Quebec (Martignole and Martelat, 2005). An extended complement of Zr vs major and trace element diagrams as well as MgO vs compatible and incompatible elements for the unknown samples, is presented in the appendix (Fig. B.11-12). 91

Figure 3.7. Geochemical classification of the unknown mafic samples according to immobile trace element concentrations. Samples are subdivided according to the tectonic domains (i.e. different symbols) from which they were collected. Those from the RDT are further subdivided into the RDT-1 and RDT-2 types. The geochemical classification (color coded) is based on shared chondrite REE (left) and N-MORB immobile multi element (right) normalized patterns. A detailed description of the geochemical classification and anomalous samples within the groups is discussed in the text. The chondrite and MORB normalized fields of the geochemical groups are presented in (I) and (J) respectively. Normalized after Sun and McDonough (1989). 94

Figure 3.8. A $(Th/Ta)_{N\text{-}MORB}$- $(Ti/Sm)_{N\text{-}MORB}$ ratio-ratio diagram used to aid in the visualization of the HFSE anomalies from the N-MORB normalized spider profiles in Fig. 3.7. 96

Figure 3.9. MORB-normalized immobile spider diagram comparison of the geochemical groups defined in this study compared against reference suites with an autochthonous affinity. Abbreviations: Allochthonous Belt/Lac Dumoine Terrane (AB), Back-Arc-Basin-Basalt (BABB), Chondrite (CH), Continental-Arc Andesite (CAA), Continental Arc Basalt (CAB), Enriched Mid-Ocean Ridge Basalt (E-MORB), Ocean-Island Basalt (OIB) Ocean-Island Arc Basalt (OIAB), Primitive mantle (PM), (Reservoir Dozois Terrane (RDT), Southern Volcanic Zone (SVZ) and Verendrye Terrane (VT). Data for PM, CH, E-MORB and OIB from Sun and McDonough (1989), for OIAB and CAB from Kelemen *et al.* (2014) and for BABB from Fretzdorff *et al.* (2002). Symbology as in figure 3.5.....100

Figure 3.10. MORB-normalized (Sun and McDonough, 1989) immobile spider diagram comparisons of the geochemical groups defined in this study versus reference suites with an allochthonous affinity. Note that samples from group U2 in this study and those from the RT reference suite are subdivided into groups with a negative (C-D) and a positive $(Ti/Sm)_{NMORB}$ ratio (E). Symbology as in figure 3.5. 104

Figure 3.11. Incompatible element ratio-ratio diagrams of the unknown samples in this study compared to the reference suites considered in this study. Trend lines define the range of possible REE_{CN} profiles defined by magmatic fractionation of a reference suite. (A) Total REE slope ($(La/Yb)_{CN}$) versus LREE $(La/Sm)_{CN}$ for unknown mafic samples compared to the Abitibi Greenstone metavolcanics and Proterozoic mafic dyke swarms. Total REE slope ($(La/Yb)_{CN}$) versus LREE $(La/Sm)_{CN}$ for unknown mafic samples compared to the Renzy Terrane and Algonquin metagabbro suites (C) HREE fractionation $(Gd/Yb)_{CN}$ versus LREE $(La/Sm)_{CN}$ for unknown mafic samples compared to the Abitibi Greenstone metavolcanics, Proterozoic mafic dyke swarms and Algonquin coronitic metagabbro suite. After Álvaro *et al.* (2014) and Rogers *et al.*, (2019), used as a proxy for depth of mafic source melting and degree of enrichment/degree of partial melting. (D) LREE $(La/Sm)_{CN}$ versus $(Tb/Yb)_{CN}$ as a non-quantitative proxy for depth of mafic source melting to include the RT groups, where Gd was not measured (Montreuil and Constantin, 2010). 108

Figure 3.12. Geotectonic diagrams mafic samples collected in this study and select reference suites. (A) Th-Tb-Ta ternary diagram of Cabanis and Thieblemont (1988). (B) Th-Hf-Ta ternary diagram of Wood (1980). (C) Zr/Nb vs Nb/Th diagram of Condie (2015) showing the fields for various mantle sources of Proterozoic oceanic basalts (i.e. not contaminated by crustal components). (D) Nb/Yb – Th/Yb diagram of Pearce (2008). Andean mafic geochemistry derived from the GEOROCK database and Espanon *et al.* (2014). (E) Th vs Nb N-MORB normalized (Sun and McDonough, 1989) diagram of Saccani (2015). Back-arc A: back-arc basin basalts (BABB) characterized by input of subduction or crustal components (e.g. immature intra-oceanic or ensialic back-arcs). Back-arc B: BABBs showing no input of subduction or crustal components (e.g. mature intra-oceanic and ensimatic back-arcs). Abbreviations: Assimilation-fractional crystallization (AFC); Crustal components (C); Depleted mantle (DM); Enriched mantle (EM); Fractional crystallization of Ol + Cpx + Pl (F); Fractional crystallization (FC); Hydrated mantle (HM); Mantel source variation (M); OCTZ: ocean-continent transition zone. Ocean island-type (plume-type) component enrichment (OIB-CE); Partial melting (P-melt); Subduction components (S); Supra-subduction zone enrichment (SSZ-E). Symbology as in figure 3.5. 114

Figure 4.1.Location and subdivision of the Grenville Province (above) and tectonic architecture along the Hw117 transect in western Quebec (below). The location of samples analyzed in

this study and those from published datasets along the transect are shown. Note that the Baskatong Shear Zone (BSZ) is interpreted to record both early dextral and late sinistral movement (Martignole, 1995) and reworks the tectonic boundary separating the Vérendrye Terrane and Lac Dumoine Terrane, previously called the Baskatong Desert Lineament (see Sharma *et al.*, 1995 and references therein). Grenville Province locality map modified after Rivers (2008), Jannin *et al.* (2018) and Dickin *et al.* (2020). Transect map compiled from field work conducted as part of this study as well as previous studies across the area (e.g. Indares and Martignole, 1990; Martignole and Pouget, 1994; Martignole, 1995; Guo and Dickin, 1996; Montreuil and Constantin, 2010; Dickin *et al.*, 2014; Lambert *et al.*, 2018, 2019). Published U-Pb zircon and monazite ages data derived from Childe *et al.* (1993); Martignole and Friedman (1998); Martignole and Martelat (2005) and from the MERN online database (2020). 125

Figure 4.2. Field outcrop photos of typical Renzy Terrane gneisses (A-B) and gneisses from the Vérendrye Terrane along Highway 117 (C-D). (A) Interbanded felsic, intermediate and mafic metavolcanics with centimetric garnet porphyroblasts (red circles and inset). (B) Augen gneiss indicative of relatively high finite subsolidus strain. (H) Sheath folds with asymmetrical 'z-shaped geometries and numerous recumbent folds. White box marks the location of the injected vein sample CL6135 (Fig. 4.9A). (I) One of many meter-scale mafic boudins in the Vérendrye Terrane that are rotated counter-clockwise (sinistral), indicating a top to the NW sense of shear. 128

Figure 4.3. Field outcrop photos of typical Reservoir Dozois Terrane gneisses. (A) Nebulitic and stromatic migmatites (trondhjemite composition) with centimetric hornblende. (B-C) Stromatic migmatites of granitic composition with abundant undeformed quartz grains (e.g. yellow outlines) and centimetric, subhedral hornblende crystals in the pink leucosome that are much larger than the millimeter-scale hornblende in the host gneiss. Note the stair-stepping leucosome (top right) and sigmoidal feldspar phenocrysts (lower left) indicating a top to the NW sense of shear in (B). (D) Diatexites with pegmatitic phase that contain centimetric, euhedral clusters of hornblende crystals. (E-F) Stromatic metatexites that locally lose structural coherence to represent diatexites that often contain variably folded dismembered mafic rafts. Note that the light-colored vertical artefacts seen along the face of the outcrop at (E) are created by drill holes and are not primary geological features. (G) Horizontal, banded

straight gneisses of the Teddy Bear Shear Zone, with a rotated, garnet-bearing mafic mega-boudin (NW-SE rock face). Sample CL6106 (see Fig. 4.6) is collected from this same outcrop to the left (NE) of the picture frame. 129

Figure 4.4. Sample CL6070. (A) Sample taken at X, from a granitic leucosome in the neck of a boudinaged mafic dyke in the RDT. (B). Examples of zircon morphologies and the types of zones defined herein. (C) REE_{CN} normalized (S.S. Sun and McDonough, 1989) spider-diagram of Grenvillian zones (type 2 &3). (D) U-Th bivariate diagram. (E) Kernel density plot of all individual $^{207}Pb/^{206}Pb$ dates within the sample. (F) Weighted mean $^{207}Pb/^{206}Pb$ age for types 2 & 3 (dark shading with stippled line) and their combined age (light shading with solid line). 139

Figure 4.5. Sample CL6098. (A) Sample taken from a pegmatitic phase (P) of diatexites interpreted to be part of the PB, that intrude into gneisses that have garnet rich lithologies comparable Renzy Terrane elsewhere. (B) The pegmatite phase is mostly concordant to the leucosomes within coherent parts of the diatexite and appears interconnected as it lacks discrete truncating geometries with the stromatic leucosome. Although deformed, the diatexites and pegmatitic phase lack evidence for subsolidus strain. (C) Sample location at X, where the pegmatitic phase cuts into the Renzy mafic and intermediate gneisses. (D) Prominently banded Renzy gneisses with abundant garnet porphyroblast aggregates and concordant quartz ribbons. (E) Examples of zircon morphologies and the types of zones defined herein. (F) REE_{CN} normalized (S.S. Sun and McDonough, 1989) spider-diagram of Grenvillian zones (type 2 & 3). (G) U-Th bivariate diagram. (H) Kernel density plot of all individual $^{207}Pb/^{206}Pb$ dates within the sample. (I) Weighted mean $^{207}Pb/^{206}Pb$ age for types 2 & 3. 144

Figure 4.6. Sample CL6106 (next page). (A) Sample taken at X, from a deformed trondhjemitic sill within gneisses of the Teddy Bear Shear Zone in the RDT (see Fig. 4.3G). The sill also contains rafts of ultramafic rocks (B). Elsewhere in this outcrop, the same sill thins and envelopes a rotated block of host gneisses but contains undeformed quartz grains where it protrudes between the foliation planes within the rotated block (this was a cut oblique to the face shown in A and Fig. 4.3A). (C) Examples of zircon morphologies and the types of zones defined herein. Note that although at least 5 types are identified, types 2 & 3 were excluded as they yielded anomalously low element concentrations (e.g. U < 27ppm) during analysis (see Fig. D.9). (D) REE_{CN} normalized (S.S. Sun and McDonough, 1989) spider-diagram of

the remaining Grenvillian zones (types 4 & 5). (E) U-Th bivariate diagram. (F) Kernel density plot of all individual $^{207}Pb/^{206}Pb$ dates within the sample. (G) Weighted mean $^{207}Pb/^{206}Pb$ age for types 4 & 5 (dark shading with stippled line) and their combined age (light shading with solid line).....148

Figure 4.7. Sample CL6112. (A) Sample taken at X from a granitic dykes at intrudes mafic and garnet bearing intermediate gneisses of the Renzy Terrane, which structurally overlie garnet-free migmatites of the PB. (B-C) The sampled dykes form part of a network of magmatic phases that pool along the contact between the PB and AB gneisses. Here the phases are distinguished based on migmatitic textures, geometry, color and grain size. They include pink, concordant to variably folded leucosomes within PB metatexites (G1) that coalesce to form discordant dykes of similar composition (G2). The dykes extend into a pink nebulitic phase (G3) with mafic rafts at the contact with the Renzy mafic body. The contacts between G2 and G3 are however, diffuse and difficult to trace. These phases are overprinted by finer-grained, white-pink (G4) and a coarse grained, white (G5) diatexites. (D) The concordant veins (G1) contain abundant undeformed quartz grains indicating they deformed under suprasolidus conditions. (E-F) The contact between the garnetiferous gneisses of the RT and the garnet-free underlying PB gneisses is characterized by an increase in strain, defined by mylonitic fabrics. If the mylonites constitute a tectonic boundary between PB and AB rocks, this boundary should represent the Allochthon Boundary Thrust (ABT). (G) Examples of zircon morphologies and the types of zones defined herein. (H) REE_{CN} normalized (S.S. Sun and McDonough, 1989) spider-diagram of the Grenvillian zones (types 3 & 4). (I) U-Th bivariate diagram. (J) Kernel density plot of all individual $^{207}Pb/^{206}Pb$ dates within the sample. Note that only the ca. 1400 Ma analysis is concordant within the inherited zones. (K) Weighted mean $^{207}Pb/^{206}Pb$ age for types 3 & 4.....153

Figure 4.8. Sample CL6127. (A) Sample taken from a granitic dyke that cuts the gneissic fabric within highly migmatitic granodiorites of the RDT (see also Fig. 4.3E) but also contains apophyses transposed within the gneissic fabric (B). Note the large hornblende crystals in the dyke (inset of B). (C) Examples of zircon morphologies and the types of zones defined herein. (D-E) REE_{CN} normalized (S.S. Sun and McDonough, 1989) spider-diagrams of Grenvillian zones only. (F) U-Th bivariate diagram. (G) Kernel density plot of all individual $^{207}Pb/^{206}Pb$ dates within the sample. (H) Weighted mean $^{207}Pb/^{206}Pb$ age for types 3, 4 & 5 (dark shading

with stippled line) and their combined age (light shading with solid line). Note that analyses one types 1 & 2 are not included in the weighted mean age calculation due to their distinct morphological and chemical traits compared to types 3-5. 157

Figure 4.9. Sample CL6135. (A) Sample taken at X, from a granitic injection vein that cuts across the ductile fabric but is folded by sheath folds (see Fig. 4.2C) in the VT. (B) Concordant portion of the vein commonly contain abundant undeformed quartz grains. (C) Discordant portions of the vein contain quartz ribbons aligned parallel to the gneissic fabric. (D) Examples of zircon morphologies and the types of zones defined herein. (E) REE_{CN} normalized (S.S. Sun and McDonough, 1989) spider-diagram of the Grenvillian zone (type 5). (F) U-Th bivariate diagram. (G) Kernel density plot of all individual $^{207}Pb/^{206}Pb$ dates within the sample. (H) Weighted mean $^{207}Pb/^{206}Pb$ age for type 5. 161

Figure 4.10. A graphical summary of the geochronology (black; age Y-axis on the left) and Ti-in-zircon thermometry (red; temperature Y-axis on the right) results from the samples presented in this study. Only the weighted mean ages of the Grenvillian zircon populations are presented. See Table 4.2 for details on all of the zircon age populations. Stippled black lines indicate the standard calibration error propagated into the error on the weighted mean age, whereas solid black error bars do not. Temperatures are reported as best conservative estimates using the upper limit of the interquartile range for pressures between 550 and 1000 MPa (pressure estimates from Indares and Martignole, 1990). Red error bars indicate a ±30°C error on the temperature to account for analytical and statistical errors (following Tomkins *et al.,* 2017). See Methodology section for further details of the age and temperature calculations. 164

Figure 4.11. Cartoon for the proposed evolution of the Grenville Province in the study region, based on the geochronology results from the samples collected herein. (A) Under-thrusting of the Laurentian basement and onset of probably fluid-fluxed melting in the Parautochthonous Belt (PB). (B) Continued melting and formation of a partially molten zone within the RDT rocks that may have intruded into, and brecciated the lower part of the AB, incorporating relatively ridged slab of the Renzy Terrane into the parautochthonous channel. (C) Continued melting and foreland-ward exhumation of the channel and dismemberment of the Renzy Terrane (RT) into km-sized and variably deformed rafts. See text for detailed description of the model. Colored stars represent the relative movement of various structural levels through the different stages of the model. Abbreviations: Allochthon Boundary Thrust (ABT); Dorval Detachment

(DD); Superior Province (SP). Model inspired by Rivers (2009), Jamieson and Beaumont (2013) and Jannin *et al.* (2018). 169
Figure A.1. Cathodoluminescence images of all zircons separated from sample CL6144 from stop 16, v-chapter 2. 231
Figure A..2. Cathodoluminescence images of all zircons separated from sample CL8025 from stop 17, v-chapter 2. 232
Figure B.1. Ni-Zr/TiO_2 of Winchester *et al.*, (1980) to identify metasedimentary protoliths and mineral cumulates. 233
Figure B.2. Co, Sc, (Al2O3 x 4) ternary diagram after Rogers *et al.* (2019) used to test for fractional crystallization. Samples fall away from the main cluster were likely affected by fractional crystallization or crystal accumulation that drew the magma composition away from the main cluster. Trends away from Co indicate excess olivine fractionation, trends away from Sc indicate excess pyroxene fractionation and trends away from Al_2O_3 indicate excess plagioclase fractionation. Trends towards the apices indicate corresponding crystal accumulation in the melt. 233
Figure B.3. Bivariate plots of Zr vs select trace elements to test for trace element mobility. Symbology represents the field-based subdivision and geochemical classification defined in this study. See legend in Figure. B.8. 234
Figure B.4. The K/Rb ratio diagram to test for element mobility in metamorphosed mafic rocks collected in this study and mafic granulites of the Renzy Terrane, Bondy Gneiss complex and Canyon Domain. After Rudnick *et al.* (1985). 236
Figure B.5. Ta/Yb – Th/Yb diagram of Schandl and Gorton (2002) that was employed by La Flèche *et al.* (2005) to test for Th mobility. 236
Figure B.6. La/Th and Th/U diagram to test for U and Th loss within metamorphosed mafic rocks collected in this study and mafic granulites of the Renzy Terrane, Bondy Gneiss complex and Canyon Domain. After Rudnick *et al.* (1985), modified by Maity and Indares (2018). 237
Figure B.7. Zr/Hf – Y/Ho diagram to assess REE mobility by metasomatic fluids of mafic rocks collected in this study and mafic granulites of the Renzy Terrane, Bondy Gneiss complex and Canyon Domain. After of Bau (1996). 237
Figure B.8. Geochemical rock classification schemes for all the mafic suites discussed in this study according to the Trace-element TAS proxy diagram (A,C,E) of Winchester and Floyd, 1977

(modified by Pearce, 1996) and the Al_2O_3-($FeO+Fe_2O_3+TiO_2$)-Mg cation diagram (B,D,F) after Jensen (1976). (A, B) Mafic samples collected during this study. Note that all possible mafic entries classified as calc-alkaline on Jensen (1976) diagram were excluded for correlative purposes in this study. 238

Figure B.9. Zr/Y – Th/Yb mafic affinity classification diagram of Ross and Bédard (2009). Symbology as in figure. B.8. 239

Figure B.10. Nb – Nb/La diagram to differentiate between uncontaminated intra-crustal and arc basalts. After (Xia, 2014b). Symbology as in figure. B.8. 239

Figure B.11. Bivariate plots of MgO vs select trace elements to asses if the geochemical groups defined herein form distinct groups, define fractionation trends and/or are contiguous....240

Figure B.12. Bivariate MgO (wt%) vs Zr (ppm) diagrams for (A) samples collected in this study, superimposed over the lines of best fit derived from the respective PMEs. (B) Mafic metavolcanics from SVZ and Chibougamau regions in the Abitibi Belt of the Superior Province. (C) Proterozoic mafic dyke swarms. (D) Mafic groups in the Renzy Terrane and Algonquin Suite. Note the trend line for the Algonquin PME suite is derived from datapoints (small grey boxes) digitized from Ketchum and Davidson (2000) . Symbology as in figure 3.S11....242

Figure D.1. Tera-Wasserburg plots for zircon populations in sample CL6070. 263

Figure D.2. (A) Tera-Wasserburg plots for zircon populations in sample CL6098 and (B) $^{207}Pb/^{206}Pb$ weighted mean average age for type 1 zones. 263

Figure D.3. Tera-Wasserburg plots for zircon populations in sample CL6106. 263

Figure D.4. Tera-Wasserburg plot for zircon populations in sample CL6112. 264

Figure D.5. Tera-Wasserburg plots for zircon populations in sample CL6127. 264

Figure D 6. (A) Tera-Wasserburg plots for zircon populations in sample CL6135 and $^{207}Pb/^{206}Pb$ weighted mean average age for (B) type 1, (C) type 2, (D) type 3 and (F) type 4 zones. (E) $^{207}Pb/^{206}Pb$ weighted mean average if types 1-3 are combined. 265

Figure D.7. Trace element diagrams used for geochemical differentiation of the various zircon populations in sample CL6070. (A-B) Various bivariate diagrams. (C-D) Chondrite normalized (Sun and McDonough, 1989) REE spider-diagrams. Image of zircon morphologies supplied for reference to the various zones. 266

Figure D.8. Trace element diagrams used for geochemical differentiation of the various zircon populations in sample CL6098. (A-B) Chondrite normalized (Sun and McDonough, 1989) REE spider-diagrams. (C-E) Various bivariate diagrams. Image of zircon morphologies supplied for reference to the various zones. 267
Figure D.9. Trace element diagrams used for geochemical differentiation of the various zircon populations in sample CL6106. (A-B) Chondrite normalized (Sun and McDonough, 1989) REE spider-diagrams. (C-E) Various bivariate diagrams. Note all analyses with triangle symbology were not used in weighted mean age calculations due to element loss. Image of zircon morphologies supplied for reference to the various zones. 268
Figure D.10. Trace element diagrams used for geochemical differentiation of the various zircon populations in sample CL6112. (A-B) Chondrite normalized (Sun and McDonough, 1989) REE spider-diagrams. (C-G) Various bivariate diagrams. Image of zircon morphologies supplied for reference to the various zones. 269
Figure D.11. Trace element diagrams used for geochemical differentiation of the various zircon populations in sample CL6127. (A) Chondrite normalized (Sun and McDonough, 1989) REE spider-diagrams. (B-D) Various bivariate diagrams. Image of zircon morphologies supplied for reference to the various zones. 270
Figure D.12. Trace element diagrams used for geochemical differentiation of the various zircon populations in sample CL6135. (A-C) Chondrite normalized (Sun and McDonough, 1989) REE spider-diagrams. (D-F) Various bivariate diagrams. Image of zircon morphologies supplied for reference to the various zones. 271
Figure D.13. Cathodoluminescence images of all zircons separated from sample CL6070.....272
Figure D.14. Cathodoluminescence images of all zircons separated from sample CL6098.....273
Figure D.15.Cathodoluminescence images of all zircons separated from sample CL6106.....274
Figure D.16. Cathodoluminescence images of all zircons separated from sample CL6112.....275
Figure D.17. Cathodoluminescence images of all zircons separated from sample CL6127.....276
Figure D.18. Cathodoluminescence images of all zircons separated from sample CL6135.....277

LIST OF SYMBOLS AND ABBREVIATIONS

AB	Allochthonous Belt
A.I	Alteration index
ABT/ABD	Allochthon Boundary Thrust/ Detachment
AFC	Assimilation fractional crystallization
AGB	Abitibi Greenstone Belt
AMCG	Anorthosite-mangerite-charnockite-granite
BABB	BABB Back-arc basin basalt
CAB	Continental Arc Basalts
CCPI	Carbonate-chlorite-pyrite index
CL	Cathodoluminescence
CMSB	Central Metasedimentary Belt
CN	Chondrite normalized
DD	Dorval Detachment
E-/N-/MORB	Enriched-/Normal-/Mid-ocean ridge basalt
FUS-ICP-MS	Fusion–inductively coupled plasma–mass spectrometry
GF	Grenville Front
GFTZ	Grenville Front Thrust Zone
HFSE	High field-strength element
Hw117	Highway 117
IAT	Island Arc Tholeiites
L/M/HREE(s)	Light/Middle/Heavy Rare earth element(s)
LA-ICP-MS	Laser ablation- inductively coupled- plasma mass spectrometry
LDT	Lac Dumoine Terrane
LHO	Large hot (long-duration) orogens
LILE	Large ion lithophile element
MERNQ	Ministère de l'Énergie et des Ressources naturelles du Québec
Minerals	Mineral abbreviations after Whitney and Evans (2010).
OIB	Ocean island basalt
OIB	Oceanic Island Basalt
OOL	Orogenic lid
PB	Parautochthonous Belt
PM	Primitive Mantle
P-T-t-D	Pressure – Temperature – time – Deformation
RDT	Reservoir Dozois Terrane
RSZ	Renzy Shear Zone
RT	Renzy Terrane
TBSZ	Teddy Bear Shear Zone
TTG	Tonalite–trondhjemite–granodiorite
v-chapter 2	Virtual chapter 2 in Google Earth
VT	Vérendrye Terrane

LIST OF APPENDICES

Appendix A Supplementary tables and figures for geochronology data presented in the virtual tour (chapter 2) 227
Appendix B Supplementary geochemical diagrams 233
Appendix C Extended geochronology methodology and selection of isotopic systems 259
Appendix D Supplementary geochronology Figures and tables 263

CHAPTER 1 INTRODUCTION

1.1 Overview and scope of study

Collisional orogens are complex tectonic systems that played vital roles in remolding the Earth's crust. The tectonic processes leading to the burial and exhumation of mid-to lower-crustal rocks in these orogens remain poorly understood and have been a contentious topic of debate in several ancient and currently active orogens (see reviews by Beaumont and Jamieson, 2010; Gervais and Brown, 2011; Jamieson and Beaumont, 2013; Cottle *et al.*, 2015).

There are three tectonic processes that are generally considered in the evolution of mountain belts (see detailed reviews by Jamieson and Beaumont, 2013 and Cottle *et al.*, 2015). These are illustrated in Fig 1.1. The first, and most classical orogenic models, were built on critical taper theory and the maintenance of a rheologically dependent critical angle of taper within an orogenic prism/wedge (e.g. Platt, 1986; Dahlen, 1990). The critical angle of taper is maintained mainly through basal accretion, leading to thickening and an increase in the angle, foreland-ward thrust-propagation and folding. Then thinning due to erosion or isostatic rebound leads to faulting in the upper part of the wedge and a decrease in the angle (Fig. 1.1A; Jamieson and Beaumont, 2013). In the orogenic wedge deformation is typically characterized by under-thrusting, with burial and exhumation of various structural levels resulting in fold and thrust-belts (e.g. Platt, 1986; Dahlen, 1990) and/or the formation of tectonic duplexes (e.g. Decelles *et al.*, 2001; Robinson and Martin, 2014; He *et al.*, 2015).

The second and more recent hypotheses, based largely on the results of numerical modeling, evoke various models of ductile flow (Fig. 1.1B), commonly referred to as channel flow (Grujic *et al.*, 1996; Vanderhaeghe *et al.*, 1999; Beaumont *et al.*, 2001, 2004, 2006; Godin *et al.*, 2006; Grujic, 2006; Rivers, 2008; Vanderhaeghe, 2009). Channel flow typically occurs within the hot, mid-lower crustal infrastructure of doubly thickened orogenic plateaux, when a package of melt-weakened (i.e. partially molten) rocks reaches a critically low viscosity, decouples from the stronger overlying superstructure, and flows over the (former) foreland of the orogen (Beaumont *et al.*, 2006; Grujic, 2006; Vanderhaeghe, 2009) in response to lithostatic pressure gradients (Gervais and Ranalli, 2017). Channel flow is considered homogeneous when flow occurs through compositionally and rheologically homogenous mid-crustal rocks (see orange zone in Fig. 1.1B). Alternatively, channel

flow is considered to be heterogenous, when it involves crustal segments with a contrasting rheological competencies, defined for example by lower-viscosity mid-crust and more competent lower crustal segments (Beaumont *et al.*, 2006). Heterogenous flow can also include the tectonic forcing of hot ductile nappes over strong, under thrusted indenters (Fig. 1.1B; Beaumont *et al.*, 2006; Fritz *et al.*, 2009; Grujic *et al.*, 2011; Jamieson and Beaumont, 2013).

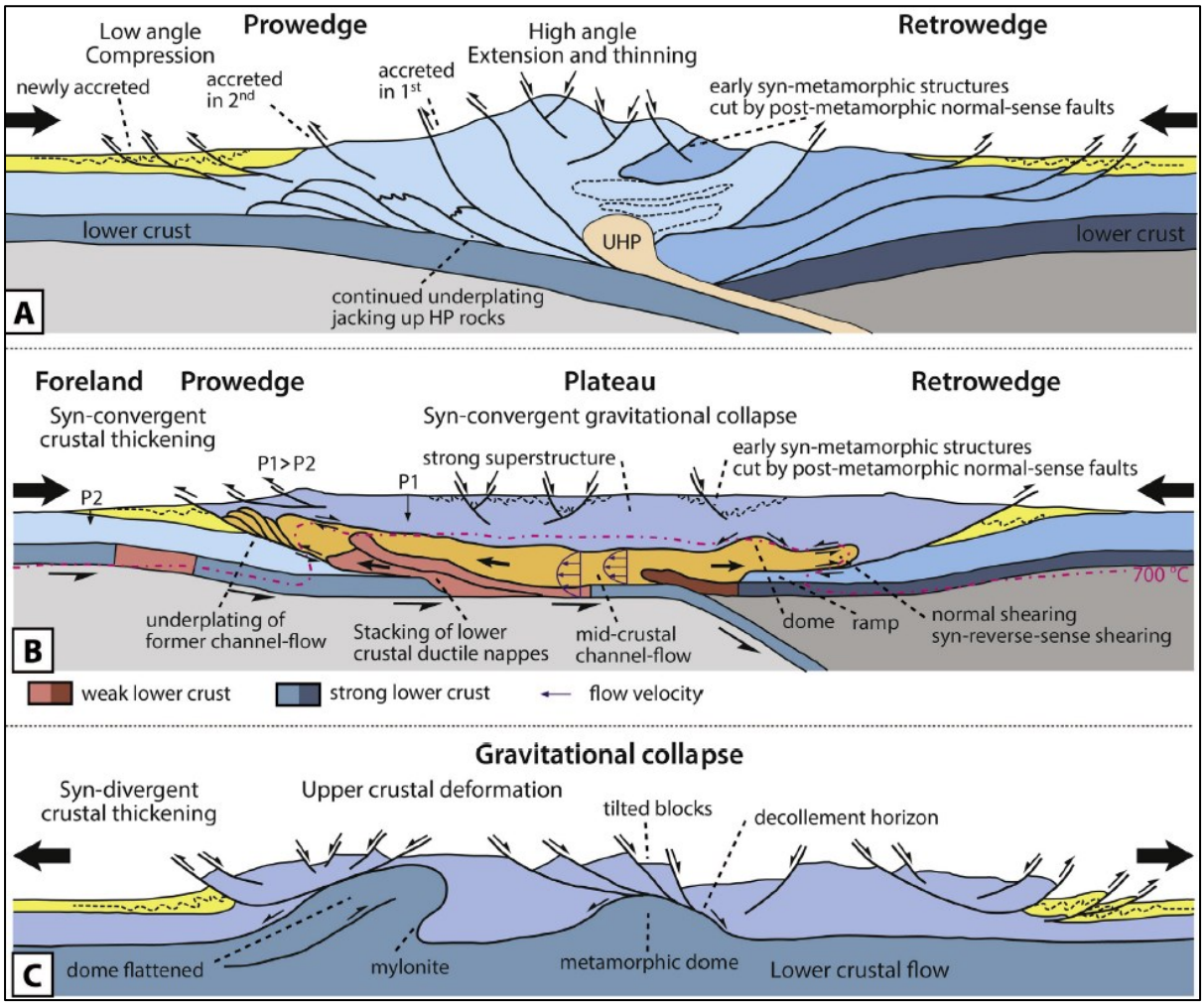

Figure 1.1. Schematic diagram summarising the tectonic processes considered to be active during orogenesis (Taken from Jannin *et al.*, 2018). (A). Orogenic wedge model (after Platt, 1986; Jamieson and Beaumont, 2013). (B) Model showing various forms of ductile flow (i.e. channel flow and hot nappes) typically considered active in long-hot-duration orogens (LHOs; after Beaumont *et al.*, 2006; Jamieson and Beaumont, 2013; Larson and Cottle, 2014). (C) Gravitational collapse model (after Rey *et al.*, 2001; Tirel *et al.*, 2008).

Lastly, once a orogen is built up and it becomes gravitationally unstable, the orogen may collapse on itself (Fig. 1.1C) if the potential energy exceeds the convergence forces (Rey *et al.*, 2001). Collapse typically results in exhumation of lower crustal rocks in the orogenic core, which form core-complexes that are associated with normal-sense ductile and even brittle detachments and faults (Dewey, 1988; Rey *et al.*, 2001; Tirel *et al.*, 2008; Platt *et al.*, 2015).

The modern consensus is that mountain belts evolve through various stages as a factor of their temperature, duration and magnitude (see detailed review by Jamieson and Beaumont, 2013). Orogenesis is considered to start with a cold-short-duration orogenic phase, where deformation is governed by critical taper theory (e.g. present day Pyrenees; Beaumont *et al.*, 2010). If convergence continues, the orogen may develop through a long-hot-duration orogenic phase (LHO; e.g. present day Himalayas; Beaumont *et al.*, 2010). Then once the mid-crust becomes thermally or melt-weakened beyond a critical value or the convergence forces wane (Rey *et al.*, 2001; Vanderhaeghe, 2009), typically during orogenic decline, both 'colder'-wedges or LHOs may be subject to orogenic collapse (e.g. present-day Western Alps, Pichon *et al.*, 2010) and while core-complexes would typically develop in the core of the orogen, deformation could also be propagated towards the flanks (Fig. 1.1C).

During the LHO phase in particular, tectonic processes have been the focus of topical debates (see review by Cottle *et al.*, 2015) due to the opposing models derived from either critical taper or channel flow theories (e.g. Searle *et al.*, 2007; Kohn, 2008; Gervais and Brown, 2011; Simony and Carr, 2011). A further complication arises as processes involving critical taper and ductile flow, are not necessarily spatially or temporally exclusive (Fig. 1.1B) and can include a continuum, as predicted by various numerical models (e.g. Vanderhaeghe *et al.*, 2003; Jamieson and Beaumont, 2011, 2013) and demonstrated by field-based studies (e.g. Larson *et al.*, 2010, 2013; Larson and Cottle, 2014; Cottle *et al.*, 2015). Furthermore, advancements in numerical models for tectonic collapse have demonstrated that they may also be associated with syn-extensional shortening within an orogenic prism along the orogen flanks (Fig. 1.1C; Jamieson and Beaumont, 2011, 2013) or may even be affected by a form of ductile flow (Vanderhaeghe, 2009; Jamieson *et al.*, 2010; Jamieson and Beaumont, 2013; Jannin *et al.*, 2018). The combination of these processes result in intricate tectonic architectures where distinction of the preceding evolutionary stages and tectonic processes is complex and requires discriminatory tests. These tests are typically based on modern structural, metamorphic and geochronological data from different structural levels within the

orogen (Gervais and Brown, 2011; Table 1.1). Therefore, unravelling the tectonic architecture in orogenic belts and a knowledge of how and when deformation was accommodated within distinct parts of these orogen, is critical to feeding the ever-shifting scientific understanding of how mountain belts evolved.

Table 1.1. Summary of the key characteristics used to distinguish between the different tectonic models (taken from Gervais and Brown, 2011).

Model	**Spatial distribution of finite strain patterns**	**Metamorphic field gradient**	**Spatial distribution of cooling ages**	**Spatial distribution of P-T-t paths**
Orogenic wedge	Reverse shearing and steep flattening	Gradual in hanging wall. Sharp in the footwall of retro-shear zone	Important gradient in all thermos-chronometers: Younger toward deeper structural levels.	Exhumation at higher structural levels coeval with burial at deeper structural levels
Channel flow model	Coeval normal and reverse shearing at the roof and base of the channel, respectively	Sharp in footwall of the channel. Gradual to sharp in the hanging wall of the channel	Lateral gradient: younger toward the front of the channel Uniform cooling at any given longitudinal section of the channel	Broadly synchronous exhumation throughout the channel coeval with burial of footwall rocks Protracted residence time in the middle crust
Gravitational collapse	Prevalence of horizontal flattening and outward verging shear zones at dome margins	Sharp at supra-infra-structure contact	Model-dependent	Exhumation paths only, variable timing

The Meso-Neoproterozoic Grenville Orogen, partially preserved as the Grenville Province in Canada (Fig. 1.2), is a dynamic collisional system where orogenic tectonic process are debated and are not yet fully understood (see detailed review by Rivers, 2015 for list of unresolved issues). The diachronous metamorphic and deformation histories in the Grenville Province have led to a 1st order tectonic architecture that is defined by the juxtaposition of lower-middle and upper-crustal levels (Rivers, 2008, 2012), rather than exposing just the root of this ancient orogen (Fig. 1.2B).

The exposure of these different structural levels makes the Grenville Province an ideal candidate for investigating the tectonic processes active during orogenesis. Furthermore, the Grenville Orogen is also of particular interest as it straddles the transition between ancient (e.g. Precambrian) and modern (e.g. Phanerozoic) tectonic regimes (Sizova *et al.*, 2014; Weller and St-Onge, 2017).

While some authors consider that the Grenvillian Orogeny evolved as a thick-skinned orogenic belt with the main panels being juxtaposed by mostly in-sequence thrusting, leading to the formation of tectonic duplexes (e.g. Martignole *et al.*, 2000; Herrell *et al.*, 2006; Dickin *et al.*, 2014, 2017), comprehensive compilations from the Grenville Province have led to conceptual (e.g. Rivers, 2008, 2009, 2012) and 2-D thermomechanical numerical models (e.g. Jamieson *et al.*, 2007, 2010; Rivers, 2008, 2009, 2012) that largely consider the Grenville Orogen evolved as an LHO model. The latter model broadly proposes that, during the initial Ottawan phase (1090-1020 Ma) of the orogeny, the orogen evolved from an accretionary stage to the large-hot stage, to a stage of gravitational collapse (Rivers, 2012; Rivers and Schwerdtner, 2015). During the Ottawan phase, only the mid-lower crustal levels of the Allochthonous[1] Belt, comprising a collage of peri-cratonic to exotic rocks that were variably accreted to Laurentia before Grenvillian orogenesis (Rivers *et al.*, 1989, 2012), were deformed and metamorphosed to upper amphibolite and granulite grades (Fig. 1.2). Then, during the younger Rigolet phase (1005-980 Ma; Rivers, 2008), the Laurentian basement and its Proterozoic cover sequences which define the Parautochthonous Belt, were reworked to amphibolite and locally higher (granulite) metamorphic grades, either through the formation of thrust-fold belts in the orogenic wedge (Jamieson *et al.*, 2007; Rivers, 2009, 2012; Jamieson and Beaumont, 2011; Fig. 1.2), or by a second phase of ductile flow (e.g. Jamieson *et al.* 2010; Jannin, 2017; Jannin *et al.*, 2018). Evolution of the Parautochthonous Belt during the Rigolet phase (Fig.

[1] In this study the term allochthonous follows the terminology of Rivers *et al.* (1989) that refers to far-travelled domains with a distinct structural and metamorphic histories but is somewhat contentious, as they are not necessarily exotic to Laurentia.

1.2B) is poorly understood and is of particular interest amidst the recent attention in how the effects of deformation in the orogenic basement may have shaped modern mountain belts (e.g. Gervais *et al.*, 2010; Godin *et al.*, 2019; Soucy La Roche and Godin, 2019; Duvall *et al.*, 2020).

Although the recent conceptual (e.g. Rivers 2008, 2009, 2012) and numerical LHO models (Jamison *et al.*, 2007, 2010) are broadly consistent with the geometry of some of the regional scale cross-sections across the Grenville Province, the 1st order architecture along these transects requires clarification/refinement and the models require testing, to ultimately understand which tectonic processes were active within a specific part of the province at a given time in its evolution. Testing requires modern structural, metamorphic and geochronological studies, collectively known as pressure-temperature-time-deformation studies (P-T-t-D) that are anchored in detailed field-investigations (Table 1.1). As a consequence, the Grenville Province has been the focus of many such studies in western Ontario (e.g. Marsh, 2013; Marsh and Culshaw, 2014; Schwerdtner *et al.*, 2014; Marsh and Stockli, 2015; Rivers and zSchwerdtner, 2015; Culshaw *et al.*, 2016; Dickin *et al.*, 2020) and the Manicouagan Reservoir area of eastern Quebec (e.g. Indares *et al.*, 2008; Lasalle *et al.*, 2013; Lasalle and Indares, 2014; Jannin, 2017; Jannin *et al.*, 2018; Indares, 2020; Lazzbat *et al.*, 2020, Kavanagh-Lepage, 2022). In western Quebec however, there is a lack of field-based data constraints on both the conceptual and numerical models, especially modern geochronological data. This means several aspects of the tectonic evolution of this part of the province remain poorly constrained, especially the reworking of the tectonic basement (i.e. the Parautochthonous Belt). While there is some existing data within the region (see section 1.2 & 1.3 for detailed references), the large majority was acquired during the late 80's and early 90's, including the results of the deep-crustal LITHOPROBE seismic program (e.g. Martignole *et al.*, 2000), but require re-investigation in light of the recent advancements in collisional and Grenvillian tectonic processes.

The aim of this study is therefore, to contribute to the understanding of the spatial and temporal tectonic evolution of the Grenville Orogen, more specifically, to contribute towards a better understanding of the deformation processes within the Parautochthonous Belt of western Quebec by filling in some of these fundamental data gaps (e.g. structure, geochronology; discussed in detail in section 1.3).

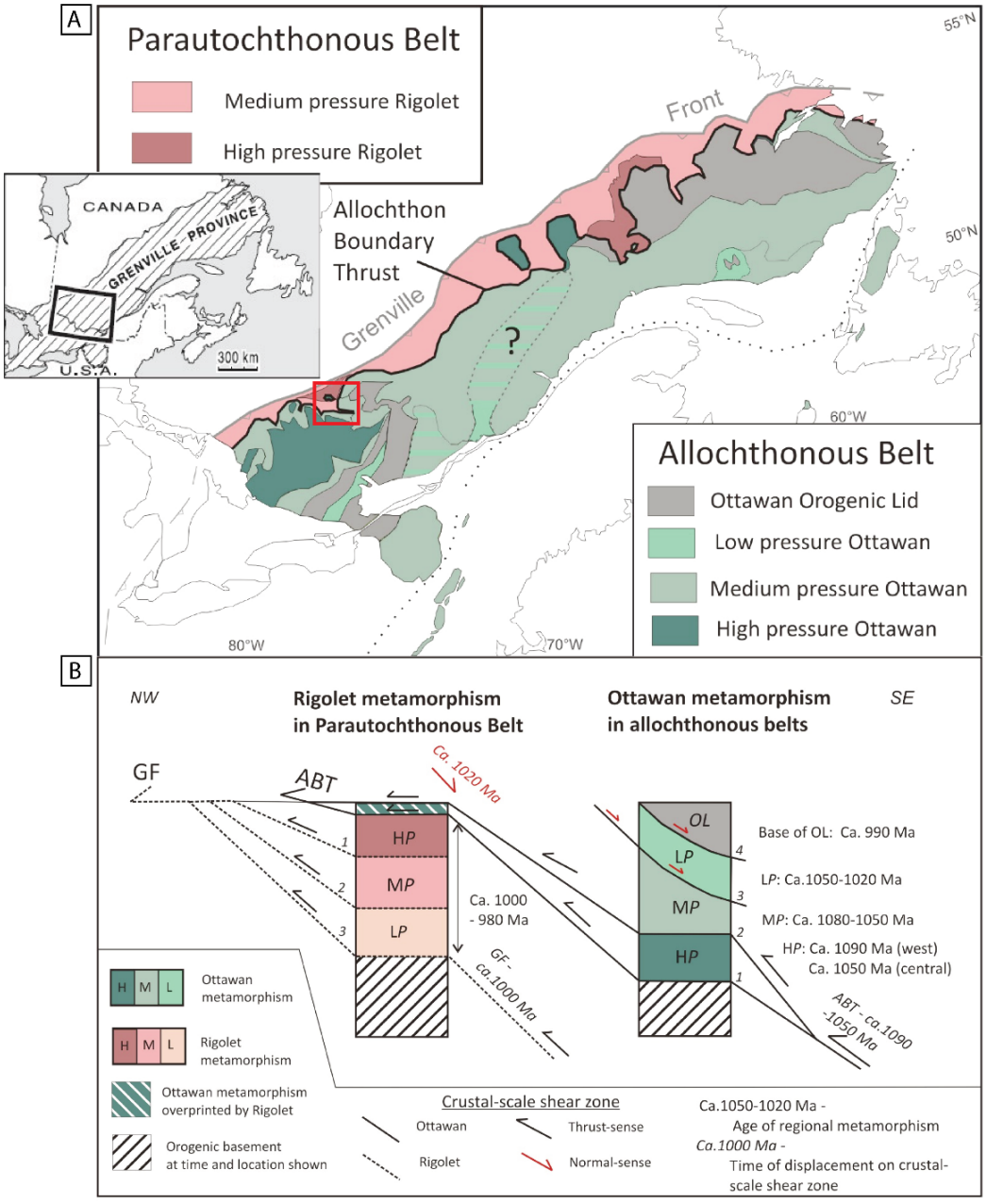

Figure 1.2. (A) Location of the Grenville Province (inset; modified after Martignole, *et al.*, (2000)), subdivision of the Grenville Province and location of the study area (red box). (B) Schematic illustration of the tectonic architecture of the Grenville Province with proposed timing and direction of movement across the primary tectono-metamorphic boundaries during the respective phases of the Grenvillian Orogeny according to Rivers (2008). Note the different timing of deformation in western and central segments and the difference between out-of-sequence and in-sequence thrusting above and below the Allochthon Boundary Thrust (ABT). Figure modified from Rivers (2015).

1.1.1 Study area

The study region for this project is located along highway 117 (Hw117) between Louvicourt and Grand-Remous in western Quebec, cutting across the 31N and the northeast corner of the 31K NTS 1:250 000 map sheets (Fig. 1.2A; also see Indares and Martignole, 1985). Hw117 provides an accessible, near perpendicular and continuous cross section through the tectonic basement (i.e. Parautochthonous Belt) into the lower-mid crustal and upper crustal levels (i.e. Allochthonous Belt), where the roadcuts offer some of the best exposed outcrops within the region.

1.2 Regional geology

1.2.1 Tectonic setting

The Grenville Province in Canada is a > 600 km wide tectono-metamorphic belt of Archean and Mesoproterozoic rocks developed on the southeast margin of Laurentia (current co-ordinates) that were variably deformed during the Mesoproterozoic-Neoproterozoic Grenvillian Orogeny (Fig. 1.2A; Hoffman, 1989, 1991). The Grenvillian Orogeny (*sensu stricto*) is generally accepted as the orogenic cycle between ca. 1090 – 950 Ma (Gower and Krogh, 2002; Rivers, 1997, 2008, 2015; Tollo *et al.*, 2004), when Laurentia collided with what was possibly Amazonia (Li *et al.*, 2008).

1.2.2 Pre-Grenvillian evolution

The evolution of the Grenville Province prior to the Grenvillian Orogeny is complex and remains contentious but is considered by most to have represented a Andean-style margin, with subduction underneath Laurentia, which recorded multiple episodes of back-arc opening and closures between ca. 1850-1140 Ma (Corrigan, 1995; Rivers, 1997; Rivers and Corrigan, 2000; Maity and Indares, 2018; Groulier *et al.*, 2020) as well as localized arc accretion (Corrigan and van Breemen, 1997; Sappin *et al.*, 2009). The earliest of these pre-Grenvillian cycles was the ca. 1850-1700 Ma Makkovickian and Penokean orogens that affected the eastern and western parts of the Grenville Province respectively (Rivers *et al.*, 2012). This was followed by the ca. 1710-1600 Ma Labradorian orogen in the east and the ca. 1520-1460 Ma Pinwarian event (synonymous to the Geon 14 period of Gower and Tucker, 1994), which is evident throughout the Grenville Province (Bethune, 1997; Rivers, 1997; Carr *et al.*, 2000; Rivers and Corrigan, 2000; Gower and Krogh, 2002; Rivers *et al.*, 2012). Accretion to the Laurentian margin during the latter event has been

contended (e.g. Hanmer *et al.*, 2000) but was recently shown to record intermittent extensional back-arc magmatism within an overall compressional arc regime onboard Laurentia (Maity and Indares, 2018). Two final accretionary phases, namely the 1290 -1220 Ma Elzevirian and 1180-1140 Ma Shawinigan orogenies are proposed to precede the Grenvillian Orogeny (Rivers, 1997; Rivers and Corrigan, 2000; Rivers *et al.*, 2012), although some authors consider the Shawinigan accretionary phase to be part of the greater Grenvillian event (e.g. Bartholomew and Hatcher, 2010; Carr *et al.*, 2000; Dufréchou and Harris, 2013; Dickin *et al.*, 2017).

Anorthosite, mangerite, charnockite and granite (AMCG) complexes are a signature element of the Mesoproterozoic crust (Bedard, 2010) and are particularly abundant in and adjacent to the Grenville Province (Rivers 2015). A critical factor in the formation of AMCG complexes is the arrival of large volume of asthenospheric magma at the base of the crust (Emslie, 1978), commonly linked to an arc-related origin, which includes: back-arc rifting; rollback of a subducted slab; and delamination of an overthickened crust leading to underplating by mafic magmatism (Bedard, 2010; Rivers 2015). Widespread AMCG magmatism preceding Grenvillian orogenesis is dated between 1640- 1140 Ma, with several AMCG massifs emplaced shortly after crustal thickening and metamorphism related to the Labradorian, Elzevirian and Shawinigan events (McLelland *et al.*, 2010; Rivers *et al.*, 2012), which would support cyclic arc to back-arc activity along an Andean style margin.

1.2.3 Tectonic subdivision of the Grenville Province

In the Grenville Province, the spatial and temporal distribution of metamorphism and deformation has led to its subdivision into two main tectono-metamorphic belts: the Allochthonous Belt (AB) and the Parautochthonous Belt (PB), which form the hanging wall and footwall of the Allochthonous Boundary Thrust (ABT), respectively (Fig. 1.2A-B; Wynne-Edwards, 1972; Rivers *et al.*, 1989). The AB represents part of the thickened hinterland and is composed of an assemblage of peri-cratonic to exotic rocks previously accreted to Laurentia. The AB is further subdivided (Fig. 1.2A-B) into a lower structural level, which was deformed at high (amphibolite to granulite and eclogite) metamorphic grades during the initial Ottawan (1090-1020 Ma) phase of the Grenvillian Orogeny (Rivers *et al.*, 1989, 2008), whereas the upper structural level largely escaped penetrative Grenvillian deformation and metamorphism, and is therefore considered the orogenic lid to the orogen (Rivers, 2008, 2012). The PB in contrast, forms part of the Laurentian margin and its cover

sequences that were only reworked during the Rigolet (1010-950 Ma) phase of the orogeny (Rivers, 2008, 2009). The PB is separated from the Archean Superior Province along the Grenville Front, the youngest of a series of foreland propagating, thrust sense shear zones (Fig. 1.2B) that constitute the Grenville Front Tectonic Zone (GFTZ; Wynne-Edwards, 1972; Green et al, 1988; White *et al.*, 2000) and therefore, is considered be the spatial and temporal limit of Grenvillian reworking at ca. 1000 Ma (Wynne-Edwards, 1972; Rivers *et al.*, 1989; Rivers, 2008).

1.2.4 Evolution of the Grenville Orogen

Unravelling the evolution of the Grenvillian Orogeny is complex, especially as deformation and high-grade metamorphism are diachronous along the strike of the Grenville Province (Fig. 1.2B; Carr *et al.*, 2000; Gower and Krogh, 2002), with documented variation in the age and grade of the tectono-metamorphic events between the Ontario region (e.g. Easton, 2000), SW Quebec (e.g. Indares and Martignole, 1990), central to NE Quebec (e.g. Indares, 2020) and Labrador (e.g. Krauss and Rivers, 2004). In a series of key contributions, Rivers (2008, 2009, 2012; see also the review of Rivers, 2015) integrated metamorphic, structural, and geochronological data collected from these various sections of the Grenville Province, with 2-D numerical models for LHO's (e.g. Beaumont *et al.*, 2001, 2004, 2006; Jamieson *et al.*, 2007, 2010) to develop comprehensive, regional-scale conceptual tectonic models that are broadly consistent with the tectonic architecture of the Grenville Province, interpreted from the series of regional, deep-crust LITHOPROBE seismic cross-sections imaged along its length (Fig. 1.3; Kellett, *et al.*, 1994; Martignole and Calvert, 1996; Gower *et al.*, 1997; Hynes *et al.*, 2000; White *et al.*, 2000a,b).

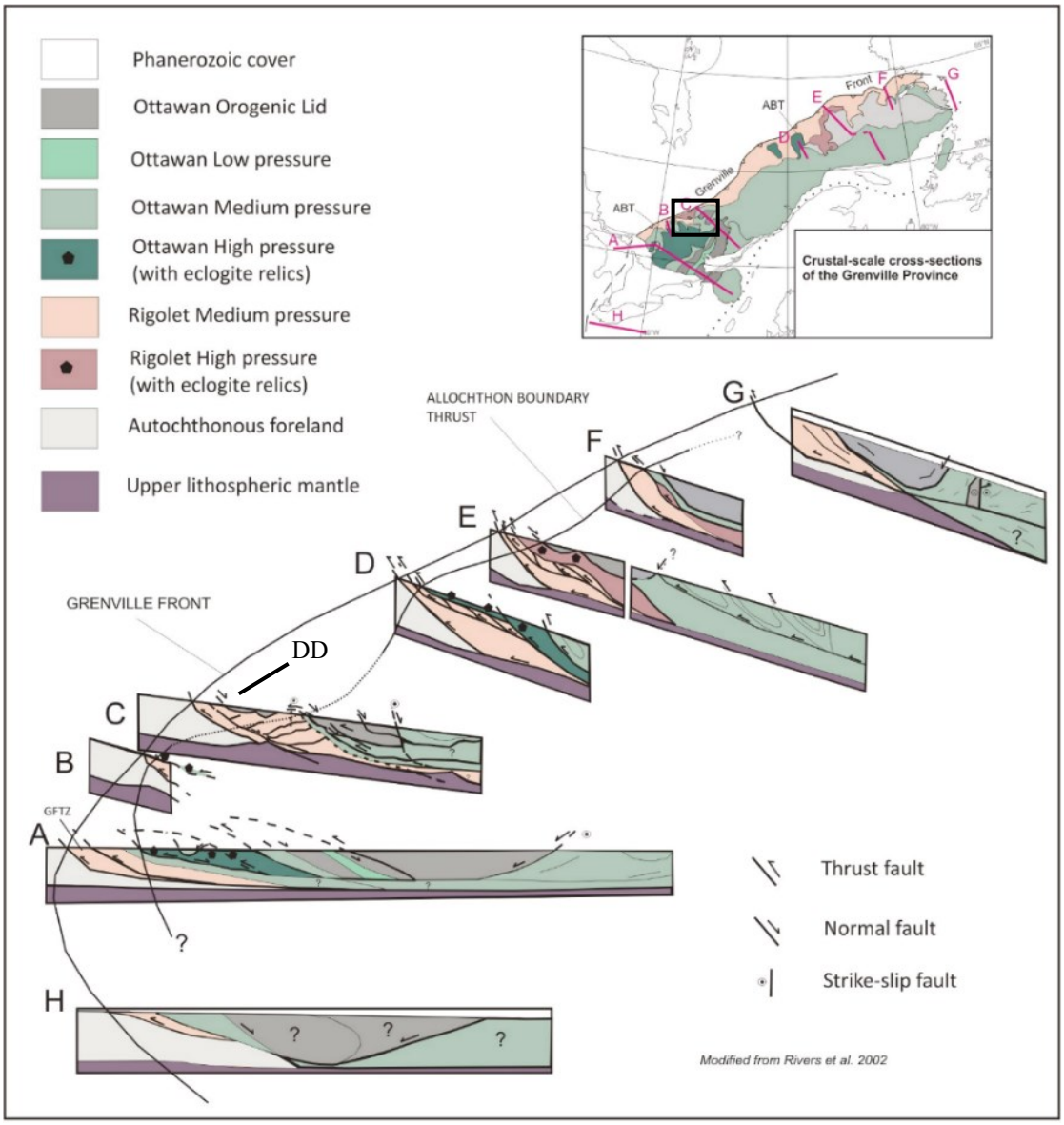

Figure 1.3. Schematic crustal-scale cross sections of the Grenville Province that were redrawn from results of the LITHOPROBE-seismic data. Study area is indicated by the black box and represented by cross-section C. Colors reflect tectonic subdivision and metamorphism from Fig. 1.2. GFTZ = Grenville Front Thrust Zone. DD = Dorval Detachment. From Rivers (2015), modified after Ludden and Hynes (2000).

The numerical models developed for the Grenville Province (Jamieson *et al.*, 2007, 2010) used data (available at the time) to reconstruct a series of time-dependant (i.e. duration of compression) iterations that evoked channel flow and/or ductile-nappe deformation mechanisms so that their terminal geometries matched the tectonic architecture defined by Rivers *et al.* (1989) and the LITHOPROBE program for these various transects through the Grenville Province. They attributed the overall geometric variation observed from west to east across the province (Fig. 1.3) to differences in erosion rates, the amount of convergence and degree of under-thrusting across the orogen. In western Quebec, the architecture was explained by a relatively low rate of erosion (GO-2 model) relative to models along the other transects. Whereas some recent studies in Ontario favor an evolutionary model involving the progressive downcutting of the basal décollement, extending from the Shawinigan to the end of the Ottawan (ca 1190-1020 Ma), typical of thick-skinned, in-sequence thrust tectonics (e.g. Dickin *et al.*, 2017, 2020), the following section provides an overview of the regional-scale processes conceptualized by Rivers (2008, 2009, 2012) and presented in numerical models (see review by Jamieson and Beaumont, 2013), focusing on those specific to western Quebec.

1.2.4.1 Ottawan Phase

Between 1090 – 1050 Ma (Fig. 1.2B & Fig. 1.4A) continental collision promoted the development of a thick (ca. 60 km) orogenic plateau, which created vertical and horizontal pressure gradients (Gervais and Ranalli, 2017) that led to the extrusion of thermally and melt weakened lower-to middle-crust from the orogenic core (i.e. hinterland) over the SE margin (current coordinates) of Laurentia (Rivers, 2008). Extrusion resulted in the juxtaposition of AB rocks over the PB along the ABT (Fig. 1.2B). In support of this model, the allochthonous rocks below the orogenic lid are regionally characterized by metamorphic temperatures in excess of 700ºC, ductile deformation styles, subhorizontal fabrics and long thermal histories, the latter marked by large differences between the peak metamorphic U-Pb-ages and hornblende $^{40}Ar/^{39}Ar$ cooling ages in the rocks above the ABT (Rivers, 2008, 2012), compared to those below the ABT (Rivers, 2009). Rivers (2008) initially proposed that deformation occurred as a form of homogeneous flow in a 20-30 km thick channel above the ABT (e.g. Beaumont *et al.*, 2006), whereas the original numerical models (GO-series) of Jamieson *et al.* (2007) considered that the mode was more heterogeneous, characterized by the formation of hot ductile nappes incorporating different structural segments of the AB with contrasting rheological competencies. While the numerical models for lower-crustal

ductile nappes induced by under-thrusting of a stiff indenter, such as the undeformed PB, would produce comparable structural and metamorphic signatures to heterogenous channel flow (Jamieson and Beaumont, 2013), the initial models of Jamieson *et al.* (2007) could not reproduce regional scale normal sense features observed in the Grenville Province (discussed below) and did not account for the 20 Ma "hiatus" period between the Ottawan and Rigolet phases inferred by Rivers (2008). However, as all models can only be compared with the final architecture of the province, the driving force and exact mode (channel flow vs ductile nappes) of deformation beneath the Grenville plateau during this stage remains somewhat enigmatic (Rivers, 2015).

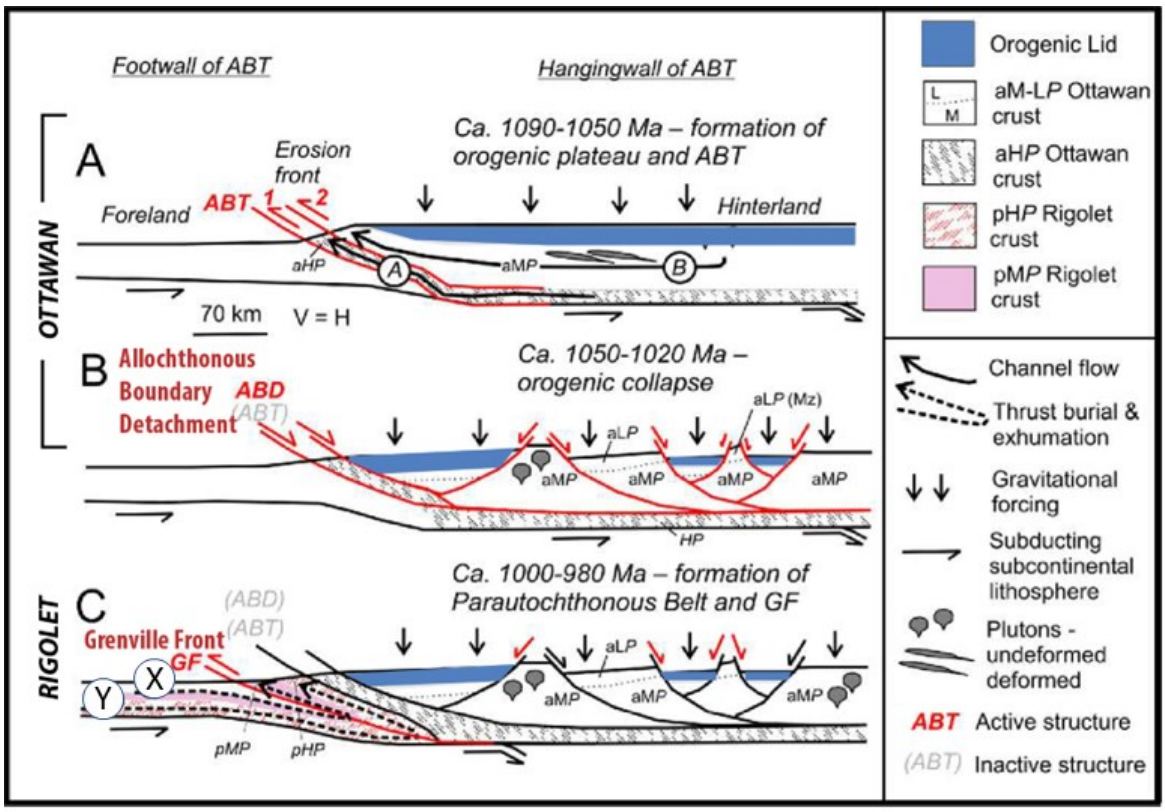

Figure 1.4. Schematic evolution of the Grenville Orogen. The proposed model shows an evolution in mode of deformation from (A) a form of ductile flow to (B) orogenic collapse and (C) renewed reworking in the Parautochthonous Belt, where the (X) mid and (Y) lower crust of the Laurentian margin are rapidly buried then thrusted in the foreland orogenic wedge. Abbreviations: ABT(D) = Allochthon Boundary Thrust (Detachment); GF = Grenville Front; Mz = Mazinaw terrane; a = allochthonous; p = parautochthonous. From Rivers (2008).

As compressional forces began to wane the Grenville Orogen underwent gravitational collapse between 1050 and 1020 Ma (Fig. 1.2B & Fig. 1.4B), which resulted in the diachronous formation of metamorphic core-complexes (e.g. Rivers, 2012; Rivers *et al.*, 2012; Rivers and Schwerdtner, 2015; Soucy La Roche *et al.*, 2015) and the development of extensive normal-sense faults or thick (ca. 7 km) detachment zones (e.g. Rivers and Schwerdtner, 2015). Normal sense shearing may also have reactivated earlier thrust-sense structures such as the ABT at 1020 Ma (see ABD in Fig. 1.4B; Culshaw *et al.*, 1994). Rivers and Schwerdtner (2015) proposed that during this stage, the formation of a large-scale core complex (the Ottawa River Gneiss Complex) triggered thinning in the upper crust, whereas the underlying middle crust, characterized by fluid ingress, abundant leucosome formation and fluid-fluxed retrogression, flowed into the intervening "megaboudin neck" regions. Rivers (2009) suggested that normal shearing and exhumation during this phase ultimately resulted in the cooling and eventual termination of channel flow above the ABT. To account for the cessation of convergence Jamieson *et al.* (2010), modified their original numerical models (GO-series; discussed above) to explain features consistent with normal-sense structures, such as the ABD (1.4C). In these later models (i.e. GO-ST-series) they investigated post-convergent flow where hot weak infrastructure flows outwards from the orogenic core towards the foreland in response to the difference in potential energy between the built up plateau and the foreland (Jamieson *et al.,* 2010). Outward spreading drives thrusting along the flanks (Fig. 1.1B), synchronous with extension thinning in the core, and the development of normal sense shears between the melt-weakened mid-crust and the underlying lower crustal ramps (Jamieson *et al.,* 2010).

1.2.4.2 Rigolet Phase

The Rigolet phase of the Grenvillian Orogeny (1005-980 Ma) marks the stage of deformation and metamorphism in the Laurentian basement and its cover sequences as the focus of tectonic thickening and the compressional front shifted from the orogen core (i.e. ABT) to the flanks (i.e. Grenville Front; Fig. 1.2B and Fig. 1.4C). Reworking during this phase defines the extent of the PB in the Grenville Province (Wynne-Edwards, 1972; Rivers 1986) and was proposed to either be in response to the foreland-ward propagation of deformation during gravitational collapse of the core (Jamieson *et al.*, 2010; Rivers, 2012; Rivers and Schwerdtner, 2015) or during renewed convergence (Rivers, 2009; Maity and Indares, 2018). Rivers (2009) proposed that cessation of channel flow above the ABT led to the inability of the orogen to accommodate further compression

through ductile flow, which triggered the switch from the long hot phase (Ottawan) to a cold-short phase (Rigolet), which would explain the ca. 20 Ma "hiatus" between the Ottawan and Rigolet phases and diachronous and contrasting tectono-metamorphic histories above and below the ABT, respectively. Recently, Maity (2019), proposed that the "hiatus" marks a period of post-Ottawan lithospheric extension and associated orogenic collapse due to lithospheric delamination of the overthickened orogenic root to the Grenville Orogen and that the Rigolet phase defines a distinct phase of renewed subduction-related convergence. Whether renewed contraction or syn-extensional compression along the flanks, the conceptual and numerical models for the Rigolet phase considered that an orogenic prism developed along the orogenic flank, which was characterised by stacked and folded thrust sheets (Fig. 1.2C) for the eastern Grenville Province (e.g. van Gool *et al.*, 2008; Rivers, 2009). More recently however, the comprehensive works by Jannin (2017) and Jannin *et al.* (2018) and subsequent studies (e.g. Labat *et al.*, 2020) in the Manicouagan Reservoir area of the central Grenville Province, proposed that the PB was reworked by a form of heterogenous channel flow between 990 Ma – 960 Ma (Fig. 1.5). Furthermore, they presented evidence that emplacement of Rigolet age (993-961) dykes (Turlin, 2017; Jannin *et al.* 2017a,b; 2018) in the AB may have led to strain weakening in the lower AB (see B3 in Fig. 1.5) and the incorporation of lower allochthonous crust into the parautochthonous channel during the Rigolet phase (see B4 in Fig. 1.5).

In western Quebec the evolution of the PB is characterized by the rapid burial, heating and exhumation of middle (X in Fig. 1.4C) and lower (Y in Fig. 1.4C) crustal levels of the contiguous Superior Province by foreland-ward thrusting ca. 1000 Ma (Rivers 2008; Martignole and Martelat, 2005). In contrast to the Ottawan phase, here the PB records lower metamorphic temperatures during the Grenvillian temperatures (Rivers, 2009; Martignole and Martelat, 2005) and only a small difference between U-Pb peak metamorphic ages and hornblende $^{40}Ar/^{39}Ar$ cooling ages (Rivers, 2012). Based largely on the limited data sets that existed in western Quebec, Jamieson *et al.*, (2007) matched the 1st order architecture that was previously interpreted from the LITHOPROBE program through this section (Martignole *et al.,* 2000) with the GO-2 type (continued convergence, low erosion and 700^{o}C geotherm) model, which depicts the PB as ductile nappes forced over the more rigid Superior Province (Fig. 1.6). Like all of the convergence models (GO-series), this model still fell short in explaining the diachronous evolutions of the PB and AB or development of post-collisional normal-sense ductile shears such as the Dorval Detachment (Fig. 1.3C). While

Jamieson *et al.* (2010) developed a post-convergent model (GO-ST type) that was compatible with the 1st order architecture of the Grenville Province in the Georgian Bay area of Ontario, a GO-ST model was not evaluated for the section through the western Quebec. Notably, most of the data that was used in the models of Rivers (2009) and Jamieson *et al.*, (2007) for the evolution of the PB in western Quebec was limited and mostly derived from the Grenville Front Thrust Zone, where the age of pervasive Grenvillian deformation is debated (see section 1.2.5).

Structural data for the Grenville Province is also relatively sparce in western Quebec. Field based studies in the Clova region suggest that regional NW-verging folds with NE-plunging fold axes, probably derived from NW-directed thrusting during the Rigolet phase, led to the development and orientation of the main gneissic foliation in the PB (Gervais and Moukhsil, 2016). Furthermore, sinistral-transpressional folding, inferred to be Ottawan in age, that led to the formation of the NW-SE elongated geometry of Algonquin/Lac Dumoine nappe along the Ontario-Quebec border, as well as NW-SE trending fold axes in the Georgian Bay area, may also have affected the orientation of the tectonic fabrics in the PB in western Quebec (Rivers and Schwerdtner, 2015; Dickin *et al.*, 2017). However, the age of these fabric in the PB of western Quebec remains to be supported by geochronology. Along the Hw117 transect interpretations of localized fabric development proposed thrusting during the Rigolet was oblique to the NW-SE shortening axis (Martignole and Calvert, 1996), likely influenced by basement topography, late (1020-980 Ma) transcurrent shear zones (Martignole and Friedman, 1998) or the reactivation and/or NW-SE trending Paleoproterozoic basement structures (Martignole and Calvert, 1996; Dufréchou and Harris, 2013; Dufréchou *et al.*, 2014).

Ultimately, the tectonic processes implicit in the deformation of the PB during the Rigolet phase are poorly understood, particularly along the Hw117 transect and require field data, petrographic and geochronological and structural and metamorphic studies to constrain the existing tectonic models or develop new ones.

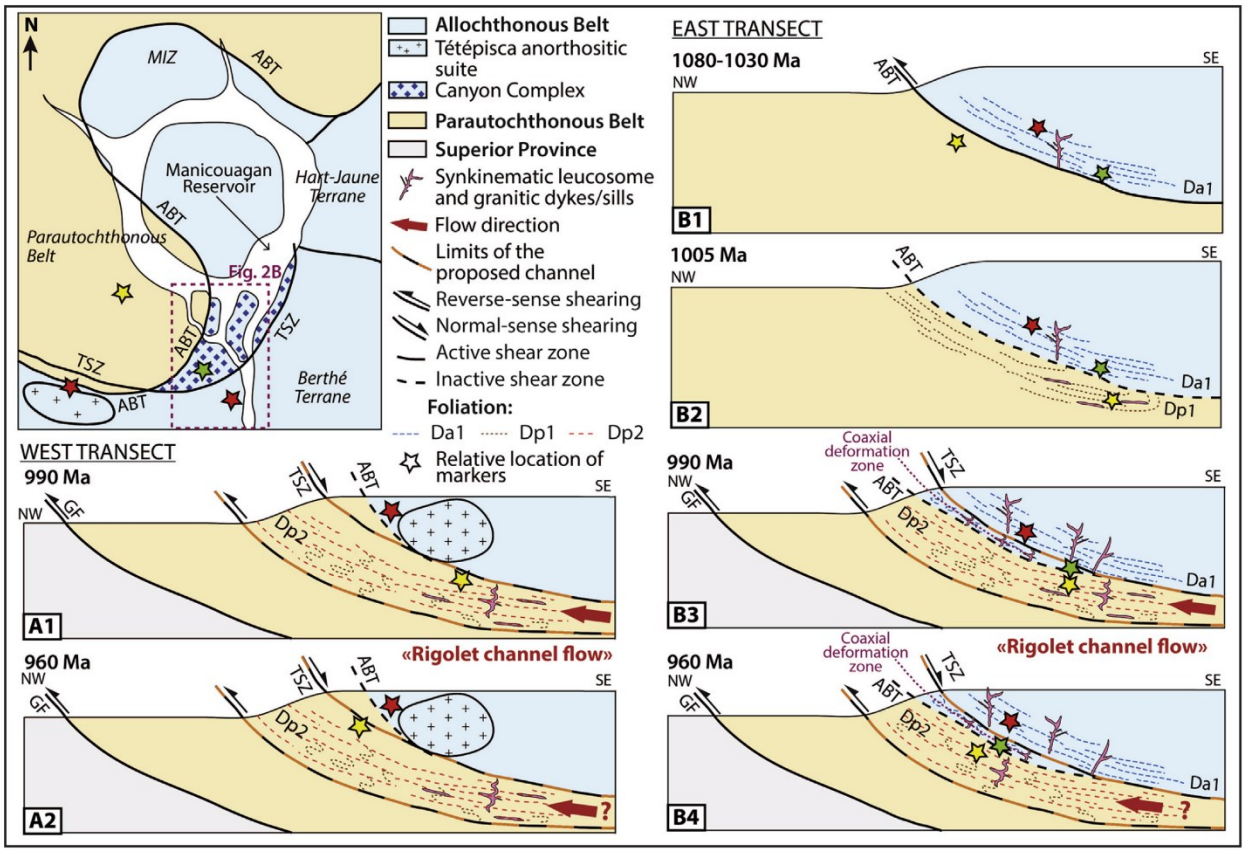

Figure 1.5. Schematic model for the tectonic evolution of the Grenville Province in the central Grenville Province, specifically the development of a parautochthonous channel during the Rigolet phase. (A1-A2) Cross section of the western transect through their study area that accounts for the possible influence of the stiff Tétépisca anorthositic pluton during the development of the channel. (B1-B4) Cross section that shows the progressive development of the parautochthonous channel in the eastern section. Without the influence of the Tétépisca pluton, the model in B1 shows the development of a ductile fabric (Da1) in the Allochthonous Belt (AB) during the Ottawan phase whereas the model in B2 shows the development of a ductile fabric (Da2) in the parautochthonous belt (PB) during the Rigolet phase. In B3 the intrusion of felsic dykes, generated in the PB, into the overlying AB, facilitated strain weakening and the development of a Rigolet fabric in the AB, which may then have promoted the development of a ductile channel that incorporates part of the lower AB during the Rigolet phase in B4 . ABT = Allochthon Boundary Thrust; TSZ = Thachic shear zone. From Jannin *et al.*, (2018)

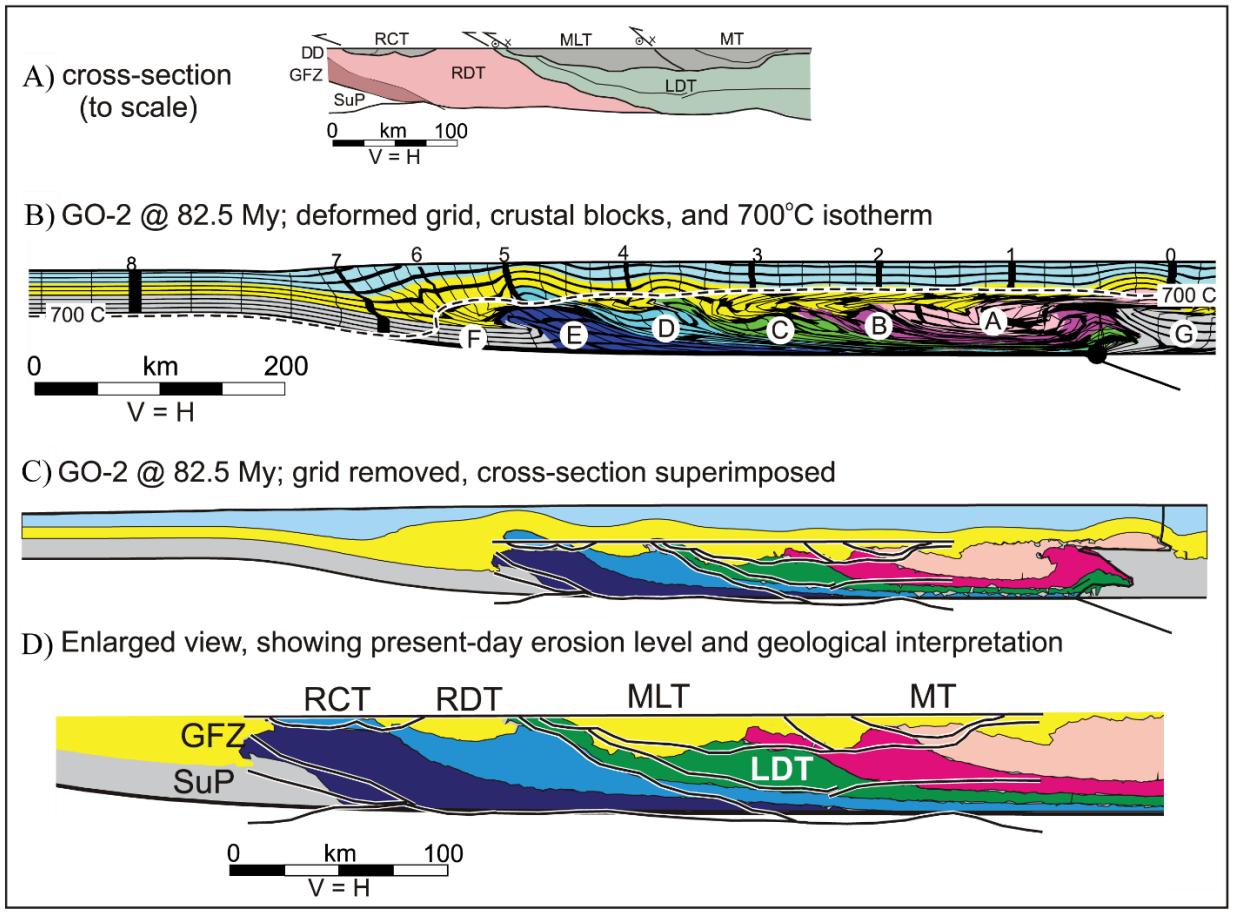

Figure 1.6. GO-2 numerical model stopped at 82.5 Ma convergence and compared against the Montreal-Val d'Or cross section. (A) Cross section interpreted from the LITHOPROBE seismic survey (Martignole, *et al.*, 2000). Colors correspond to the division of the Grenville Province shown in Fig. 1.2. (B) Model result that shows ductile nappes (blocks E-D) stacked against an indenter (block F), whereas the core is defined by moderate dipping thrust sheets. (C-D) Models overlain by cross section outline. Abbreviations: Dorval Detachment (DD); Grenville Front Thrust Zone (GFTZ); Lac Dumoine Terrane (LDT); Mont Laurier Terrane (MLT); Morin Terrane (MT); Reservoir Cabonga Terrane (RCT); Reservoir Dozois Terrane (RDT); Superior Province (SuP). From Jamieson *et al.* (2007).

1.2.5 Geology along Hw117

Prior to this study, the tectonic architecture of the Grenville Province along Hw117 in western Quebec was defined by a series of tectonic domains/terranes based largely on regional-scale investigations (e.g. Indares and Martignole, 1985, 1990; Guo and Dickin, 1996; Martignole *et al.*, 2000; Dickin *et al.*, 2014). The groundwork for the present study included geological mapping to characterize these previous and newly proposed (sub)domains, the results of which were largely presented in preliminary geological reports (Lambert *et al.*, 2018, 2019), the re-imagined virtual field trip (Lambert *et al.*, 2020) and a novel virtual chapter (chapter 2) presented in this thesis. Based on Lambert et al (2018, 2019, 2020), the following section provides an overview of the geology within the study area from NW to SE (Fig. 1.7). This will provide geological context for chapter 3. Detailed lithological descriptions are presented in the preliminary reports (Lambert *et al.*, 2018, 2019), whereas the descriptions and figures of the key outcrops and structures are presented as virtual stops chapter 2 of this thesis.

1.2.5.1 Parautochthonous Belt

1.2.5.1.1 The Grenville Front Thrust Zone

In the study region the Grenville Front Thrust Zone (GFTZ) constitutes a ca. 50 km wide zone of tectonically stacked slices of Archean rocks located between the Grenville Front in the NW and the Dorval Detachment to the SE (Fig. 1.7. Wynne-Edwards, 1972; Indares and Martignole, 1985, 1990). This stack is broadly subdivided into a lower stack of muscovite-sillimanite-garnet schists of the Lac Témiskamingue terrane metamorphosed to amphibolite-facies and an upper sheet of migmatitic-orthogneisses and charnockites of the X-terrane metamorphosed to granulite facies, locally defining the footwall and hanging wall of the McLaurin Thrust respectively (Indares and Martignole, 1985, 1990; Martignole and Martelat, 2005)

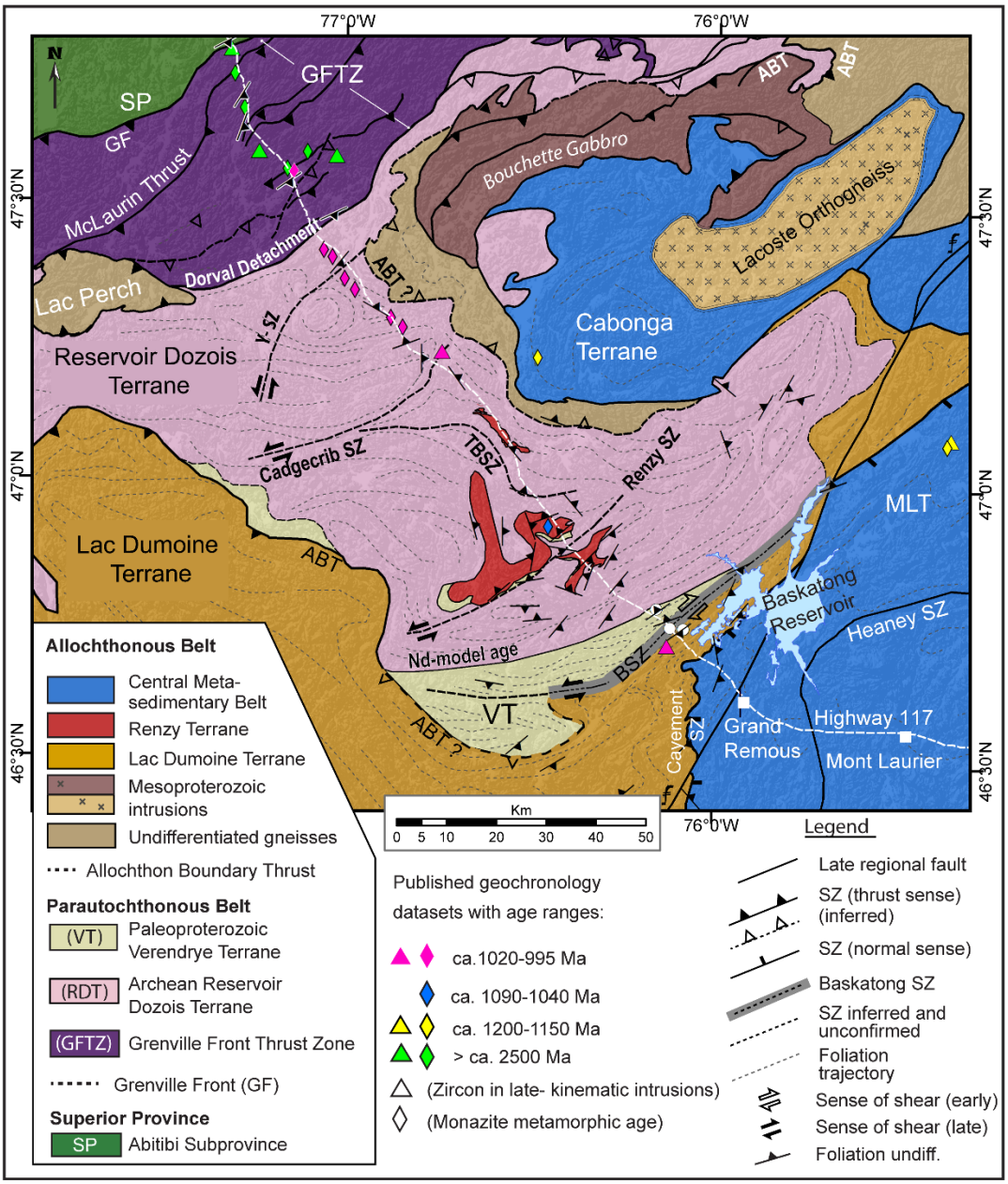

Figure 1.7. Location and subdivision of the study area along the Hw117 transect, focused between Val-d'Or and Grand Remous in western Quebec. Location of existing geochronology data sets are also shown. Map compiled from field work conducted as part of this study, integrated with previous interpretations (e.g. Indares and Martignole, 1990; Martignole and Pouget, 1994; Martignole, 1995; Guo and Dickin, 1996; Montreuil and Constantin, 2010; Dickin *et al.*, 2014; Lambert *et al.*, 2018, 2019). Published U-Pb zircon and monazite ages data derived from Childe *et al.* (1993); Martignole and Friedman (1998); Martignole and Martelat (2005) and from the MERN SIGEOM online database. Baskatong Shear Zone = BSZ.

Mafic dykes within the GFTZ show a geochemical (major and some trace elements) similarity with mafic dyke swarms emplaced in the Superior Province, equated to the ca. 2452 Ma Matachewan, 2214 Ma Senneterre-Preissac, 1240 Ma Sudbury and 1141 Ma Abitibi dyke swarms (Martignole and Martelat, 2005; see chapter 3 for more detail on the chemistry of these suites), which supports the extension of the Superior Craton basement rocks SE of the Grenville Front and suggests that similar mafic bodies may occur elsewhere in the PB within the study region (see chapter 3). Many of these mafic bodies cross-cut the gneissic fabric, have chilled margins, preserve igneous layering, and were interpreted to only record the Rigolet metamorphic event (Martignole and Martelat, 2005). As such, they were used to calculate peak P-T-conditions of 1.2-1.5 GPa at 800^{o}C during burial, which was followed by a quasi-thermal decompression to 0.9 GPa at 700^{o}C (Martignole and Martelat, 2005). The difference in the metamorphic grade of the subdomains across the MacLaurin Thrust were inferred to be the result of NW-directed thrusting of different structural levels during the Rigolet (see X and Y in Fig. 1.4.C; Martignole and Martelat, 2005). Whereas the gneisses in the X-terrane record evidence for granulite facies metamorphism during the Archean (ca. 2700-2800 Ma; Berclaz *et al.,* 1995; Martignole and Martelat, 2005) and localized Grenvillian reworking (ca. 1020-945 Ma) in discrete extensional mylonites (Martignole and Martelat, 2005), metamorphism in the dykes was not directly dated and the age of both metamorphism and NW-directed thrusting is debated (see virtual stops 3-4 in chapter 2).

1.2.5.1.2 Reservoir Dozois Terrane

The Reservoir Dozois Terrane (RDT; Fig. 1.7) is inferred to represent the Superior Province to the SE of the DD that was reworked during the Rigolet phase (Indares and Martignole, 1990; Childe *et al.*, 1993) with the occurrence of Nd-model ages older than ca. 2300 Ma (Doig, 1977; Guo and Dickin, 1996; Dickin *et al.*, 2014) largely defining its geographic extent within the study area.

U-Pb monazite ages (ca. 1000-1020 Ma) of limited geographical extent in the RDT (Fig. 1.7), suggest that metamorphism occurred during the Rigolet phase (Childe *et al.*, 1993) and in contrast to the granulite facies metamorphic grades recorded elsewhere along the transect (i.e. GFTZ, Renzy Terrane, Lac Dumoine Terrane; Indares and Martignole, 1990; Martignole and Martelat, 2005), there is little evidence that metamorphism exceeded amphibolite grade in the RDT (Indares and Martignole, 1990). Here metamorphism was estimated at approximately 0.75-0.85 GPa at 750^{o}C (Indares and Martignole, 1990) based on the occurrence of kyanite and sillimanite in aluminous gneisses and the general absence of garnet-orthopyroxene metamorphic assemblages in the mafic

rich assemblages. Based on the drop in metamorphic grade, from granulite to amphibolite facies across the Dorval Detachment, Martignole and Martelat (2005) suggested that the boundary is a ca. 1000 Ma old normal sense shear zone, but modern studies are still required to fully understand the P-T-t-D history and significance of this boundary.

Rocks within the RDT are mostly shallow dipping, highly migmatitic (>30% rock volume) to diatexite gneisses that are generally hornblende-rich and garnet-poor (chapter 2). They have mostly tonalite-trondhjemite-granodiorite (TTG) compositions that contain variably transposed and folded mafic layers. Localized biotite-sillimanite rich gneisses and granitic gneisses, commonly with pink, K-feldspar rich injections veins, are also present (Indares and Martignole, 1985, 1990; Martignole *et al.*, 2000; Lambert *et al.*, 2018). Mafic bodies in the RDT mostly occur as variably folded and dismembered lenses, rotated boudins or rafts within the migmatitic gneisses (see chapter 3). Most of the disaggregated bodies are variably retrogressed to amphibolites, probably in the presence of aqueous phases (see chapter 4) but in rare cases, localized leucosome with peritectic orthopyroxene garnet and clinopyroxene preserved in the core of some bodies, present evidence for dehydration melting at granulite metamorphic grades (Lambert *et al.*, 2019; chapter 2). Concordant and highly strained mafic layers associated with garnet-bearing units are also mapped within the greater RDT (Lambert *et al.*, 2018, 2019) but may be part of a different domain (see RT below).

As noted in this study, the gneissic fabric in this study is defined by syn-tectonic leucosome/injections, which commonly contain subrounded to rounded quartz grains or the outcrops are characterized by extensive diatexites (>60% rock volume) that contain numerous deformed and partially dismembered mafic rafts (chapter 2). Due to the lack of elongated quartz grains (or aggregates and ribbons), and the abundant rootless mafic rafts in the diatexites, the dominant deformation phase in the RDT most likely occurred under suprasolidus conditions. This is in stark contrast to the gneisses of the GFTZ (Martignole and Martelat, 2005; Lambert *et al.*, 2018, 2019) and Renzy Terrane (see below; Indares and Martignole, 1990) that record pervasive solid-state (subsolidus) deformation textures, such as elongated quartz grains or aggregates (quartz ribbons) and mylonitic planar fabrics (Lambert *et al.*, 2019; Lambert *et al.*, 2020). Some rock packages in the RDT do however, show a high level of subsolidus strain (Lambert, *et al.* 2018, 2019), the most prominent defined by a package of tonalitic and granitic gneisses that preserve evidence for thermally annealed subsolidus deformation, as indicated by recrystallized feldspar porphyroclasts, straight gneissic banding and transposition of K-feldspar injection veins and

commonly contain rotated and transposed, granulitic mafic-boudins that can define meter-scale kinematic indicators (chapter 2). This description is identical to those described elsewhere in the Grenville Province, which are colloquially called ‘straight gneisses’ and are considered to represent shear zones, characterized by mostly pure shear strain (e.g Hanmer, 1988; Nadeau and Hanmer, 1992; MacKinnon, 1994; MacKinnon *et al.*, 1996). For these reasons, the “straight gneisses” observed in this study were also interpreted as shear zones. One such example is the previously unidentified Teddy Bear Shear Zone (TBSZ; see chapter 2 for more detail). However, within the RDT, characterization and timing of transport on such shear zones and pervasive suprasolidus deformation in particular, are still required and their tectonic implications in the evolution of this domain during the Grenvillian Orogeny is yet to be considered.

1.2.5.1.3 The Vérendrye Terrane

The Vérendrye Terrane (VT) is the new name suggested by Lambert *et al.*, (2019) for the previously unnamed domain (formerly part of the Reservoir Baskatong Promontory SE of the Renzy Shear Zone; see *RBT* in Indares and Martignole, 1990) that is wedged between the RDT and Lac Dumoine Terranes (Fig. 1.7). The extent of the VT is delineated exclusively by the distribution Nd-model ages between ca. 2100-1800 Ma, collected from biotite gneisses and intermediate orthogneisses, compared to numerous older (>2300 Ma) and limited younger (1790-1550 Ma) model ages in the RDT and the Lac Dumoine Terrane (see below) respectively (Guo and Dickin, 1996; Dickin *et al.*, 2012, 2014). The ‘Nd-model age boundary’ (Fig. 1.7) is a cryptic boundary that separates the VT from the RDT to the NE (Doig, 1977; Guo and Dickin, 1996; Dickin *et al.*, 2014), whereas the boundary with the LDT is obscured by the subvertical, high strain fabrics of the Baskatong Shear Zone (BSZ) to the SE (chapter 2). Dickin *et al.* (2014) also identified similar Paleoproterozoic Nd-model ages along the base of the Renzy Terrane, which are tentatively interpreted to be part of the VT in this study (Fig. 1.7). Based on the Nd-model ages, the VT is broadly equated to other Paleoproterozoic crustal domains in the PB, such as the Britt Domain in Ontario (see Rivers *et al.*, 2012; Dickin *et al.*, 2014, 2020 and refrences therein), but apart from the Nd-model age data, there is limited evidence to support the correlation of the VT domain to others in the Grenville Province.

Mapping proximal to the Nd-model age sample localities, complemented previous studies (e.g. Indares and Martignole, 1985, 1990) and revealed that rocks within the VT exposed along the highway are similar to those in the RDT, comprised of garnet-free, migmatitic, hornblende-bearing

granodiorites (chapter 2), although localized syeno-granitic gneisses are also present in this domain (Lambert *et al.*, 2018). Like the mafic rocks in the RDT, those in the VT along the highway constitute decameter-sized amphibolite and metagabbro blocks and boudins, commonly rotated within the ductile fabric. In contrast, small (<20 m^2) isolated outcrops were also mapped in SW part of the VT that consist of mixed garnetiferous mafic and intermediate gneisses but it remains unclear if they are indeed part of the VT.

As the VT (and other Paleoproterozoic crustal domains in the Grenville Province) is interpreted to occupy a structural position below the AB, the upper boundary is inferred to represent the ABT and they were included within PB of the Grenville Province (after Rivers *et al.*, 1989; Rivers *et al.*, 2012; Ketchum and Davidson, 2000; Dickin *et al.*, 2014, 2017). Dickin *et al.* (2014, 2017) however, proposed that these Paleoproterozoic domains represent ”parautochthonous duplex structures” that formed during “thrusting” of the AB over the PB (e.g. Herrell *et al.*, 2006), with transport along the cryptic lower boundary inferred to be over 200 km (Dickin *et al.*, 2014). In this case, they define “allochthonous” terranes that would have a penetrative fabric that is older than the Rigolet phase, which would make them part of the AB. The upper boundary of the VT however remains ambiguous and until now, the timing of deformation within the VT had not been determined, meaning the affinity and the role this crustal segment during either the Ottawan or Rigolet phase of the Grenvillian Orogeny remains ambiguous.

1.2.5.2 Allochthonous Belt

1.2.5.2.1 The Renzy Terrane (RT)

The Renzy Terrane (formerly ‘Renzy Shear Belt’ in Indares and Martignole, 1990) defines two, kilometer-sized, amoeboid-shaped domains located to the NW and SE of the Renzy Shear Zone (RSZ) in the study area (Fig. 1.7). The RT is interpreted to represent juvenile arc/back-arc fragments based on the results of mafic geochemistry (Montreuil, 2010; Montreuil and Constantin, 2010; Verma *et al.*, 201) and the difference between the minimum depositional age (ca. 1400 Ma; Martignole and Ringuette, 1998; Montreuil and Constantin, 2010) and Nd-model ages (1670-1410 Ma; Dickin *et al.* 2014). RT gneisses were metamorphosed at upper amphibolite to granulite facies grades, with peak conditions estimated at 0.975 GPa and 745°C (Indares and Martignole, 1990) at ca. 1072 Ma, based on a single concordant monazite date (Childe *et al.*, 1993). This is ca. 50-70 Ma older than peak amphibolite grades in the RDT and ca. 100 Ma older than metamorphism

recorded in the Cabonga Terrane (1180-1145 Ma; Friedman and Martignole, 1995), part of the orogenic lid (see the Central Metasedimentary Belt below).

Rocks of the RT are distinctly different to those of the surrounding PB. They are characterized by garnet-rich gneisses that range from tectonically interleaved mafic and felsic aluminous gneisses (chapter 2), most likely of volcano-sedimentary protoliths (e.g. metamorphosed pelitic, quartzite and carbonate units); charnockitic augen-gneisses; mafic amphibolites to granulites and deformed ultramafic intrusions (Indares and Martignole, 1985, 1990; Montreuil, 2010; Montreuil and Constantin, 2010; Lambert *et al.*, 2018, 2019). Sulphurous alteration zones are also commonly observed within the RT (Montreuil, 2010; Lambert *et al.*, 2018). In general, the protoliths for the mafic rocks in the RT are inferred to be volcanic flows, small sills and/or intrusive sheets intercalated within the other RT gneisses (Montreuil and Constantin, 2010). The ultramafic rocks specifically, were interpreted as part of a disaggregated stratiform layered complex (Johnson, 1972).

Structural features of the RT also contrast with the shallow dipping RDT and VT gneisses. RT outcrops are characterized by variably dipping successions, defining tight disharmonic folds on decameter scale (Sabourin, 1963; Lambert *et al.*, 2019), or by moderate to steep dipping gneisses that likely represent the limbs of 1st order, kilometer-scale folds with similar complex fold geometries (Lambert *et al.*, 2019; chapter 2). In further contrast to the migmatitic RDT gneisses, all RT gneisses have prominent subsolidus deformation textures, such as penetrative pyroxene and plagioclase stretching lineations (Hanmer and Ciesielski, 1984; Indares and Martignole, 1990; Lambert *et al.*, 2018, 2019). The contrast in lithology and structure effectively differentiates Renzy outcrops from those of the PB and VT in the field, while the timing and degree of metamorphism combined with younger model ages, confirms that the RT is part of the lower-middle part of the AB that was deformed during the Ottawan phase.

Dickin *et al.* (2014) proposed that as fragments of the AB, the RT represent tectonic klippe that structurally overly the PB, initially forming part of a continuous allochthonous sheet that was thrust over Laurentia sometime during the Ottawan phase (1090-1040 Ma). The Lac Perche Terrane, located along the SE margin of the DD (Fig. 1.7), is also inferred to be part of these AB klippen based on similar Nd-model ages (Dickin *et al.*, 2012, 2014). As the AB is located structurally above

the PB in the Grenville Province, the boundary between these klippen and PB should then be the ABT, although the implications of a discontinuous ABT are not discussed in these earlier studies.

Building on the work of Lambert *et al.* (2019), mapping in this study identified numerous, previously uncharacterized, decameter-sized outcrops dispersed amongst RDT gneisses exposed >20 km NW of the RT (*sensu stricto*), that have structural and lithological characteristics similar to those described for the RT (chapter 2). Many of these outcrops contain tightly folded mafic layers associated with garnetiferous aluminous gneisses, augen gneisses and zones of sulphurous alteration (chapters 2 & 3). These characteristics, combined with earlier (e.g. Sabourin, 1963) and new structural mapping along the NW contacts of the RT (chapter 2), led to a hypothesis that these outcrops were RT-equivalents and that they, with the RT (*sensu stricto*), were not tectonic klippen, but rather completely enveloped in the PB gneisses. This was already hinted at in the original investigations along the transect (see RSB in Indares and Martignole, 1990), although the implications were not discussed at the time. This would then suggest they represent disaggregated remnants of the RT, now completely enveloped in the RDT gneisses. The structural (chapter 2) and geochemical (chapter 3) studies presented in this study aims at testing this hypothesis.

1.2.5.2.2 The Lac Dumoine Terrane

The Lac Dumoine Terrane along the transect is a ca. 8-10 km wide zone of subvertical-dipping gneisses wedged between the VT in the NW and the Mont Laurier Terrane of the Central Metasedimentary Belt to the SE (Fig. 1.7). It was previously mapped as part of the 'Lac Dumoine nappe' (Martignole *et al.*, 2000; Dickin *et al.*, 2012; Dickin *et al.*, 2014), an extension of the Algonquin Terrane in Ontario (Ketchum and Davidson, 2000; Rivers *et al.*, 2002). The Algonquin Terrane consists predominately of Paleo- and Mesoproterozoic gneisses (ca. 1715-1600 Ma and ca. 1470-1430 Ma) and meta-granitoid rocks (Ketchum and Davidson, 2000) and exhibits widespread granulite-facies metamorphism and partial melting between ca. 1080 -1045 Ma (Bussy *et al.*, 1995), that overprints earlier eclogite-facies metamorphism (Davidson and van Breemen, 1988).

Little data exists for this narrow wedge of LDT gneisses along Hw117, apart from two Paleo-Mesoproterozoic Nd-model ages (between 1790-1550 Ma; Dickin *et al.*, 2012), which means the location and transport directions along the lower (i.e. ABT) and upper (i.e. Cayamant Shear Zone) boundaries in particular, are poorly constrained. Mapping during this study revealed the LDT

consisted mostly garnet rich and highly strained gneisses comprised of migmatites with granitic and amphibolitic protoliths, high-pressure mafic granulites, undifferentiated biotite-gneisses and charnockite augen-gneisses (see also Lambert *et al.*, 2018, 2019). The contrast in lithology to the RDT and VT, younger Nd-model ages and preservation of eclogite-looking mafic rocks along the Baskatong Reservoir (Lambert *et al.*, 2019; chapter 2), would tentatively support the correlation to the Lac Dumoine Terrane to the allochthonous Algonquin Terrane, although Ottawan deformation ages in the LDT are required to confirm this correlation.

In addition to the LDT, a slice of undifferentiated rocks wedged between the PB and the Cabonga Terrane are interpreted to be allochthonous (Fig. 1.7) based on similar Nd-model ages (Dickin *et al.*, 2014). Lambert *et al.* (2018, 2019) demarcated this domain based on garnetiferous lithologies, high magnetic reflectors that in parts, show a stronger magnetic response in the AB compared to the PB (Montreuil and Constantin, 2010). The affinity and extent of this domain however, remains to be confirmed by detailed P-T-t-D investigations.

1.2.5.2.3 The Central Metasedimentary Belt (Mont Laurier and Cabonga Terranes)

The Mont Laurier and Cabonga Terranes (Fig. 1.7) are part of the Central Metasedimentary Belt, that with the Morin Terrane (see chapter 2), form part of the orogenic lid to the Grenville Orogen (Rivers *et al.*, 1989; Rivers, 2008). The Mont Laurier and Cabonga Terranes are composed of amphibolite-facies marble and granulite-facies quartzite domains respectively (Martignole and Pouget, 1993, 1994), metamorphosed to upper amphibolite to granulite facies grades as a result of the pre-Grenvillian Shawinigan Orogeny. Hornblende $^{40}Ar/^{39}Ar$ cooling ages of >1090 Ma confirm these rocks formed the upper lid of the crust during the Grenvillian Orogeny that was taking place structurally underneath (Rivers, 2012; Schneider *et al.*, 2013).

1.3 Thesis objectives

The Grenville Province serves as a natural laboratory for the investigation of deep crustal processes in collisional orogens whilst the conceptual and numerical models developed for the Grenville Province (e.g. Jamieson *et al.*, 2007; Rivers, 2008, 2009, 2012) serve as working hypothesis upon which these processes can be tested. Across the Hw117 transect in western Quebec however, there are limited field-based data to constrain the tectonic models for this part of the Grenville Province, especially in the tectonic segments located between the GFTZ and the orogenic lid (i.e. RDT, VT, LDT). The primary objective of this thesis was therefore:

(1) To collect and compile a robust dataset from a transect through part of this generally understudied section of the Grenville Province in western Quebec, by mapping and using modern analytical techniques, to move towards a better understanding of the evolution of the Grenville Orogen.

In order to realize this fundamental question, a series of secondary objectives are outlined below:

(2) Unravel and characterise the tectonic architecture across the Hw117 transect.

The Grenville Province in the study area preserves a series of AB remnants (e.g. Lac Perche & RT) distributed between the GFTZ and the LDT (Fig. 1.7). Collectively they were considered tectonic klippe overlying the PB, formed as remnants of a continuous sheet, comprised of a stacked AB crust, that was thrust over the tectonic basement during the Ottawan phase and subsequently eroded (e.g. Martignole *et al.*, 2000; Dickin *et al.*, 2014, 2017). Although this broadly fits with the geometry of the GO-2 numerical model of Jamieson *et al.* (2007) along the Montreal-Val-d'Or transect, the architecture at the time of the modelling was largely defined by regional-scale investigations (e.g. Indares and Martignole, 1985, 1990; Guo and Dickin, 1996; Martignole *et al.*, 2000; Dickin *et al.*, 2014) and lacked structural and modern geochronology controls, especially within the PB and along key structures (e.g. DD, TBSZ, RSZ, BSZ) that would ultimately have been required to feed the conceptual or numerical models for this transect.

One of the key questions in this study driving the re-investigation of the architecture across Hw117 is the hypothesis that numerous garnet-rich mafic and aluminous gneissic outcrops dispersed within the migmatitic TTG gneisses of the PB, are disaggregated remnants of the initially overlying RT (see section 1.2.5.2.1). This hypothesis then progressed to also include decameter-scale garnet-rich mafic boudins with high-grade (granulite facies) mineral assemblages and those variably retrogressed to generic amphibolite assemblages, which may also represent RT-type equivalents. The possible affinity of these outcrops/bodies to the allochthonous RT points to a more complex 1st order tectonic architecture than was defined in previous regional scale studies (e.g. Indares and Martignole, 1985, 1990; Martignole *et al.*, 2000; Dickin *et al.*, 2014) and would impact previous conceptual and numerical models for the evolution of the PB during the Rigolet phase, especially those that advocated for thick-skinned thrusting (e.g. Martignole and Martelat, 2005; Rivers, 2009). There is thus, a fundamental need to identify, characterize and delimit the various tectonic domains along the transect and re-interpret the tectonic architecture.

Straightforward identification of various tectonic domains (subdomains) is however, often hindered by poly-phase deformation and complex metamorphic histories, which can obscure the primary structures and precursor lithologies that are typically used to distinguish between the domains. The presence or absence of distinctive pre-orogenic plutonic suites, such as mafic complexes or dyke suites however, has proven to be a particularly useful tool for tectono-stratigraphic delineation within orogenic provinces, as the correlation of mafic bodies within different tectono-stratigraphic domains can confirm the continuity of structurally coherent crust (Bleeker and Ernst, 2006). Several workers have successfully identified different domains/terranes using U-Pb geochronology, geochemical and textural traits to correlate variably deformed and metamorphosed mafic and anorthosite bodies within different structural levels of the Grenville Province, to equivalent bodies elsewhere in the province or to lesser deformed suites within neighbouring provinces (e.g. Birkett *et al.*, 1991; Indares and Dunning, 1997; Ketchum and Davidson, 2000; La Flèche *et al.*, 2005; Martignole and Martelat, 2005; Montreuil and Constantin, 2010; Bédard *et al.*, 2009). In a landmark contribution, Ketchum and Davidson (2000) used the geochemical and textural correlation of deformed mafic bodies in the Grenville Province to mafic suites with either an autochthonous (e.g. 1238 Ma Sudbury dyke swarm; Fahrig and West, 1986; Condie *et al.*, 1987) or an allochthonous (e.g. 1170-1150 Ma Algonquin meta-gabbro suite; Davidson and Grant, 1986; Grant, 1987; Davidson and van Breemen, 1988) affinity, to separate the Georgian Bay area of Ontario into different structural levels (i.e. the PB and AB respectively; Fig. 3.1). This technique was subsequently tested in western Quebec by Martignole and Martelat (2005), who correlated several dykes in the PB to various Proterozoic dyke suites that intruded the Superior Province (e.g. Matachewan, Sudbury and Abitibi suites; Fahrig and West, 1986; Condie *et al.*, 1987). La Flèche *et al.* (2005) additionally showed that mafic and ultramafic granulitic gneisses in the PB to the N-NW of the Cabonga Terrane had major and trace element geochemical signatures that overlapped with the Archean Abitibi metavolcanic rocks.

To these ends, various parts of this thesis were geared to characterize the lithologies and structures across the transect to allow the tectonic architecture to be documented. The contributions of these parts are outlined in the following tertiary objectives:

2.1) Conduct detailed lithological and structural mapping through the AB and PB segments exposed along the transect (all chapters but summarized in the virtual chapter 2), including microstructural investigations. More specifically to characterize the structural fabrics in the

RDT (linear, planar and kinematics), how they vary across the transect and their tectonic significance (chapter 2). This includes existing and newly proposed key structures, such as the DD, TBSZ, BSZ, RSZ.

2.2) Build on the work of Ketchum and Davidson (2000) and subsequent authors, by comparing the geochemistry of mafic bodies collected within the PB of the study to mafic suites known to have either an autochthonous or allochthonous affinity (chapter 3), in order to define the extent of the different structural levels along the transect and more explicitly, to confirm/disprove the initial hypothesis made from the field observations (section 1.2.5.2.1; Lambert *et al.*, 2019) that suggest they may be part of the RT (chapter 3; see also Lambert *et al.,* 2019).

2.3) Use new geochronology results to aid in the delineation of the various tectonic domains/subdomains/structural levels and where possible, better constrain the age of deformation and possibly even the timing of tectonic transport across key structures, namely the TBSZ, BSZ and RSZ (chapters 2 & 4; discussed in more detail in objective 3).

2.4) Integrate the results from the above objectives, with those of existing (although limited) datasets, to construct a novel cross-section through the study area (chapter 2) that is constrained by a comprehensive dataset (e.g. surface geology as well as structural and U-Pb geochronology data).

2.5) Provide an explanation for the ambiguous location of the ABT along the transect.

(3) Present new age data acquired through modern techniques:

Existing age data within the study area is sparse (Fig. 1.7), with the most recent data confined to the GFTZ (e.g. Martignole and Martelat, 2005). Existing crystallization ages collected SE of the DD are mostly based on upper intercept ages from late-tectonic intrusions within Grenvillian (ca. 980-1000 Ma) shear zones that intersect various segments of the transect (Martignole and Friedman, 1998), some of which may be contentious (e.g. RSZ; chapter 2). While the existence and significance of a laterally extensive sinistral RSZ is yet to be confirmed, the age and kinematics across this shear zone and the BSZ are highly debated (cf. Martignole, 1995; Sharma *et al.*, 1995). Although interpreted as a sinistral shear at 1020 Ma based on the clockwise deflection of the gneissic fabric (Martignole and Friedman, 1998), numerous macro-scale kinematics in the BSZ are indicative of dextral shear sense, inferred to represent an earlier phase of shearing that may have

been related to thrusting of the AB over the PB (Martignole and Pouget, 1994; Martignole, 1995; Sharma *et al.*, 1995; Martignole and Friedman, 1998). This earlier dextral phase however, has not been dated and is of particular interest because as the boundary is inferred to divide PB and AB rocks, the age would then represent the timing of deformation along the ABT. In addition to existing crystallization ages, geochronology data in the area includes a series of mostly discordant, single grain monazite ages from undefined domains NW of the RT (including the RT) by Childe *et al.*, (1993). Furthermore, many of these samples were collected and ages interpreted before the architecture of the transect was fully characterized, which has implications on these previous tectonic models. Outside of these data, there is a notable lack of new age data, particularly for the age of pervasive deformation in the gneisses of the RDT, VT and LDT. There is thus, a need to collect new geochronological data and interpret the results within the construct of a revised architecture.

Zircon grains from igneous rocks can potentially preserve complex morphologies. The formation of multiple, texturally and/or chemically distinct zones around inherited cores, typically reflects changes in their thermo-mechanical conditions during their formation (Harley *et al.*, 2007; Kohn, 2016), specifically the fluctuation in PT-conditions and/or variation in the magma chemistry due to new magma or fluid influx at different stages of their evolution (Rubatto, 2002; Corfu *et al.*, 2003; Harley *et al.*, 2007; Rubatto *et al.*, 2009; Kohn, 2016). Zircons derived from samples in this study are no exception and have complex morphologies (see chapter 4), which can provide clues as to the thermo-mechanical conditions during a specific stage of the Grenvillian evolution. Inherited cores on the other hand, have the potential to provide clues as to the age of their protoliths and consequently, the affinity of the domains from which they were sampled.

To this end, a key component of this thesis was to obtain new zircon U-Pb zircon ages, using modern analytical techniques (e.g. LA-ICP-MS), from syn-late tectonic, leucosomes, granitic injections and pegmatites in order to determine the age of deformation of select fabrics and structures. Whereas the choice of zircon and analytical methods is discussed further in the methodology (section 1.4) section of this chapter, the results of geochronology presented herein were specially used to address the following:

3.1) Integrate field observations, zircon textures, trace-element geochemistry, age data and Ti-in-zircon thermometry to explain the complex zircon morphologies.

3.2) Determine the age of pervasive deformation in the gneisses of the RDT, VT and LDT domains (including subdomains or various structural levels; chapters 2 & 4, see objective 2). These ages are used to delimit between the tectonic domains as those deformed during the Ottawan phase are expected to record ages between 1090-1020 Ma while those deformed during the Rigolet are expected to only record ages between 1005-980 Ma (Rivers, 2008). Although, as documented by Gervais and Moukhsil (2016) and Jannin *et al.* (2018), the AB rocks may be reworked during the later phase. Distinction/differentiation may however, be aided by inherited ages if the sampled intrusive rocks were not far travelled.

3.3) Of specific interest, is the age of deformation and inherited ages in the LDT (chapter 2) and Paleoproterozoic VT (chapter 4), as their affinity to either the parautochthonous or allochthonous belts remains to be confirmed (see section 1.2.5).

3.4) Determine or constrain the age of tectonic transport across key structures (chapters 2 & 4), particularly the newly recognised TBSZ, the contentious RSZ and the age of dextral kinematics long the BSZ.

3.5) Integrate all field observations and geochronology results with the newly proposed tectonic architecture (objective 2) to better the understand the conditions during deformation of the PB.

(4) Present a model for deformation in the PB during the Grenvillian Orogeny

As summarized by Rivers, 2015, there are many aspects of the conceptual and numerical models for the Grenville Orogen that require detailed testing through dedicated field-based and analytical studies. One of the key aspects that remains unresolved is the evolution of the tectonic basement (i.e. PB) during the Rigolet phase in western Quebec. As discussed in section 1.2.5, this transect through the Grenville Province was proposed to have accommodated NW-directed thrust stacking and rapid exhumation in a fold and thrust-belt of an orogenic wedge (Martignole and Martelat, 2005; Rivers, 2009). Alternatively, the PB may have been reworked during the formation of core-complexes and normal sense detachment zones within the AB (e.g. Rivers and Schwerdtner, 2015). Notably however, as shown by the recent comprehensive works of Jannin (2017) and Jannin *et al.*, (2018) and subsequent studies (e.g. Labat *et al.*, 2020) in the central Grenville Province, reworking of the PB by heterogenous channel flow cannot be ruled out and deformation may have even affected the overlying AB crust during the Rigolet phase. Determining which of these tectonic

processes were active during the final Grenvillian phase (i.e. Rigolet) would have a significant impact on the interpretation of the resulting tectonic architecture of the Grenville Province across the Hw117 transect (e.g. Gervais *et al.*, 2010).

As summarized by Gervais and Brown (2011), there are distinctive features that can be used to discriminate which tectonic processes were active (Table 1.1). In an orogenic wedge, pervasive reverse-sense shearing that results in moderate-steeply dipping, non-coaxial fabrics, generally define the finite strain patterns, although normal-sense overprinting is possible (Platt, 1986). Deformation ages are expected to be younger towards the flanks and as reverse-shearing occurs during tectonic under thrusting and burial of various levels, fabrics are dominated by prograde to peak-metamorphic mineral assemblages. In models of channel flow or ductile nappes, key characteristics include coeval timing of the upper, thrust sense and the lower, normal sense boundaries to the channel. Between these boundaries, rocks are typically characterized by highly migmatitic packages of rocks. Similar to the thrusting model, the age of deformation decreases away from the core and fabrics may also be defined by prograde or near-peak assemblages if flow was lateral (Jamieson *et al.*, 2004), although if extruded along an inclined plane, would be defined by high-temperature retrograde assemblages (Gervais and Ranalli, 2017). In contrast, a diagnostic feature for the orogenic collapse model is the formation of domal core-complexes (Vanderhaeghe, *et al.*, 1999; Platt et al, 2015). In this case, the cores are typically characterized by co-axial fabrics with retrograde assemblages (Vanderhaeghe, *et al.*, 1999), whereas numerous brittle-ductile normal sense faults in the upper crust and outward dipping normal-sense shears are expected along the margins of the domes (Platt *et al.*, 2015). If collapse is associated with syn-extensional shortening towards the flanks (Jamieson and Beaumont, 2013), characteristics consistent with either thrusting in an orogenic wedge or even channel flow would be expected.

To this end, this study aims to present a model for deformation within the PB by considering the following two sub-objectives:

4.1) Assess if the re-defined architecture (objective 2), largely summarized by the new cross section (chapter 2), combined with the structural elements and geochronology results (objective 3), are consistent with the previous models proposed for deformation during the Rigolet phase in this section of the Grenville Province. It is important to note that as the transect largely consists of homogenous quartzo-feldspathic gneisses metamorphosed to

amphibolite facies grades, obtaining accurate P-T data constraints for the construction of detailed P-T-t-D paths that are ultimately needed to test theses models (Table 1.1; e.g. Gervais and Brown, 2011) is problematic (Peterman *et al.*, 2009) and outside the scope of this study.

4.2) Integrate the results from the three core chapters to develop and propose a tectonic model, which is consistent with the newly proposed architecture along the transect (objective 2) and may explain how and when the PB gneisses to the SE of the DD were deformed during the Grenvillian Orogeny.

(5) Present part of this research in a novel and widely accessible digital format.

Since the beginning of the 21st century there has been a push to present scientific data digitally and make it widely available, particularly following the global pandemic (ca. 2019-2021) that was brought on by the novel coronavirus (SARS-CoV-2). With the goal of integrating into this increasingly virtual era and ultimately, to expose and drive further research into collisional orogens and the Grenville Province especially, the final objective of this study is to publish part of this research as a novel virtual tour hosted in Google Earth (v-chapter 2). More detail on the format and which data of the thesis are presented in this format see section 1.5 (structure of thesis).

1.4 Methodology

1.4.1 Background, outcrop exposure and accessibility

Field work for this study was conducted over two field seasons, consisting of 6- & 5-week stints in the summers of 2017 and 2018, respectively. Most efforts in the field were spent mapping each of the outcrops that were exposed along the Hw117 segment between Louvicourt and Grand Remous, easily accessible with motor vehicles. Outcrops not occurring along the highway were accessed with a pick-up truck along select logging roads, by boats along the lakes (Reservoir Dozois and Reservoir Baskatong) and/or by foot. Some road-cuttings offer impressive 3-D exposures and while outcrops forming islands in the lakes are also relatively well exposed, exposure along the logging roads varies and outcrops typically occur as partially revealed pavements. Along the highway, outcrops typically occur more than 1 km apart, whereas along the logging roads they are sporadically distributed, ranging from hundreds of meters to tens of kilometers. Reasonable measures were taken at all times to ensure the health and safety of the field

personnel, namely the use of reflective vests, orange safety cones, hard hats as well as consistent radio communication along the logging roads.

1.4.2 Pre-field preparation and field mapping information and techniques

Prior to the fields seasons, literature review and desktop studies were conducted using the SIGEOM database (2017) and historical guidebooks, maps and figures (e.g. Indares and Martignole 1990; 1985; Martignole and Martelat 2005; Sabourin 1963; Montreuil and Constantin 2010; Dufréchou *et al.*, 2014). Geophysical datasets, specifically 1st vertical derivative magnetics, were particularly useful in delineating large, linear features denoting possible structures (e.g. faults and shear zones; e.g. Fig. 4.6 in Dufréchou *et al.,* 2014). While effective in distinguishing between the Superior Province and the PB, due to their varying magnetic signatures (Bartholomew and Hatcher, 2010; Dufréchou and Harris, 2013; Dufréchou *et al.*, 2014), the magnetics were less effective in distinguishing between the PB and AB or domains within them, due to the low spatial resolution within the study region (ca. 100 m). These data were obtained free of charge from the Geoscience Data Repository for Geophysical Data, Canada or super-imposed from existing figures (Montreuil and Constantin, 2010; Dufréchou and Harris, 2013).

Mapping was conducted with the aid of a handheld tablet ('geofiche'), equipped with onboard camera, GPS (projected coordinate system: NAD 1983, UTM zone 18N) and the proprietary software of the Ministère de l'Énergie et des Ressources naturelles du Québec (MERNQ), to record various geological attributes at each outcrop. Geo-referenced base-maps, including aerial photos, geophysical (magnetics and gravity) datasets as well as historical maps were loaded onto the tablet prior to the field-seasons.

At each location, outcrops were generally characterized according to the rock types present and respective relationships, magnetic susceptibility (non-magnetic, weak or strongly magnetic) and migmatitic characteristics, specifically textures and percentage of leucosome or injected magma relative to the rock volume (migmatite terminology after Sawyer and Brown 2008; Maxeiner *et al.*, 2017). Gneissic foliations, later discrete shear planes, dyke orientations, fold axes and if visible, axial planes were measured at each outcrop, while kinematic indicators were described and samples were collected for various analytical purposes (see below). Field data was compiled and curated in ArcGiS (ArcMap 10), whereas maps and line drawings were compiled and edited using one or a

combination of ArcGIS, GCDKit (Janoušek *et al.*, 2006), Python and Adobe Illustrator (CS6) software programs.

All structural readings were recorded using a Brunton compass, with a magnetic declination of 12^{o} to the west. Planar structural readings presented herein are reported as dip azimuth and dip angle, whereas all linear readings are reported as plunge azimuth and plunge angle. Structure data presented as part of this thesis is mostly new data collected in this study, unless otherwise specified, where structures were supplemented by undifferentiated foliation and/or lineation data of Sabourin (1963) around the RT or from the MERNQ database covering part of the LDT to the NE of the study area. The geological cross section for the ca. 140 km section of the transect between the GFTZ and the Mont Laurier Terrane, presented in chapter 2 was created with a 20x vertical (elevation) exaggeration and was drawn using dip angles corrected for the apparent dip, which accounts for the oblique trend of the gneissosity relative to the strike of the section profile. Notably, dip angles were not corrected for vertical exaggeration in order to depict the general geometries of the structures in the field. Structural data represented on stereoplots (chapter 2) are plotted as equal area plots in the lower hemisphere using the Steronet program (Allmendinger *et al.*, 2013; Cardozo and Allmendinger 2013). Most planar fabrics are represented by density distribution plots of poles-to-the-plane, contoured according to the internal Kamb method of the software, while fold axial planes are plotted as great-circles (annotated accordingly). Linear data is presented as un-contoured data points. Rose diagrams depict the direction of ductile tectonic transport (as 'rose petals'), by considering the movement of the upper/top of the rock packages relative to N (0^{o}), irrespective of normal, thrust, or strike slip type tectonics. The plotted points on the rose diagram function as linear features and provide an indication of the plunge angle that correspond to the respective directions and can be used as a rough indicator of down dip (steep lineation = thrust/normal sense) or strike-slip (shallow) type tectonics. A detailed legend is provided with the cross sections in the virtual and analog/physical chapter 2 formats of this thesis.

Sample selection at each outcrop included those required for petrography or were prioritized based on potential for PT-determinations from metasedimentary and meta-basic rocks (although not presented in this study), kinematic analysis (as orientated samples), geochemical analysis and potential for geochronology studies. Samples were collected using rock-picks, sledgehammers and a rock saw, when necessary. In all cases, care was taken to collect (or cut) fresh samples that best represented the rock types in question, away from zones of surficial and fluid-chemical alteration,

partial melts or zones defined by mineral cumulates (see section 1.4.3). A combined total of 350 potential samples were collected during this study. Samples selected for analyses, including samples orientated in the field, were prepped and cut with a rock saw at Polytechnique Montréal according to the requirements and specifications of the respective analyses. For example, samples for microstructural analyses were cut parallel to the stretching lineation and marked in order to retain their geographic orientation once made into thin sections.

All standard, polished and/or unpolished thin sections were made by IOS Services géoscientifiques Inc, including those cut from orientated samples, select lithologies, and all samples sent for geochemical and geochronology analyses. Thin sections were inspected under a polarizing microscope for petrological and microstructural descriptions.

1.4.3 Geochemistry considerations

Samples collected for both whole-rock major and trace element geochemistry were mostly from intermediate to mafic bodies with granulite grade metamorphic assemblages or variably retrogressed to amphibolite metamorphic assemblages. After they were cleaned and cut, fresh ca. 1000 cm^3 sized blocks (with some size variation due to different grain sizes) were sent to Activation Laboratories (Actlabs) Ltd in Ontario, Canada, for crushing and whole rock, major and trace element geochemical analysis by fusion–inductively coupled plasma–mass spectrometry (FUS-ICP-MS) technique. Samples were crushed to 2mm, mechanically split for subsamples and pulverized to at least 105 µm using a (mild) steel mill. The detection limits for the analyses were in the range of 0.01%-0.001% for major elements and 1-30 ppm for trace elements. All trace element concentrations presented herein are in ppm. Further details on all analytical protocols and quality assurance during analysis can be found on the Actlabs website (www.actlabs.com).

Notably samples collected from high grade metamorphic terranes such as the Grenville Province, may be subject to significant alteration and bulk element mobility, especially of the major elements (e.g. Ca, Na, Si), during metamorphism and/or hydrothermal alteration (Rollinson, 1993). For these reasons, once analysed, the samples were screened for major and trace element mobility and while some major element chemistry is considered, this study mostly focuses on the REEs and HFSEs trends as they are largely resistant to partial melting (Vigneresse *et al.*, 1996) and mostly preserve their immobile element compositions, even during granulite facies metamorphism (Pearce, 1983;

Tatsumi *et al.*, 1986). A detailed description of the screening processes, and strategy for the geochemical investigations is presented in chapter 3.

1.4.4 U-Pb zircon dating considerations

Dating deformation events in LHOs such as the Grenville Province, requires geochronometers such as zircon, that are stable at high (>700^{o}C) temperatures and are able to record a series of individual tectono-metamorphic events during orogenesis and not just the final phase (Harley *et al.*, 2007). For this reason, samples collected to determine/constrain the age of deformation, included granitic leucosomes, injections and pegmatite dykes that were emplaced during or shortly after the observed deformational phase in the host rocks, which can be inferred from their location within deformation-induced structures (e.g. strain-shadows and boudin necks) or their cross-cutting relationships with the gneissosity of the host rocks respectively. Folded pegmatites or granitic dykes that cross-cut the tectonic fabrics but lack evidence of strongly deformed quartz grains, suggest that the intrusion was emplaced during a deformational event, shortly after the main fabric in the host rocks was developed but quartz had not yet crystallized and deformed plastically (herein referred to as suprasolidus deformation). Ages derived from these samples are therefore, representative of syn-to late-deformation events.

Once the samples were cleaned and cut, the appropriate rock volumes (grain size dependent) were sent for crushing, zircon mounting, cathodoluminescence (CL) imaging and analysis by laser ablation inductively coupled plasma mass spectrometry (LA-ICP-MS) at the Boise State University Isotope Geology Laboratory. Analysis by LA-ICP-MS was favored due to the potential development of multiple zones within the zircons and the high spatial resolution (ca. 20 microns) of this technique, which means individual zones can be targeted. In addition this technique allows for the higher number of analytical points that is required for a statistically robust dataset (Spencer *et al.*, 2016) and the ability to yield trace element values for the zircon spots. Trace elements are particularly useful in calculating temperature information (Ti-in-zircon thermometry; e.g. Watson *et al.*, 2006) and for discriminating between different age populations that may have resulted due to differing geochemical or metamorphic conditions during grain growth (Kohn, 2016)

Analyses and the presentation of age data follows the recommendations of (Horstwood *et al.*, 2016). All ages in this study are reported using the $^{207}Pb/^{206}Pb$ isotopic system, either as individual spot dates or as weighted mean ages. It is important to note that for each age population with

equivalent dates a $^{207}Pb/^{206}Pb$ weighted mean age (probability of fit, PF > 0.05) is first calculated using errors on individual dates that do not include a standard calibration uncertainty (annotated within parentheses), and then a standard calibration uncertainty is propagated into the error on the weighted mean date (annotated without parentheses). Not propagating the standard calibration uncertainty is warranted for data acquired during the same analytical session and with the same standards, which allows to evaluate if the respective age populations define distinct ages or overlap with each other. On the other hand, standard calibration uncertainties need to be propagated for those analyzed in different sessions or compared to ages in other studies. Temperatures for zircon crystallization were calculated from the pressure dependant Ti-in-zircon thermometer calibration of Hofmann *et al.* (2014) and presented as the upper limit of the interquartile range (UQ), following Tomkins *et al.* (2007). Further detailed descriptions of the processes and specifications for geochronology and geo-thermometry analyses are found in section chapter 4.

1.5 Structure of thesis and co-author statement

1.5.1 Structure of thesis

Following this introduction (chapter 1), which provides an overview and objectives of the project, the results of this work are presented in three core chapters (2-4). Each represents a stand-alone study, either as a novel virtual presentation within Google Earth (chapter 2), a conventional thesis chapter (chapter 3) or an accepted manuscript (chapter 4). The findings from the three chapters collectively provide for an improved understanding of the Grenville Orogen in western Quebec and allow for a new geodynamic model to be proposed for the evolution of the Parautochthonous Belt during the Rigolet phase (see summary in chapter 5).

Chapter 2 is entitled *"Transect of a Large Hot Orogen: A novel virtual tour through the Grenville Province of Western Quebec*" and is co-authored by Christopher Lambert, Félix Gervais, James Crowley, Charles Kavanagh-Lepage and Abdelali Moukhsil. This chapter is presented as a novel, self-guided virtual tour, hosted within a Google Earth digital platform. Initially created as the virtual replacement for a guidebook and physical field excursion along the Hw117 transect for the GSA annual meeting (Lambert *et al.*, 2020), this new contribution was refined and supplemented to constitute a chapter of this thesis as a novel way to present field-based data and integrate into a new era of virtual and interactive publications, and ultimately, to increase the visibility of

geological research in the Grenville Province. Designed as a stand-alone tour and as the first of the core-chapters to this thesis, the virtual tour provides an overview of the project and examples of various key outcrops along the transect investigated to meet research objectives. The content of this tour also includes data that augments the findings presented in the two other chapters of this document (chapters 3-4); new U-Pb geochronology results from syn-late deformational pegmatites and granitic samples that provide clues as to the age of deformation within the various tectonic segments along the Hw117 transect; detailed descriptions of the dominant structures within the various tectonic domains along the transect; and a new geological cross section. It is important to note that while the one objective (no 5 in section 1.3) of the thesis was to present this chapter in a virtual format (referred to as v-chapter 2 hereafter), new data that forms part of the v-chapter 2, particularly new geochronology and structural observations, are also presented in the physical chapters of this thesis document (analog chapter 2) as they form a crucial part of this study and are not presented elsewhere in this dissertation. Furthermore, detailed figures and annotated field photos pretended in the virtual tour also form a significant contribution to the thesis but as there are too many to present in the physical chapter of this thesis, they are annotated with the prefix 'v2' (see detailed explanation in section 2.3).

As a virtual and interactive tour, this section fulfils object 5, whereas the data presented in this section collectively contributes to objectives 1-4, by providing an improved understanding of the geology along the transect. Furthermore, abundant pictures and tips on how to explore the outcrops in 'Google Street View' aims to place reader in the shoes of the geologist in the field. Instructions on accessing the virtual tour (v-chapter 2) are found here: https://drive.google.com/file/d/1a_r9LhmVNSqsz_TtO1AIK0hwE8FruyBg/view?usp=sharing.

Chapter 3 is entitled "*Unravelling The Tectonic Architecture Of The Grenville Province Along Hw117: Insights From The Geochemical Correlation Of Mafic Suites*". While this chapter follows the format of a conventional thesis chapter, it forms the backbone of a stand-alone investigation into understanding the complex 1st order architecture across the Hw117 transect that is highlighted by the presence of numerous allochthonous RT rocks distributed within the 'sea' of parautochthonous gneisses (see sections 1.2.5 and objective no. 2 in section 1.3). As such, the geological context required for this section is presented in section 1.2. This investigation builds on pre-established and innovative methods that delineated major tectonic boundaries (e.g. the ABT) of the Grenville Province in Ontario, by comparing the major and trace element geochemistry of

unknown mafic bodies to those that have a known magmatic affinity to different structural levels of the Grenville Orogen (Ketchum and Davidson, 2000). This chapter systematically compares the geochemistry, specifically key immobile trace elements (REEs and HFSEs), from thirty mafic samples collected within parautochthonous domains exposed along the Hw117 transect, against various pre-Grenvillian mafic suites that have a known age and a magmatic affinity to either the Superior Province (i.e. autochthonous) or the AB surrounding the study area. Integrated with field observations in this chapter and those presented later in the thesis (chapters 1, 2 & 4), the results of this chapter contribute to objectives 1, 2 and 4 by showing that the 1st order architecture of the Grenville Province is characterized by numerous mafic-dominated outcrops that likely have an affinity to the allochthonous RT, enveloped within migmatitic parautochthonous gneisses. This suggests that the architecture is more complex than previously perceived and requires an alternative tectonic model to be proposed (chapter 5) as this model is inconsistent with the current conceptual models advocating NW-directed, thick skinned thrusting for the evolution of the late-stages (Rigolet) of the Grenvillian Orogeny.

Chapter 4 is entitled "*Protracted melt-present deformation during the Rigolet phase of the Grenvillian Orogeny. Insights from geochronology along the highway 117 transect through the Grenville Province in western Quebec, Canada*" and represents a published manuscript with Precambrian Research that was accepted on 1 December 2022. The primary author of the manuscript was Christopher Lambert (Polytechnique Montréal) and was co-authored by Félix Gervais (Polytechnique Montréal), James Crowley (Boise State University), Abdelali Moukhsil (MERN), and Charles Kavanagh-Lepage (Polytechnique Montréal). In this chapter, field observations and LA-ICP-MS U-Pb zircon geochronology of six, syn-late deformational granitic leucosomes and pegmatitic dykes, are used to investigate the age of melt-present deformation within the PB of the Grenville Province in western Quebec. The new geochronology results and Ti-in-zircon thermometry presented herein, provides the first recorded evidence for variable fluid-fluxed melting and deformation within the PB over a protracted period during the Rigolet. The results of this section fulfill objectives 1-3 and are used to propose a tectonic model for the evolution of this part of the PB in western Quebec during the Rigolet phase, whereby fulfilling objective 4.

Chapter 5 integrates the findings of the three core chapters and summarizes the data that led to a new conceptual model for this area (objective 4). The chapter concludes with the outlook and recommendations for further research in the Grenville Province.

1.5.2 Co-author statement

The chapters discussed above would not have been possible without the contributions from the respective co-authors. As first author in all chapters, Christopher Lambert formulated the research questions, undertook the literature review, all data collection and structural, geochronology and geochemical data interpretations. He was also responsible for the written work (unless stated otherwise), creation of all the figures presented in these chapters, as well as the submission of chapter 4 to Precambrian Geology. As supervisor, Félix Gervais was responsible for formulation of the general research topic, recommendations and technical advice in all the disciplines addressed, as well as chapter revisions and proofreading. Félix is also responsible for most of the content presented in stops 19-21 of the virtual tour (chapter 2). Abdelali Moukhsil was responsible for general recommendations and edits of the preliminary reports for MERNQ that formed the basis of the field work required for the chapters. Because guidance/advice was required from a geochemist, Jean Bédard completed an initial review and gave general recommendations, comments and feedback for chapter 3. James Crowley was responsible for the analysis and reduction of the geochronology data presented in chapters 2 and 4, some written contributions to the methodology presented in chapter 4, as well as helpful comments and feedback of this section. Charles Kavanagh-Lepage was responsible for general reviews, helpful comments and proofreading in chapters 3 and 4, as well as figure editing and troubleshooting of the virtual tour (chapter 2).

1.5.3 Other contributions by author

The following two reports written for MERN present preliminary results of this work:

- Lambert, C. W., Gervais, F., & Moukhsil, A. (2018). Reconstruire l'architecture de l'ouest de la Province de Grenville, Québec: Résultats préliminaires de la cartographie géologique le long de la route 117. Rapport préliminaire. MB-2018-08. pp 59. Ministère de l'Énergie et des Ressources naturelles. Quebec City, Quebec.

- Lambert, C. W., Gervais, F., Moukhsil, A., Crowley, J. L., & Bonnet, A.-L. (2019). Reconstruire l'architecture de l'ouest de la Province de Grenville, Québec : résultats préliminaires de la cartographie, de l'analyse cinématique et de la géochronologie. Rapport préliminaire. MB-2019-05. pp 65. Ministère de l'Énergie et des Ressources naturelles. Quebec City, Quebec.

This work is also presented at the following conferences:

- Lambert, C. W., Gervais, F., Bédard, J. H., & Moukhsil, A. (2020). Using big datasets to trace tectonic boundaries in the western Grenville Province. Goldschmidt (Virtual). 21-26 June 2020.
- Lambert, C. W., Gervais, F., Crowley, J. L., & Moukhsil, A. (2020). Evidence for extensive melt-present deformation and dismembering of the overlying Allochthonous crust during late-Grenvillian orogenic flow. Geological Society of America. (Virtual). 26-30 October 2020.
- Lambert, C. W., Gervais, F., Kavanagh-Lepage, C., & Crowley, J. L. (2020). Transect of a Hot, Long Orogen: The Grenville Province of Western Quebec. Virtual field guidebook. Geological Society of America (Virtual). 26-30 October 2020.
- Lambert, C. W., Gervais, F., Moukhsil, A., & Crowley, J. L. (2019). Reconstructing The Evolution Of The Grenville Province In Western Quebec: Time Constraints And Modes Of Mid-Crustal Deformation During The Ottawan And Rigolet Phases Of The Grenvillian Orogeny. Petrochron 2019. Potsdam, Germany. June 2019.
- Lambert, C. W., Gervais, F., & Moukhsil, A. (2018). Delineation and Characterization of Tectonic Domains in the Western Grenville Province - Preliminary Results of Geological Mapping Along Highway 117, Québec, Canada. 53rd Annual GSA Northeastern Section Meeting. https://doi.org/10.1130/abs/2018NE-310718
- Lambert, C. W., Gervais, F., Moukhsil, A., & Crowley, J. L. (2018). The architecture of the Grenville Province in western Quebec: Insights from field work and U-Pb geochronology. Quebec Mines poster. 19-22 November 2018.

CHAPTER 2 TRANSECT OF A LARGE HOT OROGEN: A NOVEL VIRTUAL TOUR THROUGH THE GRENVILLE PROVINCE OF WESTERN QUEBEC: GEOCHRONOLOGY AND STRUCTURAL CONTRIBUTIONS

2.1 Introduction

The architecture of the Grenville Province along the Hw117 transect was previously characterized through a series of regional-scale stops that highlighted key examples of the proposed architectural superstructure at that time (e.g. Indares and Martignole, 1985, 1990). Since then, field constraints and developments in the conceptual models for the Grenville Province have led to a refined architecture and evolution for the lower crust. The new characterization of the (sub)domains along the transect, particularly those located structurally above the Grenville Front Thrust Zone (GFTZ) and below the orogenic lid (i.e. RDT, RT, LDT domains) where there was a notable lack of structural and age data (Fig. 1.7), forms a key contribution to this study and the results are largely presented in the virtual chapter 2 (v-chapter 2) of this thesis (link provided in section 1.5.1). As an independent project, the tour integrates data from other chapters of this thesis (discussed in section 1.5.1) and presents key field outcrops and findings driving this research objectives but importantly, also presents the results and interpretations of new data crucial to this study. As these new data are unpublished and not presented elsewhere the thesis, the new U-Pb geochronology results; the structural characterization of the various tectonic segments; and a novel geological cross section along a 140 km stretch of the Hw117 transect (see line A-B in Fig. 2.1), are also presented in this chapter of the document.

Detailed figures and annotated field photos that are pretended in the virtual tour form a significant contribution to the virtual chapter but as it is impractical to present them all again in this analog chapter 2 of the thesis, the figures in the tour are referenced following the example: v2.9.16B, which indicates that the figure (16B) is in virtual tour (v2) at the stop number (9). The “stop” numbers referring to the various cross section segments presented the tour are annotated by the Roman numerals (i-v; e.g. v2.ii.29F).

Finally, whereas the virtual tour presents a summary and conclusion based on data integrated from all of the chapters of this thesis, the final section of this analog chapter only provides a synopsis of the geochronology and structural findings presented in the sections below.

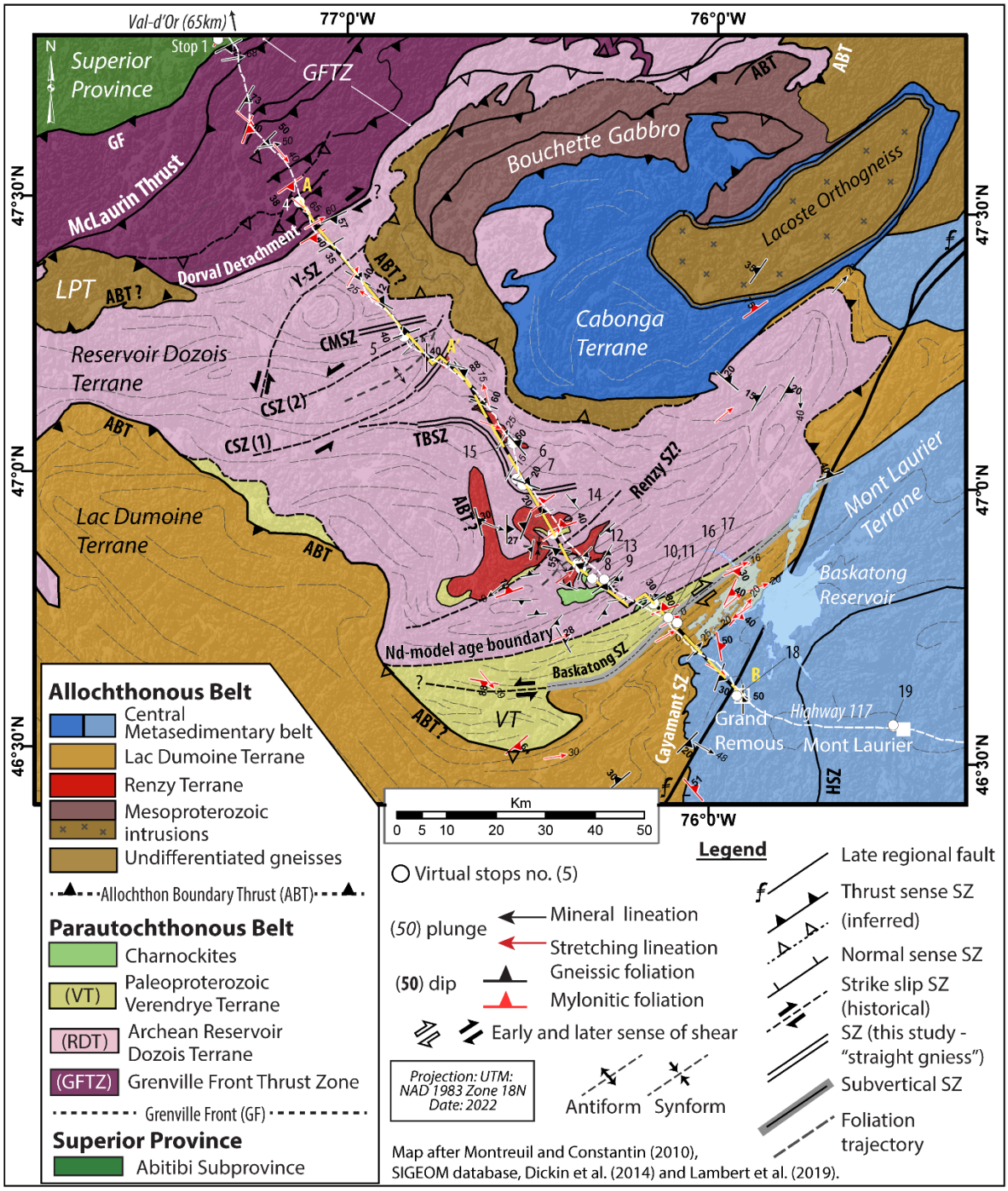

Figure 2.1. Subdivision of the Grenville Province along part of the Hw117 (white line) geo-traverse and location of the cross section (yellow line A-A'-B) that is presented later in this chapter (Fig. 2.5). Note the map also shows the virtual stop locations. References used for map creation are the same as in Fig. 1.7.

2.2 Geochronology

The following section provides a detailed description and interpretation of two syn-late granitic samples analysed for U-Pb zircon ages by LA-ICP-MS to date select deformation events along the Hw117 transect. The results of individual spot analyses and zircon images are presented in the Appendix A, whereas the detailed methodology on the procedures and decisions on isotopic systems chosen to represent these ages (i.e. $^{207}Pb/^{206}Pb$) and metadata for the analyses is presented in Appendix C and D, respectively.

2.2.1 Sample CL6144: Syeno-granite intrusion in subvertical LDT gneisses (virtual stop no. 16)

2.2.1.1 Outcrop and sample description

Sample CL6144 was collected from a 40 cm thick, pink syeno-granitic intrusion within subvertical dipping gneisses that define the core of the BSZ (Fig. 2.2A). The sampled dyke obliquely cross-cuts previously deformed gneisses (see stippled box; Fig. 2.2B) of granodioritic and charnockitic augen-gneisses compositions that are mostly garnetiferous and tentatively interpreted as part of the LDT. The dyke is thus interpreted to be intruded late, relative to deformation in the host gneisses.

2.2.1.2 Zircon morphology

Most zircon grains in this sample are stubby and range in size from 250-400 μm with euhedral dimensions and faceted edges (Fig. 2.2C). Equant grains and slender prismatic grains constitute less than ca. 10% of those in the sample. Two types of zircon zones are identified according to differences in their textures under CL. Type 1 (green in Fig. 2.2C) is characterized by prismatic (1:4, W:L) grains with low CL intensities and have homogenous to planar growth zonation patterns. Type 2 (red in Fig. 2.2C) is defined by stubby and equant grains similar in CL reflectance to type 1 but have distinctive oscillatory zonation patterns. There is no other clear textural evidence to support a relative chronological relationship between types 1 & 2.

2.2.1.3 Zircon chemistry and geochronology

Seventy-one analyses across types 1 & 2 yielded dates with < 10% discordance and all analyses yielded Grenvillian dates (Fig. 2.2G). The two populations are not easily differentiated based on their trace elements as they both have steep REE_{CN} patterns with prominent negative Eu and

positive Ce anomalies (Fig. 2.2D); similar $HREE_{CN}$ slopes and ranges in ∑REEs (Fig. 2.2F). They also have indistinguishable Th (132-548 ppm) and U (235-1030 ppm) concentrations, resulting in similar average Th/U ratios (that average 0.50, Fig. 2.2E). Despite their distinct morphologies, the similarity in their trace element characteristics and overlapping ages (excluding external calibration error) for both types lead us to combine the analyses to yield a $^{207}Pb/^{206}Pb$ weighted mean age of 1016 ± (5) 9 Ma (MSWD = 1.4, PF = 0.018, n= 67/71; Fig. 2.2I).

2.2.1.4 Interpretation

The $^{207}Pb/^{206}Pb$ age 1016 ± (5) 9 Ma is interpreted as the age of average crystallization for the dyke, which provides a minimum estimate for ductile deformation of the subvertical host gneisses. If the last movements along the BSZ are characterized by sinistral shear, as proposed by Martignole and Friedman (1998), this movement must have occurred before this date.

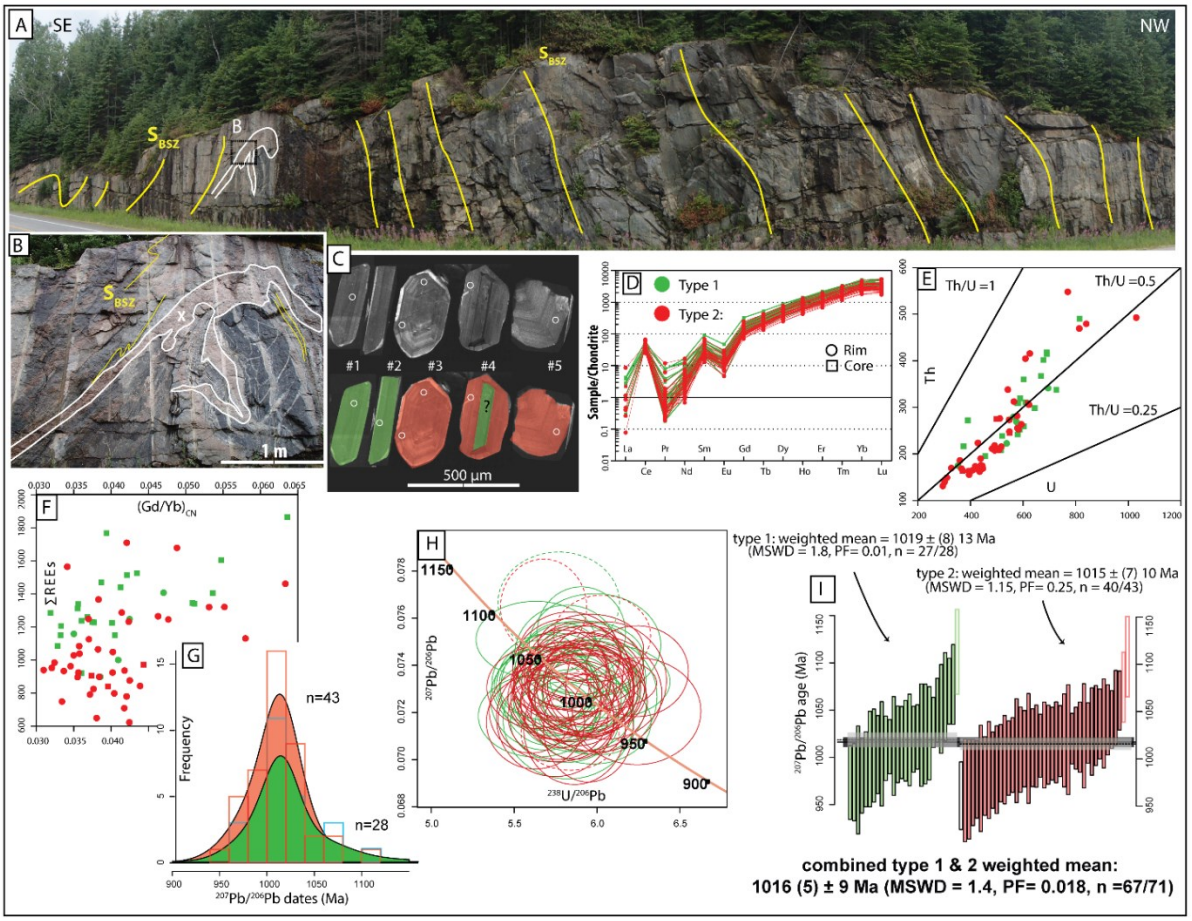

Figure 2.2. Photos and graphics summarising the field relationships and results of LA-ICP-MS geochronology from a late dyke in the BSZ (stop 16; v-chapter 2). (A) Steep dipping gneisses of the BSZ. (B) Late-tectonic pink granitic dyke that cuts the steep gneissic fabric sampled for geochronology. (C) Examples of zircon grain morphology and ablation spot locations. (D) Chondrite normalized REE spidergram and (E-F) bivariate trace element diagrams used to aid in the distinction of the various zircon zones. (G) Kernel density histogram of spot dates within the sample. (H). Tera-Wasserberg plot of the Grenvillian zircon populations. (I) Weighted mean $^{207}Pb/^{206}Pb$ ages of the Grenvillian zones. The uncertainty of the ages is reported without (in parentheses) and with the propagation of external calibration errors.

2.2.2 Sample CL8025 granitic dyke along the SE margin of BSZ (virtual stop no. 17)

2.2.2.1 Outcrop and sample description

Sample CL8025 was collected from a 30 cm thick granitic dyke that crosscuts migmatitic gneisses, likely part of the Lac Dumoine Terrane, deformed by the BSZ (Fig. 2.3A). Although this locality is ca. 2 km SE of CL6144, the affinity of these migmatitic gneisses to the LDT remains to be confirmed because the granitic and amphibolitic protoliths at this location are atypically garnet-poor (Lambert *et al.*, 2019). The subvertical planar fabric (dip direction/dip = 145/85) and shallow lineation (trend/plunge = 230/10) in the migmatitic gneisses are consistent with measurements along the BSZ (Martignole, 1995; Martignole and Friedman, 1998; Lambert *et al.*, 2019). The sampled dyke is one of multiple dykes that are emplaced throughout the outcrop and although they are largely discordant, these dykes contain numerous co-genetic stringers that extend up to a meter in length, parallel to the gneissosity and earlier generations of leucosome in the wall rocks (Fig. 2.3A). The pink color, provided by the abundance of potassic-feldspar in these dykes and their interconnected stringers allows for distinction from the relatively older, concordant and whiter-colored leucosome generations in the wall rocks. Emplacement of the dyke is interpreted to be synchronous with the latest increment of shear strain along the BSZ because the contacts of the dykes and wall rocks preserve cuspate-lobate geometries and the dyke contains quartz ribbons that are parallel to the gneissosity (Fig. 2.3A). Several winged porphyroclasts within the concordant

stringers are also consistent with dextral shearing (Figs. 2.3B-C), inferred for early stages of strain along the BSZ (Martignole, 1995; Martignole and Friedman, 1998).

2.2.2.2 Zircon morphology

Zircons in this sample are mostly whole or fractured elongated prismatic (1:5, W:L) euhedral grains that range from 250-750 μm in length (Fig. 2.4A), whereas stubby to equant grains (ca. 100-300 μm) make up <5% of those in the sample. Three types of zones are identified according to differences in their textures under CL. Type 1 (green in Fig. 2.4A) is defined by stubby to equant whole grains (#1 in Fig. 2.4A) or rare cores mantled by type 3 (#2 in Fig. 2.4A). They are characterized by euhedral habits, weak (meso-melanocratic grey) CL-reflectance and oscillatory (#3 in Fig. 2.4A) to seemingly homogeneous growth zonation patterns (Fig. #1 in Fig. 2.4A). Type 2 (blue in Fig. 2.4A) is defined by whole grains (#4 in Fig. 2.4A) or cores of prismatic grains (#5&6 in Fig. 2.4A) that have planar zonation patterns with both high (light/mesocratic) and low (dark/grey meso-melanocratic) CL intensities. Notably, no clear overprinting relationships were observed between type 1 and type 2. Type 3 (red in Fig. 2.4A) is defined as higher CL intensity rims (50-100 μm wide) around type 1 and type 2 cores (#5&6 in Fig. 2.4A) and have homogenous or broad oscillatory growth zonation patterns in both the prismatic and equant grains. No grains defined entirely by type 3 are identified in CL.

2.2.2.3 Zircon chemistry and geochronology

Thirty-seven analyses across the three different textural types yielded dates with < 10% discordance and all three zones yielded Grenvillian ages (Fig. 2.4E). They have steep $HREE_{CN}$ patterns with prominent negative Eu and positive Ce anomalies (Fig. 2.4B), although type 3 has higher Th/U ratios and generally lower ∑REE than the other two types (Figs. 2.4C-D). Despite their textural and some trace element variations, the three zones yield overlapping $^{207}Pb/^{206}Pb$ weighted mean ages (Fig. 2.4F-G) and are thus, combined to yield an average $^{207}Pb/^{206}Pb$ weighted mean age of 1040 ± (6) 9 Ma (MSWD 1.09, PF = 0.33, n = 36/37; Fig. 2.4G).

2.2.2.4 Interpretation

The 1040 ± (6) 9 Ma weighted mean age is interpreted as the average crystallization age for the dyke, which constrains the timing of the last increments of dextral shearing along the BSZ.

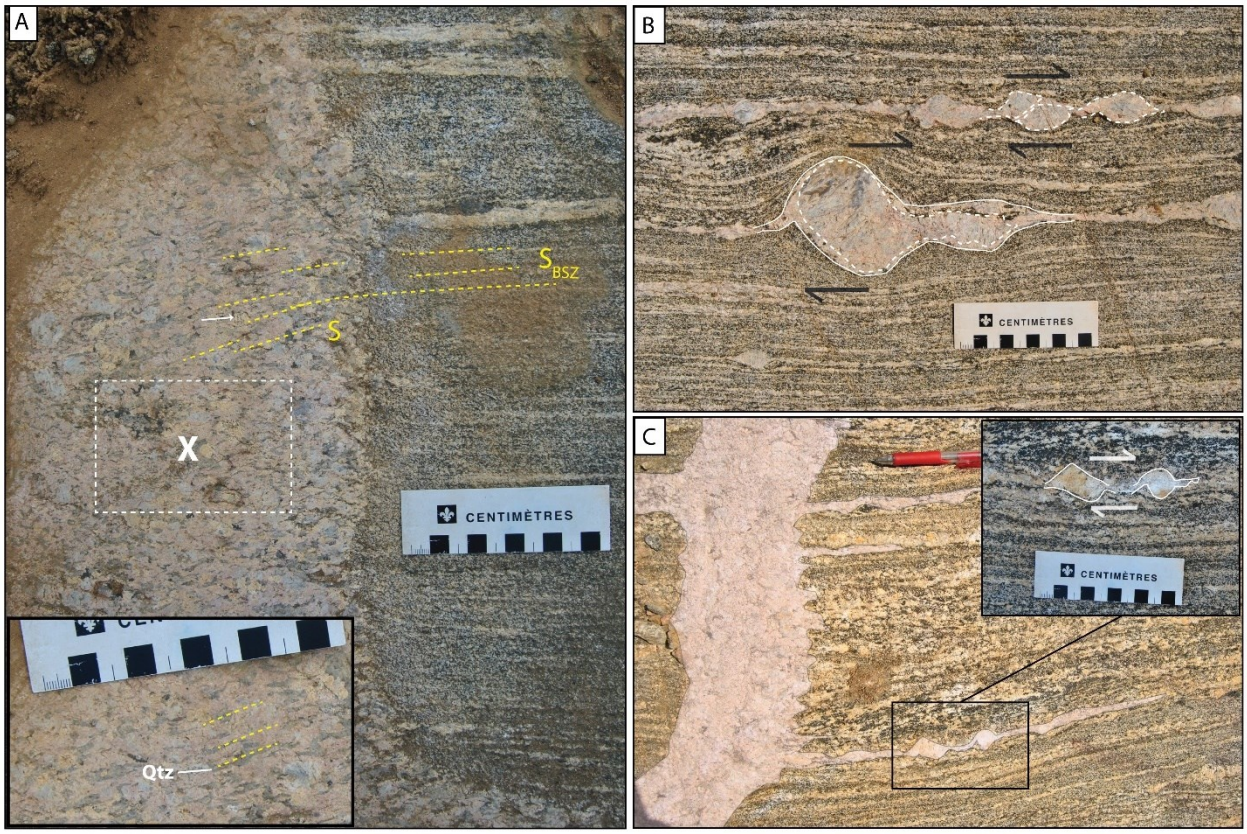

Figure 2.3. Field photos of syn-late tectonic granitic dykes and concordant stringers that intrude the BSZ (stop 17; v-chapter 2). (A) A thick (ca 30 cm) granitic dyke sampled for geochronology, crosscuts the gneissosity but also contain aligned quartz ribbons in the dyke (inset). (B) Multiple winged porphyroclasts define kinematic indicators within the granitic veins and indicate a dextral strike-slip shear component. (C) Examples of a granitic dyke that connects to cogenetic, foliation parallel veins with kinematic indicators indicating a dextral sense of shear. Note the cuspate-lobate boundaries on the dykes which indicate that they were subjected to deformation after intruding the gneisses.

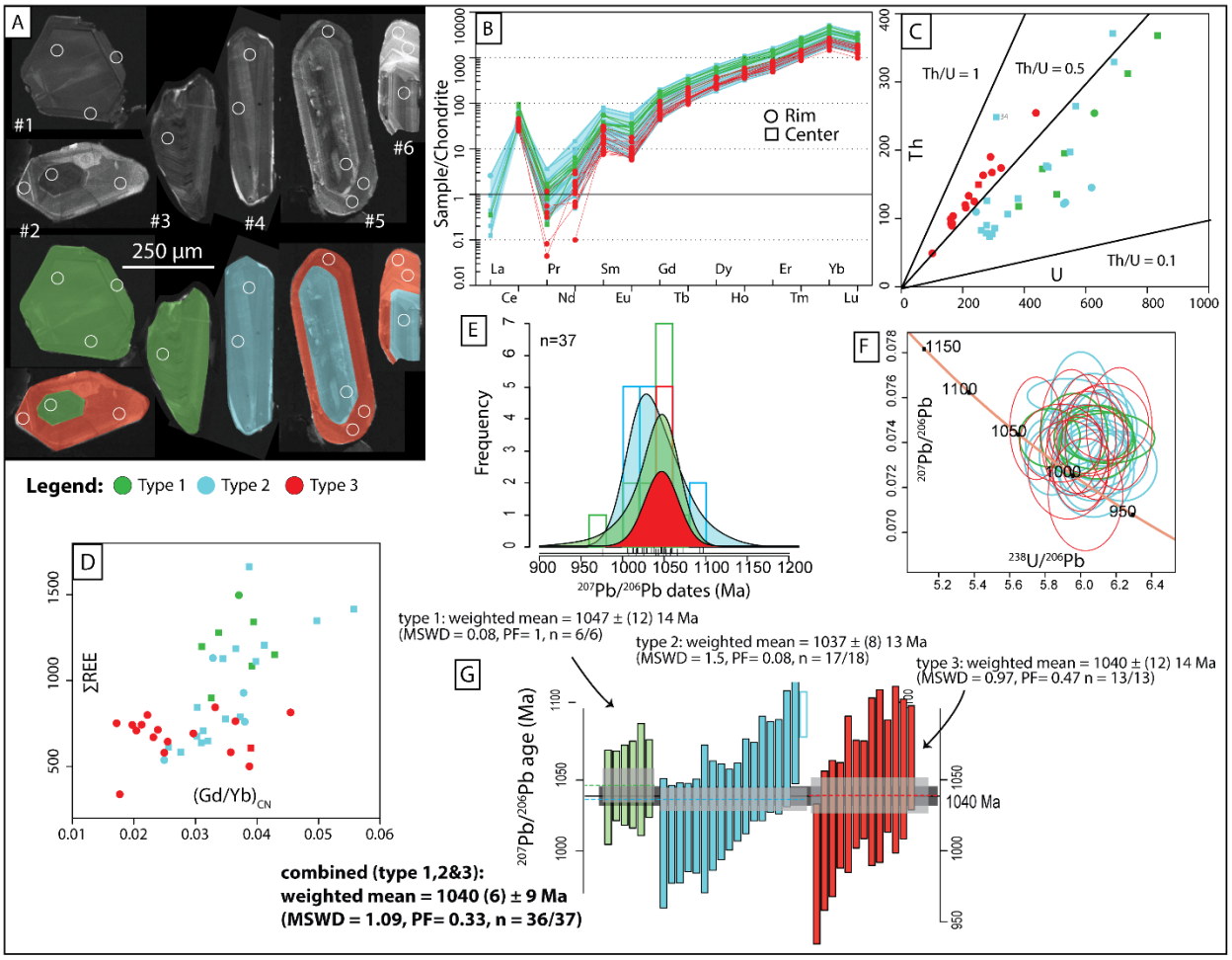

Figure 2.4. Graphics summarising the results of LA-ICP-MS geochronology for sample CL8025 (stop 17; v-chapter 2). (A) Examples of zircon grain morphology and ablation spot locations. (B) Chondrite normalized REE spidergram and (C-D) bivariate trace element diagrams used to aid in the distinction of the various zircon zones. (E) Kernel density histogram of spot dates within the sample. (F). Tera-Wasserberg plot of the Grenvillian zircon populations. (G) Graphic for a weighted mean $^{207}Pb/^{206}Pb$ ages of the Grenvillian zones. The uncertainty of the ages is reported without (in parentheses) and with the propagation of external calibration errors.

2.3 A new geological cross section for the Hw117 transect

The novel geological cross-section (Figs. 2.5-2.6) and structural summary of the domains along the Hw117 transect that are presented in the virtual tour represent fundamental contributions in this thesis. The following section presents the characterization of the various structural (sub)domains from NW to SE along the transect, with a focus on the domains located between the GFTZ and orogenic lid. Structural data discussed herein is presented along the corresponding sections on the cross-section. The number sign (octothorp #) is used in this chapter to refer to specific stereoplots and schematic diagrams presented in Figure 2.5. Information on the collection and presentation of the structural data and construction of the cross section are presented in the methodology section of this thesis (section 1.4), whereas Table 2.1 provides a summary of the structural features depicted on the cross-section, their abbreviations and literary sources.

2.3.1 Structures in the Grenville Front Thrust Zone (GFTZ)

The dominant planar fabric within the GFTZ is a gneissosity (S_A) that is defined by compositional banding of transposed migmatitic leucosomes or injected felsic magmas, as well as the preferred alignment of biotite, feldspars, and garnet aggregates (Figs. v2.i.29D-F). Granoblastic textures are common and in outcrops, where migmatitic banding is underdeveloped, planar fabrics are often difficult to discern (Fig. v2.i.29E). This foliation forms parallel and axial planar to the folded leucosomes (Fig. v2.i.29D), while transposed folds present evidence for an earlier, reworked tectonic fabrics. Despite localized, decameter scale folding around NW-verging open to closed folds, the gneissic foliation generally has moderate (30-40^o) SE dips throughout the GFTZ (#1 in Fig. 2.5).

Linear fabrics in the GFTZ are characterized by quartz and plagioclase stretching lineations (Fig. v2.i.29G) and mineral alignment of biotite and garnet aggregates (Figs. v2.i.29H). Both sets of lineations have down-dip plunges to the SE (#1 in Fig. 2.5) and although only measurements for the part of the GFTZ that intersects the cross section are shown, these measurements are consistent with those observed further NW (e.g. Martignole and Martelat, 2005; Lambert *et al.*, 2018, 2019).

Numerous SW-NE trending, discrete (<10 m wide) mylonitic shears with down-dip stretching lineations cut through the GFTZ, consistent with thrust sense (Figs v2.4.11A & Fig. v2.4.11F) and normal sense kinematics (stop 4, Fig. v2.4.11G) that are thought to correlate to Grenvillian (ca.

1000 Ma) foreland-ward thrusting and extensional reactivation respectively (Martignole and Martelat, 2005; Rivers, 2009). Whereas there is evidence for normal-sense deformation (Fig. v2.i.29F), some of which may be Grenvillian within this part of the GFTZ (Martignole and Martelat, 2005), the age of the penetrative fabric (S_A) is yet to be confirmed. Preliminary geochronology results from syn-deformation leucosomes (stop 3) and thrust-hosted pegmatites yielded Archean ages (stop no 4; Martignole and Friedman, 1998), which indicates that Grenvillian metamorphism and reworking of the Archean gneisses in this part of the GFTZ may be limited and was probably localized along discrete shear zones or was too short-lived to mobilize melt phases used for conventional geochronology. Until detailed P-T-t-D petrochronology studies are conducted, the timing of metamorphism and deformation in particular, within the GFTZ along Hw117 remains poorly constrained.

2.3.2 Structure across the Dorval Detachment (DD)

The DD separates the granulite faces gneisses of the GFTZ (stops 3-4) from the amphibolite grade Reservoir Dozois Terrane (stops 5-9) in the footwall and hanging wall respectively (Indares and Martignole, 1990; Martignole and Martelat, 2005). As such, it was previously considered as a crustal scale transtensional shear zone that offsets the Moho and played a major role in the exhumation (unroofing) of the GFTZ sometime between 1020 Ma and 960 Ma (Martignole and Martelat, 2005; Hynes and Rivers, 2010; Rivers, 2012). Despite being clearly imaged on seismic datasets (Martignole and Calvert, 1996; Martignole *et al.*, 2000) the DD is not easily identified in the field as there is no abrupt subdivision in lithology or metamorphic grade were this structure intersects the surface. Instead, a ca. 6 km wide zone across the DD is marked by the sporadic appearance of amphibole-bearing gneisses (Lambert *et al.*, 2018) and the gradual disappearance of metamorphic orthopyroxene in diorite and granodiorite gneisses and their leucosomes from the footwall into the hanging wall (Lambert *et al.*, 2019). This suggests the DD may represent an imbricated transitional zone.

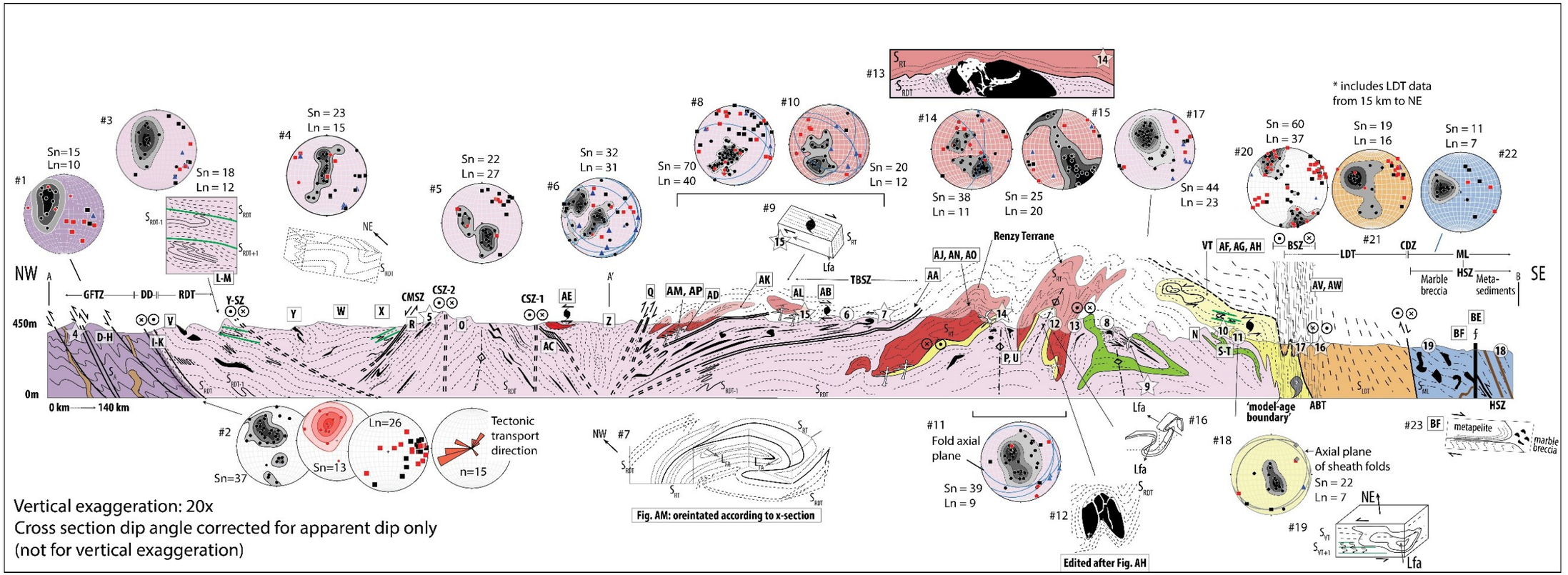

Figure 2.5. Geological cross section along line A-B (see Fig. 2.1), focusing on structural elements between the Dorval Detachment and the Baskatong Shear Zone along the Hw117 transect. Stereoplots depict planar and linear fabrics measured along the transect and summarize their trends in the different tectonic domains from NW to SE. Rose diagrams present the direction of ductile tectonic transport inferred from micro-to decameter-scale kinematic indicators. In the rose diagrams, the direction of transport ('rose petals') considers the movement of the upper/top of the rock packages relative to N (0º), irrespective of normal, thrust, or strike slip type tectonics. The points on the rose diagram function as linear features and provide an indication of the plunge angle that correspond to the respective directions and can be used as a rough indicator of down dip (steep lineation = thrust/normal sense) or strike slip (shallow) type tectonics. Schematic diagrams at select locations along the transect are also presented to aid in the visualization of various structural elements such as fold geometries and the relationship between the fabrics. Unit colors are the same as in Fig. 2.1. The location of the field stops, geochronology samples and figures discussed herein, are also annotated on the cross section. Note that the number sign (#) is used in the text to refer to specific stereoplots and schematic diagrams in the text.

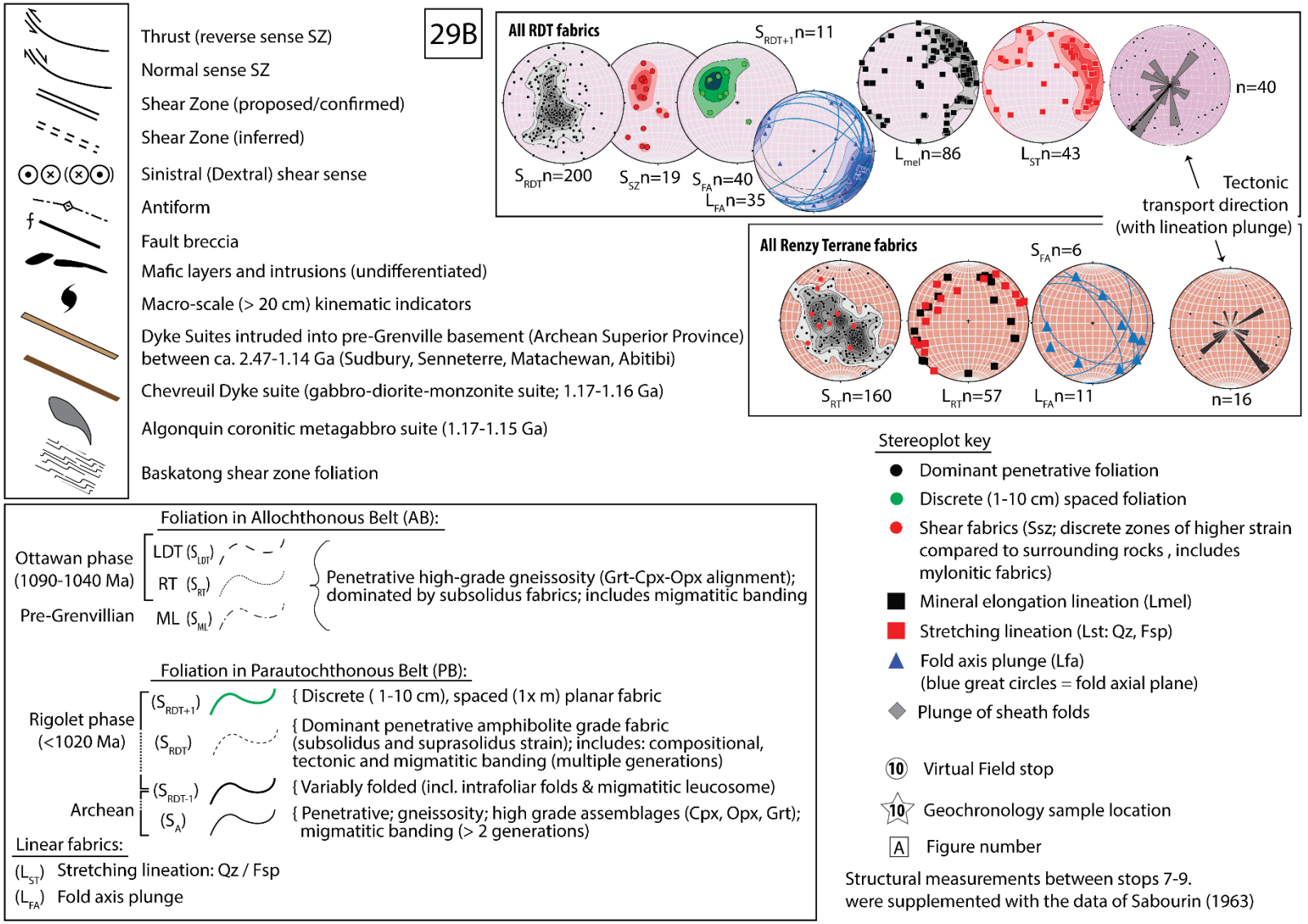

Figure 2.6. Legend to the cross-section in Fig. 2.5. Includes stereoplots summarizing tectonic fabrics collected across the RDT and RT.

Table 2.1. List of abbreviations and descriptions of structures depicted on the cross section and discussed in this chapter.

Abbreviation	Name	Characteristics/comments	Age	References
GFTZ	Grenville Front Thrust Zone	Imbricated thrusts and reactivated normal sense shear zones	Thrusting (Archean; this study and unpublished); Normal sense (Rigolet phase; Martignole & Martelat, 2005)	(Wynne-Edwards, 1972; Martignole & Martelat, 2005)
LDT	Lac Dumoine Terrane	Mid-lower crust of the Allochthonous Belt	Metamorphism (Ottawan phase; 1090-1020 Ma)	(Rivers, 2008)
ML	Mont Laurier Terrane	Orogenic lid to Grenville Orogen. Lack pervasive Grenvillian fabrics	Metamorphism (Elzevirian ca. 1245–1220 Ma and Shawinigan ~ 1245–1220 Ma)	(Rivers, 2012)
RT	Renzy Terrane	Fragments of allochthonous crust incorporated into parautochthonous belt during Rigolet phase?	Granulite facies metamorphism (1070 Ma; Childe et al., 1993)	(Indares and Martignole, 1990; Montreuil and Constantin, 2010)
RDT	Reservoir Dozois Terrane	Archean Parautochthonous Belt. Metamorphosed and deformed during Rigolet phase (1020 - 968 Ma)	Metamorphosed/deformed during Rigolet phase (ca. 1020 - 968 Ma; Rivers, 2008; this study)	(Rivers 2008, 2009; this study)
VT	The Vérendrye Terrane (previously unnamed)	Paleoproterozoic parautochthon. Extensive sheath fold development.	Deformation ca. 1008 Ma (this study)	(Guo and Dickin, 1996; Dickin et al., 2014; Lambert et al., 2018)
ABT	Allochthonous Boundary Thrust	1st order structure that juxtaposes Allochthonous Belt over the Parautochthonous Belt. Base of mid-crustal ductile channel	Convergence (ca. 1090-1040 Ma); Collapse (normal sense reactivation; ca. 1050-1020 Ma)	(Rivers, 1989, 2008, 2012, 2015 and references therein; Ketchum et al., 1998)
BSZ	Baskatong Shear Zone	Subvertical shear zone ca. 2-4 km thick	Dextral shear sense (1040 Ma; this study); Sinistral shear sense (1020 Ma; Martignole & Friedman, 1998)	(Martignole and Pouget, 1994; Martignole and Calvert, 1996)
DD	Dorval Detachment	Sinistral and normal sense (transtensional) shear zone that intersects the Moho. Responsible for exhumation of the GFTZ	Deformation: between 1020 - 960 Ma (Martignole and Martelat, 2005)	(Wynne-Edwards, 1972; Martignole et al., 2000; Martignole & Martelat, 2005)
CDZ	Cayamant Deformation Zone	Boundary between Grenvillian (NW) and Pre-Grenvillian (SE) fabrics. Dominated by marble tectonites	Deformation: before ca. 1170-1160 Ma (Corriveau and van Breemen, 2000)	(Hanmer and Ciesielski, 1984; Sharma et al., 1995)
CMSZ	Comatose Shear Zone	Banded quartzo-feldspathic gneisses (meta-tonalites and migmatites) and mafic layers; possible extension of TBSZ? Interpretation from field and VD maganetic geophysical data	Not yet determined	this study
CSZ (1 & 2)	Cadgecrib Shear zone system	Subvertical mylonitic shear zones; (2) interpreted from geophysical data (Bouger gravity "worms")	Deformation: (ca. 988 Ma; Martignole and Friedman, 1998)	(1) (Martignole and Pouget, 1994); (2) (Dufréchou et al., 2014)
HSZ	Heney Shear Zone	limited data; ca. 2 km wide; steep east dipping shear zone	Deformation: before ca. 1170-1160 Ma (Corriveau and van Breemen, 2000)	(Langlais, 1994)
RSZ	Renzy Shear Zone	Sinistral shear zone. Only confirmed along the base of the Renzy Terrane. Possible extension of the ABT?	Sinistral strike slip (1070-1040 Ma; 1003 Ma; Martignole and Friedman, 1998)	(Rivers 1989; Indares and Martignole 1990)
TBSZ	Teddy Bear Shear Zone	Subhorizontal banded quartzo-feldspathic gneisses and mafic layers (amphibolite and HP - Grt-Cpx-Pl assemblages)	Terminal deformation: (ca. 1002 Ma; this study)	proposed, this study
Y-SZ	Y-Shear Zone	From interpretation of geophysical data (Bouger gravity "worms")	No data	(Dufréchou et al., 2014)
Algonquin intrusive suite		Coronitic olivine metagabbro suite	Emplacement: ca. 1170-1150 Ma (Davidson and van Breemen, 1988; Heaman and LeCheminant, 1993)	(Davidson and Grant, 1986; Grant, 1987; Culshaw et al., 1994; Ketchum and Davidson, 2000)
Chevreuil Intrusive Suite		Gabbro, diorite and monzonite intrusions	Emplacement: ca. 1170-1160 Ma (Corriveau and van Breemen, 2000)	(Corriveau and van Breemen, 2000)
Proterozoic intrusions in pre-Grenville basement (Archean Superior Province)		Matachewan, Senneterre, Sudbury and Abitibi dyke swarms	Emplacement: ranges from ca. 2470-1140 Ma (see references)	(Condie, 1976; Krogh et al., 1987; Buchan et al., 1993; Heaman, 1997; Halls et al., 2005; Davis et al., 2018)

Across the DD zone, the increased abundance of amphibole and biotite in the hanging wall, defines a strong foliation, which is accentuated by migmatitic banding (Fig. v2.i.29K). The gneisses generally maintain moderate to steep SE dips (40-80^{o}) throughout this zone (#2 in Fig. 2.5), although steep N-dipping measurements reflect local folding at decameter-scales. Most migmatitic leucosomes within these gneisses contain quartz ribbons, indicative of strain under subsolidus conditions. In the vicinity of the DD, some discrete mylonitic zones (0.5-3 m wide) are mapped (Fig. v2.i.29J-K) with moderate-steep (30-70^{o}) dips to the SE (#2 in Fig. 2.5). In contrast to the SE-plunging lineations either side of the DD transition zone, most linear fabrics (stretching and mineral elongations; Fig. v2.i.29I) along the DD are shallow (15-20^{o}) and rotate to the east and ENE (#2 in Fig. 2.5), consistent with an oblique to strike-slip component of shear. Although the DD was inferred to record oblique, normal and sinistral shear, (Martignole and Martelat, 2005), preliminary kinematic data collected in this study are rather consistent with reverse (Fig. v2.i.29J) and dextral (Fig. v2.i.29K) shear sense and point to a predominantly oblique top-to-the SW tectonic transport direction. However, until the DD boundaries are better defined, and thorough age-constrained, kinematic analyses are conducted in both the footwall and hanging wall, it remains debatable if the DD a crustal scale transtensional or transpressional tectonic structure and what the tectonic implications during the Rigolet phase of the Grenvillian Orogeny may be.

2.3.3 Structures in the Reservoir Dozois Terrane (RDT)

Structural dissection of the RDT is challenging as the gneisses are broadly characterized by composite planar and linear fabrics and are intruded by voluminous (>30% rock volume), disharmonically folded migmatites and diatexites, likely comprised of multiple generations based on their cross-cutting relationships (Fig. v2.9.16B). In addition, the large distance between outcrops, relatively flat topography over some parts of the transect and gentle undulation in the dominant planar fabric, makes the identification of different structural levels problematic, with the transect likely intercepting the same structural levels multiple times along its length.

The dominant planar fabric (S_{RDT}) in the RDT is a penetrative amphibolite-grade gneissosity and localized schistosity, defined by compositional banding of quartzo-feldspathic and mafic minerals (clinopyroxene, amphibolite and biotite), segregated partial melts and injected felsic magmas (including tonalite–trondhjemite, granitic and K-feldspar rich compositions), as well as the transposition of mafic (e.g. metagabbro intrusions) and intermediate (e.g. tonalites and

granodiorites) and granitic lithologies (Fig. v2.ii.29L-P). The concordant felsic magmas mostly contain subrounded to rounded quartz grains (Fig. v2.ii.29M & Fig. v2.ii.29O) and as the quartz does not form elongated grains or streaked out aggregates (e.g. ribbons) on macro-scale, deformation associated with this fabric probably occurred under suprasolidus strain, although leucosome generations deformed under subsolidus conditions (i.e. contain quartz ribbons) are also present in some areas (Figs. v2.ii.29Q-R; also see stop 7). Although the gneissic fabric is variably folded on meter and decameter scales, it collectively defines relatively shallow (<40°), NNW and SE dipping successions, with localized dips to the NE (Fig. 2.6). Intrafoliar folds and variably folded migmatite generations that are cut or transposed by the penetrative fabric (S_{RDT}), are evidence of earlier (one or multiple) planar fabrics (S_{RDT-1}; Fig. v2.ii.29L & Fig. v2.ii.29N). A later, discrete (cm-thick) and spaced (0.1-3m) planar fabric (S_{RDT+1}) is documented sporadically along the length of the RDT. This fabric truncates or deflects the earlier foliations, resulting in macro-scale crenulations and drag folds (Figs. v2.ii.29L, v2.ii.29N & v2.ii.29P). This later fabric is often associated with a concordant and a weakly deformed migmatite generation but can also be cryptic and is inferred where meter thick packages with oblique penetrative foliations are juxtaposed (Fig. v2.ii.29L & Fig. v2.ii.29N). Collectively, measurements of this fabric define moderate (ca. 30°) dips to the SE (see S_{RDT+1} in Fig. 2.6). Transposition of the respective fabrics often hinders distinction between them and precise ages for the respective generations are yet to be determined.

The RDT is cut by a series of variably wide shear zones, characterized predominately by subsolidus fabrics (e.g. quartz ribbons and rotated and mantled porphyroclasts). Some of the shears manifest as discrete (centimeter to meter-scale) mylonitic zones (Fig. v2.ii.29Q), most of which are not mappable at the scale of the cross section, but predominantly trend NE-SW with moderate (30-50°) dips to the SE (see S_{SZ} in Fig. 2.6). Wider (>15-50m) shear zones depicted on the cross section include subvertical sinistral mylonite zones inferred from previous works (e.g. Y-SZ, CMZ, RSZ; see Table 2.1 for references), as well as shear zones proposed in this study (e.g. CMSZ and TBSZ respectively). Observations from the CMSZ and TBSZ are similar to those in shear zones described elsewhere in the Grenville Province (Hanmer and Ciesielski, 1984; Hanmer, 1988; Nadeau and Hanmer, 1992; MacKinnon, 1994; MacKinnon *et al.*, 1996), defined by moderate and shallow NW and NNE dipping, tectonically banded quartzo-feldspathic and mafic packages that were thermally annealed and are laterally extensive without significant changes in the X-Z plane (i.e. “straight gneisses”; see stop 7 and Fig. v2.ii.29R). The location of the Y-SZ and CSZ (1 & 2) however, could

not be confirmed in the field during this study. While extensive mylonites were confirmed along the base of the RT (stop 14 Figs. 2.8D-E), which may represent part of the contentious RSZ (discussed in section 2.3.5), this study does not consider this a laterally extensive shear zone that affected RDT gneisses as proposed by Martignole and Friedman (1998) as it could not be traced into the surrounding RDT gneisses and records contrasting shear directions along its length (discussed in further detail in section 2.3.5 below). Syn-late kinematic intrusions indicate deformation in the CSZ (ca. 988 Ma; Martignole and Friedman, 1998) and the TBSZ (ca. 1002 Ma; Fig. v2.7.14O) occurred during the Rigolet phase, the latter occurring at temperatures above the quartz solidus (see stop 7).

Linear fabrics in the RDT are mostly defined by mineral elongation (L_{mel}; amphibole and plagioclase) and stretching (Lst; quartz and plagioclase) lineations (Figs v2.ii.29S-T). However, the former lineations are perplexingly underdeveloped in the RDT and the gneisses are mostly S>>L tectonites. Both lineation types generally have predominately shallow (5-25^{o}) plunges to the NE, although subordinate populations also define plunges to the NW and SE (Fig. 2.6). In contrast to the NE-plunging elongation and stretching lineations, the collation of the fold axial plunges within the RDT, predominantly shows shallow (<25^{o}) plunges to the SE (Fig. 2.6), likely related to folding along NW-SE trending axes within the RDT gneisses.

Most of the migmatitic leucosome/injections within the RDT lack distinct peritectic phases (Figs. v2.8.15A-E), except for hornblende (Fig. v2.9.16F). This is a typical characteristic for melts derived in the presence of fluid (Weinberg and Hasalová, 2015). Fluid fluxed melting is also supported by the succession of similar, Rigolet-aged zircon zones within the samples collected in this study (Rubatto *et al.*, 2009; see stops 5, 7 & 9 and discussion in chaper 4). Leucosomes with peritectic garnet in the RDT are however, readily observed within the first ca. 10 km from the DD despite occurring in similar host rock lithologies. The reason for this somewhat localized garnet occurrence in the RDT is unresolved.

In addition to mafic sequences interleaved with the tonalite and granodiorite gneisses, mafic bodies within the RDT include centimeter to decameter sized, folded lenses that are variably boudinaged (Figs. v2.5.12A & v2.7.14A) and dismembered to form rafts within metatexites and diatexites (Figs. v2.8.15A-E & v2.9.16A). Whereas these mafic bodies are mostly retrogressed to amphibolites, the cores of larger (decameter scale) bodies commonly preserve clinopyroxene-

garnet-plagioclase rich assemblages, where plagioclase commonly forms as a pseudomorphs of garnet (Fig. v2.7.14E). The latter texture is interpreted to record decompression from high-pressures. In rare cases, melt phases within the cores contain clinopyroxene, orthopyroxene and garnet peritectic minerals (Fig. v2.ii.29U), which presents evidence for partial melting at granulite facies conditions, although the age for this metamorphism is undetermined.

The cross section and accompanying stereoplots in Figure. 2.5 highlight the variation in the tectonic fabrics within the RDT from NW to SE. In the hanging wall of the DD the gneissic fabric generally dips to the SE (Fig. v2.ii.29V) and mostly has down-dip lineations (#3 in Fig. 2.5). In contrast, gneisses SE of the Y-SZ mostly have shallow to moderate (0-25^{o}) dips (#4 in Fig. 2.5) that rotate from NE (Fig. v2.ii.29W) to S and SW (Fig. v2.ii.29Y) along the margin of a kilometer-wide domal structure that is visible on geophysical datasets and Google Earth imagery SW of the transect (Figs. 2.1 & v2.7B in Overview of virtual stops), to NW dipping gneisses further along the transect (Fig. v2.ii.29X). In this section of the RDT mineral and stretching lineations are still mostly down-dip (#4 in Fig. 2.5) and rare 3D-exposures reveal disharmonic recumbent folding of the gneiss at meter-scale, with shallow SE (and NW) plunging fold axes (Figs. v2.ii.29X-Y). Recumbent folding combined with the rotation of the gneissic fabric in this section suggests that the gneisses were doubly folded (#5 in Fig. 2.5) and may explain the formation of the dome-shaped fold to the SW. Across the CMSZ, the gneisses define a kilometer-scale, tight antiform, gently verging to the SE and plunging to the NE (#5 in Fig. 2.5). The transition across the CMSZ also marks the change between predominately SE to NE plunging lineations for the remainder of the transect. To the SE of the CSZ-1, RDT gneisses are wedged between what are interpreted as SE and NW dipping shear zones based on decameter-scale gneissic imbrications, mylonitic fabrics (S_{sz} in Fig. v2.ii.29AC) and distinct linear magnetic features that trend NE-SW and W-E respectively (see Overview of virtual stops, Fig. v2.7B). Between these two shear zones the gneisses define a zone of chaotic folding (#6 in Fig. 2.5) where multiple sheath folds with subvertical axial planes were observed (Fig. v2.ii.29Z). Further SE, the gneisses are locally folded and attain steep (up to 70^{o}) dips along the margins of proposed Renzy-equivalent outcrops (see S_{RDT} of #8 in Fig. 2.5) but generally shallows (10-15^{o}) and dips to the NE and NNE within the TBSZ (see S_{SZ} of #8 in Fig. 2.5; see also Figs. v2.7.14A-D). The gneisses of the TBSZ do however, steepen (20-30^{o}) further SE along the transect to extend over the NW-margin Renzy Terrane (Figs. v2.ii.29AA). This interpretation is supported by both historic (e.g. Sabourin, 1963) and newly acquired field data (Lambert *et al.*,

2019; this study). Below the RT (*sensu stricto*), the RDT gneisses define a gentle, upright antiform between the two Renzy components (#11 in Fig. 2.5) but pinch into an isoclinal antiform between the limbs of the SE-most Renzy component (see #12 in Fig. 2.5 & Fig. v2.iii.29AH). SE of the RT components, the RDT gneisses define an open antiform but attain consistently moderate-steep (30-60^{o}) dips further SE along the transect (#17 in Fig. 2.5). Diatexites appear to be concentrated in the roof zone of the antiform (Figs. v2.8.15A-D). In addition to the similar RDT lithologies NW of this section, large charnockite bodies (Fig. 2.5) are also present within the RDT SE of the RT. Although only weakly developed in the larger (2 km), more massive outcrops, the gneissosity (S_{RDT}) is observed in all of the charnockitic gneisses that intruded the RDT and is especially evident where they are retrogressed. Interestingly, the charnockites in the RDT preserve evidence of an earlier high-grade linear fabric that is overprinted by amphibolite metamorphic assemblages, specifically ESE-plunging orthopyroxene crystals mantled by NE-plunging hornblende and biotite assemblages (Fig. v2.ii.29T).

Probably the most notable feature of the cross section, is the interpretation that the RDT consists of structural levels that extend both above (i.e. NW of #14 in Fig.2.5) and below (i.e. SE of #14 in Fig. 2.5) components of the RT. The geochronology results (see chapter 4) from syn-late deformation granitic leucosome and granite dykes indicate that deformation in the upper structural level (stops 5 & 7) and lower structural levels (stop 9) of the RDT, was roughly contemporaneous (1002 ± 16 Ma and 1011 ± 10 Ma respectively; see chapter 4). Collectively, these data indicate that the Renzy components would not represent tectonic klippe (e.g. Dickin *et al.*, 2014), but were likely incorporated as disaggregated allochthonous remnants into the RDT during the Rigolet deformation phase. This hypothesis is also supported by the geochemical similarity of many large (meter to kilometer-scale) mafic bodies within the RDT to those in the RT (see chapters 3 & 5).

A preliminary kinematic investigation (based on a limited number of observations) across the RDT gneisses (excluding measurements adjacent to the DD) indicate that the principal tectonic transport direction was towards the SW (Fig. 2.6), parallel to the length of the orogen. However, subordinate NE, NW and S transport trends are also visible based on numerous kinematic indicators within RDT (Figs. v2.ii.29AB-AE), which suggests transport was not necessarily unidirectional (monoclinic) and was probably diachronous, based on the cross-cutting planar fabrics. It is noted that in many cases, meter-scale rotated mafic bodies that indicate top-to-the NW kinematics (Fig. v2.7.14A), are perpendicular to the dominant NE-plunging lineations in these gneisses and may be

related to an earlier phase of transport or to concurrent NW and SE directed transpressive deformation within the RDT (as previously noted by Hanmer and Ciesielski, 1984; Indares and Martignole, 1990). In general, the SW-directed transport, NE-plunging lineations, predominantly shallow N-NE dipping gneissic fabric and SE dipping fold axes (Fig. 2.6), does not seem consistent with a model for NW-directed thrusting during the Rigolet phase (e.g. Martignole, *et al.*, 2000; Rivers, 2009; Dickin *et al.*, 2014). Instead, this study proposes that deformation during the Rigolet phase probably correlates to triclinic (e.g. Fossen and Tikoff, 1993; Jiang and Williams, 1998; Lin *et al.*, 1998), ductile extrusion of the RDT against the relatively rigid GFTZ, likely controlled by a combination of the transpressional dextral shear along the DD (this study), NW-SE trending pre-Grenvillian basement structures (e.g. Mont Laurier Lineament; Dufréchou and Harris, 2013; Dufréchou *et al.*, 2014) and Rigolet-aged NE-SW trending sinistral shear zones (e.g. CSZ, CMSZ, BSZ?) that cross-cut the transect (Martignole and Pouget, 1994; Martignole and Calvert, 1996; Dufréchou *et al.*, 2014). To evaluate this hypothesis a statistically robust, age-constrained analysis of kinematic indicators throughout the RDT would be required.

2.3.4 Structures in the Vérendrye Terrane (VT)

Tectonic fabrics in the VT have similar characteristics to those in RDT and there is no clear physical distinction between them in the field. Like the RDT, the planar fabrics in the VT are defined by amphibolite grade gneissic banding (S_{VT}; Figs. v2.10.17A-F & Figs. v2.11.18A-D) and a later, discrete (centimeter-scale), subhorizontal spaced fabric (S_{VT+1}) that truncates and shears the earlier gneissosity (Fig. v2.iii.29AF). Although gneisses of the VT predominantly outcrop between the 'model-age boundary' and the LDT (Fig. 2.5) along the transect, recent Nd-model age data (1.8-2.1 Ga; Dickin *et al.*, 2014) suggests that narrow slices entrained along the base of the RT may also constitute part of the VT. However, as there is no clear distinction in the lithology or metamorphic grades, it is difficult to distinguish between RDT and VT tectonic fabrics at the latter locations. Furthermore, ages that constrain deformation of the gneissic fabric (chapter 4) within the VT (1008 ± 10 Ma; see stop 10) and RDT (ca. 1002-1011 Ma; see stops 5, 7 & 9) overlap, which suggests the VT and RDT both underwent deformation during the Rigolet phase.

The gneissic fabric (S_{VT}) within the VT changes along the transect from subhorizontal-NNW dipping successions in the vicinity of the 'Nd-model-age boundary' (#18 in Fig. 2.5) to subvertical gneisses ca. 2 km away, as they approach and extend into the BSZ (#20 in Fig. 2.5). Cliff faces

through the former subhorizontal successions, expose impressive examples of ductile deformation (stops 10 & 11) where the gneissosity is deflected around large meter-sized mafic boudins (see stop 11) and pinches tightly between the limbs of mafic bodies that were folded concurrent to deformation of the host gneisses (Fig. 2.7). Numerous sheath folds exposed in this subhorizontal section (see stop 10), mostly with shallow axial planes (#18 & 19 in Fig. 2.5), display both symmetrical (Figs. v2.10.17E-F) and complex, asymmetrical geometries (Fig. v2.10.17A). The latter geometries, along with rotated mafic boudins (stop 11) and macroscale mantled porphyroclasts (Fig. v2.iii.29AG) are used to infer the tectonic transport direction within the VT. Although data is limited (n = 10), the tectonic transport is predominately shows a top-to-N sense of shear along S-plunging lineations, but is at right angles to the NE plunging sheath fold axes (Hanmer and Ciesielski, 1984; Indares and Martignole, 1990; this study). Thus, similar to the RDT, the VT records either two distinct phases of monocyclic deformation or transverse shearing (e.g Kuiper *et al.*, 2007).

The recent geochemical comparison of the mafic bodies within the VT to possible equivalent suites elsewhere in the Grenville Province that have either an autochthonous or allochthonous affinity (see chapter 3), suggests that these mafic bodies have similar trace element signatures to allochthonous suites of either the 1.17 – 1.15 Ga coronitic metagabbros of the Algonquin suite (Ketchum and Davidson, 2000) or a mafic group previously defined for the RT (Montreuil and Constantin, 2010). However, Dickin *et al.* (2017) proposed that the Algonquin suite in Ontario is restricted to the 'Paleoproterozoic parautochthon' and as the geochronology results from this study support a phase of Rigolet deformation within the VT (see stop 10), the affinity of the VT remains somewhat ambiguous within the context of how the Grenville Province is subdivided (e.g. Rivers *et al.*, 1989; Rivers, 2008; see section 1.2.5.1.3).

Interestingly, the relationship between the gneissic fabric in the VT and a deformed mafic boudin (Fig. 2.7) may be used as an analogue for how the RDT gneisses pinch between the limbs of the folded Renzy antiformal nappe (#12 & 15 in Fig. 2.5). In addition, the brecciation of this mafic body by the granitic intrusions extending from within the VT are similar to the field observations at stop 14 (Fig 2.7) and could serve as an analogue for regional scale brecciation of the RT by felsic dykes from the RDT during the Rigolet (#13 in Fig. 2.5).

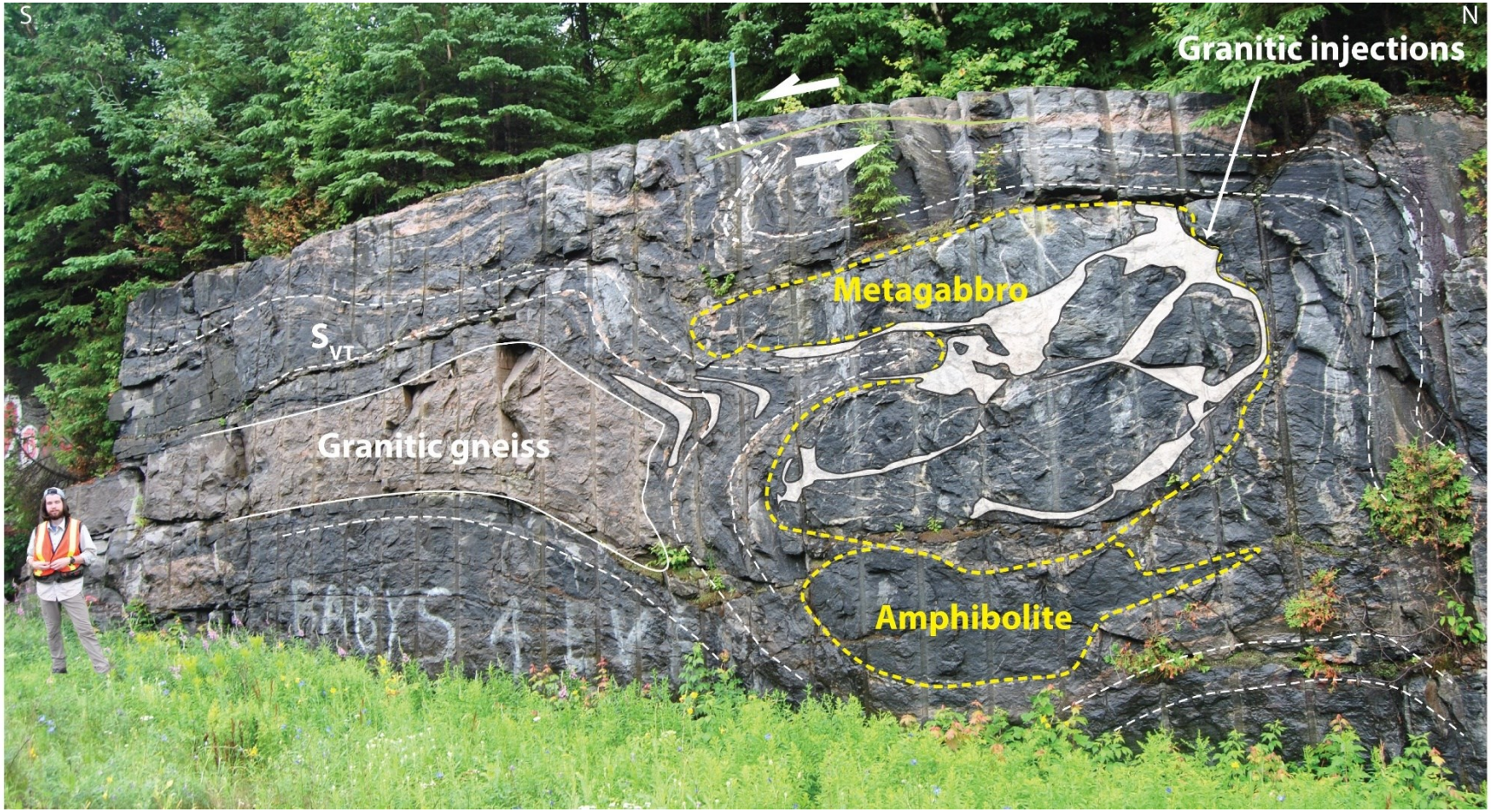

Figure 2.7. An impressive outcrop ca. 50m north of stop 11 shows a subhorizontal gneissosity that 'flows' around mafic boudins within the Vérendrye Terrane. Notice how the gneisses pinch tightly into the neck of the metagabbro, which may be used as a meter-scale analogue for the interpretation of the fabrics where RDT gneisses pinched into the inter-limb region of the Renzy Terrane on a kilometer-scale (#15 in Fig. 2.5). In addition, here granitic injections extend from the VT gneisses at the inter-boudin neck, into the metagabbro where they started to brecciate the mafic body, similar to the relationships observed at stop 14 (Fig. 2.8).

2.3.5 Structures in the Renzy Terrane (RT)

Strain in the RT and the proposed equivalent outcrops (e.g. stop 15), is generally high, evidenced by extensive grain size reduction, transposition of the gneissic layers (Fig. v2.iv.29AL), and attenuation of porphyroclasts/blasts (Fig. v2.iv.29AI-AJ) and development of isoclinal intrafoliar folds (Fig. v2.15.22D). RT rocks commonly have annealed (high temperature recrystallization) textures (Figs. v2.iv.29AK-AL), which in addition to the ubiquitous high strain, makes the distinction between different planar generations problematic. However, this study attempts to differentiate between the penetrative gneissosity (S_{RT}) and zones of apparent higher strains (S_{SZ}). The former is defined by tectonically interleaved mafic and felsic lithologies (stop 13), metamorphic differentiation of mafic (biotite, orthopyroxene, clinopyroxene ± hornblende) and felsic minerals (Fig. v2.15.22A & Fig. v2.15.22D) or banding of migmatitic leucosome (Fig. v2.15.22E). The latter is defined by mylonitic textures (Fig. v2.iv.29AK) or zones where clear local strain gradients were developed over several meters (Figs. v2.iv.29AI-AJ compared to Fig. v2.15.22F). Although a dedicated structural investigation across the RT is still required, the generally higher strains and presence of large rotated (<1-5cm) garnet porphyroblasts along the foliation planes in the vast majority of the gneisses, served as a rudimentary means of distinguishing between these RT fabrics and those of the predominately-garnet-free, suprasolidus fabrics of the RDT and VT in the field. A ca. 1070 Ma age for the penetrative fabric is estimated based on syn-kinematic garnet growth during upper-amphibolite to granulite facies metamorphism (Indares and Martignole, 1990; Childe *et al.*, 1993; Martignole and Pouget, 1993, 1994).

The orientation of S_{RT} varies significantly across the disaggregated RT segments dispersed along the transect (e.g. #10 & #15 in Fig. 2.5), likely reflecting the variation in fold geometries within the gneisses at these different locations. For example, contrasting fold patterns are observed in the segmented outcrops proposed to be part of the RT. One outcrop is characterized by non-cylindrical, reclined to recumbent isoclinal folds with both NE and SE plunging fold axes, possibly representing the nose of a sheath fold (Fig. v2.iv.29AM & #7 in Fig. 2.5). In the other outcrop, the gneisses attain consistently steep (60-70^{o}) dips towards the NE, representing the limb of a subvertical isoclinal folds (Fig. v2.15.22G & #15 in Fig. 2.5). Elsewhere in the RT (*sensu stricto*), gneisses along the ca. 1 km long section define open, upright to NE-plunging antiform-synform pairs (Fig. v2.iv.29AN) as well as N-S trending, overturned folds that verge to the E (not shown in

Fig. v2.iv.29AN). Further SE along the cross section, the gneisses mostly have moderate to steep (40-80 º) NW dips and define a ca. 4 km wide, SE verging antiformal nappe in the RT, with RDT gneisses pinching between the two limbs (#15 in Fig. 2.5). Notably, if both the RT and the inter-limb RDT gneisses were folded around the same axis, the formation of the antiformal RT nappe should be concurrent to deformation of the RDT gneisses during the Rigolet phase (see Fig. 2.7 and #12 in Fig. 2.5 for meter-scale analogues of this relationship). In addition, a 50 m wide outcrop defined by non-cylindrical, box-type folds was also identified in outcrops along the inner limb of this antiformal nappe (#16 in Fig. 2.5). In general, the fold patterns in the Renzy are chaotic and complex, mostly non-cylindrical and often have doubly plunging axes.

Linear fabrics in the RT are mostly characterized by quartz and plagioclase stretching lineations (L_{st}), whereas biotite and aligned pyroxene aggregates (Fig. v2.12.19C), define high-grade mineral lineations (L_{mel}). Despite the complex folding within the RT, both sets of lineations are consistently shallow and plunge towards the SW to N and NE around the girdle of the stereoplot in Figure 2.6.

As touched on in previous sections, the tectonic significance of the RSZ has not been discussed in much detail in previous studies in the area. Initially mapped as an isolated belt of sheared allochthonous gneisses (see RSB; Indares and Martignole, 1985, 1990), it was subsequently interpreted (and re-interpreted) as a laterally continuous, sinistral shear zone that separated parautochthonous RDT gneisses in the NW, from an unconstrained domain to the SE (see Baskatong Promontory in Indares and Martignole, 1990; Martignole *et al.*, 2000; Montreuil and Constantin, 2010; also see Fig. 53 in Rivers *et al.*, 2012). Martignole and Friedman (1998) subsequently used a ca. 1003 Ma age from late pegmatite dykes that cut sheared RT gneisses, to suggest that the RSZ was one of the many sinistral shear zones (including the CMSZ, BSZ) that controlled transverse deformation during the latter stages of the Grenvillian orogeny. Alternatively, due to the allochthonous affinity of RT, it was also inferred to represent the extension of the ABT (Rivers *et al.*, 1989), although the significance of allochthonous outliers NW of the Lac Dumoine Terrane was not recognized at that time. There is limited data to support a steep late, laterally extensive RSZ that deforms the surrounding RDT parautochthonous gneisses. The results of subsequent lithological (Lambert *et al.*, 2018, 2019) and Nd-model age (Guo and Dickin, 1996; Dickin *et al.*, 2014) mapping along the transect, indicate that the RSZ does not separate two distinctly different domains (RDT to the NW and former Baskatong Promontory to the SE). These data then question the existence of a late (ca. 1003 Ma), laterally extensive NE-SW trending RSZ.

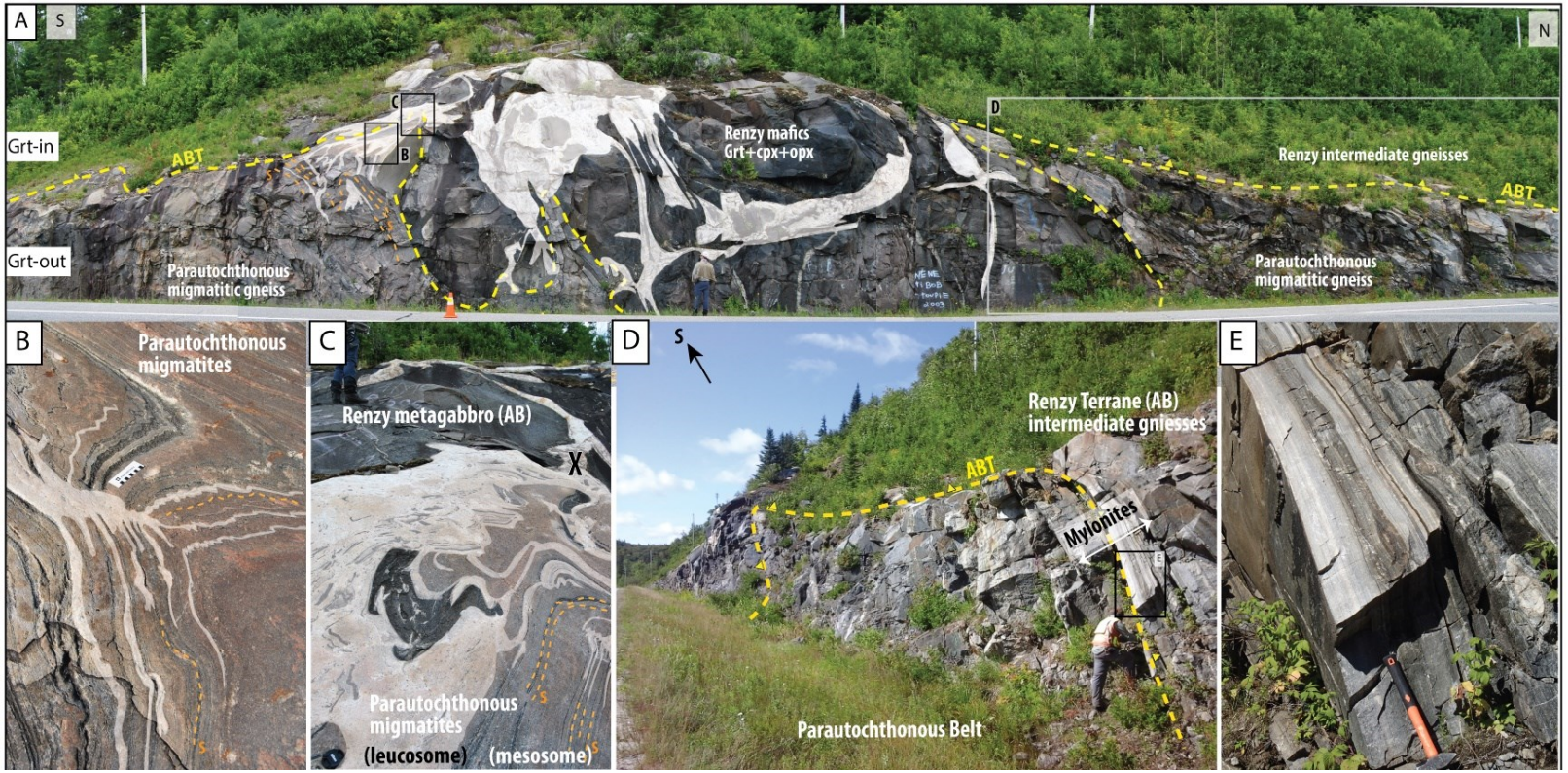

Figure 2.8. Outcrop photos from stop 14. (A) An annotated interpretation of the contact between the parautochthonous Lac Rolland and allochthonous Renzy Terrane units in the footwall and hanging wall of what is possibly the ABT. Note how the granitic dykes intrude and partially brecciate the mafic Renzy unit. (B-C). Folded leucosome in the Lac Rolland gneiss (B) forms a connected network of syn-deformational granite that coalesces, pools and intrudes the metagabbro boudin of the Renzy Terrane (C). The location of the sample collected for geochronology is indicated by 'X'. (D) Oblique view of the proposed ABT, separating gneisses from the Parautochthonous Belt (bottom) and Renzy Terrane units in the footwall and hanging wall respectively. (E) Mylonite units at the contact of volcano-sedimentary units of the Renzy Terrane (top right) and the parautochthonous Lac Rolland gneisses (bottom left), which are interpreted to represent the ABT.

Although observations in this study confirm that the base of these Renzy components are characterized by moderate-steep dipping mylonitic foliations (Fig. v2.14.21E & Fig. v2.iv.29AR) with mostly NE-SW trends and subhorizontal lineations (Fig. v2.13.20G & Fig. v2.14.21I), the mylonites previously mapped as the RSZ probably represent the original tectonic boundary between the overlying allochthonous RT and underlying RDT parautochthonous gneisses and as such, should represent the original trace of the ABT as initially inferred by Rivers *et al.,*(1989). However, as discussed at stop 14 , subsequent dismemberment of the RT by felsic intrusions (#12 in Fig. 2.5 & Figs. 2.8A) coeval to melt-present Rigolet deformation in the PB, would result in a now cryptic ABT along the transect.

Preliminary kinematic investigations reveal a range of tectonic transport directions across the RT (Fig. 2.6). In some places macro and microscale kinematic indicators record top to the NW and SE transport directions along down-dip lineations in shallow dipping gneisses (Figs. v2.iv.29AO-AP), whereas the mylonites along the base of the RT (ABT?) record apposing senses of strike-slip shear, with dextral shear (Fig. v2.iv.29AQ) observed at some locations and sinistral shears at others (Fig. v2.13.20H & Fig. v2.14.21J). This disparity in shear-sense is probably due to the complexity in RT folding or the mylonites representing the ABT/ABD may record the apposing directions of tectonic transport at ca. 1090-1050 Ma (e.g. thrust sense) and ca. 1020 Ma (e.g. normal sense; Culshaw *et al.*, 1994; Ketchum *et al.*, 1998; Rivers, 2008; see also see Fig. 1.4).

2.3.6 Structures of the Lac Dumoine Terrane (LDT) and Central Metasedimentary Belt (including the Baskatong and Cayamant shear zones)

Deformation throughout the narrow LDT strip exposed along the transect also occurred at generally high strains (Figs. v2.v.29AS-AW & Fig. v2.v.29AY). The entire ca. 10 km width of the LDT was previously interpreted to represent the BSZ, defined by NNE-trending gneisses with moderate to steep dips and shallow mineral and stretching lineations (Martignole and Pouget, 1994; Martignole, 1995; Martignole and Friedman, 1998). However, the extent and tectonic significance of the BSZ remains contentious (cf. Martignole, 1995 vs. Sharma *et al.*, 1995). This study noted that deformation along the NW margin of the LDT occurs at upper amphibolite to granulite metamorphic grades, defined by the preferred alignment of orthopyroxene-and garnet-rich mineral assemblages (Figs. v2.v.29AV-AW). Towards the SE margin of the LDT however, mafic bodies

that were originally metamorphosed at high-grades (eclogite?) and variably retrogressed to amphibolite along their margins, were also mapped (Figs. v2.v.29BA-BD). The LDT gneisses along the NW margin are consistently steep (>75°), dipping to both the NW and SE and have sub-horizontal to shallow NE and SW plunging lineations (#20 in Fig. 2.5). Elsewhere along the transect, including a similarly narrow LDT zone along the Baskatong Reservoir ca. 15 km to the NE of Hw117, the gneisses have shallower (25-65°), NNE trending foliations and although they have the ubiquitous, shallow NE-plunging lineations, they lack those that plunge to the SW. Along the SE margin of the LDT, localized lineations that plunge to the SE (#21 in Fig. 2.5) were also noted. Based on the subtle differences in the orientation of the foliation and lineations along the NW and SE margins of the LDT, this study considers that only the NW margin (coinciding with the Baskatong Desert Lineament of Sharma *et al.*, 1992) likely represents the BSZ, deforming gneisses from both the VT and LDT sometime before the emplacement of late granites that cut the steep gneissic fabrics at 1016 ± (5) 9 Ma (Fig. 2.2). In contrast, the SE margin should constitute the roof zone of the LDT and would coincide with the Cayamant Shear Zone to the S and SE of Hw117 (Sharma *et al.*, 1995 and references therein) that may have recorded a separate (later) deformation event (discussed below).

The LDT preserves macroscale evidence (e.g. C/S fabrics, asymmetrical mantled porphyroclasts) for dextral shearing (Fig. v2.v.29AW & Figs. 2.3B-C; see stop 17), whereas the counter-clockwise rotation of the gneisses on map-scale were inferred to be the result of later sinistral shearing (Martignole and Pouget, 1994; Martignole, 1995; Martignole and Calvert, 1996; Martignole and Friedman, 1998). In the roof zone of the LDT (the Cayamant Shear Zone?), this study mapped variably strained gneisses (Fig. v2.v.29AS), localized mylonites and macroscale evidence for both normal-sense (Fig. v2.v.29AX) and sinistral strike-slip shearing (Figs. v2.v.29AY-AZ) at separate locations respectively. Dextral shearing in the BSZ was correlated to initial oblique-NW directed thrusting of mid-lower allochthonous crust over the PB along a shallow dipping crustal ramp (Martignole, 1995; Martignole and Friedman, 1998; Corriveau and Morin, 2000; Martignole *et al.*, 2000) which should, by definition (after Rivers, 2008), occur along the ABT (see Fig. 1.4; Rivers, 2008). Based on the new geochronology data from the BSZ (see stop 17, section 2.2.2), this dextral movement (to more oblique if associated with thrusting) along the ABT would then have ceased at ca. 1040 Ma. Normal-sense displacement in the roof zone of the LDT correlates to the top-down movement of the CMB relative to the LDT, consistent with a model for ductile channel flow of the

lower AB (e.g. Rivers, 2008), although it remains to be determined if shearing was coeval to the 1040 Ma "thrusting" in the base of the LDT (i.e. BSZ) to test this hypothesis. Finally, sinistral shearing within the LDT (and other shears along the transect, e.g. Y-shear zone; Cadgecrib SZ) are considered the result of late (1020-1000 Ma) transpressional shearing along the transect (Martignole and Pouget, 1994; Martignole and Calvert, 1996; Martignole and Friedman, 1998; Dufréchou *et al.*, 2014), although the timing of this movement is yet to be confirmed by modern analyses. A detailed structural investigation is still required across the LDT, specially to confirm where stain is partitioned and to constrain the age and dominant directions of tectonic transport.

Few structures were measured in the CMB along the Hw117 transect as detailed mapping of this area falls outside the scope of this study. The 'Marble domain' is typically separated from the 'Metasedimentary' domain' by the N-S orientated Heney Shear Zone (Corriveau and van Breemen, 2000), but along the Hw117 transect, they appear to be split across a major (50 m wide) NNE-trending brittle-fault zone (Fig. v2.v.29BE). Foliations measured within the marble breccias define shallow-moderate, ESE dipping successions with mostly down dip lineations (#22 in Fig. 2.5). The mafic rafts and calc-silicate boudins within the marbles are variably deformed and do not show preferred orientations. With the exception of stop 18 that has steep E and NE dipping successions and NE-and SE-plunging lineations, few outcrops of the 'Metasedimentary domain' occur along the transect. However, one other impressive outcrop has a shallow SE-dipping discrete, normal sense shear zone in garnet-rich metasediments, which records a top-to-the SE sense of shear (Fig. v2.v.29BF), consistent with normal displacement of the CMB relative to the LDT. In general, all ductile fabrics in the Marble and Metapelite domains are cut by the 1170-1160 Ma Chevreuil Intrusive Suite (Corriveau and van Breemen, 2000; Corriveau *et al.*, 2018; Fig. v2.18.25C). In the former domain the Chevreuil dykes undulate while retaining the overall net-like structures (Corriveau *et al.*, 2018), whereas the formation of the gneissic foliation and crystallization of migmatitic leucosomes in the latter domain, is estimated between 1200-1180 Ma (Corriveau *et al.*, 2018).

2.4 Synopsis of the structural characterization along Hw117

The Hw117 transect exposes various structural domains through the PB and AB of the Grenville Province in western Québec. In the hanging wall of the Grenville Front (stops 1 & 2), the GFTZ records Archean deformation with little evidence for pervasive Grenvillian deformation (stops 3 &

4), whereas the RDT (stops 5-9) are Archean gneisses that record protracted deformation during the late, Rigolet, phase of the Grenvillian Orogeny for ca. 30 Ma (using uncertainties on the 1020-968 Ma weighted mean ages; discussed further in chapter 4). Although previously interpreted as a normal and sinistral sense shear zone, kinematic indicators derived along DD in this study are more consistent with dextral and reverse shearing. If true, the GFTZ probably represented a strong structural block, above which rocks of the RDT were extruded during the Rigolet phase, although transport was likely not perpendicular to the length of the orogen (NW-SE) but probably triclinic in western Quebec, controlled by basement structures and syn-late tectonic shear zones.

Structurally overlying the RDT, Paleo-Mesoproterozoic rocks of the AB are ubiquitously garnet-rich and record subsolidus strain with strong subhorizontal stretching lineations. The stops in the tour present evidence that indicates the components of the allochthonous RT (stops 12-15), previously interpreted to represent tectonic klippe overlying the RDT, were rather dismembered as a result of brecciation by felsic intrusions (Fig. 2.8) and subsequently incorporated into the underlying parautochthonous gneisses (RDT & VT) that were deformed under suprasolidus conditions during the Rigolet phase (stop 14; discussed in more detail in chapter 4). These results highlight the complexity in delineating various structural domains and their major boundaries, such as the ABT, in the Grenville Province.

Sandwiched in between the RDT and the LDT, the Paleoproterozoic (Nd-model ages) VT (stops 10-11) have lithologies and tectonic fabrics indistinguishable from the RDT and also record the Rigolet deformation event (ca. 1008 Ma; stop 10). In this domain the gneissosity is subhorizontal along the 'Nd-model age boundary' in the NW (stops 10 & 11), but then attain subvertical dips proximal with the BSZ in the SE (stop 16). Notably however, the subvertical fabric in the BSZ is interpreted to have developed before ca. 1016 Ma (stop 16; section 2.2.1), which is somewhat contradictory if the younger Rigolet gneissosity in the VT was affected by this older shear zone (see section 5.2.2).

Further SE along the transect, the lower-mid crustal rocks of the AB, represented by the LDT (stops 16-17), recorded dextral strike-slip shearing along the BSZ during the Ottawan phase of the orogeny (ca. 1040 Ma; section 2.2.2), but also contain evidence of sinistral strike-slip kinematics along the SE margin of the LDT. Although inferred to occur at 1020 Ma (Martignole and Friedman, 1998), sinistral shearing remains to be precisely dated. Furthermore, normal sense indicators in the

roof zone of the LDT (i.e. the Cayamant shear zone) would correlate to top-to-the SE movement of the orogenic lid relative to the LDT, although precise dating of this event is required to test the hypothesis of channel flow inferred for these LDT gneisses (Rivers, 2008).

Finally, Central Metasedimentary Belt (stops 18-19), with the Morin Terrane (stop 21) were deformed, metamorphosed and exhumed to upper crustal level before the Grenvillian Orogeny, which implies that this transect does not intersect the root of the crustal orogen but all structural levels from the reworked basement to the orogenic lid.

CHAPTER 3 UNRAVELLING THE TECTONIC ARCHITECTURE OF THE GRENVILLE PROVINCE ALONG HW117: INSIGHTS FROM THE GEOCHEMICAL CORRELATION OF MAFIC SUITES

3.1 Introduction

Determining the magmatic affinities of mafic components within the parautochthonous gneissic rocks, to known mafic reference suites from different structural levels of the Grenville Province, helps to establish the 1st order tectonic architecture of the Grenville Province in the study area. Once the tectonic architecture has been established, the large-scale tectonic processes that were active at different stages during the evolution of the orogen can be better understood (see section 5). As discussed in section 1.3 (see objective no. 2), delineation of various tectonic domains is often hindered by poly-phase deformation and metamorphic histories, which can obscure primary structures and protoliths. The architecture along Hw117 is no exception and as revealed by recent mapping (see section 1.2.5 & v-chapter 2), the allochthonous Renzy Terrane (RT), as well as numerous outcrops with lithological and structural characteristics similar to the RT, appear to be completely enveloped within the migmatitic gneisses of the parautochthonous Reservoir Dozois (RDT) and Vérendrye (VT) terranes (Fig. 2.5). This architecture is more complex than was initially proposed (e.g. Indares and Martignole, 1985, 1990; Martignole *et al.*, 2000; Dickin *et al.*, 2014) and suggests that deformation of the underlying parautochthonous basement rocks may have affected the overlying allochthonous crust.

To confirm the hypothesis that allochthonous rocks of the Renzy Terrane are enveloped within the parautochthonous gneisses, this chapter builds on the approach pioneered by Ketchum and Davidson (2000) and subsequent studies in the Grenville Province (e.g. Birkett *et al.*, 1991; Indares and Dunning, 1997; La Flèche *et al.*, 2005; Martignole and Martelat, 2005; Montreuil and Constantin, 2010; Bédard *et al.*, 2009), who showed that different structural levels of the Grenville Province could be identified and delineated based on the occurrence of distinct pre-orogenic plutonic mafic suites (see section 1.3). In contrast to previous studies that focused primarily on major element chemical characteristics and trends of trace elements that are typically more mobile (e.g. Rb, Ba) in their geochemical comparisons (e.g. Ketchum and Davidson, 2000; Martignole and Martelat, 2005), this chapter compares the immobile trace element signatures (REE and HFSE) of granulitic to amphibolitic mafic bodies collected from tectonic subdomains across the Hw117

transect to mafic suites with known ages that have magmatic affinities to either the Superior Province (i.e. autochthonous) or the AB (i.e. allochthonous) surrounding the study area (Fig. 3.1).

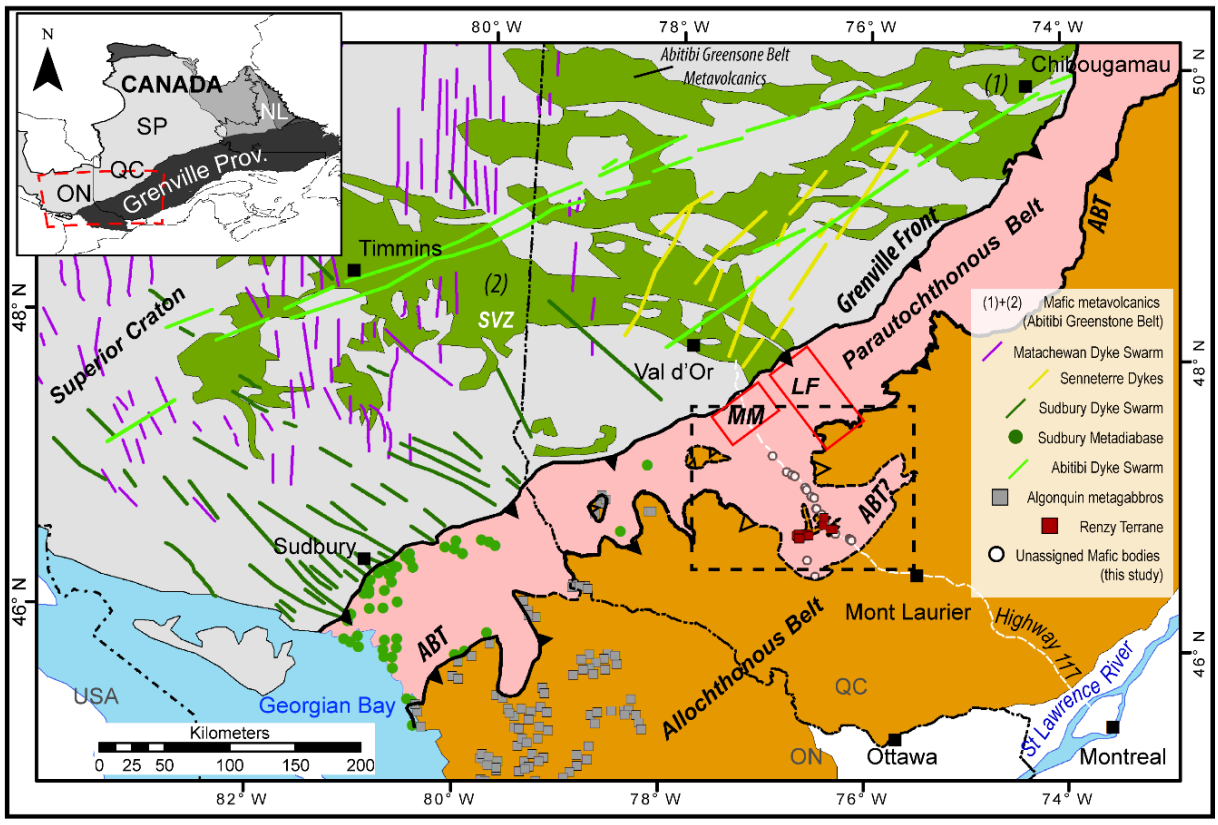

Figure 3.1. The 1st order tectonic architecture of the western Grenville Province and the distribution or orientation of the various mafic suites discussed in this study. Dashed box indicates the study region and location of Fig. 3.2. Red boxes indicate the previous areas of study by La Flèche *et al.*, (2005; LF) and Martignole and Martelat (2005; MM). Abbreviations: Allochthonous Boundary Thrust (ABT); Ontario (ON); Quebec (QC); Southern Volcanic Zone (SVZ). Compiled after Fahrig and West (1986); Wheeler *et al.* (1996); Ketchum and Davidson (2000); Rivers, (2008) and Montreuil and Constantin (2010). Data sources presented in Table 3.3.

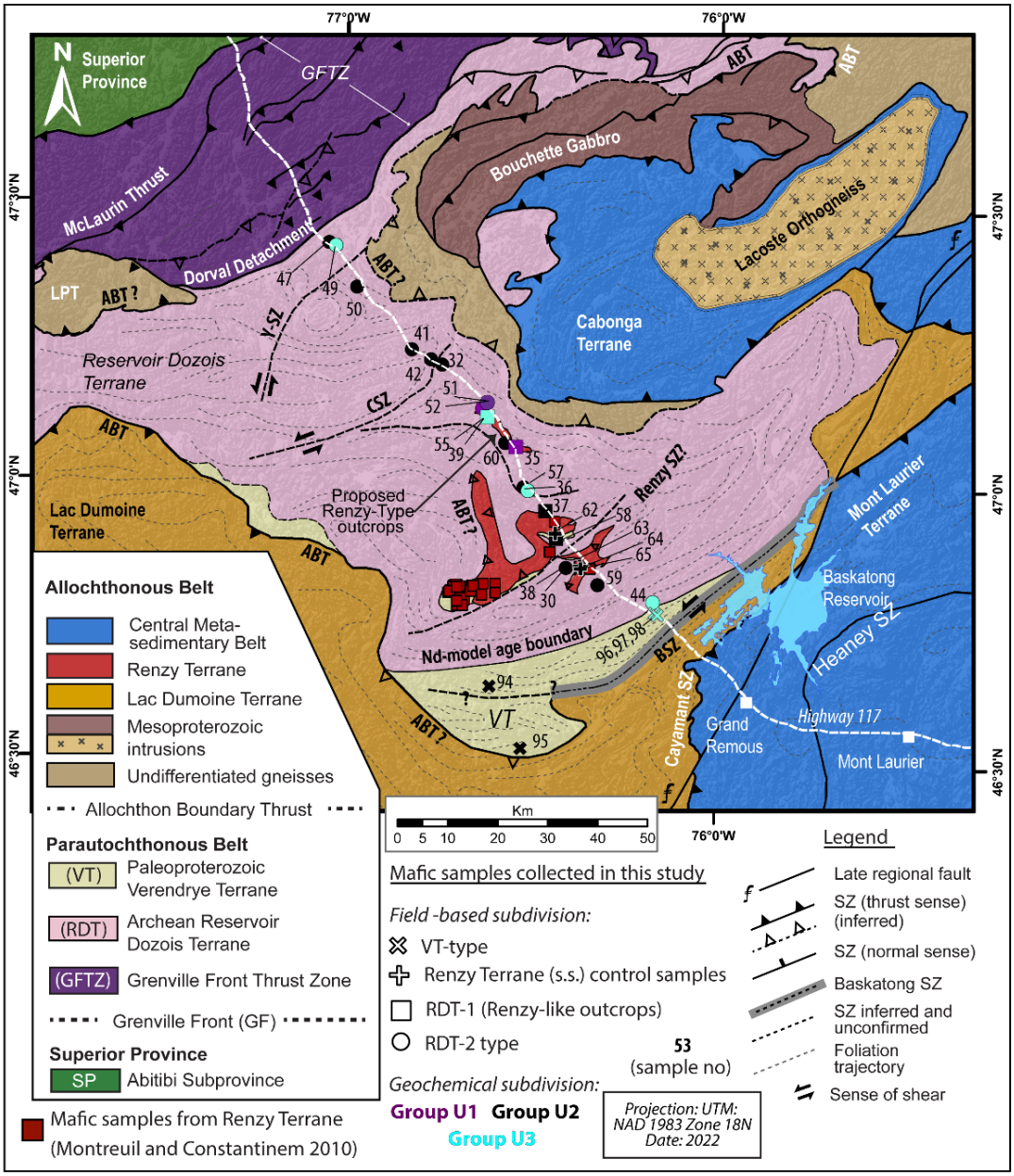

Figure 3.2. Location of the study area and distribution of mafic samples collected in this study. A description of the various segments is presented in section 1.2.5. See text for detailed discussion of the subdivision of the unknown samples according to field-based and geochemical characteristics (section 3.3). Abbreviations: Allochthonous Boundary Thrust (ABT); Baskatong Shear Zone (BSZ); Cadgecrib Shear Corridor (CSZ); Grenville Front Thrust Zone (GFTZ); Lac Perche Terrane (LPT); Shear Zone (SZ); Vérendrye Terrane (VT). Map modified after Martignole and Pouget (1994); Montreuil and Constantin (2010); Lambert *et al.* (2019) and the SIGEOM database (2020).

3.2 Methodology

3.2.1 Unknown mafic samples in this study: sample collection and analyses

In this study twenty-five samples were collected from deformed and variably retrogressed mafic bodies that were identified in the parautochthonous RDT and VT terranes along the Hw117 transect (Fig. 3.2; Lambert *et al.*, 2018, 2019; this study). Four samples, that are referred to as "RT control samples", were also collected from outcrops known to be part of the RT (Fig. 3.2) for control purposes and to complement the existing database of the mafic bodies within the RT (e.g. Montreuil, 2010; Montreuil and Constantin, 2010).

All samples were collected from texturally homogenous zones representative of the mafic body at each outcrop. In order to minimize the geochemical impact of partial melting and retrograde chemical mass transfer (Weber and Hecht, 2003) the samples were also collected as far away as possible from visible alteration zones or zones with macroscopic evidence of felsic magma injections or partial melt segregation. Samples were analysed to determine whole-rock major and trace-element concentrations (Table B.1) in two batches (2017 and 2018), which included duplicate samples that were selected at random. Detailed analytical procedures and specifications are provided in the methodology section (section 1.4.3). The geochemical results were evaluated, and applicable figures were created using the R-based GCDKit software package (Janoušek *et al.*, 2006).

3.2.2 Screening out metasedimentary and cumulate rocks

As the methodology is based on comparison of mafic magmatic rocks that approximate liquid compositions, it is 1st necessary to screen out metasedimentary and cumulate rocks from the initial batch of 40 mafic samples that were analysed for this investigation. The first step was to filter the analysed samples to only include samples with $SiO_2 < 58$ wt% and $MgO > 2$ wt%, which represents a reasonable range for mafic rocks. Samples were subsequently screened in order to exclude possible metasedimentary protoliths or those considered non-representative mafic cumulates, following the recommendations by Pearce (1996). On the Zr/TiO_2 vs Ni diagram of Winchester *et al.* (1980) three samples were excluded as they had high Zr/Ti ratios (> ca. 200), which suggests they may represent metasedimentary protoliths (Fig. B.1). On the same diagram, two samples with Ni > 200 ppm were also excluded as they are considered to have accumulated olivine (Fig. B.1).

None of the samples analysed herein had Al2O3 > 20 wt%, which is considered indicative of accumulated plagioclase (Pearce, 1996). Samples with Sc >50 pm may be indicative of accumulated clinopyroxene (recommended by Pearce, 1996) but as numerous samples from the comparative datasets (e.g. the RT; Montreuil and Constantin, 2010) have Sc concentrations between 50-54 ppm, the cut-off limit of 55 ppm for Sc is considered to be acceptable in this study. As a result, none of the samples were excluded based on possible accumulated clinopyroxene.

A newly defined ternary Co-Sc-(Al2O3 x 4) diagram of Rogers *et al.*, (2019) was also used to test for the effects of crystal fractionation or accumulation (Fig. B.2). On this diagram, samples that plot away from the main data cluster are likely affected by crystal accumulation or crystal fractionation. Trends away from the apexes indicate fractionation of olivine (Co), plagioclase ((Al2O3 x 4)) or pyroxene (Sc), whereas trends towards the apexes are indicative of crystal accumulation in the melt (Rogers *et al.*, 2019). As a result, five of the samples analysed herein were excluded as they may have accumulated plagioclase, while one is excluded due to possible pyroxene accumulation (Fig. B.2). In total, ten of the thirty-nine samples originally collected in this study were excluded from further comparison due to possible metasedimentary protoliths or cumulate effects. The geochemistry of the thirty remaining samples that were analysed is presented as supplementary material (Appendix B).

3.2.3 Major and trace element mobility

Samples from high grade metamorphic terranes such as the Grenville Province, may be subject to significant alteration and bulk element mobility during metamorphism and/or hydrothermal alteration, especially of the major elements (e.g. Ca, Na, Si; see Table 3.4, p72 in Rollinson, 1993). The unknown mafic samples collected in this study have been subjected to at least upper amphibolite and in places granulite to eclogite facies metamorphism during the different phases of the Grenvillian evolution (Indares and Martignole, 1990; section 1.2.5), in addition to pre-burial greenschist hydrothermal overprints. Therefore, it is necessary to assess the degree of element mobility in the samples collected in this study before comparing the samples to known reference suites.

3.2.3.1 Major element mobility

Most samples collected in this study have a alteration index (A.I. = 100 × (MgO + K2O)/(MgO + K2O + Na_2O + CaO); Ishikawa *et al.*, 1976) between 30-42, which is similar to fresh MORB and arc-related volcanic rocks (A.I. = 36 ± 8; see La Flèche *et al.*, 1992). Four samples (#51,52,60,35) have an A.I. = 46-56 which suggest they experienced some Na and/or Ca loss. Of these samples, one (#35) has an Al_2O_3/Na_2O > 10, which suggests that alteration resulted in Na loss (Pearce, 1996). The K/Na ratio indicates that most samples may have been moderately Na-altered (K/Na = 0.1-0.5) and two samples (#51,60) may have moderate to strong K-alteration (K/Na > 2; Nielsen *et al.*, 2013). None of the samples in this study have a chlorite–carbonate–pyrite alteration index > 90 (CCPI = 100 ×(MgO + FeOt)/(MgO + FeOt + K2O + Na2O)), which importantly, indicates that MgO and FeO were not mobilized due to Mg-Fe chlorite development or enriched by pyrite, magnetite and hematite additions (Large *et al.*, 2001). Overall, the major element data suggests that some of the unknown samples experienced alteration and major element mobility, especially with respect to the alkali elements.

3.2.3.2 Trace element mobility

Some elements that are considered immobile (e.g. Th, Nb, Ta, Hf, Ti, Y, and Zr) are useful in terms of interpreting the petrogenetic processes of the mafic magmas (Pearce, 1983; Tatsumi *et al.*, 1986). Nonetheless, care is required because several studies have shown that some of these elements can be mobile in unusual magmatic and hydrothermal environments or high grade metamorphic conditions (Hynes, 1980; Rubin *et al.*, 1993; Jenner, 1996; Woodhead *et al.*, 2001; Kamber *et al.*, 2002; Guice *et al.,* 2018). As a result, before a systematic comparison of trace element signatures between ‘unknowns’ and the reference suites is conducted, the degree of reliability that can be assigned to the different trace elements in this sample set must first be assessed.

The relative mobility of the key trace elements are first checked following the approach of Cann (1970) and Pearce (2014). This approach correlates pairs of highly incompatible elements within samples from a single magma source and that share a similar crystallization history. If the elements in question are relatively immobile, all samples should follow the correlated trends. However, samples in this study likely represent numerous different mafic suites, possibly derived from different sources or experienced different crystallization histories. In this case, multiple, evolutionary trends are expected. Overall, most HFS show a strong correlation to Zr (Fig. B.3),

except for the LREE, Ba, Rb and Th, which suggests these elements in particular, have been more mobile and need further evaluation.

All samples have $(La/Sm)_{CN} \geq 1$, which suggests that they are unlikely to have been affected by significant LREE loss. The samples all lack pronounced negative or positive Eu anomalies (Eu/Eu* = 0.83-1.25) which suggests that Eu was relatively immobile (Rudnick, 1992). An Eu/Eu* < 1.5 suggest that these samples did not incorporate excess plagioclase during fractionation of the lower crust (Rudnick, 1992), which is expected as samples that may represent plagioclase cumulates were already filtered out based on major element ratios (section 3.2.2). In addition, Ti/Eu (<11 000) suggest that the samples were not significantly modified by plagioclase or ilmenite crystallization (Maity and Indares, 2018). The K/Rb ratios for most samples is > 500 ppm. These values supports Rb loss (Rudnick, 1992), a typical trend in mafic granulites (Rudnick *et al.*, 1985; Fig. B.4), although minor K-gain due to the breakdown of biotite during metamorphism cannot be ruled out.

Th mobility is checked with the Ta/Yb-Th/Yb bivariate diagram (Fig. B.5) of Pearce (1983) and Schandl and Gorton (2002; also see La Flèche *et al.* 2005) and the Th/U - La/Th bivariate diagram (Fig. B.6) of Rudnick *et al.* (1985) and Maity and Indares (2018). On the Ta/Yb-Th/Yb diagram (Fig. B.5), all samples plot within the fields of normal basaltic rocks from within-plate, MORB and arc environments, which suggests Th mobility was limited (La Flèche *et al.* 2005) within the samples of this study. On the Th/U - La/Th bivariate diagram the majority of the samples plot within the acceptable field for igneous rocks (La/Th <21, Sun and McDonough, 1989), including samples (#51,52,58) mentioned above that have a high A.I. (>44). With the exception of one sample (#60), the samples with a high La/Th (> 21) do not correlate with a high A.I. or Na-and Ca-loss indicators and plot within the same range of other amphibolite to granulite samples (Fig. B.6) that have successfully been used for petro-and-tectonic discrimination in the Grenville Province (e.g. Blein *et al.*, 2003; Montreuil and Constantin, 2010; Maity and Indares, 2018). As a high La/Th (> 20) is common in fresh back-arc basin basalts (e.g. Taylor and Martinez, 2003), and there is no evidence for systematic post-magmatic gains or losses of La or Th, the La/Th of samples in this study is considered to be magmatic (Valverde Cardenas *et al.* 2012).

REE mobility by metasomatic fluids was checked using the Zr/Hf – Y/Ho diagram of Bau (1996; Fig. B.7). Metasomatic alteration by F-rich fluids should increase the Y/Ho and decrease Zr/Hf in the samples (La Flèche *et al.*, 2005). However, all unknown samples have Zr/Hf and Y/Ho ratios

that fall within the field of normal igneous rocks (Fig. B.7), which suggests no significant REE mobility or fractionation as a result of metamorphic, metasomatic or hydrothermal fluids (La Flèche *et al.*, 2005).

In summary, samples from this study are found to have experienced some major and trace element mobility, particularly in the alkali and large ion lithophile elements (LILE; e.g. Rb, Ba) respectively. In contrast, the HFSEs were shown to have a limited mobility. For these reasons, and in contrast to previous comparative studies within the Grenville Province (e.g. Ketchum and Davidson, 2000; Martignole and Martelat, 2005), this study limits the use of major element geochemistry and prioritizes the use of the immobile HFSE for the comparison of unknown samples to the mafic reference suites.

3.2.4 Reference suites: data sources and screening

Numerous reference suites were selected for the geochemical comparison to the unknown samples analysed in this study. Justification for the choice of the reference suites, and their geochemical characteristics, will be discussed later (section 3.4). The whole rock geochemistry of these reference suites was compiled from published literature (discussed below), including the *'Geochemical database of Proterozoic intraplate mafic magmatism in Canada* (Ernst and Buchan, 2010; and the *Geochemistry of Rocks of the Oceans and Continents* (GEOROCK) online database.

Filtering and screening of the reference suites entries follows that of the unknown samples described above. Only entries with SiO_2 (<58 w%) and MgO (2-15.5 wt%) concentrations were retained, comparable with the variably evolved set of mafic samples collected in this study. The reference suites were further filtered to exclude any entries that were 'unclassified' on the trace-element TAS proxy diagram of Winchester and Floyd, 1977 (modified by Pearce, 1996) or the Al_2O_3-($FeO+Fe_2O_3+TiO_2$)-Mg cation diagram of Jensen (1976), which are the principal mafic composition and series classification schemes used in this study. Importantly, as none of the unknown samples analyzed herein were classified as calc-alkaline on the latter diagram (Fig. B.8B), reference suite entries with a calc-alkaline classification on the same diagram (Jensen, 1976; Fig. B.8D & B.8F) were also excluded. From the filtered datasets, only samples with concentrations REEs, Ta, Nb, Th, Y, Yb and Zr well above the detection limits were retained as these elements form the principal components of the classification and multi-element normalized diagrams deployed in this contribution. Average normalized patterns were also derived for each of the

reference suites in this study. Reference samples with a difference from the mean > 2σ were excluded as it is reasonable to assume that these outliers are non representative of the original reference suite datasets. After refinement of the reference suites, 683 samples were retained for comparison. While the reference suites are briefly described herein, and although geochemical data/figures of the respective reference suites are presented for comparative purposes, it is important to note that the petrogenesis of the reference suites are not re-interpreted in this study.

3.2.5 Strategy of investigation and comparison to reference suites

This contribution presents a systematic process by which unknown mafic samples are compared to a series of reference suites. Prior to comparison, the unknown samples are first classified according to both their field-based (see section 3.3.1) and geochemical (see section 3.3.2) characteristics (Table 3.1). The field-based subdivision is based on the terranes from which the samples were collected and are described according to their, peak metamorphic minerals (classified after Green *et al.* (2016) for MORB-type basalt bulk compositions), mineral assemblages and the associated lithologies. The geochemical classification of the unknown samples is based on the bulk composition, mafic series (tholeiitic vs komatiitic; discussed below) and importantly, similarity in chondrite REE (REE_{CN}) and N-MORB normalized (normalizations after Sun and McDonough, 1989) immobile element profiles.

In contrast to previous comparative investigations that used major element classifications and differences in LILEs (e.g. Ketchum and Davidson, 2000; La Flèche, Birkett and Corriveau, 2005) this study uses the extended immobile-element N-MORB-normalized spider diagrams (after Sun and McDonough, 1989) and bi-variate REE_{CN} ratio-ratio plots to test putative correlations between the unknown samples and the reference suites. This study focuses on the key geochemical characteristics that allow us to eliminate reference suites as candidates, rather than presenting a complete geochemical characterization and comparison of each of the reference suites. Insomuch, if only one classification diagram is needed to eliminate a reference suites from consideration, the data from the reference suites that was eliminated will not be presented on subsequent diagrams. A quantitative comparative table is presented in the supplementary material (Table B.2).

Table 3.1. Field and geochemical grouping for each sample analysed in this study.

Reference no.	Sample Number	Geochemical Group	Sample location (field based subdivision)	Proposed Affinity
62	17CL6111A3	Group 2	RT-Type control sample	RT-Group 2
63	17CL6119C3	Group 2	RT-Type control sample	RT-Group 2
64	17CL6120A2	Group 2	RT-Type control sample	RT-Group 2
65	17CL6120A1	Group 2	RT-Type control sample	RT-Group 2
35	18CL6098B	Group 1	RDT-1	RT-Group 1
51	17CL6089A1	Group 1	RDT-2	RT-Group 1
52	17CL6089A2	Group 1	RDT-2	RT-Group 1
30	18CL6118D1	Group 2	RDT-2	RT-Group 2
32	17CL6022B	Group 2	RDT-2	RT-Group 2
37	18CL6109C1	Group 2	RDT-1	RT-Group 2
38	18CL6118D2	Group 2	RDT-2	RT-Group 2
39	18CL6091 Y	Group 2	RDT-1	RT-Group 2
41	18CL6073C	Group 2	RDT-2	RT-Group 2
42	17CL6075C	Group 2	RDT-2	RT-Group 2
47	17CL6054C2	Group 2	RDT-2	RT-Group 2
50	17CL6062C1	Group 2	RDT-2	RT-Group 2
57	17CL6105C1	Group 2	RDT-2	RT-Group 2
58	17CL6112D1	Group 2	RDT-1	RT-Group 2
59	17CL6125C1	Group 2	RDT-2	RT-Group 2
60	17CL6152C1	Group 2	RDT-2	RT-Group 2
94	18CL8081C1	Group 2	VT-type	RT-Group 2
95	18CL8021B1	Group 4	VT-type	RT-Group 2
36	18CL60106C1	Group 3	RDT-2	Algonquin/RT-Group 3
44	18CL6133B1	Group 3	RDT-2	Sudbury suite/RT-Group 3
49	17CL6055C2	Group 3	RDT-2	Sudbury suite/RT-Group 3
55	17CL6091A2	Group 3	RDT-1	RT-Group 3
96	17CL6135C1	Group 3	VT-type	Algonquin/RT-Group 3
97	17CL6137C1	Group 3	VT-type	Algonquin/RT-Group 3
98	17CL6136D1	Group 3	VT-type	Algonquin/RT-Group 3

3.3 Unknown mafic samples collected along Highway 117

3.3.1 Sample descriptions and field-based subdivision

3.3.1.1 Renzy Terrane control samples (RT-type)

Four mafic samples (#62-65) were collected from outcrops previously identified as the RT (*sensu stricto*) within the study area (Fig. 3.2; Table 3.1; Indares and Martignole, 1990; Montreuil, 2010; Montreuil and Constantin, 2010). These samples include those collected from conformable (>30 cm thick) fine-medium grained mafic units within variably folded packages of mafic, felsic and intermediate gneisses of possible volcano-sedimentary origin (e.g. Fig. 3.3F) and from isolated 10-20 m thick, strongly foliated mafic outcrops that lack other lithologies (Fig. 3.3G).

The RT-type samples are garnet-granulites with porphyroblastic (Fig. 3.4A) and granoblastic to nematoblastic textures (Fig. 3.4B). All four samples have mineral assemblages dominated by Hbl-Pl-Cpx-Grt±Opx±Bt (Figs. 3.4A-B) with minor quartz and accessory amounts of zircon, apatite, ilmenite and rutile. Clinopyroxene is variably retrogressed to green or pale green-brown hornblende (Figs. 3.4A-B) and the relative abundance of garnet, orthopyroxene and biotite especially, varies from sample to sample. Garnet grains commonly have plagioclase rims (Figs. 3.4A), which are interpreted as decompression textures, and while garnet is present in all four of the collected samples, some of the mafic rocks within the RT may lack garnet (Montreuil and Constantin, 2010).

3.3.1.2 Reservoir Dozois Terrane type-1 bodies (RDT-1)

Five samples (#35,37,39,55,58) were collected from mafic units within decameter-sized outcrops scattered within the greater RDT but, unlike the garnet-poor migmatitic gneisses of the RDT (Figs. 3.3A-C; RDT-2 type discussed below), the associated gneisses have lithological and structural characteristics typical of the RT (Lambert *et al.*, 2018; 2019; section 1.2.5.2.1; chapter 2). Most of these mafic samples (#35,37,39,55) came from fine- to medium-grained, meter-thick, conformable mafic layers embedded within packages of variably folded gneisses, which include garnetiferous intermediate and felsic layers (Fig. 3.3H) and subordinate augen orthogneisses. One sample (#58) was collected from a decameter-scale, coarse-grained boudin along a tectonic contact that is proposed to juxtapose garnetiferous volcano-sedimentary units of the overlying RT and the

underlying parautochthonous gneisses (see stop no. 14 in v-chapter 2; Fig. 2.8), which constitutes a key outcrop in establishing a tectonic model for the area (see chapters 4 and 5). It is emphasized that all gneisses (including the mafic samples) in these outcrops are characterized by penetrative subsolidus deformation fabrics and define distinct marker units scattered within migmatitic meta-tonalites and granitic gneisses of the RDT (see chapter 2).

RDT-1 samples include two (#55,58) garnet-granulite gneisses with porphyroblastic and granoblastic textures respectively and have mineral assemblages rich in hornblende and garnet (Hbl-Pl-Cpx-Grt±Opx±Bt; Figs. 3.4A-B), similar to RT-type samples. Conversely, two RDT-1 samples (#37,39) are garnet-free (Hbl-Pl±Bt) amphibolites with minor quartz and accessory amounts of zircon, apatite and ilmenite (Fig. 3.4E). A further sample (#35) has a Cpx-Pl-Opx-Bt±Hbl assemblage with large (5-10mm) relict (primary) clinopyroxene and orthopyroxene (Fig. 3.4D). It is important to note that samples collected from mafic units in the same outcrops may have different mineral assemblages (e.g. #39 vs #55).

Figure 3.3 (next page) Examples of field outcrops from which mafic samples analysed in this study were collected. (A-C) Examples of RDT-2 type outcrops within the Reservoir Dozois Terrane. (D-E) Examples of VT-type outcrops from the Vérendrye Terrane. (F-G) Examples of RT-type outcrops from the RT (*sensu stricto*). (H). Example of the RDT-1 type subdivision, defined by decameter-scale outcrops within the RDT but have lithological and structural characteristics rather similar to outcrops within the RT. (A) Rotated garnet-bearing gabbroic boudin in tonalitic gneisses and locality of sample #36 (geochemical group U3). (B) Gabbroic and amphibolite rafts in diatexites and locality of sample #59 (geochemical group U2). (C) Sigmoidal garnet-bearing gabbroic boudin in migmatitic granodiorite gneisses and locality of samples #30 & #38 (geochemical groups U2). (D) Rounded amphibolitic boudin within migmatitic granite to granodiorite gneisses and locality of sample #98 (geochemical group U3). (E) Transposed succession of garnet-bearing mafic and intermediate gneisses and locality of sample #95 (geochemical group U2). (F) Interleaved garnet-rich felsic to mafic gneisses (metavolcanics), typical of the RT. (G) Deformed garnetiferous granulites and sample locality of sample #64 (RT control sample). (H) Concordant folded mafic layers in a mixed package of garnet-bearing felsic to intermediate gneisses, typical of the RT. Locality of samples #39 (geochemical group U2) & #55 (geochemical group U3).

A
NW
SE
B
Diatexite
C
SE
NW
D
E
F
Interbanded felsic to intermediate and mafic Grt-rich gneisses
G
H
S
S
Mafic gneiss (±Grt)
Felsic to intermeidate and mafic Grt-rich gneisses

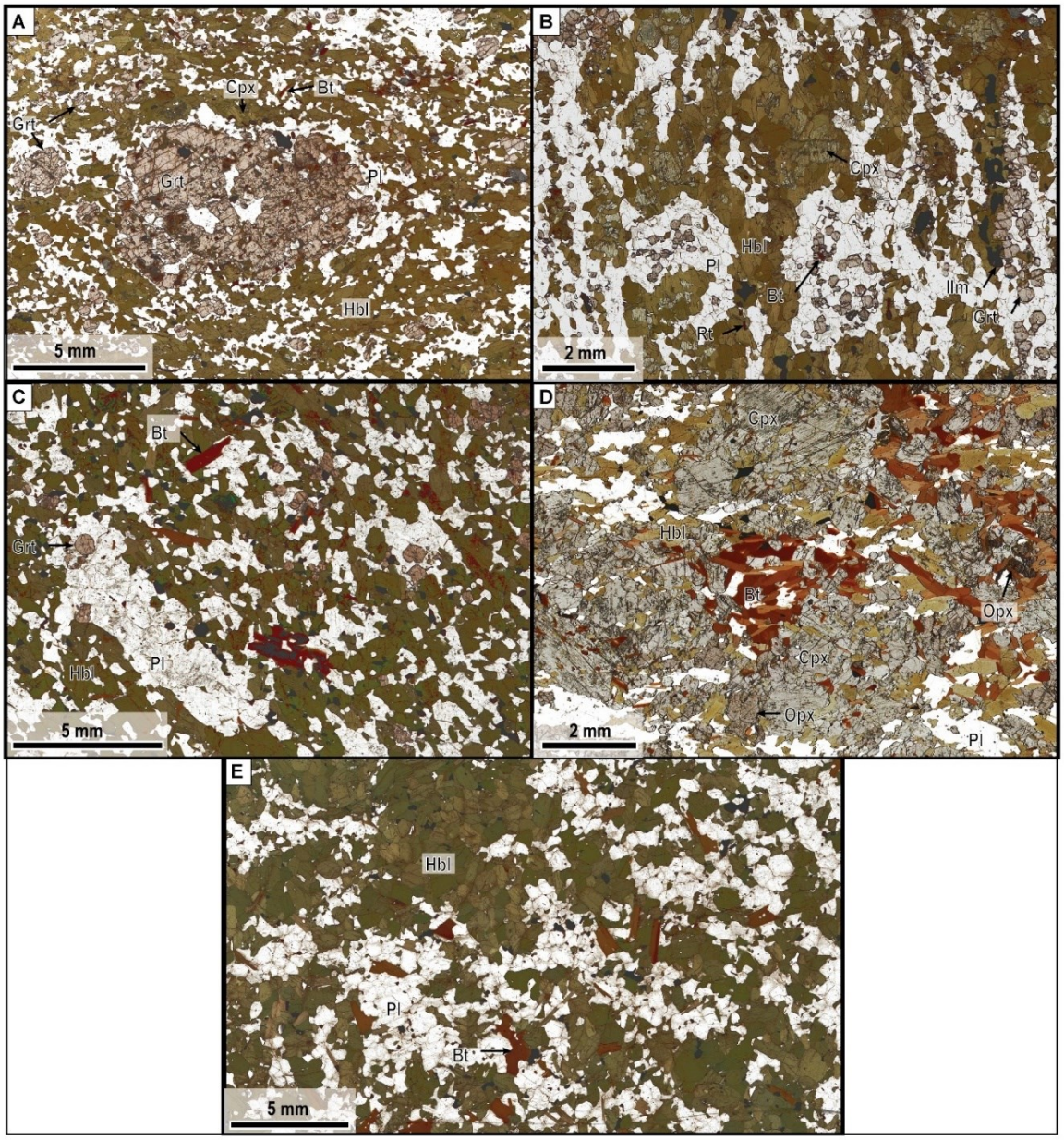

Figure 3.4. Photomicrograph examples of the principal mineral assemblages observed across all mafic samples collected within this study. (A) Hbl-Pl-Cpx-Grt±Opx±Bt dominated assemblages with porphyroblastic textures. (B) Hbl-Pl-Cpx-Grt±Opx±Bt dominated assemblages with granoblastic to nematoblastic textures. (C) Clinopyroxene free Hbl-Pl-Grt±Bt assemblages. (D) Garnet free Cpx-Pl-Opx-Bt±Hbl assemblages with relict, cumulate clinopyroxenes and orthopyroxenes. (E) Amphibolites with Hbl-Pl±Bt dominated assemblages. See text for detailed descriptions. All sections in plane polarized light. Mineral abbreviations after Whitney and Evans (2010).

3.3.1.3 Reservoir Dozois Terrane type-2 bodies (RDT-2)

The majority of the unknown samples (twenty-one; see Table 3.1) were collected from meter-decameter sized, disaggregated and rotated mafic boudins and rafts within meta-tonalitic and granodioritic migmatitic to diatexite gneisses of the RDT (Figs. 3.3A-C). In contrast to the gneisses that host RT and RDT-1 mafic samples, gneisses enveloping the RDT-2 mafic bodies are garnet-poor and generally lack prominent subsolidus strain markers (section 1.2.5.2; chapter 2). On a macro-scale, the mafic bodies are mostly medium- to coarse-grained and have weakly developed foliations or granoblastic textures at the center of the larger (>ca. 3 m) bodies, whereas penetrative foliations are developed along their margins and throughout the smaller bodies. In rare cases, localized leucosome with peritectic orthopyroxene-garnet-and clinopyroxene suggest dehydration melting at granulite grade (Lambert *et al.*, 2019), although the age of this event is unconstrained.

Most (#32,41,42,44,50,59,60) of the RDT-2 samples constitute generic, garnet-free amphibolites (Hbl-Pl±Cpx±Bt) with granoblastic to nematoblastic textures (Fig. 3.4E). Three samples (#30,36,38) are garnet-granulites (Hbl-Pl-Cpx-Grt±Opx±Bt) similar to RT and RDT-1 samples (Fig. 3.4A-B), whereas three samples (#47,49,57) contain garnet but lack pyroxene (Hbl-Pl-Grt±Bt; Fig. 3.4C), typical of garnet amphibolites which reached at least upper-amphibolite conditions (Green *et al.*, 2016). Furthermore, two RDT-2 samples (#51, 52) are hornblende granulites with Cpx-Pl-Opx±Bt±Hbl assemblages, where primary igneous textures are partially preserved (Fig. 3.4D).

3.3.1.4 Vérendrye Terrane type bodies (VT-type)

The mafic rocks within the VT, specifically those along Hw117 constitute meter-sized amphibolite and metagabbro blocks and boudins (Fig. 3.3D), commonly rotated within the ductile fabric (chapter 2). Small (<20 m^2) isolated outcrops that consist of mixed garnetiferous mafic and intermediate gneisses (Fig. 3.3E) were also mapped in the SW part of the VT (Fig. 3.2), although it remains unclear if they are indeed part of the VT. Three samples (#96,97,98) were collected from mafic boudins hosted within granitic and granodiorite gneisses (Fig. 3.3D). These samples are within 1 km of each other (Fig. 3.2) and are medium grained, generic Hbl-Pl-Bt amphibolites with neither pyroxene nor garnet (Fig. 3.4C). Two samples (#94,95) were collected from the flat exposures located to the SW of the highway (Fig. 3.2) that occur within garnet-bearing, transposed mafic and felsic gneisses, deformed under subsolidus conditions (Fig. 3.3G). Sample #94 is a fine-

grained granoblastic garnet granulite with a Hbl-Pl-Cpx-Grt±Opx±Bt assemblage (Fig. 3.4B); while #95 is a hornblende granulite with a Cpx-Pl-Opx-±Bt±Hbl assemblage. (Fig. 3.4D).

3.3.2 Geochemical classification

3.3.2.1 Bulk chemical composition and mafic series

Mafic bodies investigated in this contribution have a restricted compositional range. On the Zr/Ti vs Nb/Y TAS-proxy diagram (Winchester and Floyd, 1977; modified by Pearce, 1996), most samples are classified as subalkaline basalts, with four unknown samples and three of the RT control samples classing as basaltic andesites to andesites (Fig. 3.5A). On the AFM diagram of Jensen (1976) most samples are classified as high-Fe and high-Mg tholeiites, with three (#35,51,52) classified as komatiitic basalts (Fig. 3.5B). For simplicity, the Jensen classification is used in this contribution to separate the data sets (both from unknowns and reference suites) as "tholeiitic" and "komatiitic", although it is acknowledged the latter are high magnesian basalts (5-15 wt% MgO) that may not meet all the geochemical criteria to be named as komatiitic (i.e. none of the unknown samples have MgO >18 wt% and SiO2 < 45 wt% that would classify them as true komatiites or can be texturally or genetically linked to komatiites; (Le Bas *et al.*, 1986; Arndt and Lesher, 2006) see below).

The unknown samples examined herein show a wide range of MgO (15.2-4.3 wt%; Fig. 3.6; Table 3.2 & Table B.1). Those classified as 'komatiitic basalts' on the Jensen (1976) diagram (Fig. 3.5B) have MgO concentrations between 13.8-15.2 wt% (Mg# = 70.88-76.11), whereas those classified as tholeiites on the same diagram have a MgO concentrations of 4.3-8.01 wt% (Mg# = 34.39-57.82). The distribution of the unknown samples on major and trace element bivariate diagrams relative to a decreasing MgO (i.e. to more evolved samples), indicates that while linear trends may be approximated through the tholeiitic samples (e.g. MgO vs Fe_2O_3; and MgO vs P_2O_5), they are not colinear with those classified as komatiitic basalts and are thus, likely unrelated (Figs. 3.6A-D; see also Fig. B.11-12).

In comparison to examples of MgO-element bivariate diagrams that were used in previous studies (e.g. Ketchum and Davidson, 2000; Martignole and Martelat, 2005) to differentiate between unknown mafic samples and reference suites, the concentrations of the same elements that were derived from the samples analysed herein, overlap with more than one of the reference suites (Figs.

3.6A & 3.6D) and thus, suggests a similar comparative approach is not realistic for this study. For example, the 4 control samples collected from the RT have Fe_2O_3 (Fig. 3.6A) and Zr (Fig. 3.6D) concentrations that overlap with the trend lines defined by the different reference suites considered in both the previous and current investigations (e.g. Algonquin metagabbro, Senneterre tholeiites and Abitibi dykes). While the element concentrations selected in previous investigations may be distinctive when compared against fewer reference suites, it is also likely that many of the elements, such as the major and LIL (e.g. Rb, Ba) elements were mobile (as discussed in section 3.2.3). This is one of the reasons why differentiation using immobile trace elements on normalized diagrams was considered as an alternative approach for this study.

Figure 3.5. (next page). Geochemical rock classification schemes for all the mafic suites discussed in this study according to the trace-element TAS proxy diagram (see A,C,E) of Winchester and Floyd, (1977; modified by Pearce, 1996) and the Al_2O_3-(FeO+Fe_2O_3+TiO_2)-Mg cation diagram (see B,D,F) after Jensen (1976). (A, B) Mafic samples collected during this study .Symbology represents both their field-based subdivision and geochemical classification, with each geochemical group annotated with the prefixes U1, U2 and U3. Reference suites include: (C,D) komatiites, komatiitic basalts and tholeiitic basalts from the Southern Volcanic Zone and Chibougamau areas of the Abitibi Greenstone Belt in the Superior Province; (E, F) Paleo-Mesoproterozoic mafic dyke suites that part of the autochthonous Archean crust of Laurentia (i.e. Superior Province) and mafic suites considered unique to the Allochthonous Belt in the Grenville Province, such as the Algonquin metagabbro suite and mafic suites of the Renzy Terrane. Note that some reference suites do contain entries classified as calc-alkaline basalts on the Jensen diagram (not shown here; see Fig. B.8), which were excluded from further comparisons as none of the unknown samples collected in this study have a similar calc-alkaline classification. Abbreviations: Allochthonous Belt (AB), Calc-alkaline (CA), Southern Volcanic Zone (SVZ), Tholeiitic or tholeiite (TH), Verendrye Terrane (VT). Data sources are discussed in the literature and presented in Table 3.3.

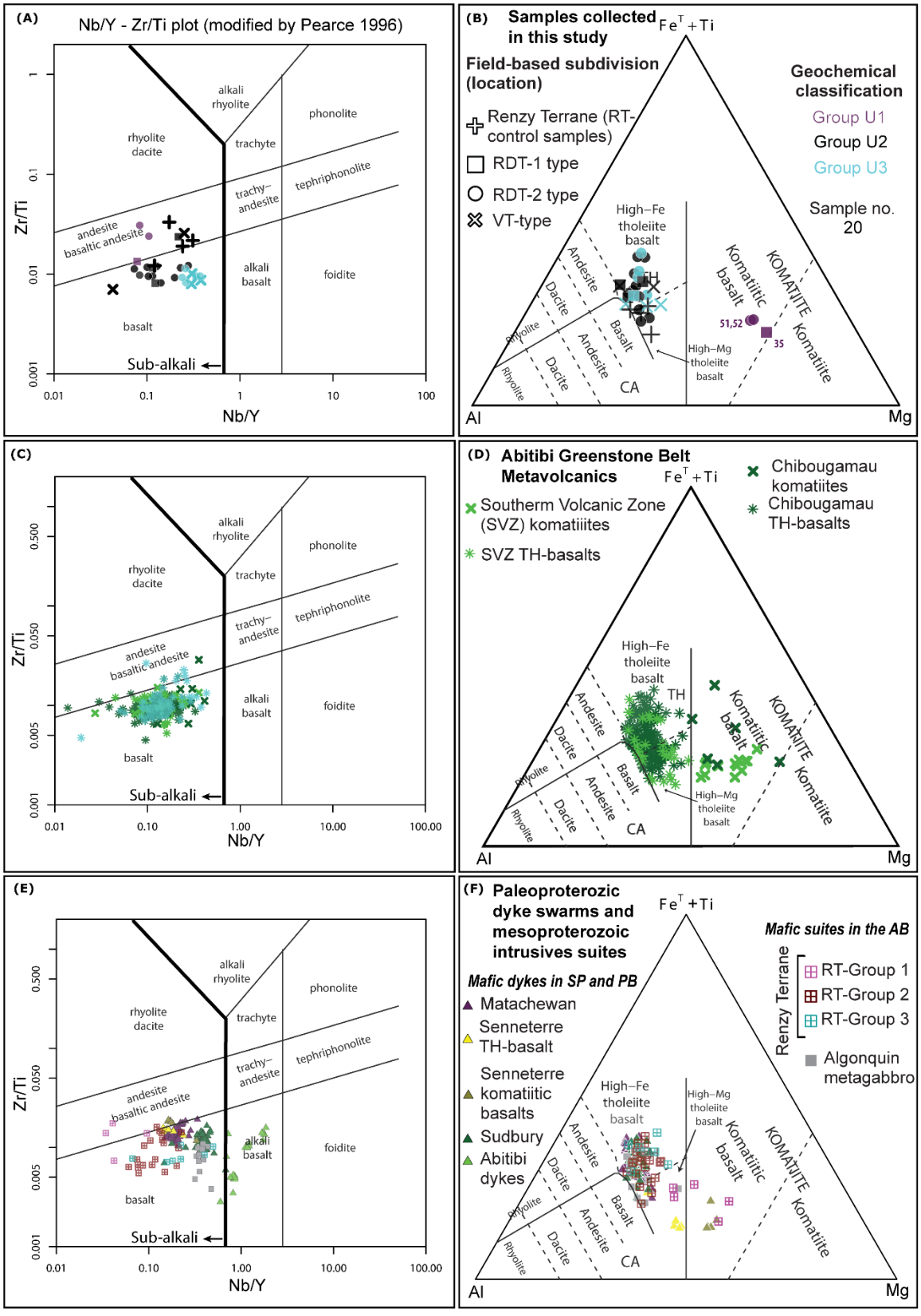
(A)
Nb/Y - Zr/Ti plot (modified by Pearce 1996)
alkali rhyolite
phonolite
rhyolite dacite
trachyte
trachy–andesite
tephriphonolite
andesite basaltic andesite
alkali basalt
foidite
basalt
Sub-alkali
Zr/Ti
Nb/Y
(B)
Samples collected in this study
Field-based subdivision (location)
Renzy Terrane (RT-control samples)
RDT-1 type
RDT-2 type
VT-type
Geochemical classification
Group U1
Group U2
Group U3
Sample no.
20
Fe^T +Ti
High–Fe tholeiite basalt
Andesite
Dacite
Rhyolite
Basalt
Komatiitic basalt
KOMATIITE
Komatiite
51,52
35
High–Mg tholeiite basalt
CA
Al
Mg
(C)
(D)
Abitibi Greenstone Belt Metavolcanics
Southern Volcanic Zone (SVZ) komatiites
SVZ TH-basalts
Chibougamau komatiites
Chibougamau TH-basalts
TH
(E)
(F)
Paleoproterozic dyke swarms and mesoproterozoic intrusives suites
Mafic dykes in SP and PB
Matachewan
Senneterre TH-basalt
Senneterre komatiitic basalts
Sudbury
Abitibi dykes
Mafic suites in the AB
Renzy Terrane
RT-Group 1
RT-Group 2
RT-Group 3
Algonquin metagabbro

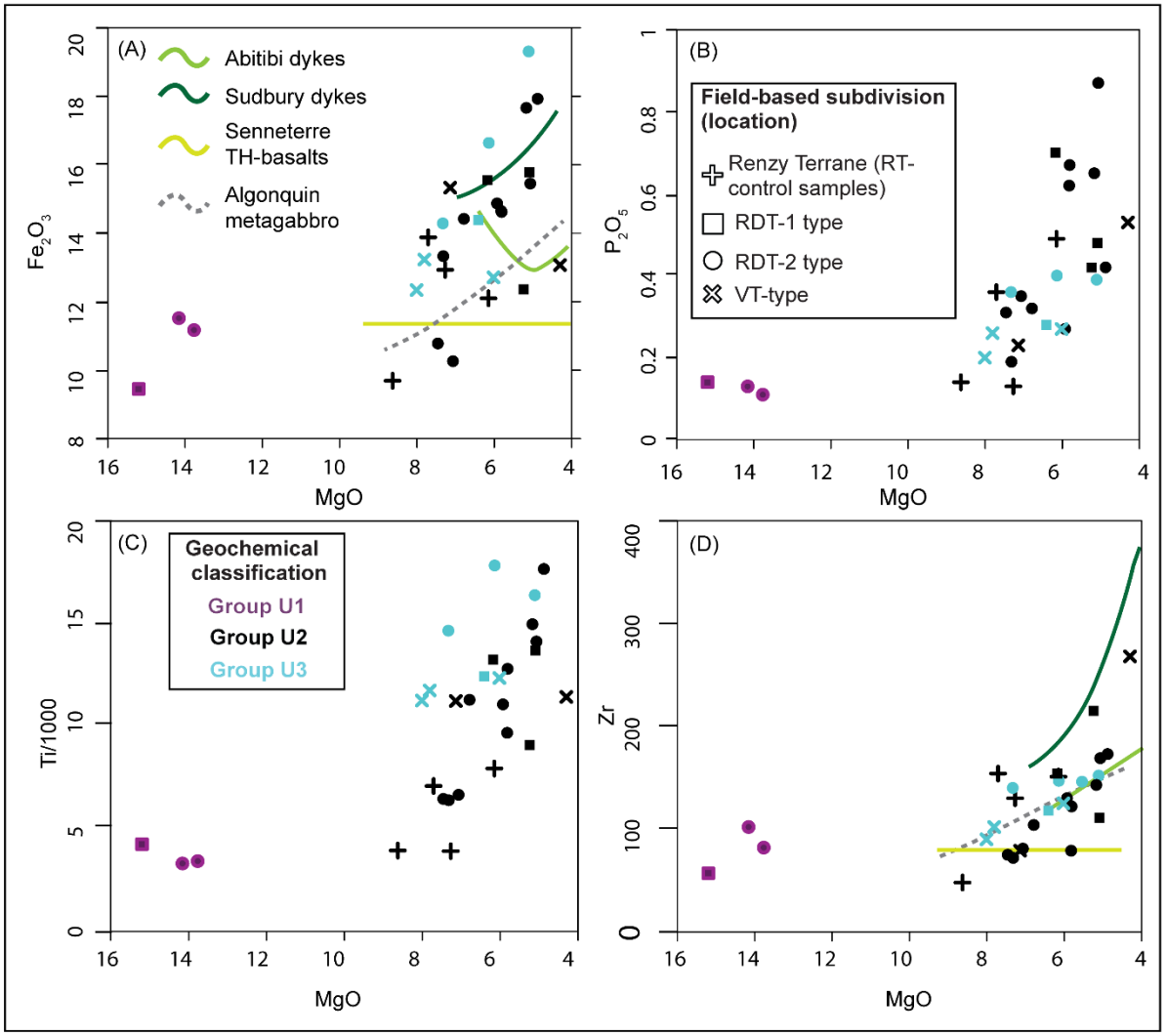

Figure 3.6. MgO vs select major and trace elements for the unknown samples collected in this study. Symbology as in Fig. 3.5. Colored lines in (A) and (D) represent the elemental trend lines that were used to correlate unknown samples to reference suites with either an autochthonous (Abitibi, Sudbury, Senneterre dyke suites) or allochthonous (Algonquin coronitic metagabbro) affinity in the previous studies around the Georgian Bay area of Ontario (Ketchum and Davidson, 2000) and the Grenville Front Thrust Zone of western Quebec (Martignole and Martelat, 2005). An extended complement of Zr vs major and trace element diagrams as well as MgO vs compatible and incompatible elements for the unknown samples, is presented in the appendix (Fig. B.11-12).

Table 3.2. Summary of the geochemical characteristics used to define geochemical groups U1-3 in this study

Group		Mafic series (Jensen, 1976)	Trace element alkalinity (Nb/Y)	MgO range (wt%)	HFSE anomaly **	REECN* slopes	HREE slope (Gd/Yb)CN* (depth of source melting)	HREE slope (Tb/Yb)CN*	Zr (ppm)****	Field Grouping/Host rocks	Mineral assemblages***
This study	**Group U1**	Komatiitic basalts	0.08-0.1	13.77-15.2 (ave: 14.38)	Deep Nb-Ta troughs and negative Ti anomlay; (Ti/Sm)NMORB = 0.3-0.52; (Th/Ta)NMORB = 5.61-14.08	(La/Sm)CN = 1.39-2.08; (La/Yb)CN = 4.42-4.96	1.73-2.34	1.46-1.92	57-102	RDT-2	Cpx-opx-pl-bt
	Group U2 (with negative Ti anomlay)	High-Fe and high-Mg TH	0.07-0.28 (ave: 0.16)	4.3-7.46 (ave: 5.94)	Deep Nb-Ta troughs and prominent negative Ti anomlay; (Ti/Sm)NMORB = 0.37-0.95; (Th/Ta)NMORB = 1.27-9.24	(La/Sm)CN = 1.67-2.74 (ave: 2.16); (La/Yb)CN = 2.89-7.29 (ave 5.3)	1.50-2.30 (ave: 1.78)	1.27-1.84 (ave: 1.49)	72-268	RDT-1, RDT-2, VT	Hbl-Pl-Bt±Grt Cpx-Hbl-Pl-Grt±Opx
	Group U2 (with nil-positive Ti anomaly)		0.04-0.2	4.88-7.14 (ave: 5.98)	Deep Nb-Ta troughs weak negative Ti anomaly; (Ti/Sm)NMORB = 1.02-1.09; (Th/Ta)NMORB = 3.68-11.47	(La/Sm)CN = 0.96-1.84 (ave 1.50); (La/Yb)CN = 1.45-4.53 (ave 2.97)	1.40-1.95 (ave: 1.62)	1.30-1.61	79-173		
	Group U3	High-Fe and high-Mg TH	0.24-0.38 (ave: 0.31)	5.11-8.01 (6.55)	Weak Ta-Nb troughs, flat to positive Ti anomlay; (Ti/Sm)NMORB = 1.05-1.24; (Th/Ta)NMORB = 0.75-2.14	(La/Sm)CN = 1.32-2.23 (ave 4.30); (La/Yb)CN = 3.13-5.50 (ave 3.67)	1.53-2.47 (1.91)	1.38-1.8 (ave: 1.61)	90-152	RDT-1, RDT-2, VT-type	Hbl-Pl-Bt±Grt Cpx-Hbl-Pl-Grt±Opx
	Renzy Terrane control samples	High-Fe high-Mg TH	0.12-0.31	6.15-8.63 (ave: 7.44)	Strong Nb-Ta and Ti troughs; (Ti/Sm)NMORB = 0.3-0.56; (Th/Ta)NMORB = 1.02-16.5	(La/Sm)CN = 1.68-2.76 (ave 2.32); (La/Yb)CN = 3.69-7.36 (ave 3.47)	1.4-2.1 (ave: 1.63)	1.27-1.55	48-154	RDT-1	Cpx-Hbl-Pl-Grt±Opx

* Chondrite normalized ($_{CN}$) after Sun and McDonough (1989)

** MORB normalized (after Sun and McDonough, 1989)

*** Mineral abbreviations after Whitney *et al.* (2010)

**** Zr concentration given for similarly evolved samples (defined by change in MgO)

3.3.2.2 Immobile trace elements: Three geochemical groups

The unknown mafic samples investigated herein are divided into 3 principal groups (groups U1 to U3) based on their geochemical characteristics (Tables 3.2). The three samples (#35, 51, 52) that are komatiitic-basalts on the Jensen diagram (Fig. 3.5B) are classed as group U1. They have moderate, negative-dipping negative REE_{CN} slopes characterized by flatter LREE (La-Sm) profiles enriched relative to HREEs (Fig. 3.7I) and large negative HFSE (Ta-Nb, Zr-Hf, Ti) anomalies on the N-MORB profiles (Fig. 3.7J). All three samples are hornblende granulites with similar Cpx-Pl-Opx±Bt±Hbl assemblages (Fig. 3.4D).

The remaining groups are both tholeiitic but show distinct Nb-Ta-Ti signatures (Figs. 3.7I-J & Fig. 3.8). Group U2 includes fifteen tholeiitic basalts that mostly have LREE-enriched profiles with flat to HREE-depleted segments, and with Th-LREE abundances higher than N-MORB (Fig. 3.7I) and show deep negative Ta-Nb-Ti anomalies on N-MORB-normalized spidergrams (Fig. 3.7J). To aid in the distinction between groups U2 and U3 based on the HFSE anomalies, the samples are plotted on a bivariate $(Th/Ta)_{N\text{-}MORB}$-$(Ti/Sm)_{N\text{-}MORB}$ ratio-ratio diagram (Fig. 3.8). This diagram highlights that group U2 contains samples with both flatter-positive Ti anomalies ($(Ti/Sm)_{N\text{-}MORB} \geq 1$) and samples with prominent negative Ti anomalies, whereas the negative Ta-Nb anomalies ($(Th/Ta)_{N\text{-}MORB}$) are generally pronounced ($(Th/Ta)_{N\text{-}MORB} \geq 3$). Although samples #39 from the RDT-1 (Fig. 3.7B), #94 from the VT (Fig. 3.7F and Fig. 3.8) and a control sample from the RT (#65; Fig. 3.7H and Fig. 3.8) have shallower Ta-Nb troughs compared to the rest of the profiles within group U2, they are distinguished from group U3 by their strong negative Ti anomalies and are thus, included in group U2. Five of the samples (#47,58,59,95), including one (#95) with a notably flat REE_{CN} slope (Fig. 3.7E and Fig. 3.8), have weakly negative to flat Ti anomalies but are also included in group U2 due to their distinct negative Ta-Nb throughs (Fig. 3.7F and Fig. 3.8). Samples from group U2 could be split into two subgroups at this stage, defined by those with flatter-positive Ti anomalies ($(Ti/Sm)_{N\text{-}MORB} \geq 1$) and those with prominent negative Ti anomalies (Fig. 3.7 and Fig. 3.8). However, for the sake of simplicity, group U2 is discussed as a single dataset until the differences in these HFSE are required for discrimination from the reference suites (see section 3.5). The seven tholeiites classed as group U3 resemble U2 rocks in having weakly- to moderately LREE-enriched profiles but tend to have steeper HREE segments on the REE_{CN} profiles (Fig. 3.7I). In contrast to U2, group 3 have very weak to absent negative Ta-Nb-Ti anomalies (Fig. 3.7J & Fig.

3.8). The group U2-U3 subdivision is also independent of the metamorphic mineral assemblage (Table 3.2). For example, group U2 includes garnet granulites (e.g. #30; Figs. 3.4A-B), garnet amphibolites (e.g. #47; Fig. 3.4C) as well as generic, garnet-poor amphibolites (e.g. #37; Fig. 3.4E).

Samples with different geochemical classifications (U1-3) were collected from various tectonic subdomains within in the study area (Fig. 3.2) and thus, fall within different field-based subdivisions (RDT-1, RDT-2 and VT-type; Fig. 3.7). RDT-1 type outcrops contain 1 x group U1, 3 x group U2 and 1 x group U3 samples (Figs. 3.7A-B). RDT-2 type outcrops contain 2 x group U1, 10 x group U2 and 3 x group U3 samples (Figs. 3.7C-D). The VT-type samples include 2 x group U2 and 3 x group U3 samples (Figs. 3.7E-F). The RT-type is however an exception, with all 4 control samples classified as group U2 (Fig. 3.7G-H). The three geochemical groups define herein are thus, not confined to specific localities within the field area, are not dependant on the field-based subdivision (Fig. 3.2) nor are they dependant on their mineral assemblages.

Figure 3.7. (next page) Geochemical classification of the unknown mafic samples according to immobile trace element concentrations. Samples are subdivided according to the tectonic domains (i.e. different symbols) from which they were collected. Those from the RDT are further subdivided into the RDT-1 and RDT-2 types. The geochemical classification (color coded) is based on shared chondrite REE (left) and N-MORB immobile multi element (right) normalized patterns. A detailed description of the geochemical classification and anomalous samples within the groups is discussed in the text. The chondrite and MORB normalized fields of the geochemical groups are presented in (I) and (J) respectively. Normalized after Sun and McDonough (1989).

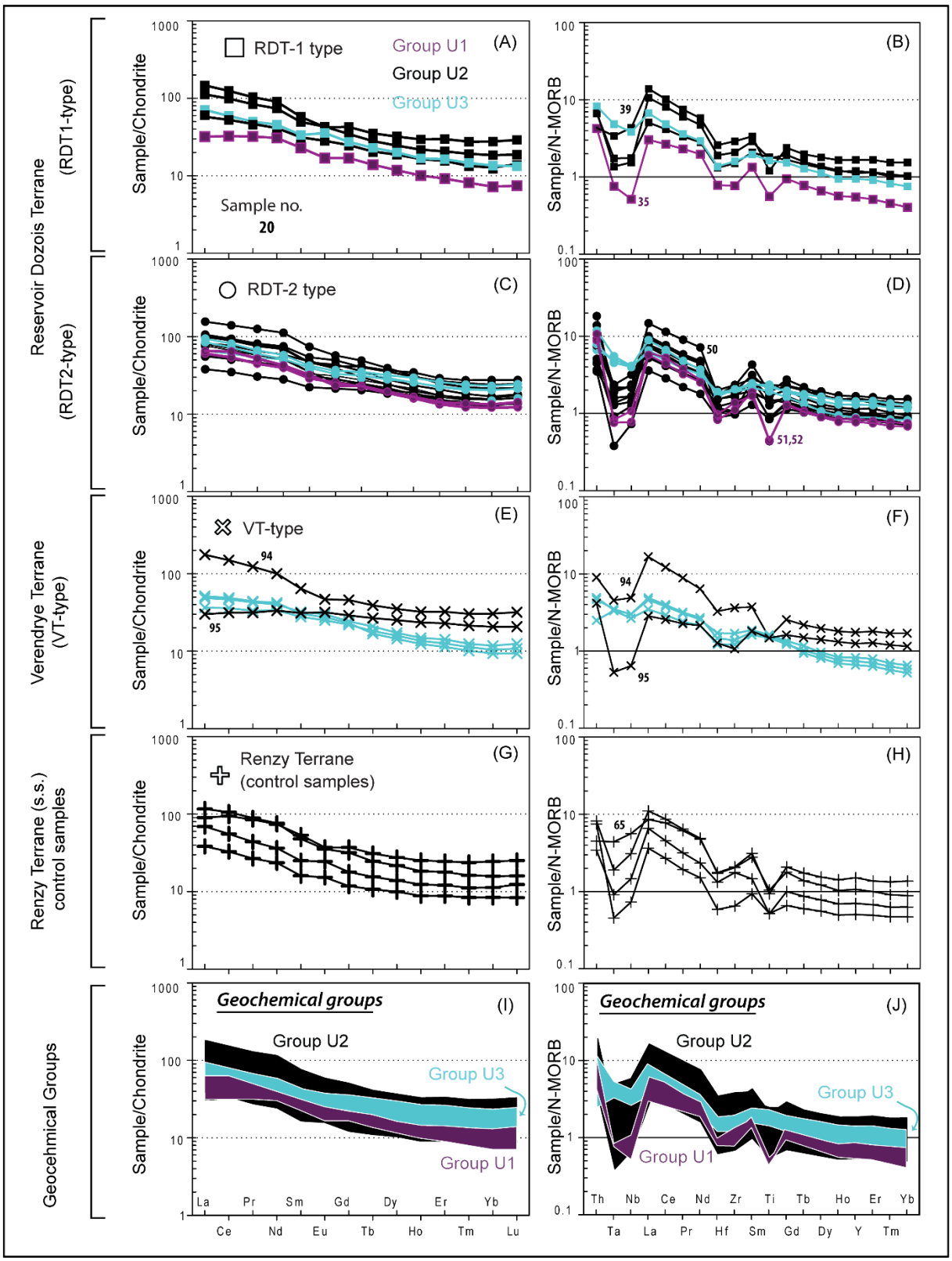
Reservoir Dozois Terrane (RDT1-type)
(RDT2-type)
Verendrye Terrane (VT-type)
Renzy Terrane (s.s.) control samples
Geochemical Groups
Sample/Chondrite
Sample/N-MORB
RDT-1 type
Group U1
Group U2
Group U3
(A)
(B)
Sample no.
20
39
35
RDT-2 type
(C)
(D)
50
51,52
VT-type
(E)
(F)
94
95
Renzy Terrane
(control samples)
(G)
(H)
65
Geochemical groups
(I)
(J)
La Pr Sm Gd Dy Er Yb
Ce Nd Eu Tb Ho Tm Lu
Th Nb Ce Nd Zr Ti Tb Ho Er Yb
Ta La Pr Hf Sm Gd Dy Y Tm

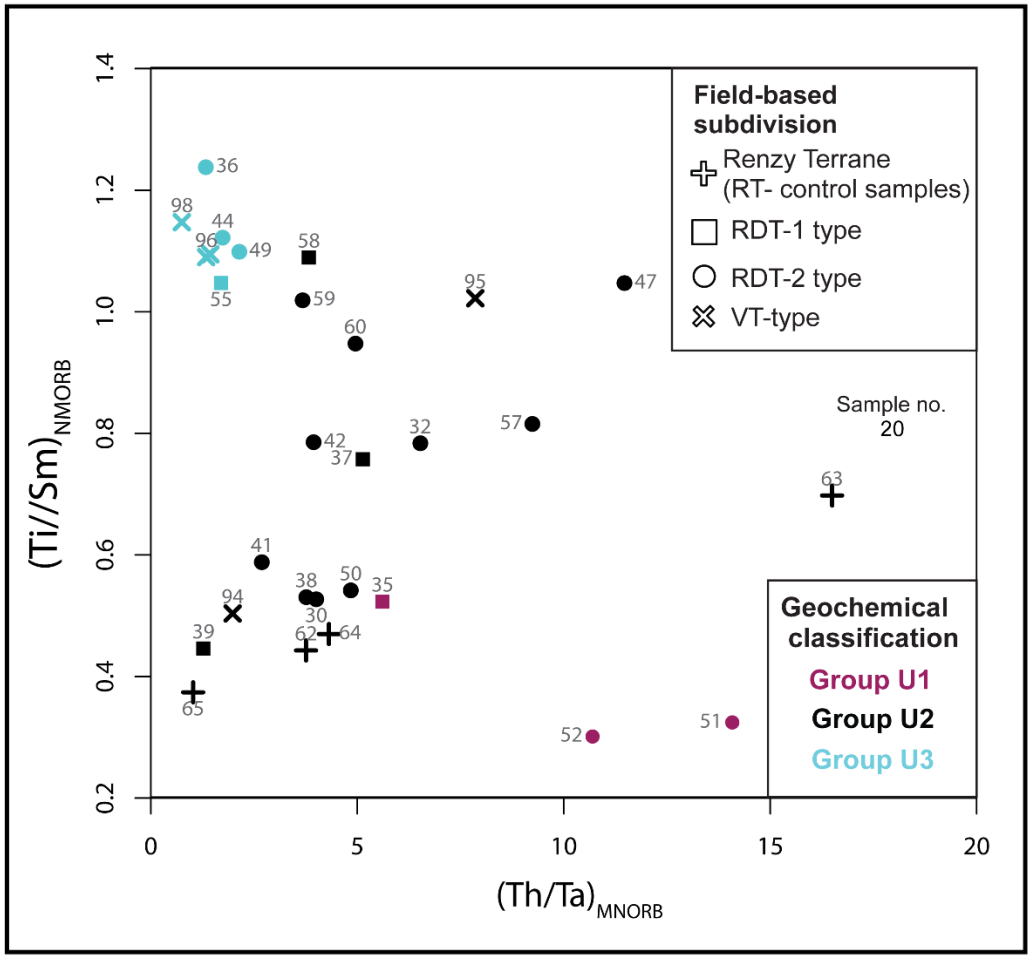

Figure 3.8. A $(Th/Ta)_{N\text{-}MORB}$- $(Ti/Sm)_{N\text{-}MORB}$ ratio-ratio diagram used to aid in the visualization of the HFSE anomalies from the N-MORB normalized spider profiles in Fig. 3.7.

3.4 Reference Suites

The reference suites considered for comparison to the unknown samples are subdivided into those that have an affinity to mafic and ultramafic metavolcanics suites and dyke swarms that intruded in the Archean Superior Province, (thus have a potentially autochthonous affinity) and those that belong to the Allochthonous Belt of the Grenville Province (Fig. 3.1, Table. 3.3), which could represent accreted terranes or a post accretion Andean-type margin or AMCG magmas. While each reference suites is briefly described below, their quantitative geochemical characteristics are presented in the supplementary material (Table B.2).

The reference suites derived from the Archean Superior Province include metavolcanics of the Archean Abitibi Greenstone Belt, in addition to the Proterozoic Matachewan, Senneterre, Sudbury and Abitibi dyke swarms (Condie, 1976). Metavolcanics from the Abitibi Greenstone Belt are considered because they occur only ca. 50 km to the NW of the RDT (Fig. 3.1) and have been correlated to mafic granulite bodies within the GFTZ to the north-east of the study region (e.g. Birkett *et al.*, 1991; La Flèche *et al.*, 2005; Fig. 3.1). The oblique trends of the Proterozoic dyke swarms relative to the Grenville Front (e.g. Fahrig and West, 1986; Fig. 3.1) and their correlation to variably deformed and metamorphosed mafic bodies in the PB of western Quebec (e.g. Indares and Dunning, 1997; La Flèche *et al.*, 2005; Martignole and Martelat, 2005; Fig. 3.1) and Ontario (e.g. Palmer *et al.*, 1977; Dudás *et al.*, 1994; Bethune and Davidson, 1997; Ketchum and Davidson, 2000; Fig. 3.1) establish their selection as reference suites in this study.

Reference suites with an allochthonous affinity include rocks of the Mesoproterozoic RT, located within the immediate study area (Figs. 3.1 and 3.2) as well as the Algonquin coronitic olivine metagabbro suite (Algonquin Suite after Rivers, 1997 and Ketchum and Davidson, 2000), identified within the allochthonous terranes of Ontario (e.g. Davidson and Grant, 1986; Ketchum and Davidson, 2000; Fig. 3.1). These two reference suites have geochemical (e.g. Ketchum and Davidson, 2000; Montreuil and Constantin, 2010), metamorphic (e.g. Indares and Martignole, 1990; Indares and Dunning, 1997), U-Pb age (e.g. Davidson and van Breemen, 1988; Childe, Doig and Gariepy, 1993; Heaman and LeCheminant, 1993; Indares and Dunning, 1997) and Nd-isotope (e.g. Dickin *et al.*, 2014) characteristics typical of the mid-lower crustal segments deformed during the Ottawan phase of the Grenvillian orogeny and thus, supports their affinity to the AB.

Table 3.3. Summary of reference suites considered in this study.

Mafic Suite	Tectonic affinity	Geographic trend and morphology	Age	Geochemical series	Paleo-tectonic setting	Number of samples	Data Source
Abitibi Greenstone Belt	Autochthonous (Superior Province)						
Chibougamau region: Roy Group		W-E trending Greenstone Belt in Superior Province	2734-2711 Ma	Komatiites; basalts to andesitic tholeiites (high Mg and Fe); transitional to calc-alkaline andesites (minor basalts)	Within plate (stagnent-ild system)	28	**Leclerc et al. (2016)**
SVZ (Blake River Group)			2704-2695 Ma			491	**GEOROC online database**
Proterozoic Mafic Suites							
Matachewan Suite		N-S and NW-SE dykes	2473-2446 Ma	Basaltic high-Mg and high-Fe tholeiites (Jensen, 1976) or transitional to calc-alkaline (Ross and Bédard, 2009)	Within plate	47	**Geochemical database of Proterozoic intraplate mafic magmatism in Canada (Ernst and Buchan, 2010)**
Senneterre Suite		NE to ENE dykes	2221±4 Ma-2214±12 Ma	Basaltic to andesitic high-Mg tholeiites and komatiitic (Jensen, 1976) or transitional to calc-alkaline (Ross and Bédard, 2009)	Within plate	13	
Sudbury dykes and metadiabase bodies in PB		NW-SE to N-S dykes; dismembered dykes and isolated bodies in PB	1238±4 Ma	Olivine-diabase alkali (major elements) or tholeiitic basalts (trace elements)	Within plate (Superior Craton)	15	
Abitibi Dyke Suite		NE-SW dykes; deformed dykes	1141±4 Ma	Olivine-diabase alkali (major and trace elements)	OIB-type; Within plate (Laurentia margin)	21	
Algonquin-type coronitic metagabbro	Allochthonous Belt	Clusters of mafic boudins; dismembered components of larger intrusions in Algonquin Terrane (Ontario)	ca. 1170-1150 Ma (1070-1047 Ma metamorphic age)	Olivine alkali (major element) or tholeiitic to transitional basalts (trace element)	Within plate (post Shawinigan orogeny)	10	
Renzy Terrane							
RT-Group 1		Deformed concordant sills and boudins or layers in mixed gneissic packages	ca. 1400 Ma (1072 Ma metamorphic age)	High Mg-tholeiitic basalts and andesites; komatiitic basalts	Arc/back-arc (oceanic)	5	**Montreuil and Constantine (2010) supplementary data**
RT-Group 2				High-Fe (minor high-Mg) tholeiites and transitional basalts, andesite and basaltic andesite		19	
RT-Group 3				High-Fe tholeiitic basalts	Within plate (E-MORB and rare OIB)	7	

3.4.1 Mafic suites with an autochthonous affinity

3.4.1.1 Metavolcanics of the Abitibi Greenstone Belt (AGB)

The Abitibi Greenstone Belt (AGB) in the Superior Province represents one of the largest preserved Archean greenstone belts in the world (Goodwin and Ridler, 1970; Daigneault *et al.*, 2004; Mole *et al.*, 2021). Volcanism in the ABG was characteristically bimodal, with the mafic component being mostly tholeiitic, with associated transitional[2] to calc-alkaline facies, while the felsic volcanic and pyroclastic rocks are mostly calc-alkaline (Thurston *et al.*, 1985; Barrie *et al.*, 1993; Sterckx *et al.*, 2013, 2014). This study uses geochemical data from mafic suites of the Blake River Group (2704-2695 Ma; Ross *et al.*, 2011; McNicoll *et al.*, 2014) and Roy Group (2734-2711 Ma; Ayer *et al.*, 2002; Leclerc *et al.*, 2011), which constitute important and representative volcanic packages in the Southern Volcanic Zone (SVZ) and Chibougamau regions of the Abitibi belt respectively (Fig. 3.1). It is important to reiterate that Abitibi metavolcanics that plot in the calc-alkaline fields in the Jensen (1976) diagram (Fig. B.8) and the Th/Yb vs Zr/Y plot (Ross and Bédard, 2009; Fig. B.9) were not included in the comparison as none of the unknown samples (groups U1-3) plotted in the same (calc-alkaline) fields on the corresponding diagrams. The dominant Abitibi mafic metavolcanic population plots in the sub-alkali field on the Zr/Ti vs Nb/Y diagram (Fig. 3.5C) and in the high-Fe to high-Mg tholeiite and komatiitic basalt fields on the Jensen diagram (Fig. 3.5D). Most are fractionated multiply-saturated basalts. In general, the average komatiitic and tholeiitic basalts from the AGB dataset broadly have flat N-MORB-normalized profiles (Fig 3.9A & Fig. 3.9C) that lack the prominent HFSE (i.e. negative Ta-Nb troughs and Ti anomalies) and are typical of Archean mafic suites derived from a fertile or primitive mantle source and lacking a strong crustal contamination signature (Bédard, 2018).

[2] The 'transitional' geochemical affinity refers to a sub-alkali geochemical series of rocks that plot within the 'transitional' field between tholeiitic and calc-alkaline fields on the Zr/Y vs Th/Yb diagram of Ross and Bédard (2009). Note that samples in this transitional field commonly cluster along the dividing line between the tholeiitic and calc-alkaline fields on the Al-FeT+Ti-Mg (AFM) cation diagram of Jensen (1976). See supplementary figure B.9.

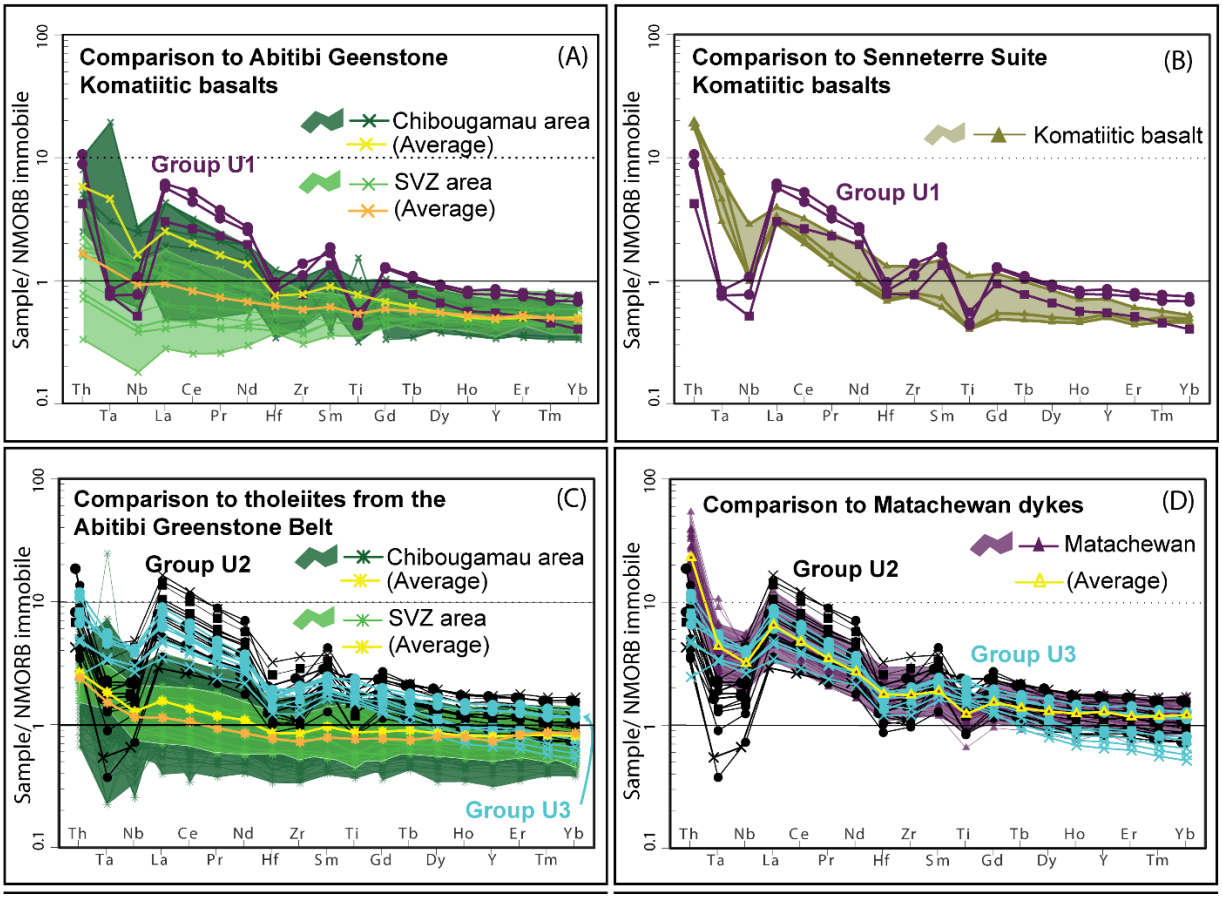

Figure 3.9. MORB-normalized immobile spider diagram comparison of the geochemical groups defined in this study compared against reference suites with an autochthonous affinity. Abbreviations: Allochthonous Belt/Lac Dumoine Terrane (AB), Back-Arc-Basin-Basalt (BABB), Chondrite (CH), Continental-Arc Andesite (CAA), Continental Arc Basalt (CAB), Enriched Mid-Ocean Ridge Basalt (E-MORB), Ocean-Island Basalt (OIB) Ocean-Island Arc Basalt (OIAB), Primitive mantle (PM), (Reservoir Dozois Terrane (RDT), Southern Volcanic Zone (SVZ) and Verendrye Terrane (VT). Data for PM, CH, E-MORB and OIB from Sun and McDonough (1989), for OIAB and CAB from Kelemen *et al.* (2014) and for BABB from Fretzdorff *et al.* (2002). Symbology as in figure 3.5.

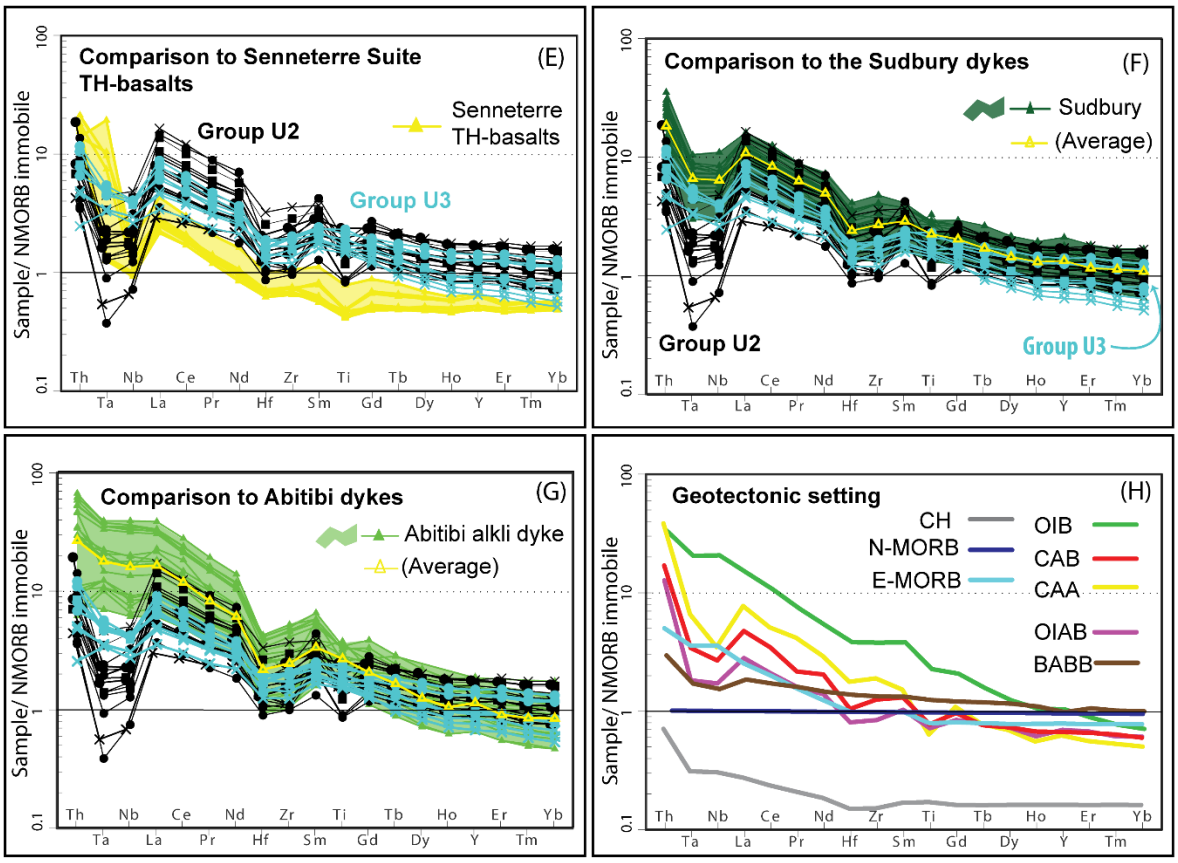

Figure. 3.9. (cont'd).

3.4.1.2 Proterozoic Mafic dyke suites

The Matachewan dyke suite is composed of quartz-normative mafic dykes and is part of the Proterozoic Matachewan Large Igneous Province, which constitutes dyke swarms, layered intrusions and continental flood basalts emplaced in the Superior Province at ca. 2473-2446 Ma (Heaman, 1997; Halls *et al.*, 2005). The dykes are classified as subalkali basalts (Fig. 3.5E), mostly from the high-Fe tholeiitic series (Fig. 3.5F). Although the Matachewan Suite rocks show arc-like MORB-normalized signatures, defined by negative Ta-Nb-Ti anomalies and LILE-enrichment (Fig. 3.8D), previous studies concluded that their chemistry reflects crustal contamination of primary magmas derived from a compositionally heterogeneous mantle plume (Condie, 1997; Phinney and Halls, 2001; La Flèche *et al.*, 2005; Ciborowski *et al.*, 2015).

The Senneterre suite is composed of quartz-normative dykes that formed part of the giant radiating Ungava swarm (Buchan *et al.*, 1998, 2007). Dykes of the Senneterre Suite were emplaced between ca. 2221±4 Ma (Davis *et al.*, 2018) and 2214±12 Ma (Buchan *et al.*, 1993), possibly as a plume-rift system along the eastern Superior Province (Buchan *et al.*, 1998; Hamilton and Buchan, 2016). The dykes are classified as sub-alkali basaltic to andesite and basaltic andesites (Fig. 3.5E) from both the tholeiitic and komatiitic-basalt series (Fig. 3.5F) but are largely considered a relatively primitive suite, compared to the rest of the Proterozoic swarms in the Superior Province (Buchan *et al.*, 2007). Both the komatiitic (Fig. 3.9B) and tholeiitic (Fig. 3.9E) basalts have MORB-normalized profiles with particularly high Th concentrations, that result in steep Th/Nb and Th/La segments, which were interpreted to record contamination by crustal material during plume ascent (Dunphy *et al.*, 1995).

The Sudbury dyke swarm is composed of olivine diabase dykes emplaced at ca. 1238 Ma (Krogh *et al.*, 1987) along the south eastern Laurentian margin (Condie, 1997). Emplacement was originally correlated to a plume-rift system (e.g. Fahrig, 1987; Ernst and Buchan, 2001; Condie, 1997) that led to break up of the Mesoproterozoic Columbia supercontinent (Ernst and Buchan, 1994; Hou *et al.*, 2008) but recent studies suggest the dykes could have exploited regional scale heterogenies during the closure of the Elzevir basin (ca .1250 -1190 Ma; e.g. Shellnutt and MacRae, 2012). Although considered an alkali suite based on major element classification schemes and in previous investigations (e.g. Ketchum and Davidson, 2000; Condie, 1997; Martignole and Martelat, 2005), the Sudbury dykes are classified as a sub-alkali (Fig. 3.5E) and high-Fe tholeiitic basalts (Fig. 3.5F) on the TAS and Jensen diagrams used in this study respectively. Interestingly, previous studies (e.g. Ketchum and Davidson, 2000; Martignole and Martelat, 2005) used the high Zr concentrations of the Sudbury dykes as one of the key geochemical traits that differentiated them from other deformed Proterozoic bodies in the Grenville Province, a distinction which is not necessarily evident in this study (Fig. 3.6D). In general, their enrichment in the most incompatible elements, small negative Nb-Ta and Hf-Zr troughs, and nil-to-positive Ti anomalies also characterize this suite (Fig. 3.9F), which is distinctly different to the other autochthonous reference suites. Based mainly on their trace element characteristics, such as their steep $HREE_{NMOB}$ slopes, the Sudbury dykes were considered products of low degrees (ca. 2%) of partial melting from a subcontinental, garnet-rich lithospheric mantle (Condie, 1997; Shellnutt and MacRae, 2012) or derived from a subduction-modified mantle source (Shellnutt and MacRae, 2012).

The Abitibi dyke suite, not to be confused with the Archean metavolcanics from the Abitibi Belt, is an olivine-bearing diabase dyke swarm (Fahrig *et al.*, 1965; Condie *et al.*, 1987) that was emplaced at ca. 1141 Ma (Krogh *et al.*, 1987). Emplacement was attributed to asthenospheric upwelling (Ernst and Bell, 1992) within, or along the margin of the Superior craton (Condie, 1997) as part of the Keweenwan Rift system (Ernst and Bell, 1992). The Great Abitibi dyke is the largest (ca. 250 m wide and 700 km long) and most studied of the swarm (e.g. Ernst *et al.*, 1987; Ernst and Bell, 1992). The Abitibi dykes have a distinctly more alkaline chemistry according to both major elements (Condie, 1976; Ernst and Bell, 1992) and trace element proxies (Figs. 4.5E). The alkaline signature is also reflected in their incompatible-element-enriched profiles (Fig. 3.9G), typical of ocean island basalts (Sun and McDonough, 1989; Pearce, 1996, 2014; Xia, 2014; Fig. 3.9H).

3.4.2 Mafic suites with an allochthonous affinity

3.4.2.1 Algonquin-type coronitic metagabbro suite

The Algonquin suite are coronitic olivine metagabbros and lesser amphibolite bodies dated at ca. 1170-1150 Ma (Davidson and van Breemen, 1988; Heaman and LeCheminant, 1993; Culshaw *et al.*, 1994) and overprinted by metamorphic ages of ca. 1060-1050 Ma metamorphic ages (Davidson and van Breemen, 1988; Heaman and LeCheminant, 1993; Kendrick and Jamieson, 2016), that have been extensively mapped as clusters and dismembered mafic bodies within the AB of Ontario (Ketchum and Davidson, 2000). The genesis of the Algonquin suite sensu stricto has not been constrained in detail but based on the geochemical interpretations of similar aged (ca. 1160-1145 Ma; McLelland *et al.*, 2004) coronitic metagabbros in the Adirondack Highlands (Regan *et al.*, 2011), they may be related to the AMCG complexes emplaced within the Grenville Province shortly after the Shawinigan orogeny (ca. 1160 Ma; McLelland *et al.*, 2004; McLelland *et al.*, 2010; Regan *et al.*, 2011). The Algonquin suite are classified as sub-alkaline basalts (Fig. 3.5E) from the high-Fe and high-Mg tholeiitic series, with few datapoints falling within the calc-alkaline field (Fig. 3.5F), which were excluded from further comparison. Although the Algonquin dykes have somewhat similar trace element characteristics to the Sudbury suite, with N-MORB normalized profiles enriched in the most incompatible elements and weak negative Ta-Nb anomalies, they differ by having distinct positive Ti anomalies (Fig. 3.10A), distinctly flatter $LREE_{CN}$ profiles (i.e. plot to the left in 3.11C) and lower Zr concentrations (Fig. 3.6D).

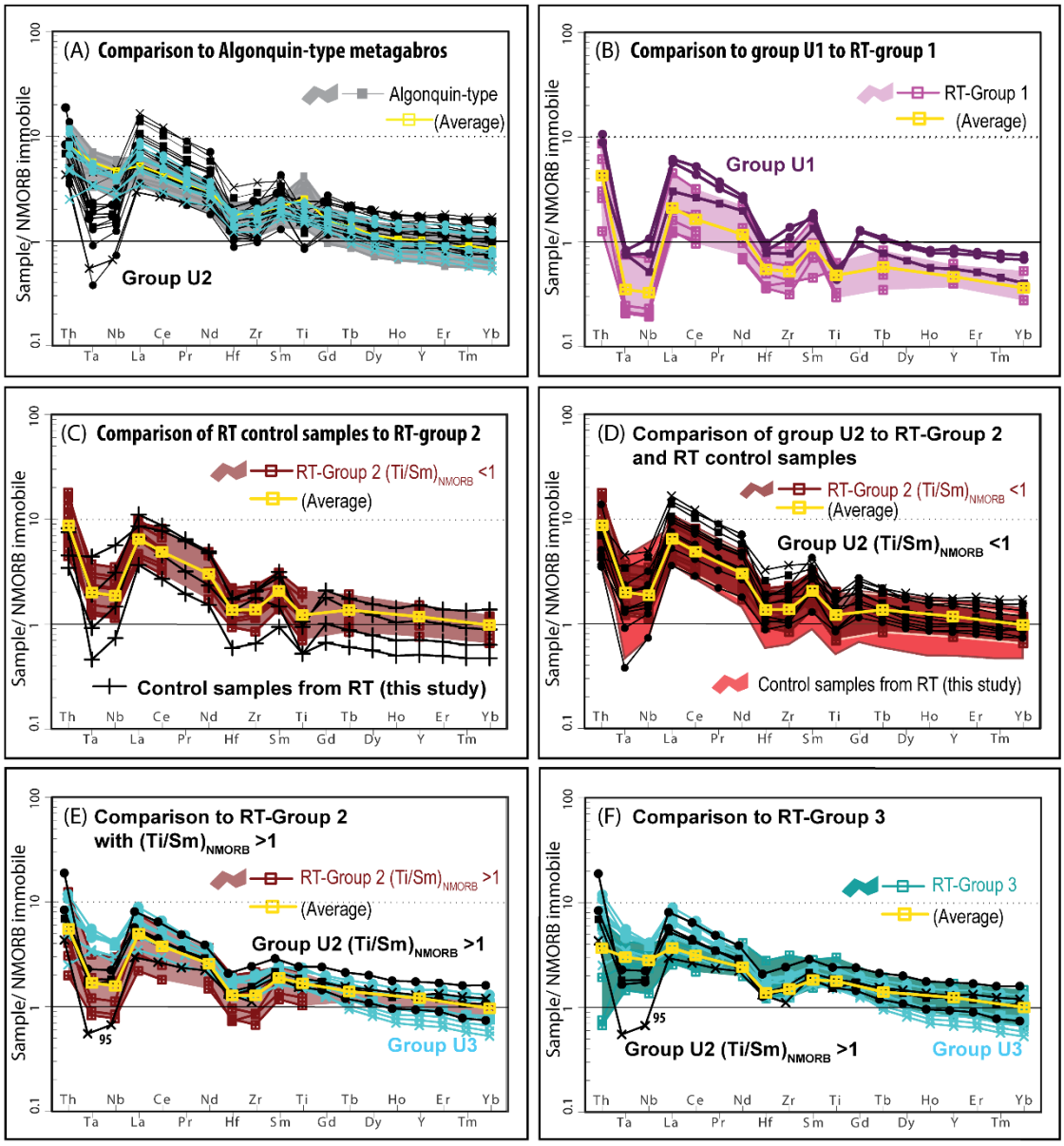

Figure 3.10. MORB-normalized (Sun and McDonough, 1989) immobile spider diagram comparisons of the geochemical groups defined in this study versus reference suites with an allochthonous affinity. Note that samples from group U2 in this study and those from the RT reference suite are subdivided into groups with a negative (C-D) and a positive $(Ti/Sm)_{NMORB}$ ratio (E). Symbology as in figure 3.5.

3.4.2.2 Renzy Terrane mafic suites

The mafic bodies from the RT dataset are interpreted to represent disaggregated fragments of laterally continuous mafic intrusions or layered volcanic flows that are spatially associated with meta- volcano-sedimentary sequences (Montreuil, 2010; Montreuil and Constantin, 2010). The mafic bodies are variably retrogressed, with assemblages ranging from granulite-facies to amphibolite-facies (Montreuil and Constantin, 2010). Although the mafic gneisses are undated, they were interpreted to be ca. 1400 Ma old, based on detrital U-Pb zircon ages from the associated meta- volcano-sedimentary lithologies in the RT (Martignole and Ringuette, 1998), as well as their geochemical affinity to ca. 1400 Ma mafic suites (e.g. Bondy Gneiss Complex; Blein *et al.*, 2003) dated elsewhere in the Grenville Province (Montreuil and Constantin, 2010). Notably, the spatial association with volcano-clastic rocks, the difference in age and metamorphic history (Indares and Martignole, 1990) indicates that the RT outcrops do not constitute intrusive complexes within the RDT but rather part of a distinctly different terrane.

The Renzy mafic bodies were originally subdivided into three groups (RT-groups 1-3) based on differences in petrology and geochemistry (Montreuil, 2010; Montreuil and Constantin, 2010). RT-group 1 in the RT are garnetiferous, two-pyroxene meta-gabbro sills (Montreuil and Constantin, 2010) that are classed as sub-alkaline basalts, basaltic andesites and andesites (Fig. 3.5E), from both the high-Mg tholeiite and komatiitic basalt series (Fig. 3.5F). In general, Montreuil and Constantin (2010) proposed that RT-group 1 may represent a suite of cumulates, rather than a primitive suite and that their trace element characteristics, such as high Th/Ta ratios and strong negative anomalies in the HFSE (Ta, Ti, Zr, Hf; Fig. 3.10B), reflect an arc-metasomatized mantle source.

RT-group 2 bodies dominate the mafic constituents of the RT. They are described as fine to medium grained mafic bands and lenses that extend laterally for less than 5 km or are tightly folded within the meta-volanosedimentary sequences (Montreuil and Constantin, 2010). RT-group 2 represent mafic bodies metamorphosed to granulite facies and those partially to completely retrogressed to amphibolite facies, with variable mineral assemblages, including those with and without garnet (Montreuil and Constantin, 2010). RT-group 2 are mostly classed as sub-alkaline basalts and basaltic andesites with some andesites and one dacite (Fig. 3.5E). On the Jensen diagram, most are high-Fe tholeiites with a few high-Mg tholeiites (Fig. 3.5F). The four RT-group 2 datapoints classed as calc-alkaline basalts and andesites and the one dacitic sample on the same

diagram, are excluded from further comparison with the unknown tholeiitic samples. Whereas all RT-group 2 have prominent negative Nb-Ta troughs on the MORB-normalized diagram, Montreuil and Constantin (2010) showed that they include those with (Fig. 3.10C & Fig. 3.10D) and without (Fig. 3.10E) prominent negative Ti anomalies. It is important to note that the Ti anomalies defined for RT-group 2 samples by Montreuil and Constantin (2010) were based on PM-normalized (Sun and McDonough, 1989) concentrations for Eu, Ti, and Tb. However, because of the selection of the immobile element MORB-normalized diagram in this study, the Ti anomaly in RT-group 2 samples is defined by $(Ti/Sm)_{N_MORB}$, as Gd was not measured in the initial study of Montreuil and Constantin (2010). Montreuil and Constantin (2010) ultimately proposed that an arc/bac-arc setting related to a subduction zone offshore of the Laurentian margin was the most likely geodynamic setting for emplacement of this mafic suite.

RT-group 3 mafic bodies were defined as fine to medium grained granulite bands that contain abundant (cm-sized) garnet (Montreuil and Constantin, 2010). Clinopyroxene-ilmenite symplectite textures in these samples were inferred to represent relics of an eclogitic precursor event (e.g. Indares, 1993; Montreuil and Constantin, 2010). RT-Group 3 samples are classed as sub-alkaline basalts (Fig. 3.5E) and are all high-Fe tholeiites (Figs. 3.5F). Notably they have MORB-normalized profiles with weak-to nil-Ta-Nb troughs and flat to weakly positive Ti anomalies (Fig. 3.10E). In general, RT-group 3 lack evidence for significant crustal input and are interpreted as E-MORB and rare OIB type basalts (Montreuil and Constantin, 2010).

3.5 Comparing unknown samples and reference suites

3.5.1 Comparison to reference suites with an autochthonous affinity

It is unlikely that the any of the samples investigated herein have an affinity to the Abitibi dyke swarm because the unknown samples have sub-alkali compositions (Fig. 3.5A), whereas the Abitibi dykes are an alkali suite (Fig. 3.5E). The Abitibi dykes also have contrasting N-MORB-normalized spidergrams to the unknown samples, characterized by the enrichment of highly incompatible elements compared to the geochemical groups defined herein (Fig..10G).

Komatiitic basalts of the AGB and Senneterre suites are potentially correlative with group U1 samples, which are high-Mg basalts and are classified as ‘komatiitic basalt’ on the Jensen (1976) diagram (Fig. 3.5B). However, the komatiitic basalts of the AGB generally lack the pronounced

Ta-Nb troughs and negative Ti anomalies that characterise group U1 samples (Figs. 3.9A). Komatiitic basalts from the Senneterre suite have prominent Nb-Ta troughs but are more depleted in HREE-Y than group U1 rocks and lack prominent negative Ti anomalies (Fig. 3.9B). Moreover, group U1 rocks have higher $(La/Yb)_{CN}$, $(La/Sm)_{CN}$ and $(Gd/Yb)_{CN}$ ratios than the Archean komatiites and BK (Fig. 3.11A & Fig. 3.11C).

It is unlikely that the Group U2 & U3 tholeiites have an affinity to the tholeiites of the ABG reference suite as the ABG samples generally show flatter N-MORB spidergrams with weak to no absent Nb-Ta and Ti anomalies and are more depleted in all immobile elements compared group U2 and U3 rocks (Fig. 3.9C). Although sample #95 may have a flat REE_{CN} profile comparable to the AGB tholeiites, highlighted by similar $(La/Yb)_{CN}$, $(La/Sm)_{CN}$ or $(Gd/Yb)_{CN}$ ratios (Figs. 3.11A & 3.11C), sample #95 has a distinct Nb-Ta trough (Fig. 3.7F & Fig. 3.8), which discriminates it from this reference suite.

The tholeiites of the Senneterre reference suite are also an unlikely equivalent suite to group U2 and U3 tholeiites. Although the Senneterre tholeiites have weakly negative Ti and strong negative Ta anomalies, HFSE characteristics observed in group U2, the Senneterre tholeiites are more enriched in Th and are depleted in HREE-Y, which define flatter $HREE_{N\text{-}MORB}$ profiles when compared to groups U2 & U3 (Fig. 3.9E). Furthermore, the Senneterre tholeiites have lower $(La/Yb)_{CN}$ and $(Gd/Yb)_{CN}$ ratios (Fig. 3.11A & 3.11C) compared to all samples investigated herein.

In contrast to the previous reference suites, the Matachewan tholeiites have similar N-MORB spider-profiles to tholeiites of group U2 tholeiites (those that are enriched in the incompatible elements), as well as all group U3 samples (Fig. 3.9F). On the incompatible element ratio-ratio diagrams however, the Matachewan suite defines a strongly differentiated suite, defined by combined lower $(La/Yb)_{CN}$ and higher $(La/Sm)_{CN}$ ratios compared to all samples investigated herein (Fig. 3.11A). In addition the Matachewan tholeiites all have lower $(Gd/Yb)_{CN}$ ratios (i.e. flatter HREE profiles) compared to groups U2 & U3 (Fig. 3.11C). Because none of the group U2 & U3 samples plot along the trend line ($r = 0.87$) defined by the Matachewan samples (Fig. 3.11A), nor do they have similar depths for source melting (Fig. 3.11C), it is unlikely that group U2 & U3 have an affinity to the Matachewan reference suite.

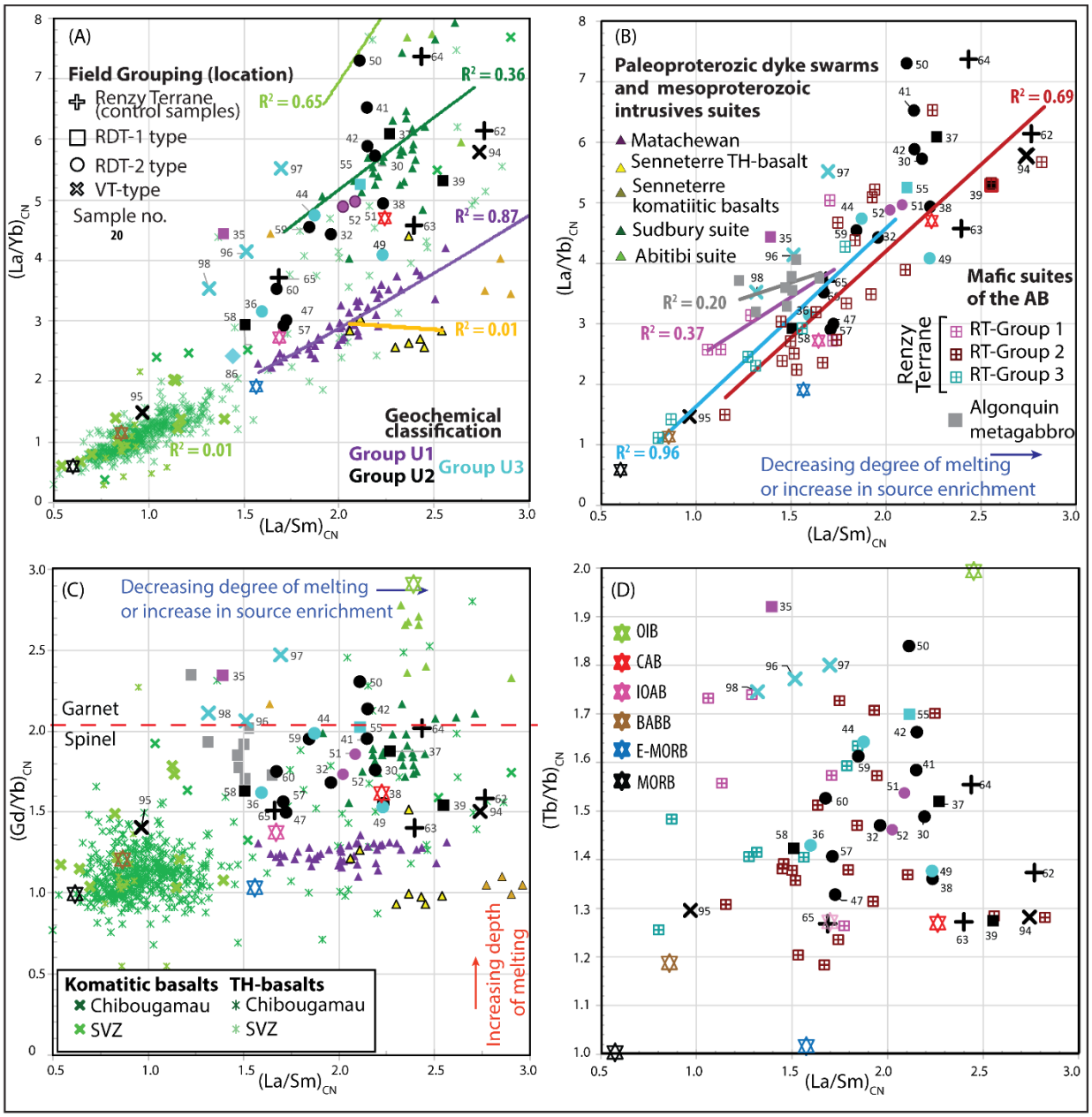

Figure 3.11. Incompatible element ratio-ratio diagrams of the unknown samples in this study compared to the reference suites considered in this study. Trend lines define the range of possible REE_{CN} profiles defined by magmatic fractionation of a reference suite. (A) Total REE slope ($(La/Yb)_{CN}$) versus LREE $(La/Sm)_{CN}$ for unknown mafic samples compared to the Abitibi Greenstone metavolcanics and Proterozoic mafic dyke swarms. Total REE slope ($(La/Yb)_{CN}$) versus LREE $(La/Sm)_{CN}$ for unknown mafic samples compared to the Renzy Terrane and Algonquin metagabbro suites (C) HREE fractionation $(Gd/Yb)_{CN}$ versus LREE $(La/Sm)_{CN}$ for

unknown mafic samples compared to the Abitibi Greenstone metavolcanics, Proterozoic mafic dyke swarms and Algonquin coronitic metagabbro suite. After Álvaro *et al.* (2014) and Rogers *et al.*, (2019), used as a proxy for depth of mafic source melting and degree of enrichment/degree of partial melting. (D) LREE $(La/Sm)_{CN}$ versus $(Tb/Yb)_{CN}$ as a non-quantitative proxy for depth of mafic source melting to include the RT groups, where Gd was not measured (Montreuil and Constantin, 2010).

The Sudbury reference suite is more enriched in incompatible elements compared to most group U2 rocks (Fig. 3.9F). Of the group U2 samples that overlap with the Sudbury suite on the N-MORB spidergrams (Fig. 3.9F), such as samples #39, 94, which are characterized by similar weak Nb-Ta troughs (Fig. 3.7B & Fig. 3.7F), these samples do not plot along the trend line or within the range of the Sudbury samples on the incompatible element ratio-ration diagrams due to the lower $(La/Yb)_{CN,}$ higher $(La/Sm)_{CN}$ (Figs. 3.11A) and lower $(Gd/Yb)_{CN}$ ratios (Fig. 3.11C). It is thus unlikely that group U2 samples have an affinity to the Sudbury reference suite.

The Sudbury reference suite does however, have similar N-MORB spidergram profiles as samples from group U3, all defined by weakly negative Ta-Nb troughs and flat to positive Ti anomalies (Fig. 3.9F). Again the incompatible element ratio-ration diagrams are used to evaluate which of the overlapping group U3 samples also have similar REE characteristics to the Sudbury suite. Samples #96, #97, #98, and #36 all plot away from the Sudbury trend line and are mostly outside the range of the individual Sudbury samples due to their lower $(La/Sm)_{CN}$ and $(La/Yb)_{CN}$ ratios (Fig. 3.11A and Fig. 3.11C). This suggests an affinity of these samples to the Sudbury suite is unlikely. In contrast, samples #44 & #55 plot along Sudbury trendline (Fig. 3.11A) and plot within the main Sudbury data cluster at the transition between the spinel and garnet stability fields in Figure 3.11C. This suggests that samples #44 & #55 may have an affinity to the Sudbury suite. Furthermore, because samples #48 & #49 have similar $(La/Sm)_{CN}$, $(La/Yb)_{CN}$ and $(Gd/Yb)_{CN}$ ratios to some of the outlying Sudbury datapoints (Fig. 3.11A & 3.11C), an affinity of these samples to the Sudbury suite cannot be ruled out.

3.5.2 Comparison to reference suites with an allochthonous affinity

Tholeiites of the Algonquin reference suite differ from group U2 rocks in having deeper Nb-Ta troughs and negative Ti anomalies on the N-MORB spidergrams. Rocks of group U3 however, show similar profiles to the Algonquin suite (in addition to their similarity to the Sudbury reference suite), in particular the presence of flat to positive Ti anomalies (Fig. 3.10A). The incompatible element ratio-ratio diagrams demonstrate that group U3 samples can be subdivided into two subgroups: samples #96, #98 and #36, that plot roughly within the same fields as the Algonquin samples; and samples #44, #48, #49, #55 and #97 that do not (Fig. 3.11B & C). The latter group of samples is thus, not likely part of the Algonquin suite.

The second comparison to reference suites with an allochthonous affinity is to the three geochemical suites already known to exist in the RT (RT-groups 1-3; Montreuil and Constantine, 2010). Group U1 and RT-group 1 both plot within the 'komatiitic basalt' field (Fig. 3.5B & D) and have remarkably similar N-MORB-normalized profiles (Fig. 3.10B). Following the subdivision of the RT-group 2 into samples with and without negative Ti anomalies (after Montreuil and Constantin, 2010), group U2 is now subdivided into samples with negative (Fig. 3.10C-D) and flat to positive $(Ti/Sm)_{N\text{-}MORB}$ ratios (Fig. 3.10E) to aid in the comparative process. Control samples collected from RT in this study (RT-type) have remarkably similar N-MORB-normalized profiles to RT-group 2 rocks with prominent negative Nb-Ta troughs and negative Ti anomalies ($(Ti/Sm)_{N\text{-}MORB} < 1$; Fig. 3.10C). Group U2 have remarkably similar N-MORB spider-profiles to the RT-type (Fig. 3.10D) and to RT-group 2 samples, both with ($(Ti/Sm)_{N\text{-}MORB} < 1$; Figs. 3.10D) and without ($(Ti/Sm)_{N\text{-}MORB} > 1$; Figs. 3.10E) prominent negative Ti anomalies. The negative Nb-Ta troughs of group U2 are also reflected in the RT-type and RT-group 2 samples (Figs. 3.10D-E). Group U2 samples cannot be differentiated further from the RT-group 2 samples on the incompatible element ratio-ration diagrams as group U2 falls within the range defined by the $(La/Sm)_{CN} - (La/Yb)_{CN}$ ratios of the RT-type and RT-group 2 samples (Fig. 3.11B). With the exception of sample #50, group U2 also falls within the same HREE ranges defined by the $(Gd/Yb)_{CN}$ ratios of the RT-type (Fig. 3.11C) and $(Tb/Yb)_{CN}$ ratios of RT-group 2 samples (Fig. 3.11D). Group U3 have remarkably similar N-MORB spider-profiles to RT-group 3, characterized by shallow Ta-Nb troughs and flat to positive Ti anomalies (Fig. 3.10F). Most group U3 samples (including sample #36) plot within the same range as RT-group 3 samples on the incompatible element ratio-ration diagrams (Fig. 3.11B & D), except for samples #96, #97, #98 that have slightly steeper $HREE_{CN}$ slopes on the

$(Tb/Yb)_{CN}$ proxy diagram (Fig. 3.11D). Insomuch as samples from group U1-3 have -N-MORB profiles and REE characteristics that are remarkably similar to predefined groups of the RT, most of the unknown samples herein may have an affinity to the allochthonous RT.

3.6 Discussion

3.6.1 Allochthonous affinity for most samples in the RDT and VT

Immobile trace element geochemical comparisons presented above (also see quantitative Table B.2) allows for the correlation of most investigated samples to a specific reference suite. While the element concentrations selected in previous investigations (e.g. Ketchum and Davidson, 2000; La Flèche *et al.,* 2005) may be distinctive when compared against fewer reference suites, it is also likely that many of the elements, such as the major and LIL (e.g. Rb, Ba) elements were mobile (as discussed in section 3.2.3). This is one of the reasons why differentiation using immobile trace elements on normalized diagrams was considered as an alternative approach for this study.

All three samples from group U1 (#35,51,52) are correlated with the RT-group 1 reference suite. They are all high Mg-basalts (MgO >9 wt%) with 'komatiitic basalt' affinities (Fig. 3.5), share similar HFSE characteristics such as deep negative Ta-Nb and Ti troughs (Fig. 3.10) and group U1 has REE_{CN} profiles that can be explained by variable magmatic differentiation of the RT-group 1 samples (Fig. 3.11).

The RT-type control samples from this study have immobile elements concentrations that are remarkably similar to the RT-group 2 mafic characterized by negative Ta-Nb troughs and $(Ti/Sm)_{N\text{-}MORB} < 1$ (Fig. 3.10C; (Table B.2). This correlation confirms that previously mapped RT outcrops (Montreuil, 2010; Montreuil and Constantine, 2010) were successfully identified in this study based on their lithological and structural characteristics (discussed in sections 1.2) and suggests that the unknown samples classified as RDT1-1 type (see section 3.3.1) are also likely part of the RT. Furthermore, as the mafic rocks of the RT are associated with sub-aerial volcano-clastic succession, it is unlikely that the unknown samples collected from outcrops that physically resemble the RT outcrops (RDT-1 type), represent feeder dykes that intruded the deep crust (e.g. AGB dykes, Matachewan and Sudbury reference suite).

Most samples from group U2 also show a strong resemblance to with RT-group 2. Although sample #50 from group U2 has a higher $(Tb/Yb)_{CN}$ ratio (Fig. 3.11B), it is tentatively correlated with RT-

group 2 based on the large negative Ta-Nb and Ti anomalies (Figs. 3.7D & 3.10D). Although samples #94, #95 are from the VT as previously defined (Fig. 3.2), their group U2 geochemical classification and the dominance of subsolidus deformation textures (Fig. 3.2E), which contrast with the textures generally observed elsewhere within the VT (Lambert *et al.*, 2019), suggests that they are more likely RT-group 2 rocks.

Three group U3 samples (#96, #98 and #36) closely resemble both the RT-group 3 and the Algonquin suite, both of which have an allochthonous tectonic affinity, although none of these group U3 samples contain the coronitic textures typical of the Algonquin suite. Sample #97 from group U3 resembles none of the reference suites considered, but as it was collected < 200 m away from samples #96 & 98 in the VT (Fig. 3.2), it probably has the same allochthonous affinity (RT-group 3 or the Algonquin suite) as these two samples. A further three group U3 samples (#44, #49 and #55) could be correlated either with the autochthonous Sudbury suite or with the allochthonous RT-group 3. Inasmuch as sample #55 comes from a garnet-bearing layered and variably folded package (Fig. 3.3H) with gneisses exhibiting subsolidus strain (i.e. RDT-1 type field grouping), which is typical of the RT (Montreuil and Constantin, 2010), a correlation with the RT-group 3 is proposed. Consequently, only two of the unknown samples (#44, and #49) could still be correlated to a reference suite with an autochthonous affinity (i.e. the Sudbury dike suite), whereas all the others, including those hosted in migmatitic parautochthonous rocks of the RDT (RDT-2 type) and VT (VT-type), are most similar to allochthonous reference suites.

3.6.2 Tectonic setting of the protoliths

Although they could yield contradictory information (Xia and Li, 2019), geochemical tectonic discrimination diagrams are useful in assessing possible tectonic settings that generated the mafic magmas of our unknows. Most of group U1 and U2 plot in the island arc tholeiites (IAT) to back-arc basin basalts (BABB) and continental arc basalts (CAB) on the geotectonic diagrams of Cabanis and Thieblemont (1988; Fig. 3.12A) and Wood (1980; Fig. 3.12B). These groups also mostly fall within the hydrated mantle source field on the Zr/Nb – Nb/Th diagram (Fig. 3.12C), typical for subduction related settings (Condie, 2015). Some samples from group U2 however (including some RT-control samples), fall within the N-MORB and E-MORB fields on the same diagrams (Figs. 3.12A-B) or trend from the hydrated mantle to the enriched mantle fields (Fig. 3.12C). The Th/Yb vs Nb/Yb diagram of Pearce (2008) reveals a similar trend, where group U1 and group U2 mostly

cluster within the oceanic arc field but some group U2 samples plot along the mantle array (Fig. 3.12D), a trend which is a common characteristic for mafic suites within modern-day back-arc basin (Pearce, 2014). On the more recent N-MORB-normalized Th-Nb diagram of Saccani (2015) group U1 falls within the BABB field, characterized by the input of subduction components (e.g. immature intra-oceanic or ensialic back-arcs), similar to RT-group U1 (Fig. 3.12E), whereas group U2 are spread across the arc-influenced (back-arc A) and extensional N-MORB-influenced (back-arc B) fields, similar to RT-group 2 samples (Fig. 3.12E). Based on these geochemical signatures (Fig. 3.9H & Fig. 3.12), the geotectonic characteristics for group U1 and group U2 are therefore, most consistent with a back-arc setting characterized variable input of the subduction component. These characteristics are consistent with the paleotectonic environment suggested for the arc-modified RT-group 1 and back arc basin RT-group 2 suites for the RT (Montreuil and Constantin, 2010).

The geotectonic signatures for group U3 samples are distinctly different from the arc-modified mantle signatures of groups U1 and U2. N-MORB-normalized patterns of group U3 rocks are most similar to enriched (E)-MORB profiles (Fig. 3.9H). They also mostly plot in E-MORB field on the tectonic diagrams of Cabanis and Thieblemont (1988; Fig. 3.12A), Wood (1980; Fig. 3.12B) and the enriched mantle (EM) field of Condie (2015; Fig. 3.12C). The location near the E-MORB poles of the mantle array on the diagrams of Pearce (2008; Fig. 3.12D) and Saccani (2015; Fig. 3.12E), support an E-MORB intraplate environment for group U3. The enriched E-MORB signature for group U3 is thus, consistent with the tectonic settings proposed for the autochthonous Sudbury suite, or with the allochthonous Algonquin and RT-3 suites (Fig. 3.12E).

Interestingly, none of the group U1 and group U2 samples with arc or back-arc signatures, plot within the continental-arc field on the diagram of Pearce (2008; Fig. 3.12D). Nor do they cluster with Andean mafic rocks (Fig. 3.12D). Notably, the Andean dataset in Figure 3.12D includes basaltic lavas from the Payenia Basaltic Province, a typical back-arc basin to the Andean arc-front (Espanon *et al.*, 2014 and references therein) and consist of basalts both with (e.g. Llancanelo) and without (e.g. Payún Matrú) strong arc-like signatures (Espanon *et al.*, 2014), similar to what is observed across the group U2 samples in this study. If the correlation of group U1 & group U2 samples to suites of the ca. 1400 Ma RT (Montreuil and Constantin, 2010) is correct, these data provide no support for models involving a continental Andean-style active margin along the SE-margin of Laurentia (current coordinates) at this time (Geon 14; e.g. Carr *et al.*, 2000; Rivers and

Corrigan, 2000; Rivers *et al.*, 2012; Maity and Indares, 2018). Instead, these data support the models of Montreuil and Constantin (2010) and others in the Grenville Province (e.g. Sappin *et al.*, 2009) that propsoed the mafics rocks are derived from one of the numerous arc/back-arc systems that were subsequently accreted to Laurentia during one of the orogenic events that preceaded the Grenvillian Orogeny (see section 1.2.2).

Figure 3.12 (next page). Geotectonic diagrams mafic samples collected in this study and select reference suites. (A) Th-Tb-Ta ternary diagram of Cabanis and Thieblemont (1988). (B) Th-Hf-Ta ternary diagram of Wood (1980). (C) Zr/Nb vs Nb/Th diagram of Condie (2015) showing the fields for various mantle sources of Proterozoic oceanic basalts (i.e. not contaminated by crustal components). (D) Nb/Yb – Th/Yb diagram of Pearce (2008). Andean mafic geochemistry derived from the GEOROCK database and Espanon *et al.* (2014). (E) Th vs Nb N-MORB normalized (Sun and McDonough, 1989) diagram of Saccani (2015). Back-arc A: back-arc basin basalts (BABB) characterized by input of subduction or crustal components (e.g. immature intra-oceanic or ensialic back-arcs). Back-arc B: BABBs showing no input of subduction or crustal components (e.g. mature intra-oceanic and ensimatic back-arcs). Abbreviations: Assimilation-fractional crystallization (AFC); Crustal components (C); Depleted mantle (DM); Enriched mantle (EM); Fractional crystallization of Ol + Cpx + Pl (F); Fractional crystallization (FC); Hydrated mantle (HM); Mantel source variation (M); OCTZ: ocean-continent transition zone. Ocean island-type (plume-type) component enrichment (OIB-CE); Partial melting (P-melt); Subduction components (S); Supra-subduction zone enrichment (SSZ-E). Symbology as in figure 3.5.

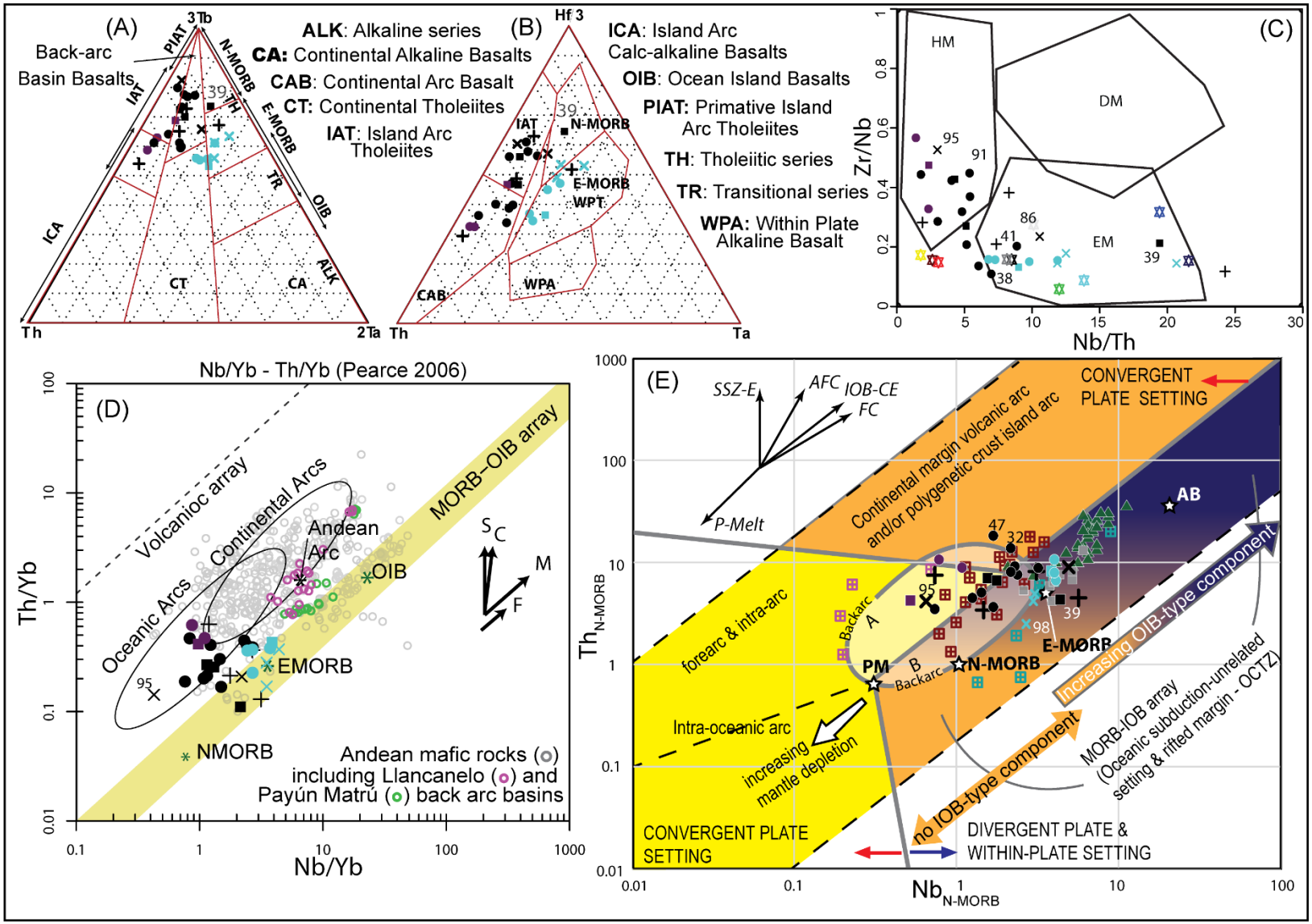
(A)
3Tb
Back-arc
Basin Basalts
PIAT
IAT
N-MORB
E-MORB
TR
OIB
ICA
CT
CA
ALK
TH
39
Th
2Ta
ALK: Alkaline series
CA: Continental Alkaline Basalts
CAB: Continental Arc Basalt
CT: Continental Tholeiites
IAT: Island Arc Tholeiites
(B)
Hf 3
IAT
N-MORB
E-MORB
WPT
CAB
WPA
Th
Ta
ICA: Island Arc Calc-alkaline Basalts
OIB: Ocean Island Basalts
PIAT: Primative Island Arc Tholeiites
TH: Tholeiitic series
TR: Transitional series
WPA: Within Plate Alkaline Basalt
(C)
HM
DM
EM
95
91
86
41
38
39
Zr/Nb
Nb/Th
Nb/Yb - Th/Yb (Pearce 2006)
(D)
Volcanioc array
Continental Arcs
Andean Arc
Oceanic Arcs
MORB–OIB array
OIB
EMORB
NMORB
Andean mafic rocks (o) including Llancanelo (o) and Payún Matrú (o) back arc basins
Th/Yb
Nb/Yb
(E)
SSZ-E
AFC
IOB-CE
FC
P-Melt
CONVERGENT PLATE SETTING
Continental margin volcanic arc and/or polygenetic crust island arc
forearc & intra-arc
Backarc A
Backarc B
PM
N-MORB
E-MORB
AB
47
32
95
98
39
Intra-oceanic arc
increasing mantle depletion
Increasing OIB-type component
MORB-IOB array (Oceanic subduction-unrelated setting & rifted margin - OCTZ)
no IOB-type component
CONVERGENT PLATE SETTING
DIVERGENT PLATE & WITHIN-PLATE SETTING
Th N-MORB
Nb N-MORB

3.6.3 The tectonic architecture for the Grenville Orogen in western Quebec and geodynamic implications

The identification of the inferred allochthonous rocks within the PB have implications on the geodynamic model for structural reworking of the Grenville Province PB in western Quebec during the last (Rigolet) phase of the Grenville Orogeny because they provide a better understanding of the 1st order architecture along the Hw117 transect. More specifically, the distribution of the mafic bodies can help define the Allochthon Boundary Thrust (ABT) which should separate the AB from the PB (Rivers *et al.*, 1989; Rivers, 2008).

Firstly, the distribution of the two group U3 samples (#44, #49) that are potentially correlatable to the Sudbury suite, supports the southeastern extension of the contiguous Superior Province to the Nd-model age boundary in the RDT (Dickin *et al.*, 2014; Dickin and Guo, 2001; Guo and Dickin, 1996). However, a geochronology investigation is still required to confirm the affinity of these two samples to either the ca. 1230 Ma Sudbury or ca. 1400 Ma Renzy mafic gneisses.

Secondly, the majority of the unknown samples collected within the migmatitic gneisses of parautochthonous RDT show a strong affinity to geochemical groups defined for the allochthonous RT (RT-groups 1-3; Montreuil and Constantin, 2010). These findings support the field-based hypothesis that numerous Renzy-looking outcrops dispersed within the greater RDT are indeed part of the RT (Lambert *et al.*, 2019; see sections 1.2.5 & chapter 2). The distribution of these allochthonous rocks also suggest that parts of the RT are found further NW than was previously identified along the Hw117 transect (e.g. Indares and Martignole, 1990; Montreuil and Constantin, 2010; Dickin *et al.*, 2014) and suggests that the ABT is a dismembered and cryptic boundary in the study area.

Finally, four group U3 samples (#36, #96, #97, #98) are potentially correlated to either the allochthonous RT-group 3 and Algonquin metagabbro reference suites. Although the coronitic metagabbros of the Algonquin suite were originally used to delineate the AB from the PB (Ketchum and Davidson, 2000), Dickin *et al.* (2017) argued that the Algonquin suite rocks are only found in Paleoproterozoic crust (T_{DM} ages 1.65-1.79 Ga), located structurally below the AB in Ontario. As samples #96, #97, #98 were sampled within the Paleoproterozoic VT domain (Fig. 3.2) the possible geochemical affinity of these samples to the Algonquin suite would support the

arguments of Dickin *et al.* (2017) and infers that the ABT lies to the SE of sample #98, likely disguised by late (ca. 1020 Ma; Martignole and Friedman, 1996 deformation along the Baskatong Shear Zone (Fig. 3.2). In this model, the Nd-model age boundary along the NW margin of the VT (Fig. 3.2) could then define the basal thrust to 'parautochthonous duplex' structures, proposed to be the result of NW-directed in-sequence, thick-skinned thrusting of Paleoproterozoic or magmatically reworked Archean crust over the PB (Herrell *et al.*, 2006; Dickin *et al.* 2017). However, as noted by Dickin *et al.* (2017), this thrusting would have accommodated crustal shortening of at least 200 km, which infers the VT represents a variably transported domain and is thus, still 'allochthonous' according to the definition of Rivers *et al.* (1989) and Ketchum and Davidson (2000). Consequently, clarification of the 'allochthonous' terminology and the unification of the structural context of the ABT in the Grenville Province is still required. Until the 'allochthonous' problematic is resolved, the affinity of samples #96,#97, #98 to the AB or PB remains to be confirmed. Alternatively, as samples #96,#97, #98 as well as #36 do not contain the distinct coronitic textures of the Algonquin metagabbro suite (e.g. Indares and Dunning, 1997; Ketchum and Davidson, 2000), the possible affinity of these four samples to the RT-group 3 reference suite cannot be ruled out.

To integrate the field based (see sections 1.2.5 & 2.3) and geochemical data into a coherent model, this study proposes that the lower part of the AB in western Quebec, comprised predominately of mafic rocks from the RT, was reworked during deformation of the underlying parautochthonous rocks (RDT and VT) during late Grenvillian deformation (Rigolet phase; see chapter 4) and now represent variably dismembered mafic fragments of allochthonous crust within a 'sea' of parautochthonous gneisses. These observations seem inconsistent an architecture previously defined for the Hw117 transect (Martignole 2000; Dickin *et al.*, 2014). Dickin *et al.* (2014) proposed that the remnants of the RT, and by extrapolation these newly correlated Renzy mafic bodies, represent tectonic klippen structurally overriding the parautochthonous rocks of the RDT. However, the geochemical comparisons provided in this chapter show that many of the allochthonous mafic bodies, especially RDT-2 type, constitute boudins and blocks completely enveloped by highly migmatitic parautochthonous gneisses within the RDT (Fig. 3.3A-C) and possibly the VT gneisses (samples #96, #97, #98; Fig. 3.3D). Alternatively, the architecture now preserved along Hw117 could be explained by a tectonic model similar to that proposed for the Central Grenville Province, where partial melting and strain localization during the Rigolet phase

promoted the incorporation of relatively rigid allochthonous crust into a flowing parautochthonous channel (e.g. Jannin, 2017; Jannin *et al.*, 2018; Labat *et al.*, 2020). The results of this geochemical investigation are combined with structural (chapter 2) and geochronological studies (chapter 4) to further support this model and are discussed in detail in chapter 5.

3.7 Conclusions

To better understand the 1st order architecture of the Grenville Province in western Quebec, this chapter investigates the geochemistry of mafic granulite to amphibolitic bodies hosted by gneissic rocks distributed within well exposed subdomains (RDT, VT, RT) along the Hw117 transect that straddles the boundary between the AB and PB in the Grenville Province. Herein the immobile element geochemical signatures of these mafic bodies are systematically compared with those of numerous reference suites derived from the autochthonous Superior Province or the AB of the Grenville Province. The findings of this study allow us to conclude the following:

- Twenty-nine unknown mafic samples collected across the RDT and VT subdomains of the PB can be subdivided into three geochemical groups irrespective of their field relationships or mimic mineral assemblages. Group U1 and are classified as 'komatiitic basalts' on the diagram of Jensen (1976) and have large negative Ta-Nb and Ti anomalies on N-MORB-normalized spidergrams. Group U2 and group U3 are tholeiitic basalts (and lesser basaltic andesites). Group U2 is characterized by N-MORB-normalized profiles with large negative Ta-Nb and variable negative Ti anomalies, whereas group U3 has N-MORB-normalized profiles characterized by only weak Ta-Nb troughs and flat to positive Ti anomalies in the latter groups.
- The majority (22) of the newly classified samples are correlated to mafic groups defined for the allochthonous RT (RT-groups 1-3). Group U1 is correlated to the 'komatiitic basalts of RT-group 1'. Group U2 is most likely correlated with RT-group 2 tholeiitic basalts. Four of the group U3 samples have characteristics similar to both the Algonquin suite and to a suite of the RT (RT-group 3), both of which are considered allochthonous reference suites. Two remaining samples could be correlated to either the autochthonous Proterozoic Sudbury dyke suite or those of the RT (RT-group 3) but require additional geochronology investigations to distinguish between the two reference suites.

- Group U1 mafic rocks have geochemical signatures that indicate they were derived from a mantle modified by subduction processes, whereas group U2 samples have characteristics of a back-arc basin basalts with variable subduction input. Notably, none of the samples from these two groups have Andean-style continental signatures, which supports previous models that proposed these mafic rocks were formed in arc/back-arc system outboard of Laurentia at this time and were accreted to the Laurentian margin before Grenvillian orogenesis (e.g. Sappin *et al.*, 2009; Montreuil and Constantin, 2010) Group U3 have trace element signatures typical of E-MORB basalts, which is consistent with those of their possible correlative suites: the RT-group 3; the coronitic metagabbro Algonquin suite; and the Sudbury suite.
- The geochemical correlation of multiple mafic bodies within the PB to mafic suites with an allochthonous affinity, support the field observations that many of these mafic bodies may represent variably retrogressed granulitic fragments of the structurally overlying RT.
- The architecture along Hw117 is now defined by a series of allochthonous rocks enveloped within the highly migmatitic parautochthonous gneisses along the Hw117 transect.
- This architecture could be explained by a model similar to recent models proposed in the central Grenville province, where the lower part of the AB was dismembered and incorporated into a ductile PB channel during the later Rigolet phase of the Grenvillian Orogeny.
- The 1st order architecture of the western Grenville Province is more complex than was previously perceived and suggests that, until the mode of deformation within the PB is better constrained, the delineation of upper and lower structural levels and their boundaries (e.g. ABT), solely through the correlation of mafic suites unique to each level, may be problematic elsewhere in the Grenville Province.

CHAPTER 4 ARTICLE 1: PROTRACTED MELT-PRESENT DEFORMATION DURING THE RIGOLET PHASE OF THE GRENVILLIAN OROGENY. INSIGHTS FROM GEOCHRONOLOGY ALONG THE HIGHWAY 117 TRANSECT THROUGH THE GRENVILLE PROVINCE IN WESTERN QUEBEC, CANADA

Christopher William Lambert, Félix Gervais, James Crowley, Abdelali Moukhsil (MERN), Charles Kavanagh-Lepage.

Article accepted by the Journal of Precambrian Research on 1 December 2022.

4.1 Abstract

In this contribution we use U-Pb zircon geochronology to investigate the age of melt-present deformation within the various structural levels of the Mesoproterozoic Grenville Orogen that are exposed along the Highway 117 transect in western Quebec, Canada. Samples include six syn- to late-deformational felsic leucosomes and injection veins. Four of them are physically linked with hornblende-bearing leucosome in their host gneiss and all six contain undeformed quartz grains, implying they were deformed while still partially molten. Zircon from all samples reveal complex morphologies defined by inherited cores and successions of texturally distinct zones, that mostly share trace element characteristics and yield overlapping Grenvillian $^{207}Pb/^{206}Pb$ weighted mean ages between ca. 1020-968 Ma. A crustal panel charactered by pervasive migmatites that present evidence for protracted suprasolidus deformation, are key characteristics of channel flow during the youngest phase (Rigolet) of the Grenville Orogen. Field data also indicate that, coeval to deformation in the lower structural level, felsic dykes brecciated mafic components within the upper level; these components were subsequently incorporated into the ductile channel as decametre-sized mafic boudins. The findings from this study are comparable to recent models advocating Rigolet ductile flow within the Parautochthonous Belt in eastern Quebec but differ from the current conceptual models viewing proposed for the evolution of the orogen during this phase.

4.2 Introduction

Continental collisional orogens are dynamic and complex tectonic systems that played vital roles in remolding the Earth's crust. Their dynamic nature commonly results in the preservation of spatially and temporally distinct, deformation and metamorphic histories, across the orogen.

Knowledge of how and when deformation was accommodated within distinct parts of these orogens (Cottle *et al.*, 2015) is thus, critical to feeding the ever-shifting scientific understanding of how mountain belts evolve, particularly those that straddle the transition between ancient (e.g. Precambrian) and modern (e.g. Phanerozoic) tectonic regimes (cf. Sizova *et al.*, 2014; Weller and St-Onge, 2017).

Conceptual models for collisional convergent orogens are broadly subdivided into two end-members on the basis of their increasing temperature (T) and magnitude (M): small cold orogens (low-T-M) and large-hot and long-duration orogens (LHO; high T-M) (Beaumont *et al.*, 2006; Jamieson and Beaumont, 2013). Whereas the tectonic processes leading to burial and exhumation within small cold orogens are largely considered to be dominated by critical taper theory, processes within LHOs have been the focus of topical debate (see Jamieson and Beaumont, 2013 and Cottle *et al.* 2015 for detailed reviews), mostly due to opposing models derived from either critical taper or channel flow theories (e.g. Searle *et al.*, 2007; Kohn, 2008; Gervais and Brown, 2011; Simony and Carr, 2011). Critical taper theory is based on the maintenance of a critical angle of taper within an orogenic thrust-wedge by processes such as basal accretion, foreland-ward thrust propagation and/or thinning by normal-sense faulting and erosion (Platt, 1986; Dahlen, 1990). Rocks are coupled through the evolution within the thrust-wedge and deformation results in pervasive reverse-sense finite-strain patterns and foreland-propagating thrust stacks (Gervais and Brown, 2011), typical of fold-and-thrust belts (e.g. Elliott, 1976; Davis *et al.*, 1983; Dahlen, 1990) and tectonic duplexes (e.g. Decelles *et al.*, 2001; Robinson and Martin, 2014; He *et al.*, 2015). In contrast, channel flow typically occurs within the hot, mid-lower crustal infrastructure of the thickened orogenic plateau, when a package of melt weakened (i.e. partially molten) rocks reach a critically low viscosity, decouple from the stronger overlying superstructure, and flows over the (former) foreland of the orogen (Beaumont *et al.*, 2006; Grujic, 2006; Vanderhaeghe, 2009) in response to lithostatic pressure gradients (Gervais and Ranalli, 2017). Channel flow can be homogeneous, when the channel occurs within a sufficiently weak, compositionally homogenous mid-crust or flow can be heterogeneous when it involves a combination of lower-viscosity mid-crust and stronger lower crustal segments (Beaumont *et al.*, 2006). A variation of ductile flow can also include the tectonic forcing of ductile nappes over a strong, under thrusted indenter (Beaumont *et al.*, 2006; Fritz *et al.*, 2009; Grujic *et al.*, 2011; Jamieson and Beaumont, 2013). Tectonic fabrics resulting from lateral channel flow should mostly be shallow dipping and can consist of near-peak

metamorphic assemblages, whereas if the channel is exhumed during flow, high-temperature retrograde mineral assemblages are expected (Jamieson *et al.*, 2004; Vanderhaeghe, 2009; Gervais and Brown, 2011).

The Grenville Province in Canada is the largest and best exposure of the Mesoproterozoic Grenville Orogen, an archetypal candidate for a LHO (Jamieson *et al.*, 2007, 2010; Rivers, 2008, 2015). The Grenville Orogen is considered to be the result of the continental collision between Laurentia and possibly Amazonia (Li *et al.*, 2008) between ca. 1090 – 980 Ma (Gower and Krogh, 2002; Rivers, 2015; Tollo *et al.*, 2004). The Grenville Province is principally subdivided into two structural levels, juxtaposed along the regionally continuous Allochthon Boundary Thrust (ABT; Fig. 4.4.1; Rivers *et al.*, 1989; Rivers, 2008). In the footwall of the ABT, the Parautochthonous Belt (PB) consists mostly of Laurentian basement gneisses of the contiguous Archean Superior Province and its Proterozoic sedimentary cover sequences that were reworked to amphibolite and local granulite grades during the younger (1005-960 Ma) Rigolet phase (Wynne-Edwards, 1969, 1972; Rivers, 1997, 2009). In the hanging wall, the Allochthonous[3] Belt (AB) is composed of an assemblage of Mesoproterozoic peri-cratonic to exotic rocks variably accreted to the Laurentian margin before the Grenville orogenesis (Rivers *et al.*, 2012; Rivers, 2015 and references therein). The AB is further subdivided into a lower structural level, part of the mid-lower crust of the orogenic hinterland that was deformed at high (granulite-eclogite facies) metamorphic grades during the Ottawan phase (1090-1020 Ma) of the orogeny (Rivers, 2008; Rivers, 2009) and an upper structural level, that largely escaped this event and formed the 'Orogenic Lid' (Rivers *et al.*, 2008 & 2012). The 'Orogenic Lid' regroups all rocks that recorded cooling below ca. 500-550ºC and/or deformation during prior to the main deformation and metamorphic event associated with the Grenville Orogen 1090-980 Ma). They would have formed a passive upper crustal lid while high-grade metamorphism and deformation took place at lower structural levels during the Grenville Orogeny. This concept revolutionized the understanding of Grenvillian tectonics because it implies that the Grenville Orogen is not only a slice through the deep root of an ancient orogen, as was commonly assumed (see numerical models of Jamieson *et al.*, 2007 for example), but is a collage of crustal blocks deformed and metamorphosed at different times and places across an orogen,

[3] In this study the term allochthonous follows the terminology of Rivers *et al.* (1989) that refers to far-travelled domains with a distinct structural and metamorphic histories but is somewhat contentious, as they are not necessarily exotic to Laurentia.

similar to the Canadian Cordillera (Gervais and Brown, 2011) or the Himalayan (Cottle *et al.*, 2015) orogens, although unmetamorphosed rocks are absent from the Grenville Province.

Recent conceptual and numerically-derived models for the Grenvillian Orogeny proposed diachronous metamorphic and structural histories for the PB and AB (Rivers, 2009; see Rivers, 2015 for a comprehensive review). Evolution of the AB would have involved heterogeneous channel flow of the mid and lower crust (Beaumont *et al.*, 2006; Rivers, 2008; Jamieson *et al.*, 2010) and/or expulsion of ductile nappes (Jamieson *et al.*, 2007, 2010) during convergence. Reduction of the convergence rate at the end of this first orogenic phase would have led to gravitational collapse of the hot orogen with the formation of core complexes (Rivers *et al.*, 2012; Rivers and Schwerdtner, 2015; Soucy La Roche *et al.*, 2015) and/or expulsion of partially molten crust towards the foreland (Jamieson *et al.* 2007). Renewed convergence at ca. 1000 Ma would have shifted the focus of thickening from the hinterland toward the foreland, where different crustal levels of the Laurentian basement were reworked by under-thrusting, followed by rapid burial and subsequent foreland-ward directed, thrust stacking within an orogenic wedge (Martignole and Martelat, 2005; Rivers, 2008, 2009; van Gool *et al.*, 2008). The youngest of these thrusts, the Grenville Front, is a crustal scale structure that separates the Grenville Province from the Archean Superior Province for most of its length (Fig. 4.1; Wynne-Edwards, 1972; Rivers *et al.*, 1989). Rivers (2009) proposed that the diachronous tectono-metamorphic histories and ca. 20 Ma hiatus between the Ottawan and Rigolet phases marked the switch from a long hot phase (Ottawan) to a cold-short phase (Rigolet). Subsequent studies in the central Grenville Province, rather documented a protracted period of partial melting and heterogeneous channel flow during the Rigolet phase (e.g. Jannin, 2017; Jannin *et al.*, 2018).

In this study we present the results of LA-ICP-MS U-Pb zircon geochronology from six samples that represent felsic leucosome, injection veins and dykes, within PB and AB orthogneisses exposed along the Hw117 transect in western Quebec (Fig. 4.1). The new age data for the age of penetrative ductile deformation in the PB furthers the understanding of Grenvillian geodynamics within western Quebec and thus, allow us to propose an alternative model for deformation during the Rigolet phase of the Grenville Orogeny in western Quebec.

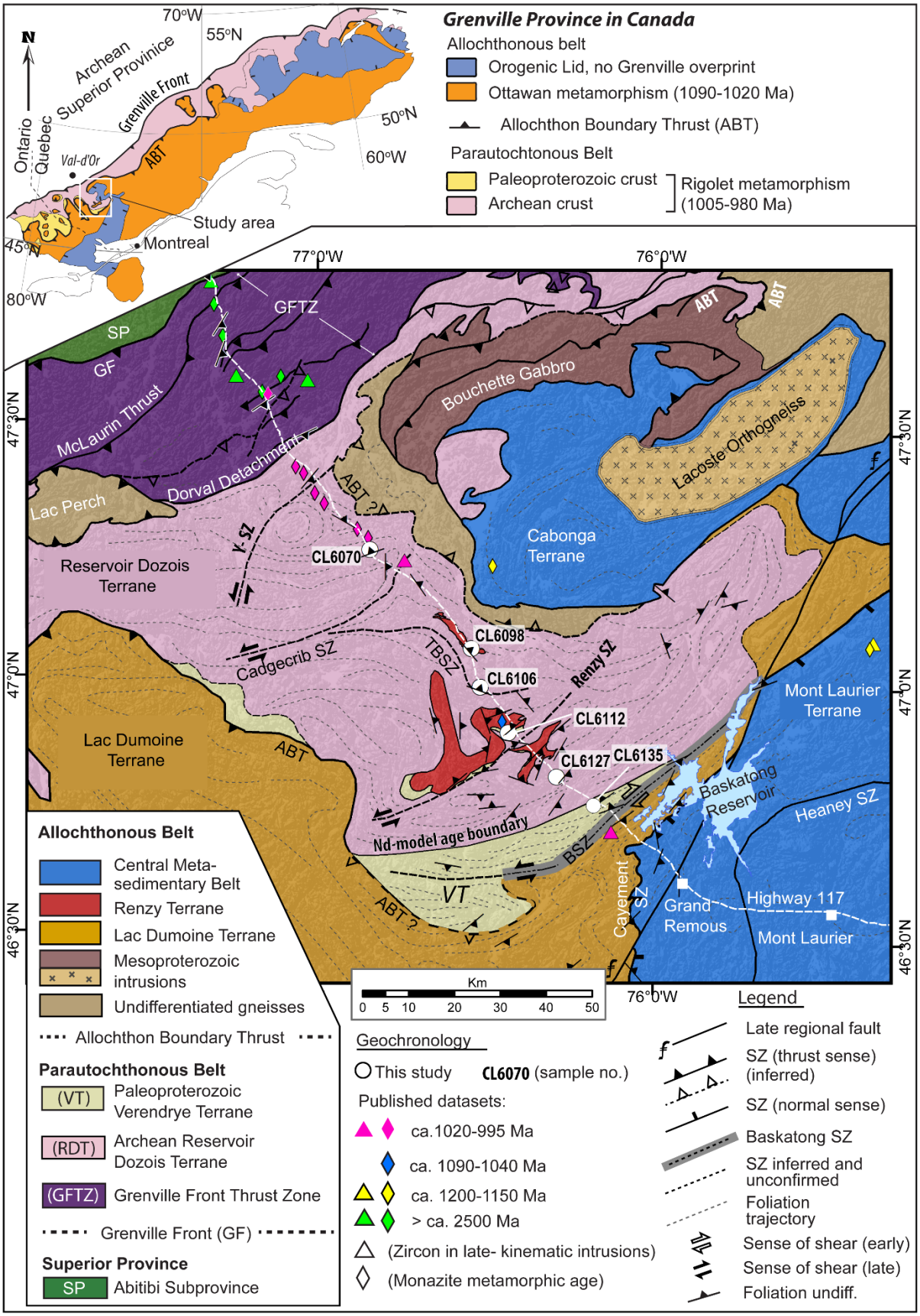
Grenville Province in Canada
Allochthonous belt
Orogenic Lid, no Grenville overprint
Ottawan metamorphism (1090-1020 Ma)
Allochthon Boundary Thrust (ABT)
Parautochtonous Belt
Paleoproterozoic crust
Archean crust
Rigolet metamorphism (1005-980 Ma)
Archean Superior Province
Grenville Front
Ontario
Quebec
Val-d'Or
ABT
Study area
Montreal
70°W
55°N
50°N
60°W
45°N
80°W
77°0'W
76°0'W
47°30'N
47°0'N
46°30'N
GFTZ
SP
GF
McLaurin Thrust
Dorval Detachment
Lac Perch
Reservoir Dozois Terrane
Y-SZ
CL6070
ABT ?
Bouchette Gabbro
Lacoste Orthogneiss
Cabonga Terrane
CL6098
CL6106
CL6112
CL6127
CL6135
Cadgecrib SZ
TBSZ
Renzy SZ
Lac Dumoine Terrane
Nd-model age boundary
BSZ
VT
Mont Laurier Terrane
Baskatong Reservoir
Heaney SZ
Cayemont SZ
Grand Remous
Highway 117
Mont Laurier
Km
0 5 10 20 30 40 50
Allochthonous Belt
Central Meta-sedimentary Belt
Renzy Terrane
Lac Dumoine Terrane
Mesoproterozoic intrusions
Undifferentiated gneisses
Allochthon Boundary Thrust
Parautochthonous Belt
(VT) Paleoproterozoic Verendrye Terrane
(RDT) Archean Reservoir Dozois Terrane
(GFTZ) Grenville Front Thrust Zone
Grenville Front (GF)
Superior Province
SP Abitibi Subprovince
Geochronology
This study CL6070 (sample no.)
Published datasets:
ca.1020-995 Ma
ca. 1090-1040 Ma
ca. 1200-1150 Ma
> ca. 2500 Ma
(Zircon in late- kinematic intrusions)
(Monazite metamorphic age)
Legend
Late regional fault
SZ (thrust sense) (inferred)
SZ (normal sense)
Baskatong SZ
SZ inferred and unconfirmed
Foliation trajectory
Sense of shear (early)
Sense of shear (late)
Foliation undiff.

Figure 4.1. (previous page) Location and subdivision of the Grenville Province (above) and tectonic architecture along the Hw117 transect in western Quebec (below). The location of samples analyzed in this study and those from published datasets along the transect are shown. Note that the Baskatong Shear Zone (BSZ) is interpreted to record both early dextral and late sinistral movement (Martignole, 1995) and reworks the tectonic boundary separating the Vérendrye Terrane and Lac Dumoine Terrane, previously called the Baskatong Desert Lineament (see Sharma *et al.*, 1995 and references therein). Grenville Province locality map modified after Rivers (2008), Jannin *et al.* (2018) and Dickin *et al.* (2020). Transect map compiled from field work conducted as part of this study as well as previous studies across the area (e.g. Indares and Martignole, 1990; Martignole and Pouget, 1994; Martignole, 1995; Guo and Dickin, 1996; Montreuil and Constantin, 2010; Dickin *et al.*, 2014; Lambert *et al.*, 2018, 2019). Published U-Pb zircon and monazite ages data derived from Childe *et al.* (1993); Martignole and Friedman (1998); Martignole and Martelat (2005) and from the MERN online database (2020).

4.3 Geological context

4.3.1 Geological subdivision along the highway 117 transect

The tectonic architecture along Hw117 was initially subdivided according to regional-scale investigations (e.g. Indares and Martignole, 1985, 1990; Martignole *et al.*, 2000) and the distribution of different Nd-model ages from felsic and intermediate gneisses within various domains (Guo and Dickin, 1996; Dickin *et al.*, 2014). The groundwork for this contribution included new geological mapping that was presented in geological reports (Lambert *et al.*, 2018; Lambert *et al.*, 2019) and a novel digital version of a field guide "book" (Lambert *et al.*, 2020). In addition to common field-based geological features (e.g. lithologies, structural characterisation and measurements), great care was also placed on the aspect of minerals present in leucosome. Euhedral minerals larger than those found in the matrix that share crystal faces against quartz and feldspar in leucosome were interpreted as peritectic. When the mineral was hydrous, such as hornblende, great care was taken to ascertain that it does not overgrow an earlier anhydrous phase. The presence of melt during deformation has also been systematically assessed at each of the visited outcrops, based on the deformation state of quartz grains in leucosome layers parallel with the gneissic (or stromatic) banding. In igneous rocks, quartz is generally the last mineral to crystallize at the solidus,

which is ca. 650ºC for granitic rocks (Yakymchuk, 2019). In contrast, quartz is the mineral with the lowest temperature for ductile deformation at ca. 300-350ºC (Stipp *et al.*, 2002). Consequently, quartz grains in any granitic layer submitted to the same strain field as their host should be deformed (i.e. attain a preferred grain orientation). To avoid complexities related to the orientation of the layer, we only observed the deformation state of quartz in leucosome layers showing some form of deformation (e.g. folding and structurally controlled emplacement) and parallel gneissic banding in the host gneiss. Deformed quartz that would later be submitted to static recrystallization would see the size of individual (sub)grains increase, but they should not loose their preferred orientation. The absence of deformation in quartz from these leucosome layers therefore, implies that these leucosomes were still partially molten (i.e. suprasolidus conditions) during deformation of the host gneiss and that minimal strain was recorded in these rocks after their crystallization.

Below we briefly outline the geological subdivision of the Hw117 transect through progressively deeper structural levels of the Grenville Province, which generally shows younger ages of deformation and metamorphism. This study however, focusses on the three structurally deepest panels: the Renzy, Vérendrye and Reservoir Dozois terranes.

4.3.1.1 The Central Metasedimentary Belt

The Mont Laurier and Cabonga Terranes (Fig. 4.1) form part of the Central Metasedimentary Belt within the AB. In the study area, these rocks consist of marble intruded by mafic and felsic dykes, which are commonly brecciated together; as well as garnet-bearing metasediments and pink orthogneiss. The tectonic fabric presents evidence of subsolidus textures such as mineral alignment and flattened layers of recrystallized feldspar and quartz or mafic mineral aggregates. Undeformed mafic dykes typical of the ca. 1150 Ma Chevreuil Suite (Corriveau *et al.*, 2018) crosscut the foliation, but contains a weak mineral alignment. This cross-cutting relationship supports the interpretation that the Central Metasedimentary Belt belongs to the 'Orogenic Lid' of the Grenville Orogen (Rivers, 2008).

4.3.1.2 The Lac Dumoine Terrane (LDT)

Across the Hw117 transect, the Lac Dumoine Terrane defines a narrow, ca. 8 km wide zone of highly strained, subvertical gneisses wedged between the VT and the Mont Laurier Terrane (Fig. 4.1). The geographic extent of the Lac Dumoine Terrane increases west of the highway, where it extends towards the Lac Dumoine Nappe of Dickin *et al.* (2012) and is considered the extension

of the Algonquin Terrane in Ontario (Ketchum and Davidson, 2000; Rivers *et al.*, 2002), based on the occurrence of high grade (granulite and relict eclogitic) assemblages (Indares and Dunning, 1997; Indares and Martignole, 1990) and Sm-Nd model ages between ca. 1790-1550 Ma (Dickin *et al.*, 2012). While the Lac Dumoine Terrane along the highway is also considered as part of the AB in this study, the age of pervasive Grenvillian deformation (Rigolet or Ottawan) in western Quebec is yet to be determined. On the highway, subvertical, garnet and biotite rich granodioritic gneisses, metagabbroic units and variably deformed charnockitic augen gneisses are exposed as a ca. 2 km long continuous panel. These gneisses record high subsolidus strain and have well-developed, shallow lineations that are probably related to deformation along the Baskatong Shear Zone (Fig. 4.1).

4.3.1.3 The Renzy Terrane (RT)

The RT (formerly 'Renzy Belt', Indares and Martigole, 1990) defines two kilometer-sized, amoeboid-shaped domains within the RDT (Fig. 4.1; Montreuil, 2010; Montreuil and Constantin, 2010). Geochemical studies indicate that the RT represent Mesoproterozoic juvenile arc/back-arc fragments (e.g. Montreuil, 2010; Montreuil and Constantin, 2010; Verma *et al.*, 2015) with Sm-Nd model ages of 1670-1410 Ma (Guo and Dickin, 1996; Dickin *et al.*, 2014). Metamorphism in the RT is characterized by upper amphibolite to granulite facies metamorphism (Indares and Martignole, 1990) with monazite yielding a concordant ca. 1072 Ma age (Fig. 4.1), which was estimated as the timing of peak metamorphism (Childe *et al.*, 1993). These geochemical and isotopic characteristics are typical of the AB (Rivers, 2008).

Rocks of the RT are distinctly different to those of the surrounding migmatitic gneisses of the PB (RDT and VT, described below). In particular, the RT is comprised of ubiquitously garnet-rich, tectonically interleaved mafic–to-felsic gneisses, likely of volcano-sedimentary origin (Fig. 4.2A), charnockitic augen-gneisses (Fig. 4.2B) and ultramafic (meta - dunites, pyroxenites, and lherzolites) rocks (Indares and Martignole, 1985, 1990; Martignole *et al.*, 2000; Montreuil, 2010; Montreuil and Constantin, 2010; Lambert *et al.*, 2018, 2019).

The fabrics observed in the RT are also distinctive. Planar fabrics are generally steeply dipping and preserve high strain, subsolidus deformation textures, particularly the development of stretching lineations (variable orientations to the NE, NW and SE), as well as abundant asymmetrical mantled porphyroclasts and the transposition of augen porphyroclasts (Fig. 4.2B; Hanmer and Ciesielski,

1984; Indares and Martignole, 1990; Lambert *et al.*, 2018, 2019). The contrast in lithology, the presence of garnet in the rocks and the subsolidus structures effectively discriminate the Renzy outcrops from the RDT and VT gneisses in the field (Indares and Martignole, 1990; Lambert *et al.*, 2018, 2019).

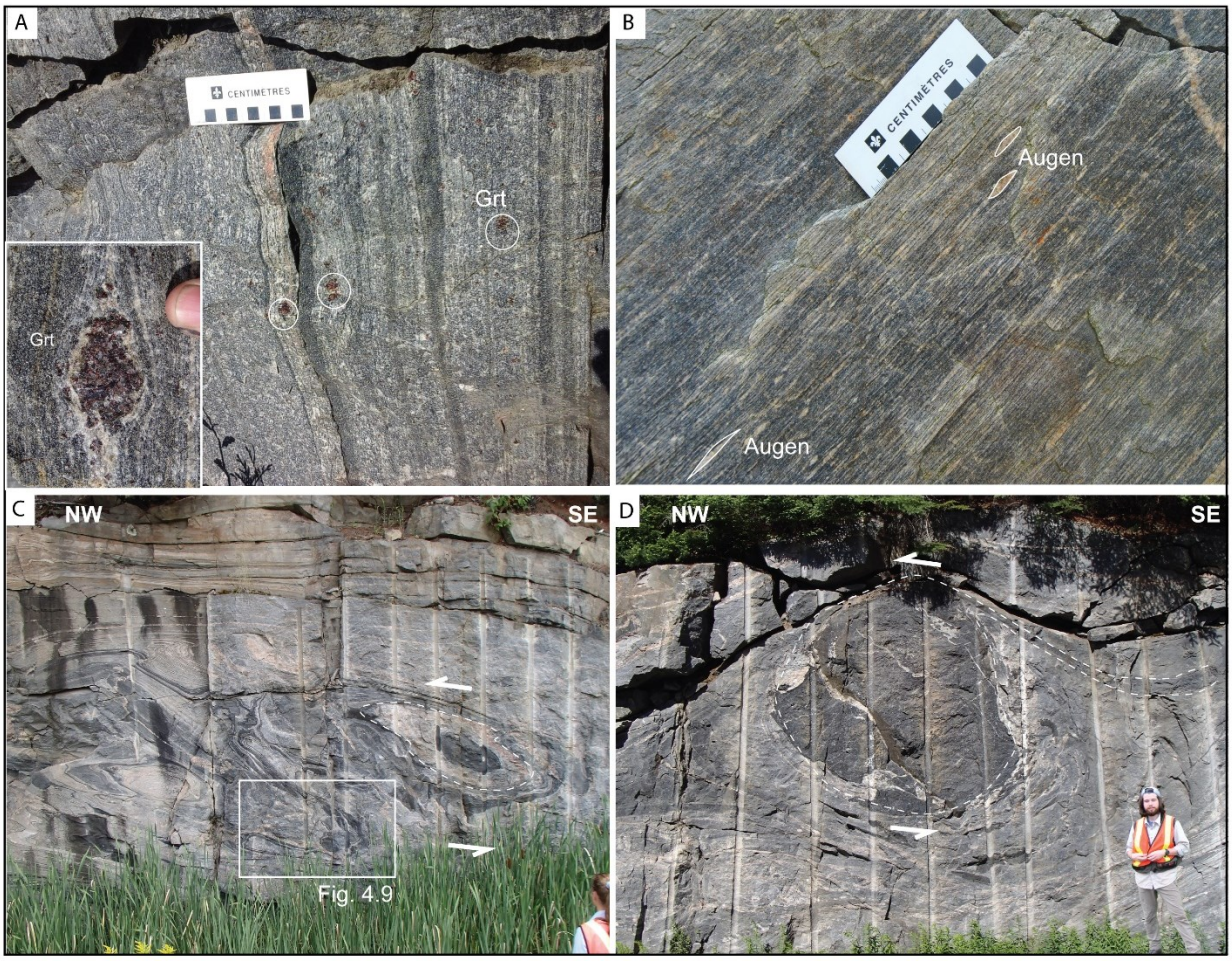

Figure 4.2. Field outcrop photos of typical Renzy Terrane gneisses (A-B) and gneisses from the Vérendrye Terrane along Highway 117 (C-D). (A) Interbanded felsic, intermediate and mafic metavolcanics with centimetric garnet porphyroblasts (red circles and inset). (B) Augen gneiss indicative of relatively high finite subsolidus strain. (H) Sheath folds with asymmetrical 'z-shaped geometries and numerous recumbent folds. White box marks the location of the injected vein sample CL6135 (Fig. 4.9A). (I) One of many meter-scale mafic boudins in the Vérendrye Terrane that are rotated counter-clockwise (sinistral), indicating a top to the NW sense of shear.

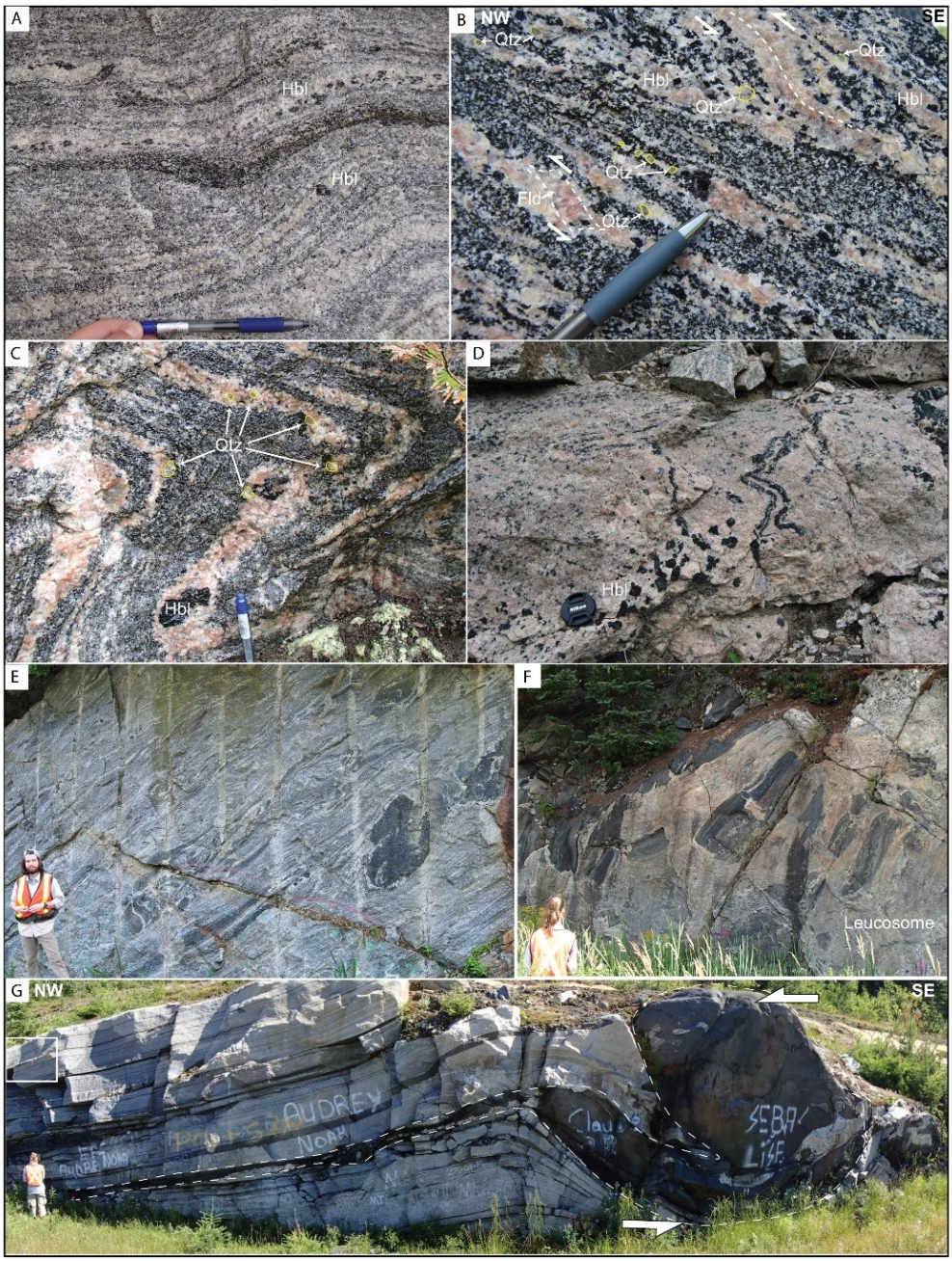

Figure 4.3. Field outcrop photos of typical Reservoir Dozois Terrane gneisses. (A) Nebulitic and stromatic migmatites (trondhjemite composition) with centimetric hornblende. (B-C) Stromatic migmatites of granitic composition with abundant undeformed quartz grains (e.g. yellow outlines) and centimetric, subhedral hornblende crystals in the pink leucosome that are much larger than the millimeter-scale hornblende in the host gneiss. Note the stair-stepping leucosome (top right) and sigmoidal feldspar phenocrysts (lower left) indicating a top to the NW sense of shear in (B). (D)

Diatexites with pegmatitic phase that contain centimetric, euhedral clusters of hornblende crystals. (E-F) Stromatic metatexites that locally lose structural coherence to represent diatexites that often contain variably folded dismembered mafic rafts. Note that the light-colored vertical artefacts seen along the face of the outcrop at (E) are created by drill holes and are not primary geological features. (G) Horizontal, banded straight gneisses of the Teddy Bear Shear Zone, with a rotated, garnet-bearing mafic mega-boudin (NW-SE rock face). Sample CL6106 (see Fig. 4.6) is collected from this same outcrop to the left (NE) of the picture frame.

4.3.1.4 Vérendrye Terrane (VT)

The VT (name suggested by Lambert *et al.*, 2019) constitutes part of the previously unnamed, 'Paleoproterozoic parautochthon' (see Dickin *et al.*, 2014 and references therein), located between the RDT to the NW and the LDT to the SE (Fig. 4.1). Indares and Martignole (1990) conducted conventional thermobarometry on a series of metasedimentary and mafic samples across the transect. All the metasedimentary samples investigated in that study show evidence of a significant net-transfer reaction involving garnet breakdown and, therefore, yielded doubtful pressure-temperature conditions. The mafic samples, however, do not seem to present such evidence and we consider the results more realistic and are herein interpreted as conditions at which chemical composition was homogenized, probably but not necessarily, near peak temperature. Hence, their mafic sample (15-78b) from the VT (part of what they called the Reservoir Baskatong Terrane) yielded a peak temperature of ca. 680ºC at 725-740 MPa and retrogression down to 620ºC at ca. 680 MPa (Indares & Martignole, 1990). The VT is delineated exclusively by the distribution of Paleoproterozoic Nd-model ages (Guo and Dickin, 1996; Dickin *et al.*, 2012, 2014). Dickin *et al.* (2014) also identified Paleoproterozoic Nd-model ages along the base of the Renzy Terrane (Fig. 4.1) and proposed that the VT could be part of 'Paleoproterozoic duplex structures' located between the Archean PB and components of the overriding AB. It remains to be determined whether the VT is part of the PB or the AB.

On Hw117, the VT consists of migmatitic, garnet-free, hornblende-bearing orthogneisses, but also include syenogranitic gneisses that are less readily observed elsewhere (Indares and Martignole, 1985, 1990; Lambert *et al.*, 2018). Where the VT intersects the highway (Fig. 4.1), it is characterized by subhorizontal and gently undulating gneissic banding that progressively steepens

towards the Baskatong Shear Zone in the SE (Lambert *et al.*, 2019). The subhorizontal gneisses contain numerous spectacular metric sheath folds defined by gneissic banding and mafic layers closing on themselves and by asymmetrical folds on both sides of a given sheath folds having axes converging towards the apex. The long axes of these sheath folds plunge shallowly towards the NE. In contrast, on faces perpendicular to this axis, the sheath folds are asymmetrical and have a sigmoidal shape systematically indicating a top-to-the NW sense of shear (Fig. 4.2C). Mafic boudins contained within the gneisses (Fig. 4.2D) present the same morphology and sense of shear that is typical of the general NW-directed Grenvillian tectonic transport direction observed elsewhere along the highway (Hanmer and Ciesielski, 1984; Indares and Martignole, 1985, 1990; Lambert *et al.*, 2018).

4.3.1.5 The Reservoir Dozois Terrane (RDT)

The RDT is an amphibolite facies domain of inferred reworked Archean gneisses (Fig. 4.1; Indares and Martignole, 1990; Martignole and Martelat, 2005). Indares and Martignole (1990) investigated one reliable mafic sample (47-55) from the RDT. It yielded peak temperature of 695-740°C at 875-915 MPa and retrogression down to 650°C at 650-740 MPa. Peak PT are compatible with the presence of kyanite in the rare leucosome in migmatitic pelitic schist they have observed (we did not find any). Furthermore, discordant U-Pb monazite dates between 1020 Ma and 995 Ma were acquired from samples collected within ca. 30 km of the NW boundary of this domain (Fig. 4.1; Childe *et al.*, 1993). At the southeastern margin of the RDT, the 'Nd-model age boundary' (Doig, 1977; Guo and Dickin, 1996; Dickin *et al.*, 2014), separates the RDT from the VT (Fig. 4.1). This boundary is cryptic in the field (Lambert *et al.*, 2018, 2019) and marked only by the division of older Nd-model ages (> 2300 Ma) in the RDT from the younger ages (2100-1800 Ma) in the Vérendrye Terrane (Doig, 1977; Guo and Dickin, 1996; Dickin *et al.*, 2014).

Our detailed investigation of the mineralogy in the field revealed some key information on the metamorphic evolution of the RDT. Rocks are generally migmatitic orthogneisses that are hornblende-rich and garnet-poor (Figs. 4.3A-C). Despite the detailed investigation in the field, no other mineral than hornblende was observed in the leucosomes. Furthermore, no evidence for replacement of a dry minerals, such as garnet or pyroxene, has been observed in the core of the generally sub- to euhedral hornblende crystals that are typically much larger than hornblende in the matrix (2-10 cm vs < 0.5 cm; Figs. 4.3C-D). Boudinaged mafic bodies within these gneisses

locally preserve garnet-clinopyroxene assemblages in their centers, but are largely retrogressed to amphibolites (Lambert *et al.*, 2018, 2019).

Structures within the RDT are strikingly different to those in the RT. Here the structures are characterized by shallow-dipping (<25°) gneisses and poorly developed linear fabrics (Indares and Martignole, 1990; Lambert *et al.*, 2018). The penetrative foliation is syn-migmatitic and mostly lacks evidence for pervasive solid-state deformation, such as mylonitic textures (i.e. grain size reduction), streaked-out quartz grains (Figs. 4.3A-C), or prominent stretching lineations. Migmatitic textures (terminology after Sawyer and Brown 2008; Maxeiner *et al.*, 2017) range from metatexites to diatexites (30 to >60% leucosome respectively) and include: nebulitic to stromatic leucosomes with diffuse contacts (Figs. 4.3A-C); injected net-like arrays and patchy type leucosomes (Fig. 4.4A). Mafic boudins within the RDT, which can be several meters in diameter (e.g. Fig. 4.3G), are generally found as isolated or dismembered and folded lenticular rafts in the migmatites and diatexites (e.g. Fig. 4.3F). The presence of high-grade assemblages (Cpx-Opx-Grt) and subsolidus strain in many of these mafic bodies, allowed us to ascribe several previously unmapped, isolated outcrops (e.g. locality of sample CL6098; Fig. 4.1) and most of the mafic boudins found in the RDT, to the structurally overlying allochthonous RT (see Lambert *et al.*, 2019, 2020 for detailed discussion). This is further supported by published dataset (e.g. Sabourin, 1963 ; Lambert *et al.*, 2019) that indicate the gneisses of the RDT extend structurally above the RT. Consequently, there are RDT rocks both structurally above and below the RT.

Within the RDT, however, the 'Teddy Bear Shear Zone' (TBSZ; Lambert *et al.*, 2019) preserves evidence for annealed subsolidus deformation. It consists of a litho-structural packages of tonalitic and granitic gneisses in which quartz is deformed, feldspar porphyroclasts recrystallized, contains straight gneissic banding (Fig. 4.3G), and ubiquitous transposition of pink K-feldspar veins. Furthermore, mafic boudins within these gneisses are commonly rotated and transposed with the tectonic fabric, some of which define meter-scale kinematic indicators (Fig. 4.3G). The shear zone is relatively thin with a ~10-20 m thickness but is exposed for 10-15 km because of the undulating subhorizontal dip of the gneissic banding.

While limited U-Pb zircon and monazite ages from syn-and-post kinematic pegmatites in the RDT suggest that localized sinistral shearing along subvertical mylonitic zones (e.g. Cadgecrib SZ, RSZ;

Fig. 4.1) occurred at ca. 1000 Ma (Martignole and Friedman, 1998), the age of pervasive syn-migmatitic deformation across the RDT is not constrained.

4.4 Methodology

4.4.1 Methodology LA-ICP-MS preparation and analytical procedure

Zircon grains were separated from the sampled rocks, imaged with cathodoluminescence (CL), and analyzed by laser ablation inductively coupled plasma mass spectrometry (LA-ICP-MS) at the Boise State University Isotope Geology Laboratory. Data for the samples discussed in this chapter were collected over two analytical sessions in April 2018 (see experimental session numbers 2 & 3 in Table 4.1) and two sessions in October 2019 (sessions 5 & 6 in Table 4.1). The standards and reference zircons that were used, as well as the preparation and analytical procedures are found in Table 4.1, while the detailed descriptions are presented in the supplementary material (Appendices C-D).

4.4.2 Presentation of ages and calibration of errors

Ages for each of the unknown samples in this study are reported for zircon grains or zones within individual grains (e.g. rims and cores). The ages for each population are presented as weighted mean ages, calculated using Isoplot 4, a Microsoft Excel Toolkit (Ludwig, 2003, 2008) in conjunction with Isoplot-R (Vermeesch, 2018). For all samples, the reduced chi-squared statistic (also known as the Mean Square of Weighted Deviates or MSWD; McIntyre *et al.*, 1966; Wendt and Carl, 1991) and the probability of fit (PF) are presented.

The choice of isotopic system used to interpret zircon ages between ca. 800 – 1500 Ma is generally problematic (Spencer *et al.*, 2016), with populations where dates > ca. 1200-1500 Ma commonly reported as $^{207}Pb/^{206}Pb$ weighted mean ages and as $^{206}Pb/^{238}U$ weighted mean ages in younger populations (Puetz, 2018; Puetz *et al.*, 2021). However, in cases where data is discordant, the weighted mean $^{207}Pb/^{206}Pb$ age typically offers more robust data (Spencer *et al.* 2016). In addition, LA-ICPMS analysis with the $^{206}Pb/^{238}U$ system can result in dates having a younger, or less frequently, an older bias due the matrix effect (Herriott *et al.*, 2019). Furthermore, caution is advised for $^{206}Pb/^{238}U$ age calculations for zircons that have U > 700 ppm (Williams, 1992; Vavra *et al.*, 1999). With these considerations in mind, we report the ages (or individual dates) determined

herein, with the $^{207}Pb/^{206}Pb$ system because many of the samples in this study have U concentrations > 700 ppm and in some cases, yielded reversely-discordant data (Fig. D.6A). All analytical results, including the $^{207}Pb/^{206}Pb$ and $^{206}Pb/^{238}U$ individual dates and trace element geochemistry for each sample as well as a comparison between of the $^{207}Pb/^{206}Pb$ and $^{206}Pb/^{238}U$ weighted mean ages determined for each of the various populations identified herein, are presented in the supplementary material (Figs. D.2-6; Tables D.2-8).

Radiogenic isotope ratio and age error propagation for all analyses includes uncertainty contributions from counting statistics and background subtraction. Errors on the individual dates are reported at 2σ. Analyses with dates >10% positive or >10% negative discordance (at 2σ) between the $^{206}Pb/^{238}U$ and $^{207}Pb/^{206}Pb$ systems are not considered in the age calculations.

For each age population with equivalent dates a $^{207}Pb/^{206}Pb$ weighted mean age (probability of fit, PF > 0.05) is first calculated using errors on individual dates that do not include a standard (external) calibration uncertainty (standard error annotated within parentheses), and then a standard calibration uncertainty is propagated into the error on the weighted mean date (error annotated without parentheses). In this way, we can first evaluate if the respective age populations that are obtained from a single sample, derived during the same analytical session and with the same standards, define distinct ages or overlap with each other. Conversely, age populations across different samples are only compared once the standard calibration uncertainty is propagated into the error, in order to mitigate differences across the different analytical sessions, the use of different standards and for subsequent comparison to ages reported elsewhere in the Grenville Province, determined in different laboratories. The standard calibration uncertainty for U/Pb is the local standard deviation of the polynomial fit to the fractionation factor of the primary standards OG1 (sessions 2 & 3) and FC1 (sessions 5 & 6) versus time. For $^{207}Pb/^{206}Pb$ the standard calibration uncertainty is the standard error of the mean of the fractionation factor of the primary standards for each session respectively. For sessions 2 & 3, these uncertainties were 1.50-1.82% (2σ) for $^{206}Pb/^{238}U$ and 0.18-0.32% (2σ) for $^{207}Pb/^{206}Pb$ (Table 4.1). For sessions 5 & 6 the uncertainties are 0.52-0.60% (2σ) for $^{206}Pb/^{238}U$ and 0.32-0.42% (2σ) for $^{207}Pb/^{206}Pb$ (Table 4.1).

Table 4.1. Metadata for LA-ICP-MS U-(Th-)Pb analyses of samples analysed in this study.

Laboratory and Sample Preparation	
Laboratory name	Boise State University Isotope Geology Laboratory
Sample type/mineral	Zircon
Sample preparation	Conventional mineral separation, 1 inch resin mount, 0.3 μm polish to finish
Imaging	CL, JEOL T300, 10 nA, 17 mm working distance
Laser ablation system	
Make, Model and type	ESI/New Wave Research, UP213
Ablation cell and volume	Standard ablation cell
Laser wavelength (nm)	213 nm
Pulse width (ns)	4 ns
Fluence (J cm^{-2})	~5 J cm^{-2}
Repetition rate (Hz)	5 Hz
Ablation duration (s)	30 s
Ablation pit depth / ablation rate	15 μm pit depth, measured using an optical microscope, equivalent to 0.05 μm/pulse
Spot diameter (μm)	25 μm
Sampling mode / pattern	Static spot ablation
Carrier gas	100% He in the cell, Ar make-up gas combined using a Y-piece 70 cm from the torch.
Cell carrier gas flow (l min^{-1})	1.15 l min^{-1}
ICP-MS Instrument	
Make, Model and type	ThermoElectron, X-series II, quadrupole
Sample introduction	Ablation aerosol transported through 90 cm long, 1.5 cm dia. tygon tubing coil
RF power (W)	1400 W
Make-up gas flow (l min^{-1})	0.74 l min^{-1} Ar
Detection system	single ion-counting SEM
Masses measured	29, 91 (5); 202–207, 235, 238
Masses measured and dwell times per peak (ms)	29,91(5); 31,89,93,139,140,141,146,147,153,157,159, 163,165,166,169,172,175,177,181(10); 202,204,208,232,238(40); 206(80); 49,207(200)
Total integration time per output data point (s)	~ 0.895 s
'Sensitivity' as useful yield (%, element)	0.01% U ((#ions detected/#atoms sampled)*100; Schaltegger *et al.* 2015)
IC Dead time (ns)	29 ns

Laboratory and Sample Preparation	
Data Processing	
Gas blank	30 s on-peak zero subtracted
Calibration strategy	In session 1, OG1 used as primary reference material and 91500 and FC1 used as secondary reference materials. In session 2, FC1 used as primary reference material and 91500 and Plešovice used as secondary reference material.
Reference Material info	OG1 (3465 Ma; Boise State University, unpublished data) 91500 (1065 Ma; Wiedenbeck et al., 1995) FC1 (1098 Ma; Boise State University, unpublished data) Plešovice (337 Ma; Slama et al., 2008)
Data processing package used / Correction for LIEF	ThermoElectron Plasmalab TRA software for integrated cps acquisition; in-house Microsoft VBA coded spreadsheet for data normalization, concentration calibration, uncertainty propagation and age calculation.
Mass discrimination	$^{207}Pb/^{206}Pb$ and $^{206}Pb/^{238}U$ normalized to reference material
Common-Pb correction, composition and uncertainty	No common Pb correction applied; ablation sweeps with mass 204 signals above background rejected.
Uncertainty level and propagation	Ages are quoted at 2 sigma absolute, propagation is by quadratic addition. Systematic errors based upon reproducibility of reference material are propagated where appropriate: 1.82% (2 sigma) for Pb/U and 0.32% (2 sigma) for Pb/Pb in session 1 and 0.60% (2 sigma) for Pb/U and 0.42% (2 sigma) for Pb/Pb in session 2 .
Quality control / Validation	See accompanying data tables.

Experimental session number	Samples analysed	Primary standard	Published age (207Pb/206Pb)	Secondary reference zircon	Published age (Ma)	Calculated (207Pb/206Pb) age on secondary reference	±2s (Ma)*	Mean Square of Weighted Deviates and probability of fit	Standard error on 207Pb/206Pb (%)	Standard error on 206Pb/238U (%)
2	**CL6070**	OG1	3465	Zircon 91500	1065	1027	39	MSWD = 0.6, pof = 0.80	0.24	1.5
	CL6106			FC1	1098	1085	12	MSWD = 1.6, pof = 0.10		
3	**CL6127**	OG1	3465	Zircon 91500	1065	1054	28	MSWD = 1.8, pof = 0.06	0.3	1.58
				FC1	1098	1086	14	MSWD = 1.5, pof = 0.12		
5	**CL6098**	FC1	1098	Zircon 91500	1065	1081	20	MSWD = 0.9, pof = 0.53	0.32	0.52
	CL6112									
6	**CL6135**	FC1	1098	Zircon 91500	1065	1063	18	MSWD = 1.8, pof = 0.07	0.42	0.6

* Weighted mean dates with errors that include standard calibration uncertainty.

4.4.3 Ti-in-zircon thermometry

Temperatures for zircon crystallization were calculated from the pressure dependant Ti-in-zircon thermometer calibration of Hofmann *et al.* (2014). For this calibration, as all samples contain undeformed and thus likely igneous quartz, the activity for SiO_2 ($aSiO_2$) was set to 1. While we acknowledge that the $aSiO_2$ may be less than 1 in silica undersaturated melts (Kriegsman and Hensen, 1998), a lower $aSiO_2$ (0.99-0.90) is considered to have a relatively negligible effect on the reduction of the calculated temperatures (<10ºC; Schiller and Finger, 2019). Following the recent recommendations of Schiller and Finger (2019), who modelled the activity for TiO_2 ($aTiO_2$) in numerous ilmenite bearing S-and some I-type granites, the $aTiO_2$ in all samples of this study was set to 0.5, as they contained ilmenite and no rutile was observed. A $aTiO_2$ of 0.5 is also in agreement with the average $aTiO_2$ (0.5 ± 0.2) modelled from a compilation of numerous ilmenite-bearing rhyolites and dacites analyzed by Gualda and Ghiorso (2013).

A broad range of pressures between 550 and 1000 MPa were used in this pressure dependant thermometer (Hofmann *et al.*, 2014) based on the range of peak to retrograde thermobarometric results from mafic samples in the RDT and VT (Indares and Martignole, 1990; see above), which includes an added uncertainty of ± 100 MPa (not cited in their study, but we consider this as a minimum error for conventional barometry).

We report the calculated temperature range as a best conservative estimate for the temperatures using the upper limit of the interquartile range (UQ) for these pressures (Table D.9), as was suggested by Tomkins *et al.* (2007). Following Tomkins *et al.* (2007), an uncertainty of ± 30ºC on the UQ temperatures is considered acceptable to account for statistical and analytical errors.

4.4.4 Classification of multiple zircon zones

The zircon dataset in this study is complex, with zircon grains generally characterized by several zones. Our strategy was to first subdivide zircon into different types based on their morphology and zonation. In some samples, these types correlated with groups defined by chemical discrimination diagrams (e.g. REE_{CN} and U vs Th) or by weighted mean ages, but in others no correlation was observed. In some instances, zones that could not be defined by their morphology or internal zonation patterns, were classified based on overgrowing relationships with better defined zones or by their chemical composition or age group. Although we acknowledge that

having several zones for several samples could become confusing, we consider this a clear and robust approach. In the figures below, we present only a subset of the zircon morphologies and diagrams used for geochemical discrimination; all other zircon CL-images and geochemical traits that are discussed herein are found in the supplementary material (Appendix D).

4.5 Geochronology results

4.5.1 Sample CL6070: inter-boudin granitic leucosome in the RDT

4.5.1.1 Outcrop and sample description

Sample CL6070, the north-western most sample (Fig. 4.1), is a granitic leucosome hosted in a migmatitic, garnet-free granodiorite gneiss of the RDT (Fig. 4.4A). The leucosome specimen was collected in the neck of a boudinaged mafic dyke. At this outcrop, leucosome in the boudin neck does not contain crystals that could be interpreted as peritectic and is connected to stringers of leucosome that are parallel to stromatic migmatite in the wall rocks (Fig. 4.4A). These relationships suggest that the host gneiss was still partially molten at the time of boudinage and that the boudin necks functioned as a low pressure sink for the melt (Van Der Molen, 1985; Sawyer, 2001).

4.5.1.2 Zircon morphology

Zircon grains in this sample have stubby to equant habits and vary between ca. 100 to 500 μm in diameter (Fig. 4.4B). Three different types of zircon zones are identified across these grains. Type 1 (yellow in Fig. 4.4B) define grains with high CL intensities and constitute both entire grains or are resorbed cores (#3 in Fig. 4.4B). Type 2 (blue in Fig. 4.4B) are defined by stubby to equant habits, have weaker (mesocratic grey) CL intensities and homogenous to sector growth zonation patterns (#4 in Fig. 4.4B). Type 3 (red in Fig. 4.4B) define a population of thin (<120 μm) rims around type 1 (#3 in Fig. 4.4B) and type 2, with slightly higher (mesocratic grey) CL intensities compared to type 2 and have (seemingly) homogenous (#1 in Fig. 4.4B) and oscillatory growth zonation patterns (#3 in Fig. 4.4B). Distinction between types 2 & 3 is not always clear when zonation is underdeveloped with only one grain analysed in both the core (type 2) and rim (type 3) to confirm this textural relationship (#2 in Fig. 4.4B).Zircon chemistry and geochronology

Nineteen analyses conducted across all three types yielded dates with <10% discordance. Three bright-CL, type 1 cores, yielded Archean $^{207}Pb/^{206}Pb$ dates of 2703 ± 64 Ma, 2691 ± 41 Ma and

2566 ± 37 Ma, (Fig. 4.4E). They have steep positive REE_{CN} profiles with negative Eu anomalies (Fig. D.7C), low U (48-103 ppm), moderate Th (32-61 ppm) concentrations and a Th/U > 0.5 (Fig. 4.4D). The remaining analyses on type 2 & 3 domains all yielded concordant Grenvillian dates (Fig. 4.4E). Both types 2 & 3 have steep REE_{CN} profiles with slight variations in the depth of the negative Eu anomaly (Fig. 4.4C) and slope of the $HREE_{CN}$ slopes (Fig. D.7B). Both have a similar ranges in ∑REEs concentrations (Fig. D.7B) and have moderate U (305-589 ppm) and Th (34-127 ppm) concentrations that yield Th/U ratios between 0.1 and 0.3 (Fig. 4.4D). In addition, both types 2 and 3 have similar Ti concentrations (UQ: 1.77 and 1.59 ppm, respectively) that yield temperatures between 667-717°C and 659-709°C respectively (Table 4.2). As these two populations cannot be differentiated based on their trace elements and their textural relationship are ambiguous (e.g. similar CL intensity and zonation patterns), types 2 & 3 are combined to yield a $^{207}Pb/^{206}Pb$ weighted mean age of 1010 ± (10) 14 (MSWD = 1.6, PF = 0.08, n= 16/16; Fig. 4.4F).

4.5.1.3 Interpretation

We interpret the Archean dates to be xenocrystic cores. Despite the clear overprinting relationships between type 2 and 3 zircon zones observed on CL images (Fig. 4.4B), it is not possible to distinguish them based on their REE_{CN} profiles and Ti-in zircon temperatures. We interpret them as distinct growth phases, but the lack of precision of LA-ICP-MS precludes distinguishing them based on their ages. Therefore, the combined 1010 ± (10) 14 Ma age of types 2 and 3 is interpreted as the timing of crystallisation of the leucosome synchronous with boudinage of the mafic dyke.

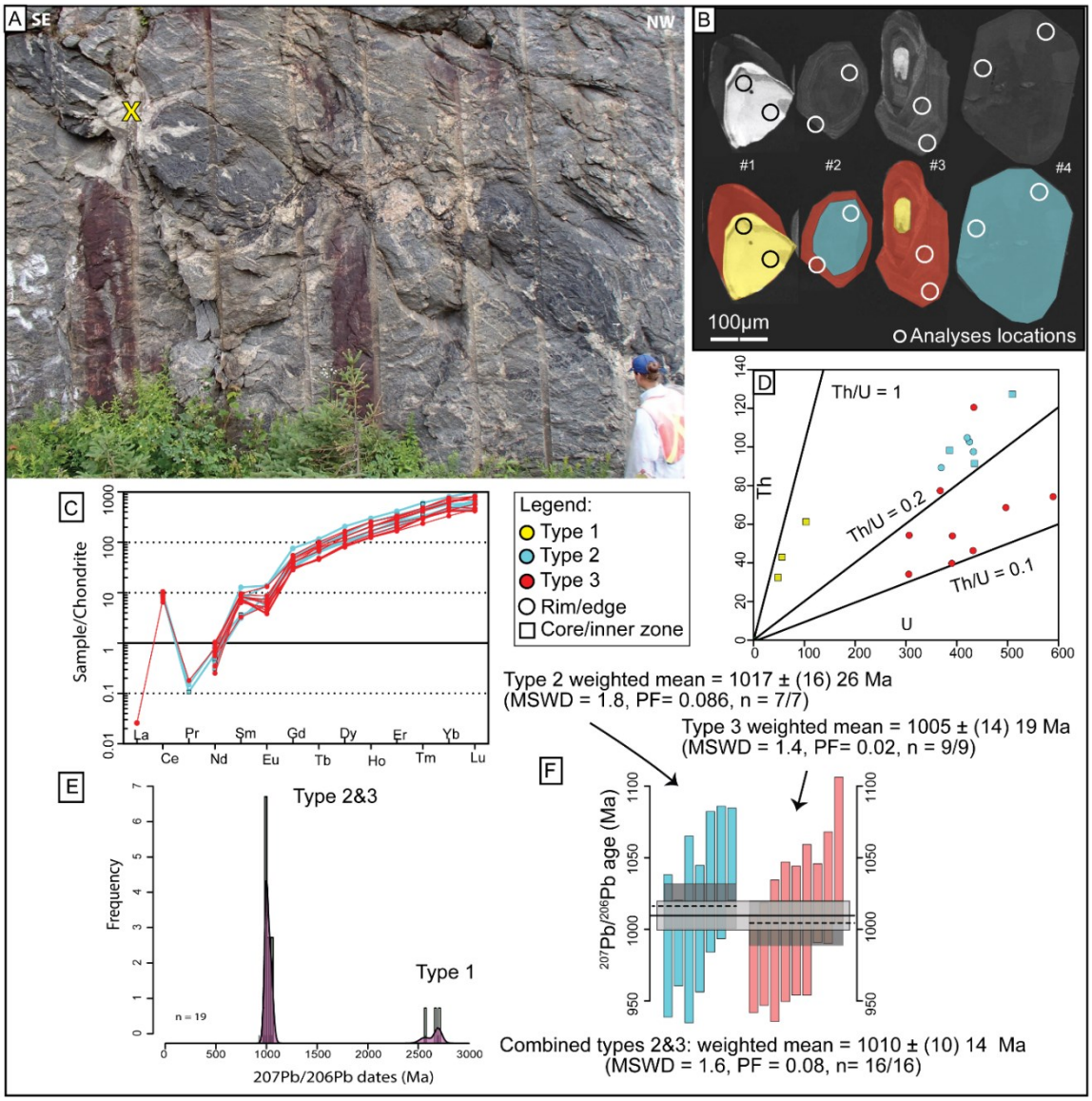

Figure 4.4. Sample CL6070. (A) Sample taken at X, from a granitic leucosome in the neck of a boudinaged mafic dyke in the RDT. (B). Examples of zircon morphologies and the types of zones defined herein. (C) REE_{CN} normalized (S.S. Sun and McDonough, 1989) spider-diagram of Grenvillian zones (type 2 &3). (D) U-Th bivariate diagram. (E) Kernel density plot of all individual $^{207}Pb/^{206}Pb$ dates within the sample. (F) Weighted mean $^{207}Pb/^{206}Pb$ age for types 2 & 3 (dark shading with stippled line) and their combined age (light shading with solid line).

Table 4.2. Summary table of the geochronology and Ti-in-zircon thermometry results from this study.

Sample	Sample coordinates (WGS94)		Location (structural domain)	Description	Population (zircon type)	Weighted mean age	Error (excl. cal)	Error (incl. cal)	*Ti in Zr temperature (°C)	Concordant inherited dates	Interpretation
	lat_y	long_x									
CL6070	47.265	-76.8301	RDT	Leucosome in boudin neck	Type 1	na	na	na	na	2703 ± 64 Ma; 2691 ± 41 Ma; 2566 ± 37 Ma	Inherited Archean
					Type 2	**1010**	10	14	667-717		Similar textural and geochemical characteristics
					Type 3				659-709		
CL6098	**47.07505**	-76.5327	Renzy-type?	Folded pegmatite intruding RT	Type 1	1428	7	14	na		Inherited from Renzy?
					Type 2	**1020**	6	13	678-729		Protracted growth in diatexite
					Type 3	**1001**	6	10	713-766		Pegmatite crystallization age
CL6106	**46.9999**	-76.5094	RDT (structurally above RT)	Syn-late tonalitic-trondhjemite sill	Type 1	na	na	na	na	2617 ± 39 Ma	Inherited Archean
					Type 4	**1002**	11	16	673-724		Crystallization age of sill and min. age for top-to-NW shearing
					Type 5				678-729		
CL6112	**46.9117**	-76.4226	Renzy s.s.	Granitic dykes intruding RT synchronous to deformation in the RT	Type 2	na	na	na	na	1438 ± 23 Ma; 1436 ± 23 Ma	Inherited from Renzy?
					Type 3	**979**	6	11	665-715		Earlier crystallization phase in dykes
					Type 4	**968**	4	10	627-675		Final crystallization phase of dyke
CL6127	46.8265	-76.3002	RDT (structurally below RT)	Syn-late granitic dyke	Type 1	na	na	na	na	2647 ± 51 Ma (core); 977 ± 65 Ma (rim)	Inherited Archean
					Type 2	na	na	na	724-778	1015 ± 24 Ma; 989 ± 36 Ma	
					Type 3				682-733		Final crystallization phase of dyke
					Type 4	**1011**	7	10	684-735		
					Type 5				689-741		
CL6135	**46.791**	-76.1563	VT	Granitic intrusion dating sheath folds	Type 1-3	1663	6	14	na	1276 ± 63 Ma	Inherited from Paleo-Mesoproterozoic host rocks?
					Type 4	1445	7	10	na	1157 ± 63 Ma	
					Type 5	**1008**	7	10	725-778		Final crystallization phase of dyke

*Temperatures are reported as best conservative estimates using the upper limit of the interquartile range for pressures between 550 and 1000 MPa (pressure estimates from Indares and Martignole, 1990) and do not contain the ±30C error to account for analytical and statistical errors (following the recommendations of Tomkins *et al.* 2017).

4.5.2 Sample CL6098: diatexites and pegmatites intruding Renzy-type gneisses

4.5.2.1 Outcrop and sample description

Sample CL6098 is a granitic pegmatite that crosscuts a garnetiferous mafic gneiss, located ca. 20 km NW of the RT (Fig. 4.1 & Fig. 4.5A). The mafic gneiss is part of a mixed package with garnetiferous intermediate, migmatitic and charnockitic augen gneisses that display subsolidus strain (e.g. quartz ribbons and pervasive quartz and feldspar stretching lineations; Fig. 4.5D; Lambert *et al.*, 2019), which are diagnostic lithologies and structural characteristics of Renzy-type rocks (Figs. 4.2A-B). At the outcrop-scale, the gneissosity in the Renzy-type rocks is cut by migmatitic orthogneisses (Fig. 4.5A). Where the migmatites locally preserve a structural coherency (Fig. 4.5B) they can be described as metatexites; where they lack structural coherency, they can be described as diatexites (Fig. 4.5A). Like the migmatitic gneisses of RDT (Figs. 4.3A-F), these migmatitic orthogneisses are garnet-free and lack evidence of subsolidus strain and are therefore, interpreted as an "intrusion" of RDT gneisses into the Renzy-type rocks.

Hosted in the orthogneiss are pegmatitic dykes that are locally concordant with the main migmatitic banding in the metatexite and have diffuse contacts with the granitic leucosome network (Fig. 4.5B) but are discordant and variably folded within the diatexite (Fig. 4.5A). The pegmatitic phase contains centimetric, euhedral to subhedral hornblende crystals that can form aggregates (Fig. 4.3D). One of these pegmatite dykes intruded the overlying Renzy gneiss and clearly crosscuts the (subsolidus) gneissosity (Fig. 4.5A & Fig. 4.5C. This is where sample CL6098 was collected (see X in Fig. 4.5C).

4.5.2.2 Zircon morphology

Zircon grains recovered from this sample range in size between 100-300 um in length with stubby to prismatic (3:1 L:W ratio) habits. Three types have been identified in the imaged crystals. Type 1 (green in Fig. 4.5E) includes all morphologies that contain a high CL intensity. Zonation in type 1 includes oscillatory (#1 & #2 in Fig. 4.5E) and convoluted patterns or are defined by broad-banded (25-50μm) patterns of alternating bright and darker grey reflectance in CL (#3 & #4 in E). Type 2 (blue in Fig. 4.5E) define lower CL intensity (mesocratic grey) zircon, with homogeneous to weak sector zonation patterns in stubby-prismatic grains (#2, #3 & #4 in Fig. 4.5E). Type 3 (red

in Fig. 4.5E) is defined by extremely low (black) CL intensities that have no clear growth zonation patterns but generally have faceted edges. Type 1 zircon can encompass the whole grain (#1 in Fig. 4.5E) but mostly define resorbed cores, mantled by types 2 (#2-4 in Fig. 4.5E) or type 3 zircon (#4 & #5 in Fig. #5E), although the exact boundary between type 1 and type 2 can be ambiguous due to the similarity in the CL-intensity (#4 in Fig. 4.5E). Type 2 are commonly mantled by narrow (<100 μm) type 3 zircon (#3 & #4 in Fig. 4.5E). In addition to forming rims, type 3 also constitutes a subordinate population (<5%) of grains that lack cores (#6 in Fig. 4.5E) and can have metamict textures. The textural relationship between these types is summarized in grain #4 & #5 (Fig. 4.5E), where a bright core inferred to be type 1, is successively mantled by types 2 and 3. Importantly, in this grain and others both type 2 and 3 zircon are faceted with no sign of resorption in between growth phases.

4.5.2.3 Zircon chemistry and geochronology

Forty-seven analyses across the different textural types yielded ages with <10 % discordance and yielded Mesoproterozoic and Grenvillian dates (Fig. 4.5H). The nineteen analyses on type 1 yielded a $^{207}Pb/^{206}Pb$ weighted mean ages of 1428 ± (7) 14 Ma (MSWD = 2.4, PF = 0.01, n = 18/19; Table 4.2; Fig. D.2B). The trace element geochemistry of type 1 is defined by steep positive REE_{CN} profiles with large negative Eu anomalies and strong positive Ce anomalies, although their $HREE_{CN}$ defines moderate slopes (see Fig. D.8). In addition, they have a range of U (67-502 ppm) and Th (34-257 ppm) concentrations and a Th/U > 0.1 (0.28-0.86; Fig. 4.5G).

Types 2 & 3 define two distinct Grenvillian zircon populations. Twenty-one analyses on type 2 domains yielded a wide range of $^{207}Pb/^{206}Pb$ dates, from 966-1061 Ma that when combined, yield a $^{207}Pb/^{206}Pb$ weighted mean age of 1020 ± (6) 13 Ma (MSWD = 3.40, PF = 0, n = 20/21; Fig. 4.5I). Type 2 zircon all share similar trace element compositions, defined by: steep positive REE_{CN} slopes with prominent Eu anomalies (Fig. 4.5F); similar ∑REE concentrations and $HREE_{CN}$ slopes (Fig. 4.5F); moderate-high U (395-1516, average = 832 ppm) concentrations, with low Th (6-55, average = 28 ppm) concentrations (Fig. 4.5G); and a low Th/U ratio (<0.05; Fig. 4.5G). Type 3 have similar, steeply dipping REE_{CN} profiles to type 2, with deep negative Eu anomalies (Fig. 4.5F). In contrast to type 2 however, they have steeper $HREE_{CN}$ slopes, are enriched in ∑REEs (average = 807 ppm; Fig. 4.5F & Fig. D.8D), have higher U (1129-4215, average = 2923 ppm) and Th (33-80, average = 46 ppm) concentrations but a lower average Th/U (average < 0.02; Fig. 4.5G).

Type 3 have similar, steeply dipping REE_{CN} profiles to type 2, with deep negative Eu anomalies (Fig. 4F). In contrast to type 2 however, they have steeper $HREE_{CN}$ slopes, are enriched in ∑REEs (average = 807 ppm; Fig. 4F & Fig. D.8D), have higher U (1129-4215, average = 2923 ppm) and Th (33-80, average = 46 ppm) concentrations but a lower average Th/U (average < 0.02; Fig. 4G). Types 2 and 3 also show notable differences in their Nb/Ta ratios (Fig. D.8E) and Ti concentrations, with higher Ti (UQ: 3.24 ppm) in type 3 compared to type 2 (UQ: 2.05 ppm), that correspond to temperatures between 628-729ºC and 713-766ºC respectively (Table 4.2). Eight analyses on the high-U type 3 domains yielded reversely discordant data (Fig. D.2A) with a $^{207}Pb/^{206}Pb$ weighted mean age of 1001 ± (6) 10 Ma (MSWD = 1.35, PF = 0.02, n= 8/8; Fig. 4.5J).

4.5.2.4 Interpretation

The distinct zircon morphologies (Fig. 4.5E), chemical composition (Figs. 4.5F-G), age (Fig. 4.5H) and location of the cores mantled by types 2 and 3 strongly suggest that type 1 zircons represent a xenocrystic population inherited from a ca. 1400 Ma protolith, which is the accepted age for the formation of the RT (Martignole and Ringuette, 1998; Montreuil and Constantin, 2010). Because types 2 and 3 show overprinting relationships (Fig. 4.5E), have a slightly different REE_{CN} profile (Fig. 4.5F), distinct U-Th composition (Fig. 4.5G) and yielded a statistically different age without propagating the external calibration (1001 ± 6 vs 1020 ± 6 Ma; Fig. 4.5I), then types 2 and 3 can be considered as two distinct populations. Types 2 and 3 zircon have an elongated morphology and distinct crystal faces (Fig. 4.5E), high U content and REE_{CN} profiles (Fig. 4.5F) that are all key characteristics of igneous zircon (Corfu, 2003). Furthermore, as it is unlikely that type 2 originated from the garnet-rich Renzy gneisses as it lacks the flat $HREE_{CN}$ profiles expected for concurrent growth with garnet during the Ottawan phase (Fig. 4.5F; Rubatto, 2002). It is also unlikely that they form in distinct melt phases because of their similar composition. Instead, the two types likely grew during partial melting of the migmatitic orthogneiss. Importantly, the absence of resorption textures between types 2 & 3 suggests continuous growth in the same melt phase. Based on these constraints, the most logical interpretation would be that type 2 zircons are those that grew for a protracted period of time at 1020 ± (6) 13 Ma in the partially molten gneiss and that type 3 zircon records final zircon growth during the crystallization of the pegmatite at ca. 1001 Ma. Statistical parameters associated with the two ages are compatible with this interpretation with a high MSWD of 3.4 for type 2, which would reflect true geological scatter (Ludwig, 2003). This interpretation is also compatible with field observations suggesting that the hornblende-bearing pegmatite was

extracted from the partially molten orthogneiss to intrude the diatexites and rocks of the structurally overlying RT. To estimate the duration of this anatectic event, we can use the relative difference between the age of the two types (i.e. without external calibration errors). It yields at least 7 Myrs and could have been as long as 30 Myrs. We consider the alternative hypothesis of protracted crystallization of zircon within the dyke as less likely. Nevertheless, the absence of subsolidus deformation features, such as elongated quartz, in a well-layered metatexite (Fig. 4.5B) further suggests protracted melt-present deformation.

Figure 4.5 (next page). Sample CL6098. (A) Sample taken from a pegmatitic phase (P) of diatexites interpreted to be part of the PB, that intrude into gneisses that have garnet rich lithologies comparable Renzy Terrane elsewhere. (B) The pegmatite phase is mostly concordant to the leucosomes within coherent parts of the diatexite and appears interconnected as it lacks discrete truncating geometries with the stromatic leucosome. Although deformed, the diatexites and pegmatitic phase lack evidence for subsolidus strain. (C) Sample location at X, where the pegmatitic phase cuts into the Renzy mafic and intermediate gneisses. (D) Prominently banded Renzy gneisses with abundant garnet porphyroblast aggregates and concordant quartz ribbons. (E) Examples of zircon morphologies and the types of zones defined herein. (F) REE_{CN} normalized (S.S. Sun and McDonough, 1989) spider-diagram of Grenvillian zones (type 2 & 3). (G) U-Th bivariate diagram. (H) Kernel density plot of all individual $^{207}Pb/^{206}Pb$ dates within the sample. (I) Weighted mean $^{207}Pb/^{206}Pb$ age for types 2 & 3.

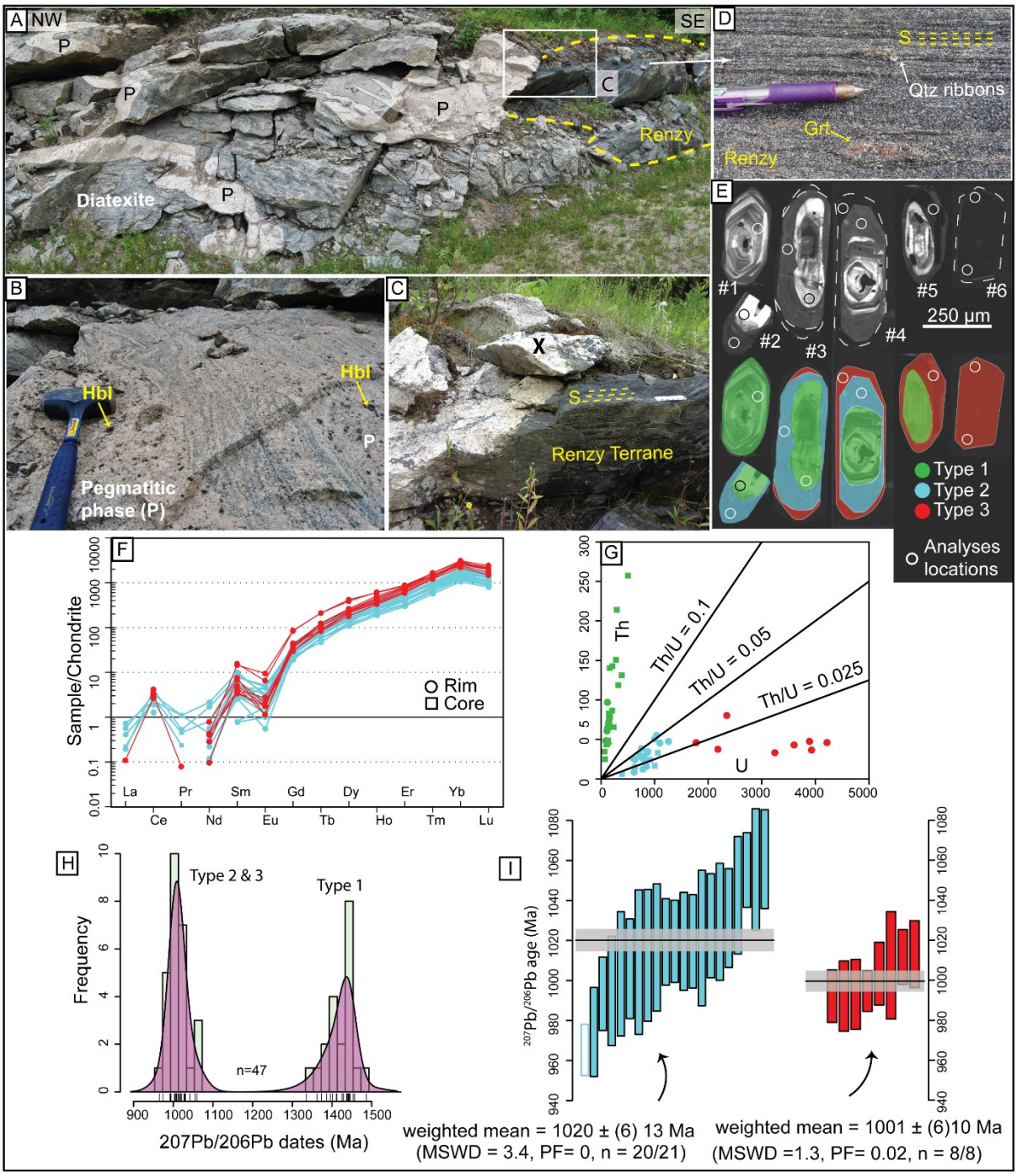
A
NW
SE
P
C
Renzy
Diatexite
D
S
Qtz ribbons
Grt
Renzy
E
#1
#2
#3
#4
#5
#6
250 µm
Type 1
Type 2
Type 3
Analyses locations
B
Hbl
P
Pegmatitic phase (P)
C
X
S
Renzy Terrane
F
Sample/Chondrite
Rim
Core
La
Ce
Pr
Nd
Sm
Eu
Gd
Tb
Dy
Ho
Er
Tm
Yb
Lu
G
Th
U
Th/U = 0.1
Th/U = 0.05
Th/U = 0.025
H
Frequency
Type 2 & 3
Type 1
n=47
207Pb/206Pb dates (Ma)
I
207Pb/206Pb age (Ma)
weighted mean = 1020 ± (6) 13 Ma
(MSWD = 3.4, PF= 0, n = 20/21)
weighted mean = 1001 ± (6)10 Ma
(MSWD =1.3, PF= 0.02, n = 8/8)

4.5.3 Sample CL6106: tonalitic-trondhjemitic intrusion in the Teddy Bear Shear Zone

4.5.3.1 Outcrop and sample description

Sample CL6106 represents a tonalitic-trondhjemite intrusion hosted within the shallow dipping to subhorizontal, banded gneisses of the Teddy Bear Shear Zone (TBSZ; Fig. 4.6A). The sample locality is within the RDT, NW of the RT (Fig. 4.1) and steepen along strike to attain shallow-NW dips (15-20o) and extend structurally above the RT (Lambert *et al.*, 2019; this study). Distinctive features of the TBSZ are the continuous 'straight' gneissic banding, developed under subsolidus strain and annealed at high temperatures, as well as the presence of decameter-sized mafic (metagabbro to amphibolite) boudins within the host gneiss (Fig. 4.3G) One of these boudins defines a δ-shaped kinematic marker that indicates the gneisses recorded a top-to-the NW sense of shear (Fig. 4.3G). Where sampled, the intrusion forms a ca. 30 cm thick pegmatitic sill that is mostly concordant, but also cuts the gneissic banding (Fig. 4.6A) that defines the shear fabric. The sampled sill contains numerous xenoliths of ultramafic (olivine-bearing) rocks (Fig. 4.6A) and was traced for more than 5 m along strike, to where it less than ca. 5 cm thick, is folded, and locally surrounds blocks of foliated gneiss (Fig. 4.6B). The origin of these ultramafic xenoliths is unknown but they were probably transported in the felsic sill as they have not been observed elsewhere and there are no rocks with a transitional composition. Although mostly concentrated around the margins, apophyses from the intrusion also extend parallel to the foliation within the segmented block (Fig. 4.6B). Where concordant with the migmatitic banding, the apophyses of the sampled leucosome contain abundant ovoidal quartz grains without preferred elongation (inset in Fig. 4.6B). Combined, these relationships indicate that the emplacement of the sample was synchronous to late, relative to deformation in TBSZ, while the sill was partially molten.

4.5.3.2 Zircon morphology

Zircon grains are mostly well preserved, equant (ca. 250 μm diameter), stubby and prismatic (<1 mm in length, Fig. 4.6C). Five types of zircon are identified across these grains. Type 1 (yellow in Fig. 4.6C) have a high CL intensity, variably resorbed cores mantled by lower CL-intensity zones of both type 3 (#1 in Fig. 4.6C) and those inferred to be type 2 (#6 in Fig. 4.6C). Type 2 (green in Fig. 4.6C) have lower CL-intensity zones with sector zonation patterns and form stubby prism (#4

in Fig. 4.6C), or subrounded cores mantled by a higher CL-intensity type 3 (#5 & #6 in Fig. 4.6C), although no analyses were conducted in these cores to confirm their affinity. In addition to higher CL intensities, type 3 (pink in Fig. 4.6C) have homogenous to weak sector growth zonation patterns in comparison to type 2. While type 3 mostly defines a population of thick rims, they are themselves also mantled by texturally younger type 4 zircon (#1 in Fig. 4.6C). Type 4 (blue in Fig. 4.6C) are mostly defined by well-faceted prismatic cores mantled by euhedral type 5 zircon (#2 & #3 in Fig. 4.6C). Rare rims with similar traits are also considered type 4 (#1 in Fig. 4.6C) and although they have similar CL-intensities and homogenous zonation to type 3, they are distinguished based on their geochemical traits (see below). Type 5 (red in Fig. 4.6C) are characterized by distinctively darker, low CL-intensity (black) zircon with oscillatory zonation patterns and constitute both a population of rims (#2 & #3 in Fig. 4.6C) and stubby whole grains (#7 in Fig. 4.6C). While no grain preserves all five zircon types, the relationships define a succession of progressively younger textures from type 1 to type 5. Importantly, several grains (such as #2 and #3 shown on Fig. 4.6C) present faceted types 4 mantled by oscillatory-zoned and faceted type 5 with no evidence for resorption in between the two growth phases.

4.5.3.3 Zircon chemistry and geochronology

Twenty-six of the fifty-five analyses, including all on types 2 and 3 zones, yielded dates with >10 % discordance, had U concentrations too low (U< 27 ppm) for accurate age determinations, or had large uncertainties (>100 Ma; Table S4). Therefore, these dates will not be discussed further. One analysis on a type 1 core yielded a discordant $^{207}Pb/^{206}Pb$ date of 2617 ± 39 Ma, whereas the remaining dates (types 4 & 5) were Grenvillian (Fig. 4.6F). The analysis on the Archean core shows a distinctly different trace element chemistry to those with Grenvillian dates (types 4 & 5) and is characterized by positive sloping REE_{CN} profiles with a negative Eu anomaly but a flatter HREECN slope, higher ∑REE concentrations (669 ppm) and Th/U (0.77) than the rest of the types in this sample (Fig. D.9).

The Grenvillian type 4 and 5 zircons are all characterized by similar steep $HREE_{CN}$ sloped profiles with variable, negative to flat Eu anomalies (Fig. 4.6D & Fig. D.9D), similar ∑REE concentrations (Fig. D.9C) and low Th/U (<0.1; Fig. 4.6E). Although types 4 and 5 show distinct morphologies and type 5 has higher U and Th concentrations, they have similar Th/U ratios (ca. 0.05; Fig. 4.6E). They also have and similar Ti concentrations (UQ: 1.93 and 2.07 ppm respectively), that yield

essentially the same Ti-in-zircon temperatures, 673-724ºC and 678-729ºC, for types 4 and 5 respectively (Table 4.2). Types 4 and 5 cannot be distinguished based on other trace element compositions (see Fig. D.9). Furthermore, their ages are within error of each other and all dates from type 5 fall within the range of type 4 (Fig. 4.6G). For these reasons they are combined and define a $^{207}Pb/^{206}Pb$ weighted mean age of 1002 ± (11) 16 Ma (MSWD = 1.5, PF = 0.05, n = 27/27; Fig. 4.6G).

4.5.3.4 Interpretation

Geochronological results for sample CL6106 provide information on the nature of the host gneiss as well as the timing of shearing along the TBSZ. The distinct chemical composition and resorbed morphology of type 1 zircon, which yielded a date of ca. 2617 Ma, indicate they are inherited from an Archean protolith. Types 4 and 5 zircon have an elongated morphology and crystal faces (Fig. 4.6C), and REE_{CN} profiles (Fig. 4.6D) that are all key characteristics of igneous zircon (Corfu, 2003). Although their distinct morphologies and overprinting relationships could suggest they represent two different generations, we cannot distinguish them based on REE_{CN} profiles, Th/U ratio and U-Pb geochronology. Hence, the weighted mean average age of 1002 ± (11) 16 Ma for the combined types 4 and 5 is interpreted as the timing of crystallisation for the sill. Inasmuch as field relationships indicate that crystallization occurred under suprasolidus conditions, synchronous to the latest increments of strain relative to the deformation along the TBSZ, the age for this sample also constrains the youngest possible age for rotation of the mafic boudins and top-to-the NW directed shear within the TBSZ.

Figure 4.6. Sample CL6106 (next page). (A) Sample taken at X, from a deformed trondhjemitic sill within gneisses of the Teddy Bear Shear Zone in the RDT (see Fig. 4.3G). The sill also contains rafts of ultramafic rocks (B). Elsewhere in this outcrop, the same sill thins and envelopes a rotated block of host gneisses but contains undeformed quartz grains where it protrudes between the foliation planes within the rotated block (this was a cut oblique to the face shown in A and Fig. 4.3A). (C) Examples of zircon morphologies and the types of zones defined herein. Note that although at least 5 types are identified, types 2 & 3 were excluded as they yielded anomalously low element concentrations (e.g. U < 27ppm) during analysis (see Fig. D.9). (D) REE_{CN} normalized

(S.S. Sun and McDonough, 1989) spider-diagram of the remaining Grenvillian zones (types 4 & 5). (E) U-Th bivariate diagram. (F) Kernel density plot of all individual $^{207}Pb/^{206}Pb$ dates within the sample. (G) Weighted mean $^{207}Pb/^{206}Pb$ age for types 4 & 5 (dark shading with stippled line) and their combined age (light shading with solid line).

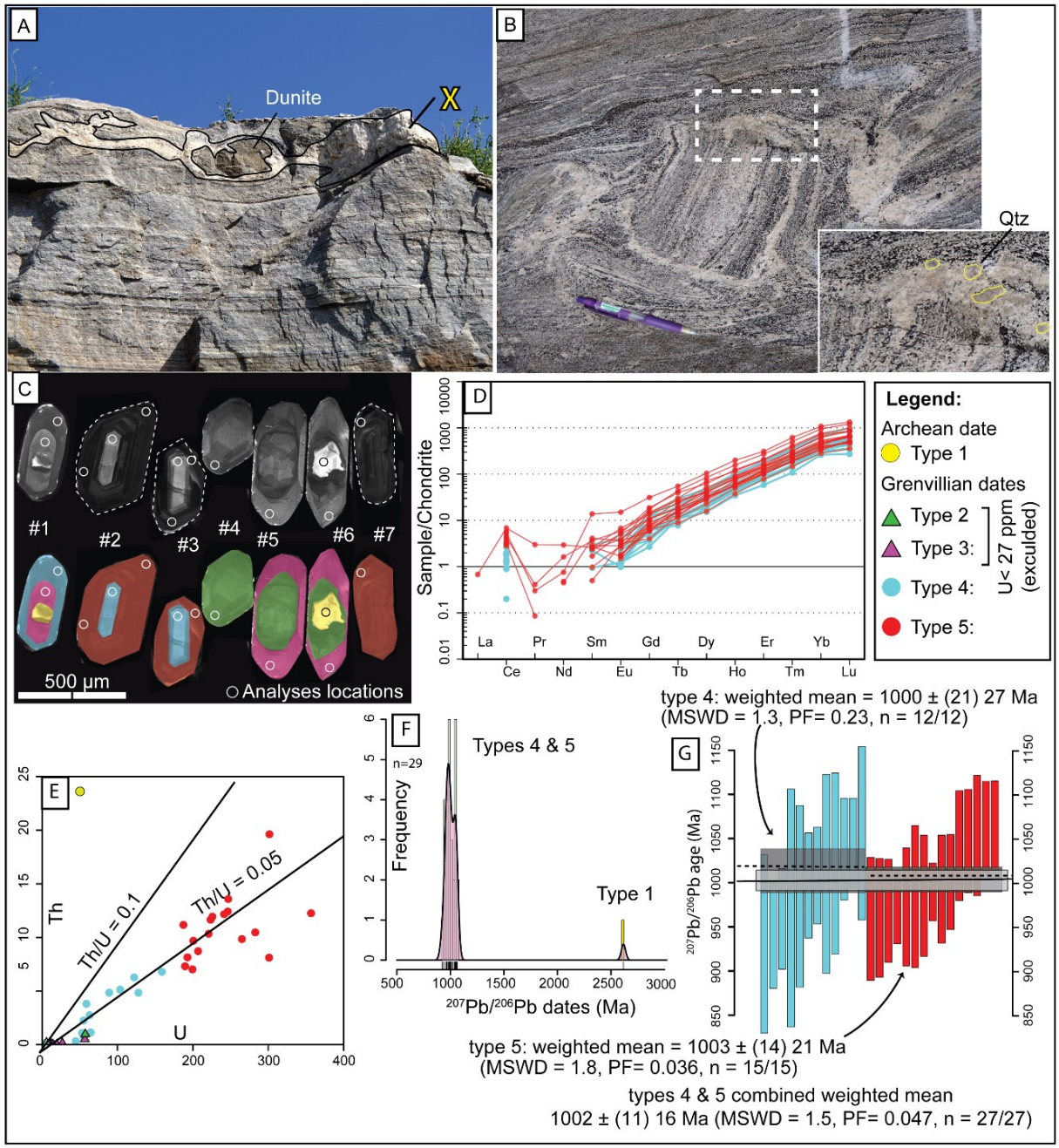

4.5.4 Sample CL6112 granitic dykes intruding the Renzy Terrane

4.5.4.1 Outcrop and sample description

The outcrop where sample CL6112 was collected is key to unravelling the tectonic evolution of the study area. It consists of migmatitic granodiorite gneiss that lacks garnet, typical of the parautochthonous rocks in the study area (Fig. 4.7A). These gneisses are probably part of the 'Paleoproterozoic Parautochthon' that is identified based on Nd-model age mapping by Dickin *et al.* (2014; Fig. 4.1). These migmatitic gneisses are structurally overlain by garnetiferous intermediate gneisses and a granulitic (Cpx-Opx-Pl-Grt-Hbl) metagabbro (Fig. 4.7A) that are typical of the Renzy-type rocks and form part of the RT (*sensu stricto*) outcrops that were identified in previous studies (e.g. Indares and Martignole, 1990; Montreuil and Constantin, 2010). At the northern end of the outcrop, the contact between these two gneissic packages is characterized by a ca. 3 m wide package of mylonitic gneisses that should then represent the first-order boundary between the Parautochthonous and Allochthonous Belts (i.e. the ABT; Figs. 4.7E-F). The underlying migmatitic gneiss has stromatic leucosomes that parallel the gneissic layering (Fig. 4.7B) in which, quartz is not deformed (Fig. 4.7D). The leucosome coalesce to form veins and dykes that pool at the contact between the migmatitic PB gneiss and AB mafic gneisses (Figs. 4.7B-C) and brecciate the latter. Mafic enclaves in the felsic granitic range from decameter-sized detached blocks (Fig. 4.7A) to metric distorted rafts (see at G3 in Fig. 4.7C) to centimetric schlieren (G4 in Fig. 4.7C); altogether forming a diatexite. Based on differences in their grain size, weathering colors and distribution of mafic enclaves, there seem to be multiple granitic phases (see G1-G5 in Fig. 4.7C) although the contacts between these phases are vague. Sample CL6112 was collected from the youngest apparent granitic phase, is devoid of minerals that could be interpreted as peritectic and intrudes and brecciates the mafic gneisses of the RT at the collection site (G5, X in Fig. 4.7C).

4.5.4.2 Zircon morphology

Zircons recovered from this sample include roughly equal proportions of subrounded, equant shaped and stubby-prismatic grains with faceted edges (Fig. 4.7G). The subrounded grains are ca 200-300 μm in diameter and mostly have metamict interiors, while the stubby and prismatic grains are 250 to 500 μm in length, or longer, as some grains are partial fragments. Four distinct types are distinguished based on their textures. Type 1 (yellow in Fig. 4.7G) are cores with high CL-

intensities and are mantled by lower (grey) CL intensity type 3 zones (#1 & #7 in Fig. 4.7G), although there are no analyses in the rims to confirm this affinity. Metamict textures in the zircons are abundant and can be randomly distributed throughout entire grains (#3 in Fig. 4.7G) or define distinct, subrounded xenocrystic cores mantled by the non-metamict zircon domains of types 3 (#5 in Fig. 4.7G) and type 4 (#2 in Fig. 4.7G). While type 2 (green in Fig. 4.7G) are considered the homogenous and seemingly undamaged zones between those with metamict textures, none of the proposed type 2 cores had undamaged zones sufficiently wide (>25 μm) for analysis and as a result, their affinity could not be confirmed. Most (ca. 60%) grains in the sample contain type 3 zircon (blue in Fig. 4.7G), defined by wide zones, low-CL (mesocratic grey) intensities, with homogenous to weak sector growth zonation patterns. Type 4 (red in Fig. 4.7G) are exclusively defined as low CL-intensity (black) rims that mantle type 3 zones (#4, #6, #8 in Fig. 4.7G). Notably, some of the type 3 cores may themselves contain variably resorbed cores interpreted as type 2 (#2 in Fig. 4.7G). In some grains the boundaries between types 3 and 4 are sharp (#6 in Fig. 4.7G) but in general, they are diffuse and are defined by a gradual change from a grey interior (type 3) to a darker (black) rim (type 4; #4 in Fig. 4.7G). The low CL intensity mostly obscures zonation patterns in type 4 but in some cases, sector zonation patterns are visible, although these may still constitute part of the texturally older type 3 (#4 in Fig. 4.7G). Due to the diffuse boundaries and possible overlap in zonation textures, distinction between these two successive types based on morphology alone was tentative and relied on their trace element characteristics.

4.5.4.3 Zircon chemistry and geochronology

Forty-nine analyses across the four different morphological types yielded ages with < 10% discordance. Types 1 and 2 yielded Mesoproterozoic dates (Fig. 4.7J) but the single analysis on type 1 reveals distinctly different trace element traits compared to those of type 2. While both types have a positive REE_{CN} slope with weakly negative Eu anomalies, type 1 has a strong positive Ce anomaly and a shallower dipping $HREE_{CN}$ slope compared to type 2 and is more enriched in ∑REEs (Fig. D.10A). Type 1 also has a low U (40 ppm), low Th (36 ppm) concentration and notably a higher Th/U = 0.90, in comparison to the U (472-816 ppm), Th (28-38 ppm) concentrations and exceptionally low Th/U ratios (0.05-0.06) of type 2 (Fig. 4.7I). This single analysis on the type 1 zone yields a discordant $^{207}Pb/^{206}Pb$ date of ca. 1590 Ma (Fig. D.4), whereas two of the three analyses on type 2 yielded concordant $^{207}Pb/^{206}Pb$ dates of ca. 1440 ± 23 Ma and

1436 ± 23 Ma (Figs. 4.7J-K). The remaining analysis on type 2 yielded a single $^{207}Pb/^{206}Pb$ date of 1264 ± 29 Ma but as it is also discordant (Fig. D.4), it will also not be discussed further.

Types 3 & 4 define Grenvillian populations (Fig. 4.7J) with different trace element signatures. Both have steep REE_{CN} patterns with variable (where measured) weak to strong Eu anomalies (Fig. 4.7H) but type 4 mostly has steeper $HREE_{CN}$ slopes and are enriched in the total ∑REE concentrations (average = 781) compared to type 3 (average = 418 ppm; Fig. D.10D). Type 4 also have higher U concentrations (>1496 ppm), but a lower Th/U (< 0.01) ratio compared to the U concentration (549-985, average = 705 ppm) and Th/U (0.01-0.05) of type 3 (Fig. 4.7I). In addition, type 4 zones have notably lower Ti concentrations (UQ = 0.99 ppm) compared to type 3 (UQ= 1.72 ppm), which yield Ti-in-zircon temperatures between 627-675ºC and 665-715ºC respectively (Table 4.2). Twenty-five analyses on type 3 domains yielded a $^{207}Pb/^{206}Pb$ weighted mean age of 979 ± (6) 11 Ma (MSWD = 1.52, PF = 0.05, n = 24/25; Fig. 4.7K) and twenty analyses on the high-U type 4 domains yielded reversely discordant data (Fig. D.4) with a $^{207}Pb/^{206}Pb$ weighted mean age of 968 ± (4) 10 Ma (MSWD = 1.31, PF = 0.17, n= 18/20; Fig. 4.7K). Combined, these two types do not yield a statistically robust age (972 ± (3) Ma with MSWD = 2 and PF = 0.00).

4.5.4.4 Interpretation

Geochronological results for sample CL6112 provide information on the nature of the host gneiss as well as the timing of deformation in PB rocks and the incipient brecciation of the overlying RT. Because they form rounded cores and are much older than the younger populations, types 1 and 2 zircons are considered inherited and their ages suggest they were extracted from the Mesoproterozoic RT rocks that are crosscut and brecciated by granitic dykes similar to that of the collected specimen. Types 3 and 4 zircon have an elongated morphology and crystal faces (Fig. 4.7G), and REE_{CN} profiles (Fig. 4.7H) that are all key characteristics of igneous zircon (Corfu, 2003). Because type 4 overgrow the faceted and euhedral type 3 zircons (e.g. grain #6 & #8 in on Fig. 4.7G), they have distinct chemical compositions (Fig. 4.7I) and distinct ages, we consider them as two distinct populations. The absence of resorption textures between these two types indicates there was no dissolution and that zircon growth was protracted for a minimum of 1 Myr. A more precise geochronological method would be required to confirm this hypothesis. Interestingly, field relationships clearly show that the melt from which specimen CL6112 was collected, was extracted from the underlying PB migmatitic gneiss (Figs. 4.7B-C). The absence of deformation in quartz

grains from concordant leucosome in the migmatitic gneiss indicates that part of the strain in the underlying metatexites of the PB was acquired in the presence of melt at ca. 968 Ma, the age of the youngest type 4 zircon.

Figure 4.7 (next page). Sample CL6112. (A) Sample taken at X from a granitic dykes at intrudes mafic and garnet bearing intermediate gneisses of the Renzy Terrane, which structurally overlie garnet-free migmatites of the PB. (B-C) The sampled dykes form part of a network of magmatic phases that pool along the contact between the PB and AB gneisses. Here the phases are distinguished based on migmatitic textures, geometry, color and grain size. They include pink, concordant to variably folded leucosomes within PB metatexites (G1) that coalesce to form discordant dykes of similar composition (G2). The dykes extend into a pink nebulitic phase (G3) with mafic rafts at the contact with the Renzy mafic body. The contacts between G2 and G3 are however, diffuse and difficult to trace. These phases are overprinted by finer-grained, white-pink (G4) and a coarse grained, white (G5) diatexites. (D) The concordant veins (G1) contain abundant undeformed quartz grains indicating they deformed under suprasolidus conditions. (E-F) The contact between the garnetiferous gneisses of the RT and the garnet-free underlying PB gneisses is characterized by an increase in strain, defined by mylonitic fabrics. If the mylonites constitute a tectonic boundary between PB and AB rocks, this boundary should represent the Allochthon Boundary Thrust (ABT). (G) Examples of zircon morphologies and the types of zones defined herein. (H) REE_{CN} normalized (S.S. Sun and McDonough, 1989) spider-diagram of the Grenvillian zones (types 3 & 4). (I) U-Th bivariate diagram. (J) Kernel density plot of all individual $^{207}Pb/^{206}Pb$ dates within the sample. Note that only the ca. 1400 Ma analysis is concordant within the inherited zones. (K) Weighted mean $^{207}Pb/^{206}Pb$ age for types 3 & 4.

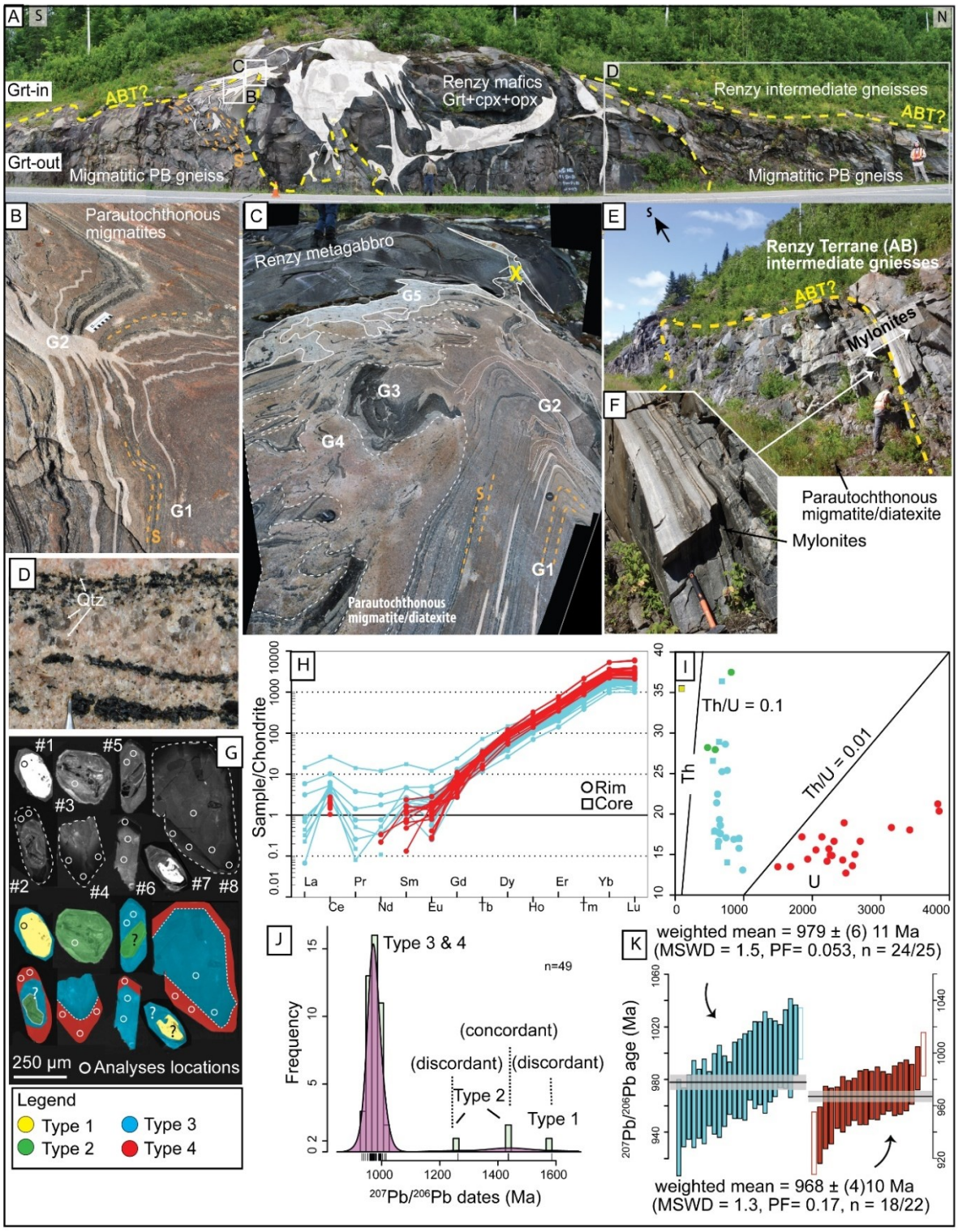
A
S
N
Grt-in
Grt-out
ABT?
C
B
Renzy mafics
Grt+cpx+opx
D
Renzy intermediate gneisses
ABT?
Migmatitic PB gneiss
Migmatitic PB gneiss
B
Paraautochthonous migmatites
G2
G1
S
C
Renzy metagabbro
G5
X
G3
G2
G4
S
G1
Paraautochthonous migmatite/diatexite
E
S
Renzy Terrane (AB) intermediate gneisses
ABT?
Mylonites
F
Paraautochthonous migmatite/diatexite
Mylonites
D
Qtz
G
#1
#5
#3
#2
#4
#6
#7
#8
250 µm
Analyses locations
Legend
Type 1
Type 3
Type 2
Type 4
H
Sample/Chondrite
Rim
Core
La
Pr
Sm
Gd
Dy
Er
Yb
Ce
Nd
Eu
Tb
Ho
Tm
Lu
I
Th/U = 0.1
Th/U = 0.01
Th
U
J
Type 3 & 4
n=49
Frequency
(concordant)
(discordant)
(discordant)
Type 2
Type 1
207Pb/206Pb dates (Ma)
K
weighted mean = 979 ± (6) 11 Ma
(MSWD = 1.5, PF= 0.053, n = 24/25)
207Pb/206Pb age (Ma)
weighted mean = 968 ± (4)10 Ma
(MSWD = 1.3, PF= 0.17, n = 18/22)

4.5.5 Sample CL6127: Granitic dyke in RDT gneisses

4.5.5.1 Outcrop and sample description

Sample CL6127 was collected from a pegmatitic, hornblende-bearing, granite dyke that cuts through a package of migmatitic gneisses in the RDT (Fig. 4.8A) that are located SE of the RT (Fig. 4.1). We interpret this outcrop as structurally below the RT due to the shallow NW dips of the gneisses and the drop in elevation (150 m over 5 km) between the RT and this locality. The migmatites are generally stromatic metatexites that, in places, are isoclinally folded (Fig. 4.8A) and locally loose structural integrity to become diatexites (Fig. 4.3E). Like the leucosome in these migmatites, the sampled dyke is devoid of garnet but contains euhedral hornblende crystals that are much larger (> 5 cm vs < 0.5 cm) than those in the gneiss (see inset in Fig. 4.8B). Although discordant to the foliation, the margins of the dyke have cuspate-lobate fold geometries and have concordant apophyses that are transposed parallel to the gneissosity in the wall rocks (Fig. 4.8A). Importantly, the contact between these apophyses and the migmatitic layering in the gneiss is diffuse (Fig. 4.8B) and quartz grains within apophyses do not show any preferred orientation. Zircon morphology

Zircon grains recovered from this sample occur as stubby and equant grains ranging between 100-500 μm in size (Fig. 4.8C). Rare prismatic grains make up less than 5% of the imaged populations. Five distinct types of zircon zones are identified across the grains. Type 1 (yellow in Fig. 4.8C) are defined by high CL-intensities consisting of entire zoned grains or cores (#1 and #2 in Fig. 4.8C). Type 2 (pink in Fig. 4.8C) are defined by distinctly low (black) CL-intensities consisting of whole unzoned grains (e.g. #3 in Fig. 4.8C) or cores within other grains (e.g. #4 in Fig. 4.8C). Type 3 (green in Fig. 4.8C) were identified in ca. 10% of the grains and are defined by prismatic (ca. 3:1 W:L ratio) habits and planar growth zonation patterns (#5 & #6 in Fig. 4.8C). They can consist of entire grains (#5 in Fig. 4.8C) or rims around weakly zoned cores with contrasting CL-intensities and an unknown affinity (#6 in Fig. 4.8C). There are no clear textural relationships between type 3 and the rest of the zircon types in this sample. Types 4 & 5 define the dominant morphologies in this sample. Types 4 (blue in Fig. 4.8C) define zircon with sector zonation patterns and moderate CL-intensities (grey) in whole euhedral grains (#7 in Fig. 4.8C) or as cores in stubby grains (#8 & #9 in Fig. 4.8C) that are rimmed by type 5 (red in Fig. 4.8C). Type 5 only define a population of

rims around type 4 and have variably wide (25-200 μm) subrounded to euhedral habits (#8 & #9 in Fig. 4.8C).

4.5.5.2 Zircon chemistry and geochronology

Thirty-seven analyses across the different morphologies yielded dates with <10% discordance. One spot from the core of a type 1 grain (#1 in Fig. 4.8C) yielded a concordant $^{207}Pb/^{206}Pb$ Archean date of 2647 ± 51 Ma (Fig. D.5A), whereas all other analyses yielded concordant Grenvillian dates (Fig. 4.8G). One analysis in the type 1 rim (#1 in Fig. 4.8C) yielded a concordant $^{207}Pb/^{206}Pb$ date of 977 ± 65 Ma and two analyses in type 2 zones yielded concordant $^{207}Pb/^{206}Pb$ dates of 989 ± 36 Ma and 1015 ± 24 Ma. However, these three analyses do not share the same trace-element characteristics as the remaining types 3-5 zircons, notably in terms of U concentration (Fig. 4.8F; Fig. D.11). One analysis in the type 1 rim (#1 in Fig. 4.8C) yielded a concordant $^{207}Pb/^{206}Pb$ date of 977 ± 65 Ma and two analyses in type 2 zones yielded concordant $^{207}Pb/^{206}Pb$ dates of 989 ± 36 Ma and 1015 ± 24 Ma (Fig. D.5B). Types 3-5 have similar steep positive $HREE_{CN}$ slopes, with variable negative Eu anomalies and strong positive Ce anomalies (Figs. 4.8D-E), similar ranges in their ∑REEs (262-586 ppm; Fig. D.11C) and Th (80-184 ppm) and U (246-649 ppm) concentrations, with Th/U ratios mostly between 0.1-0.2 (Fig. 4.8F). In addition, types 3-5 have similar Ti concentrations (UQ: 2.16, 2.23 and 2.38 respectively) and corresponding Ti-in-zircon temperatures (between 682-741°C; Table 4.2). In contrast, the type 1 rim, lacks the prominent Eu anomaly (Fig. 4.8D), has lower ∑REEs (Figs. D.11C-D) and Th-U concentrations (Fig. 4.8E). In addition to higher U concentrations (Fig. 4.8E), type 2 has higher Ti concentrations (UQ: 3.73 ppm) and a higher range in corresponding temperatures (724-778°C) compared to types 3-5 (Table 4.2). The distinct chemical and morphology traits of types 1 & 2 zircons differentiates them from the remaining Grenvillian populations and as such, these three dates are excluded from further weighted mean age calculations. Although types 3, 4, and 5 have different morphologies, they cannot be distinguished based on their geochemistry or individual weighted mean ages and are thus, combined to yield a $^{207}Pb/^{206}Pb$ weighted mean age of 1011 ± (7) 10 Ma (MSWD = 1.15, PF = 0.26, n = 32/34; Fig. 4.8H).

4.5.5.3 Interpretation

Geochronological results for sample CL6127 provide information on the nature of the host gneiss as well as the timing of deformation in PB rocks. The one Archean date from a type 1 core suggests that Archean rocks were involved somehow in the production of this granitic dyke, which is expected since this outcrop was considered part of the PB (Dickin *et al.*, 2014). Types 3, 4 and 5 zircon have an elongated morphology, crystal faces (Fig. 4.8C), and REE_{CN} profiles (Fig. 4.8D-E) that are all key characteristics of igneous zircon (Corfu, 2003). Because type 5 zircon overgrow faceted and euhedral type 4 zircons (e.g. grain #2, #4, #8 and #9 on Fig. 4.8C), they likely reflect several crystallization events without resorption in between. The combined age of 1011 ± (7) 10 Ma for these three zircon types is interpreted as the timing of crystallization for this late-kinematic dyke. Furthermore, the diffuse contact between the dyke and leucosome in its host gneiss as well as the absence of deformation in quartz located in apophyses parallel with the migmatitic banding constitute strong evidence for melt-present deformation of the gneiss at the time of intrusion.

Figure 4.8 (next page). Sample CL6127. (A) Sample taken from a granitic dyke that cuts the gneissic fabric within highly migmatitic granodiorites of the RDT (see also Fig. 4.3E) but also contains apophyses transposed within the gneissic fabric (B). Note the large hornblende crystals in the dyke (inset of B). (C) Examples of zircon morphologies and the types of zones defined herein. (D-E) REE_{CN} normalized (S.S. Sun and McDonough, 1989) spider-diagrams of Grenvillian zones only. (F) U-Th bivariate diagram. (G) Kernel density plot of all individual $^{207}Pb/^{206}Pb$ dates within the sample. (H) Weighted mean $^{207}Pb/^{206}Pb$ age for types 3, 4 & 5 (dark shading with stippled line) and their combined age (light shading with solid line). Note that analyses one types 1 & 2 are not included in the weighted mean age calculation due to their distinct morphological and chemical traits compared to types 3-5.

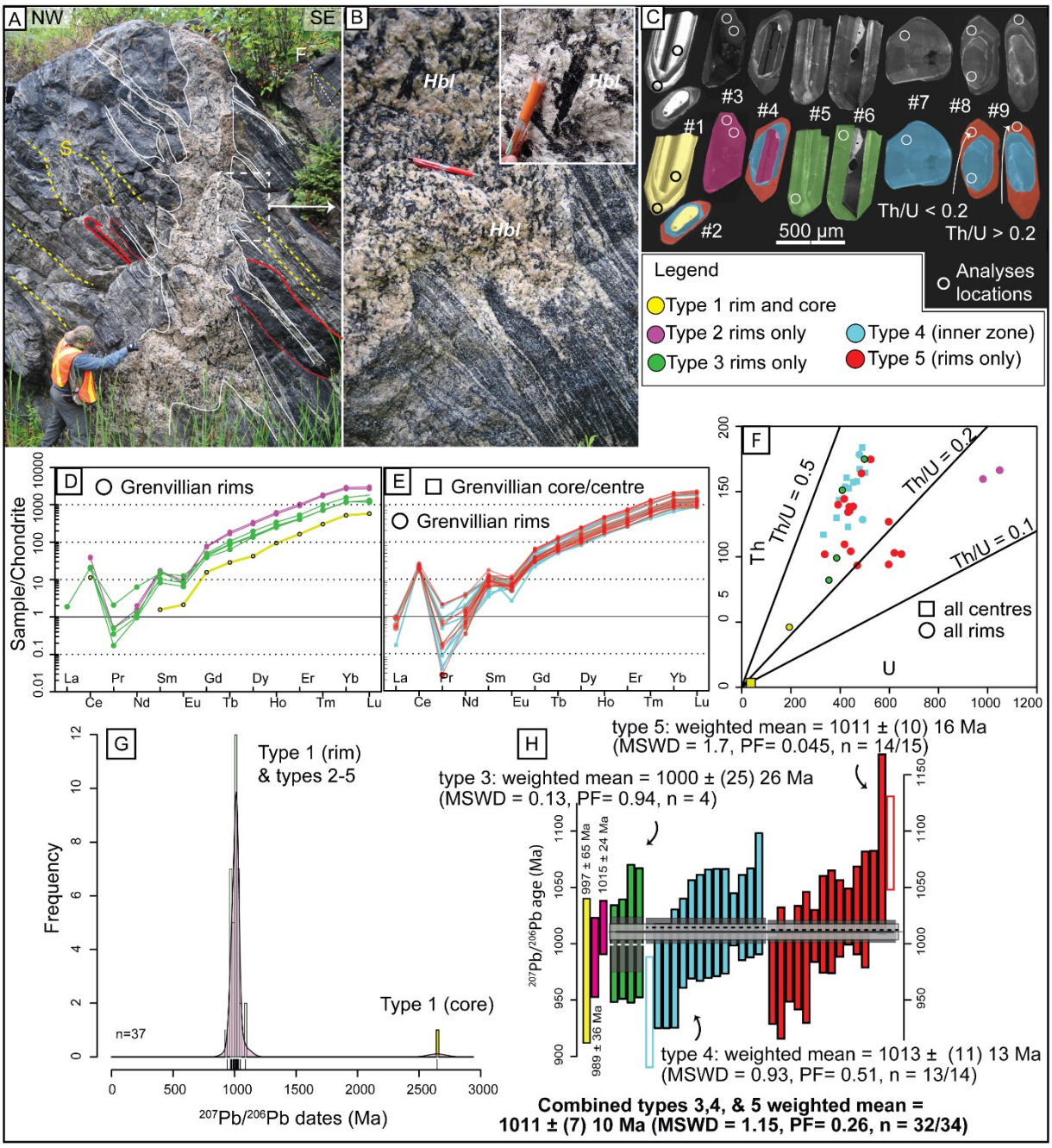
A
NW
SE
F
S
B
Hbl
Hbl
Hbl
C
#1
#2
#3
#4
#5
#6
#7
#8
#9
500 µm
Th/U < 0.2
Th/U > 0.2
Legend
Analyses locations
Type 1 rim and core
Type 2 rims only
Type 3 rims only
Type 4 (inner zone)
Type 5 (rims only)
D
Grenvillian rims
Sample/Chondrite
La Ce Pr Nd Sm Eu Gd Tb Dy Ho Er Tm Yb Lu
E
Grenvillian core/centre
Grenvillian rims
F
Th
U
Th/U = 0.5
Th/U = 0.2
Th/U = 0.1
all centres
all rims
G
Type 1 (rim)
& types 2-5
Type 1 (core)
n=37
Frequency
207Pb/206Pb dates (Ma)
H
type 5: weighted mean = 1011 ± (10) 16 Ma
(MSWD = 1.7, PF= 0.045, n = 14/15)
type 3: weighted mean = 1000 ± (25) 26 Ma
(MSWD = 0.13, PF= 0.94, n = 4)
997 ± 65 Ma
1015 ± 24 Ma
989 ± 36 Ma
207Pb/206Pb age (Ma)
type 4: weighted mean = 1013 ± (11) 13 Ma
(MSWD = 0.93, PF= 0.51, n = 13/14)
Combined types 3,4, & 5 weighted mean =
1011 ± (7) 10 Ma (MSWD = 1.15, PF= 0.26, n = 32/34)

4.5.6 Sample CL6135: granitic injection in the VT

4.5.6.1 Outcrop and sample description

Sample CL6135 (Fig. 4.1) was collected from a granitic injection vein within the migmatitic gneisses of the VT that is dominated by sheath folds (Fig. 4.2C). The vein is folded by one of the asymmetrical sheath folds within the gneisses (Fig. 4.2C and Fig. 4.9A), but also cuts across the gneissic fabric and the limbs of the same sheath fold (Fig. 4.9A). Where the vein is parallel with the gneissosity in the host, quartz within the vein is generally rounded to subhedral (Fig. 4.9B), whereas in the hinge of the fold it forms lenses roughly aligned with the axial-plane (Fig. 4.9C). The 'z-shaped' asymmetry of the sheath folds (Fig. 4.2C) define a top-to-the NW shear component, consistent with other centimetric (e.g. δ-shaped feldspar porphyroclasts) to meter-scale (e.g. mafic boudins; Fig. 4.2D) kinematic indicators in this part of the VT (Hanmer and Ciesielski, 1984; Indares and Martignole, 1990; Lambert *et al.*, 2019).

4.5.6.2 Zircon morphology

Zircons recovered from this sample include mostly ca. 250 μm long, stubby grains with a few (< 10%), larger (ca. 500-600 μm) grains with prismatic habits and rare (<2%) equant subrounded grains (Fig. 4.9D). Five different types of zircon zones are identified across the grains based on their internal textures. Type 1 (yellow in Fig. 4.9D) defines euhedral cores with high CL intensities and, although the reflectance typically obscures the internal zonation patterns, oscillatory zonation patterns are visible in some grains (#1 Fig. 4.9D). Type 1 is always mantled by type 2 zircon (#1 & 5 in Fig. 4.9D), which may be followed by a succession of other zones (#2 in Fig. 4.9D). Type 2 (green in Fig. 4.9D) defines growth zones with lower CL intensity (grey), homogenous and oscillatory growth zonation patterns. In grains where a type 1 core is not preserved, type 2 encompasses the entire grains (#4 in Fig. 4.9D). Type 2 also represent cores, mantled by types 3 (#2 in Fig. 4.9D), type 4 (#5 & #6 in Fig. 4.9D) and type 5 (#9 in Fig. 4.9D). Notably, where margins between type 2 are blurred by the bright reflectance of type 1 in our CL images (#6 in Fig. 4.9D), the two populations are distinguished based on their trace element characteristics (see below). Type 3 (pink in Fig. 4.9D) constitute a subordinate population of textures (ca. 10%) that have convoluted growth patterns, characterized by mixed CL intensities (see white and mesocratic grey colors of #2 & #3 in Fig. 4.9D). These textures encompass entire grains (#3 in Fig. 4.9D), mantle cores inferred as types 1 and 2 (#2 in Fig. 4.9D) or themselves may be mantled by type 5

(#8 in Fig. 4.9D), although no type 3 cores were analyzed to confirm the latter relationship. We also note that there are no clear textural links between type 3 and type 4. Type 4 (blue in Fig. 4.9D) and type 5 (red in Fig. 4.9D) are both defined as broad (<100 μm) homogenous zircon rims, with low (mesocratic to melanocratic grey) CL intensities. In addition to rims around type 2, type 4 also mantles vague and zones that are possibly resorbed type 2 zircon (#6 & 7 in Fig. 4.9D). Type 5 mantles both those inferred as type 2 (#9 in Fig. 4.9D) and type 3 (#8 in Fig. 4.9D). There are no clear textural relationships between types 4 and 5, but they are confidently differentiated from each other based on both geochemistry and age (see below).

4.5.6.3 Zircon chemistry and geochronology

Sixty-nine analyses across the different zircon types yielded dates with <10% discordance (Table S7). Except for one concordant Mesoproterozoic date (1276 ± 63 Ma), thirty-three analyses from types 1-3 yield mostly concordant Paleoproterozoic dates between 1777-1510 Ma (Fig. 4.9G & Fig. D.6A) and broadly have similar trace element traits (Fig. D.12). In particular, they all have steep positive REE_{CN} profiles with negative Eu and a positive Ce anomalies, similar ∑REE concentrations and have similar Th (<135 ppm) and U (<205) concentrations with average Th/U ratios > 0.25 (Fig. 4.9F). Due to the poorly constrained textural relationships, similarity in chemistry and overlapping weighted mean ages of these three populations (Figs. D.6B-D), they are combined to yield a weighted mean age of 1663 ± (6) 14 Ma (MSWD = 3.1, PF = 0, n = 31/33; Fig. D.6E).

Type 4 and 5 zircons are characterized by steep positive REE_{CN} profiles with, moderately negative Eu and strong positive Ce anomalies (Fig. 4.9E). They have similar ∑REE (Fig. D.12C) and U (200-600 ppm) concentrations and although they have variable Th and concentrations, they both yield Th/U ratios between 0.1-0.5 (Fig. 4.9F). Type 5 have distinctly lower Ti concentrations (UQ: 3.76 ppm) compared to the rest of the zones (UQ: 4.73-6.27 ppm) with corresponding temperatures between 725-778ºC (Table 4.2). Despite their morphological and chemical similarities, types 4 and 5 zircon are clearly distinguished by their U-Pb ages (Fig. 4.9G). Except for one analysis that yielded a concordant date of 1157 ± 68 Ma, all other type 4 zircon analyses had similar dates to yield a $^{207}Pb/^{206}Pb$ weighted mean age of 1445 ± (7) 10 Ma (MSWD = 2.06, PF = 0.01, n = 16; Fig. D.6F). In contrast, all type 5 zircon analyses yielded a weighted mean age of 1008 ± (7) 10 Ma (MSWD = 1.64, PF = 0.52; n=17; Fig. 4.9H).

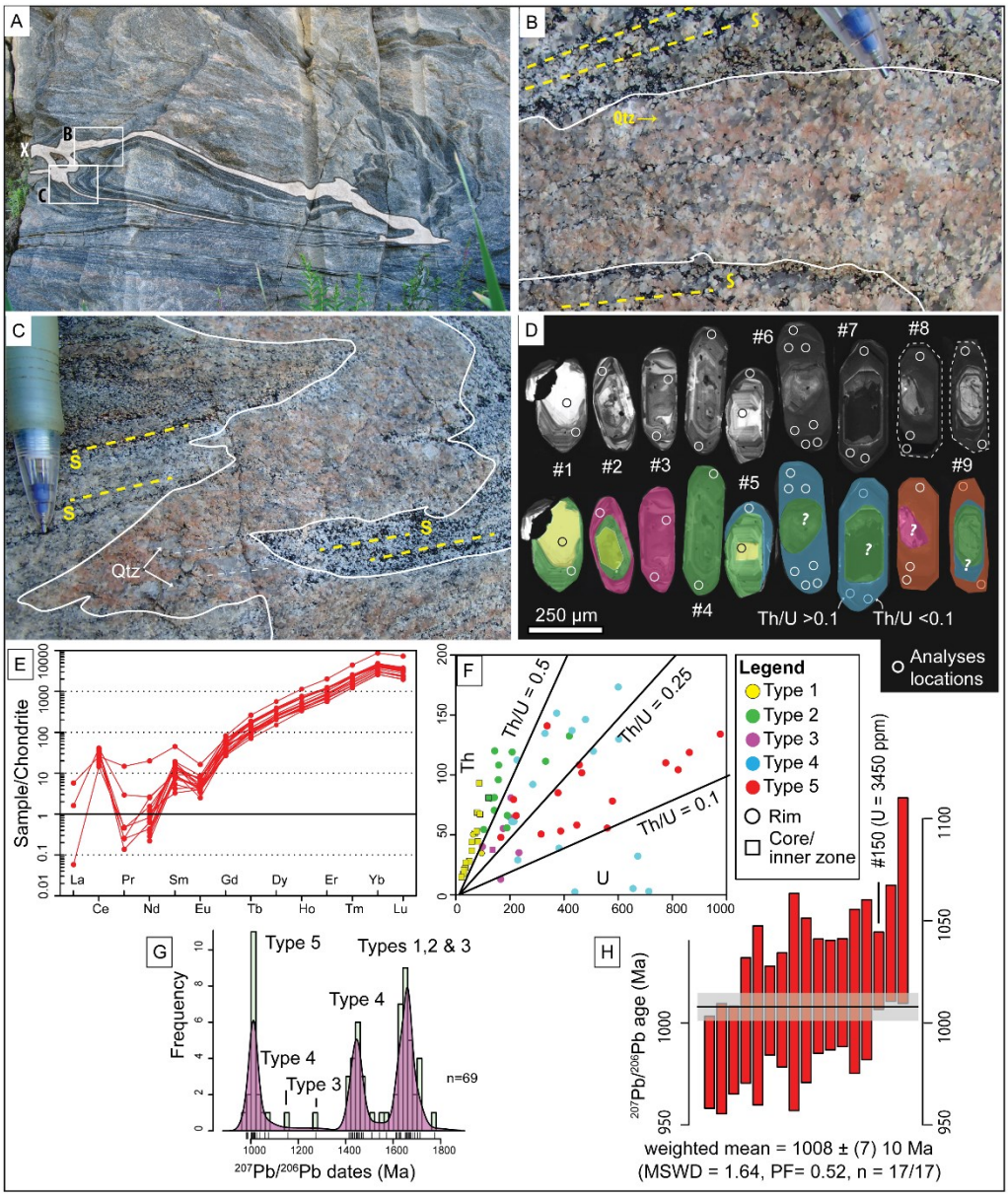

Figure 4.9. Sample CL6135. (A) Sample taken at X, from a granitic injection vein that cuts across the ductile fabric but is folded by sheath folds (see Fig. 4.2C) in the VT. (B) Concordant portion of the vein commonly contain abundant undeformed quartz grains. (C) Discordant portions of the vein contain quartz ribbons aligned parallel to the gneissic fabric. (D) Examples of zircon morphologies and the types of zones defined herein. (E) REE_{CN} normalized (S.S. Sun and McDonough, 1989) spider-diagram of the Grenvillian zone (type 5). (F) U-Th bivariate diagram. (G) Kernel density plot of all individual $^{207}Pb/^{206}Pb$ dates within the sample. (H) Weighted mean $^{207}Pb/^{206}Pb$ age for type 5.

4.5.6.4 Interpretation

As types 1-4 generally consist of rounded cores (Fig. 4.9D) and have distinctly older ages compared to type 5 (Fig. 4.9G), they are interpreted as inherited grains. Type 5 zircon has an elongated morphology, crystal faces (Fig. 4.9D), and REE_{CN} profiles (Fig. 4.9E) that are all key characteristics of igneous zircon (Corfu, 2003). The 1008 ± (7) 10 Ma weighted mean age of type 5 is thus interpreted as the crystallization age of the injection vein. Field relationships indicate that the sampled vein crosscuts the gneissosity but the vein is itself, folded into a sheath (Fig. 4.9A) and that quartz grains within the part of the veins that parallel the gneissosity are undeformed (Fig. 4.9B). This is strong evidence that the age of the vein is that of sheath folding. Here the absence of quartz deformation further implies that the top-to-the NW shear strain within this part of the VT occurred under suprasolidus conditions. Elsewhere in the sampled vein, the preservation of both ovoid undeformed quartz grains and ribbons aligned with the gneissic fabric suggests that deformation probably started under suprasolidus conditions but transitioned to subsolidus conditions by the time of crystallization.

4.6 Discussion

4.6.1 Petrogenesis of felsic igneous rocks

Key geochemical and morphological traits can help unravel the complex textural relationships preserved within the Grenvillian zircon populations presented herein. The majority of zircon grains observed herein, preserve compelling morphological and chemical evidence that they crystallized within anatectic melts, in particular: their prismatic (1:4 width: length) and faceted igneous habits (type 2 & 3 in Fig. 4.5E; type 4 in Fig. 4.6C; type 3 in Fig. 4.7G; types 3 & 5 in Fig. 4.8C; type 5 in Fig. 4.9D); distinct oscillatory zonation patterns (type 3 in Fig. 4B and type 5 in Fig. 4.6C); and positive $HREE_{CN}$ profiles (Fig. 4C, Fig. 4.5H, Figs. 4.8D-E, Fig. 4.9E) and Th/U > 0.1 (Fig. 4D, Fig. 4.8F, Fig. 4.9F; Corfu. 2003; Hinton and Upton, 1991; Hoskin and Black, 2000; Hoskin and Ireland, 2000; Paterson *et al.*, 1992; Rubatto, 2002). Inasmuch as the zircons in most samples show evidence for more than one Grenvillian zone mantling another, with limited evidence for resorption in between, we consider that they represent multiple episodes of Grenvillian zircon growth.

There is some evidence that suggests the igneous rocks studied herein were derived from the melt in their host rocks. First, the age of inherited zircon systematically matches that expected of their

host gneisses. The samples (CL6070, CL6106, CL6127) located in the RDT contain Archean xenocrystic cores, the sample located in the VT terrane (CL6135) contain inherited Paleo-and Mesoproterozoic xenocrystic cores and samples intruding the RT contains ca. 1400 Ma cores (Table 4.2). Moreover, at several outcrops, there was a physical link between the sampled intrusive rocks and leucosome in their host gneiss (Fig. 4.4A, Fig. 4.5B, Figs. 4.7A-C, Figs. 4.8A-B) and some show diffuse contacts (Fig. 4.5B & Fig. 4.8B). It is therefore likely that the earlier Grenvillian zircon types were generated from the melting of the host gneiss and that the later types record crystallization of the igneous rocks. Furthermore, at two outcrops, the dated igneous rocks are physically linked to diatexites (Fig. 4.5A, Fig &.Fig. 4.7A-C).

Zircons with multiple growth zones that are similar in age, could be explained by continuous crystallization during protracted cooling or the result of episodic melting (re-melting or melt rejuvenation) of the same melt phase (Rubatto *et al.*, 2009). In the former case, we expect to see chemical changes in zircon that correspond to an evolving mineral paragenesis during cooling; examples include the deepening of the Eu anomaly as feldspar begins to crystallize (Rubatto *et al.*, 2013) and a decrease in Ti concentrations (Watson *et al.*, 2006) from inner to outer zones. Furthermore, zircons recording protracted crystallization should reflect a continuum of concordant dates, resulting in a larger statistical spread (MSWD > 2; Rubatto *et al.*, 2009). Examples of episodic melting (and subsequent crystallization) have been documented within amphibolite grade migmatites from the Central Alps by Rubatto *et al.* (2009). In that study, multiple generations of zircon growth zones with distinct 'Alpine' ages (ca. 32-22 Ma) and chemical signatures, were interpreted as the result of repeated melting during sporadic and localized fluid influx. The slight variation in age, combined with uniformly low Ti concentrations across their samples and/or within the different zones of individual zircon grains, led Rubatto *et al.* (2009) to suggest that melting of these zones occurred intermittently and repeatedly at roughly constant temperatures (~620-700^{o}C) as fluid became available, over a protracted period of ca. 10 My during exhumation.

Most of the Grenvillian populations analyzed herein, display a number of strikingly similar traits to those described by Rubatto *et al.* (2009). There is no evidence for progressively deeper Eu anomalies within the zircon types within a sample and, with the exception of sample CL6112 (types 3 & 4), the overgrowing zircon zones record uniform Ti concentrations (Table S10), which does not support protracted crystallization during cooling. Furthermore, Ti-in-zircon temperatures are all below 800^{o}C (Fig. 4.10; Table 4.2), which is on the lower limit of dehydration melting of Bt-

Qtz-Pl rocks derived from experiments (see summary of various melting reactions in Weinberg and Hasalová, 2015). Although some studies have shown that Ti-in-zircon thermometry can yield lower temperatures than constrained by other geo-thermometers (e.g. Hofmann *et al.*, 2014; Gervais and Crowley, 2017), Schiller and Finger (2019) noted that the unrealistically low temperatures in such previous studies, may in fact, be attributed to the common over-estimation of the aTiO2 (>0.5) in rutile-free granitic rocks. Moreover, we observed that zircon grains contain multiple, texturally distinct Grenvillian zones, mostly sharing geochemical characteristics and overgrow each other, generally without signs of resorption of the previous phase (e.g. #2 in Fig. 4B; #3 & #5 in Fig. 4.5E; #2 & #3 in Fig. 4.6C; #6 & #8 in Fig. 4.7G; #2, #4 & #8 in Fig. 4.8F). Notably, in sample CL6098, euhedral type 3 zones are faceted and mantle type 2 that is also faceted (#4 in Fig. 4.5E). U-Pb geochronology on this sample yields statistically distinct ages (Fig. 4.5I & Fig. 4.10) suggesting a first phase of zircon crystallisation following partial melting and crystallization of the host zircons at 1020 ± (6) 13 Ma and then a second phase following crystallisation of the pegmatite at 1001 ± (6) 10 Ma. Relative geochronology (i.e. without calibration error), thus suggests that these rocks remained partially molten for a minimum of 7 Myrs (Fig. 4.10).

Figure 4.10 (next page). A graphical summary of the geochronology (black; age Y-axis on the left) and Ti-in-zircon thermometry (red; temperature Y-axis on the right) results from the samples presented in this study. Only the weighted mean ages of the Grenvillian zircon populations are presented. See Table 4.2 for details on all of the zircon age populations. Stippled black lines indicate the standard calibration error propagated into the error on the weighted mean age, whereas solid black error bars do not. Temperatures are reported as best conservative estimates using the upper limit of the interquartile range for pressures between 550 and 1000 MPa (pressure estimates from Indares and Martignole, 1990). Red error bars indicate a ±30^{o}C error on the temperature to account for analytical and statistical errors (following Tomkins *et al.,* 2017). See Methodology section for further details of the age and temperature calculations.

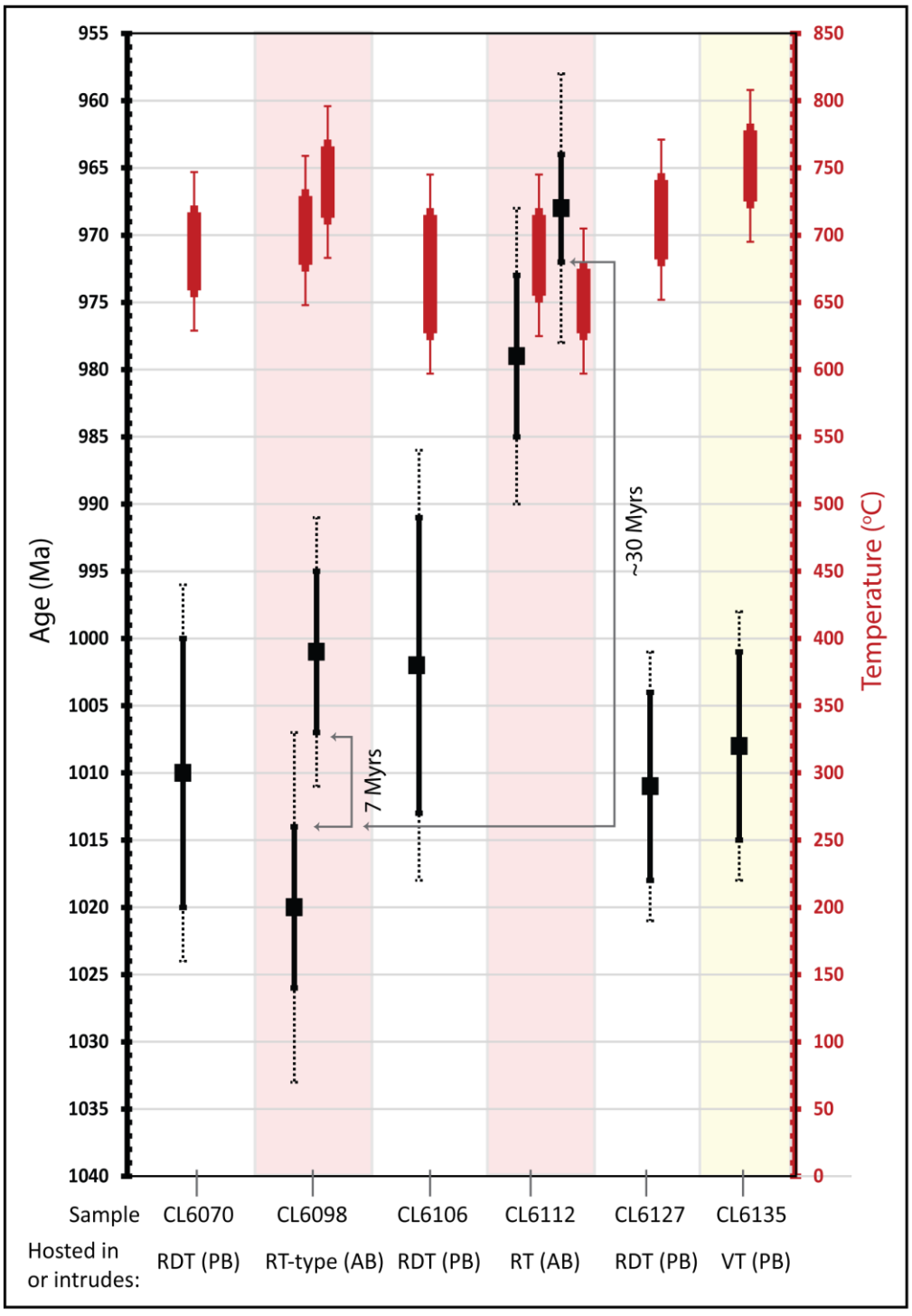
Age (Ma)
955
960
965
970
975
980
985
990
995
1000
1005
1010
1015
1020
1025
1030
1035
1040
Temperature (°C)
850
800
750
700
650
600
550
500
450
400
350
300
250
200
150
100
50
0
~30 Myrs
7 Myrs
Sample
CL6070
CL6098
CL6106
CL6112
CL6127
CL6135
Hosted in or intrudes:
RDT (PB)
RT-type (AB)
RDT (PB)
RT (AB)
RDT (PB)
VT (PB)

If the early Grenvillian zircons in the dated igneous rocks were formed during melting of their host gneiss, it is important to evaluate the melting process. First, our systematic investigation of leucosomes in the field indicate a lack of common peritectic phases indicative of dehydration melting such as garnet, orthopyroxene or clinopyroxene (Weinberg and Hasalová, 2015). There is also a general lack of melanosomes associated with the migmatitic neosomes (Figs. 4.3A-D, Fig. 4A, Figs. 4.5A-B & Fig. 4.6B). Instead, euhedral hornblende crystals that are much larger than in their host gneiss are common. (e.g. Figs. 4.3C-D & inset in Fig. 4.8B). Partial melting experiments (Gardien *et al.*, 2000), crystallisation experiments (Naney, 1983) and phase equilibria modeling (Green *et al.*, 2016) clearly demonstrate that hornblende-bearing leucosomes require a significant (ca. 4 wt %) input of external water (see also the review by Weinberg and Hasalová, 2015). The addition of water is supported by the hydration of dry clinopyroxene-garnet assemblages observed in the center of mafic boudins to hornblende-plagioclase at their margin where in contact with leucosome. Water-present melting is also supported by the high leucosome fraction (>30-50% of the wall rock volume; Figs. 4.3E-F & Fig. 4.5A), which is more typical of water-fluxed rather than dehydration melting (Brown, 2013; Sawyer, 2008, 2010; Sawyer and Brown, 2008; Weinberg and Hasalová, 2015). Thus, like the migmatites in the Central Alps, we propose that the Grenvillian zones in the zircons presented in this study, potentially crystallized during multiple fluid-assisted (re-)melting or fluid present crystallization events/pulses. Further petrological studies and more precise geochronology to distinguish the age of the different types would, however, be required to test this hypothesis and determine the source of the fluid.

4.6.2 Tectonic implications

The main implication of the current study is the documentation of widespread, and likely protracted, melt present deformation during the latest phase of the Grenvillian Orogeny (the Rigolet). Four samples from the RDT (CL6070, CL6098, CL6112 and CL6127) are felsic igneous rocks that can be physically linked to leucosomes in their host gneiss (Fig. 4.4A, Figs. 4.5A-B, Figs. 4.7B-C & Fig. 4.8B) and these leucosomes do not show evidence for subsolidus strain as the quartz grains within them are undeformed (Figs. 4.3B-C, Fig. 4.7D). Three of these samples yield overlapping ages at ca. 1000 Ma and at least one sample (CL6098) indicates a protracted partial melting event of at least 7 Myrs (Fig. 4.10). Sample CL6112 yields younger ages of ca. 979 ± (6) 11 Ma and ca. 968 ± (4) 10 Ma (Fig. 4.10; Table 4.2). Although we cannot rule out that this outcrop

recorded a younger melt-present deformation event, we have observed no structural discontinuity or differences in outcrop features to suggest that this outcrop is distinct from all the other migmatites and diatexites in the RDT. Therefore, we interpret the spread of crystallization ages as a protracted event of melt-present deformation for a minimum of 30 Myrs (difference with errors between the oldest and youngest Grenvillian age; Fig. 4.10). Furthermore, the two samples from gneisses (TBSZ & VT respectively) that recorded subsolidus conditions (CL6106 and CL6135), yielded ages overlapping with the timing of melt-present deformation recorded in the other samples (CL6106 at ca. 1002 and CL6135 at ca. 1008 Ma; Fig. 4.10). This demonstrates that the migmatites crystallized locally to record the regional top-to-NW shearing evidenced by the asymmetry of delta-shaped meter-scale mafic boudins (Fig. 4.2D) and of sheath folds at outcrops CL6135 (Fig. 4.2C). Shallow dipping migmatites and diatexites recording protracted melt-present deformation (Sabourin, 1963; Martignole, 1995; Martignole *et al.*, 2000; Lambert *et al.*, 2018, 2019) are characteristics of lateral ductile flow (i.e. channel flow; Beaumont *et al.*, 2004; Gervais and Brown, 2011; Vanderhaeghe, 2009 and references therein).

Field observations and geochronological data presented herein allow us to propose a novel tectonic model for the western Grenville Province during the Rigolet phase of the Grenvillian Orogeny. First, under-thrusting of the Laurentian basement may have brought metasediments to lower crustal levels (Fig. 4.11A). Metasediments are abundant in the PB NW of the map shown on figure 1 (see Lac Témiskamingue Terrane; Indares and Martignole, 1989, 1990; Martignole and Martelat, 2005). Dehydration of these sediments may have transported water upward into the orthogneiss of the RDT and triggered their partial melting starting sometimes before ca. 1020 Ma (Fig. 4.11A; see the age of the oldest type in sample CL6098; Fig. 4.10). Once thick enough, a partially molten panel of RDT rocks started to flow towards the foreland. Melt within the channel migrated upward, intruded and brecciated the stiff structurally overlying mafic rocks of the RT (Fig. 4.11B). The brecciated blocks were incorporated into the flowing partially molten channel and now forms rafts of various size in the RDT (Fig. 4.11C). The amoeboid shape of the map-scale RT (Fig. 1) that our work shows to be surrounded both structurally above, below and sideways by RDT migmatites (see also Sabourin, 1963) likely reflect a km size block of RT rocks that was engulfed by the flowing channel. Finally, locality CL6112, which records the youngest melt present deformation (Fig. 4.10), probably captures an incipient snapshot of this process, but was stopped as convergence ceased at the end of the Grenvillian Orogeny.

This model differs from models proposed for the regional tectonic evolution, specifically the Rigolet phase of the Grenvillian Orogeny (Rivers, 2009). Because we have mapped RDT rocks structurally above and below the RT, the model viewing the RT as a tectonic klippen overlying the parautochthonous gneisses, (e.g. Dickin *et al.*, 2014) does not seem likely. The Rigolet phase of the Grenvillian Orogeny is generally viewed as a relatively cold and short event (Van Gool *et al.*, 2008; Rivers, 2009). Thermomechanical numerical model applied for this transect also largely agrees with this view (see Fig. 4 in Jamieson *et al.*, 2010). In stark contrast, we documented protracted melt-present deformation, with flowing migmatites dismembering and incorporating rocks of the overlying structural panel, which strongly argues against the currently accepted model. Jannin *et al.* (2018), however, documented remarkably similar features in the Manicouagan area of eastern Quebec. They showed that felsic dykes migrated upward from the PB into the overlying AB during the Rigolet phase, leading to strain localization and formation of a ductile channel in partially molten crust between ca. 990-960 Ma. They also proposed that part of the lower AB was detached as a rigid "allochthonous slice" into the flowing channel, formed largely in PB rocks. Consequently, we propose that the RT is analogous to the "allochthonous slice" in the model of Jannin *et al.* (2018). These two contributions are the first two modern geochronological studies, conducted in two distinct parts of the PB, to demonstrate that the Rigolet was a major orogenic phase involving protracted melting and flow of the deep crust.

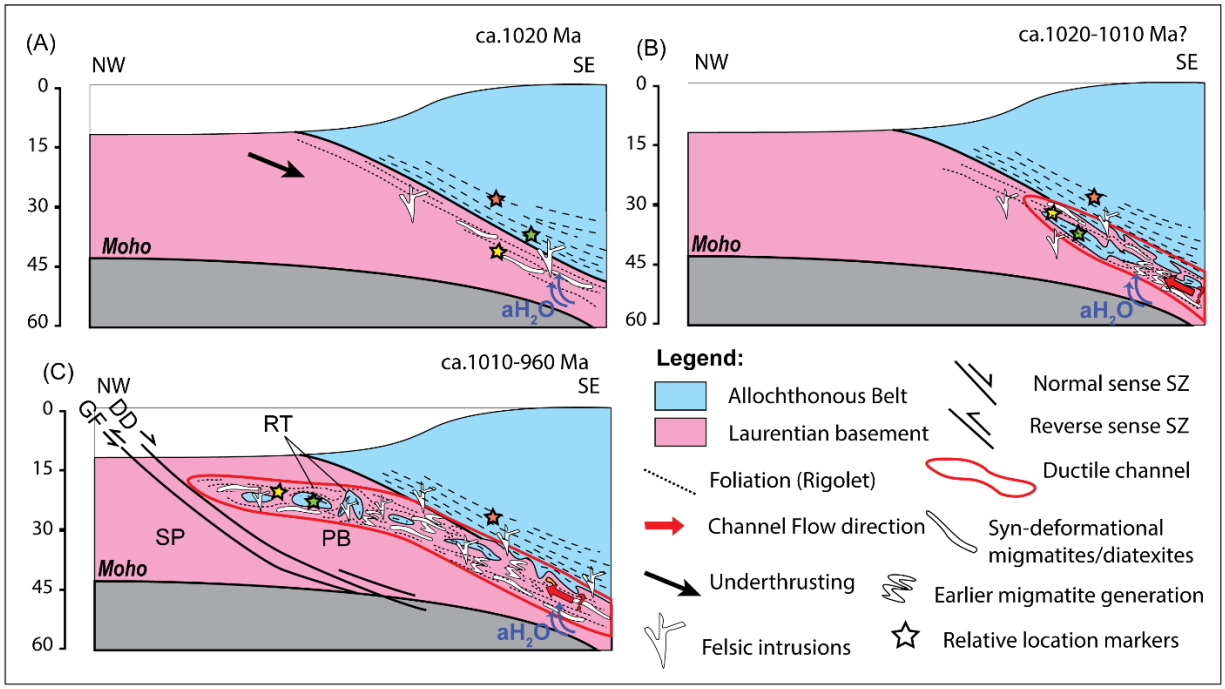

Figure 4.11. Cartoon for the proposed evolution of the Grenville Province in the study region, based on the geochronology results from the samples collected herein. (A) Under-thrusting of the Laurentian basement and onset of probably fluid-fluxed melting in the Parautochthonous Belt (PB). (B) Continued melting and formation of a partially molten zone within the RDT rocks that may have intruded into, and brecciated the lower part of the AB, incorporating relatively ridged slab of the Renzy Terrane into the parautochthonous channel. (C) Continued melting and foreland-ward exhumation of the channel and dismemberment of the Renzy Terrane (RT) into km-sized and variably deformed rafts. See text for detailed description of the model. Colored stars represent the relative movement of various structural levels through the different stages of the model. Abbreviations: Allochthon Boundary Thrust (ABT); Dorval Detachment (DD); Superior Province (SP). Model inspired by Rivers (2009), Jamieson and Beaumont (2013) and Jannin *et al.* (2018).

4.7 Conclusions

- LA-ICP-MS U-Pb geochronology on zircon from six syn-late deformational felsic dykes, pegmatites, and injection veins provides constraints on the age of deformation within the Reservoir Dozois (RDT) and Verendrye terranes of the Grenville Province along the Hw117 transect in western Quebec. Four of them present field evidence that they were extracted from their partially molten migmatitic host gneiss. An interpretation supported by the ages of inherited cores that systematically fit with the age expected from previously published studies. All six specimens present evidence that they were deformed while still being partial molten.

- Zircons within the samples contain several textural zones, sharing geochemical and morphological characteristics typical of igneous grains. They yield $^{207}Pb/^{206}Pb$ weighted mean ages of: i) 1010 ± (10) 14 Ma for sample CL6070 (error in parentheses does not include the external calibration error), a leucosome in a boudin neck (Fig. 4A-F); ii) 1020 ± (6) 13 Ma and 1001 (6) 10 Ma for sample CL6098, a hornblende-bearing pegmatite derived from diatexite intruding mafic rocks of the Renzy Terrane (Fig. 4.5A-I); iii) 1002 ± (11) 16 Ma for sample CL6106, a granitic dyke crosscutting a top-to-the-NW subsolidus shear zone enveloped by migmatites of the RDT (Fig. 4.6A-G); iv) 979 ± (6) 11 Ma and 968 ± (4) 10 Ma for sample CL6112 a pegmatite extracted from the host gneiss that brecciates the overlying mafic rocks of the Renzy Terrane (Fig. 4.7A-K); 1011 ± (7) 10 Ma for sample CL6127, a hornblende-bearing pegmatite that crosscut the gneissosity but has apophyses within it as well (Fig. 4.8A-H); 1008 ± (7) 10 Ma for sample CL6135, a granitic veins synchronous with sheath folding in the Vérendrye Terrane (Fig. 4.9AH).

- $^{207}Pb/^{206}Pb$ weighted mean ages between ca. 1020-968 Ma (Fig. 4.10) demonstrate that pervasive melt-present deformation during the Rigolet phase was protracted (>40 Myrs). The incipient brecciation of mafic rocks belonging to the Renzy Terrane (outcrop CL6112; Fig. 4.7A-C),which is part of the Allochthonous Belt, and the intrusion of diatexites of the RDT into similar Renzy mafic rocks (outcrop CL6098; Figs. 4.5A-B), as well as the numerous garnet-bearing mafic boudins ascribed to the RT isolated within in the migmatites of the RDT, advocates for the dismemberment and incorporation of overlying

allochthonous components within a partially molten parautochthonous channel during the Rigolet phase.

- This model is in stark contrast to previously proposed models of a short orogenic cycle in a relatively cold orogenic wedge of the Grenville Orogen (Rivers, 2009), but is similar to a model proposed for the evolution of a similar structural level in the Eastern Grenville Province (Jannin *et al.*, 2018).
- Melt-weakened crust along this section of the Grenville orogen likely facilitated ductile lateral flow during the Rigolet phase. However, the hypothesis for channel flow within the PB of western Quebec still requires further data and testing, particularly the identification of the upper and lower channel boundaries within the PB, which should record a synchronous but an opposite sense of shear (Gervais and Brown, 2011).

CHAPTER 5 CONCLUSION (AND RECOMMENDATIONS)

5.1 Summary and conclusions

The primary objective of this thesis, as outlined in section 1.3, was to collect and compile a robust dataset from a transect through part of this generally understudied section of the Grenville Province in western Quebec, by mapping and applying modern structural, geochemical and geochronology analytical techniques in order to move towards a better understanding of the evolution of the Grenvillian Orogen. As summarized below, data presented in the three core-chapters of this study contributes towards this fundamental objective. More specifically, the integrated datasets (chapters 2-4) are used to understand and characterize the tectonic architecture along a critical transect through the Grenville Province in western Quebec (objective no. 2) by: mapping and characterizing the structure along the transect (chapter 2); comparing mafic bodies collected in the Parautochthonous Belt (PB) to known reference suites in different structural levels of the Grenville Province in the study area (chapter 3); and determining the age of pervasive deformation in various tectonic segments along this transect (chapter 2 & chapter 4). The new U-Pb age data from this study is the first modern geochronological dataset along this transect (objective no. 3). These integrated datasets are then used to propose a new model for how and when the PB (objective no. 4). Finally, much of this data was presented in a novel, interactive and digital format (see v-chapter 2) to increase the exposure of the research and encourage further research in the Grenville Province (objective no. 5).

The final section of this chapter highlights key questions that surfaced throughout this study that remain unresolved and make some suggestions for future research in the Grenville Province.

5.1.1 Towards a new model for deformation of the PB in western Quebec

5.1.1.1 The tectonic architecture along the Hw117 transect

By integrating the lithological and structural characteristics of the various tectonic domains of the Hw117 transect (v-chapter 2 & chapter 2), with the likely allochthonous geochemical affinity of most mafic bodies collected within the PB along the transect (chapter 3) and the new U-Pb geochronology results (chapters 2 & 4; discussed in section 5.1.1.2), this study complements the sparse geological datasets that exists throughout this critical section of the Grenville Province and provides for a better understanding of the architecture preserved along the Hw117 transect.

Furthermore, these new field data can be used for future development of the conceptual (e.g. Martignole and Martelat, 2005; Rivers, 2009) and the numerical models that exists along this transect (e.g. GO-2 Montreal-Val d'Or; Jamieson *et al.*, 2007). This section summarizes the tectonic architecture according to the findings in this study.

In general, mapping in the Grenville Front Thrust Zone (GFTZ) confirms earlier interpretations of Indares and Martignole (1990) and Martignole and Martelat (2005). High-grade (granulite) gneissic fabrics in the GFTZ trend SW-NE and have prominent down dip lineations that are consistent with NW-directed brittle-ductile thrusting and subsequent SE-directed normal sense displacement (Montreuil and Constantin, 2010). Although rare monazite with Grenvillian ages (964 ± 28 Ma; 956 ± 27 Ma; 945 ± 17 Ma) presents some evidence for Grenvillian reworking in the GFTZ (Martignole and Martelat, 2005), the age of pervasive deformation and metamorphism (Archean or Grenvillian) remains debatable as preliminary ages presented for both syn-tectonic partial melting and NW-directed thrusting are Archean and preserves no younger Grenvillian age populations (see stops 3-4 in v-chapter 2).

The manifestation and exact location of the Dorval Detachment, boundary between the GFTZ and the structurally overriding Reservoir Dozois Terran (RDT) remains cryptic in the field. However, this study proposes the Dorval Detachment coincides with a ca. 6 km wide (imbricated?) zone of alternating gneissic packages with either amphibolite or granulite grade mineral assemblages and is marked in the field by a progressive disappearance of orthopyroxene in the migmatitic leucosomes and the host gneisses from the NW to the SE across the Dorval Detachment.

New structural (chapter 2), geochemical (chapter 3) and geochronological (chapters 2 & 4) data from the RDT and Vérendrye Terrane (VT) parautochthonous domains to the SE of the Dorval Detachment in this study, presents the first coherent dataset along the length of the Hw117 transect. In these domains, the highly migmatitic, TTG- and granitic gneisses preserve amphibolite facies metamorphic assemblages (Indares and Martignole, 1990) and record at least 3 deformation fabrics, namely a transposed fabric ($S_{n-1;}$; Archean?), a pervasive gneissosity (S_n) and a spaced, subhorizontal planar fabric (S_{n+1}). The gneisses in the RDT and VT are mostly S>>L tectonites, with mineral and stretching lineations generally under-developed. Although the gneissosity is predominantly shallow dipping and where measured, the mineral lineations mostly define shallow NE-plunges parallel to the orogen, the new geological cross section (Fig. 2.5) highlights a

significant variation in the orientation of the planar and linear fabrics from NW to SE along the length of the transect and for the first time, this study demonstrates that the RDT can be subdivided into numerous structural segments/subdomains. Furthermore, although this study area describes the existence of a laterally extensive and sub-horizontal Teddy Bear shear zone (TBSZ), systematic mapping throughout the study area revealed a notable lack of discrete, brittle-ductile NW-directed thrusts, which would be expected within a fold and thrust belt type tectonic model for the area (e.g. Rivers, 2009).

Geochronology results from this study (chapters 2 & 4) provide essential data needed to understand the tectonic architecture along the Hw117 transect. As will be discussed in the section that follows (section 5.1.1.2), ages between ca. 1020 ± 13 Ma and 968 ± 10 Ma provide the first proof that gneisses within both the RDT and VT were deformed during the Rigolet phase of the Grenville Orogen. Abundant undeformed quartz grains in the samples and the abundant syn-tectonic migmatites and general lack of subsolidus deformation features (outside of the TBSZ) indicate that deformation occurred largely under suprasolidus conditions, in stark contrast to gneisses in the GFTZ. The inherited Archean ages found in the samples (CL6070, CL6106, CL6127) support the physical extension of the reworked Archean basement to the SE of the Dorval Detachment, which was inferred by Nd-model age data in the RDT (> 2300 Ma; Guo and Dickin, 1996; Dickin *et al.*, 2014). Sample CL6127 in particular, also supports the Nd-model age data that indicates that the RDT physically extends SE of the Renzy Shear Zone (Fig. 1.7), rather than constituting a distinctly different terrane (see Reservoir Baskatong Terrane in Indares and Martignole, 1990; Baskatong Promontory; Martingole *et al*, 2000). Samples CL6127 and CL6135 also present the first evidence of Rigolet reworking of the PB to the SE of the Renzy Shear Zone, which previously only defined by the monazite ages further to the NW (Childe *et al.*, 1994).

Although the age of the host rocks in the VT are yet to be studied in detail, inherited ca. 1445 and 1660 Ma dates from the granitic sample cutting through the VT gneisses (CL6135) would support the correlation of this domain to the Paleoproterozoic Britt Domain in Ontario, which is also shown to have ca. 1690-1640 Ma and 1450 Ma aged gneisses (e.g. Culshaw *et al.,* 1994, 2016; Ketchum *et al.,* 1994; Rivers *et al.,* 2012).

In the Lac Dumoine Terrane (LDT), crystallization ages (1040 ± 9 Ma) from sample CL8025 and the lack of Archean inherited cores, present the first conclusive evidence that this domain forms

part of the Allochthonous Belt (AB), which was deformed during the Ottawan phase (section 2.2.2 & stop 17, v-chapter 2; Rivers, 2008) and thus, supports the correlation of the LDT to the Algonquin Terrane in Ontario (e.g. Ketchum and Davidson, 2000).

The geochronology results also provide insight on the age of tectonic transport at distinct locations along the Hw117 transect. Ages of 1002 ± 16 Ma (CL6106) and 1008 ± 12 Ma (CL6135), define a minimum age for NW-directed tectonism, manifested by the rotation of large mafic boudins, within the newly recognized TBSZ and VT respectively. Dextral shearing along the Baskatong Shear Zone (Fig. 1.7) is also dated for the first time, with the terminal stages of shearing occurring at 1040 ± 9 Ma (CL8025). If this dextral shearing is related to initial extrusion/thrusting of the AB over the PB (i.e. along the Allochthon Boundary Thrust; ABT), as suggested by Martignole and Friedman (1998), then the ca. 1040 Ma age would also represent the age of juxtaposition of the AB over the PB. Any subsequent sinistral shearing along the Baskatong Shear Zone that was suggested by those authors, must have occurred before 1016 ± 9 Ma (CL6144; section 2.2.1 & stop 16, v-chapter 2).

One of the key findings from mapping the in the RDT and VT was the revelation that several newly identified outcrops may be part of the allochthonous RT based on lithological and structural similarities to the RT (*sensu stricto*) components (Lambert *et al.*, 2019; section 1.2.5) that were already identified within the study region (e.g. Indares and Martignole, 1990; Montreuil and Constantin, 2010). Unlike the mostly shallow dipping, migmatitic TTG- and granitic gneisses of the RDT and VT (Lambert *et al.,* 2018; chapter 2), the RT outcrops: are ubiquitously garnetiferous; consisted of mafic bodies with granulite facies metamorphic assemblages, mafic to intermediate and felsic meta-volcano-sedimentary units and augen gneisses; have steep planar fabrics; are deformed at generally higher strains; and contained abundant subsolidus deformation textures (see 2.3.5). In this study, the ca. 1400 Ma inherited dates and ages from pegmatitic (CL6098) and granitic dykes (CL6112) that intruded the RT and proposed equivalent outcrops, are also consistent with the ca. 1400 Ma age inferred for the RT (Martignole and Ringuette, 1998). Most notable however, is the similarity of the immobile trace elements of the mafic bodies sampled within the PB, to the mafic suites of the RT (chapter 3), which supports the initial field-based hypothesis and allows us to propose a formal correlation to the RT for them.

In addition, ca. 1400 Ma inherited zircon cores within pegmatitic (CL6098) and granitic dykes (CL6112) that intruded the outcrops are consistent with the age inferred for the RT (Martignole and Ringuette, 1998).

The RT components (*sensu strico*) along the transect were previously interpreted to represent tectonic klippe, remnants of a buckled and subsequently eroded, allochthonous slab thrust over the PB (Martignole *et al.*, 2000; Dickin *et al.*, 2014). However, the combined results of this study indicate that the 1st order tectonic architecture is more complex and the RT is rather interpreted as disaggregated allochthonous components, completely enveloped and sporadically dispersed within a 'sea' of migmatitic PB gneisses as decameter- to kilometer-scale boudins. This interpretation is supported by: the formal correlation of mafic boudins enveloped by PB gneisses to suites of the RT (chapter 3); and new (chapter 2) and pre-existing structural data (e.g. Sabourin, 1963) that shows that RDT gneisses extend both structurally above and below the previously mapped RT components (summarized by the cross section through the PB; Fig. 2.5). Furthermore, the presence of inherited Archean zircons and Rigolet crystallization ages from syn-late deformational intrusions into the structural levels both above (CL6070, CL6106) and below (CL6127) the RT, confirm that the RDT gneisses enveloping the RT are indeed part of the reworked PB (chapter 4).Insomuch as the allochthonous RT is enveloped by parautochthonous gneisses and that the RT-like outcrops and boudins are sporadically dispersed among these PB gneisses, the 1st order boundary (i.e. the ABT) between the parautochthonous rocks of the RDT and formerly overlying allochthonous RT, would now be cryptic and explains why it is rarely exposed (e.g. stop 14, v-chapter 2; Fig. 4.7E-F within the study area. Consequently this serves to caution that delineation of upper and lower structural levels and their boundaries, solely through the correlation of igneous suites unique to each level, may be problematic elsewhere in the Grenville Province or other LHOs.

5.1.1.2 Insights from new U-Pb zircon geochronology

This study presents a series of new U-Pb ages and Ti-in-zircon thermometry results, derived through LA-ICP-MS analyses of zircons in syn-late deformational granitic dykes in order to complement the sparce geochronological dataset that existed through the study area. New U-Pb crystallization ages in this study present the first modern evidence that pervasive deformation of the gneisses in both the RDT and VT occurred in the presence of melt during the Rigolet phase (chapter 4), whereas inherited dates from these samples systematically matched the ages expected

for their host gneisses and supports the architecture discussed above (section 5.1.1.1). These findings, also have important implications on how deformation in the parautochthonous domains SE of the Dorval Detachment was accommodated during the evolution of the PB.

Firstly, zircons from the samples analyzed in this study displayed complex zircon morphologies, defined by more than one Grenvillian zone mantling another (chapter 4). On this basis, and with steeply positive REE_{CN} slopes and limited evidence for resorption between the Grenvillian zones, the successive zones are interpreted as multiple episodes of magmatic Grenvillian zircon growth. The successive Grenvillian zones in the zircons, combined with evidence of Ti-in zircon temperatures (ca. 625-778^{o}C) that are at the lower limit (< ca. 800^{o}C) of dehydration melting in Bt-Qtz-Pl rocks; and the general lack of peritectic phases in the samples and surrounding migmatites of the RDT and VT, other than peritectic hornblende, which requires the addition of ca. 4 wt% of water to form in melt (Naney, 1983; Weinberg and Hasalová, 2015 and references therein); and that many of the samples (CL6070, CL6098, CL6112, CL6127) were physically linked to leucosomes in the host gneisses (chapter 4); this study suggests that most of the leucosome and intrusions in the RDT and VT were the products of water-present melting (and subsequent crystallization) events (Rubatto *et al.*, 2009; Weinberg and Hasalová, 2015) between 1020 ± 13 Ma and 968 ± 10 Ma. The source of fluids in the deep orogenic crust dominated by orthogneisses, such as those found in the study area, is not obvious. In the NW of the study area, reworked Archean rocks of the GFTZ (Fig. 4.1), include large tracts of muscovite-sillimanite schists of the Lac Témiskamingue terrane (Indares and Martignole, 1989). Furthermore, Laurentian rocks NW of the Grenville Front consists of volcano-sedimentary sequences of the Abitibi sub-province that have been metamorphosed and hydrated during greenschist facies metamorphism in the Archean (Powell *et al.*, 1995). As both hydrous rock packages probably underly the RDT at depth (Martignole *et al.*, 2000), they may have served as significant water-rich protoliths, similar to under-thrusted hydrous wedges or basement ramps (e.g. Cloos, 1984; Le Fort *et al.*, 1987). These fluids could have been carried along crustal scale shear zone such as the Dorval Detachment (Martignole *et al.*, 2000). Although water fluxed melting was considered to have a minor significance within tectonic terranes (Clemens and Vielzeuf, 1987; Vernon and Clarke, 2008; Brown, 2007, 2013), recent studies have shown that water-fluxed melting is a widespread processes that plays a significant role in the evolution of anatectic terranes (e.g. Berger *et al.*, 2008; Rubatto *et al.*, 2009; Weinberg and Hasalová, 2015 and references therein) and, as shown in this study (see

summary in 5.1.1.3), may play a particularly important role in the evolution of the basement (e.g. RDT and VT) within collisional orogens (e.g. Gervais *et al.,* 2010; Jannin *et al.*, 2018).

Secondly, based on the spread of crystallization ages, melt-present deformation in the RDT and VT parautochthonous gneisses is interpreted as a protracted event, lasting at least 30 Myrs (difference between the minimum and maximum errors of CL6098 and CL6112 respectively; Fig. 4.10). Protracted melt-present deformation, combined with the presence of voluminous syn-deformational migmatites and diatexites (up to 60% rock volume), which ubiquitously contain undeformed quartz grains, indicates these (RDT & VT) basement gneisses were probably deformed at suprasolidus conditions and suggests that the parautochthonous RDT and VT represented a portion of melt-weakened crust within the Grenville Orogen during the Rigolet phase.

5.1.1.3 A new model for deformation in the PB during the Rigolet phase

A better understanding of the tectonic architecture, structures and rheological conditions during deformation, sets the foundation to test or refine existing conceptual and numerical models or develop new models to explain the Rigolet phase of the Grenvillian Orogeny.

The structural characteristics from the parautochthonous RDT and VT domains discussed above (section 5.1.1.1) and evidence from the new geochronology (section 5.1.1.2), which suggests that parautochthonous gneisses (RDT & VT) that were sandwiched between the more rigid GFTZ and the Allochthonous Belt domains (LDT), constituted a melt-weakened zone within the crust for several ten's of Ma during the Rigolet phase, seem inconsistent with a cold, short-duration orogenic model for this phase of the Grenvillian Orogeny (Rivers, 2009). In the latter model, deformation should be dominated by fold-and-thrust tectonic styles within an orogenic wedge (e.g. van Gool *et al.*, 2008; Martignole and Martelat, 2005; Rivers, 2009), where orogen-perpendicular (NW-directed in the Grenville Province) thrusting of coherent rock-stacks is expected (Gervais and Brown, 2011). The same arguments would apply if thrusting along the flanks of the orogen was induced by foreland-ward expulsion of ductile nappes from the core (Jamieson *et al.*, 2007, 2010). As noted in chapter 2, the parautochthonous RDT and VT domains do not preserve evidence for brittle-ductile thrusting or the formation of duplex structures. Furthermore, ages for protracted melt-present deformation in the PB (1020 ± 13 Ma and 968 ± 10 Ma Ma) presented in this study overlap with the ca. 20 Ma "hiatus" between the Ottawan and Rigolet phases (1020-1005 Ma;

Rivers, 2008), which questions the switch in the tectonic regimes from the long-hot orogenic phase (Ottawan phase) to a shorter-colder-orogen that was proposed for the Rigolet phase (Rivers, 2009).

While the structural data from this study (chapter 2) may be consistent with a mode ductile PB nappes extruding over the under-thrusted Superior Province as suggested by Jamieson *et al.*, (2007) and the apparent absence of pervasive Grenvillian deformation in the GFTZ suggests that this domain may have represented such an indenter, the lack of Ottawan ages populations in the samples analyzed from the RDT and VT in this study shows that such an extrusion could not have been concurrent with Ottawan deformation in the orogenic core (Jamieson *et al.*, 2007).

Structural and geochronological data from this study also seem inconsistent with recent conceptual models for gravitational collapse and the formation of core complexes (e.g. the Ottawa River Gneiss Complex; Rivers, 2012; Rivers and Schwerdtner, 2015); which mostly concerns flow of the AB crust. The notable lack of Ottawan inner rims or cores within the zircons analysed in this study provide no support for models that predict that the PB gneisses in the study area were involved in the initial doming, or in uplift of the basement during orogenic collapse. Furthermore, systematic structural mapping along the transect (chapter 2) noted a lack of evidence for steep, outward dipping (i.e. towards the SE following Rivers and Schwerdtner, 2015), normal sense shears and/or brittle faults that are expected in collapsed orogens (Gervais and Brown, 2011). The preservation and of NW-directed tectonism, manifested by the rotation of decameter-scale mafic boudins (CL6106) and asymmetrical sheath folds formed during the Rigolet phase (1008 ± 10; CL6135) and the dominance of NE-directed transport (chapter 2; Fig. 2.5) also seems inconsistent normal-sense (southeastward) re-activation of the ABT around1020 Ma (see ABD in Fig. 1.2B; Rivers, 2008). Further comparisons to this gravitational collapse model would require modern P-T-t-D data from the parautochthonous rocks in the Ottawa River Gneiss (core) Complex. Notably, the difficulties of obtaining accurate P-T constraints from the homogeneous amphibolite grade quartzo-feldspathic gneisses (discussed by Peterman *et al.*, 2009) that characterize the study area (v-chapter 2) and are required for detailed P-T-t-D determinations, also hinders further testing of the tectonic models.

The widespread, and likely protracted (>30 Ma) melt-present (suprasolidus) deformation of the generally shallow dipping migmatite and diatexite gneisses of the RDT and VT during the Rigolet phase, that is documented in this study (chapter 2; sections 5.1.1.1 and 5.1.1.2), is however,

consistent with the characteristics of lateral ductile flow models (i.e. channel flow; Beaumont *et al.*, 2004; Gervais and Brown, 2011; Vanderhaeghe, 2009 and references therein). As touched on in the introduction of this study (section 1.2.4.2), Jannin (2017) and Jannin *et al.*, (2018) presented the first evidence for lateral ductile flow during the Rigolet phase in the Manicouagan area of eastern Quebec; where they showed that felsic dykes, dated between ca. 990-960 Ma migrated upward from the PB into the overlying AB, leading to strain localization and formation of a ductile channel in partially molten crust that engaged portions of the parautochthonous and lower allochthonous crust and promoted the detachment of part of the lower AB as a rigid "allochthonous slice" into the flowing channel (see B3-B4 in Fig. 1.5).

To integrate the data from the three core-chapters and to explain the tectonic architecture preserved within the PB to the SE of the DD, this study considers a similar model to that proposed by Jannin *et al.*, (2018) for Rigolet deformation of the PB in eastern Quebec (see B2-B4 in Fig. 1.5). In western Quebec, under-thrusting of the Laurentian basement may have brought metasediments, such as those abundant in the Lac Témiskamingue Terrane of the GFTZ (Indares and Martignole, 1989, 1990; Martignole and Martelat, 2005), to lower crustal levels (Fig. 4.11A). Dehydration of these sediments may have transported water upward into the orthogneiss of the RDT and triggered their partial melting, starting sometime before ca. 1020 Ma (Fig. 4.11A). Continued melting and migration of melt into the RDT and VT domains would have promoted the development of a partially molten, melt-weakened panel, that once thick enough started to flow towards the foreland by a mode of heterogeneous ductile flow (e.g. channel flow or ductile nappes; Fig. 4.11B). The upward migration of melt in the panel could have led to the intrusion and brecciation of the stiff structurally overlying mafic rocks of the RT (Fig. 4.11B). Then analogous to the "allochthonous slice" in the model of Jannin *et al.* (2018), the RT components were incorporated into the flowing partially molten 'channel' and now forms rafts of various size in the RDT and VT (Fig. 4.11C). Stop 14 (v-chapter 2) and Figure 2.8 may capture an incipient snapshot of this process, where diatexites and felsic intrusions coeval to Rigolet deformation are traced from the underlying parautochthonous gneisses, are shown to intrude and brecciate the mafic components of the RT (also see analogue example in Fig. 2.7); but as this outcrop records the youngest age for melt present deformation (968 ± 10 Ma; Fig. 4.7), disaggregation was stopped as convergence ceased at the end of the Grenvillian Orogeny.

Flow of the RDT and VT parautochthonous gneisses during the Rigolet phase was not perpendicular to the length of the orogen (i.e. NW-SE) in western Quebec and was probably triclinic (Fossen and Tikoff, 1993; Jiang and Williams, 1998; Lin *et al.*, 1998), as indicated by the bimodal (NW-SE and NE-SW) tectonic transport directions (Fig. 2.5). The dominant direction of flow is not easily estimated due to the shallow dips and folding of the gneisses but was likely controlled by a combination of features, including: the underlying basement topography, which was shown to be an important feature in the Manicouagan Reservoir area (Jannin, 2017); reactivation of the various NW-SE trending basement structures (e.g. Dufréchou *et al.*, 2014); and oblique strike-slip shearing along late-Grenvillian shear zones (Martignole and Friedman, 1998; Dufréchou and Harris, 2013). As the GFTZ represents a terrane metamorphosed to granulite-facies and records little evidence for pervasive Grenvillian deformation (section 5.1.1.1), it may have represented the strong structural indenter (e.g. Beaumont *et al.*, 2004, 2006; Vanderhaeghe, 2009; Jamieson *et al.*, 2010, Jamieson and Beaumont, 2013), above which rocks of the RDT and VT flowed and were exhumed. In addition to hydration by fluids, exhumation along an incline may explain the dominant retrograde mineral assemblages (Gervais and Brown, 2011). This is also partially supported by reverse-sense kinematic indicators reported in the hanging wall of the Dorval Detachment (chapter 2). Whereas this study advocates for protracted ductile flow during the Rigolet phase in this part of the Grenville Province, it is plausible that thrust-dominated tectonics were active synchronously in other parts of the orogen (e.g. Ontario, e.g. Dickin *et al.*, 2017), as documented in the Himalayan orogen (Cottle *et al.*, 2015 and references therein).

This study and that of Jannin *et al.* (2018), are the first two modern geochronological studies, conducted independently in two distinct parts of the PB, to demonstrate that the Rigolet event was a major orogenic phase involving protracted melting and flow of the deep crust. Thus, the results of this contribution have significant implications regarding the tectonic evolution of the Grenvillian Orogeny in its type locality that is the Grenville Province, as well as implications for the evolution of the tectonic basement in other LHOs and how it may impact the overlying crustal infrastructure (e.g. Gervais *et al.*, 2010).

5.2 Recommendations and future work

Whereas findings in this study largely contribute to the growing understanding for the evolution of the Grenvillian Orogeny, there are many unanswered questions that were identified throughout this research. The following section highlights some of these key questions and suggests avenues for future research within the Grenville Orogen.

5.2.1 The ABT problem

A fundamental problem that remains to be solved along the transect and various locations elsewhere in the Grenville Province, is the location and manifestation of the ABT. As the RT in the study area is considered part of the AB, and the AB is generally located structurally above the PB, the contact between the RT and underlying parautochthonous gneisses should demarcate the ABT (Fig. 2.8D-E). However, variable dismemberment of the RT would result in a now cryptic ABT boundary and explain why this formally continuous 1st order tectonic boundary, was not easily identified along the Highway 117 transect. A question that then remains is, where does the ABT continue along the transect and what domains does it subdivide?

As one of the pioneers in establishing the current subdivision of the Grenville Province, Rivers *et al.* (1989) and Rivers (2008, 2009) considered the ABT as a 1st order structure that marks *"...a major break in the distribution of lithologic units, structural fabrics, and in the age and character of metamorphism..."*. To emphasize the division of the Grenville province, Rivers *et al.* (1989) and Ketchum and Davidson (2000) referred to the domains in the footwall as parautochthonous (i.e. PB) and those in the hanging wall as "allochthonous" (i.e. AB), inferring the latter were far travelled but not necessarily exotic to Laurentia. This definition of the ABT however, is somewhat contradictory, as highlighted by the arguments below for the two possibly locations for the ABT along the Hw117.

Firstly, as shown in this study, the high-grade (granulite facies metamorphism) LDT was deformed during the Ottawan (ca. 1040 Ma) phase, whereas the VT, with amphibolite grade assemblages, was deformed during the Rigolet (ca. 1008 Ma) and lacks distinct Ottawan-aged zircon populations. Following the definition for the ABT of Rivers *et al.*, (1989) and Rivers (2008, 2009), the ABT should then delimit these two domains, probably along the BSZ. Although, as shown by

Jannin *et al.* (2018) and inferred in this study, strain localization and Rigolet deformation is not necessarily limited to the PB but may also affect the overlying units of the AB.

Secondly, from the younger Paleo-Mesoproterozoic Nd-model ages (ca. 2100-1800 Ma; Dickin *et al.*, 2014) in the VT, the inferred Paleo-Mesoproterozoic (ca. 1445 and 1660 Ma) protolith ages derived from this study in this domain and general lack of evidence for Archean crust, indicates that the VT was transported (i.e. allochthonous) to the Archean Laurentian basement sometime before Grenvillian orogenesis. Although not necessarily considered the principal focus of deep crustal exhumation, Dickin *et al.* (2017) suggested that basal structures to the VT and other the "Paleoroterozoic Parautochthon" domains in Ontario, would have accommodated crustal shortening of at least 200 km. Thus, following a definition of the AB to represent "*variably transported domains*" of Rivers *et al.* (1989); Ketchum and Davidson (2000), the ABT would then be located along the informally named 'Nd-model age boundary' in the study area where the impressive sheath folds are developed (stop 10, v-chapter 2). In addition, inherited dates (ca. 1245-1140 Ma) that were also present in the granitic sample from the VT (Fig. 4.9G), correlate to the pre-Grenvillian Elzevirian (ca. 1245-1255 Ma) and Shawinigan (ca. 1190-1140 Ma) orogenic events that are only recorded in in the AB (McLelland *et al.*, 2004, 2013; Rivers, 2012 and references therein).

Detailed petrochronology studies as well as systematic and statistically robust protolith geochronology and geochemistry sampling is still required within the VT and correlative "Paleoproterozoic parautochthon" domains, such as the Britt Domain in Ontario, to unravel their tectonic history and affinity to the PB or AB. Ultimately however, the resolution of the location of the ABT along the transect and elsewhere in the Grenville Province, first calls for a better definition of the 'allochthonous' terminology and unification of the structural context for the ABT in the Grenville Province.

5.2.2 General questions raised and recommendations for future work

- While this study shows tectonic fabrics within the GFTZ are consistent with NW-directed thrust sense and SW-normal sense tectonics (Martignole and Martelat, 2005) and although Martignole and Martelat (2005) presented evidence for Grenvillian monazite in the matrix of normal sense shear zones, new modern LA-ICP-MS geochronology results (unpublished) indicate that partial melting (stop 3, v-chapter 2) and NW-directed thrusting (stop 4, v-chapter 2) was Archean. This questions the age of pervasive Grenvillian metamorphism and NW-directed thrusting proposed for the GFTZ along the transect (Martignole and Martelat, 2005; Rivers, 2009). Detailed P-T-t-D petrochronology is required to resolve this problematic. The migmatitic muscovite-sillimanite ± garnet metasediments of the Lac Témiskamingue terrane in the hanging wall of the Grenville Front, should offer ideal samples for such analyses.
- The expression of the DD remains cryptic in the field and requires detailed mapping and characterization both across it and along its length. Although it was proposed to represent a transitional crustal scale detachment (Martignole and Martelat, 2005), defined by normal-and sinistral-sense kinematics, kinematic indicators in the footwall of the DD are more consistent with a reverse and dextral-sense of shear (chapter 2). A detailed and statistically robust kinematic analysis is required to better understand deformation along the DD and its subsequent tectonic implications, particularly if the metamorphic gradient across the DD is the result of normal-sense juxtaposition of different crustal levels (Martignole and Martelat, 2005) or ductile exhumation of the RDT against a rigid GFTZ indenter as inferred in this study.
- This study presents a model for a melt-weakened crust within the PB to the SE of the GFTZ that may have facilitated lateral ductile flow during the Rigolet phase, with exhumation possibly even along the Dorval Detachment. However, this study falls short in attaining all the evidence required to implicitly prove deformation occurred as channel flow, particularly PT-constraints along the proposed channel and the identification of the exact upper and lower channel boundaries within the PB, which should record a synchronous but an opposite sense of shear (Gervais and Brown, 2011).
- Due to the complex zonation of the zircons grains in the samples that intruded the PB rocks, the LA-ICP-MS geochronological method (chapter 4) was an effective choice, due to its small analytical spot size (ca. 20 microns) and ability to yield a statistically robust number of analyses. However, this analytical method typically yields results that have an uncertainty between 1-6%

(Košler *et al.*, 2013; Schoene, 2014), which means that the Grenville samples have an error of 15-20 Ma. Although none of the Rigolet crystallization ages had errors that extended across the lower limit of the Ottawan phase (1020 Ma), some are within error of each other (e.g. samples CL6070, CL6106 and CL6127). Therefore, to better constrain the age of deformation at different points along the transect (i.e. within the proposed ductile channel), more precise methods are required. Isotope dilution-thermal ionization mass spectrometry (ID-TIMS), with a precision 0.1% (Bowring, *et al.*, 2006; Schoene, 2014) is a possibility, but must be conducted on Grenvillian zircons confidently identified as morphologically and chemically homogeneous or on Grenvillian rims that are mechanically (or by laser?) separated from inner or inherited zones (e.g. Jannin, 2017; Jannin *et al.*, 2018).

- At least three deformation phases are preserved within the PB (chapter 2), as evidenced by intrafoliar folds (S_{n-1}), a pervasive gneissosity (S_n) and a later, discrete planar fabric (S_{n+1}). In each case, the fabrics are commonly associated with migmatitic leucosome or felsic injections, which presents the opportunity to precisely date each deformation phase, although high precision sampling and analytical techniques (ID-TIMS) would likely be required.
- This study shows that the RDT can be subdivided into various structural subdomains, but other than the variation in the orientation of structural fabrics, the potential differences (e.g. deformation age, metamorphism) between them and the geodynamic implications, require further investigation.
- Migmatites in the RDT are generally garnet-free but leucosomes with peritectic garnet are, however, observed within the first ca. 10 km SE of the GFTZ. The reason for this localized garnet occurrence in the RDT remains to be understood but it is tentatively suggested that gneisses near the Dorval Detachment may represent deeper crustal segments compared to RDT gneisses further SE, where temperatures were higher and biotite-dehydration melting conditions could be supported.
- Undifferentiated AB domains tentatively equated to the AB, such as the Lac Perch (Fig. 1.7) and the domain wedged between the PB and Cabonga Terrane require further investigation through detailed P-T-t-D investigations. Notably, if the Lac Perch domain is part of the RT, as suggested by Dickin *et al.* (2012, 2014) and the tectonic model presented in this thesis is valid, the location of the Lac Perch domain along the Dorval Detachment, would support the notion that the gneisses of the RDT extruded above the GFTZ. Detailed mapping of the boundaries of

these proposed allochthonous domains would also further refine the architecture along this transect.

- In contrast to the surrounding terranes, the RDT gneisses are mostly S>>L tectonites, with lineations notably underdeveloped, which is perplexing if the gneisses were deformed in a fold-thrust belt (e.g. Martingole and Martelat, 2005; Rivers, 2009) and requires further investigation. The extensive development of fluid-fluxed migmatites and diatexites within this domain and deformation under mostly suprasolidus conditions is speculated as one explanation.
- Conversely, rare outcrops in the RDT contain evidence for earlier high-grade linear fabrics that are overprinted by amphibolite metamorphic assemblages, specifically the ESE-plunging orthopyroxene (±garnet) aggregates mantled by NE-plunging hornblende and biotite (Fig. v2.ii.29ST). The age of these two fabrics and the tectonic implications for each of their orientations remains unresolved and may provide further clues as to the evolution of the parautochthonous gneisses SE of the GFTZ.
- With a better understanding of the tectonic architecture along the Hw117 transect, there is also an opportunity to complement and re-evaluate existing hornblende-cooling age data (e.g. Martignole and Reynolds, 1997) to determine if there is a systematic changes from NW to SE, in order to support or contest a mode for channel flow (i.e. younger towards the front of the channel; Gervais and Brown, 2011).
- Mapping along the transect presents evidence for new shear zones that accommodated Rigolet deformation (e.g. The Teddy Bear Shear Zone; TBSZ; stop 7 in v-chapter 2; Fig. 4.3G). In the TBSZ shear zone (and elsewhere along the transect) rotation of mafic boudins indicate a clear top-to-the NW direction for tectonic transport but is near perpendicular to the NE-plunging lineations measured in these gneisses (stop 7, v-chapter 2) and sheath fold stretching-axes elsewhere (stop 10, v-chapter 2). Whereas quartz c-axis fabric analyses were considered as an alternative to traditional optical microstructural analyses in the TBSZ, due to their ability to provide information on the type and direction of bulk strain, deformation temperatures and vorticity (Kruhl, 1998; Passchier and Trouw, 2005; Larson *et al.*, 2013; Law, 2014), the gneisses lack homogenous quartz-dominated layers, making this approach problematic. Nonetheless, the tectonic implications of this laterally continuous (ca. 10 km), subhorizontal shear zone must still be considered.

- While the subhorizontal gneisses in the VT record a Rigolet deformation event at ca. 1008 ± (7) 10 Ma (section 4.5.6), they are interpreted to attain subvertical dips along the Baskatong Shear Zone (v-chapter 2), where deformation is interpreted to be older than ca. 1016 Ma (stop 16; section 2.2.1). These temporal relationships are thus, contradictory and require further resolution.
- The Renzy Shear Zone was interpreted as a late-Grenvillian (ca. 1003 Ma), sinistral shear zone that played an significant role in the late-stage evolution of the Grenville Province (Martignole and Friedman, 1998). However, evidence presented in this study suggests that the mylonitic gneisses at the base of the RT outcrops, rather represent the ABT and record both dextral and sinistral strike slip shearing (section 2.3.5; v-chapter 2). It is noted that the two directions of tectonic transport recorded along this boundary may correlate to an initial thrust-sense movement (ca. 1040 Ma?) and subsequent normal- sense shearing along the ABT (i.e. Allochthon Boundary Detachment, 1020 Ma) proposed by Rivers (2008). In-situ dating techniques such as petrochronology, are required in mylonites along the base of various RT bodies to fully characterize the timing and direction of transport along this potential 1st order tectonic boundary.
- The three mafic suites defined for RT are inferred to be ca. 1400 Ma based on detrital zircon from the associated meta-volanosedimentary units (Martignole and Ringuette, 1998) but they have not been directly dated. Dating the mafic suites, integrated with the paleo-tectonic interpretation that the different suites represent intraplate E-MORB basalts and arc/back arc basalts offshore the Laurentian margin (Montreuil and Constantin, 2010; this study), would further the understanding of the tectonics along the pre-Grenville Laurentian margin and its evolution. Specifically, were these suites emplaced contiguously or define a change in the paleo-tectonic setting over time? Was the 1400 Ma period along Laurentia really dominated by continental Andean style tectonics (Corrigan and Hanmer, 1995; Hanmer *et al.*, 2000; Maity and Indares, 2018)?
- The methods employed in geochemistry chapter (chapter 2) allow for a second, targeted zircon/baddeleyite geochronology investigation of the samples that still require distinction. In particular, two samples (#44, #49) collected within the RDT gneisses remain undifferentiated from the ca. 1230 Ma Sudbury and the mafic RT-group 3 suite of the RT. Similarly, four samples (#36, #96, #97, #98) in the VT remain undifferentiated from the allochthonous RT-group 3 and

ca. 1170-1150 Ma Algonquin metagabbro suite (Davidson and van Breemen, 1988; Heaman and LeCheminant, 1993; Culshaw *et al.*, 1994). Furthermore, dating samples correlated to the RT in this contribution is still required to support the interpretations made in chapter 3.

- Conceptual models for deformation during the Ottawan phase was characterized by ductile channel flow (Rivers, 2008) and probably subsequent orogenic collapse (Rivers, 2012; Rivers and Schwerdtner, 2015). While geochronology results from sample CL8025 (1040 ± (6) 9 Ma) confirm the LDT gneisses were deformed during the Ottawan phase, the mode of deformation and exhumation must still be determined/assessed in this AB domain. Whereas dextral strike-slip deformation in the base of the LDT (BSZ) may correlate to initial thrust-sense tectonics (Martignole and Friedman, 1998) at ca. 1040 Ma and evidence for an opposite (i.e. normal and sinistral) sense of shear in the roof of the LDT is presented in this study (chapter 2), which is one of the requirements to prove channel flow (Gervais and Brown, 2011), the coeval timing of these two boundaries must still be determined. In addition, the 1020 Ma age and tectonic significance of the sinistral shearing in the Baskatong Shear Zone proposed by Martignole and Friedman (1998) requires resolution. As this study only recorded evidence for sinistral shearing in the roof zone of the LDT, along the Baskatong Reservoir to the NE of Hw117 (chapter 2), sinistral movement was likely not related to the BSZ but rather movement along the Cayamant Shear Zone that forms the boundary with the orogenic lid, as suggested by (Sharma *et al.*, 1995).
- The combined data from geochemical (e.g. Montreuil and Constantin, 2010), isotopic (e.g. Dickin *et al.*, 2014), conventional thermobarometry (Indares and Martignole, 1990) and importantly, monazite geochronology that yielded a 1072 Ma metamorphic age (Childe *et al.*, 1993), indicates that the RT is part of the AB affected by the Ottawan phase of the Grenvillian Orogeny. The age of the high-grade penetrative fabric in the RT is also estimated to be ca. 1070 Ma based on syn-kinematic garnet growth during peak metamorphism (Martignole and Pouget, 1993, 1994). Modern petrochronological analyses (P-T-t-D) are however still required to confirm the timing and peak metamorphic (PT) conditions, age (t) and if possible – initial direction of deformation (D) – in order to constrain the tectonic evolution of this terrane, in particular if these gneisses record both Ottawan and Rigolet deformation events. This study also shows that the kinematic direction of tectonic transport varies significantly in the different segments identified along the transect (Fig. 2.5), which means P-T-t-D must be conducted in the different segments and subsequently reconstructed.

REFERENCES

Allen, C. M., & Campbell, I. H. (2012). Identification and elimination of a matrix-induced systematic error in LA-ICP-MS 206Pb/ 238U dating of zircon. *Chemical Geology*, *332–333*, 157–165. https://doi.org/10.1016/j.chemgeo.2012.09.038

Allmendinger, R. W., Cardozo, N. C., & Fisher, D. (2013). *Structural Geology Algorithms: Vectors & Tensors* (p. 289). Cambridge University Press.

Álvaro, J. J., Pouclet, A., Ezzouhairi, H., Soulaimani, A., Bouougri, E. H., Imaz, A. G., & Fekkak, A. (2014). Early Neoproterozoic rift-related magmatism in the Anti-Atlas margin of the West African craton, Morocco. *Precambrian Research*, *255*(P1), 433–442. https://doi.org/10.1016/j.precamres.2014.10.008

Arndt, N. T., & Lesher, C. M. (2006). Komatiite. In *Encyclobedia of Geology* (pp. 260–268). Elsevier.

Ayer, J., Amelin, Y., Corfu, F., Kamo, S., Ketchum, J., Kwok, K., & Trowell, N. (2002). Evolution of the southern Abitibi greenstone belt based on U–Pb geochronology: autochthonous volcanic construction followed by plutonism, regional deformation and sedimentation. *Precambrian Research*, *115*(1–4), 63–95. https://doi.org/10.1016/S0301-9268(02)00006-2

Barrie, C. T., Ludden, J. N., & Green, T. H. (1993). Geochemistry of volcanic rocks associated with Cu-Zn and Ni-Cu deposits in the Abitibi Subprovince. *Economic Geology*, *88*(6), 1341–1358. https://doi.org/10.2113/gsecongeo.88.6.1341

Bartholomew, M. J., & Hatcher, R. D. (2010). The Grenville orogenic cycle of southern Laurentia : Unraveling sutures , rifts , and shear zones as potential piercing points for Amazonia. *Journal of South American Earth Sciences*, *29*(1), 4–20. https://doi.org/10.1016/j.jsames.2009.08.007

Bau, M. (1996). Controls on the fractionation of isovalent trace elements in magmatic and aqueous systems: Evidence from Y/Ho, Zr/Hf, and lanthanide tetrad effect. *Contributions to Mineralogy and Petrology*, *123*(3), 323–333. https://doi.org/10.1007/s004100050159

Beaumont, C., & Jamieson, R. A. (2010). *Himalaya-Tibetan orogeny: channel flow versus (critical) wedge models, a false dichotomy?*

Beaumont, C., Jamieson, R. A., Nguyen, M. H., & Lee, B. (2001). Himalayan tectonics explained by extrusion of a low-viscosity crustal channel coupled to focused surface denudation. *Nature*, *414*(6865), 738–742. https://doi.org/10.1038/414738a

Beaumont, C., Nguyen, M. H., Jamieson, R. A., & Ellis, S. (2006). Crustal flow modes in large hot orogens. *Geological Society, London, Special Publications2*, *268*, 91–145. https://doi.org/10.1144/GSL.SP.2006.268.01.05

Beaumont, Christopher, Jamieson, R. A., Nguyen, M. H., & Medvedev, S. (2004). Crustal channel flows: 1. Numerical models with applications to the tectonics of the Himalayan-Tibetan orogen. *Journal of Geophysical Research: Solid Earth*, *109*(6), 1–29. https://doi.org/10.1029/2003JB002809

Beaumont, Christopher, Jamieson, R., & Nguyen, M. (2010). Models of large, hot orogens containing a collage of reworked and accreted terranesThis article is one of a series of papers published in this Special Issue on the theme Lithoprobe — parameters, processes, and the evolution of a continent. *Canadian Journal of Earth Sciences*, *47*(4), 485–515. https://doi.org/10.1139/E10-002

Bédard, J. H. (2010). Parental magmas of Grenville Province massif-type anorthosites, and conjectures about why massif anorthosites are restricted to the Proterozoic. Earth and Environmental Science Transactions of the Royal Society of Edinburgh, 100(1–2), 77–103. https://doi.org/10.1017/S1755691009016016

Bédard, J. H. (2018). Stagnant lids and mantle overturns: Implications for Archaean tectonics, magma genesis, crustal growth, mantle evolution, and the start of plate tectonics. *Geoscience Frontiers*, *9*(1), 19–49. https://doi.org/10.1016/j.gsf.2017.01.005

Bédard, J. H., Leclerc, F., Harris, L. B., & Goulet, N. (2009). Intra-sill magmatic evolution in the Cummings Complex, Abitibi greenstone belt: Tholeiitic to calc-alkaline magmatism recorded in an Archaean subvolcanic conduit system. *Lithos*, *111*(1–2), 47–71. https://doi.org/10.1016/j.lithos.2009.03.013

Berclaz, A., Hébert, R., & Rocheleau, M. (1995). La zone tectonique du front de Grenville à l'est de Louvicourt, Québec : exhumation de la croûte archéenne pendant l'orogénie grenvillienne. *Canadian Journal of Earth Sciences*, *32*(11), 1899–1920. https://doi.org/10.1139/e95-146

Bethune, K M, & Davidson, A. (1997). Grenvillian Metamorphism of the Sudbury Diabase Dyke Swarm: From protolith to two-pyroxene garnet coronite. *Canadian Mineralogist*, *35*, 1191–1220.

Bethune, Kathryn M. (1997). The Sudbury dyke swarm and its bearing on the tectonic development of the Grenville Front, Ontario, Canada. *Precambrian Research*, *85*(3–4), 117–146. https://doi.org/10.1016/S0301-9268(96)00052-6

Bird, P. (1991). Lateral extrusion of lower crust from under high topography in the isostatic limit. *Journal of Geophysical Research: Solid Earth*, *96*(B6), 10275–10286. https://doi.org/https://doi.org/10.1029/91JB00370

Birkett, T., Marchildon, N., Paradis, S., & Godue, R. (1991). The Grenville Province to the east of Val d'Or, Quebec: a geological reconnaissance and a possible extension of the Abitibi greenstone belt in the Grenville parautochthonous belt. In *Current research, part C. Canadian Shield* (Paper 91-1, p. 216). Geological Survey of Canada.

Bleeker, W., & Ernst, R. (2006). Short-lived mantle generated magmatic events and their dyke swarms: The key unlocking Earth's palaeogeographic record back to 2.6 Ga. In E. Hanski, S. Mertanen, T. Ramo, & J. Vuollo (Eds.), *Dyke Swarms - Time Markers of Crustal Evolution* (pp. 3–26). Taylor & Francis.

Blein, O., LaFlèche, M. R., & Corriveau, L. (2003). Geochemistry of the granulitic Bondy gneiss complex: a 1.4 Ga arc in the Central Metasedimentary Belt, Grenville Province, Canada. *Precambrian Research*, *120*(3–4), 193–217. https://doi.org/10.1016/S0301-9268(02)00112-2

Bonnet, A. L., Corriveau, L., & La Flèche, M. R. (2005). Chemical imprint of highly metamorphosed volcanic-hosted hydrothermal alterations in the La Romaine Supracrustal Belt, eastern Grenville Province, Quebec. *Canadian Journal of Earth Sciences*, *42*(10), 1783–1814. https://doi.org/10.1139/e05-098

Bowring, S. A., Schoene, B., Crowley, J. L., Ramezani, J., & Condon, D. C. (2006). High-precision U–Pb zircon geochronology and the stratigraphic record: Progress and promise. In T. Olszewski (Ed.), *Geochronology: Emerging Opportunities. Paleontological Society Papers* (pp. 25–45). The Paleontological Society.

Brown, M. (2013). Granite: From genesis to emplacement. *Bulletin of the Geological Society of*

America, *125*(7–8), 1079–1113. https://doi.org/10.1130/B30877.1

Buchan, K. L., Mortensen, J. K., & Card, K. D. (1993). Northeast-trending early Proterozoic dykes of southern Superior Province: multiple episodes of emplacement recognized from integrated paleomagnetism and U-Pb geochronology. *Canadian Journal of Earth Sciences*, *30*(6), 1286–1296. https://doi.org/10.1139/e93-110

Buchan, Kenneth L., Goutier, J., Hamilton, M. A., Ernst, R. E., & Matthews, A. (2007). Paleomagnetism, U–Pb geochronology, and geochemistry of Lac Esprit and other dyke swarms, James Bay area, Quebec, and implications for Paleoproterozoic deformation of the Superior Province. *Canadian Journal of Earth Sciences*, *44*(5), 679–694. https://doi.org/10.1139/E06-131

Buchan, Kenneth L., Mortensen, J. K., Card, K. D., & Percival, J. A. (1998). Paleomagnatism and U-Pb geochronology of diabase swarms of the Minto block, Superior Province, Quebec, Canada. *Canadian Journal of Earth Sciences*, *35*, 1054–1069. https://doi.org/https://doi.org/10.1139/e98-054

Bussy, F., Krogh, T. E., Klemens, W. P., & Schwerdtner, W. . (1995). Tectonic and metamorphic events in the westernmost Grenville Province, central Ontario: new results from high precision U–Pb geochronology. *Canadian Journal of Earth Sciences*, *671*(32:), 660–671.

Cabanis, B., & Thieblemont, D. (1988). La discrimination des tholeiites continentales et des basaltes arriere-arc; proposition d'un nouveau diagramme, le triangle Th-3xTb-2xTa. *Bulletin de La Societe Geologique de France*, *IV*(6), 927–935. https://doi.org/10.2113/gssgfbull.iv.6.927

Cann, J. R. (1970). Rb, Sr, Y, Zr and Nb in some ocean floor basaltic rocks. *Earth and Planetary Science Letters*, *10*, 7–11.

Cardozo, N., & Allmendinger, R. W. (2013). Spherical projections with OSXStereonet: *Computers & Geosciences* (No. 51). https://doi.org/doi:10.1016/j.cageo.2012.07.021

Carr, S. D., Easton, R. M., Jamieson, R. a, & Culshaw, N. G. (2000). Geologic transect across the Grenville orogen of Ontario and New York. *Canadian Journal of Earth Sciences*, *37*(2–3), 193–216. https://doi.org/10.1139/e99-074

Chiarenzelli, J., Lupulescu, M., Cousens, B., Thern, E., Coffin, L., & Regan, S. (2010). Enriched

Grenvillian lithospheric mantle as a consequence of long-lived subduction beneath Laurentia. *Geology*, *38*(2), 151–154. https://doi.org/10.1130/G30342.1

Childe, F., Doig, R., & Gariepy, C. (1993). Monazite as a metamorphic chronometer, south of the Grenville Front, western Quebec. *Canadian Journal of Earth Sciences*, *30*, 1056–1065. https://doi.org/10.1139/e93-089

Ciborowski, T. J. R., Kerr, A. C., Ernst, R. E., McDonald, I., Minifie, M. J., Harlan, S. S., & Millar, I. L. (2015). The early proterozoic Matachewan large Igneous Province: Geochemistry, petrogenesis, and implications for earth evolution. *Journal of Petrology*, *56*(8), 1459–1494. https://doi.org/10.1093/petrology/egv038

Clemens, J. D., & Vielzeuf, D. (1987). Constraints on melting and magma production in the crust. *Earth Planet. Sci. Lett.*, *86*(null), 287.

Cloos, M. (1984). Landward-dipping reflectors in accretionary wedges: Active dewatering conduits? *Geology*, *12*(9), 519–522. https://doi.org/10.1130/0091-7613(1984)12<519:LRIAWA>2.0.CO;2

Condie, K. (2015). Changing tectonic settings through time: Indiscriminate use of geochemical discriminant diagrams. *Precambrian Research*, *266*, 587–591. https://doi.org/10.1016/j.precamres.2015.05.004

Condie K. C., Bobbrow, D. ., & Card, K. D. (1987). Geochemistry Of Precambrian Mafic Dykes From The Southern Superior Province Of The Canadian Shield. *Geological Association of Canada*, *34*, 95–108.

Condie, K. C., Bobrow, D. J., & Card, K. D. (1987). Geochemistry of Precambrian mafic dykes from the southern Superior Province of the Canadian Shield. *Geological Association of Canada, Special Paper*.

Condie, Kent C. (1976). Plate Tectonics and Crustal Evolution (p. 492). Pergamon.

Condie, Kent C. (1997). Sources of Proterozoic mafic dyke swarms: Constraints from Th/Ta and La/Yb ratios. *Precambrian Research*, *81*(1–2), 3–14. https://doi.org/10.1016/s0301-9268(96)00020-4

Corfu, F., Hanchar, J. M., Hoskin, P. W. O., & Kinny, P. (2003). Atlas of Zircon Textures. *Reviews*

in Mineralogy and Geochemistry, *53*(1), 469–500. http://dx.doi.org/10.2113/0530469

Corrigan, D, & Hanmer, S. (1995). Arc accretion, thickening, post-collisional extension and plutonism in the Grenville orogen; constraints from the Mauricie region, south-central Quebec. *Precambrian '95, International Conference on Tectonics and Metallogeny of Early–Mid Precambrian Orogenic Belts*, 106.

Corrigan, David. (1995). Mesoproterozoic evolution of the south-central Grenville orogen: structural, metamorphic and geochronologic constraints from the Mauricie transect. Carleton University, Ottawa, Ontario.

Corrigan, David, & van Breemen, O. (1997). U–Pb age constraints for the lithotectonic evolution of the Grenville Province along the Mauricie transect, Quebec. *Canadian Journal of Earth Sciences*, *34*, 299–316. https://doi.org/10.1139/e17-027

Corriveau, L., & Spry, P. G. (2014). Metamorphosed Hydrothermal Ore Deposits. *Treatise on Geochemistry*, 175–194. https://doi.org/10.1016/B978-0-08-095975-7.01107-4

Corriveau, L, Blein, O., Gervais, F., Trapy, P. H., De Souza, S., & Fafard, D. (2018). Iron-oxide and alkali-calcic alteration, skarn, and epithermal mineralizing systems of the Grenville Province: the Bondy gneiss complex in the Central Metasedimentary Belt of Quebec as a case example - a field trip to the 14th Society for Geology Applied. *Geological Survey of Canada, Open File*, *8349*, 1–125. https://doi.org/10.4095/311230

Corriveau, L, & van Breemen, O. (2000). Docking of the Central Metasedimentary Belt to Laurentia in geon 12: evidence from the 1.1W_1.16 Ga Chevreuil intrusive suite and host gneisses, Quebec. *Canadian Journal of Earth Sciences*, *37*, 253–269.

Corriveau, Louise, & Morin, D. (2000). Modelling 3D architecture of western Grenville from surface geology, xenoliths, styles of magma emplacement, and Lithoprobe reflectors 1. *Canadian Journal of Earth Sciences*, *37*(1), 235–251. https://doi.org/10.1139/e99-121

Cottle, J. M., Larson, K. P., & Kellett, D. A. (2015). How does the mid-crust accommodate deformation in large, hot collisional orogens? A review of recent research in the Himalayan orogen. *Journal of Structural Geology*, *78*, 119–133. https://doi.org/10.1016/j.jsg.2015.06.008

Culshaw, N., Foster, J., Marsh, J., Slagstad, T., & Gerbi, C. (2016). Kiosk domain, Central Gneiss

Belt, Grenville Province, Ontario: A Labradorian palimpsest preserved in the ductile deep crust. *Precambrian Research*, *280*, 249–278. https://doi.org/10.1016/j.precamres.2016.05.002

Culshaw, N. G., Ketchum, J. W. F., Wodicka, N., & Wallace, P. (1994a). Deep crustal ductile extension following thrusting in the southwestern Grenville Province, Ontario. *Canadian Journal of Earth Sciences*, *31*(1), 160–175. https://doi.org/10.1139/e94-013

Culshaw, N. G., Ketchum, J. W. F., Wodicka, N., & Wallace, P. (1994b). Deep-crustal ductile extension following thrusting in the southwestern Grenville Province, Ontario. *Canadian Journal of Earth Sciences*, *31*(1), 160–175. https://doi.org/10.1139/e94-013

Dahlen, F. A. (1990). Critical Taper Model of Fold-And-Thrust Belts and Accretionary Wedges. *Annual Review of Earth and Planetary Sciences*, *18*(1), 55–99. https://doi.org/10.1146/annurev.ea.18.050190.000415

Daigneault, R., Mueller, W. U., & Chown, E. H. (2004). Abitibi greenstone belt plate tectonics: the diachronous history of arc development, accretion and collision. In P. G. Eriksson, W. Altermann, D. R. Nelson, W. U. Muelle, & O. Catuneanu (Eds.), *Precambrian times, tempos and events* (pp. 88–103). Elsevier.

Davidson, A., & Grant, S. M. (1986). Reconnaissance geology of western and central Algonquin Park and detailed study of coronitic olivine metagabbro, Central Gneiss Belt, Grenville Province of Ontario. In *Current research, part B.* (pp. 837–848). Geological Survey of Canada.

Davidson, A., & van Breemen, O. (1988). Baddeleyite-zircon relationships in coronitic metagabbro, Grenville Province, Ontario: implications for geochronology. *Contributions to Mineralogy and Petrology*, *100*(3), 291–299. https://doi.org/10.1007/BF00379740

Davis, D. W., Lafrance, I., Goutier, J., Takam, F. T., Bandyayera, D., Gigon, J., Francis, C. :, & Takam, T. (2018). *Datations U-Pb dans les provinces de Churchill et du Supérieur effectuées au JSGL en 2013-2014*. http://gq.mines.gouv.qc.ca/documents/EXAMINE/RP201701/RP201701.pdf

Decelles, P. G., Robinson, D. M., Quade, J., Ojha, T. P., Garzione, C. N., Copeland, P., & Upreti, B. N. (2001). Himalayan fold-thrust belt in western Nepal. *Tectonics*, *20*(4), 487–509.

Dewey, J. F. (1988). Extensional collapse of orogens. *Tectonics*, *7*(6), 1123–1139. https://doi.org/https://doi.org/10.1029/TC007i006p01123

Dickin, A. P, Herrell, M., Moore, E., Cooper, D., & Pearson, S. (2014). Nd isotope mapping of allochthonous Grenvillian klippen: Evidence for widespread "ramp-flat" thrust geometry in the SW Grenville Province. *Precambrian Research*, *246*, 268–280. https://doi.org/10.1016/j.precamres.2014.03.012

Dickin, A. P., Krivankova-Smal, L., Strong, J., & Swing, M. (2020). Nd isotope mapping of a tectonic window near Chalk River, Ontario: Implications for large-scale Grenvillian tectonics. *Precambrian Research*, *350*, 105904. https://doi.org/10.1016/j.precamres.2020.105904

Dickin, A. P, Strong, J., Arcuri, G., Van Kessel, A., & Krivankova-Smal, L. (2017). A revised model for the crustal structure of the SW Grenville Province, Ontario, Canada. *Geological Magazine*, *154*(4), 903–913. https://doi.org/10.1017/S001675681700005X

Dickin, A.P., & Guo, A. (2001). The location of the Allochthon Boundary Thrust and the Archean–Proterozoic suture in the Mattawa area of the Grenville Province: Nd isotope evidence. *Precambrian Research*, *107*(1–2), 31–43. https://doi.org/10.1016/S0301-9268(00)00153-4

Dickin, A., P., Cooper, D., Guo, A., Hutton, C., Martin, C., Sharma, K. N. M. M., & Zelek, M. (2012). Nd isotope mapping of the Lac Dumoine thrust sheet: Implications for large-scale crustal structure in the SW Grenville Province. *Terra Nova*, *24*(5), 363–372. https://doi.org/10.1111/j.1365-3121.2012.01074.x

Doig, R. (1977). Rb–Sr geochronology and evolution of the Grenville Province in northwestern Quebec, Canada. *Geological Society of America Bulletin1*, *88*, 1843–1856.

Dudás, F. Ö., Davidson, A., & Bethune, K. M. (1994). Age of the Sudbury diabase dykes and their metamorphism in the Grenville Province. In *Radiogenic age and isotopic studies* (Report 8:, pp. 97–106). Geological Survey of Canada.

Dufréchou, G., & Harris, L. B. (2013). Tectonic models for the origin of regional transverse structures in the Grenville Province of SW Quebec interpreted from regional gravity. *Journal of Geodynamics*, *64*, 15–39. https://doi.org/10.1016/J.JOG.2012.12.001

Dufréchou, G., Harris, L. B., & Corriveau, L. (2014). Tectonic reactivation of transverse basement structures in the Grenville orogen of SW Quebec, Canada: Insights from gravity and

aeromagnetic data. *Precambrian Research*, *241*, 61–84. https://doi.org/10.1016/j.precamres.2013.11.014

Dunphy, J. M., Ludden, J. N., & Francis, D. (1995). Geochemistry of mafic magmas from the Ungava orogen, Québec, Canada, and implications for mantle reservoir compositions at 2.0 Ga. *Chemical Geology*, *120*(3–4), 361–380. https://doi.org/10.1016/0009-2541(94)00146-Y

Duvall, M. J., Waldron, J. W. F., Godin, L., & Najman, Y. (2020). Active strike-slip faults and an outer frontal thrust in the Himalayan foreland basin. *Proceedings of the National Academy of Sciences of the United States of America*, *117*(30), 17615–17621. https://doi.org/10.1073/pnas.2001979117

Easton, R. M. (2000). Metamorphism of the Canadian Shield, Ontario, Canada II. Proterozoic metamorphic history. *The Canadian Mineralogist*, *38*, 319–344.

Elliott, D. (1976). The motion of thrust sheets. *Journal of Geophysical Research (1896-1977)*, *81*(5), 949–963. https://doi.org/https://doi.org/10.1029/JB081i005p00949

Erdmann, S., Scaillet, B., & Kellett, D. A. (2012). Textures of Peritectic Crystals as Guides to Reactive Minerals in Magmatic Systems: New Insights from Melting Experiments. Journal of Petrology, 53(11), 2231–2258. https://doi.org/10.1093/petrology/egs048

Ernst, R.E., & Bell, K. (1992). Petrology of the Great Abitibi Dyke, Superior Province, Canada. *Journal of Petrology*, *33*(2), 423–469. https://doi.org/10.1093/petrology/33.2.423

Ernst, Richard E., Bell, K., Ranalli, G., & H.C., H. (1987). The Great Abitibi Dyke, Southeastern Superior Province, Canada. In Henry C. Halls & W. F. Fahrig (Eds.), *Mafic Dyke Swarms* (Special Pa, pp. 123–135). Geological Association of Canada.

Ernst, Richard E., & Buchan, K. L. (1994). Mapping the magma flow pattern in the Sudbury dyke swarm in Ontario using magnetic fabric analysis. Geological Survey of Canada, Current Research 1994-E. p183-192

Ernst, Richard E., & Buchan, K. L. (2001). Large mafic magmatic events through time and links to mantle-plume heads. In *Special Paper of the Geological Society of America* (Vol. 352). https://doi.org/10.1130/0-8137-2352-3.483

Espanon, V. R., Chivas, A. R., Kinsley, L. P. J., & Dosseto, A. (2014). Geochemical variations in

the Quaternary Andean back-arc volcanism, southern Mendoza, Argentina. *Lithos*, *208*, 251–264. https://doi.org/10.1016/j.lithos.2014.09.010

Fahrig, W. F. (1987). The tectonic settings of continental mafic dyke swarms: Failed arm and early passive margin. In Henry C. Halls & W. F. Fahrig (Eds.), *Mafic Dyke Swarms* (Special Pa, pp. 331–348). Geological Association of Canada.

Fahrig, W. F., Gaucher, E. H., & Larochelle, A. (1965). Palaeomagnetism of Diabase Dykes of the Canadian Shield. *Canadian Journal of Earth Sciences*, *2*(4), 278–298. https://doi.org/10.1139/e65-023

Fahrig, W. F., & West, T. D. (1986). Diabase dykes swarms of the Canadian Shield – Essaims de dykes diabasiques du Bouclier canadien. Commission géologique du Canada.

Fossen, H., & Tikoff, B. (1993). The deformation matrix for simultaneous simple shearing, pure shearing and volume change, and its application to transpression-transtension tectonics. *Journal of Structural Geology*, *15*(3–5), 413–422. https://doi.org/10.1016/0191-8141(93)90137-Y

Fretzdorff, S., Livermore, R. A., Devey, C. W., Leat, P. T., & Stoffers, P. (2002). Petrogenesis of the Back-arc East Scotia Ridge, South Atlantic Ocean. *Journal of Petrology*, *43*(8), 1435–1467. https://doi.org/10.1093/petrology/43.8.1435

Friedman, R. M., & Martignole, J. (1995). Mesoproterozoic sedimentation, magmatism, and metamorphism in the southern part of the Grenville Province (western Quebec): U–Pb geochronological constraints. *Canadian Journal of Earth Sciences*, *32*(12), 2103–2114. https://doi.org/10.1139/e95-164

Fritz, H., Tenczer, V., Hauzenberger, C., Wallbrecher, E., & Muhongo, S. (2009). Hot granulite nappes - Tectonic styles and thermal evolution of the Proterozoic granulite belts in East Africa. *Tectonophysics*, *477*(3–4), 160–173. https://doi.org/10.1016/j.tecto.2009.01.021

Gardien, V., Thompson, A. B., & Ulmer, P. (2000). Melting of Biotite + Plagioclase + Quartz Gneisses: the Role of H2O in the Stability of Amphibole. *Journal of Petrology*, *41*(5), 651–666. https://doi.org/10.1093/petrology/41.5.651

Gariépy, C., Verner, D., & Doig, R. (1990). Dating Archean metamorphic minerals southeast of the Grenville front, western Quebec, using Pb isotopes. *Geology*, *18*(11), 1078.

https://doi.org/10.1130/0091-7613(1990)018<1078:DAMMSO>2.3.CO;2

Gehrels, G. E., Valencia, V. A., & Ruiz, J. (2008). Enhanced precision, accuracy, efficiency, and spatial resolution of U-Pb ages by laser ablation-multicollector-inductively coupled plasma-mass spectrometry. *Geochemistry, Geophysics, Geosystems*, *9*(3). https://doi.org/10.1029/2007GC001805

Gervais, F., & Brown, R. L. (2011). Testing modes of exhumation in collisional orogens: Synconvergent channel flow in the southeastern Canadian Cordillera. *Lithosphere*, *3*(1), 55–75. https://doi.org/10.1130/L98.1

Gervais, Félix, Brown, R. L., & Crowley, J. L. (2010). Tectonic implications for a Cordilleran orogenic base in the Frenchman Cap dome, southeastern Canadian Cordillera. *Journal of Structural Geology*, *32*(7), 941–959. https://doi.org/10.1016/j.jsg.2010.05.006

Gervais, Félix, & Moukhsil, A. (2016). *Analyse structurale préliminaire de trois régions clés du secteur Oskélanéo, région de Clova, Québec.*

Gervais, Félix, & Ranalli, G. (2017a). The effects of lateral density gradients, slopes and buoyancy on channel flow: 1D analytical solutions and applications to the SE Canadian Cordillera. *Tectonophysics*, *712–713*, 578–588. https://doi.org/10.1016/j.tecto.2017.06.023

Gervais, Félix, & Ranalli, G. (2017b). The effects of lateral density gradients, slopes and buoyancy on channel flow: 1D analytical solutions and applications to the SE Canadian Cordillera. *Tectonophysics*, *712–713*, 578–588. https://doi.org/10.1016/j.tecto.2017.06.023

Godin, L., Grujic, D., Law, R. D., & Searle, M. P. (2006). Channel flow, ductile extrusion and exhumation in continental collision zones: An introduction. *Geological Society Special Publication*, *268*, 1–23. https://doi.org/10.1144/GSL.SP.2006.268.01.01

Godin, Laurent, Roche, R. S. LA, Waffle, L., & Harris, L. B. (2019). Influence of inherited indian basement faults on the evolution of the himalayan orogen. *Geological Society Special Publication*, *481*(1), 251–276. https://doi.org/10.1144/SP481.4

Goodwin, A. M., & Ridler, R. H. (1970). The Abitibi Orogenic Belt. In A. J. Baer (Ed.), *Symposium on basins and geosynclines of the Canadian Shield.* (Paper, pp. 1–31). Geological Association of Canada.

Gower, C. F., & Tucker, R. D. (1994). Distribution of pre-1400 Ma crust in the Grenville Province: implications for rifting in Laurentia-Baltica during geon 14. *Geology*, *22*(9), 827–830. https://doi.org/10.1130/0091-7613(1994)022<0827:DOPMCI>2.3.CO;2

Gower, C.F., Hall, J., Kilfoil, G. J., Quinlan, G. M., & Wardle, R. J. (1997). Roots of the Labradorian orogen in the Grenville Province in southeast Labrador: Evidence from marine, deep-seismic reflection data. *Tectonics*, *16*, 795–809.

Gower, Charles F, & Krogh, T. E. (2002). A U–Pb geochronological review of the Proterozoic history of the eastern Grenville Province. *Canadian Journal of Earth Sciences*, *39*(5), 795–829. https://doi.org/10.1139/e01-090

Grant, S. M. (1987). *The petrology and structural relations of metagabbros from the western Grenville Province, Canada.* University of Leicester, Leicester, UK.

Green, A. G., Milkereit, B., Davidson, A., Spencer, C., Hutchinson, D. R., Cannon W.F, Lee, M. W., Agena, W. F., Behrendt, J. C., & Hinze, W. J. (1988). Crustal structure of the Grenville front and adjacent terranes. *Geology*, *16*(9), 788–792. https://doi.org/10.1130/0091-7613(1988)016<0788:CSOTGF>2.3.CO;2

Green, E. C. R., White, R. W., Diener, J. F. A., Powell, R., Holland, T. J. B., & Palin, R. M. (2016). Activity–composition relations for the calculation of partial melting equilibria in metabasic rocks. *Journal of Metamorphic Geology*, *34*(9), 845–869. https://doi.org/10.1111/jmg.12211

Guice, G. L., McDonald, I., Hughes, H. S. R., Schlatter, D. M., Goodenough, K. M., MacDonald, J. M., & Faithfull, J. W. (2018). Assessing the Validity of Negative High Field Strength-Element Anomalies as a Proxy for Archaean Subduction: Evidence from the Ben Strome Complex, NW Scotland. In Geosciences (Vol. 8, Issue 9). https://doi.org/10.3390/geosciences8090338

Grujic, D. (2006). Channel flow and continental collision tectonics: an overview. *Geological Society, London, Special Publications*, *268*, 25–37.

Grujic, D., Warren, C. J., & Wooden, J. L. (2011). Rapid synconvergent exhumation of Miocene-aged lower orogenic crust in the eastern Himalaya. *Lithosphere*, *3*(5), 346–366. https://doi.org/10.1130/L154.1

Grujic, Djordje, Casey, M., Davidson, C., Hollister, L. S., Kündig, R., Pavlis, T., & Schmid, S.

(1996). Ductile extrusion of the Higher Himalayan Crystalline in Bhutan: evidence from quartz microfabrics. *Tectonophysics*, *260*(1), 21–43. https://doi.org/10.1016/0040-1951(96)00074-1

Gualda, G. A. R., & Ghiorso, M. S. (2013). The Bishop Tuff giant magma body: An alternative to the Standard Model. *Contributions to Mineralogy and Petrology*, *166*(3), 755–775. https://doi.org/10.1007/s00410-013-0901-6

Guo, A., & Dickin, A. P. (1996). The southern limit of Archean crust and significance of rocks with Paleoproterozoic model ages: Nd model age mapping in the Grenville Province of western Quebec. *Pre*, *77*, 231–241.

Halls, H. C, Stott, G. M., & Davis, D. W. (2005). Paleomagnetism, geochronology and geochemistry of several Proterozoic mafic dike swarms in northwestern Ontario. Open file Report 617L. (pp 59). Ontario Geological Survey.

Hamilton, M. A., & Buchan, K. L. (2016). A 2169 Ma U–Pb baddeleyite age for the Otish Gabbro, Quebec: Implications for correlation of Proterozoic magmatic events and sedimentary sequences in the eastern Superior Province. *Canadian Journal of Earth Sciences*, *53*(2), 119–128. https://doi.org/10.1139/cjes-2015-0131

Hanmer, S. (1988). Ductile thrusting at mid-crustal level, southwestern Grenville Province. *Canadian Journal of Earth Sciences*, *25*(3), 1049–1059. https://doi.org/10.1139/e88-102

Hanmer, S., Corrigan, D., Pehrsson, S., & Nadeau, L. (2000). SW Grenville Province , Canada : the case against post – 1 . 4 Ga accretionary tectonics. *Geographical*, *319*, 33–51.

Hanmer, S. K., & Ciesielski, A. (1984). A structural reconnaissance of the northwest boundary of the Central Metasedimentary Belt, Grenville Province, Ontario and Quebec. In *Current research, part B.* (Paper 84-1, pp. 121–131). Geological Survey of Canada.

Harley, S. L, Kelly, N. M., & Möller, a. (2007). Zircon behaviour and the thermal history of mountain belts. *Elements*, *3*(1), 25–30; DOI: 10.2113/gselements.3.1.25. https://doi.org/10.2113/gselements.3.1.25

Harley, S. L, Kelly, N. M., & Möller, A. (2007). Zircon Behaviour and the Thermal Histories of Mountain Chains. *Elements*, *3*(1), 25–30. http://dx.doi.org/10.2113/gselements.3.1.25

Harris, L. B., Godin, L., & Yakymchuk, C. (2012). Regional shortening followed by channel flow induced collapse: A new mechanism for "dome and keel" geometries in Neoarchaean granite-greenstone terrains. *Precambrian Research*, *212–213*, 139–154. https://doi.org/10.1016/j.precamres.2012.04.022

He, D., Webb, A. A. G., Larson, K. P., Martin, A. J., & Schmitt, A. K. (2015). Extrusion vs. duplexing models of Himalayan mountain building 3: Duplexing dominates from the Oligocene to Present. *International Geology Review*, *57*(1), 1–27. https://doi.org/10.1080/00206814.2014.986669

Heaman, L. M., & LeCheminant, A. N. (1993). Paragenesis and U-Pb systematics of baddeleyite (ZrO2). *Chemical Geology*, *110*(1–3), 95–126. https://doi.org/10.1016/0009-2541(93)90249-I

Heaman, Larry M. (1997). Global mafic magmatism at 2.45 Ga: Remnants of an ancient large igneous province? *Geology*, *25*(4), 299–302. https://doi.org/10.1130/0091-7613(1997)025<0299:GMMAGR>2.3.CO;2

Herrell, M. K., Dickin, A. P., & Morris, W. A. (2006). A test of detailed Nd isotope mapping in the Grenville Province: Delineating a duplex thrust sheet in the Kipawa-Mattawa region. *Canadian Journal of Earth Sciences*, *43*(4), 421–432. https://doi.org/10.1139/E06-008

Herriott, T. M., Crowley, J. L., Schmitz, M. D., Wartes, M. A., & Gillis, R. J. (2019). Exploring the law of detrital zircon: LA-ICP-MS and CA-TIMS geochronology of Jurassic forearc strata, Cook Inlet, Alaska, USA. *Geology*, *47*(11), 1044–1048. https://doi.org/10.1130/G46312.1

Hinton, R. W., & Upton, B. G. J. (1991). The chemistry of zircon: Variations within and between large crystals from syenite and alkali basalt xenoliths. *Geochimica et Cosmochimica Acta*, *55*(11), 3287–3302. https://doi.org/https://doi.org/10.1016/0016-7037(91)90489-R

Hoffman, P. F. (1989). Precambrian geology and tectonic history of North America. In A. W. Bally & A. R. Palmer (Eds.), *The Geology of North America – an overview* (Decade of, pp. 447–512). Geological Society of America.

Hoffman, P. F. (1991). Did the breakup of Laurentia turn Gondwanaland inside out? *Science*, *252*, 1409–1411.

Hofmann, A. E., Baker, M. B., & Eiler, J. M. (2014). Sub-micron-scale trace-element distributions in natural zircons of known provenance: implications for Ti-in-zircon thermometry. *Contributions to Mineralogy and Petrology*, *168*(3), 1–21. https://doi.org/10.1007/s00410-014-1057-8

Horstwood, M. S. A., Košler, J., Gehrels, G., Jackson, S. E., McLean, N. M., Paton, C., Pearson, N. J., Sircombe, K., Sylvester, P., Vermeesch, P., Bowring, J. F., Condon, D. J., & Schoene, B. (2016). Community-Derived Standards for LA-ICP-MS U-(Th-)Pb Geochronology – Uncertainty Propagation, Age Interpretation and Data Reporting. *Geostandards and Geoanalytical Research*, *40*(3). https://doi.org/10.1111/j.1751-908X.2016.00379.x

Hoskin, P. W. O., & Black, L. P. (2000). Metamorphic zircon formation by solid-state recrystallization of protolith igneous zircon. *Journal of Metamorphic Geology*, *18*(4), 423–439. https://doi.org/10.1046/j.1525-1314.2000.00266.x

Hoskin, P. W. O., & Ireland, T. R. (2000). Rare earth element chemistry of zircon and its use as a provenance indicator. *Geology*, *28*(7), 627–630. https://doi.org/10.1130/0091-7613(2000)028<0627:REECOZ>2.3.CO;2

Hou, G., Santosh, M., Qian, X., Lister, G. S., & Li, J. (2008). Tectonic constraints on 1.3~1.2 Ga final breakup of Columbia supercontinent from a giant radiating dyke swarm. *Gondwana Research*, *14*(3), 561–566. https://doi.org/10.1016/j.gr.2008.03.005

Hynes, A., Indares, A., Rivers, T., & Gobeil, A. (2000). Lithoprobe line 55: integration of out-of-plane seismic results with surface structure, metamorphism, and geochronology, and the tectonic evolution of the eastern Grenville Province. *Canadian Journal of Earth Sciences*, *37*, 341–358.

Hynes, A. (1980). Carbonatization and mobility of Ti, Y, and Zr in Ascot Formation metabasalts, SE Quebec. *Contributions to Mineralogy and Petrology*, *75*(1), 79–87. https://doi.org/10.1007/BF00371891

Hynes, A., & Rivers, T. (2010). Protracted continental collision — evidence from the Grenville Orogen. *Canadian Journal of Earth Sciences*, *47*(5), 591–620. https://doi.org/10.1139/E10-003

Indares, A. (1993). Eclogitized gabbros from the eastern Grenville Province: textures, metamorphic

context, and implications. *Canadian Journal of Earth Sciences*, *30*(1), 159–173. https://doi.org/10.1139/e93-015

Indares, A. (2020). Deciphering the metamorphic architecture and magmatic patterns of large hot orogens: Insights from the central Grenville Province. *Gondwana Research*, *80*, 385–409. https://doi.org/10.1016/j.gr.2019.10.013

Indares, A., & Dunning, G. (1997). Coronitic metagabbro and eclogite from the Grenville Province of western Quebec: interpretation of U–Pb geochronology and metamorphism. *Canadian Journal of Earth Sciences*, *34*(7), 891–901. https://doi.org/10.1139/e17-074

Indares, A., & Martignole, J. (1985). The Montreal - Val D'Or Geotraverse. Field guide book. *Friends of the Grenville Province* (p. 73).

Indares, A., & Martignole, J. (1989). The Grenville Front south of Vald'Or. *Tectonophysics*, *157*, 221–239.

Indares, A., & Martignole, J. (1990a). Metamorphic constraints on the evolution of the gneisses from the parautochthonous and allochthonous Polycyclic Belts, Grenville Province, Western Quebec. *Canadian Journal of Earth Sciences*, *27*(3), 357–370. https://doi.org/10.1139/e90-033

Indares, A., White, R. W., & Powell, R. (2008). Phase equilibria modelling of kyanite-bearing anatectic paragneisses from the central Grenville Province. *Journal of Metamorphic Geology*, *26*(8), 815–836. https://doi.org/10.1111/j.1525-1314.2008.00788.x

Ishikawa, Y., Sawaguchi, T., Iwaya, S., & Horiuchi, M. (1976). Delineation of prospecting targets for Kuroko deposits based on modes of volcanism of underlying dacite and alteration halos. *Mining Geology*, *26*, 105–117. https://doi.org/10.11456/shigenchishitsu1951.26.105.

Jamieson, R. A., & Beaumont, C. (2011). Coeval thrusting and extension during lower crustal ductile flow - implications for exhumation of high-grade metamorphic rocks. *Journal of Metamorphic Geology*, *29*(1), 33–51. https://doi.org/10.1111/j.1525-1314.2010.00908.x

Jamieson, R. A., & Beaumont, C. (2013). On the origin of orogens. *Bulletin of the Geological Society of America*, *125*(11–12), 1671–1702. https://doi.org/10.1130/B30855.1

Jamieson, R. A., Beaumont, C., Nguyen, M. H., & Culshaw, N. G. (2007). Synconvergent ductile

flow in variable-strength continental crust: Numerical models with application to the western Grenville orogen. *Tectonics*, *26*(5), 1–23. https://doi.org/10.1029/2006TC002036

Jamieson, R. A., Beaumont, C., Warren, C. J., & Nguyen, M. H. (2010). The Grenville Orogen explained? Applications and limitations of integrating numerical models with geological and geophysical data. *Canadian Journal of Earth Sciences*, *47*(4), 517–539. https://doi.org/10.1139/E09-070

Jamieson, R. A., Culshaw, N. G., & Corrigan, D. (1995). North-west propagation of the Grenville orogen: Grenvillian structure and metamorphism near Key Harbour, Georgian Bay, Ontario, Canada*. *Journal of Metamorphic Geology*, *13*(2), 185–207. https://doi.org/10.1111/j.1525-1314.1995.tb00213.x

Jamieson, R. A., Beaumont, C., Medvedev, S., & Nguyen, M. H. (2004). Crustal channel flows: 2. Numerical models with implications for metamorphism in the Himalayan-Tibetan orogen. *Journal of Geophysical Research: Solid Earth*, *109*(6), 1–24. https://doi.org/10.1029/2003JB002811

Jannin, S. (2017). Exhumation de la Ceinture parautochtone par fluage chenalisé tardi-grenvillien (réservoir Manicouagan, Province de Grenville central) : identification et rôle de la structuration du socle (PhD thesis, École Polytechnique de Montréal). [École Polytechnique de Montréal]. https://publications.polymtl.ca/2958/

Jannin, Sophie, Gervais, F., Moukhsil, A., & Augland, L. E. (2018). Late-Grenvillian channel flow in the central Grenville Province (Manicouagan Reservoir area): New constraints from a structural and geochronological study of the Allochthon Boundary Thrust. *Journal of Structural Geology*, *115*(July), 132–151. https://doi.org/10.1016/j.jsg.2018.07.019

Jannin, S., Gervais, F., Moukhsil, A., Crowley, J. L., & Augland, L. E. (2017a). Datations U/Pb des deformations inverses et normales dans la partie centrale de la Province de Grenville (Manicouagan, Québec): évidence d'un chenal orogénique dans le Parautochtone. In J. Nadeau & M. Racine (Eds.), Géologie, Potentiel Minéral et Cadre Géodynamique des Roches de la Région du Réservoir Daniel-Johnson (Manicougan), Partie Centrale de la Province De Grenville. Report MM 2017-01 (p. 307). Ministère de l'Énergie et des Ressources naturelles.

Jannin, S., Gervais, F., Crowley, J. L., Augland, L. E., & Vanderhaeghe, O. (2017b). Linking channel-flow processes to pegmatite potentially mineralized in REE in the central Grenville Province. In P. MercierLangevin, B. Dube, M. Bardoux, P. S. Ross, & C. Dion (Eds.), 14th SGA Biennial Meeting on Mineral Resources to Discover (pp. 1297–1300).

Janoušek, V., Farrow, C. M., & Erban, V. (2006). Interpretation of Whole-rock Geochemical Data in Igneous Geochemistry: Introducing Geochemical Data Toolkit (GCDkit). *Journal of Petrology*, *47*(6), 1255–1259. http://dx.doi.org/10.1093/petrology/egl013

Jenner, G. A. (1996). Trace element geochemistry of igneous rocks: geochemical nomenclature and analytical geochemistry. In D. A. Wyman (Ed.), *Trace Element Geochemistry of Volcanic Rocks: Applications for Massive Sulphide Exploration* (Vol 12, pp. 51–77). Geological Association of Canada.

Jensen, L. S. (1976). New Cation Plot for Classifying Subalkalic Volcanic Rocks. *Ont Div Mines Misc Pap*, *66*.

Jiang, D., & Williams, P. F. (1998). High-strain zones : a unified model. *Journal of Structural Geology*, *20*(8), 1105–1120. https://doi.org/0191-8141/98

Johnson, W. L. (1972). Copper-nickel sulphides in a layered ultramafic body, Renzy mine, southwestern Quebec. Msc Thesis. The University of Western Ontario, London.

Kamber, B. S., Ewart, A., Collerson, K. D., Bruce, M. C., & McDonald, G. D. (2002). Fluid-mobile trace element constraints on the role of slab melting and implications for Archaean crustal growth models. *Contributions to Mineralogy and Petrology*, *144*(1), 38–56. https://doi.org/10.1007/s00410-002-0374-5

Kelemen, P. B., Hanghøj, K., & Greene, A. R. (2014). One View of the Geochemistry of Subduction-Related Magmatic Arcs, with an Emphasis on Primitive Andesite and Lower Crust. *Treatise on Geochemistry: Second Edition*, *4*, 749–806. https://doi.org/10.1016/B978-0-08-095975-7.00323-5

Kellett, R. L., Barnes, A. E., & Rive, M. (1994). The deep structure of the Grenville Front: a new perspective from western Quebec. *Canadian Journal of Earth Sciences*, *31*(2), 282–292. https://doi.org/10.1139/e94-027

Ketchum, J. W., & Davidson, A. (2000). Crustal architecture and tectonic assembly of the Central

Gneiss Belt, southwestern Grenville Province, Canada: a new interpretation. *Canadian Journal of Earth Sciences*, *37*(2–3), 217–234. https://doi.org/10.1139/e98-099

Ketchum, J. W. F., Heaman, L. M., Krogh, T. E., Culshaw, N. G., & Jamieson, R. A. (1998). Timing and thermal influence of late orogenic extension in the lower crust: a U□Pb geochronological study from the southwest Grenville orogen, Canada. *Precambrian Research*, *89*(1–2), 25–45. https://doi.org/10.1016/S0301-9268(97)00079-X

Ketchum, J. W. F., Jamieson, R. A., Heaman, L. M., Culshaw, N. G., & Krogh, T. E. (1994). 1.45 Ga granulites in the southwestern Grenville Province: geologic setting, P-T conditions, and U-Pb geochronology. *Geology*, *22*(3), 215–218. https://doi.org/10.1130/0091-7613(1994)022<0215:GGITSG>2.3.CO;2

Kohn, M. J. (2008). P-T-t data from central Nepal support critical taper and repudiate large-scale channel flow of the Greater Himalayan Sequence. *Geological Society of America Bulletin*, *120*(3–4), 259–273. https://doi.org/10.1130/B26252.1

Kohn, Matthew J. (2016). Metamorphic chronology—a tool for all ages: Past achievements and future prospects. *American Mineralogist*, *101*(1), 25–42. https://doi.org/10.2138/am-2016-5146

Košler, J., Sláma, J., Belousova, E., Corfu, F., Gehrels, G. E., Gerdes, A., Horstwood, M. S. A., Sircombe, K. N., Sylvester, P. J., Tiepolo, M., Whitehouse, M. J., & Woodhead, J. D. (2013). U-Pb Detrital Zircon Analysis – Results of an Inter-laboratory Comparison. *Geostandards and Geoanalytical Research*, *37*(3), 243–259. https://doi.org/https://doi.org/10.1111/j.1751-908X.2013.00245.x

Krauss, J. B., & Rivers, T. (2004). High-pressure granulites in the Grenvillian Grand Lake thrust system, Labrador: pressure-temperature conditions and tectonic evolution. In R. P. Tollo, L. Corriveau, J. M. McLelland, & M. . Bartholomew (Eds.), *Proterozoic tectonic evolution of the Grenville orogen* (197th ed., pp. 105–134.). Geological Society of America Memoir.

Kriegsman, L. M., & Hensen, B. J. (1998). Back reaction between restite and melt: Implications for geothermobarometry and pressure-temperature paths. *Geology*, *26*(12), 1111–1114. https://doi.org/10.1130/0091-7613(1998)026<1111:BRBRAM>2.3.CO;2

Krogh, T. E., Corfu, F., Davis, D. W., Dunning, G. R., Heaman, L. M., Kamo, S. L., Machado, N.,

Greenhough, J. D., & Nakamura, N. (1987). Precise U–Pb isotopic ages of diabase dykes and mafic to ultramafic rocks using trace amounts of baddeleyite and zircon. In W. F. Halls, Henry C. Fahrig (Ed.), *Mafic Dyke Swarms* (Special Pa, pp. 147–152). Geological Association of Canada.

Kruhl, J. H. (1998). Reply: Prism- and basal-plane parallel subgrain boundaries in quartz: A microstructural geo- thermobarometer. *Journal of Metamorphic Geology*, *16*(5), 142–146.

Kuiper, Y. D., Jiang, D., & Lin, S. (2007). Relationship between non-cylindrical fold geometry and the shear direction in monoclinic and triclinic shear zones. *Journal of Structural Geology*, *29*(6), 1022–1033. https://doi.org/10.1016/j.jsg.2007.01.009

Le Bas, M. J. L. E., Maitre, R. W. L. E., Streckeisen, A., & Zanettin, B. (1986). A Chemical Classification of Volcanic Rocks Based on the Total Alkali-Silica Diagram. Journal of Petrology, 27(3), 745–750. https://doi.org/10.1093/petrology/27.3.745

Labat, G., Gervais, F., Kavanagh-Lepage, C., Jannin, S., & Crowley, J. L. (2020). Ductile nappe extrusion in constrictive strain at the origin of transverse segments of the Allochthon Boundary Thrust in the Manicouagan Imbricate Zone (Central Grenville Province, Québec). *Journal of Structural Geology*, *138*(June). https://doi.org/10.1016/j.jsg.2020.104117

La Flèche, M. R., Dupuy, C., & Bougault, H. (1992). Geochemistry and petrogenesis of Archean mafic volcanic rocks of the southern Abitibi Belt, Québec. *Precambrian Research*, *57*(3–4), 207–241. https://doi.org/10.1016/0301-9268(92)90003-7

La Flèche, M. R., Birkett, T. C., & Corriveau, L. (2005). "Crustal development at the pre-Grenvillian Laurentian margin: a record from contrasting geochemistry of mafic and ultramafic orthogneisses in the Chochocouane River area, Quebec." *Canadian Journal of Earth Sciences*, *42*(10), 1653–1675. https://doi.org/10.1139/e05-068

Lambert, C.W., Gervais, F., Moukhsil, A., & Crowley, J. L. (2019). Reconstructing The Evolution Of The Grenville Province In Western Quebec: Time Constraints And Modes Of Mid-Crustal Deformation During The Ottawan And Rigolet Phases Of The Grenville Orogeny. *Petrochron 2019*.

Lambert, Christopher W., Gervais, F., Kavanagh-Lepage, C., & Crowley, J. L. (2020). Transect of a Hot, Long Orogen: The Grenville Province of Western Quebec. Geological Society of

America. Virtual field guide: https://earth.google.com/earth/d/14RzCLFNPytkhhnFKjx_MxU4P8raRxtdp?usp=sharing

Lambert, Christopher W., Gervais, F., & Moukhsil, A. (2018). Reconstruire l'architecture de l'ouest de la Province de Grenville, Québec: Résultats préliminaires de la cartographie géologique le long de la route 117.

Lambert, Christopher W., Gervais, F., Moukhsil, A., Crowley, J. L., & Bonnet, A.-L. (2019). Reconstruire l'architecture de l'ouest de la Province de Grenville, Québec : résultats préliminaires de la cartographie, de l'analyse cinématique et de la géochronologie.

Large, R. R., Gemmell, J. B., Paulick, H., & Huston, D. L. (2001). The Alteration Box Plot: A Simple Approach to Understanding the Relationship between Alteration Mineralogy and Lithogeochemistry Associated with Volcanic-Hosted Massive Sulfide Deposits. *Economic Geology*, *96*(5), 957–971. https://doi.org/10.2113/gsecongeo.96.5.957

Larson, K. P., & Cottle, J. M. (2014). Midcrustal discontinuities and the assembly of the Himalayan midcrust. *Tectonics*. https://doi.org/10.1002/2013TC003452

Larson, K. P., Gervais, F., & Kellett, D. A. (2013). A P–T–t–D discontinuity in east-central Nepal: Implications for the evolution of the Himalayan mid-crust. *Lithos*, *179*, 275–292. https://doi.org/10.1016/j.lithos.2013.08.012

Larson, K. P., Godin, L., & Price, R. A. (2010). Relationships between displacement and distortion in orogens: linking the Himalayan foreland and hinterland in central Nepal. *Geological Society of America Bulletin*, *122*, 1116–1134.

Lasalle, S, & Indares, A. (2014). Anatectic record and contrasting P–T paths of aluminous gneisses from the central Grenville Province. *Journal of Metamorphic Geology*, *32*(6), 627–646. https://doi.org/https://doi.org/10.1111/jmg.12083

Lasalle, Stephanie, Fisher, C. M., Indares, A., & Dunning, G. (2013). Contrasting types of Grenvillian granulite facies aluminous gneisses: Insights on protoliths and metamorphic events from zircon morphologies and ages. *Precambrian Research*. https://doi.org/10.1016/j.precamres.2013.01.014

Law, R. D. (2014). Deformation thermometry based on quartz c-axis fabrics and recrystallization microstructures: A review. *Journal of Structural Geology*, *66*, 129–161.

https://doi.org/10.1016/j.jsg.2014.05.023

Le Fort, P., Cuney, M., Deniel, C., France-Lanord, C., Sheppard, S. M. F., Upreti, B. N., & Vidal, P. (1987). Crustal generation of the Himalayan leucogranites. *Tectonophysics*, *134*(1–3), 39–57. https://doi.org/10.1016/0040-1951(87)90248-4

Leclerc, F., Bédard, J. H., Harris, L. B., McNicoll, V. J., Goulet, N., Roy, P., & Houle, P. (2011). Tholeiitic to calc-alkaline cyclic volcanism in the roy group, chibougamau area, abitibi greenstone belt revised stratigraphy and implications for VHMS exploration. *Canadian Journal of Earth Sciences*, *48*(3), 661–694. https://doi.org/10.1139/E10-088

Li, Z. X., Bogdanova, S. V., Collins, A. S., Davidson, A., De Waele, B., Ernst, R. E., Fitzsimons, I. C. W., Fuck, R. A., Gladkochub, D. P., Jacobs, J., Karlstrom, K. E., Lu, S., Natapov, L. M., Pease, V., Pisarevsky, S. A., Thrane, K., & Vernikovsky, V. (2008). Assembly, configuration, and break-up of Rodinia: a synthesis. *Precambrian Research*, *160*, 179–210.

Lin, S., Jiang, D., & Williams, P. F. (1998). Transpression (or transtension) zones of triclinic symmetry: natural example and theoretical modelling. *Geological Society Special Publication*, *135*(January 2014), 41–57. https://doi.org/10.1144/GSL.SP.1998.135.01.04

Ludden, J., & Hynes, A. (2000). The Lithoprobe Abitibi-Grenville transect: two billion years of crust formation and recycling in the Precambrian Shield of Canada. *Canadian Journal of Earth Sciences*, *37*(2–3), 459–476. https://doi.org/10.1139/e99-120

Ludwig, K. R. (2003). Mathematical-Statistical Treatment of Data and Errors for 230Th/U Geochronology. *Reviews in Mineralogy and Geochemistry*, *52*(1), 631–656. https://doi.org/10.2113/0520631

Ludwig, K. R. (2008). User's Manual for Isoplot 3.6. A Geochronological Toolkit for Microsoft Exce. *Berkeley Geochronological Center, Special Publication*, *4*, 78.

Luth, W. C., Jahns, R. H., & Tuttle, O. F. (1964). The granite system at pressures of 4 to 10 kilobars. *Journal of Geophysical Research (1896-1977)*, *69*(4), 759–773. https://doi.org/https://doi.org/10.1029/JZ069i004p00759

MacKinnon, P. (1994). Deformation of Straight Gneisses: Rheological Modelling and Petrographic Analysis. PhD thesis. University of Toronto.

MacKinnon, P., Fueten, F., & Robin, P. Y. F. (1996). A fracture model for quartz ribbons in straight gneisses. *Journal of Structural Geology*, *19*(1), 1–14. https://doi.org/10.1016/S0191-8141(96)00073-9

Maity, B. (2019). Origin of mafic and potassic to ultrapotassic rocks, Manicouagan area, central Grenville Province: Geochemical and geochronological constraints on the evolution of the Mesoproterozoic SE Laurentian margin and the Grenvillian LHO. Memorial University of Newfoundland St. John's, Newfoundland and Labrador.

Maity, B., & Indares, A. (2018). The Geon 14 arc-related mafic rocks from the central Grenville Province. *Canadian Journal of Earth Sciences*, *55*(6), 545–570. https://doi.org/10.1139/cjes-2017-0197

Marsh, J. H., & Culshaw, N. G. (2014). Timing and conditions of high-pressure metamorphism in the western Grenville Province: Constraints from accessory mineral composition and phase equilibrium modeling. *Lithos*, *200–201*(1), 402–417. https://doi.org/10.1016/j.lithos.2014.04.016

Marsh, J. H., Culshaw, N. G., & Gerbi, C. C. (2013). Timing and conditions of poly-phase metamorphism within the Twelve Mile Bay shear zone: implications for the evolution of mid-crustal decollement zones and western Grenville tectonics. *International Geology Review*, *55*(5), 525–547. https://doi.org/10.1080/00206814.2013.773768

Marsh, J. H., & Stockli, D. F. (2015). Zircon U–Pb and trace element zoning characteristics in an anatectic granulite domain: Insights from LASS-ICP-MS depth profiling. *Lithos*, *239*, 170–185. https://doi.org/10.1016/J.LITHOS.2015.10.017

Martignole, J. (1995). A two-stage emplacement for the Cabonga allochthon (central part of the Grenville Province): evidence for orthogonal and oblique collision during the Grenville orogeny. *Canadian Journal of Earth Sciences*, *32*(9), 1478–1481. https://doi.org/10.1139/e95-120

Martignole, J., & Calvert, A. J. (1996). Crustal-scale shortening and extension across the Grenville Province of western Québec. *Tectonics*, *15*(2), 376–386. https://doi.org/10.1029/95TC03748

Martignole, J., Calvert, A. J., Friedman, R., & Reynolds, P. (2000). Crustal evolution along a seismic section across the Grenville Province (western Quebec). *Canadian Journal of Earth*

Sciences, *37*, 291–306. https://doi.org/10.1139/e99-123

Martignole, J., & Friedman, R. (1998). Geochronological constraints on the last stages of terrane assembly in the central part of the Grenville Province. *Precambrian Research*, *92*(2), 145–164. https://doi.org/10.1016/S0301-9268(98)00072-2

Martignole, J., & Martelat, J. E. (2005). Proterozoic mafic dykes as monitors of HP granulite facies metamorphism in the Grenville Front Tectonic Zone (western Quebec). *Precambrian Research*, *138*(3–4), 183–207. https://doi.org/10.1016/j.precamres.2005.05.002

Martignole, J., & Pouget, P. (1993). Contrasting zoning profiles in high grade garnets: evidence for the allochthonous nature of the Grenville province terrane. *Earth and Planetary Science Letters*, *120*, 1977–185.

Martignole, J., & Pouget, P. (1994). A two-stage emplacement for the Cabonga allochthon (central part of the Grenville Province): evidence for orthogonal and oblique collision during the Grenville orogeny. *Canadian Journal of Earth Sciences*, *31*(11), 1714–1726. https://doi.org/10.1139/e94-153

Martignole, J., & Reynolds, P. H. (1997). $^{40}Ar/^{39}Ar$ thermochronology along a western Québec transect of the Grenville Province, Canada. *Journal of Metamorphic Geology*, *15*(2), 283–296. https://doi.org/10.1111/j.1525-1314.1997.00018.x

Martignole, J., & Ringuette, L. (1998). Dating provenance of metaclastic rocks from allochthonous terranes of the western Quebec portion of the Grenville Province by 207Pb/208Pb method with La(IR)-ICP-MS. In *Annual Meeting Abstract Volume* (p. 118). Geological Association of Canada-Mineralogical Association of Canada.

Maxeiner, R. ., Ashton, K., Card, C. D., Morelli, R. ., & Knox, B. (2017). A Field Guide to Naming Migmatites and Their Textures, with Saskatchewan Examples (p. 22). Saskatchewan Geological Survey.

McIntyre, G. A., Brooks, C., Compston, W., & Turek, A. (1966). The statistical assessment of Rb-Sr isochrons. *Journal of Geophysical Research (1896-1977)*, *71*(22), 5459–5468. https://doi.org/https://doi.org/10.1029/JZ071i022p05459

McLelland, J. M., Bickford, M. E., Hill, B. M., Clechenko, C. C., Valley, J. W., & Hamilton, M. A. (2004). Direct dating of Adirondack massif anorthosite by U-Pb SHRIMP analysis of

igneous zircon: Implications for AMCG complexes. *GSA Bulletin*, *116*(11–12), 1299–1317. https://doi.org/10.1130/B25482.1

Mclelland, J. M., Selleck, B. W., & Bickford, M. E. (2013). Tectonic Evolution of the Adirondack Mountains and Grenville Orogen Inliers within the USA. *Geoscience Canada*, *44*(4), 318–352.

McLelland, J. M., Selleck, B. W., & Bickford, M. E. (2010). Review of the Proterozoic evolution of the Grenville Province, its Adirondack outlier, and the Mesoproterozoic inliers of the Appalachians. *The Geological Society of America Memoir*, *206*(02), 21–49. https://doi.org/10.1130/2010.1206(02)

McNicoll, V., Goutier, J., Dubé, B., Mercier-Langevin, P., Ross, P.-S., Dion, C., Monecke, T., Legault, M., Percival, J., & Gibson, H. (2014). U-Pb Geochronology of the Blake River Group, Abitibi Greenstone Belt, Quebec, and Implications for Base Metal Exploration*,**. *Economic Geology*, *109*(1), 27–59. https://doi.org/10.2113/econgeo.109.1.27

Mole, D. R., Thurston, P. C., Marsh, J. H., Stern, R. A., Ayer, J. A., Martin, L. A. J., & Lu, Y. J. (2021). The formation of Neoarchean continental crust in the south-east Superior Craton by two distinct geodynamic processes. Precambrian Research, 356, 106104. https://doi.org/https://doi.org/10.1016/j.precamres.2021.106104

Montreuil, J. F. (2010). Le terrane de Renzy (Province de Grenville, Québec), vestige d'un système d'arc/bassin arrière arc actif à la marge de Laurentia au Protérozoïque. Msc Thesis. Université Laval, Québec.

Montreuil, J. F., & Constantin, M. (2010). The geochemistry of mafic gneisses from the Renzy terrane, western Grenville Province, Quebec: Implications for the geodynamic setting of the early Mesoproterozoic Laurentian margin. *Precambrian Research*, *181*(1–4), 150–166. https://doi.org/10.1016/j.precamres.2010.06.001

Nadeau, L., & Hanmer, S. (1992). Deep-crustal break-back stacking and slow exhumation of the continental footwall beneath a thrusted marginal basin, Grenville orogen, Canada. *Tectonophysics*, *210*, 215–233.

Naney, M. T. (1983). Phase equilibria of rock-forming ferromagnesian silicates in granitic systems. *American Journal of Science*, *283*(10), 993–1033.

Nielsen, A. B., Thorkelson, D. J., Gibson, H. D., & Marshall, D. D. (2013). The Wernecke igneous clasts in Yukon, Canada: Fragments of the Paleoproterozoic volcanic arc terrane Bonnetia. *Precambrian Research*, *238*, 78–92. https://doi.org/https://doi.org/10.1016/j.precamres.2013.09.017

Palmer, H. C., Merz, B. A., & Hayatsu, A. (1977). Sudbury Dikes Of The Grenville Front Region: Paleomagnetism, Petrochemistry, And K-Ar Age studies. *Can J Earth Sci*, *14*(8), 1867–1887. https://doi.org/10.1139/e77-158

Passchier, C. W., & Trouw, R. A. J. (2005). Micro-tectonics (second edition). Springer.

Paterson, B. A. ., Stephens, W. E., Rogers, G., Williams, I. S., Hinton, R. W., & Herd, D. A. (1992). The nature of zircon inheritance in two granite plutons. *Transactions of the Royal Society of Edinburgh: Earth Sciences*, *83*(1–2), 459–471. https://doi.org/10.1017/S0263593300008130

Pearce, J.A. (1983). Role of the Sub-Continental Lithosphere in Magma Genesis at Active Continental Margins. In C. J. Hawkesworth & M. J. Norry (Eds.), *Continental Basalts and Mantle Xenoliths* (pp. 230–249). Shiva.

Pearce, J.A. (1996). A User's Guide to Basalt Discrimination Diagrams. In D. A. Wynam (Ed.), *Trace Element Geochemistry of Volcanic Rocks: Applications for Massive Sulphied Exploration* (volume 12., pp. 79–113). Geological Association of Canada: Short Course Notes.

Pearce, Julian A. (2008). Geochemical fingerprinting of oceanic basalts with applications to ophiolite classification and the search for Archean oceanic crust. *Lithos*, *100*(1–4), 14–48. https://doi.org/10.1016/J.LITHOS.2007.06.016

Pearce, Julian A. (2014). Immobile element fingerprinting of ophiolites. *Elements*, *10*(2), 101–108. https://doi.org/10.2113/gselements.10.2.101

Pearce, Julian A, Ernewein, M., Bloomer, S. H., Parson, L. M., Murton, B. J., & Johnson, L. E. (1994). Geochemistry of Lau Basin volcanic rocks: influence of ridge segmentation and arc proximity. *Geological Society, London, Special Publications*, *81*(1), 53 LP – 75. https://doi.org/10.1144/GSL.SP.1994.081.01.04

Peterman, E. M., Hacker, B. R., & Baxter, E. F. (2009). Phase transformations of continental crust during subduction and exhumation: Western Gneiss Region, Norway. *European Journal of*

Mineralogy, *21*(6), 1097–1118. https://doi.org/10.1127/0935-1221/2009/0021-1988

Phinney, W. C., & Halls, H. C. (2001). Petrogenesis of the early Proterozoic Matachewan dyke swarm, Canada, and implications for magma emplacement and subsequent deformation. *Canadian Journal of Earth Sciences*, *38*(11), 1541–1563. https://doi.org/10.1139/e01-044

Pichon, X. Le, Rangin, C., Hamon, Y., Loget, N., Lin, J. Y., Andreani, L., & Flotte, N. (2010). Geodynamics of the France Southeast Basin. *Bulletin de La Societe Geologique de France*, *181*(6), 477–501. https://doi.org/10.2113/gssgfbull.181.6.477

Pidgeon, R. T. (2014). Zircon radiation damage ages. *Chemical Geology*, *367*, 13–22. https://doi.org/10.1016/j.chemgeo.2013.12.010

Piwinskii, A. J. (1973). Experimental studies of granitoids from the Central and Southern Coast Ranges, California. *Tschermaks Mineralogische Und Petrographische Mitteilungen*, *20*(2), 107–130. https://doi.org/10.1007/BF01081387

Platt, J. P. (1986). Dynamics of orogenic wedges and the uplift of high-pressure metamorphic rocks. *Geological Society of America Bulletin*, *97*(9), 1037–1053. https://doi.org/10.1130/0016-7606(1986)97<1037:DOOWAT>2.0.CO;2

Platt, J. P., Behr, W. M., & Cooper, F. J. (2015). Metamorphic core complexes: windows into the mechanics and rheology of the crust. *Journal of the Geological Society*, *172*, 9–27.

Powell, W. G., Carmichael, D. M., & Hodgson, C. J. (1995). Conditions and timing of metamorphism in the southern Abitibi Greenstone Belt, Quebec. *Canadian Journal of Earth Sciences*, *32*(6), 787–805. https://doi.org/10.1139/e95-067

Prince, C., Harris, N., & Vance, D. (2001). Fluid-enhanced melting during prograde metamorphism. Journal of the Geological Society, 158(2), 233–242. https://doi.org/10.1144/jgs.158.2.233

Puetz, S. J. (2018). A relational database of global U–Pb ages. *Geoscience Frontiers*, *9*(3), 877–891. https://doi.org/10.1016/j.gsf.2017.12.004

Puetz, S. J., Spencer, C. J., & Ganade, C. E. (2021). Analyses from a validated global U–Pb detrital zircon database: Enhanced methods for filtering discordant U–Pb zircon analyses and optimizing crystallization age estimates. *Earth-Science Reviews*, *220*(February), 103745.

https://doi.org/10.1016/j.earscirev.2021.103745

Raveggi, M., Giles, D., Foden, J., & Raetz, M. (2007). High Fe-Ti mafic magmatism and tectonic setting of the Paleoproterozoic Broken Hill Block, NSW, Australia. *Precambrian Research*, *156*(1–2), 55–84. https://doi.org/10.1016/j.precamres.2007.02.006

Reddy, S. M., Timms, N. E., Trimby, P., Kinny, P. D., Buchan, C., & Blake, K. (2006). Crystal-plastic deformation of zircon: A defect in the assumption of chemical robustness. *Geology*, *34*(4), 257–260. https://doi.org/10.1130/G22110.1

Regan, S. P., Chiarenzelli, J. R., McLelland, J. M., & Cousens, B. L. (2011). Evidence for an enriched asthenospheric source for coronitic metagabbros in the Adirondack Highlands. *Geosphere*, *7*(3), 694–709. https://doi.org/10.1130/GES00629.1

Rey, P., Vanderhaeghe, O., & Teyssier, C. (2001). Gravitational collapse of the continental crust. *Tectonophysics*, *342*(3–4), 435–449. https://doi.org/10.1016/S0040-1951(01)00174-3

Rivers, T. (1997). Lithotectonic elements of the Grenville Province: review and tectonic implications. *Precambrian Research*, *86*(3–4), 117–154. https://doi.org/10.1016/S0301-9268(97)00038-7

Rivers, T. (2008). Assembly and preservation of lower, mid, and upper orogenic crust in the Grenville Province-Implications for the evolution of large hot long-duration orogens. *Precambrian Research*, *167*(3–4), 237–259. https://doi.org/10.1016/j.precamres.2008.08.005

Rivers, T. (2009). The Grenville Province as a large hot long-duration collisional orogen - insights from the spatial and thermal evolution of its orogenic fronts. *Geological Society, London, Special Publications*, *327*(1), 405–444. https://doi.org/10.1144/SP327.17

Rivers, T. (2012). Upper-crustal orogenic lid and mid-crustal core complexes: signature of a collapsed orogenic plateau in the hinterland of the Grenville Province. *Canadian Journal of Earth Sciences*, *49*(1), 1–42. https://doi.org/10.1139/e11-014

Rivers, T. (2015). Tectonic Setting and Evolution of the Grenville Orogen: An Assessment of Progress Over the Last 40 Years. *Geoscience Canada*, *42*, 321–344. https://doi.org/10.12789/geocanj.2013.40.022

Rivers, T., & Corrigan, D. (2000). Convergent margin on southeastern Laurentia during the

Mesoproterozoic: tectonic implications. *Canadian Journal of Earth Sciences*, *37*(2–3), 359–383. https://doi.org/10.1139/e99-067

Rivers, T., Culshaw, N., Hynes, A., Indares, A., Jamieson, R., & Martignole, J. (2012). The Grenville. Orogen — A post-LITHOPROBE perspective. In J. A. Percival, F. A. Cook, & R. M. Clowes (Eds.), *Tectonic Styles in Canada: The LITHOPROBE Perspective* (Special Pa, pp. 97–236). Geological Association of Canada.

Rivers, T., Ketchum, J., Indares, A., & Hynes, A. (2002). The High Pressure belt in the Grenville Province: architecture, timing, and exhumation. *Canadian Journal of Earth Sciences*, *39*(5), 867–893. https://doi.org/10.1139/e02-025

Rivers, T., Martignole, J., Gower, C. ., & Davidson, C. (1989). New tectonic divisions of the Grenville Province, southeast Canadian Shield. *Tectonics*, *8*, 63–84. https://doi.org/10.1029/TC008i001p00063

Rivers, T., & Schwerdtner, W. . (2015). Post-peak Evolution of the Muskoka Domain, Western Grenville Province: Ductile Detachment Zone in a Crustal scale Metamorphic Core Complex. *Geoscience Canada*, *42*(Andrew Hynes Series: Tectonic Processes), 403–436.

Robinson, D. M., & Martin, A. J. (2014). Reconstructing the Greater Indian margin: focusing on the Lesser Himalayan duplex. *Tectonics*, *33*(Figure 2), 1–26. https://doi.org/10.1002/2014TC003564.Received

Rogers, C., Cousens, B., Ernst, R. E., & Söderlund, U. (2019). Phosphorus and Potassium Metasomatic Enrichment in the Mantle Source of the c. 1450-1425 Ma Michael-Shabogamo Gabbro of Eastern Laurentia. *Journal of Petrology*, *60*(1), 57–83. https://doi.org/10.1093/petrology/egy104

Rollinson, H. R. (1993). Using Geochemical Data: Evolution, Presentation, Interpretation (First edition). Longman Scientific and Technical.

Ross, P. S., McNicoll, V., Goutier, J., Mercier-Langevin, P., & Dubé, B. (2011). Basaltic to andesitic volcaniclastic rocks in the Blake River Group, Abitibi Greenstone belt: 2. origin, geochemistry, and geochronology. *Canadian Journal of Earth Sciences*, *48*(4), 757–777. https://doi.org/10.1139/e10-102

Ross, P. S., & Bédard, J. H. (2009). Magmatic affinity of modern and ancient subalkaline volcanic

rocks determined from trace-element discriminant diagrams. *Canadian Journal of Earth Sciences*, *46*(11), 823–839. https://doi.org/10.1139/E09-054

Rubatto, D. (2002). Zircon trace element geochemistry: partitioning with garnet and the link between U–Pb ages and metamorphism. *Chemical Geology*, *184*(1–2), 123–138. https://doi.org/10.1016/S0009-2541(01)00355-2

Rubatto, D. (2017). Zircon: The Metamorphic Mineral. In *Reviews in Mineralogy and Geochemistry* (Vol. 83, Issue 1). https://doi.org/10.2138/rmg.2017.83.10

Rubatto, D., Chakraborty, S., & Dasgupta, S. (2013). Timescales of crustal melting in the Higher Himalayan Crystallines (Sikkim, Eastern Himalaya) inferred from trace element-constrained monazite and zircon chronology. *Contributions to Mineralogy and Petrology*, *165*(2), 349–372. https://doi.org/10.1007/s00410-012-0812-y

Rubatto, D., Hermann, J., Berger, A., & Engi, M. (2009). Protracted fluid-induced melting during Barrovian metamorphism in the Central Alps. *Contributions to Mineralogy and Petrology*, *158*(6), 703–722. https://doi.org/10.1007/s00410-009-0406-5

Rubin, J. N., Henry, C. D., & Price, J. G. (1993). The mobility of zirconium and other "immobile" elements during hydrothermal alteration. *Chemical Geology*, *110*(1–3), 29–47. https://doi.org/10.1016/0009-2541(93)90246-F

Rudnick, R.L., McLennan, S. M., & Taylor, S. R. (1985). Large ion lithophile elements in rocks from high-pressure granulite facies terrains. *Geochimica et Cosmochimica Acta*, *49*(7), 1645–1655. https://doi.org/10.1016/0016-7037(85)90268-6

Rudnick, Roberta L. (1992). Restites, Eu anomalies and the lower continental crust. *Geochimica et Cosmochimica Acta*, *56*(3), 963–970. https://doi.org/10.1016/0016-7037(92)90040-P

Sabourin, R. J. E. (1963). Géologie de la region de Bourbonnais-Limousin, Comte de Pontiac (p. 12). Ministère de l'Énergie et des Ressources naturelles.

Saccani, E. (2015). A new method of discriminating different types of post-Archean ophiolitic basalts and their tectonic significance using Th-Nb and Ce-Dy-Yb systematics. *Geoscience Frontiers*, *6*(4), 481–501. https://doi.org/10.1016/j.gsf.2014.03.006

Sawyer, E. W. (1991). Disequilibrium Melting and the Rate of Melt–Residuum Separation During Migmatization of Mafic Rocks from the Grenville Front, Quebec. Journal of Petrology, 32(4), 701–738. https://doi.org/10.1093/petrology/32.4.701

Sawyer, E. W. (2001). Melt segregation in the continental crust: Distribution and movement of melt in anatectic rocks. *Journal of Metamorphic Geology*, *19*(3), 291–309. https://doi.org/10.1046/j.0263-4929.2000.00312.x

Sawyer, E. W. (2010). Migmatites formed by water-fluxed partial melting of a leucogranodiorite protolith: Microstructures in the residual rocks and source of the fluid. *Lithos*, *116*(3–4), 273–286. https://doi.org/10.1016/j.lithos.2009.07.003

Sawyer, E. W., & Brown, M. (2008). Working with migmatites. In E. W. Sawyer & M. Brown (Eds.), *Working with migmatites* (Short Cour, p. 158). Mineralogical Association of Canada.

Sappin, A. A., Constantin, M., Clark, T., & van Breemen, O. (2009). Geochemistry, geochronology, and geodynamic setting of Ni–Cu ± PGE mineral prospects hosted by mafic and ultramafic intrusions in the Portneuf–Mauricie Domain, Grenville Province, QuebecGéologie Québec Contribution 8439-2008-2009-5. Geological Survey of C. *Canadian Journal of Earth Sciences*, *46*(5), 331–353. https://doi.org/10.1139/E09-022

Schandl, E. S., & Gorton, M. P. (2002). Application Of High Field Strength Elements To Discriminate Tectonic Settings In VMS Environments. *Economic Geology*, *97*(3), 629–642. https://doi.org/10.2113/gsecongeo.97.3.629

Schiller, D., & Finger, F. (2019). Application of Ti-in-zircon thermometry to granite studies: problems and possible solutions. *Contributions to Mineralogy and Petrology*, *174*(6), 1–16. https://doi.org/10.1007/s00410-019-1585-3

Schneider, D. A., Cope, N., & Holm, D. K. (2013). Thermochronology of the Mont Laurier terrane, southern Canadian Grenville Province, and its bearing on defining orogenic architecture. *Precambrian Research*, *226*, 43–58. https://doi.org/10.1016/j.precamres.2012.11.006

Schoene, B. (2014). U-Th-Pb Geochronology. In *Treatise on Geochemistry: Second Edition* (Vol. 4). https://doi.org/10.1016/B978-0-08-095975-7.00310-7

Searle, M., Avouac, J.-P., Elliott, J., & Dyck, B. (2017). Ductile shearing to brittle thrusting along the Nepal Himalaya: Linking Miocene channel flow and critical wedge tectonics to 25th April

2015 Gorkha earthquake. *Tectonophysics*, *714–715*, 117–124. https://doi.org/10.1016/J.TECTO.2016.08.003

Searle, M. P., Stephenson, B., Walker, J. D., & Walker, C. (2007). Restoration of the Western Himalaya: Implications for metamorphic protoliths, thrust and normal faulting, and channel flow models. *Episodes*, *30*(4), 242–257. https://doi.org/10.18814/epiiugs/2007/v30i4/001

Sharma, K. N. M., Singhroy, V. H., & Levesque, J. (1995). Discussion: A two-stage emplacement for the Cabonga allochthon (central part of the Grenville Province): evidence for orthogonal and oblique collision during the Grenville orogeny. *Canadian Journal of Earth Sciences*, *32*, 1474–1478.

Shellnutt, J. G., & MacRae, N. D. (2012). Petrogenesis of the Mesoproterozoic (1.23 Ga) Sudbury dyke swarm and its questionable relationship to plate separation. *International Journal of Earth Sciences*, *101*(1), 3–23. https://doi.org/10.1007/s00531-010-0636-9

Simony, P. S., & Carr, S. D. (2011). Cretaceous to Eocene evolution of the southeastern Canadian Cordillera: Continuity of Rocky Mountain thrust systems with zones of “in-sequence” mid-crustal flow. *Journal of Structural Geology*, *33*(9), 1417–1434. https://doi.org/10.1016/J.JSG.2011.06.001

Sizova, E., Gerya, T., & Brown, M. (2014). Contrasting styles of Phanerozoic and Precambrian continental collision. *Gondwana Research*, *25*(2), 522–545. https://doi.org/10.1016/j.gr.2012.12.011

Slagstad, T., Jamieson, R. A., & Culshaw, N. G. (2005). Formation, crystallization, and migration of melt in the mid-orogenic crust: Muskoka domain migmatites, Grenville Province, Ontario. *Journal of Petrology*, *46*(5), 893–919. https://doi.org/10.1093/petrology/egi004

Sláma, J., Košler, J., Condon, D. J., Crowley, J. L., Gerdes, A., Hanchar, J. M., Horstwood, M. S. A., Morris, G. A., Nasdala, L., Norberg, N., Schaltegger, U., Schoene, B., Tubrett, M. N., & Whitehouse, M. J. (2008). Plešovice zircon - A new natural reference material for U-Pb and Hf isotopic microanalysis. *Chemical Geology*, *249*(1–2), 1–35. https://doi.org/10.1016/j.chemgeo.2007.11.005

Smith, T. E., Harris, M. J., Huang, C. H., & Holm, P. E. (2001). The geochemical nature of the igneous rocks of the Sharbot Lake domain, Central Metasedimentary Belt, Ontario. *Canadian*

Journal of Earth Sciences, *38*(7), 1037–1057. https://doi.org/10.1139/cjes-38-7-1037

Soucy La Roche, R., & Godin, L. (2019). Inherited Cross-Strike Faults and Oligocene-Early Miocene Segmentation of the Main Himalayan Thrust, West Nepal. *Journal of Geophysical Research: Solid Earth*, *124*(7), 7429–7444. https://doi.org/10.1029/2019JB017467

Soucy La Roche, R, Gervais, F., Tremblay, A., Crowley, J. L., & Ruffet, G. (2015). Tectono-metamorphic history of the eastern Taureau shear zone, Mauricie area, Québec: Implications for the exhumation of the mid-crust in the Grenville Province. In *Precambrian Research* (Vol. 257). https://doi.org/10.1016/j.precamres.2014.11.012

Spencer, C. J., Kirkland, C. L., & Taylor, R. J. M. (2016). Strategies towards statistically robust interpretations of in situ U–Pb zircon geochronology. *Geoscience Frontiers*, *7*(4), 581–589. https://doi.org/10.1016/J.GSF.2015.11.006

Sterckx, S., Ross, P. S., & Goutier, J. (2014). Géochimie des roches volcaniques archéennes du Groupe de Blake River, Sous-province de l'Abitibi, Québec: composition des échantillons « frais » Rapport préliminaire: MB 2013-09 (p. 21). Ministère de l'Énergie et des Ressources naturelles.

Sterckx, S., Ross, P. S., & Goutier, J. (2014). Géochimie des roches volcaniques archéennes du Groupe de Blake River, Sous-province de l'Abitibi, Québec: composition des échantillons « frais ». Repport MB 2014-32 (p. 22). Ministère de l'Énergie et des Ressources naturelles du Quebec. Quebec City, Canada.

Stipp, M., Stünitz, H., Heilbronner, R., & Schmid, S. M. (2002). Dynamic recrystallization of quartz: correlation between natural and experimental conditions. *Geological Society, London, Special Publications*, *200*(1), 171–190. https://doi.org/10.1144/GSL.SP.2001.200.01.11

Sun, S.S., & McDonough, W. F. (1989). Chemical and isotopic systematics of oceanic basalts; implications for mantle composition and processes. In A. D. Saunders & M. J. Norry (Eds.), *Magmatism in the ocean basins* (pp. 319–345). Geological Society of London.

Sun, S.S., & McDonough, W. F. (1989). Chemical and isotopic systematics of oceanic basalts: Implications for mantle composition and processes. *Geological Society Special Publication*, *42*(1), 313–345. https://doi.org/10.1144/GSL.SP.1989.042.01.19

Tatsumi, Y., Hamilton, D. L., & Nesbitt, R. W. (1986). Chemical characteristics of fluid phase released from a subducted lithosphere and origin of arc magmas: Evidence from high-pressure experiments and natural rocks. *Journal of Volcanology and Geothermal Research*, *29*(1–4), 293–309. https://doi.org/10.1016/0377-0273(86)90049-1

Taylor, B., & Martinez, F. (2003). Back-arc basin basalt systematics. *Earth and Planetary Science Letters*, *210*(3–4), 481–497. https://doi.org/10.1016/S0012-821X(03)00167-5

Thurston, P. C., Ayres, L. D., Edwards, G. R., Gelinas, L., Ludden, J. N., & Verpaelst, P. (1985). Archean bimodal volcanism. In L. D. Ayres, P. C. Thurston, K. D. Card, & W. Weber (Eds.), *Evolution of Archean supracrustal sequences* (Special Pa, pp. 7–21). Geological Association of Canada,.

Tirel, C., Brun, J.-P., & Burov, E. (2008). Dynamics and structural development of metamorphic core complexes. *Journal of Geophysical Research: Solid Earth*, *113*(B4). https://doi.org/https://doi.org/10.1029/2005JB003694

Tollo, R. P., Corriveau, L., McLelland, J., & Bartholomew, M. . (2004). Proterozoic tectonic evolution of the Grenville orogen in North America: An introduction. In R. P. Tollo, L. Corriveau, J. McLelland, & M. . Bartholomew (Eds.), *Proterozoic Tectonic Evolution of the Grenville Orogen in North America* (197th ed., pp. 1–18). Geological Society of America Memoir.

Tomkins, H. S., Powell, R., & Ellis, D. J. (2007). The pressure dependence of the zirconium-in-rutile thermometer. *Journal of Metamorphic Geology*, *25*(6), 703–713. https://doi.org/10.1111/j.1525-1314.2007.00724.x

Turlin, F., André-Mayer, A. S., Moukhsil, A., Vanderhaeghe, O., Gervais, F., Solgadi, F., Groulier, P. A., & Poujol, M. (2017). Unusual LREE-rich, peraluminous, monazite- or allanite-bearing pegmatitic granite in the central Grenville Province, Québec. Ore Geology Reviews. https://doi.org/10.1016/j.oregeorev.2017.04.019

Tuttle, O. F., & Bowen, N. L. (1958). *Origin of Granite in the Light of Experimental Studies in the System NaAlSi3O8–KAlSi3O8–SiO2–H2O*. Geological Society of America. https://doi.org/10.1130/MEM74

Valverde Cardenas, C., Indares, A., & Jenner, G. (2012). Mafic and ultrapotassic rocks from the

canyon domain (Central Grenville Province): Geochemistry and tectonic implications. *Canadian Journal of Earth Sciences*, *49*(2), 412–433. https://doi.org/10.1139/E11-065

van Gool, J. A. M., Rivers, T., & Calon, T. (2008). Grenville Front zone, Gagnon terrane, southwestern Labrador: Configuration of a midcrustal foreland fold-thrust belt. *Tectonics*, *27*(1), 1–35. https://doi.org/10.1029/2006TC002095

Van Der Molen, I. (1985). Interlayer Material Transport During Layer-Normal Shortening. Part Ii. Boudinage, Pinch-And-Swell and Migmatite At Søndre Strømfjord Airport, West Greenland. *Tectonophysics*, *115*, 297–313.

Vanderhaeghe, O., Medvedev, S., Fullsack, P., Beaumont, C., & Jamieson, R. A. (2003). Evolution of orogenic wedges and continental plateaux: insights from crustal thermal-mechanical models overlying subducting mantle lithosphere. *Geophysical Journal International*, *153*(1), 27–51. https://doi.org/10.1046/j.1365-246X.2003.01861.x

Vanderhaeghe, Olivier. (2009). Migmatites, granites and orogeny: Flow modes of partially-molten rocks and magmas associated with melt/solid segregation in orogenic belts. *Tectonophysics*, *477*(3–4), 119–134. https://doi.org/10.1016/J.TECTO.2009.06.021

Vanderhaeghe, Olivier, Teyssier, C., & Wysoczanski, R. (1999). Structural and geochronological constraints on the role of partial melting during the formation of the Shuswap metamorphic core complex at the latitude of the Thor-Odin dome, British Columbia. *Canadian Journal of Earth Sciences*, *36*, 917–943.

Vavra, G., Schmid, R., & Gebauer, D. (1999). Internal morphology, habit and U-Th-Pb microanalysis of amphibolite-to-granulite facies zircons: geochronology of the Ivrea Zone (Southern Alps). *Contributions to Mineralogy and Petrology*, *134*(4), 380–404. https://doi.org/10.1007/s004100050492

Verma, S. P., Verma, S. K., & Oliveira, E. P. (2015). Application of 55 multi-dimensional tectonomagmatic discrimination diagrams to Precambrian belts. *International Geology Review*, *57*(11–12), 1365–1388. https://doi.org/10.1080/00206814.2014.921125

Vermeesch, P. (2018). IsoplotR: a free and open toolbox for geochronology. *Geoscience Frontiers*. https://doi.org/10.1016/J.GSF.2018.04.001

Vernon, R. H., & Clarke, G. L. (2008). Principles of Metamorphic Petrology. Cambridge

University Press.

Vielzeuf, D., & Schmidt, M. W. (2001). Melting relations in hydrous systems revisited: Application to metapelites, metagreywackes and metabasalts. *Contributions to Mineralogy and Petrology*, *141*(3), 251–267. https://doi.org/10.1007/s004100100237

Vigneresse, J. L., Barbey, P., & Cuney, M. (1996). Rheological transitions during partial melting and crystallization with application to felsic magma segregation and transfer. *Journal of Petrology*, *37*(6), 1579–1600. https://doi.org/10.1093/petrology/37.6.1579

Watson, E. B., Wark, D. A., & Thomas, J. B. (2006). Crystallization thermometers for zircon and rutile. *Contributions to Mineralogy and Petrology*, *151*(4), 413–433. https://doi.org/10.1007/s00410-006-0068-5

Weber, B., & Hecht, L. (2003). Petrology and geochemistry of metaigneous rocks from a Grenvillian basement fragment in the Maya block: the Guichicovi complex, Oaxaca, southern Mexico. *Precambrian Research*, *124*(1), 41–67. https://doi.org/https://doi.org/10.1016/S0301-9268(03)00078-0

Weinberg, R. F., & Hasalová, P. (2015). Water-fluxed melting of the continental crust: A review. *Lithos*, *212–215*, 158–188. https://doi.org/10.1016/j.lithos.2014.08.021

Weller, O. M., & St-Onge, M. R. (2017). Record of modern-style plate tectonics in the Palaeoproterozoic Trans-Hudson orogen. *Nature Geoscience*, *10*(4). https://doi.org/10.1038/ngeo2904

Wendt, I., & Carl, C. (1991). The statistical distribution of the mean squared weighted deviation. *Chemical Geology: Isotope Geoscience Section*, *86*(4), 275–285. https://doi.org/10.1016/0168-9622(91)90010-T

Wheeler, J. O., Hoffman, P. F., Card, K. D., Davidson, A., Sanford, B. V., Okulitch, A. V., & Roest, W. R. (1996). *Geological map of Canada*. Natural Resources Canada. https://doi.org/https://doi.org/10.4095/208175

White, D. J., Forsyth, D. A., Asudeh, I. ., Carr, S. D., Wu, H., Easton, R. M., & Mereu, R. F. (2000a). Seismic-Based Cross- Section Across the Grenville Front in Ontario. *Canadian Journal of Earth Sciences*, *37*, 183–192.

White, D. J., Forsyth, D. A., Asudeh, I., Carr, S. D., Wu, H., Easton, R. M., & Mereu, R. F. (2000b). A seismic-based cross-section of the Grenville Orogen in southernwestern Quebec. *Canadian Journal of Earth Sciences*, *37*, 183–192.

White, L. T., & Ireland, T. R. (2012). High-uranium matrix effect in zircon and its implications for SHRIMP U-Pb age determinations. *Chemical Geology*, *306–307*, 78–91. https://doi.org/10.1016/j.chemgeo.2012.02.025

Whitney, D. L., & Evans, B. W. (2010). Abbreviations for names of rock-forming minerals. *American Mineralogist*, *95*(1), 185–187. https://doi.org/10.2138/am.2010.3371

Wiedenbeck, M., Alle, P., Corfu, F., Griffin, W., Meier, M., Oberli, F., Quadt, A. V., Roddick, J., & Spiegel, W. (1995). Three Natural Zircon Standards for U-Th-Pb, Lu-Hf, Trace Element and Ree Analyses. *Geostandards Newsletter*, *19*(1), 1–23. https://doi.org/10.1111/j.1751-908X.1995.tb00147.x

Williams, I. S. (1992). Some observations on the use of zircon U-Pb geochronology in the study of granitic rocks. *Earth and Environmental Science Transactions of the Royal Society of Edinburgh*, *83*(1–2), 447–458. https://doi.org/10.1017/S0263593300008129

Williams, P. F., & Jiang, D. (2005). An investigation of lower crustal deformation: Evidence for channel flow and its implications for tectonics and structural studies. *Journal of Structural Geology*, *27*(8), 1486–1504. https://doi.org/10.1016/j.jsg.2005.04.002

Winchester, J. A., & Floyd, P. A. (1977). Geochemical discrimination of different magma series and their differentiation products using immobile elements. *Chemical Geology*, *20*, 325–343. https://doi.org/10.1016/0009-2541(77)90057-2

Winchester, J. A., Park, R. G., & Holland, J. G. (1980). The geochemistry of Lewisian semipelite schists from the Gairlch district, Wester Ross. *Scottish Journal of Geology*, *16*, 325–343.

Wood, D. A. (1980). The application of a ThHfTa diagram to problems of tectonomagmatic classification and to establishing the nature of crustal contamination of basaltic lavas of the British Tertiary Volcanic Province. *Earth and Planetary Science Letters*, *50*(1), 11–30. https://doi.org/10.1016/0012-821X(80)90116-8

Woodhead, J. D., Hergt, J. M., Davidson, J. P., & Eggins, S. M. (2001). Hafnium isotope evidence for 'conservative' element mobility during subduction zone processes. *Earth and Planetary*

Science Letters, *192*(3), 331–346. https://doi.org/10.1016/S0012-821X(01)00453-8

Wynne-Edwards, H. R. (1972). The Grenville Province. In R. A. Price & R. J. W. Douglas (Eds.), *Variations in tectonic styles in Canada* (Special Pa, pp. 263–334). Geological Association of Canada. https://books.google.com/books?id=pNkJAQAAIAAJ

Yakymchuk, C. (2019). On Granites. *Journal of the Geological Society of India*, *94*(1), 9–22. https://doi.org/10.1007/s12594-019-1261-2

Yakymchuk, C., Kirkland, C. L., & Clark, C. (2018). Th/U ratios in metamorphic zircon. *Journal of Metamorphic Geology*. https://doi.org/10.1111/jmg.12307

Xia, L., & Li, X. (2019). Basalt geochemistry as a diagnostic indicator of tectonic setting. *Gondwana Research*, *65*, 43–67. https://doi.org/10.1016/j.gr.2018.08.006

Xia, L. Q. (2014). The geochemical criteria to distinguish continental basalts from arc related ones. *Earth-Science Reviews*, *139*, 195–212. https://doi.org/10.1016/j.earscirev.2014.09.006

APPENDIX A SUPPLEMENTARY TABLES AND FIGURES FOR GEOCHRONOLOGY DATA PRESENTED IN THE VIRTUAL TOUR (CHAPTER 2)

Table A.1. Summary of geochronology analyses for sample CL6144 from stop 16, v-chapter 2.

			Apparent Ages (Ma)					Isotope ratios							
Sample No	SpotNum	Type	207Pb* 206Pb*	±2s (Ma)	206Pb* 238U*	±2s (Ma)	% disc.	207Pb* 235U*	±2s (%)	206Pb* 238U	±2s (%)	error corr.	207Pb* 206Pb*	±2s (%)	error corr.
CL6144	62	1	1112.57	46	1031	50	7.4	1.8324	5.6768	0.1733	5.1987	0.9140	0.0767	2.2802	0.0000
	41	1	1078.07	43	1008	35	6.5	1.7594	4.2789	0.1693	3.7043	0.8624	0.0754	2.1419	0.0000
	65	1	1037.84	27	1003	39	3.3	1.7155	4.3675	0.1684	4.1569	0.9489	0.0739	1.3396	0.0000
	66	1	1022.51	35	982	44	4.0	1.6628	5.1636	0.1645	4.8697	0.9410	0.0733	1.7173	0.0000
	67	1	999.19	51	1000	43	0.0	1.6759	5.2546	0.1677	4.6033	0.8739	0.0725	2.5337	0.0000
	73	1	1025.60	54	1027	39	-0.2	1.7490	4.8902	0.1728	4.1025	0.8363	0.0734	2.6615	0.0000
	74	1	1026.45	50	1008	37	1.8	1.7140	4.6498	0.1692	3.9306	0.8425	0.0735	2.4841	0.0000
	75	1	1010.54	35	1000	37	1.0	1.6868	4.3212	0.1679	3.9669	0.9150	0.0729	1.7136	0.0000
	76	1	1020.19	36	1040	41	-2.0	1.7682	4.6385	0.1751	4.2937	0.9231	0.0732	1.7550	0.0000
	83	1	1016.55	39	1044	43	-2.7	1.7711	4.8470	0.1757	4.4537	0.9165	0.0731	1.9128	0.0000
	84	1	1070.99	36	1054	51	1.6	1.8391	5.5219	0.1776	5.2314	0.9456	0.0751	1.7673	0.0000
	85	1	1052.20	48	1022	42	2.8	1.7630	5.0407	0.1719	4.4450	0.8795	0.0744	2.3771	0.0000
	262	1	981.60	40	1053	50	-7.2	1.7573	5.4947	0.1774	5.1241	0.9311	0.0718	1.9838	0.0000
	42	1	1014.69	41	1006	43	0.8	1.7008	5.0785	0.1689	4.6509	0.9136	0.0730	2.0397	0.0000
	46	1	988.39	40	1013	45	-2.5	1.6922	5.2112	0.1703	4.8173	0.9224	0.0721	1.9874	0.0000
	52	1	1004.65	56	991	43	1.3	1.6652	5.4562	0.1662	4.6984	0.8591	0.0727	2.7739	0.0000
	53	1	1050.71	34	1007	48	4.1	1.7337	5.4023	0.1691	5.1254	0.9469	0.0743	1.7075	0.0000
	56	1	1024.47	55	1003	46	2.1	1.7041	5.6284	0.1684	4.9222	0.8727	0.0734	2.7296	0.0000
	59	1	977.07	58	1021	52	-4.5	1.6961	6.2301	0.1716	5.5345	0.8869	0.0717	2.8606	0.0000
	60	1	1019.31	49	1035	51	-1.6	1.7579	5.8846	0.1742	5.3560	0.9085	0.0732	2.4377	0.0000
	63	1	1002.80	50	1043	46	-4.0	1.7586	5.4107	0.1757	4.8132	0.8876	0.0726	2.4716	0.0000
	68	1	1064.96	48	996	50	6.5	1.7240	5.9200	0.1670	5.4255	0.9149	0.0749	2.3686	0.0000
	70	1	974.57	42	997	44	-2.3	1.6517	5.1927	0.1673	4.7753	0.9175	0.0716	2.0399	0.0000
	72	1	1003.89	42	1022	43	-1.8	1.7208	5.0392	0.1718	4.5936	0.9093	0.0726	2.0717	0.0000
	77	1	974.27	40	1025	44	-5.2	1.7009	4.9930	0.1723	4.5927	0.9176	0.0716	1.9590	0.0000
	79	1	1012.90	53	1042	39	-2.9	1.7646	4.8332	0.1754	4.0539	0.8361	0.0730	2.6317	0.0000
	81	1	1012.17	29	1038	43	-2.6	1.7575	4.7081	0.1748	4.4812	0.9494	0.0729	1.4438	0.0000
	82	1	1018.56	43	1045	40	-2.6	1.7762	4.6333	0.1761	4.1068	0.8837	0.0732	2.1451	0.0000
	51	2	1023.66	56	986	45	3.7	1.6713	5.6985	0.1653	4.9726	0.8708	0.0734	2.7831	0.0000
	57	2	1014.06	46	1001	40	1.2	1.6916	4.8804	0.1681	4.3102	0.8807	0.0730	2.2892	0.0000
	64	2	1061.11	32	1000	41	5.8	1.7285	4.6681	0.1678	4.3936	0.9387	0.0747	1.5771	0.0000
	243	2	1075.22	38	989	36	8.0	1.7204	4.3853	0.1658	3.9650	0.9017	0.0753	1.8734	0.0000
	245	2	1008.04	56	993	48	1.5	1.6711	5.9327	0.1665	5.2492	0.8834	0.0728	2.7645	0.0000
	256	2	1036.22	38	1027	36	0.9	1.7583	4.2381	0.1728	3.8031	0.8947	0.0738	1.8703	0.0000
	257	2	1018.04	38	1000	33	1.8	1.6927	3.9950	0.1678	3.5212	0.8784	0.0731	1.8871	0.0000
	258	2	1010.42	59	991	26	1.9	1.6701	4.0408	0.1662	2.7926	0.6874	0.0729	2.9206	0.0000
	259	2	1021.26	33	1022	45	-0.1	1.7362	5.0316	0.1719	4.7530	0.9429	0.0733	1.6511	0.0000
	260	2	1034.66	43	958	36	7.4	1.6290	4.5843	0.1602	4.0563	0.8826	0.0738	2.1359	0.0000
	261	2	1036.81	48	1021	44	1.5	1.7474	5.2623	0.1717	4.6951	0.8905	0.0738	2.3765	0.0000
	263	2	1022.35	38	1027	39	-0.5	1.7458	4.5531	0.1727	4.1513	0.9095	0.0733	1.8703	0.0000
	264	2	987.49	41	1059	36	-7.2	1.7737	4.1941	0.1785	3.6750	0.8735	0.0721	2.0212	0.0000
	270	2	981.32	43	1031	41	-5.1	1.7181	4.7556	0.1735	4.2731	0.8965	0.0718	2.0871	0.0000
	273	2	1013.29	34	1010	40	0.3	1.7071	4.5553	0.1697	4.2355	0.9276	0.0730	1.6766	0.0000
	275	2	1003.45	40	1035	38	-3.2	1.7442	4.4407	0.1742	3.9729	0.8923	0.0726	1.9838	0.0000
	276	2	1040.95	31	1010	39	3.0	1.7298	4.4820	0.1696	4.2070	0.9364	0.0740	1.5459	0.0000
	277	2	994.78	42	1028	32	-3.3	1.7236	3.9804	0.1729	3.4117	0.8541	0.0723	2.0504	0.0000
	278	2	965.98	55	1015	40	-5.1	1.6762	5.0563	0.1705	4.2732	0.8432	0.0713	2.7029	0.0000
	279	2	1009.14	46	1025	40	-1.6	1.7309	4.8200	0.1724	4.2532	0.8804	0.0728	2.2677	0.0000
	280	2	987.91	47	1015	35	-2.7	1.6939	4.3623	0.1705	3.6892	0.8431	0.0721	2.3281	0.0000
	43	2	977.64	42	1033	48	-5.7	1.7183	5.3959	0.1738	4.9897	0.9228	0.0717	2.0540	0.0000
	44	2	1012.77	44	1006	42	0.7	1.6991	5.0244	0.1689	4.5227	0.8979	0.0730	2.1887	0.0000
	47	2	1020.79	27	998	49	2.2	1.6917	5.5188	0.1675	5.3510	0.9678	0.0732	1.3506	0.0000
	49	2	1010.07	41	1003	45	0.7	1.6905	5.2619	0.1683	4.8555	0.9207	0.0729	2.0278	0.0000
	55	2	978.73	57	1034	48	-5.7	1.7212	5.7608	0.1740	5.0287	0.8711	0.0717	2.8106	0.0000
	61	2	1000.23	40	1019	47	-1.9	1.7120	5.4118	0.1712	5.0389	0.9292	0.0725	1.9741	0.0000
	71	2	998.45	48	1006	49	-0.8	1.6872	5.7943	0.1689	5.2981	0.9127	0.0724	2.3461	0.0000
	78	2	1028.29	47	1023	34	0.5	1.7430	4.2630	0.1719	3.5668	0.8333	0.0735	2.3349	0.0000
	247	2	1040.74	38	1003	44	3.6	1.7171	5.0594	0.1684	4.6996	0.9271	0.0740	1.8736	0.0000
	248	2	1011.07	42	1016	48	-0.5	1.7156	5.5313	0.1707	5.1281	0.9256	0.0729	2.0731	0.0000
	249	2	1018.89	50	1004	45	1.5	1.7004	5.4741	0.1685	4.8824	0.8903	0.0732	2.4756	0.0000
	250	2	1016.88	44	1018	47	-0.1	1.7235	5.3960	0.1710	4.9481	0.9154	0.0731	2.1526	0.0000
	251	2	1026.65	33	1006	45	2.0	1.7108	5.0658	0.1689	4.8007	0.9459	0.0735	1.6173	0.0000
	252	2	1014.26	43	1002	35	1.3	1.6921	4.3420	0.1681	3.7999	0.8726	0.0730	2.1008	0.0000
	253	2	1019.69	59	1012	44	0.8	1.7156	5.5447	0.1700	4.7106	0.8480	0.0732	2.9246	0.0000
	254	2	967.14	54	1002	35	-3.6	1.6536	4.5547	0.1681	3.7210	0.8145	0.0713	2.6266	0.0000
	255	2	1053.39	40	1020	41	3.2	1.7596	4.7630	0.1714	4.3222	0.9054	0.0744	2.0013	0.0000
	267	2	974.34	46	1054	42	-8.2	1.7539	4.8679	0.1777	4.3042	0.8822	0.0716	2.2738	0.0000
	269	2	1015.43	39	1052	43	-3.6	1.7850	4.8708	0.1772	4.4689	0.9156	0.0731	1.9373	0.0000
	272	2	960.31	36	1019	39	-6.1	1.6794	4.5125	0.1713	4.1439	0.9161	0.0711	1.7861	0.0000
	271	2	1107.49	43	1046	36	5.6	1.8573	4.3277	0.1762	3.7420	0.8621	0.0765	2.1741	0.0000
	246	2	987.48	52	958	45	3.0	1.5920	5.6853	0.1602	5.0704	0.8904	0.0721	2.5718	0.0000

Table A.1 (cont'd).

Sample No	SpotNum	Trace element concentrations (ppm)																												Ti-in-zircon
		P	Ti	Y	Zr	Nb	La	Ce	Pr	Nd	Sm	Eu	Gd	Tb	Dy	Ho	Er	Tm	Yb	Lu	Hf	Ta	Th	U	Ce/Ce*	Eu/Eu*	ΣREE	(Gd/Yb)cn	Lu/Hf	Nb/Ta	Th/U	T(°C)
CL6144	62	791.2861	4.4091	1575.5307	430998.2691	6.3133	0.0711	24.4745	0.1034	1.8302	6.4356	0.9070	29.1102	10.9064	141.4438	53.4476	240.8970	61.8304	676.9810	90.3666	8656.6777	2.3541	298.7702	644.4902	69.9775	0.2026	1338.8048	0.0356	0.0104	2.6818	0.4636	718
	41	853.5013	4.4950	2229.0015	516025.8530	7.5692	0.6879	24.6591	0.2881	4.2515	5.9822	0.7088	46.7005	14.7887	181.2670	73.3815	333.4447	74.2041	705.8832	137.7299	12505.7652	2.8114	367.0445	668.7606	13.5803	0.1296	1603.9772	0.0547	0.0110	2.6923	0.5488	719
	65	776.9516	5.4013	1702.3013	454401.1343	5.7607	0.2650	23.5116	0.3641	3.8624	8.1813	1.3222	39.2494	12.8335	157.0960	57.5828	253.1532	65.5163	690.4877	94.4592	9000.7046	1.7866	341.2105	695.2235	18.5565	0.2256	1407.8847	0.0470	0.0105	3.2245	0.4908	736
	66	558.2672	3.7692	1657.1656	483307.2111	5.7159	0.9307	26.0422	0.7716	5.6288	8.0458	1.5185	39.3788	12.9627	154.2171	59.0630	246.2006	60.2777	636.7129	90.1946	10332.6235	2.2896	309.5759	581.9682	7.5347	0.2608	1341.9449	0.0512	0.0087	2.4965	0.5319	704
	67	599.3955	4.6082	1381.3896	486596.4045	6.3369		22.0120		0.8657	4.5933	0.9544	27.4710	9.7622	125.1387	49.0952	214.9935	53.3924	560.8564	81.5579	10684.4522	2.3200	238.8569	521.1832		0.2597	1150.6926	0.0405	0.0076	2.7314	0.4583	722
	73	632.2871	3.5193	1483.3949	486787.6422	5.5018		19.3198	0.0173	0.4617	3.4538	0.8179	24.9141	9.1369	125.3220	49.8860	209.9204	57.4080	618.3697	88.1416	10205.6212	2.4301	242.1381	579.3544	1097.1153	0.2696	1207.1693	0.0333	0.0086	2.2640	0.4179	698
	74	348.6625	4.5775	1197.4714	459577.2505	8.8463		27.2916	0.0524	1.7774	3.4673	0.5257	24.0825	8.1661	109.0867	41.7494	179.6179	46.5726	486.4316	71.7710	10044.0008	4.2062	268.9316	574.9080	511.0806	0.1759	1000.5923	0.0410	0.0071	2.1032	0.4678	721
	75	710.6341	4.2035	1438.6596	466008.7716	5.4729		19.9168	0.0290	1.4609	3.1186	0.9059	27.8447	9.9037	129.2776	49.3672	229.1753	59.0243	614.6029	86.0342	9940.2623	2.0742	252.8104	584.8051	674.4981	0.2972	1230.6608	0.0375	0.0087	2.6386	0.4323	714
	76	645.1833	4.3989	1509.5705	462854.5902	7.3821		24.7236		1.7024	5.0186	0.9398	27.4949	10.9259	135.9748	52.4930	236.0285	60.7986	617.5385	87.6953	9752.6805	2.7485	311.0152	609.8557		0.2446	1261.3340	0.0368	0.0090	2.6859	0.5100	718
	83	527.0233	4.3737	1738.0610	477530.6290	5.1502	0.6235	25.8130	0.7582	6.2023	8.2543	1.2170	38.9337	12.7939	161.7834	57.6229	247.7305	59.6350	632.6305	92.2909	10460.3542	2.1480	308.8545	578.4010	9.2049	0.2076	1346.2892	0.0509	0.0088	2.3977	0.5340	717
	84	734.4805	5.0327	1511.5632	493075.1486	7.4150		21.8195		0.7681	4.2605	0.5093	24.9310	9.4041	131.3316	51.8411	238.3394	60.7346	646.5550	94.0396	11296.1126	3.1476	216.2039	374.3253		0.1511	1284.5340	0.0319	0.0083	2.3558	0.5776	730
	85	532.2443	3.7082	1332.4004	482405.6886	6.0943		19.1543		0.7870	2.9821	0.4859	21.1347	8.4660	115.3608	43.5063	205.3956	51.3615	532.3646	83.7895	10244.8930	2.1550	207.7708	516.1839		0.1871	1084.7885	0.0328	0.0082	2.8280	0.4025	703
	262	667.6788	3.9982	2192.4045	512288.4321	7.2295		24.0334	0.0354	2.4414	5.6715	0.7587	34.3703	13.5065	164.4824	67.5647	313.3765	70.8869	675.1451	141.2717	12435.8942	2.1416	414.5316	690.9723	665.3703	0.1661	1513.5445	0.0421	0.0114	3.3758	0.5999	709
	42	756.4328	3.2177	2012.9858	545578.2869	7.5525		22.1293	0.0800	2.0370	5.3284	0.9126	33.1387	11.7474	150.0919	62.6864	294.3685	68.4914	664.0654	126.4929	12854.0270	2.3024	319.2016	588.7483	271.3829	0.2100	1441.5698	0.0413	0.0098	3.2802	0.5422	691
	46	993.1036	4.0364	2268.2437	507870.8016	7.8118		20.5268		1.7686	7.3655	0.7822	39.5242	15.3259	191.9227	77.7954	361.6858	84.2277	829.5737	137.2592	11987.7861	2.8090	418.0030	689.3438		0.1401	1767.7575	0.0394	0.0114	2.7810	0.6064	710
	52	313.5100	3.0592	1098.1351	492701.5555	6.2619		18.9286	0.0354	1.0057	2.7945	0.2686	20.8304	7.3275	88.6957	36.4418	165.5875	41.7262	447.0271	68.1224	10988.5338	3.2974	174.9044	352.5530	523.8062	0.1076	898.7913	0.0385	0.0062	1.8990	0.4961	686
	53	704.8822	3.8649	1525.0353	477502.8980	5.7054		19.7687	0.0687	1.5570	3.5867	0.6328	27.6279	10.7859	132.5151	51.8128	227.4459	58.1644	605.4706	88.8935	10053.0387	2.2264	273.6877	547.5104	282.1756	0.1943	1228.3301	0.0377	0.0088	2.5626	0.4999	706
	56	310.4194	4.5946	1246.4441	439808.1784	9.5020		24.1249	0.0948	1.0520	4.0561	0.6276	23.7863	8.7704	110.0734	42.3550	205.2380	52.3501	591.9217	85.8236	9662.7068	3.9260	211.2493	500.7512	249.5383	0.1953	1150.2740	0.0332	0.0089	2.4203	0.4219	721
	59	657.5332	3.4679	1430.7121	434750.3340	5.8212		21.4611		0.7504	4.9648	0.5964	27.3660	9.6929	137.1237	47.6519	216.9270	56.0268	627.8292	87.3407	9013.3166	1.9482	259.2355	603.2747		0.1564	1237.7310	0.0361	0.0097	2.9880	0.4297	697
	60	309.1410	4.3384	1292.5611	431606.9524	10.2454		24.7653	0.0446	1.1658	5.6495	0.8707	25.4052	9.6136	111.4571	42.2880	201.5618	51.4632	600.0847	84.4007	9070.9449	4.4033	222.5189	537.8207	544.3892	0.2222	1158.7704	0.0350	0.0093	2.3268	0.4137	716
	63	454.0953	3.6529	1008.3015	427343.5573	5.6367		20.4456		1.5625	3.3210	0.4706	20.7163	7.0662	90.5763	32.9060	164.0228	42.5854	475.9295	62.6376	9440.4256	2.8191	195.1284	456.1629		0.1734	922.2396	0.0360	0.0066	1.9995	0.4278	701
	68	663.8270	3.9875	1481.7115	498811.2761	7.0657		22.1958	0.0165	1.2725	5.3205	0.8907	29.2026	9.7955	125.9853	50.5826	229.0070	58.8407	602.2638	89.2485	10324.8779	2.4712	251.8651	587.7364	1316.9181	0.2185	1224.6222	0.0401	0.0086	2.8592	0.4285	709
	70	379.0428	4.8398	2347.6790	501415.6649	6.5739	1.0051	35.8401	0.7189	7.7915	14.1583	2.6981	66.7506	19.7065	227.3836	79.5662	339.8778	82.4618	868.7770	118.8550	10717.2976	3.0703	490.4987	814.6240	10.3377	0.2683	1865.5904	0.0636	0.0111	2.1411	0.6021	726
	72	663.9047	3.5579	1564.9117	450182.0119	5.6652		22.3676	0.0359	0.8057	4.5576	1.0971	31.1891	11.7382	139.2704	51.6327	231.8157	59.4687	607.3884	86.2307	9505.2813	2.6541	279.5263	563.5524	610.2968	0.2813	1247.5979	0.0425	0.0091	2.1345	0.4960	699
	77	633.1621	4.1464	1835.6717	474635.9872	6.2746		26.9432	0.0692	3.1695	8.0007	1.4365	39.2931	14.6747	172.0027	67.1991	273.2238	68.5682	747.4221	104.3926	9573.7660	2.4666	401.9959	676.9373	382.0417	0.2477	1526.3952	0.0435	0.0109	2.5438	0.5938	712
	79	563.3027	4.2696	1520.5586	475432.1476	10.5438		27.4181	0.0569	1.3289	4.0490	0.6239	28.7099	10.1213	131.9060	52.5373	235.6216	59.3634	668.4555	92.3086	10811.5895	4.9456	272.4575	389.9903	472.7483	0.1769	1312.5005	0.0355	0.0085	2.1320	0.6986	715
	81	387.5610	3.3347	1753.1670	460232.5596	4.9647		28.6217	0.1463	3.2605	9.3222	1.7663	41.8455	14.8484	175.6700	61.1773	264.8818	63.7847	645.8543	93.7641	10312.6436	2.8401	359.7754	602.3610	191.8323	0.2734	1404.9432	0.0536	0.0091	1.7481	0.5973	694
	82	810.2621	3.7954	1825.5584	465772.2122	6.9534		23.7900	0.0821	2.8709	5.5342	1.0219	34.1744	12.5462	161.0769	58.6967	268.1147	67.7168	730.9621	104.1217	9785.9010	2.4612	337.9289	726.3780	284.2222	0.2272	1470.7085	0.0387	0.0106	2.8252	0.4652	705
	51	693.8622	4.9125	1712.9682	486175.5478	5.9571		21.1408	0.1036	1.4864	3.7561	0.7733	30.6605	11.2635	143.9827	58.3569	268.1826	64.8664	661.9160	100.3097	10671.3215	1.9928	305.6988	622.4100	200.1051	0.2203	1366.7986	0.0383	0.0094	2.9893	0.4912	727
	57	354.5776	4.2788	1162.5874	439560.0359	7.4364		19.6769	0.0326	1.2212	2.9410	0.6514	22.0893	8.2196	105.2178	42.5796	185.0514	46.9282	522.0506	72.8276	9631.4610	5.0794	211.1875	482.1428	591.6418	0.2471	1029.4872	0.0350	0.0076	1.4640	0.4380	715
	64	603.5505	4.2739	1907.9158	435926.0749	18.9185		37.9099	0.1190	2.2960	4.8477	0.8918	32.0787	13.3895	172.3040	63.9557	285.9816	74.2267	777.5064	99.5689	10580.8185	6.9854	492.7445	1030.0816	312.4548	0.2186	1565.0758	0.0341	0.0094	2.7083	0.4784	715
	243	448.6461	2.8543	1136.0222	460831.3299	5.4038		16.8352	0.0269	0.4930	3.1636	0.4659	19.4161	7.3029	90.6569	36.4286	168.7281	43.3740	477.0290	70.5321	10101.8860	2.2238	165.9579	432.2267	612.8610	0.1818	934.4523	0.0337	0.0070	2.4300	0.3840	681
	245	255.2270	3.3811	1134.6636	463820.2315	8.5953		24.9696	0.0777	1.1371	4.1916	0.6779	23.9322	7.9603	100.1473	37.1638	164.6770	41.4545	405.5384	61.4726	10013.2657	3.4336	308.4307	617.3646	315.2874	0.2069	873.4000	0.0488	0.0061	2.5033	0.4996	695
	256	605.8674	2.9610	1286.1400	442275.8433	4.7119		19.2457	0.0501	0.4454	3.6750	0.6362	25.8722	8.8129	105.2054	41.4560	184.1780	49.9000	532.0155	77.3519	9459.2691	2.0651	215.7788	517.2786	376.9545	0.1995	1048.8443	0.0402	0.0082	2.2817	0.4171	684
	257	287.9222	3.4791	1056.1848	423327.4422	6.7272	0.2020	19.4662	0.0746	0.9464	4.2518	0.5724	22.6389	7.5647	94.5391	36.2604	162.9430	40.9620	465.8029	68.7998	8956.7549	3.8558	173.4077	418.0786	38.8815	0.1784	925.0242	0.0402	0.0077	1.7447	0.4148	697
	258	300.7225	3.8006	1107.2450	423191.7283	7.2481		20.4341		0.7824	3.1236	0.6734	20.2149	8.0129	96.7162	37.5789	173.7654	44.5069	483.5894	73.7253	8994.5422	3.8210	175.7159	439.6796		0.2591	963.1235	0.0346	0.0082	1.8969	0.3996	705
	259	306.5280	4.0709	957.9502	436352.0873	6.0565	0.0623	22.1712	0.0210	1.3497	3.4096	0.7236	19.4501	6.9246	82.2241	31.3080	139.7733	36.5462	382.4655	54.0456	9201.3866	2.9549	190.0639	438.9020	150.5086	0.2716	780.4747	0.0421	0.0059	2.0496	0.4330	711
	260	268.0897	4.3160	974.1568	425413.0007	6.3320		18.4121		0.6843	3.6323	0.6198	19.0160	6.5419	82.6411	32.1475	144.8733	38.6713	417.7876	60.8165	9144.7776	3.2601	163.0423	392.9618		0.2280	825.8437	0.0377	0.0067	1.9423	0.4149	716
	261	488.5635	3.1125	1101.8100	437027.8892	4.4891		16.8549	0.0300	0.4100	3.7304	0.5568	19.0616	7.0653	94.6944	36.6582	164.0329	43.6282	444.0766	65.7815	9605.9356	1.7528	172.6540	434.8818	550.9730	0.2019	896.5807	0.0355	0.0068	2.5611	0.3970	688
	263	301.6164	4.2002	1344.3644	491107.9799	7.3983	0.5184	22.1778	0.3157	3.6447	5.5744	0.8517	22.7985	8.6128	105.7703	43.2799	197.6614	45.9853	425.2556	90.6348	12341.4502	3.0757	274.8351	499.1211	13.4414	0.2310	973.0813	0.0443	0.0073	2.4054	0.5506	713
	264	478.2781	2.6999	1502.2083	490888.2144	4.6459		15.3991		1.0972	4.2709	0.7338	22.7863	9.1435	113.9839	46.3089	208.4538	51.0074	492.7710	99.5197	12293.5483	1.7147	223.4935	428.2653		0.2274	1065.4755	0.0383	0.0081	2.7095	0.5219	676
	270	636.7947	3.5553	1656.0628	483133.0803	5.8415		21.2875	0.0335	1.4695	4.0418	0.6879	26.7380	10.4185	127.7707	53.4151	238.2581	61.4640	598.3176	105.7220	11007.8327	2.3246	273.3412	547.5766	623.9955	0.2023	1249.6241	0.0370	0.0096	2.5128	0.4992	699
	273	455.8449	2.9370	1248.7124	474657.8330	5.2538		15.6033	0.0248	0.9225	2.7995	0.4295	18.8265	7.8710	105.2217	40.7544	182.9108	47.7235	480.1804	81.5013	11096.1181	2.2363	174.5502	444.9569	616.2179	0.1809	984.7692	0.0324	0.0073	2.3494	0.3923	683
	275	339.8419	3.4999	1756.9592	466652.8892	5.3027	0.0183	26.4180	0.1482	3.3810	7.7620	1.3609	38.8918	13.0364	157.1729	57.5847	249.1257	65.2464	605.6634	94.7166	10437.2445	2.6683	337.9468	542.1676	124.3025	0.2395	1320.5263	0.0531	0.0091	1.9873	0.6233	698
	276	282.5519	3.4060	986.4670	469822.4719	5.5288		16.1619	0.0480	0.9144	4.2636	0.7681	18.8685	6.9492	80.0938	32.4296	150.9447	37.5537	385.9672	63.7215	10165.0786	3.0666	149.2023	310.7649	329.9241	0.2618	798.6842	0.0404	0.0063	1.8029	0.4801	695
	277	222.6101	2.6500	975.3933	471148.3404	5.7099		17.3046		1.4051	2.7533	0.6070	17.1911	6.3268	82.3459	31.6052	151.5870	37.5901	382.6026	60.3772	10259.7769	2.9839	168.5864	365.8173		0.2697	791.6959	0.0372	0.0059	1.9136	0.4608	675
	278	214.5791	2.7849	908.1797	452346.4122	4.8274		16.2938		0.5444	3.1524	0.6136	15.1375	6.1321	75.3951	29.0946	136.2364	36.3516	374.5901	56.3551	10453.7518	2.8336	139.6881	301.3700		0.2716	749.8966	0.0334	0.0054	1.7036	0.4635	679
	279	258.9877	3.6401	1017.9971	437600.2157	7.4923		25.4676	0.0375	0.9661	3.8580	0.8267	21.4989	7.3617	92.6618	35.0506	152.2824	39.8661	405.2659	58.5428	9763.8858	3.3671	263.4243	594.0919	665.8467	0.2775	843.6862	0.0439	0.0060	2.2251	0.4434	701
	280	472.8022	3.7208	1178.7053	456398.0414	5.6123		15.3569	0.0308	0.7681	3.0602	0.3961	19.7207	7.5792	92.9574	38.1297	171.6464	44.2141	457.9688	73.1151	10012.9964	1.9227	168.6834	446.6719	488.7869	0.1559	924.9435	0.0356	0.0073	2.9189	0.3776	703
	43	468.3196	5.0866	1738.8848	528209.0740	10.4322		36.0982	0.0323	1.7863	5.3619	0.7772	31.3984	10.7823	139.7037	54.7571	262.0813	56.3406	561.1994	105.4582	12491.5991	3.9887	404.5441	609.1795	1096.6795	0.1831	1265.7768	0.0463	0.0084	2.6154	0.6641	731
	44	360.4774	4.9112	1610.8080	527362.0380	9.5933		28.3409	0.0339	1.2659	4.9369	0.7476	33.5217	10.7312	132.3422	52.2030	235.3221	59.2933	581.7242	105.5971	13124.5698	4.3250	312.4017	565.3291	820.7821	0.1777	1246.0601	0.0477	0.0080	2.2181	0.5526	727
	47	835.5124	4.7673	2304.8505	509732.4982	7.4055		26.9812	0.0225	2.1899	6.8707	1.0818	40.9454	16.0038	194.1403	74.6928	325.7532	80.5792	804.4960	136.5426	10473.0579	2.6739	479.3035	840.2123	1176.7685	0.1972	1710.2994	0.0421	0.0130	2.7695	0.5705	725
	49	342.5440	3.2161	1152.2204	491920.4588	6.2250		17.5402	0.0572	0.3179	3.2173	0.4499	22.9376	6.9487	96.8668	38.0896	180.1308	44.1422	453.9850	72.4338	11300.0281	3.4191	185.9869	359.8356	300.8320	0.1601	937.1170	0.0418	0.0064	1.8207	0.5169	691
	55	543.8697	3.8060	1470.4809	456597.8635	6.6132		22.1652	0.0350	2.5549	6.6658	1.2723	31.1761	10.6653	129.0145	49.5093	227.3554	55.4125	608.6931	87.9734	10027.4491	2.1286	247.9797	548.2884	620.3518	0.2698	1232.4929	0.0424	0.0088	3.1068	0.4523	705
	61	356.9649	3.7813	1023.0402	435213.7386	8.5034		27.4116	0.0268	1.3527	4.5421	0.7298	20.4683	7.8177	92.5064	35.6408	161.2956	40.5233	452.8750	60.4209	9253.6243	3.5239	245.4786	549.3820	1002.5398	0.2314	905.6109	0.0374	0.0065	2.4131	0.4468	704
	71	335.3668	4.3075	1107.2019	490567.9392	7.0364		27.5803	0.1018	1.3549	4.1591	0.8002	18.2187	7.7391	104.5087	38.9046	171.0398	45.0064	470.0276	63.2368	10877.8321	4.1010	252.8862	582.3200	265.7672	0.2810	952.6779	0.0321	0.0058	1.7158	0.4343	716
	78	693.3910	4.0218	1529.1108	468282.0385	5.2114		23.4377	0.0309	1.8210	4.4804	0.7716	31.7278	10.7034	142.7234	50.1681	237.1672	59.3758	633.4382	91.3263	9807.2590	1.5965	281.5176	577.0556	745.0169	0.1979	1287.1718	0.0414	0.0093	3.2644	0.4879	710
	247	263.5406	4.3937	1134.3376	470060.0926	7.8339	0.0956	25.9315	0.1313	1.5311	4.3464	0.4793	20.2688	8.1151	94.9382	36.9043	163.1886	41.7302	436.3842	65.1941	10497.6336	3.6906	255.4892	578.4655	56.7462	0.1561	899.2388	0.0384	0.0062	2.1226	0.4417	717
	248	288.3265	3.2139	1908.9324	450072.1861	5.2492		29.4752	0.1402	2.9870	9.9001	1.7369	51.0278	15.3991	178.6634	65.9506	279.0134	66.6104	666.4693	94.2842	9804.2925	2.4452	415.7152	625.5165	206.1632	0.2363	1461.6577	0.0633	0.0096	2.1468	0.6646	690
	249	525.8868	3.7290	1283.9311	453361.0665	5.4528		20.9123	0.0671	1.7026	3.6811	1.0298	26.0481	9.2374	112.1395	43.3475	196.8080	51.0089	581.8602	78.2242	9842.4104	2.2245	217.9777	491.6022	305.6874	0.3215	1126.0666	0.0370	0.0079	2.4512	0.4434	703
	250	484.1606	3.0661	1127.6165	444099.8443	5.8322		17.3356	0.0261	0.7422	3.2517	0.6253	17.8285	7.6279	95.5759	35.6504	169.0477	45.8822	476.0929	70.3878	9568.6748	2.2591	162.1433	434.7150	652.1091	0.2511	940.0742	0.0310	0.0074	2.5816	0.3730	687
	251	235.2829	3.5567	786.2492	468898.2055	5.7682		20.0398	0.0185	1.1292	2.1738	0.2732	14.5468	5.6063	64.7378	25.5839	120.3105	31.4373	316.1916	47.7317	10323.4190	2.8304	165.2233	409.0588	1061.7197	0.1485	649.7804	0.0381	0.0046	2.0379	0.4039	699
	252	593.8275	3.8062	1300.3157	447626.1171	5.3079		18.7147		0.9293	4.8357	0.7323	22.3965	8.6290	102.6878	42.3490	191.9724	50.8183	517.7519	77.3662	9740.6280	1.8536	207.4550	492.4519		0.2151	1039.1831	0.0358	0.0079	2.8635	0.4213	705
	253	525.1600	3.0298	1296.3462	441661.2152	5.7572		18.4978	0.0189	1.1108	3.6814	0.5829	23.6392	8.6959	110.4028	43.3213	195.1190	52.8105	547.3354	79.5418	9484.7324	2.1171	208.6323	508.1424	962.3609	0.1910	1084.7577	0.0357	0.0084	2.7194	0.4106	686
	254	242.3646	3.1125	865.7020	445247.8545	4.6588		15.0325		0.6698	1.9751	0.4557	17.9141	6.0245	74.3222	28.6547	124.2928	35.0422	354.5750	50.3303	9902.7307	2.6953	131.1944	294.9533		0.2342	709.4710	0.0418	0.0051	1.7285	0.4448	688
	255	274.1280	3.9086	742.0614	453429.5007	5.5151		18.7546	0.0177	0.7312	2.3884	0.4572	15.7498	4.9490	63.3950	24.2161	112.6651	29.5745	306.8723	43.7405	10504.3133	2.6113	155.5682	394.8803	1039.0095	0.2279	623.5115	0.0425	0.0042	2.1120	0.3940	707
	267	250.6663	3.2767	1173.4750	489209.4455	5.5946		16.7142	0.0407	1.0439	3.6646	0.5027	20.7745	7.3212	90.0178	35.8538	173.7948	41.7115	404.3503	81.2569	11786.0551	3.0924	169.4956	327.3069	402.3297	0.1761	877.0471	0.0425	0.0069	1.8091	0.5178	692
	269	365.2659	3.9236	1550.1439	492924.9463	11.4596	0.1113	40.7527	0.1793	1.8530	5.2314	0.9728	34.1659	10.6739	130.8494	50.8229	228.0584	51.3131	487.3752	88.8346	12090.3999	3.7989	547.9128	769.9034	70.7455	0.2224	1131.1939	0.0580	0.0073	3.0166	0.7117	707
	272	721.8284	4.8382	2205.7766	482763.9733	6.6316	0.2725	30.3149	0.5866	5.5441	10.6327	1.5919	46.7693	15.4140	175.7724	69.9651	321.4515	78.7545	792.5394	129.7340	10314.9595	2.6608	469.3194	813.7892	18.5896	0.2182	1679.3429	0.0488	0.0126	2.4924	0.5767	726
	271	326.9996	4.1951	1781.3897	485484.1233	7.9856	2.0301	27.9875	1.1298	7.6751	7.8486	1.3158	39.0514	13.4229	155.3414	59.7949	249.9567	61.2230	585.5390	109.1296	11298.1976	3.8053	276.1308	511.3968	4.5310	0.2298	1321.4456	0.0552	0.0097	2.0985	0.5400	713
	246	324.3689	3.1713	1039.7980	467992.4264	5.2902		17.4397	0.0391	0.5718	2.1120	0.2918	19.8760	7.1205	90.9955	33.7907	147.7642	39.4722	415.4989	64.9641	10595.3045	3.4214	163.4938	370.5416	437.9099	0.1377	839.9366	0.0396	0.0061	1.5462	0.4412	689

Isotope ratios and ages are NOT corrected for initial common Pb.
Isotope ratio and apparent age errors do NOT include systematic calibration errors of 0.32% ($^{207}Pb/^{206}Pb$), 1.82% (206Pb/238U) (all 2-sigma).
Isotope ratios and ages corrected using a measured linear secondary standard age bias - ^{206}Pb count rate relationship.
Trace element concentrations in ppm, calculated using mean count rate method.
Sweep-by-sweep downhole fractionation of U/Pb ratios NOT corrected via Si/Zr fractionation factor. Backgrounds were monitored between sweeps 5 to 20

Table A.2. Summary of geochronology analyses for sample CL8025 from stop 17, v-chapter 2.

			Apparent Ages (Ma)					Isotope ratios							
Sample No	SpotNum	Type	207Pb*/206Pb*	±2s (Ma)	206Pb*/238U*	±2s (Ma)	% disc.	207Pb*/235U*	±2s (%)	206Pb*/238U	±2s (%)	error corr.	207Pb*/206Pb*	±2s (%)	error corr.
CL8025	1	1	1047	29	1021	23	2.49	1.75648	2.80097	0.17166	2.40761	0.85956	0.07421	1.43139	0.00000
	7	1	1052	28	978	23	7.04	1.68013	2.89687	0.16381	2.54207	0.87752	0.07439	1.38916	0.00000
	9	1	1047	25	971	32	7.26	1.66274	3.72659	0.16253	3.51494	0.94321	0.07420	1.23801	0.00000
	13	1	1039	34	980	26	5.69	1.67218	3.34724	0.16412	2.89410	0.86462	0.07390	1.68172	0.00000
	21	1	1048	31	982	28	6.24	1.68460	3.40062	0.16460	3.02655	0.89000	0.07423	1.55054	0.00000
	28	1	1051	40	999	24	4.93	1.71946	3.28971	0.16771	2.61129	0.79378	0.07436	2.00084	0.00000
	3	2	1018	34	1019	20	-0.07	1.72791	2.71037	0.17129	2.13442	0.78750	0.07316	1.67045	0.00000
	17	2	1059	38	974	22	8.05	1.67863	3.10517	0.16308	2.48154	0.79916	0.07465	1.86656	0.00000
	22	2	1013	35	959	23	5.32	1.61310	3.09514	0.16037	2.56009	0.82713	0.07295	1.73948	0.00000
	23	2	1030	29	980	22	4.89	1.66566	2.78725	0.16416	2.38663	0.85627	0.07359	1.43970	0.00000
	32	2	1060	33	984	22	7.18	1.69833	2.90318	0.16491	2.40841	0.82958	0.07469	1.62111	0.00000
	33	2	1035	28	1025	15	1.02	1.75277	2.12866	0.17231	1.61409	0.75827	0.07378	1.38777	0.00000
	34	2	1047	34	1002	22	4.24	1.72050	2.88094	0.16820	2.33232	0.80957	0.07419	1.69117	0.00000
	36	2	1093	46	994	21	9.07	1.74482	3.19663	0.16668	2.24724	0.70300	0.07592	2.27340	0.00000
	37	2	1026	39	1000	25	2.55	1.69826	3.30356	0.16774	2.66921	0.80798	0.07343	1.94650	0.00000
	47	2	1029	34	980	27	4.77	1.66369	3.43244	0.16410	2.97887	0.86786	0.07353	1.70528	0.00000
	50	2	1014	36	982	25	3.08	1.65661	3.28463	0.16462	2.76532	0.84190	0.07299	1.77251	0.00000
	53	2	1050	28	998	20	4.96	1.71456	2.55300	0.16736	2.13342	0.83565	0.07430	1.40225	0.00000
	54	2	1060	34	980	25	7.60	1.69035	3.19200	0.16413	2.70934	0.84879	0.07469	1.68771	0.00000
	55	2	1017	32	971	27	4.58	1.63872	3.37026	0.16253	2.98331	0.88519	0.07313	1.56797	0.00000
	58	2	1006	47	983	28	2.31	1.65185	3.86068	0.16473	3.10461	0.80416	0.07273	2.29482	0.00000
	59	2	1073	42	984	25	8.33	1.70841	3.41201	0.16484	2.70775	0.79359	0.07517	2.07603	0.00000
	61	2	1023	53	988	21	3.42	1.67581	3.51002	0.16571	2.33302	0.66468	0.07334	2.62245	0.00000
	38	2	1097	16	1006	29	8	1.77074	3.21150	0.16880	3.10650	0.96730	0.07608	0.81450	0.00000
	10	3	1058	60	961	22	9.15	1.65463	3.84856	0.16082	2.43988	0.63397	0.07462	2.97630	0.00000
	2	3	1059	50	1034	20	2.36	1.78981	3.27787	0.17393	2.11858	0.64633	0.07464	2.50121	0.00000
	6	3	1054	62	1002	22	4.92	1.72586	3.90823	0.16813	2.40421	0.61517	0.07445	3.08124	0.00000
	16	3	1041	56	980	22	5.86	1.67453	3.67074	0.16417	2.39186	0.65160	0.07398	2.78449	0.00000
	19	3	1017	49	994	20	2.24	1.68011	3.25077	0.16670	2.17916	0.67035	0.07310	2.41221	0.00000
	42	3	1026	38	997	22	2.85	1.69329	3.05520	0.16723	2.41071	0.78905	0.07344	1.87689	0.00000
	43	3	1054	40	989	26	6.19	1.70133	3.47655	0.16573	2.84136	0.81729	0.07445	2.00327	0.00000
	44	3	1044	35	988	28	5.39	1.69157	3.54947	0.16558	3.09262	0.87129	0.07409	1.74198	0.00000
	45	3	1067	37	971	28	8.94	1.67991	3.61778	0.16261	3.10051	0.85702	0.07493	1.86420	0.00000
	48	3	977	58	990	26	-1.28	1.63994	4.04186	0.16591	2.86301	0.70834	0.07169	2.85303	0.00000
	49	3	1050	60	989	21	5.81	1.69844	3.74927	0.16578	2.25894	0.60250	0.07431	2.99236	0.00000
	56	3	1041	39	1011	30	2.84	1.73275	3.73591	0.16987	3.20530	0.85797	0.07398	1.91914	0.00000
	57	3	1008	50	1005	29	0.34	1.69277	3.98345	0.16866	3.12708	0.78502	0.07279	2.46765	0.00000

Table A.2 (cont'd)

Sample No	SpotNum	Trace element concentrations (ppm)																												Ti-in-zircon
		P	Ti	Y	Zr	Nb	La	Ce	Pr	Nd	Sm	Eu	Gd	Tb	Dy	Ho	Er	Tm	Yb	Lu	Hf	Ta	Th	U	Ce/Ce*	Eu/Eu*	ΣREE	(Gd/Yb)cn	Lu/Hf	Nb/Ta	Th/U	T(°C)
CL8025	1	383.2576	4.2748	1049.4015	462249.8564	3.5451		25.7904	0.0934	1.8172	5.5305	1.7605	27.0806	9.3424	111.3068	40.8101	177.8677	48.2448	571.8317	63.4012	9549.3253	1.5176	172.7977	459.4359	270.92	0.44	1085	0.04	0.01	2.34	0.38	690
	7	266.0041	6.5379	1128.8533	444130.0092	8.0414		52.4195	0.1499	2.3487	5.8161	1.3698	30.2924	10.6706	122.3627	43.4538	186.3813	50.1858	584.4732	61.2523	9304.3019	3.8626	312.1376	736.5972	343.02	0.32	1151	0.04	0.01	2.08	0.42	727
	9	289.7492	6.0893	1035.1345	394656.5597	6.8631		29.9724	0.0208	1.7738	5.1212	1.6906	25.4748	9.0952	110.7628	37.8180	179.9698	50.7188	678.8673	66.3850	8183.7129	3.3053	135.3838	506.0624	1412.38	0.45	1198	0.03	0.01	2.08	0.27	721
	13	405.8567	4.6147	838.0143	423802.6516	2.9524	0.0835	21.0464	0.1248	1.9996	4.2663	1.1893	19.3155	7.4391	89.2108	31.9790	142.3992	38.8022	490.2950	50.8414	8963.9979	1.3636	117.6746	381.5387	50.56	0.40	899	0.03	0.01	2.17	0.31	697
	21	334.9144	5.4761	1315.6695	437922.3542	9.5117		58.6594	0.1606	2.9737	8.2191	1.6523	32.4351	12.0167	142.5041	49.2664	224.2542	60.8163	679.9707	69.4508	9433.4880	4.6671	367.7987	833.7413	358.25	0.31	1342	0.04	0.01	2.04	0.44	711
	28	455.2441	4.4549	1243.2514	422726.4488	4.3092		31.2646	0.0742	2.0029	5.5210	1.7201	28.3757	10.6203	125.2041	47.3686	201.1479	56.4141	694.9071	73.4087	8466.5094	2.2581	195.5241	531.1847	413.18	0.42	1278	0.03	0.01	1.91	0.37	694
	3	242.5851	4.0596	628.4288	460373.7126	3.2123		16.9074	0.0323	0.6811	1.8438	0.4280	13.5317	4.8480	63.3686	24.1984	104.6340	29.6794	349.3825	40.0486	10925.7550	1.7082	82.8702	260.4453	513.30	0.26	650	0.03	0.00	1.88	0.32	686
	17	291.1472	3.1632	610.5094	400951.4537	2.8777		17.1978		1.0856	2.4594	0.7027	12.9672	4.7723	61.7462	21.7159	103.6916	28.4622	346.6092	36.4012	8986.4730	1.5691	78.3405	277.0398		0.38	638	0.03	0.00	1.83	0.28	666
	22	281.4425	3.0924	640.0774	464823.1763	3.8157		17.9171	0.0344	1.0269	2.4275	0.5988	13.4096	4.6408	67.2086	22.9264	108.8922	30.9592	366.8368	38.9731	10820.3771	2.0257	90.4167	277.7962	510.32	0.32	676	0.03	0.00	1.88	0.33	664
	23	412.8707	4.2810	1127.6514	454051.5655	3.8322		27.1742	0.0943	2.0264	6.0490	1.7710	25.0156	9.0473	116.5949	41.6831	180.3323	51.0962	600.6531	65.9091	9372.9435	2.0299	175.1366	478.0694	282.65	0.44	1127	0.03	0.01	1.89	0.37	690
	32	433.4994	5.3593	1087.0354	421938.5405	3.6319	0.2259	29.3640	0.3460	4.5597	5.5568	1.9382	28.1476	9.8067	117.7650	41.7388	176.3388	48.1627	584.6293	63.2125	8799.7929	1.8435	177.0855	471.1284	25.76	0.47	1112	0.04	0.01	1.97	0.38	710
	33	560.6941	6.6273	1590.7156	412254.3772	5.5574	0.0294	46.1335	0.1904	3.5567	10.2369	2.7799	41.0159	14.6601	174.4835	62.0131	270.9057	71.1546	875.9982	89.9640	8048.1652	2.6530	329.3496	691.9841	151.04	0.41	1663	0.04	0.01	2.09	0.48	729
	34	233.9296	3.3340	1211.7040	437450.4947	3.0076		31.4054	0.0458	1.4426	6.4665	1.1084	31.5659	10.3959	133.2037	47.3247	190.6285	53.4447	633.7795	65.7090	10001.5674	1.7473	248.6088	308.9849	672.27	0.24	1207	0.04	0.01	1.72	0.80	670
	36	364.6860	4.7003	800.5191	406585.8897	3.8572	0.0481	20.8865	0.1036	1.2235	3.1589	1.1642	16.6815	7.2936	92.2327	30.5564	128.8822	39.0252	455.0772	48.0580	9151.4491	2.1728	129.2242	379.9362	72.56	0.49	844	0.03	0.01	1.78	0.34	698
	37	308.6542	4.4243	1311.6354	404956.8015	3.9883	0.1036	31.4135	0.3476	6.8025	12.2806	3.3307	40.6269	14.2992	157.1237	53.2955	223.0906	60.5944	675.8943	68.9112	8220.3089	1.5638	264.8657	567.6615	40.58	0.46	1348	0.05	0.01	2.55	0.47	693
	47	282.0430	3.8686	672.8223	423028.8180	3.2405		18.4344	0.0620	1.3063	3.6594	0.6067	14.5095	5.8882	71.3094	24.0815	109.8066	32.8242	383.6222	40.9838	9397.1405	1.6522	85.8496	304.8477	291.82	0.25	707	0.03	0.00	1.96	0.28	682
	50	456.0062	4.7033	1142.9180	433240.0655	3.7548		29.4717	0.0866	2.0188	5.2807	1.8154	28.0646	9.9826	126.8625	43.1112	186.9812	52.8339	634.7811	65.2879	8241.1275	1.8180	197.5111	549.2735	333.72	0.46	1187	0.04	0.01	2.07	0.36	698
	53	298.4096	4.1545	851.3988	405476.4683	5.0459		30.1653	0.0788	1.4371	5.1742	1.0565	22.9454	7.3543	90.9306	31.0471	142.0003	42.1746	501.6652	52.4752	8956.9182	3.7027	145.3385	618.6673	375.59	0.30	929	0.04	0.01	1.36	0.23	688
	54	261.9684	4.7789	992.0120	406509.3353	6.3559	0.6117	26.7104	0.1892	2.3857	3.8158	1.1405	25.0621	8.2799	104.4018	39.6204	172.8264	49.8257	631.1426	65.1423	8513.0893	3.7385	121.4672	528.5868	19.25	0.36	1131	0.03	0.01	1.70	0.23	700
	55	301.8919	4.2607	745.8862	413564.7108	2.8758		20.0615	0.0629	1.5383	4.5298	0.8485	19.3282	6.2963	77.5570	28.9188	120.9142	35.6377	428.5951	44.8270	8827.3489	1.7074	106.4386	346.2941	312.82	0.28	789	0.04	0.01	1.68	0.31	690
	58	250.1996	3.9165	539.3021	411155.0314	3.0080		16.7474	0.0260	0.9019	1.6479	0.8360	10.4814	4.4658	57.5607	21.6168	94.7088	27.8061	338.6248	36.0981	9706.5707	2.1961	77.8343	295.8381	631.09	0.61	612	0.03	0.00	1.37	0.26	683
	59	249.9854	3.5309	545.5942	405384.5861	2.7746		16.0676	0.0309	0.5660	2.3854	0.3692	10.8353	4.2789	54.8971	20.4286	89.7744	24.9396	324.6639	34.6440	9703.8460	1.6883	73.6769	288.2749	509.77	0.22	584	0.03	0.00	1.64	0.26	674
	61	203.3541	4.1144	744.8546	414088.5068	2.5455		23.6751	0.0446	0.4169	3.5660	0.8799	17.3765	6.2835	79.4763	27.9419	126.7082	34.9510	412.0707	42.7155	9862.8641	1.6080	126.0802	278.1509	521.06	0.34	776	0.03	0.00	1.58	0.45	687
	38	322.6406	31.9970	1415.4485	434952.1149	6.5037	13.1315	55.0303	2.7698	19.5387	12.8198	3.4700	45.3430	14.2404	159.7939	53.1331	232.9106	60.7969	673.1278	70.0549	8480.2291	2.7628	371.0800	687.0121	2.24	0.44	1416	0.06	0.01	2.35	0.54	895
	10	240.1426	3.6238	510.7198	401618.1189	4.6171		16.6631		0.6086	2.6226	0.5370	8.7644	4.4985	54.8215	18.6740	84.6569	24.7497	290.8907	29.2576	9781.8490	2.4666	109.7927	243.8025		0.34	537	0.02	0.00	1.87	0.45	677
	2	160.7509	4.0029	672.3480	445087.9737	4.1694		19.9919		0.2503	2.8235	0.4982	13.5635	5.0730	65.7788	24.3656	112.0098	30.4416	378.1672	39.1691	11283.8630	2.3882	133.2982	219.4570		0.25	692	0.03	0.00	1.75	0.61	685
	6	244.8582	3.8270	679.1822	449769.7445	4.4764		16.9744		0.3140	1.9479	0.3426	10.7649	4.3758	63.4749	26.2349	118.1299	34.4937	418.5544	47.2647	11673.5340	2.2549	99.5072	161.3707		0.23	743	0.02	0.00	1.99	0.62	681
	16	221.9850	3.7830	609.3051	413481.0885	4.4141		18.7574		0.7258	2.2265	0.3320	10.8528	4.9084	61.9767	23.1521	103.4861	29.1100	352.1007	37.2679	10603.4578	2.6589	125.2799	237.2873		0.21	645	0.03	0.00	1.66	0.53	680
	19	229.2435	4.6428	580.4208	433639.2256	3.6321		21.1431		0.4859	2.6975	0.5293	13.0096	4.9341	64.1288	22.5808	94.7623	26.5411	301.1269	30.4443	11390.9685	3.0349	167.3565	295.2805		0.27	582	0.04	0.00	1.20	0.57	697
	42	287.8044	4.6612	824.0029	425820.7355	5.7669		27.7602	0.1109	1.4966	4.7650	1.0294	22.5166	8.1464	94.6005	31.2306	135.4834	35.9178	409.6675	41.4726	10344.1875	3.9050	254.6647	438.1523	245.48	0.30	814	0.05	0.00	1.48	0.58	698
	43	244.3355	4.7696	768.9705	428040.9839	4.6099		19.2391	0.0042	0.8394	3.8154	0.6197	17.5481	6.4949	84.5348	30.5202	126.9965	35.2193	397.7173	39.6627	10326.4754	2.8625	163.3657	266.4141	4479.97	0.23	763	0.04	0.00	1.61	0.61	700
	44	186.4410	4.2318	636.8751	418669.8959	4.1271		19.5356		0.8734	2.4709	0.8255	14.8311	5.7433	65.2938	23.0350	100.0937	27.1348	314.5034	32.2300	10240.6780	2.4216	149.8908	251.9565		0.42	607	0.04	0.00	1.70	0.59	689
	45	200.2875	3.5249	834.8549	443474.6219	3.7360		23.1972		1.3312	4.2473	0.8294	17.9144	7.4468	88.4543	33.4186	138.6311	36.8135	446.1483	45.1733	10726.7978	1.8010	190.2545	290.4874		0.29	844	0.03	0.00	2.07	0.65	674
	48	223.2822	4.2124	603.7386	419800.3800	4.6333		16.9742		0.8854	1.1658	0.3829	9.9635	4.8007	59.4410	23.0189	112.0513	31.4183	404.0515	44.2290	10797.4392	2.3414	92.4947	161.7595		0.34	708	0.02	0.00	1.98	0.57	689
	49	246.8777	3.8368	632.7050	420938.1953	4.5476		15.2189	0.0078	0.2628	1.5433	0.3631	9.0936	4.6204	60.6542	24.5695	116.0048	34.5768	437.6195	47.0697	10585.9134	1.9311	92.4835	166.4925	1916.37	0.30	752	0.02	0.00	2.35	0.56	681
	56	235.7066	4.4279	522.1307	400211.9604	4.5545		21.6982	0.0378	0.5098	2.9303	0.5882	11.6706	4.9281	60.3913	19.9888	81.2749	22.3257	248.9649	24.9999	10259.4958	2.0579	174.1878	324.8162	563.27	0.31	500	0.04	0.00	2.21	0.54	693
	57	214.3188	3.1446	583.9413	404339.3855	4.0048		16.7234	0.0300	0.5567	1.3147	0.3859	10.7877	3.5701	59.7755	22.1372	101.2654	29.8547	385.2195	38.5745	9955.0440	2.1149	89.5674	164.6086	546.69	0.31	670	0.02	0.00	1.89	0.54	665

Isotope ratio and date errors do not include systematic calibration errors of 0.32% ($^{207}Pb/^{206}Pb$) and 0.52% ($^{206}Pb/^{238}U$) (2 sigma).
Trace element concentrations in ppm, calculated using mean count rate method.
Sweep-by-sweep downhole fractionation of U/Pb ratios NOT corrected via Si/Zr fractionation factor.
Backgrounds were monitored between sweeps 5 to 20. Sample counts were integrated from sweeps 35 to 60.
Trace element concentrations from analyses with U<27 ppm and known to have intersected inclusions of other minerals based on P and Ti were not included.
Ablation used a laser spot size of 25 microns, and a laser firing repetition rate of 10 Hz.
Ti-in-zircon temperatures calculated using the pressure independent geothermometer of Watson *et al.*, (2006).
Activity of TiO2 for Ti-in-Zircon temperature calculation is 0.8.

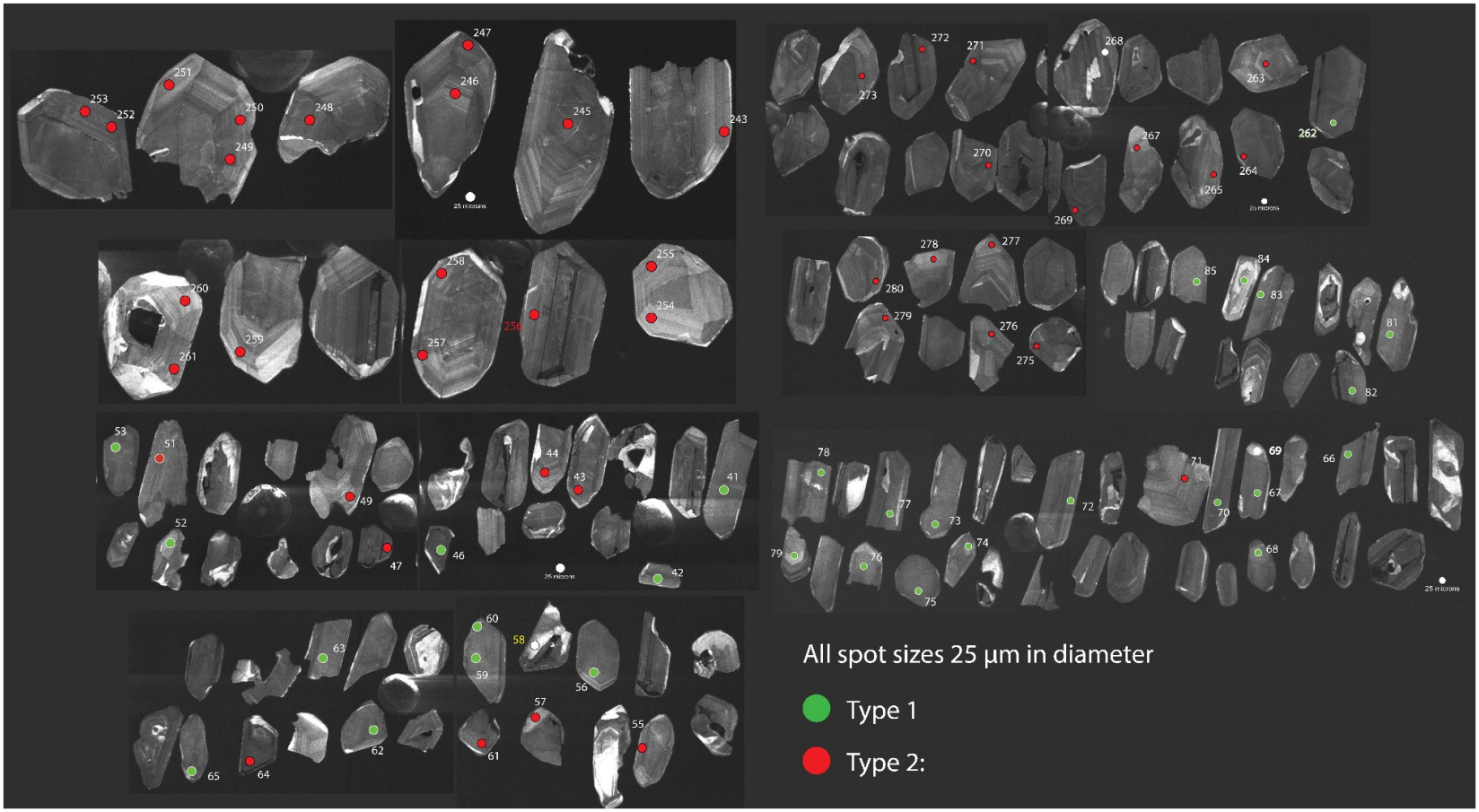

Figure A.1. Cathodoluminescence images of all zircons separated from sample CL6144 from stop 16, v-chapter 2.

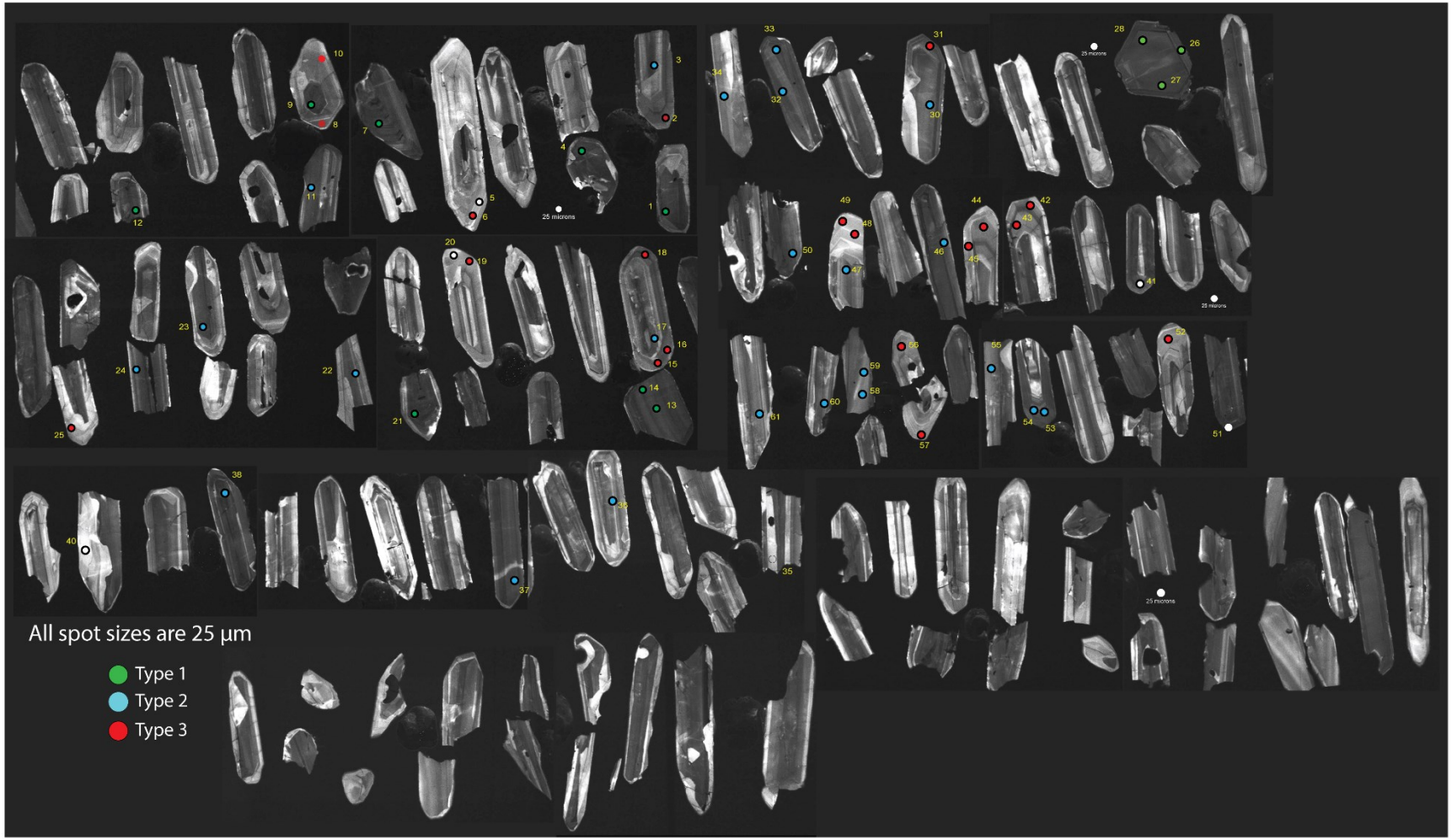

Figure A..2. Cathodoluminescence images of all zircons separated from sample CL8025 from stop 17, v-chapter 2.

APPENDIX B SUPPLEMENTARY GEOCHEMICAL DIAGRAMS

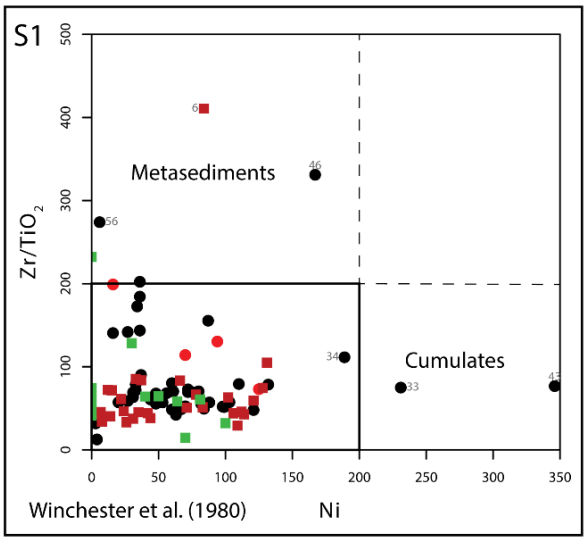

Figure B.1. Ni-Zr/TiO_2 of Winchester *et al.*, (1980) to identify metasedimentary protoliths and mineral cumulates.

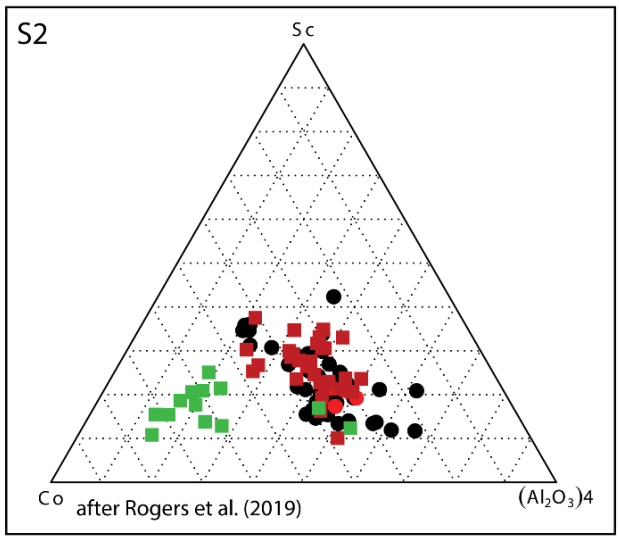

Figure B.2. Co, Sc, (Al2O3 x 4) ternary diagram after Rogers *et al.* (2019) used to test for fractional crystallization. Samples fall away from the main cluster were likely affected by fractional crystallization or crystal accumulation that drew the magma composition away from the main cluster. Trends away from Co indicate excess olivine fractionation, trends away from Sc indicate excess pyroxene fractionation and trends away from Al_2O_3 indicate excess plagioclase fractionation. Trends towards the apices indicate corresponding crystal accumulation in the melt.

Legend:

- Unknown samples (this study)
- Renzy Terrane samples (this study)
- Renzy Terrane samples (Montreuil and Constantine, 2010)
- Bondy Gneiss Complex (Blein et al., 2003)
- Canyon domain (Maity and Indares 2018)

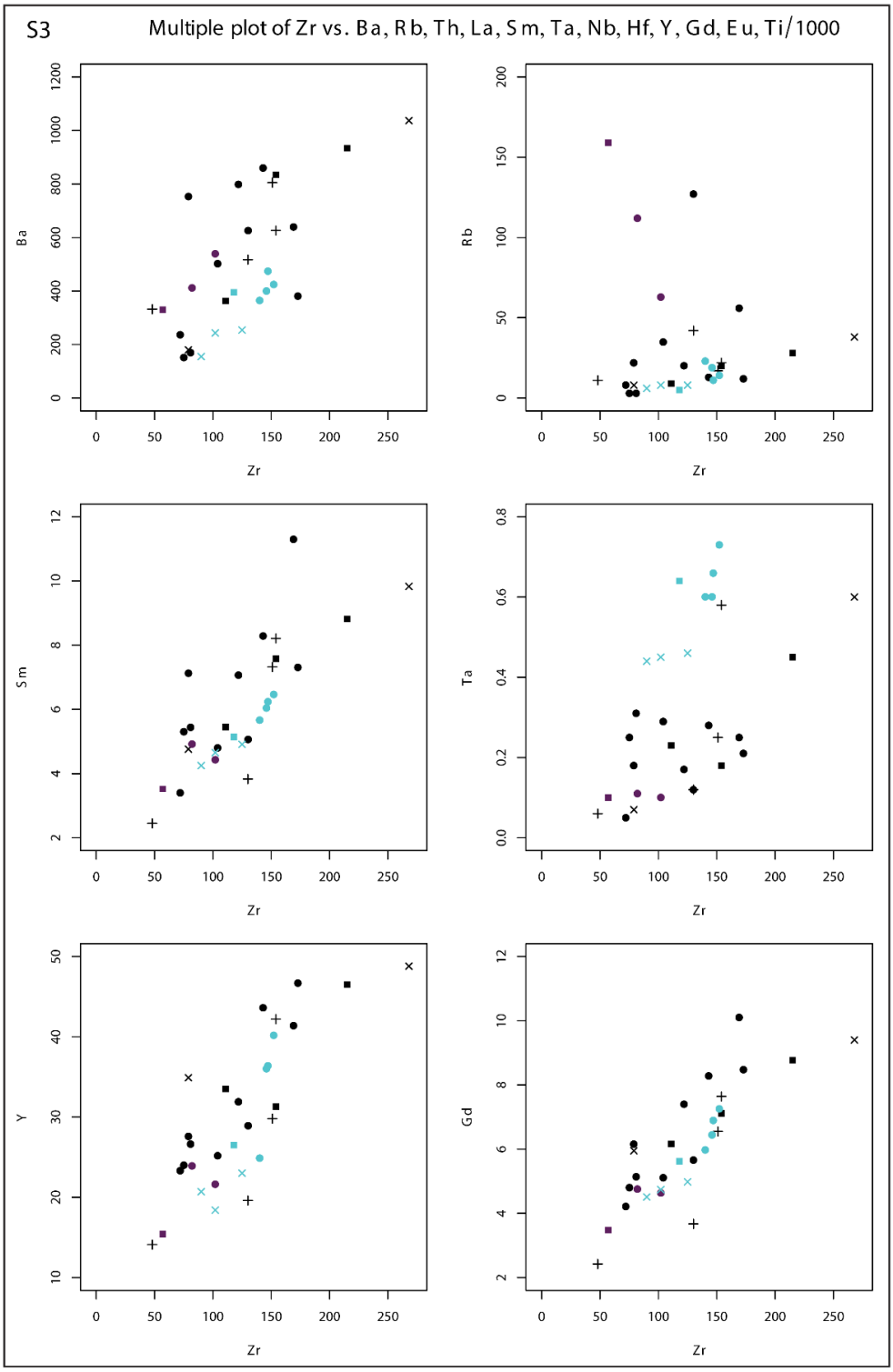

Figure B.3. Bivariate plots of Zr vs select trace elements to test for trace element mobility. Symbology represents the field-based subdivision and geochemical classification defined in this study. See legend in Figure. B.8.

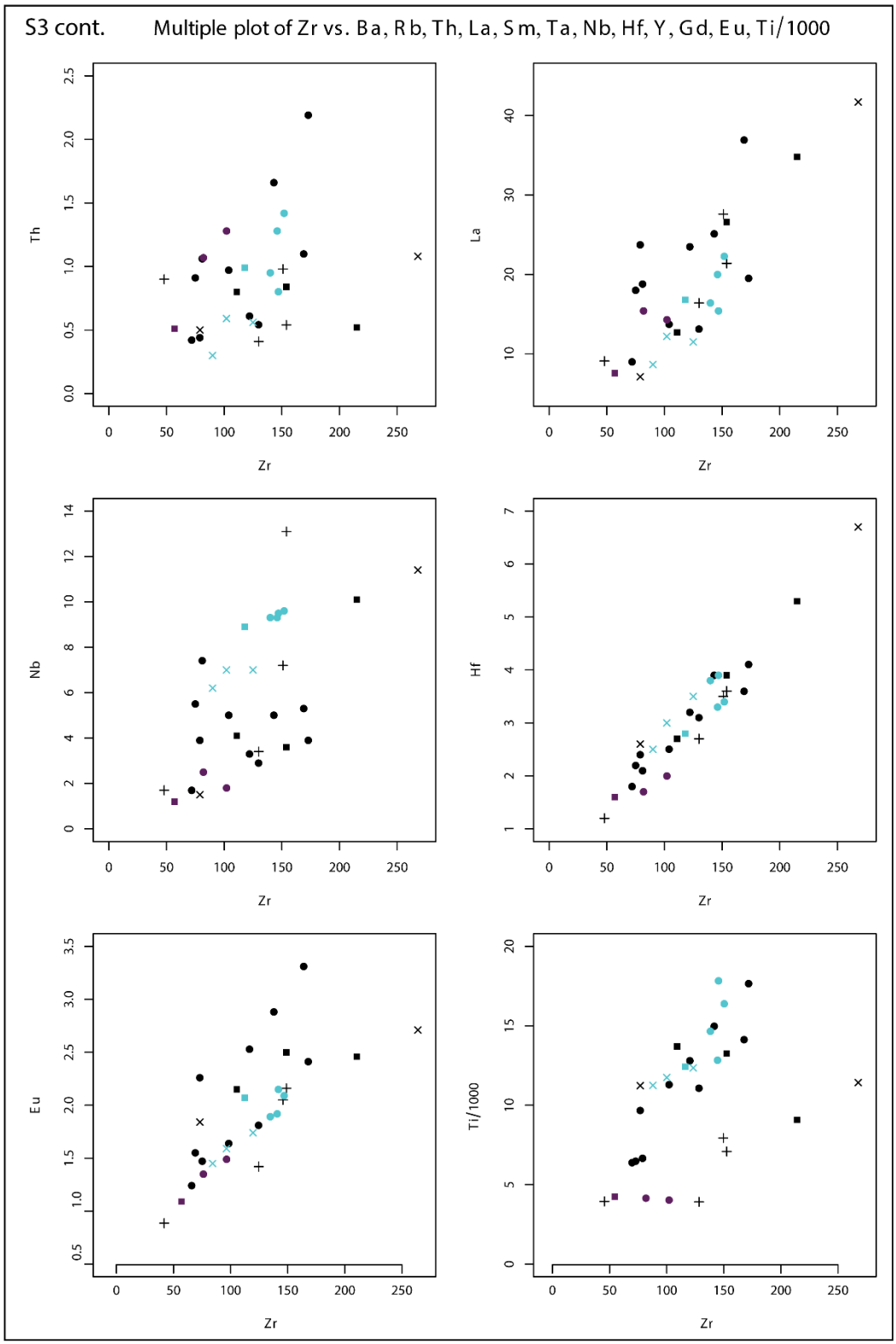

Figure B.3 (cont'd).

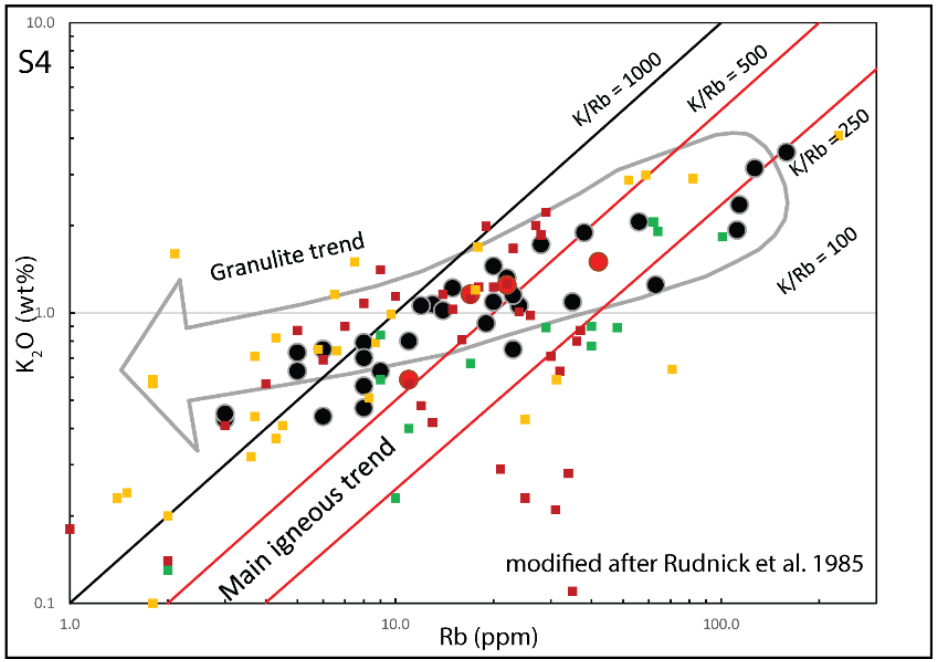

Figure B.4. The K/Rb ratio diagram to test for element mobility in metamorphosed mafic rocks collected in this study and mafic granulites of the Renzy Terrane, Bondy Gneiss complex and Canyon Domain. After Rudnick *et al.* (1985).

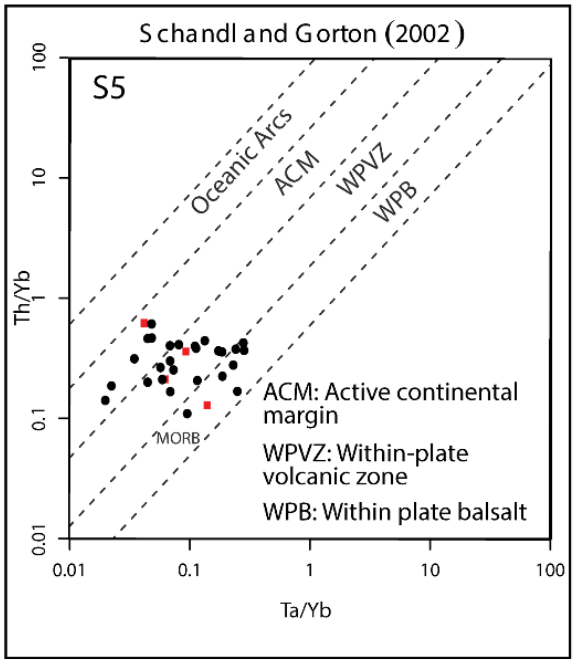

Figure B.5. Ta/Yb – Th/Yb diagram of Schandl and Gorton (2002) that was employed by La Flèche *et al.* (2005) to test for Th mobility.

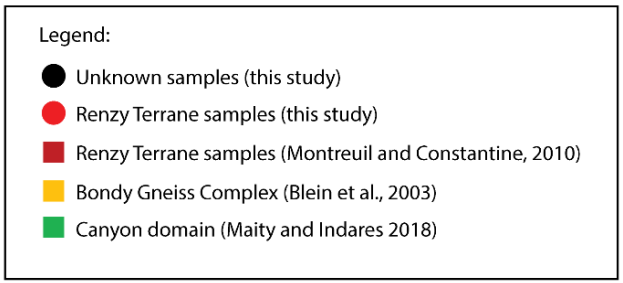

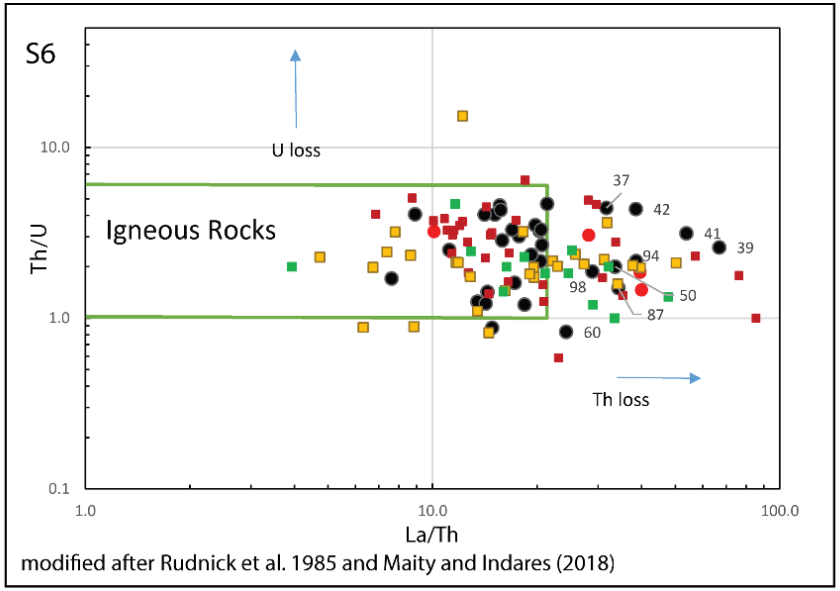

Figure B.6. La/Th and Th/U diagram to test for U and Th loss within metamorphosed mafic rocks collected in this study and mafic granulites of the Renzy Terrane, Bondy Gneiss complex and Canyon Domain. After Rudnick *et al.* (1985), modified by Maity and Indares (2018).

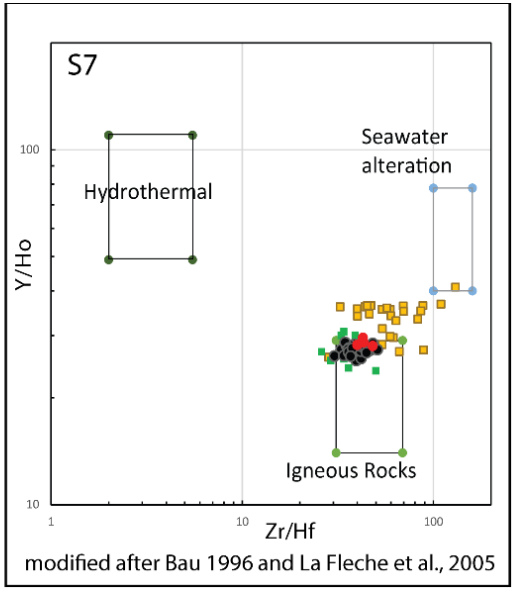

Figure B.7. Zr/Hf – Y/Ho diagram to assess REE mobility by metasomatic fluids of mafic rocks collected in this study and mafic granulites of the Renzy Terrane, Bondy Gneiss complex and Canyon Domain. After of Bau (1996).

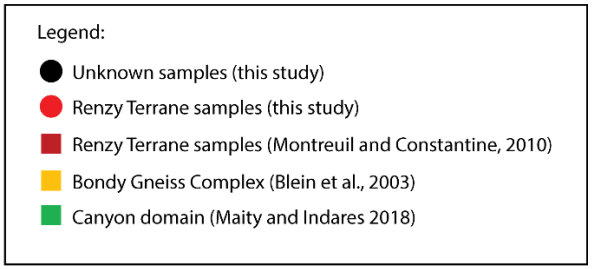

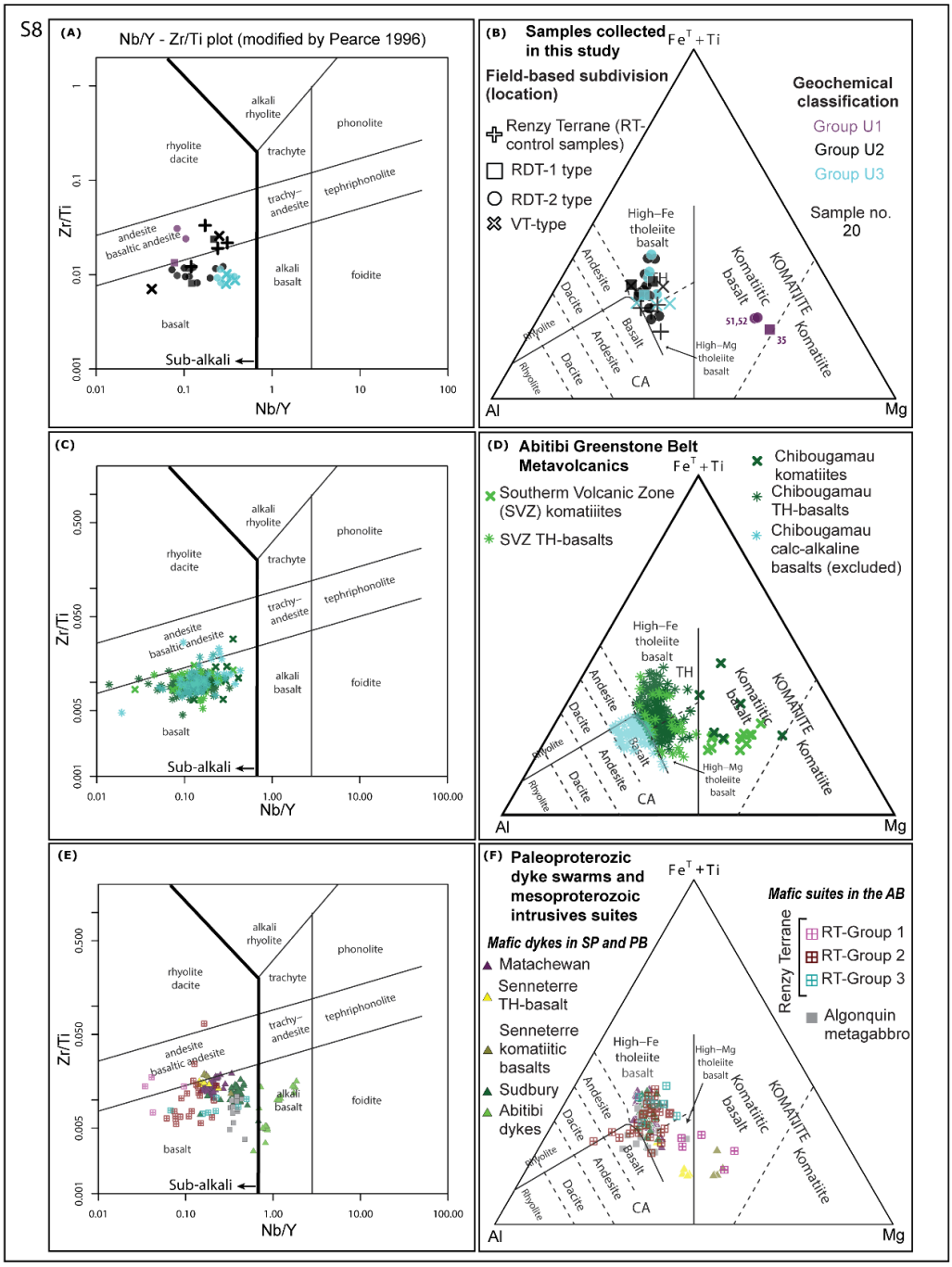

Figure B.8. Geochemical rock classification schemes for all the mafic suites discussed in this study according to the Trace-element TAS proxy diagram (A,C,E) of Winchester and Floyd, 1977 (modified by Pearce, 1996) and the Al_2O_3-($FeO+Fe_2O_3+TiO_2$)-Mg cation diagram (B,D,F) after Jensen (1976). (A, B) Mafic samples collected during this study. Note that all possible mafic entries classified as calc-alkaline on Jensen (1976) diagram were excluded for correlative purposes in this study.

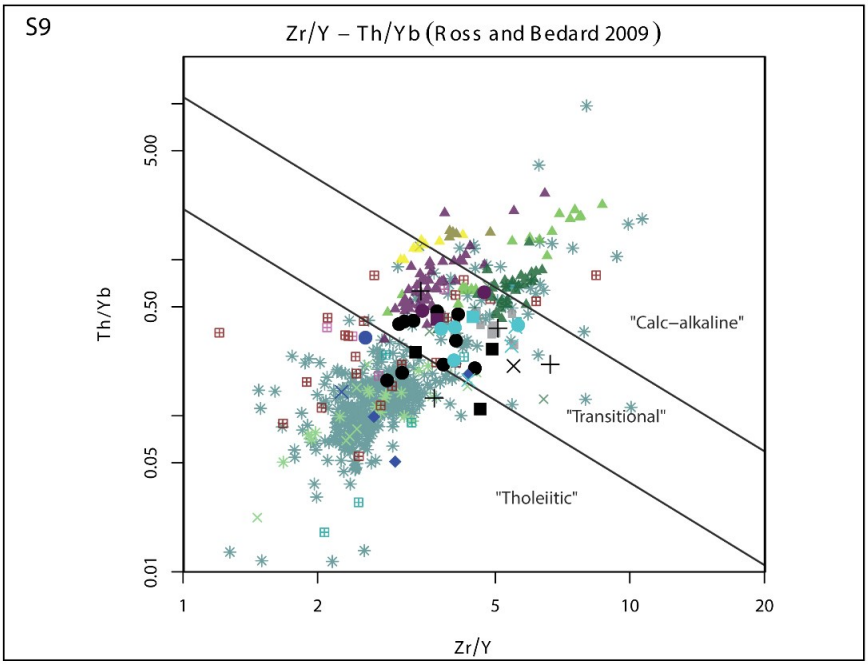

Figure B.9. Zr/Y – Th/Yb mafic affinity classification diagram of Ross and Bédard (2009). Symbology as in figure. B.8.

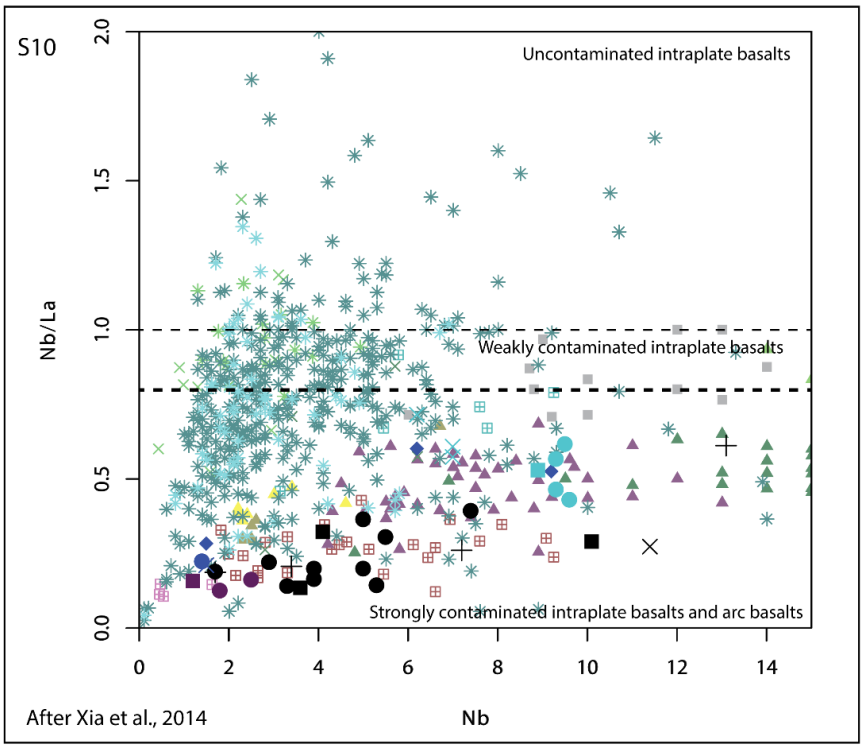

Figure B.10. Nb – Nb/La diagram to differentiate between uncontaminated intra-crustal and arc basalts. After (Xia, 2014b). Symbology as in figure. B.8.

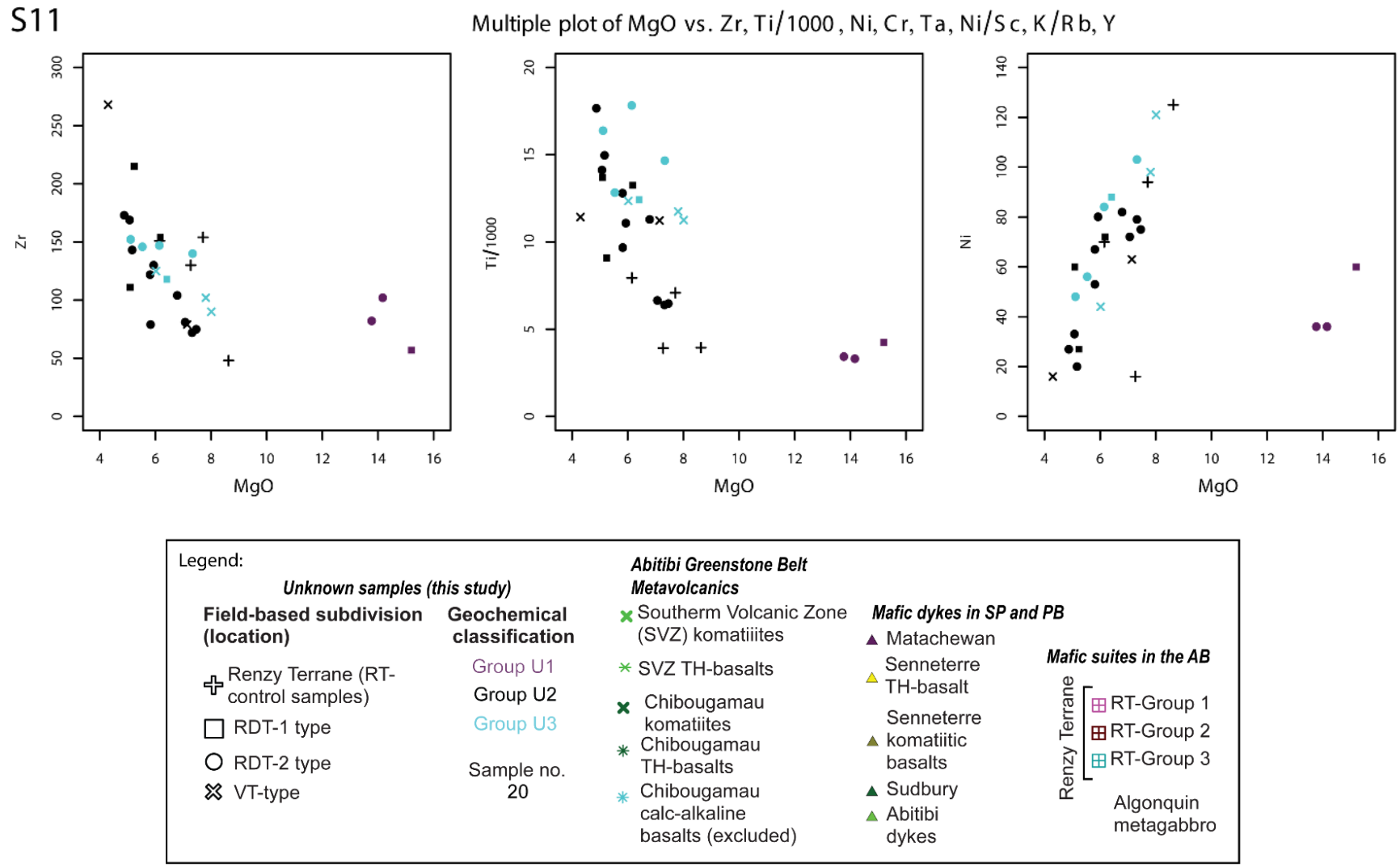

Figure B.11. Bivariate plots of MgO vs select trace elements to asses if the geochemical groups defined herein form distinct groups, define fractionation trends and/or are contiguous

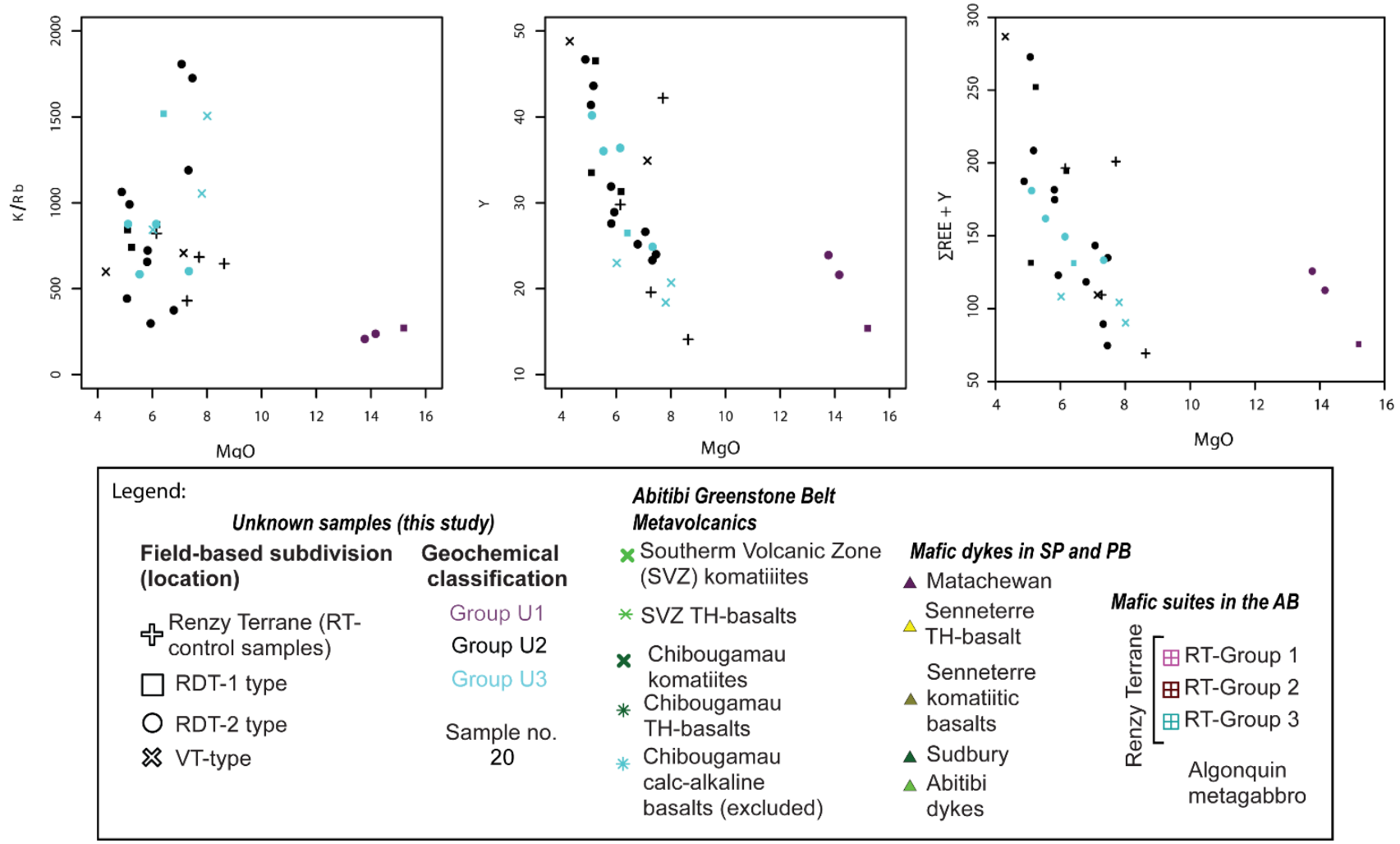

Figure B.11 (cont'd)

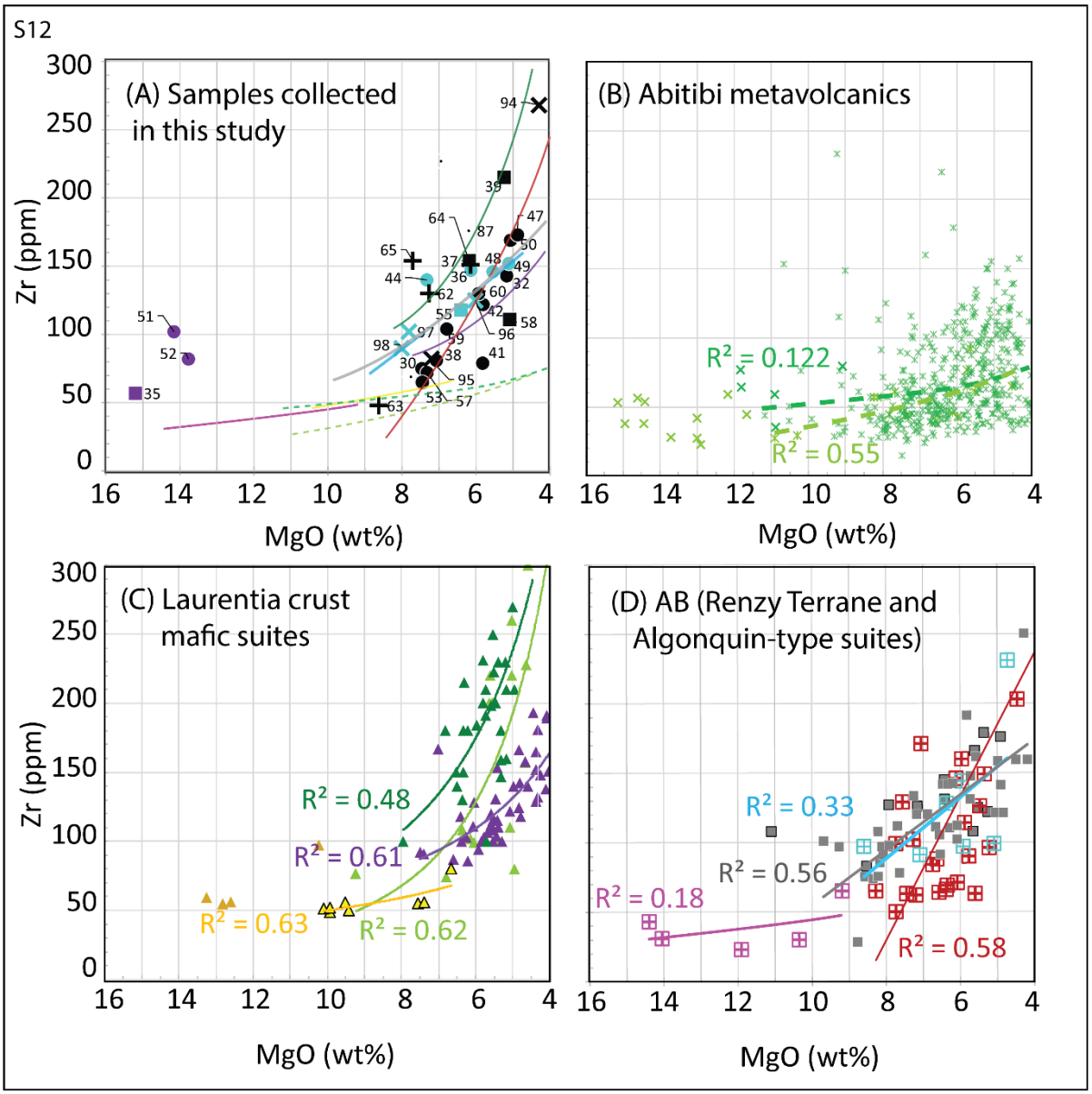

Figure B.12. Bivariate MgO (wt%) vs Zr (ppm) diagrams for (A) samples collected in this study, superimposed over the lines of best fit derived from the respective PMEs. (B) Mafic metavolcanics from SVZ and Chibougamau regions in the Abitibi Belt of the Superior Province. (C) Proterozoic mafic dyke swarms. (D) Mafic groups in the Renzy Terrane and Algonquin Suite. Note the trend line for the Algonquin PME suite is derived from datapoints (small grey boxes) digitized from Ketchum and Davidson (2000) . Symbology as in figure 3.S11.

Table B.1. Geochemistry of unknown mafic samples analyzed in this study

Sample reference no.	35	51	52
Sample Number	**18CL6098B**	**17CL6089A1**	**17CL6089A2**
Latitude (Y)	47.0751	47.1431	47.1431
Longitude (X)	-76.5327	-76.6222	-76.6222
Geochemical Group	Group U1	Group U1	Group U1
Field based subdivision	RDT-1	RDT-2	RDT-2
Proposed Affinity	RT-Group 1	RT-Group 1	RT-Group 1
SiO2 (wt%)	47.90	49.34	49.79
Al2O3	6.92	7.81	7.24
Fe2O3(T)	9.45	11.52	11.17
MgO	15.20	14.16	13.77
MnO	0.18	0.21	0.20
CaO	13.97	12.23	12.14
Na2O	0.48	1.49	1.19
K2O	3.58	1.25	1.93
TiO2	0.71	0.55	0.57
P2O5	0.14	0.13	0.11
Cr2O3	0.27	0.10	0.10
LOI	1.02	0.60	1.10
Total	99.56	99.29	99.21
FeO	8.50	10.37	10.05
#Mg*	76.11	70.89	70.95
A.I.**	56.52	52.90	54.08
K/Na	11.35	1.60	3.10
CCPI***	85.38	89.95	88.42
K/Rb	271.22	239.01	207.58
Ag (ppm)	< 0.3	< 0.3	< 0.3
As	< 0.5	< 0.5	1.10
Au (ppm)	< 0.002	< 0.002	< 0.002
Ba	330.00	539.00	412.00
Be	< 1	< 1	2.00
Bi	0.10	< 0.1	0.10
Br	< 0.5	< 0.5	< 0.5
Cd	< 0.5	< 0.5	< 0.5
Co	55.00	62.00	62.00
Cr	1440.00	535.00	551.00
Cs	6.50	0.40	1.60
Cu	15.00	36.00	36.00
Fe (ppm)	65300.00	72900.00	71500.00
Ga	10.00	10.00	10.00
Ge	1.70	1.30	1.70

*#Mg (MgO/(MgO+Fe2O3))molecular
**Alteration index: 100x(Mgo+K2O)/MgO+K2O+Na2O+CaO)
***CCPI: 100 X (MgO+FeOt)/(MgO+FeOt+K2O+N2O))
****Chondrite normalized (Sun and McDonough, 1989)
FeOt = 0.8998 × Fe2O3
Ti = 5995 × TiO2

Sample reference no.	35	51	52
Hf	1.60	2.00	1.70
In	0.10	< 0.1	< 0.1
Ir (ppm)	0.01	<0.005	<0.005
Mo	< 1	< 1	< 1
Nb	1.20	1.80	2.50
Ni	60.00	36.00	36.00
Pb	3.00	< 3	6.00
P (ppm)	610.93	567.29	480.01
Rb	159.00	63.00	112.00
S	900.00	3200.00	2900.00
Sb	0.30	< 0.1	< 0.1
Sc	46.50	49.50	50.80
Se	< 3	< 3	< 3
Sn	1.00	< 1	1.00
Sr	67.00	201.00	116.00
Ta	0.10	0.10	0.11
Th	0.51	1.28	1.07
Ti (ppm)	4250.46	3315.24	3423.15
TL	0.85	< 0.05	0.24
U	0.58	0.51	0.75
V	242.00	209.00	203.00
W	< 0.5	< 0.5	< 0.5
Zn	79.00	68.00	68.00
Zr	57.00	102.00	82.00
La	7.58	14.30	15.40
Ce	19.90	32.90	39.40
Pr	3.05	4.26	4.95
Nd	14.40	18.50	19.90
Sm	3.52	4.43	4.92
Eu	0.98	1.49	1.35
Gd	3.48	4.64	4.75
Tb	0.52	0.70	0.73
Dy	3.00	4.07	4.24
Ho	0.57	0.79	0.84
Er	1.52	2.22	2.36
Tm	0.21	0.31	0.35
Yb	1.23	2.07	2.27
Lu	0.19	0.31	0.36
Y	15.40	21.60	23.90
∑REE	60.15	91.00	101.82
(La/Yb)****	4.42	4.96	4.87
(La/Sm)****	1.39	2.08	2.02
(Gd/Yb)****	2.34	1.85	1.73
(Tb/Yb)****	1.92	1.54	1.46
Eu/Eu****	0.86	1.00	0.85

Table B.1. (cont'd). Geochemistry of unknown mafic samples analyzed in this study

Sample reference no.	62	63	64	65
Sample Number	**17CL6111A3**	**17CL6119C3**	**17CL6120A2**	**17CL6120A1**
Latitude (Y)	46.9202	46.8620	46.8581	46.8581
Longitude (X)	-76.4244	-76.3586	-76.3563	-76.3563
Geochemical Group	Group U2	Group U2	Group U2	Group U2
Field based subdivision	RT-Type	RT-Type	RT-Type	RT-Type
Proposed Affinity	RT-Group 2	RT-Group 2	RT-Group 2	RT-Group 2
SiO2 (wt%)	48.11	48.81	48.65	45.92
Al2O3	16.64	16.70	16.57	16.35
Fe2O3(T)	12.93	9.69	12.10	13.88
MgO	7.27	8.63	6.15	7.71
MnO	0.19	0.16	0.17	0.23
CaO	9.47	11.45	9.19	10.02
Na2O	2.85	2.83	3.49	2.65
K2O	1.50	0.59	1.16	1.25
TiO2	0.65	0.66	1.32	1.18
P2O5	0.13	0.14	0.49	0.36
Cr2O3	0.01	0.04	0.02	0.03
LOI	0.44	0.57	0.47	0.56
Total	100.20	100.20	99.77	100.10
FeO	11.63	8.72	10.89	12.49
#Mg*	52.69	63.82	50.17	52.39
A.I.**	41.58	39.23	36.57	41.42
K/Na	1.07	0.40	0.63	0.81
CCPI***	81.29	83.53	78.56	83.82
K/Rb	430.21	646.10	821.96	684.43
Ag (ppm)	< 0.3	< 0.3	< 0.3	< 0.3
As	0.60	< 0.5	< 0.5	< 0.5
Au (ppm)	< 0.002	< 0.002	< 0.002	< 0.002
Ba	517.00	332.00	805.00	626.00
Be	1.00	< 1	1.00	2.00
Bi	< 0.1	< 0.1	< 0.1	< 0.1
Br	< 0.5	< 0.5	< 0.5	< 0.5
Cd	< 0.5	< 0.5	< 0.5	< 0.5
Co	49.00	44.00	39.00	49.00
Cr	48.00	220.00	98.00	161.00
Cs	0.90	0.40	0.20	0.10
Cu	17.00	58.00	89.00	92.00
Fe (ppm)	77800.00	61300.00	76800.00	88000.00
Ga	17.00	15.00	20.00	21.00
Ge	0.90	1.00	1.00	1.20
Hf	2.70	1.20	3.50	3.60

In	< 0.1	< 0.1	< 0.1	< 0.1
Ir (ppm)	<0.005	<0.005	<0.005	<0.005
Mo	< 1	< 1	< 1	< 1
Nb	3.40	1.70	7.20	13.10
Ni	16.00	125.00	70.00	94.00
Pb	6.00	< 3	6.00	< 3
P (ppm)	567.29	610.93	2138.24	1570.95
Rb	42.00	11.00	17.00	22.00
S	1900.00	1200.00	1900.00	2400.00
Sb	0.30	< 0.1	< 0.1	< 0.1
Sc	24.20	29.40	25.10	31.30
Se	< 3	< 3	< 3	< 3
Sn	< 1	< 1	< 1	2.00
Sr	329.00	545.00	785.00	571.00
Ta	0.12	0.06	0.25	0.58
Th	0.41	0.90	0.98	0.54
Ti (ppm)	3914.74	3944.71	7937.38	7086.09
TL	0.06	< 0.05	< 0.05	< 0.05
U	0.28	0.28	0.32	0.29
V	230.00	179.00	234.00	270.00
W	< 0.5	< 0.5	< 0.5	< 0.5
Zn	120.00	62.00	93.00	108.00
Zr	130.00	48.00	151.00	154.00
La	16.40	9.09	27.60	21.40
Ce	34.00	20.10	65.00	57.80
Pr	4.17	2.54	8.47	8.09
Nd	17.00	11.00	35.70	34.50
Sm	3.83	2.45	7.32	8.21
Eu	1.42	0.89	2.05	2.16
Gd	3.67	2.42	6.55	7.64
Tb	0.58	0.40	0.92	1.16
Dy	3.53	2.53	5.51	7.00
Ho	0.70	0.50	1.04	1.43
Er	2.00	1.46	2.96	4.06
Tm	0.29	0.21	0.41	0.61
Yb	1.92	1.43	2.69	4.16
Lu	0.31	0.21	0.41	0.64
Y	19.60	14.10	29.80	42.20
∑REE	89.82	55.23	166.63	158.86
(La/Yb)****	6.13	4.56	7.36	3.69
(La/Sm)****	2.76	2.40	2.43	1.68
(Gd/Yb)****	1.58	1.40	2.01	1.52
(Tb/Yb)****	1.37	1.27	1.55	1.27
Eu/Eu****	1.16	1.11	0.91	0.83

Table B. 1. (cont'd). Geochemistry of unknown mafic samples analyzed in this study

Sample reference no.	30	32	37	38	39
Sample Number	18CL6118D1	17CL6022B	18CL6109C1	18CL6118D2	18CL6091 Y
Latitude (Y)	46.8657	47.2204	46.9612	46.8657	47.1274
Longitude (X)	-76.3637	-76.7309	-76.4514	-76.3637	-76.6083
Geochemical Group	Group U2	Group U2	Group U2	Group U2	Group U2
Field based subdivision	RDT-2	RDT-2	RDT-1	RDT-2	RDT-1
Proposed Affinity	RT-Group 2	RT-Group 2	RT-Group 2	RT-Group 2	RT-Group 2
SiO2 (wt%)	51.48	48.33	46.87	52.71	51.50
Al2O3	14.86	12.65	14.59	15.60	14.81
Fe2O3(T)	10.78	17.66	15.55	10.26	12.36
MgO	7.46	5.17	6.18	7.07	5.24
MnO	0.23	0.27	0.20	0.26	0.21
CaO	10.57	8.83	7.44	9.72	7.91
Na2O	2.35	2.93	3.89	2.54	3.27
K2O	0.43	1.07	1.45	0.45	1.72
TiO2	1.08	2.50	2.21	1.11	1.52
P2O5	0.31	0.65	0.70	0.35	0.42
Cr2O3	0.04	< 0.01	0.02	0.04	< 0.01
LOI	0.35	0.23	0.87	0.26	0.67
Total	99.90	100.30	99.94	100.30	99.64
FeO	9.70	15.89	13.99	9.23	11.12
#Mg*	57.82	36.71	44.05	57.72	45.65
A.I.**	37.91	34.67	40.24	38.02	38.37
K/Na	0.29	0.61	0.66	0.29	0.88
CCPI***	86.06	84.04	79.07	84.50	76.63
K/Rb	1726.59	991.48	873.34	1806.90	739.97
Ag (ppm)	< 0.3	< 0.3	< 0.3	< 0.3	< 0.3
As	4.80	4.10	3.50	4.10	5.60
Au (ppm)	< 0.002	< 0.002	< 0.002	< 0.002	< 0.002
Ba	152.00	860.00	834.00	170.00	934.00
Be	1.00	1.00	< 1	2.00	1.00
Bi	< 0.1	< 0.1	< 0.1	< 0.1	< 0.1
Br	< 0.5	< 0.5	< 0.5	< 0.5	< 0.5
Cd	< 0.5	< 0.5	< 0.5	< 0.5	< 0.5
Co	40.00	48.00	57.00	38.00	40.00
Cr	228.00	11.00	88.00	196.00	50.00
Cs	< 0.1	0.20	0.80	0.10	0.50
Cu	< 1	49.00	85.00	3.00	21.00
Fe (ppm)	76500.00	116000.00	98600.00	70800.00	82100.00
Ga	18.00	23.00	22.00	18.00	20.00
Ge	1.60	1.70	1.20	1.40	1.50
Hf	2.20	3.90	3.90	2.10	5.30

Sample reference no.	30	32	37	38	39
In	0.10	0.10	0.10	0.10	0.10
Ir (ppm)	<0.005	<0.005	<0.005	<0.005	<0.005
Mo	< 1	< 1	< 1	< 1	< 1
Nb	5.50	5.00	3.60	7.40	10.10
Ni	75.00	20.00	72.00	72.00	27.00
Pb	7.00	5.00	5.00	5.00	9.00
P (ppm)	1352.77	2836.45	3054.63	1527.32	1832.78
Rb	3.00	13.00	20.00	3.00	28.00
S	< 100	1000.00	1600.00	< 100	1700.00
Sb	< 0.1	< 0.1	< 0.1	< 0.1	< 0.1
Sc	29.10	41.00	21.20	27.40	27.30
Se	< 3	< 3	< 3	< 3	< 3
Sn	1.00	1.00	1.00	1.00	1.00
Sr	477.00	410.00	387.00	491.00	346.00
Ta	0.25	0.28	0.18	0.31	0.45
Th	0.91	1.66	0.84	1.06	0.52
Ti (ppm)	6462.61	14969.52	13248.95	6660.45	9082.43
TL	< 0.05	0.06	0.17	< 0.05	0.12
U	0.26	0.41	0.19	0.35	0.20
V	235.00	502.00	373.00	229.00	256.00
W	< 0.5	< 0.5	< 0.5	< 0.5	< 0.5
Zn	122.00	139.00	120.00	141.00	128.00
Zr	75.00	143.00	154.00	81.00	215.00
La	18.00	25.10	26.60	18.80	34.80
Ce	40.70	57.30	60.80	42.90	76.40
Pr	5.43	7.72	7.97	5.56	9.84
Nd	23.60	35.00	34.50	24.70	42.30
Sm	5.31	8.28	7.58	5.44	8.82
Eu	1.55	2.88	2.50	1.47	2.46
Gd	4.80	8.28	7.11	5.14	8.77
Tb	0.74	1.32	1.05	0.82	1.32
Dy	4.46	7.74	6.23	4.64	8.15
Ho	0.87	1.55	1.23	0.94	1.67
Er	2.53	4.41	3.42	2.75	4.93
Tm	0.37	0.64	0.49	0.39	0.70
Yb	2.26	4.08	3.14	2.74	4.71
Lu	0.35	0.62	0.48	0.44	0.74
Y	24.00	43.60	31.30	26.60	46.50
∑REE	110.97	164.92	163.10	116.72	205.61
(La/Yb)****	5.71	4.41	6.08	4.92	5.30
(La/Sm)****	2.19	1.96	2.27	2.23	2.55
(Gd/Yb)****	1.76	1.68	1.87	1.55	1.54
(Tb/Yb)****	1.49	1.47	1.52	1.36	1.27
Eu/Eu****	0.94	1.06	1.04	0.85	0.86

Table B.1 (cont'd). Geochemistry of unknown mafic samples analyzed in this study

Sample reference no.	41	42	47	50	57
Sample Number	**18CL6073C**	**17CL6075C**	**17CL6054C2**	**17CL6062C1**	**17CL6105C1**
Latitude (Y)	47.2471	47.2299	47.4363	47.3572	47.0027
Longitude (X)	-76.8109	-76.7598	-77.0368	-76.9606	-76.5094
Geochemical Group	Group U2	Group U2	Group U2	Group U2	Group U2
Field based subdivision	RDT-2	RDT-2	RDT-2	RDT-2	RDT-2
Proposed Affinity	RT-Group 2	RT-Group 2	RT-Group 2	RT-Group 2	RT-Group 2
SiO2 (wt%)	47.83	47.76	47.80	47.16	46.54
Al2O3	15.54	15.02	13.60	14.05	17.01
Fe2O3(T)	14.65	14.62	17.93	15.45	13.33
MgO	5.82	5.81	4.88	5.07	7.32
MnO	0.23	0.20	0.26	0.23	0.19
CaO	8.38	8.53	8.48	7.42	9.10
Na2O	3.65	3.69	1.96	3.55	3.68
K2O	1.32	1.09	1.06	2.06	0.79
TiO2	1.61	2.13	2.95	2.36	1.07
P2O5	0.62	0.67	0.42	0.87	0.19
Cr2O3	< 0.01	< 0.01	0.01	0.01	0.01
LOI	0.68	0.65	0.62	0.67	0.73
Total	100.30	100.20	99.95	98.88	99.95
FeO	13.18	13.16	16.13	13.90	11.99
#Mg*	44.04	44.05	35.03	39.40	52.10
A.I.**	37.25	36.09	36.26	39.39	38.82
K/Na	0.64	0.54	0.97	1.11	0.40
CCPI***	79.27	79.87	87.43	77.18	81.21
K/Rb	722.76	656.51	1064.06	443.12	1189.54
Ag (ppm)	< 0.3	< 0.3	< 0.3	< 0.3	< 0.3
As	2.70	< 0.5	0.50	< 0.5	< 0.5
Au (ppm)	< 0.002	< 0.002	< 0.002	< 0.002	< 0.002
Ba	753.00	799.00	381.00	640.00	237.00
Be	1.00	< 1	1.00	3.00	< 1
Bi	< 0.1	0.20	< 0.1	< 0.1	< 0.1
Br	< 0.5	< 0.5	< 0.5	< 0.5	< 0.5
Cd	< 0.5	< 0.5	0.70	< 0.5	< 0.5
Co	52.00	51.00	44.00	38.00	54.00
Cr	50.00	52.00	40.00	47.00	71.00
Cs	0.40	0.60	0.20	1.20	< 0.1
Cu	78.00	53.00	29.00	112.00	56.00
Fe (ppm)	99300.00	95600.00	111000.00	98000.00	86900.00
Ga	22.00	22.00	23.00	23.00	19.00
Ge	1.20	1.20	1.60	1.40	1.20
Hf	2.40	3.20	4.10	3.60	1.80

Sample reference no.	41	42	47	50	57
In	0.10	0.10	0.10	< 0.1	< 0.1
Ir (ppm)	<0.005	<0.005	<0.005	<0.005	<0.005
Mo	< 1	< 1	< 1	< 1	< 1
Nb	3.90	3.30	3.90	5.30	1.70
Ni	67.00	53.00	27.00	33.00	79.00
Pb	3.00	6.00	9.00	11.00	< 3
P (ppm)	2705.53	2923.72	1832.78	3796.47	829.12
Rb	22.00	20.00	12.00	56.00	8.00
S	1900.00	1800.00	1800.00	2000.00	1400.00
Sb	< 0.1	< 0.1	< 0.1	< 0.1	< 0.1
Sc	26.50	28.30	41.90	31.60	28.30
Se	< 3	< 3	< 3	< 3	< 3
Sn	1.00	1.00	1.00	2.00	< 1
Sr	449.00	494.00	296.00	459.00	441.00
Ta	0.18	0.17	0.21	0.25	0.05
Th	0.44	0.61	2.19	1.10	0.42
Ti (ppm)	9675.93	12793.33	17661.27	14124.22	6396.67
TL	0.10	0.08	< 0.05	0.13	< 0.05
U	0.14	0.14	0.54	0.55	0.09
V	310.00	338.00	447.00	399.00	230.00
W	< 0.5	< 0.5	0.50	< 0.5	1.10
Zn	128.00	117.00	126.00	141.00	88.00
Zr	79.00	122.00	173.00	169.00	72.00
La	23.70	23.50	19.50	36.90	8.99
Ce	54.20	54.40	46.70	85.70	21.40
Pr	7.29	7.15	6.20	11.90	2.90
Nd	33.20	32.20	27.40	52.30	13.10
Sm	7.13	7.06	7.31	11.30	3.40
Eu	2.26	2.53	2.41	3.31	1.24
Gd	6.15	7.40	8.48	10.10	4.21
Tb	0.91	1.05	1.37	1.47	0.69
Dy	5.05	5.97	8.77	7.93	4.09
Ho	1.01	1.20	1.72	1.52	0.86
Er	2.91	3.44	4.82	4.11	2.36
Tm	0.40	0.47	0.70	0.57	0.34
Yb	2.61	2.87	4.69	3.63	2.23
Lu	0.41	0.46	0.70	0.56	0.35
Y	27.60	31.90	46.70	41.40	23.30
∑REE	147.23	149.69	140.77	231.30	66.16
(La/Yb)****	6.51	5.87	2.98	7.29	2.89
(La/Sm)****	2.15	2.15	1.72	2.11	1.71
(Gd/Yb)****	1.95	2.13	1.50	2.30	1.56
(Tb/Yb)****	1.58	1.66	1.33	1.84	1.41
Eu/Eu****	1.04	1.07	0.94	0.95	1.00

Table B.1 (cont'd). Geochemistry of unknown mafic samples analyzed in this study

Sample reference no.	58	59	60	94	95
Sample Number	**17CL6112D1**	**17CL6125C1**	**17CL6152C1**	**18CL8081C1**	**18CL8021B1**
Latitude (Y)	46.9117	46.8291	47.0824	46.6440	46.5332
Longitude (X)	-76.4226	-76.3114	-76.5603	-76.5896	-76.5047
Geochemical Group	Group U2	Group U2	Group U2	Group U2	Group U2
Field based subdivision	RDT-1	RDT-2	RDT-2	VT-type	VT-type
Proposed Affinity	RT-Group 2	RT-Group 2	RT-Group 2	RT-Group 2	RT-Group 2
SiO2 (wt%)	45.39	44.60	45.22	54.29	46.01
Al2O3	17.24	16.25	16.91	14.57	14.17
Fe2O3(T)	15.78	14.42	14.87	13.07	15.33
MgO	5.09	6.79	5.93	4.30	7.14
MnO	0.21	0.22	0.20	0.21	0.26
CaO	9.39	8.40	7.11	6.93	10.68
Na2O	3.41	3.93	3.30	2.16	3.14
K2O	0.63	1.09	3.15	1.89	0.47
TiO2	2.29	1.88	1.85	1.91	1.87
P2O5	0.48	0.32	0.27	0.53	0.23
Cr2O3	0.01	0.01	0.01	< 0.01	0.03
LOI	-0.05	0.94	0.80	0.39	0.39
Total	99.85	98.83	99.61	100.30	99.69
FeO	14.20	12.98	13.38	11.76	13.79
#Mg*	38.99	48.26	44.13	39.46	47.99
A.I.**	30.89	38.99	46.59	40.51	35.51
K/Na	0.34	0.52	1.81	1.41	0.26
CCPI***	82.68	79.75	74.96	79.86	85.29
K/Rb	843.22	375.15	298.78	599.13	707.70
Ag (ppm)	< 0.3	< 0.3	< 0.3	< 0.3	< 0.3
As	1.30	0.80	< 0.5	2.80	5.70
Au (ppm)	< 0.002	< 0.002	< 0.002		
Ba	363.00	502.00	626.00	1037.00	180.00
Be	1.00	< 1	1.00	2.00	< 1
Bi	< 0.1	< 0.1	0.30	< 0.1	< 0.1
Br	< 0.5	< 0.5	< 0.5	< 0.5	< 0.5
Cd	< 0.5	< 0.5	< 0.5	< 0.5	< 0.5
Co	50.00	54.00	54.00	37.00	57.00
Cr	40.00	66.00	38.00	30.00	146.00
Cs	0.20	0.10	5.10	0.50	0.10
Cu	53.00	33.00	7.00	18.00	58.00
Fe (ppm)	98600.00	91200.00	97800.00	88800.00	104000.00
Ga	22.00	20.00	21.00	21.00	21.00
Ge	1.20	1.10	1.20	1.50	1.70
Hf	2.70	2.50	3.10	6.70	2.60

Sample reference no.	58	59	60	94	95
In	0.10	< 0.1	< 0.1	0.10	0.10
Ir (ppm)	<0.005	<0.005	<0.005	<0.005	<0.005
Mo	< 1	< 1	< 1	< 1	< 1
Nb	4.10	5.00	2.90	11.40	1.50
Ni	60.00	82.00	80.00	16.00	63.00
Pb	< 3	< 3	9.00	11.00	3.00
P (ppm)	2094.61	1396.40	1178.22	2312.79	1003.67
Rb	9.00	35.00	127.00	38.00	8.00
S	800.00	800.00	200.00	800.00	1400.00
Sb	< 0.1	< 0.1	< 0.1	< 0.1	< 0.1
Sc	26.30	21.90	22.20	27.60	43.80
Se	< 3	< 3	< 3	< 3	< 3
Sn	1.00	< 1	1.00	1.00	1.00
Sr	420.00	494.00	351.00	364.00	289.00
Ta	0.23	0.29	0.12	0.60	0.07
Th	0.80	0.97	0.54	1.08	0.50
Ti (ppm)	13698.58	11288.59	11066.77	11426.47	11228.64
TL	< 0.05	< 0.05	0.44	0.18	< 0.05
U	0.28	0.24	0.65	0.50	0.41
V	290.00	240.00	235.00	301.00	374.00
W	< 0.5	1.10	1.00	< 0.5	< 0.5
Zn	118.00	136.00	131.00	140.00	119.00
Zr	111.00	104.00	130.00	268.00	79.00
La	12.70	13.70	13.10	41.70	7.11
Ce	31.10	32.30	31.00	91.50	19.20
Pr	4.40	4.43	4.28	11.70	2.99
Nd	20.50	19.30	19.30	46.80	15.60
Sm	5.45	4.80	5.06	9.83	4.76
Eu	2.15	1.64	1.81	2.71	1.84
Gd	6.16	5.11	5.66	9.40	5.95
Tb	0.98	0.77	0.90	1.46	1.00
Dy	5.96	4.75	5.43	8.92	6.39
Ho	1.19	0.93	1.12	1.82	1.33
Er	3.38	2.57	2.91	5.35	3.79
Tm	0.47	0.34	0.42	0.77	0.55
Yb	3.13	2.17	2.68	5.18	3.51
Lu	0.48	0.36	0.40	0.81	0.53
Y	33.50	25.20	28.90	48.80	34.90
∑REE	98.04	93.17	94.07	237.95	74.54
(La/Yb)****	2.91	4.53	3.51	5.77	1.45
(La/Sm)****	1.50	1.84	1.67	2.74	0.96
(Gd/Yb)****	1.63	1.95	1.75	1.50	1.40
(Tb/Yb)****	1.42	1.61	1.53	1.28	1.30
Eu/Eu****	1.13	1.01	1.03	0.86	1.06

Table B.1 (cont'd) Geochemistry of unknown mafic samples analyzed in this study

Sample reference no.	36	44	49
Sample Number	**18CL60106C1**	**18CL6133B1**	**17CL6055C2**
Latitude (Y)	46.9999	46.7991	47.4334
Longitude (X)	-76.5049	-76.1665	-77.0281
Geochemical Group	Group U3	Group U3	Group U3
Field based subdivision	RDT-2	RDT-2	RDT-2
Proposed Affinity	Algonquin/RT-Group 3	Sudbury suite/RT-Group 3	Sudbury suite/RT-Group 3
SiO2 (wt%)	44.83	45.61	45.88
Al2O3	15.82	15.74	13.55
Fe2O3(T)	16.64	14.29	19.31
MgO	6.14	7.33	5.11
MnO	0.23	0.20	0.26
CaO	8.71	8.73	8.87
Na2O	3.18	3.30	1.92
K2O	0.80	1.15	1.02
TiO2	2.97	2.44	2.73
P2O5	0.40	0.36	0.39
Cr2O3	0.01	< 0.01	0.01
LOI	0.61	0.62	0.37
Total	100.30	99.77	99.42
FeO	14.97	12.86	17.38
#Mg*	42.23	50.40	34.39
A.I.**	36.86	41.35	36.23
K/Na	0.43	0.60	0.96
CCPI***	84.14	81.94	88.44
K/Rb	876.07	602.30	877.64
Ag (ppm)	< 0.3	< 0.3	< 0.3
As	4.00	2.90	< 0.5
Au (ppm)	< 0.002	< 0.002	< 0.002
Ba	474.00	365.00	424.00
Be	1.00	1.00	1.00
Bi	< 0.1	0.30	< 0.1
Br	< 0.5	< 0.5	10.90
Cd	< 0.5	< 0.5	< 0.5
Co	56.00	58.00	51.00
Cr	82.00	58.00	78.00
Cs	0.10	1.20	< 0.1
Cu	113.00	66.00	58.00
Fe (ppm)	103000.00	98200.00	122000.00
Ga	21.00	21.00	23.00
Ge	1.30	1.20	1.50
Hf	3.90	3.80	3.40

Sample reference no.	36	44	49
In	0.10	0.10	0.10
Ir (ppm)	<0.005	<0.005	<0.005
Mo	< 1	< 1	< 1
Nb	9.50	9.30	9.60
Ni	84.00	103.00	48.00
Pb	< 3	5.00	< 3
P (ppm)	1745.51	1570.95	1701.87
Rb	11.00	23.00	14.00
S	1200.00	1100.00	1600.00
Sb	< 0.1	< 0.1	< 0.1
Sc	26.70	23.90	35.70
Se	< 3	< 3	< 3
Sn	1.00	1.00	< 1
Sr	357.00	372.00	227.00
Ta	0.66	0.60	0.73
Th	0.80	0.95	1.42
Ti (ppm)	17829.13	14651.78	16384.34
TL	0.05	0.10	< 0.05
U	0.34	0.59	0.33
V	264.00	199.00	415.00
W	< 0.5	< 0.5	0.50
Zn	115.00	105.00	142.00
Zr	147.00	140.00	152.00
La	15.40	16.40	22.30
Ce	36.40	37.60	49.70
Pr	5.06	5.11	6.32
Nd	23.50	23.20	27.00
Sm	6.24	5.66	6.46
Eu	2.15	1.89	2.09
Gd	6.90	5.97	7.26
Tb	1.11	0.90	1.19
Dy	6.53	4.86	7.48
Ho	1.32	0.95	1.50
Er	3.80	2.64	4.30
Tm	0.55	0.38	0.61
Yb	3.53	2.49	3.93
Lu	0.54	0.40	0.62
Y	36.40	24.90	40.20
∑REE	113.03	108.45	140.76
(La/Yb)****	3.13	4.72	4.07
(La/Sm)****	1.59	1.87	2.23
(Gd/Yb)****	1.62	1.98	1.53
(Tb/Yb)****	1.43	1.64	1.38
Eu/Eu****	1.00	0.99	0.93

Table B.1 (cont'd). Geochemistry of unknown mafic samples analyzed in this study

Sample reference no.	55	96	97	98
Sample Number	**17CL6091A2**	**17CL6135C1**	**17CL6137C1**	**17CL6136D1**
Latitude (Y)	47.1274	46.7910	46.7851	46.7886
Longitude (X)	-76.6083	-76.1563	-76.1485	-76.1532
Geochemical Group	Group U3	Group U3	Group U3	Group U3
Field based subdivision	RDT-1	VT-type	VT-type	VT-type
Proposed Affinity	RT-Group 3	Algonquin/RT-Group 3	Algonquin/RT-Group 3	Algonquin/RT-Group 3
SiO2 (wt%)	44.76	48.02	45.47	46.16
Al2O3	16.68	17.19	16.50	14.02
Fe2O3(T)	14.38	12.71	13.23	12.34
MgO	6.41	6.02	7.81	8.01
MnO	0.20	0.17	0.19	0.20
CaO	10.31	8.71	9.48	11.46
Na2O	3.05	4.07	3.38	2.70
K2O	0.63	0.56	0.70	0.75
TiO2	2.07	2.06	1.96	1.88
P2O5	0.28	0.27	0.26	0.20
Cr2O3	0.01	< 0.01	< 0.01	0.04
LOI	0.67	0.90	1.14	1.18
Total	99.43	100.70	100.10	98.89
FeO	12.94	11.44	11.90	11.10
#Mg*	46.90	48.41	53.91	56.25
A.I.**	34.51	33.99	39.82	38.22
K/Na	0.41	0.26	0.36	0.45
CCPI***	84.02	79.04	82.85	84.71
K/Rb	1517.80	843.22	1054.03	1505.75
Ag (ppm)	< 0.3	< 0.3	< 0.3	< 0.3
As	< 0.5	2.20	11.40	< 0.5
Au (ppm)	< 0.002			
Ba	395.00	254.00	243.00	155.00
Be	1.00	< 1	< 1	< 1
Bi	< 0.1	< 0.1	< 0.1	< 0.1
Br	2.30	< 0.5	< 0.5	< 0.5
Cd	< 0.5	< 0.5	< 0.5	< 0.5
Co	51.00	50.00	59.00	55.00
Cr	39.00	20.00	45.00	247.00
Cs	< 0.1	< 0.1	0.10	< 0.1
Cu	17.00	15.00	41.00	15.00
Fe (ppm)	86300.00	82400.00	90900.00	86600.00
Ga	20.00	20.00	21.00	20.00
Ge	1.10	1.20	1.20	1.50
Hf	2.80	3.50	3.00	2.50

Sample reference no.	55	96	97	98
In	< 0.1	0.10	0.10	0.10
Ir (ppm)	<0.005	<0.005	<0.005	<0.005
Mo	< 1	< 1	< 1	< 1
Nb	8.90	7.00	7.00	6.20
Ni	88.00	44.00	98.00	121.00
Pb	< 3	3.00	3.00	4.00
P (ppm)	1221.85	1178.22	1134.58	872.75
Rb	5.00	8.00	8.00	6.00
S	600.00	900.00	1700.00	1200.00
Sb	< 0.1	< 0.1	< 0.1	< 0.1
Sc	25.50	18.40	21.50	29.80
Se	< 3	< 3	< 3	< 3
Sn	1.00	1.00	1.00	1.00
Sr	400.00	636.00	614.00	322.00
Ta	0.64	0.46	0.45	0.44
Th	0.99	0.56	0.59	0.30
Ti (ppm)	12421.64	12349.70	11744.21	11252.62
TL	< 0.05	< 0.05	< 0.05	< 0.05
U	0.30	0.17	0.22	0.16
V	271.00	238.00	287.00	332.00
W	7.90	< 0.5	< 0.5	< 0.5
Zn	101.00	69.00	86.00	77.00
Zr	118.00	125.00	102.00	90.00
La	16.80	11.50	12.20	8.66
Ce	36.30	28.40	29.90	22.00
Pr	4.75	4.06	4.19	3.16
Nd	21.40	18.70	19.70	15.70
Sm	5.14	4.91	4.65	4.25
Eu	2.07	1.74	1.59	1.45
Gd	5.62	4.98	4.74	4.51
Tb	0.86	0.78	0.63	0.68
Dy	5.10	4.38	3.66	4.03
Ho	0.95	0.84	0.70	0.77
Er	2.71	2.35	1.88	2.08
Tm	0.37	0.32	0.26	0.29
Yb	2.30	2.00	1.59	1.77
Lu	0.34	0.32	0.24	0.27
Y	26.50	23.00	18.40	20.70
∑REE	104.71	85.27	85.93	69.62
(La/Yb)****	5.24	4.12	5.50	3.51
(La/Sm)****	2.11	1.51	1.69	1.32
(Gd/Yb)****	2.02	2.06	2.47	2.11
(Tb/Yb)****	1.70	1.77	1.80	1.75
Eu/Eu****	1.18	1.08	1.04	1.01

Table B.2 Quantitative geochemical comparison of unknown mafic samples analyzed herein, to reference suites.

Group	Subdivision	Mafic series (Jensen, 1976)	Trace element alkalinity (Nb/Y)	MgO range (wt%)	HFSE characteristics	REECN slopes	HREE slope (Gd/Yb)CN (depth of source melting)	HREE slope (Tb/Yb)CN (depth of source melting)	Zr (ppm)*	Field Grouping/Host rocks	Mineral assemblage	Tectonic Setting
This study	Group 1	High-Mg 'komatiitic' basalts	0.08-0.1	13.77-15.2 (ave: 14.38)	Deep Nb-Ta troughs and negative Ti*; (Ti/Sm)NMORB = 0.3-0.52 (0.38 ave); (Th/Ta)NMORB = 5.61-14.08 (10.13 ave)	(La/Sm)CN = 1.39-2.08; (La/Yb)CN = 4.42-4.96	1.73-2.34	1.46-1.92	57-102	RDT-2	Cpx-opx-pl-bt	Arc-modified
	Group 2 (with Ti anomlay)	Hig-Fe high-Mg TH	0.07-0.28 (ave: 0.16)	4.3-7.46 (ave: 5.94)	Deep Nb-Ta troughs and prominent negative Ti*; (Ti/Sm)NMORB = 0.37-0.95 (0.66 ave); (Th/Ta)NMORB = 1.27-9.24 (4.39 ave)	(La/Sm)CN = 1.67-2.74 (ave: 2.16); (La/Yb)CN = 2.89-7.29 (ave 5.3)	1.50-2.30 (ave: 1.78)	1.27-1.84 (ave: 1.49)	72-286	RDT-1, RDT-2, VT (#94)	Hbl-Pl-Bt±Grt Cpx-Hbl-Pl-Grt±Opx	Oceanic back-arc
	Group 2 (without Ti anomaly)		0.08-0.2	4.88-7.14 (ave: 5.98)	Deep Nb-Ta troughs and weak negative Ti*; (Ti/Sm)NMORB = 1.02-1.09 (1.04 ave); (Th/Ta)NMORB = 3.68-11.47 (6.71 ave)	(La/Sm)CN = 0.96-1.84 (ave 1.50); (La/Yb)CN = 1.45-4.53 (ave 2.97)	1.40-1.95 (ave: 1.62)	1.30-1.61	104-173			
	Group 3	Hig-Fe high-Mg TH	0.24-0.38 (ave: 0.31)	5.11-8.01 (6.55)	Weak Ta-Nb troughs and flat to positive Ti*; (Ti/Sm)NMORB = 1.05-1.24 (1.12); (Th/Ta)NMORB = 0.75-2.14 (1.50 ave)	(La/Sm)CN = 1.32-2.23 (ave 4.30); (La/Yb)CN = 3.13-5.50 (ave 3.67)	1.53-2.47 (1.91)	1.38-1.8 (ave: 1.61)	90-152	RDT-1, RDT-2, VT	Hbl-Pl-Bt±Grt Cpx-Hbl-Pl-Grt±Opx	E-MORB
Abitibi Greenstone Blet	Southern Volcanic Zone	Komatiitic basats	0.23-0.26 (ave: 0.16)	9.1-17.74	Weak Nb-Ta depeltion and flat Ti*; (Ti/Sm)NMORB = 0.82-1.24 (1.12 ave); (Th/Ta)NMORB = no data	(La/Sm)CN = 0.48-1.40 (ave: 0.90); (La/Yb)CN = 0.28-2.03 (ave: 1.18)	0.71-1.78 (ave: 1.26)	NA	23-59 (ave: 43)	Metavolcanic layers or sills/dykes	Cpx-Opx-Grt±Ol (in GFTZ; La Flèche et al., 2005)	Intraplate (stagnet lid system)
	Chibougamau region		0.15-0.6 (ave: 0.29)		Weak Nb-Ta depeltion and flat Ti*; (Ti/Sm)NMORB = 0.62-4.99 (1.45 ave); (Th/Ta)NMORB = 0.53-6.66 (3.07 ave)	(La/Sm)CN = 0.65-1.99 (ave: 1.03); (La/Yb)CN = 0.61-2.4 (ave: 1.50)	0.93-2-15 (ave: 1.52)	NA	31-71 (ave: 57)	Metavolcanic layers or sills/dykes		
	Southern Volcanic Zone	Hig-Fe high-Mg TH, CA	0.07-0.19 (ave: 0.13)	4.0-10.0	Rare Nb-Ta troughs; Weak negative to flat Ti* (Ti/Sm)MORB = 0.91-1.60 (ave: 1.20); (Th/Ta)NMORB = 0.35-6.66 (3.07 ave)	(La/Sm)CN = 0.76-1.53 (ave 0.99); (La/Yb)CN = 0.29-2.15 (ave 0.86)	0.43-2.27 (ave 0.98)	NA	27-92 (ave: 54)	Metavolcanic layers or sills/dykes	Cpx-Opx-Grt±Ol (in GFTZ; La Flèche et al., 2005)	WPA (N-MORB)
	Chibougamau region		0.01-2 (ave: 0.16)		Rare Nb-Ta troughs; Weak negative to flat Ti*; (Ti/Sm)NMORB = 0.04-4.35 (1.10 ave); (Th/Ta)NMORB = 0.06-33.18 (2.4 ave)	(La/Sm)CN =0.50-2.16 (ave 1.00); (La/Yb)CN = 0.29-3.75 (ave 1.14)	0.68-2.48 (ave 1.10)	NA	15-391 (ave: 73)	Metavolcanic layers often associated felsic (rhyolitic layers)		WPA (N-MORB)

*Zr concentration given for similarly evolved samples (defined by the range in MgO)
Ti* refers to Ti anomaly

Table B.2 (cont'd). Quantitative geochemical comparison of unknown mafic samples analyzed herein, to reference suites.

Group	Subdivision	Mafic series (Jensen, 1976)	Trace element alkalinity (Nb/Y)	MgO range (wt%)	HFSE characteristics	REECN slopes	HREE slope (Gd/Yb)CN (depth of source melting)	HREE slope (Tb/Yb)CN (depth of source melting)	Zr (ppm)*	Field Grouping/Host rocks	Mineral assemblage	Tectonic Setting
Proterozoic dyke swarms	Matachewan Suite	Hig-Fe high-Mg TH	0.15-0.34 (ave: 0.21)	3.65-7.5 (ave: 5.2)	Weak to moderate negative Ta-Nb trough, moderate negative Ti anomlay; (Ti/Sm)NMORB = 0.67-0.98 (0.83 ave); (Th/Ta)NMORB = 1.02-15.8 (6.05 ave)	(La/Sm)CN = 1.58-3.14 (ave: 2.10); (La/Yb)CN = 2.22-4.47 (ave: 2.99)	1.10-1.36 (ave: 1.24)	NA	86-233 (ave: 132)	Dykes	Qtz-tholeiites	Intraplate
	Seneterre Suite	Komatiitic basalts	0.16-0.34 (ave: 0.21)	10.23-13.24; (ave: 12.28)	Strong Nb-Ta trough, weak negative Ti* and flat HREE; (Ti/Sm)NMORB = 0.71-0.93 (0.83 ave); (Th/Ta)NMORB = 2.31-6.33 (3.57 ave)	(La/Sm)CN = 1.64-3.15 (ave:2.66); (La/Yb)CN = 3.44-4.34 (ave: 3.88)	0.99-2.17 (ave: 1.2)	NA	55-97 (ave: 64.8)	Dykes	NA	Intraplate
		Hig-Fe high-Mg TH	0.15-0.24 (ave: 0.17)	6.66 -10.10 (ave: 8.81)	Deep Ta-trough, weak Ti*; (Ti/Sm)NMORB = 0.71-0.93 (0.83 ave); (Th/Ta)NMORB = 2.1-5.75 (3.57 ave)	(La/Sm)CN = 2.06-2.54 (ave 2.32); (La/Yb)CN = 2.56-4.38 (ave 5.43)	0.93-1.52 (ave 1.10)	NA	49-80 (ave: 56)	Dykes	Qtz-tholeiites	Intraplate
	Sudbury	Hig-Fe high-Mg TH	15-0.69 (ave. 0.40)	4.47-7.95 (ave: = 5.69)	Weak Ta-Nb, flat to positive Ti*; (Ti/Sm)NMORB = 0.72-1.28 (0.96 ave); (Th/Ta)NMORB = 1.78-4.81 (2.83 ave)	(La/Sm)CN = 1.37-2.71 (ave: 2.26); (La/Yb)CN = 4.02-8.56 (ave: 5.90)	1.55-2.52 (ave; 1.90)	NA	100-360 (ave: 203)	Dykes or dismembered bodies	Olivine tholeiites, can be corronitic	E-MORB
	Abitibi Dyke Suite	NA	>0.61	2.52-9.22 (ave: 5.34)	HFSE and LFSE enriched (Nb, Ta, Ti, Zr); (Ti/Sm)NMORB =0.58-1.85 (1.10 ave); (Th/Ta)NMORB =0.62-3.13 (1.36 ave)	(La/Sm)CN = 1.92-3.72; (La/Yb)CN = 5.95-18.42	2.32-3.63	NA	74-380 (ave: 203)	NA	NA	OIB
Mafic Suite in AB (Ontario)	Algonuqin	Hig-Fe high-Mg TH, CA	0.32-0.48 (ave. 0.37)	4.91-11.10 (ave: 7)	Weak Ta-Nb, positive average Ti*; (Ti/Sm)NMORB = 1.16-2.95 (1.65 ave); (Th/Ta)NMORB = 0.94-1.87 (1.37 ave)	(La/Sm)CN = 1.23-1.65 (ave: 1.46); (La/Yb)CN = 3.19-4.05 (ave: 3.61)	1.70-2.34 (ave: 1.91)	1.52-2 (ave: 1.654)	83-176 (ave: 129)	Dykes or dismembered bodies	Olivine tholeiites, can be corronitic	E-MORB
Renzy Terrane	RT-Group 1: High Mg-TH and komatiitic basalts	High-Mg tholeiites and komatiitic basalts	0.03-0.10 (ave: 0.05)	9.19-14.4 (ave: 12.74)	Strong Nb-Ta trough and strong negative Ti*; (Ti/Sm)NMORB = 0.42-1.5 (0.79 ave); (Th/Ta)NMORB =5.89-25.09 (14.30 ave)	(La/Sm)CN = 1.06-1.72 (ave: 1.38); (La/Yb)CN = 2.56-5.03 (ave: 3.2)	NA	1.26-1.74 (ave:1.57)	23-65 (ave: 38.4)	Metagabbro sills in Grt-bearing felsic and intermediate gneisses	Hbl–Opx–Cpx–Pl±Grt Hbl–Pl–Grt–Cpx	Arc-modified
	RT-Group 2a (with Ti anomlay)	Hig-Fe high-Mg TH, CA	0.07-0.22 (ave: 0.13)	5.22-8.28 (ave: 6.73)	Strong Nb-Ta trough and strong negative Ti*; (Ti/Sm)NMORB =0.57-0.089 (0.73 ave); (Th/Ta)NMORB = 1.35-7.42 (4.26 ave)	(La/Sm)CN = 1.44-2.82 (ave 1.93); (La/Yb)CN = 2.23-6.53 (ave 3.99)	NA	1.18-1.73 (ave: 1.39)	62-171 (ave: 100)	Granulite to amphibolite gneissic bands	Hbl–Pl–Cpx/Opx–Grt Hbl–Pl–Cpx–Bt–Grt Hbl–Cpx–Pl–Bt Pl–Hbl–Bt–Kfs–Ap–Qtz±Grt±Cpx±Zm	Arc-modified back-arc basin
	RT-Group 2b (without Ti anomlay)	Hig-Fe high-Mg TH	0.06-0.21 (ave: 0.12)	5.47-7.74 (ave: 6.44)	Strong Nb-Ta troughs, weak to flat Ti*; (Ti/Sm)NMORB =1.00-1.29 (1.10 ave); (Th/Ta)NMORB = 1.63-5.32 (3.30 ave)	(La/Sm)CN = 1.15-2.24 (ave 1.67); (La/Yb)CN = 1.48-6.53 (ave 3.67)	NA	1.31-1.73 (ave: 1.49)	50-160 (ave: 94)			
	Renzy Terrane control samples (this study)	Hig-Fe high-Mg TH	0.12-0.31	Strong Nb-Ta and Ti troughs; (Ti/Sm)NMORB = 0.3-0.56; (Th/Ta)NMORB = 1.02-16.5	Strong Nb-Ta and Ti troughs; (Ti/Sm)NMORB = 0.37-0.70 (0.50 ave); (Th/Ta)NMORB = 1.02-16.5 (6.40 ave)	(La/Sm)CN = 1.68-2.76 (ave 2.32); (La/Yb)CN = 3.69-7.36 (ave 3.47)	1.4-2.1 (ave: 1.63)	1.27-1.55	48-154	RD1-1	Cpx-Hbl-Pl-Grt±Opx	Oceanic back-arc
	RT-Group 3	Hig-Fe TH	0.07-0.5 (ave: 0.25)	4.72-8.6 (ave: 6.25)	Weak Nb-Ta troughs, weak to flat Ti*; (Ti/Sm)NMORB =0.98-1.55 (1.24 ave); (Th/Ta)NMORB = 0.28-2.11 (1.07 ave)	(La/Sm)CN = 0.80-1.84 (ave: 1.35); (La/Yb)CN = 1.10-4.26 (ave 2.66)	NA	1.25-1.63 (ave: 1.45)	91-31 (ave: 127)	Granulite to amphibolite gneissic bands	Cpx–Grt–Hbl brown green–Pl–Qtz	E-MORB

APPENDIX C EXTENDED GEOCHRONOLOGY METHODOLOGY AND SELECTION OF ISOTOPIC SYSTEMS

1. LA-ICP-MS preparation and analytical procedure

Zircon grains were separated from rocks using standard techniques, annealed at 900°C for 60 hours in a muffle furnace, and mounted in epoxy and polished until their centers were exposed. Cathodoluminescence (CL) images were obtained with a JEOL JSM-1300 scanning electron microscope and Gatan MiniCL. Zircon was analyzed by laser ablation inductively coupled plasma mass spectrometry (LA-ICP-MS) using a ThermoElectron X-Series II quadrupole ICPMS and New Wave Research UP-213 Nd:YAG UV (213 nm) laser ablation system. In-house analytical protocols, standard materials, and data reduction software were used for acquisition and calibration of U-Pb dates and a suite of high field strength elements (HFSE) and rare earth elements (REE). Zircon was ablated with a laser spot of 25 μm wide using fluence and pulse rates of 5 J/cm^2 and 10 Hz, respectively, during a 45 second analysis (15 sec gas blank, 30 sec ablation) that excavated a pit ~25 μm deep. Ablated material was carried by a 1.2 L/min He gas stream to the nebulizer flow of the plasma. Dwell times were 5 ms for Si and Zr, 200 ms for ^{49}Ti and ^{207}Pb, 80 ms for ^{206}Pb, 40 ms for ^{202}Hg, ^{204}Pb, ^{208}Pb, ^{232}Th, and ^{238}U and 10 ms for all other HFSE and REE. Background count rates for each analyte were obtained prior to each spot analysis and subtracted from the raw count rate for each analyte. Ablations pits that appear to have intersected glass or mineral inclusions were identified based on Ti and P. U-Pb dates from these analyses are considered valid if the U-Pb ratios appear to have been unaffected by the inclusions. Analyses that appear contaminated by common Pb were rejected based on mass 204 being above the baseline. For concentration calculations, background-subtracted count rates for each analyte were internally normalized to ^{29}Si and calibrated with respect to NIST SRM-610 and -612 glasses as the primary standards. Analyses on these standards are found in the supplementary material (Table D.1 & Table D.8).

Data were collected over four experiments in April 2018 (sessions 1-4) and two experiments in October 2019 (sessions 5-6). For U-Pb and ^{207}Pb/^{206}Pb dates, instrumental fractionation of the background-subtracted ratios were corrected and dates were calibrated with respect to interspersed measurements of zircon standards and reference materials. During sessions 1-4, the primary standard OG1 zircon (3465 Ma, unpublished data, Boise State University) was used to monitor time-dependent instrumental fractionation based on two analyses for every 10 analyses of unknown

zircon. A secondary correction to the $^{206}Pb/^{238}U$ dates was made based on results from the zircon standards FC1 (1098 Ma, unpublished data, Boise State University) and 91500 (1065 Ma; Wiedenbeck et al., 1995), which were treated as unknowns and measured once for every 10 analyses of unknown zircon. During sessions 5 and 6, FC1 was used as the primary standard, while zircon standards 91500 and the Plešovice (337 Ma, Sláma *et al.*, 2008) were used for secondary corrections. These results showed a linear age bias of several percent that is related to the ^{206}Pb count rate. The secondary correction is thought to mitigate matrix-dependent variations due to contrasting compositions and ablation characteristics between the Plešovice zircon and other standards (and unknowns; Herriott *et al.*, 2019; discussed below). The $^{207}Pb/^{206}Pb$ results from the secondary reference materials FC1 and 91500 show that accurate dates were obtained (Table D.1).

2. Presentation of ages and calibration of errors

Ages for each of the unknown samples in this study are reported for zircon grains or zones within individual grains (e.g. rims and cores). The ages for each population are presented as weighted mean ages, calculated using Isoplot 4, a Microsoft Excel Toolkit (Ludwig, 2003, 2008) in conjunction with IsoplotR, a free R-based software package with a graphic-friendly user interface (Vermeesch, 2018). For all samples the reduced chi-squared statistic (also known as the Mean Square of Weighted Deviates or MSWD; McIntyre *et al.*, 1966; Wendt and Carl, 1991) and the probability of fit (PF) are presented as a means to evaluate the heteroscedasticity (i.e. data with unequal measurement uncertainties).

The choice of isotopic system used to interpret zircon ages between ca. 800 – 1500 Ma is generally problematic (Spencer *et al.*, 2016). Age interpretations for populations with dates > ca. 1200-1500 Ma are commonly reported as $^{207}Pb/^{206}Pb$ weighted mean ages and as $^{206}Pb/^{238}U$ weighted mean ages in younger populations (Puetz, 2018; Puetz *et al.*, 2021). This is largely due to the greater imprecision of ^{207}Pb in younger zircons (Gehrels, *et al.*, 2008; Spencer *et al.*, 2016) and conversely, in cases where data is commonly discordant due to Pb-loss, the weighted mean $^{207}Pb/^{206}Pb$ age typically offers more robust data (Spencer *et al.* 2016). In addition, LA-ICP-MS analysis with the $^{206}Pb/^{238}U$ system can result in dates having a younger, or less frequently, an older bias due the matrix effect (Herriott *et al.*, 2019). The matrix effect is linked to the difference in Th and U concentration between the standards and unknowns (Allen and Campbell, 2012) and radiation damage (metamictization) in high U zircons (White and Ireland, 2012; Pidgeon, 2014).

Zircons with very low U concentrations relative to the standards may yield $^{206}Pb/^{238}U$ ages up to ~5% younger than the 'true age', while those with very high U concentrations may yield $^{206}Pb/^{238}U$ ages up to ~2% older than the true age (Allen and Campbell, 2012). The thresholds for low and high U concentrations are not well constrained but caution is advised for $^{206}Pb/^{238}U$ age calculations where zircons have U > 700 ppm (Williams, 1992; Vavra *et al.*, 1999), particularly when analysing the outer rims of zircon, which are more prone to radiation damage and Pb-loss (Schoene, 2014). Caution is also advised against the $^{206}Pb/^{238}U$ system within zircon that have been subject to deformation, which may lead to Pb-loss (Reddy *et al.*, 2006). Insomuch, we report the ages (or individual dates) determined herein with the $^{207}Pb/^{206}Pb$ system because many of the samples in this study have U concentrations > 700 ppm and in some cases, yielded reversely discordant data (Fig. 4.S2A, 4.S4A & 4.S6A). The analytical results ($^{207}Pb/^{206}Pb$ and $^{206}Pb/^{238}U$ individual dates) for each sample are presented in the supplementary material (Tables D.2-8) and the comparison between of the $^{207}Pb/^{206}Pb$ and $^{206}Pb/^{238}U$ weighted mean ages determined for the respective age populations of each sample is presented in Table D.8.

Radiogenic isotope ratio and age error propagation for all analyses includes uncertainty contributions from counting statistics and background subtraction. Errors on the individual dates are reported at 2σ, while those on weighted mean averages are reported at 95% confidence level. Analyses with dates >10% positive or >10% negative discordance (at 2σ) between the $^{206}Pb/^{238}U$ and $^{207}Pb/^{206}Pb$ systems are not considered in the initial age calculations.

For each age population with equivalent dates (probability of fit, PF > 0.05) a $^{207}Pb/^{206}Pb$ weighted mean age is first calculated using errors on individual dates that do not include a standard/external calibration uncertainty (standard error annotated within parentheses), and then a standard calibration uncertainty is propagated into the standard error on the weighted mean date (annotated without parentheses). In this way, we can first evaluate if different age populations obtained from a single sample, derived during the same analytical session with the same standards, define distinct ages or overlap with each other. Conversely, age populations across different samples are only compared once the standard calibration uncertainty is propagated into the error in order to mitigate differences across the different analytical sessions, the use of different standards and for subsequent comparison to ages reported elsewhere in the Grenville Province, determined in different laboratories. The standard calibration uncertainty for U/Pb is the local standard deviation of the polynomial fit to the fractionation factor of the primary standards OG1 (sessions 1-4) and FC1

(sessions 5 & 6) versus time and for $^{207}Pb/^{206}Pb$ is the standard error of the mean of the fractionation factor of the primary standards respectively. For sessions 1-4, these uncertainties are 1.50-1.82% (2σ) for $^{206}Pb/^{238}U$ and 0.18-0.32% (2σ) for $^{207}Pb/^{206}Pb$ (Table D.1B). For sessions 5 & 6 the uncertainties are 0.52-0.60% (2σ) for $^{206}Pb/^{238}U$ and 0.32-0.42% (2σ) for $^{207}Pb/^{206}Pb$ (Table D.1).

APPENDIX D SUPPLEMENTARY GEOCHRONOLOGY FIGURES AND TABLES

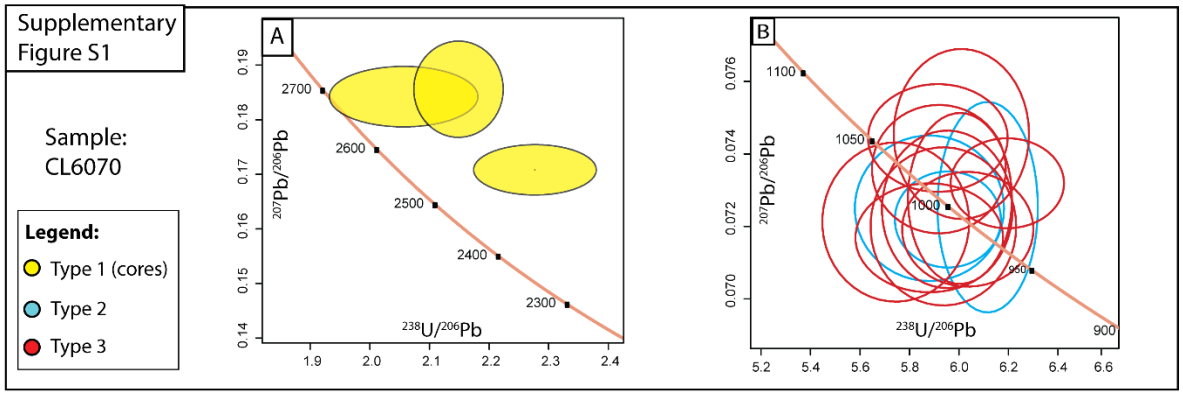

Figure D.1. Tera-Wasserburg plots for zircon populations in sample CL6070.

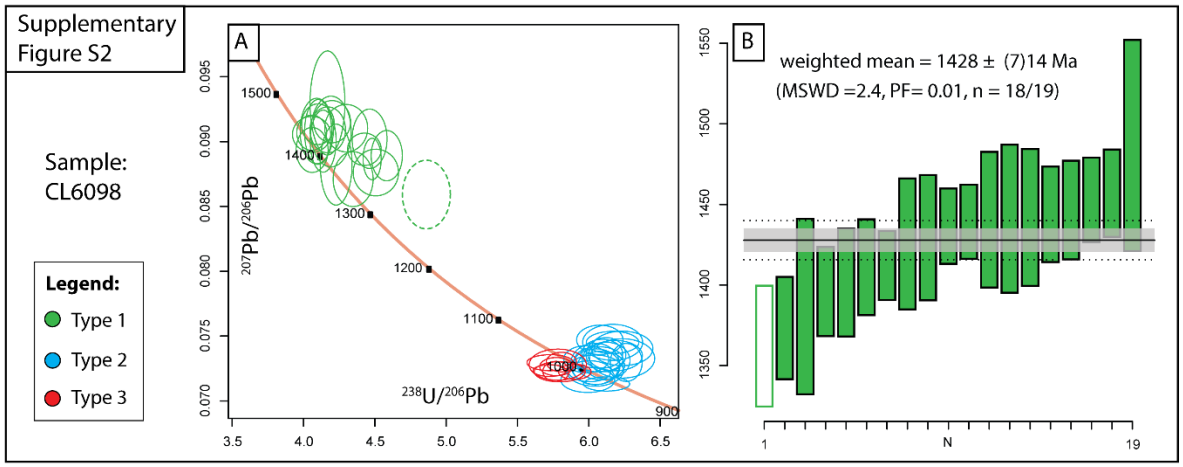

Figure D.2. (A) Tera-Wasserburg plots for zircon populations in sample CL6098 and (B) $^{207}Pb/^{206}Pb$ weighted mean average age for type 1 zones.

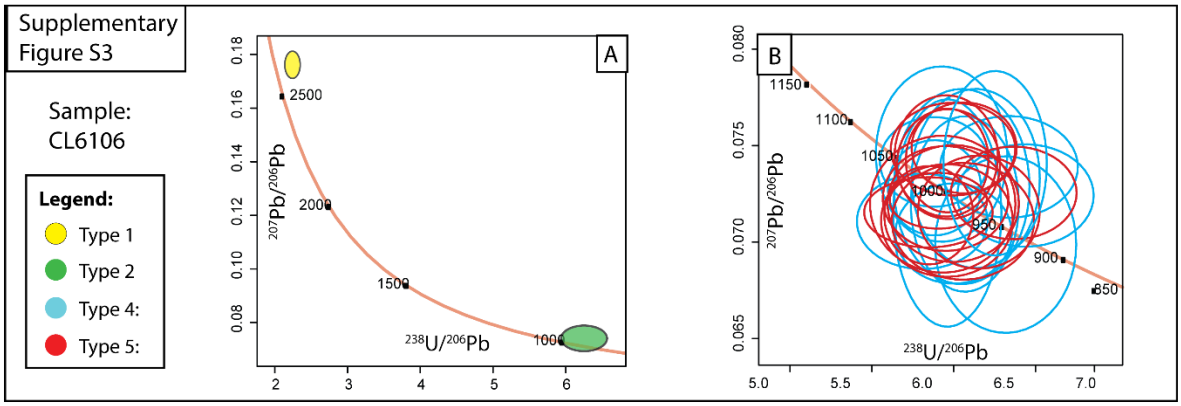

Figure D.3. Tera-Wasserburg plots for zircon populations in sample CL6106.

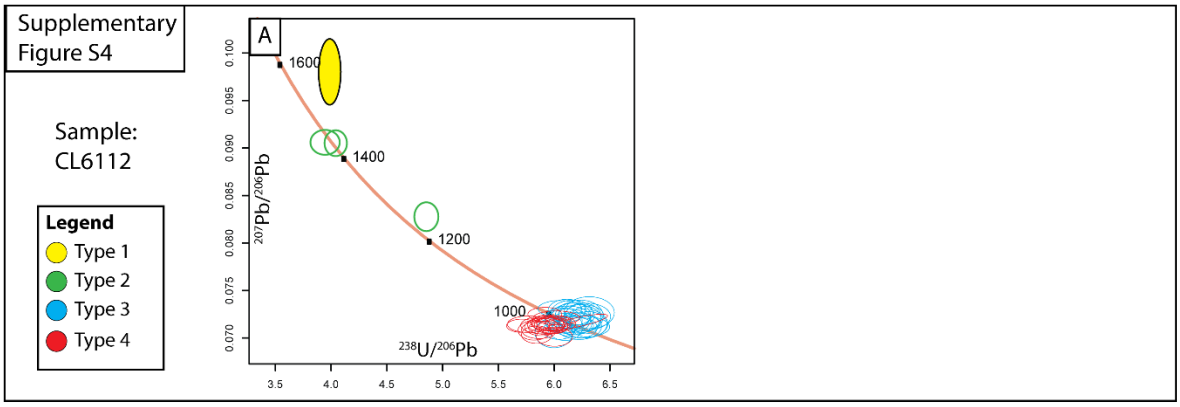

Figure D.4. Tera-Wasserburg plot for zircon populations in sample CL6112.

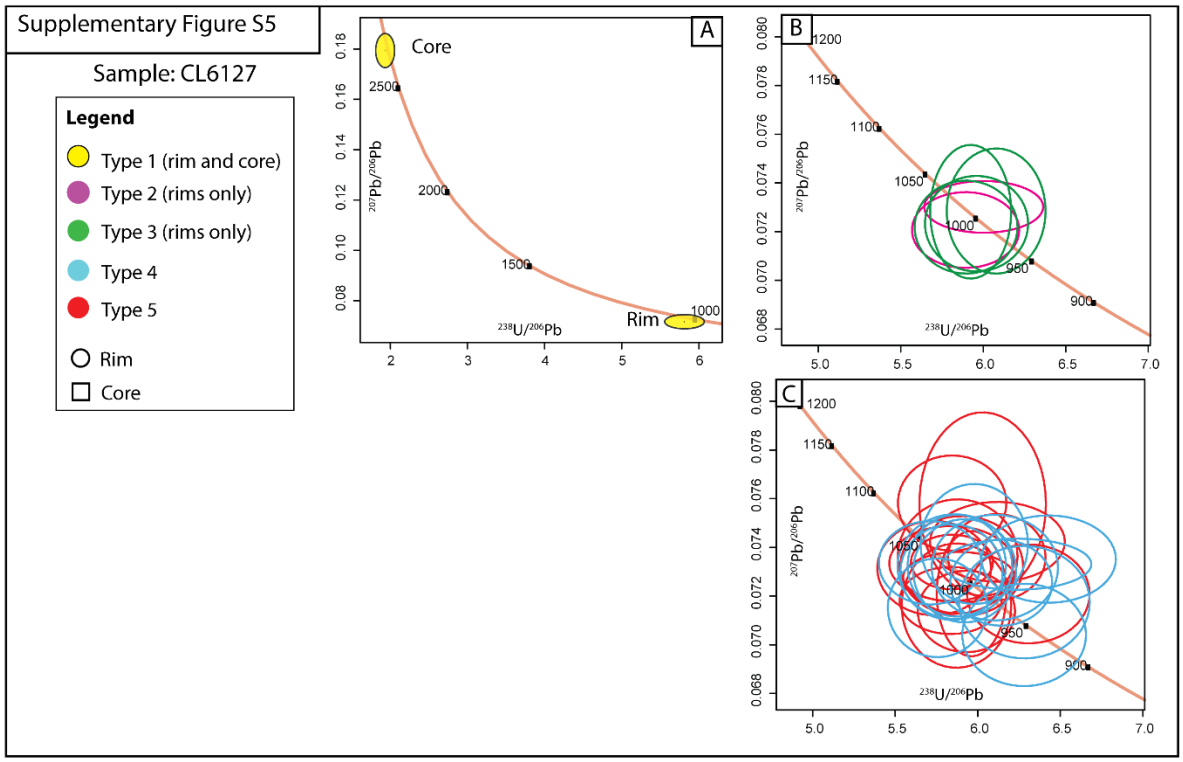

Figure D.5. Tera-Wasserburg plots for zircon populations in sample CL6127.

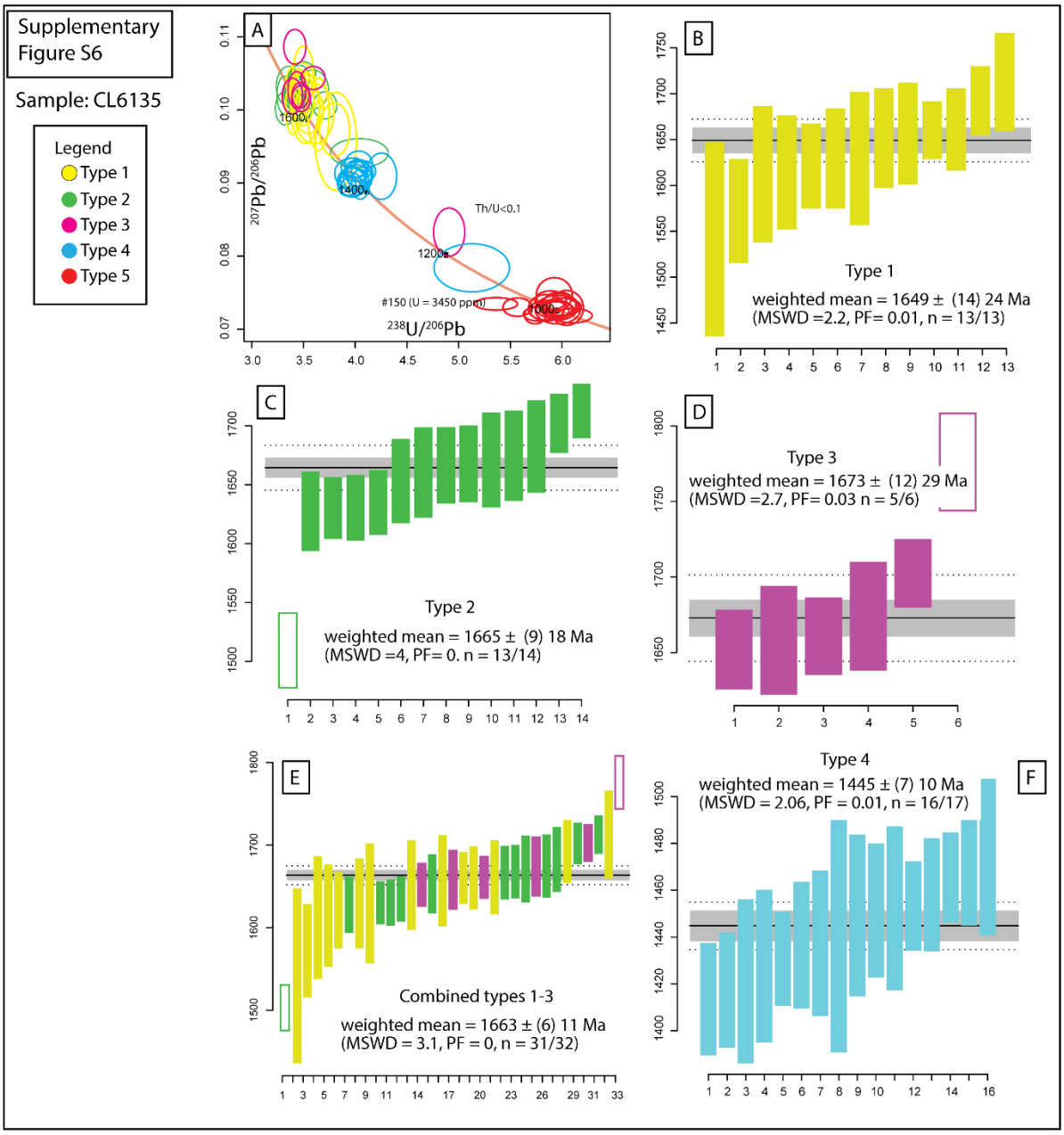

Figure D.6. (A) Tera-Wasserburg plots for zircon populations in sample CL6135 and $^{207}Pb/^{206}Pb$ weighted mean average age for (B) type 1, (C) type 2, (D) type 3 and (F) type 4 zones. (E) $^{207}Pb/^{206}Pb$ weighted mean average if types 1-3 are combined.

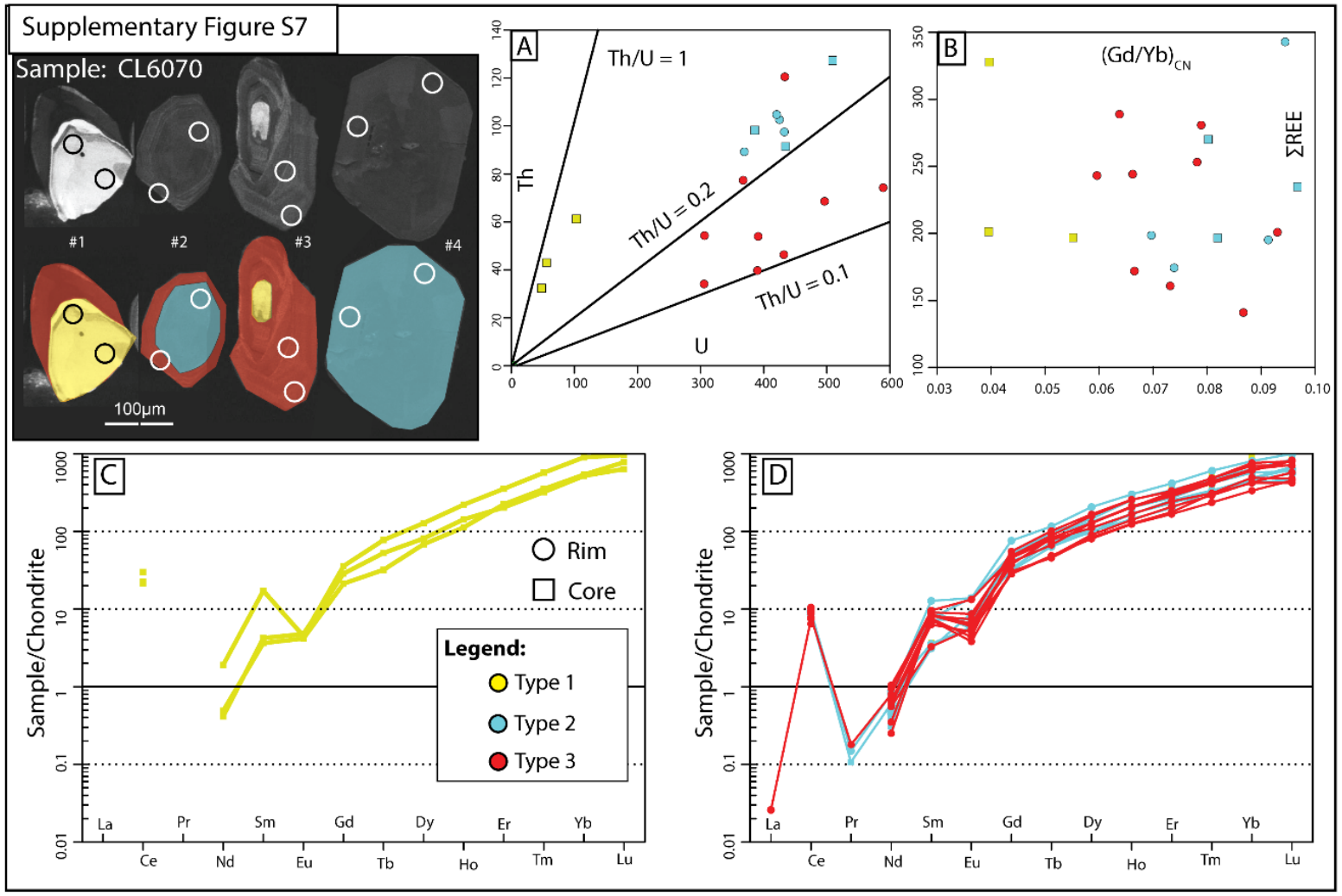

Figure D.7. Trace element diagrams used for geochemical differentiation of the various zircon populations in sample CL6070. (A-B) Various bivariate diagrams. (C-D) Chondrite normalized (Sun and McDonough, 1989) REE spider-diagrams. Image of zircon morphologies supplied for reference to the various zones.

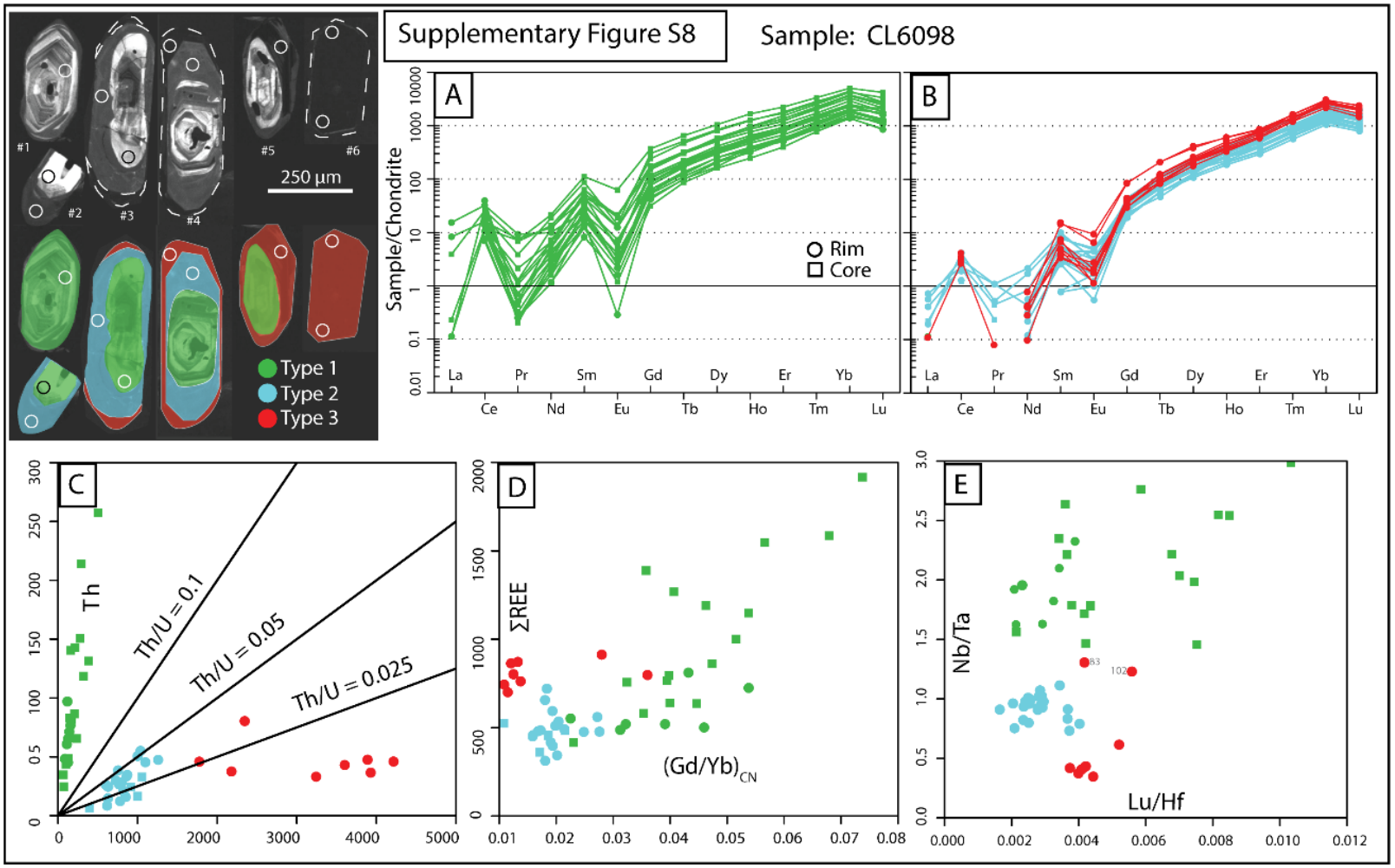

Figure D.8. Trace element diagrams used for geochemical differentiation of the various zircon populations in sample CL6098. (A-B) Chondrite normalized (Sun and McDonough, 1989) REE spider-diagrams. (C-E) Various bivariate diagrams. Image of zircon morphologies supplied for reference to the various zones.

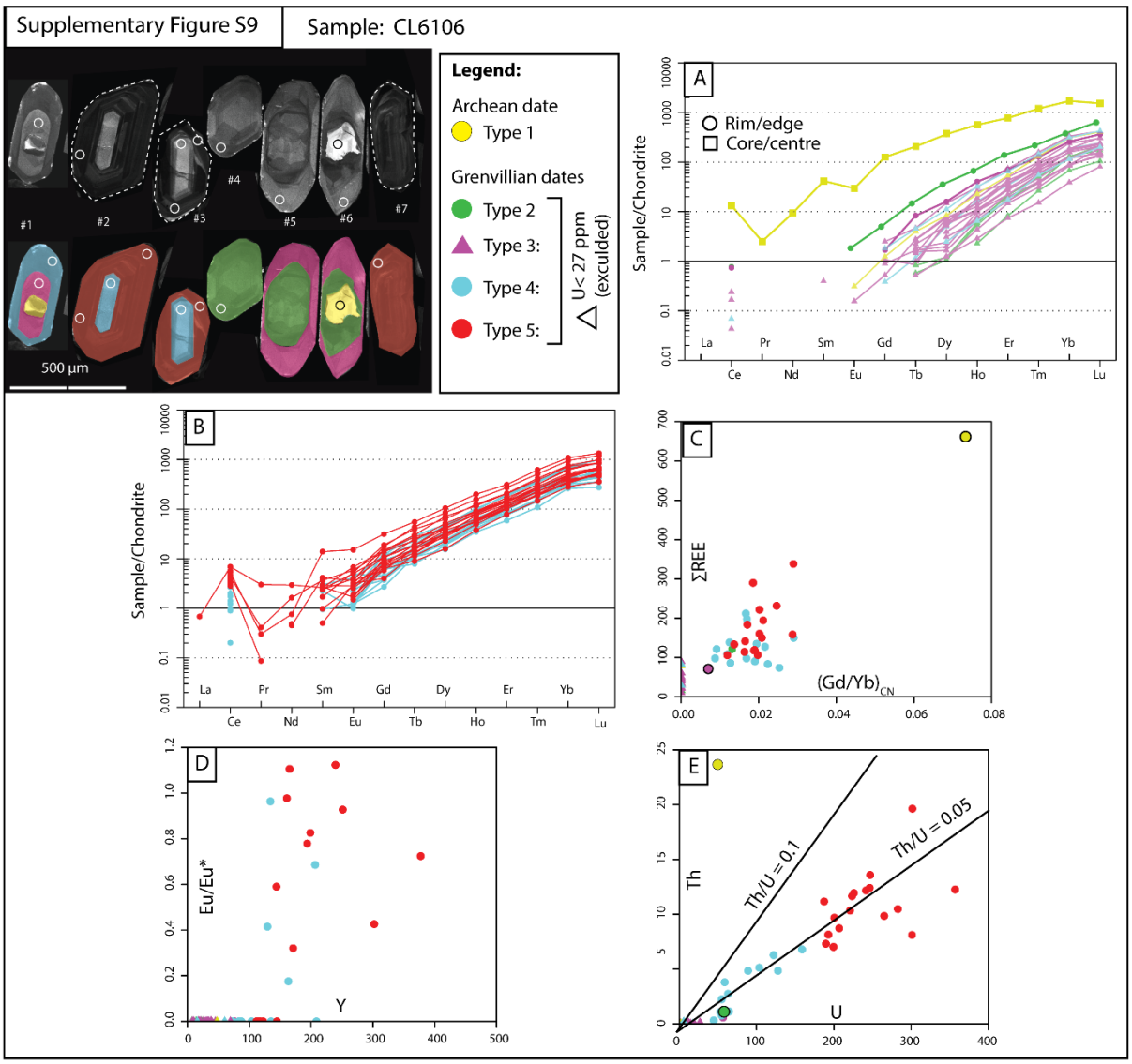

Figure D.9. Trace element diagrams used for geochemical differentiation of the various zircon populations in sample CL6106. (A-B) Chondrite normalized (Sun and McDonough, 1989) REE spider-diagrams. (C-E) Various bivariate diagrams. Note all analyses with triangle symbology were not used in weighted mean age calculations due to element loss. Image of zircon morphologies supplied for reference to the various zones.

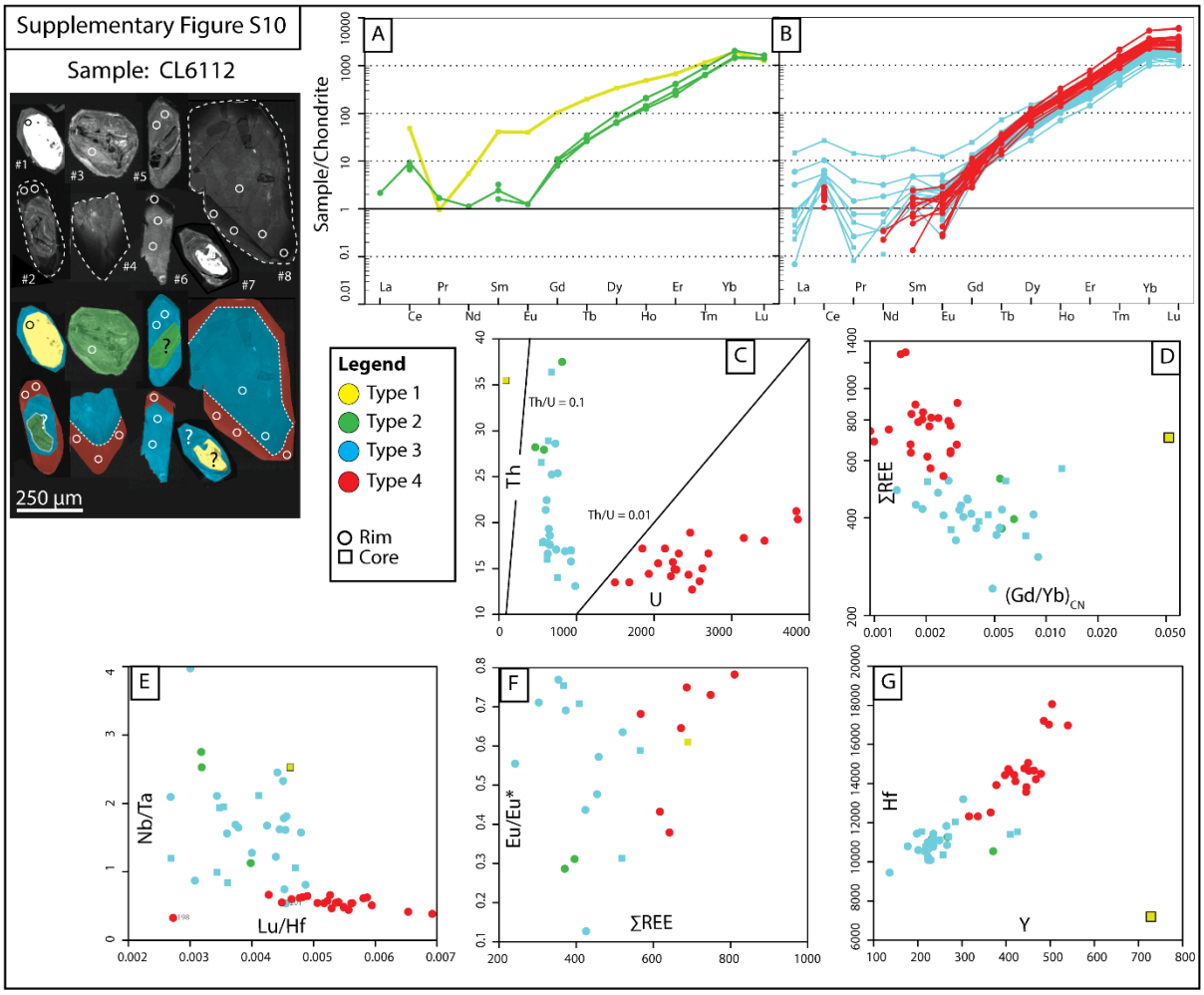

Figure D.10. Trace element diagrams used for geochemical differentiation of the various zircon populations in sample CL6112. (A-B) Chondrite normalized (Sun and McDonough, 1989) REE spider-diagrams. (C-G) Various bivariate diagrams. Image of zircon morphologies supplied for reference to the various zones.

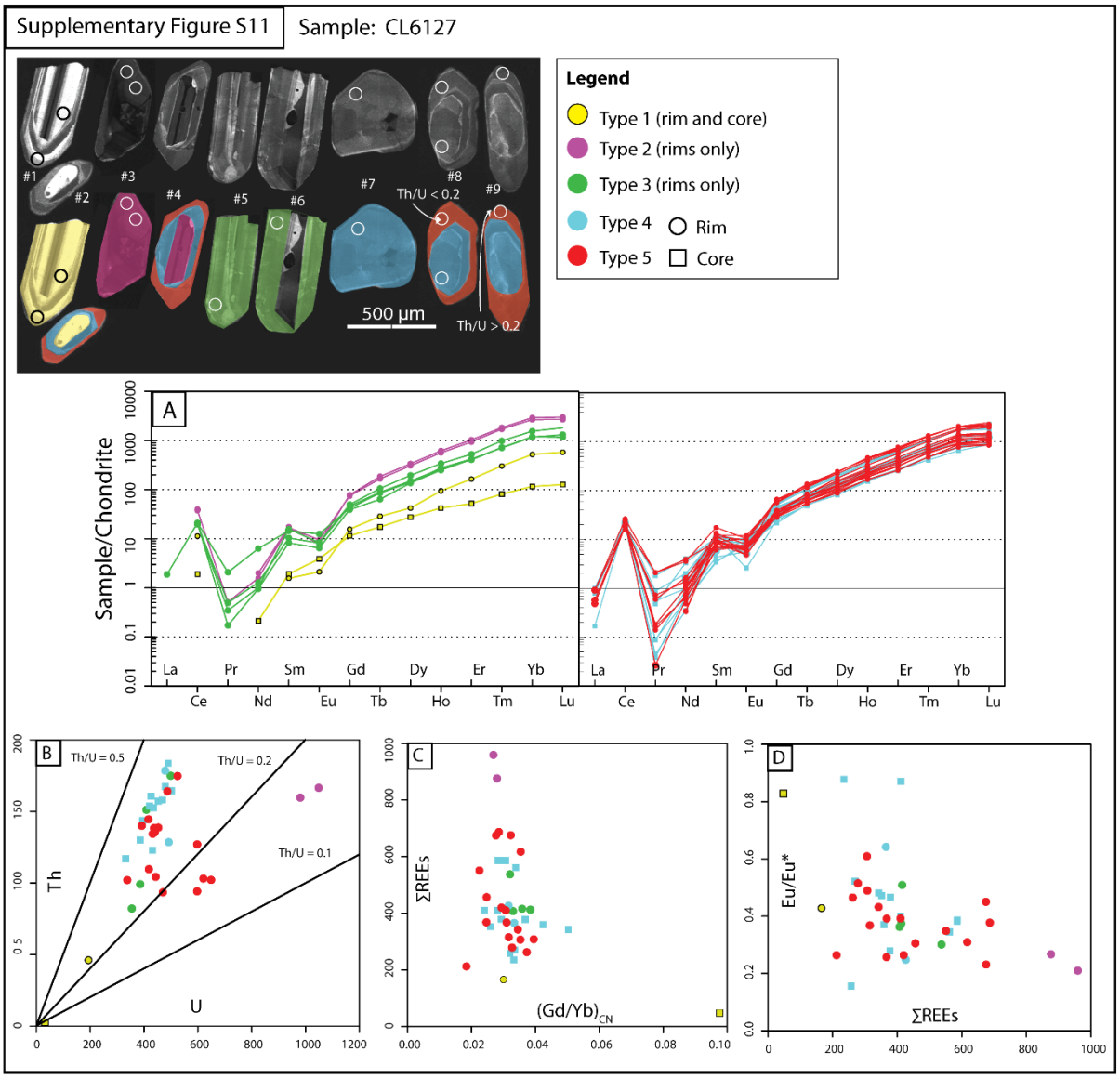

Figure D.11. Trace element diagrams used for geochemical differentiation of the various zircon populations in sample CL6127. (A) Chondrite normalized (Sun and McDonough, 1989) REE spider-diagrams. (B-D) Various bivariate diagrams. Image of zircon morphologies supplied for reference to the various zones.

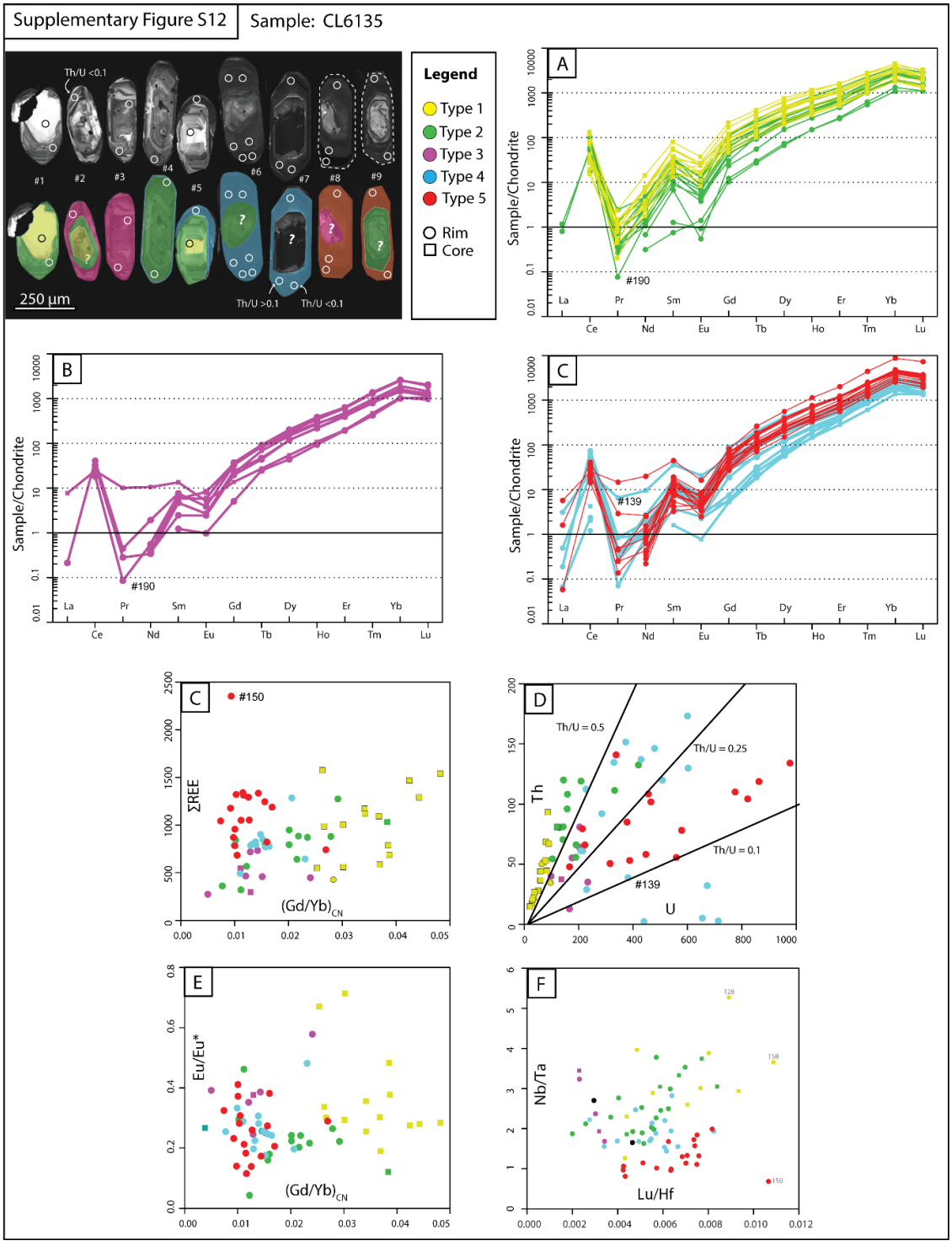

Figure D.12. Trace element diagrams used for geochemical differentiation of the various zircon populations in sample CL6135. (A-C) Chondrite normalized (Sun and McDonough, 1989) REE spider-diagrams. (D-F) Various bivariate diagrams. Image of zircon morphologies supplied for reference to the various zones.

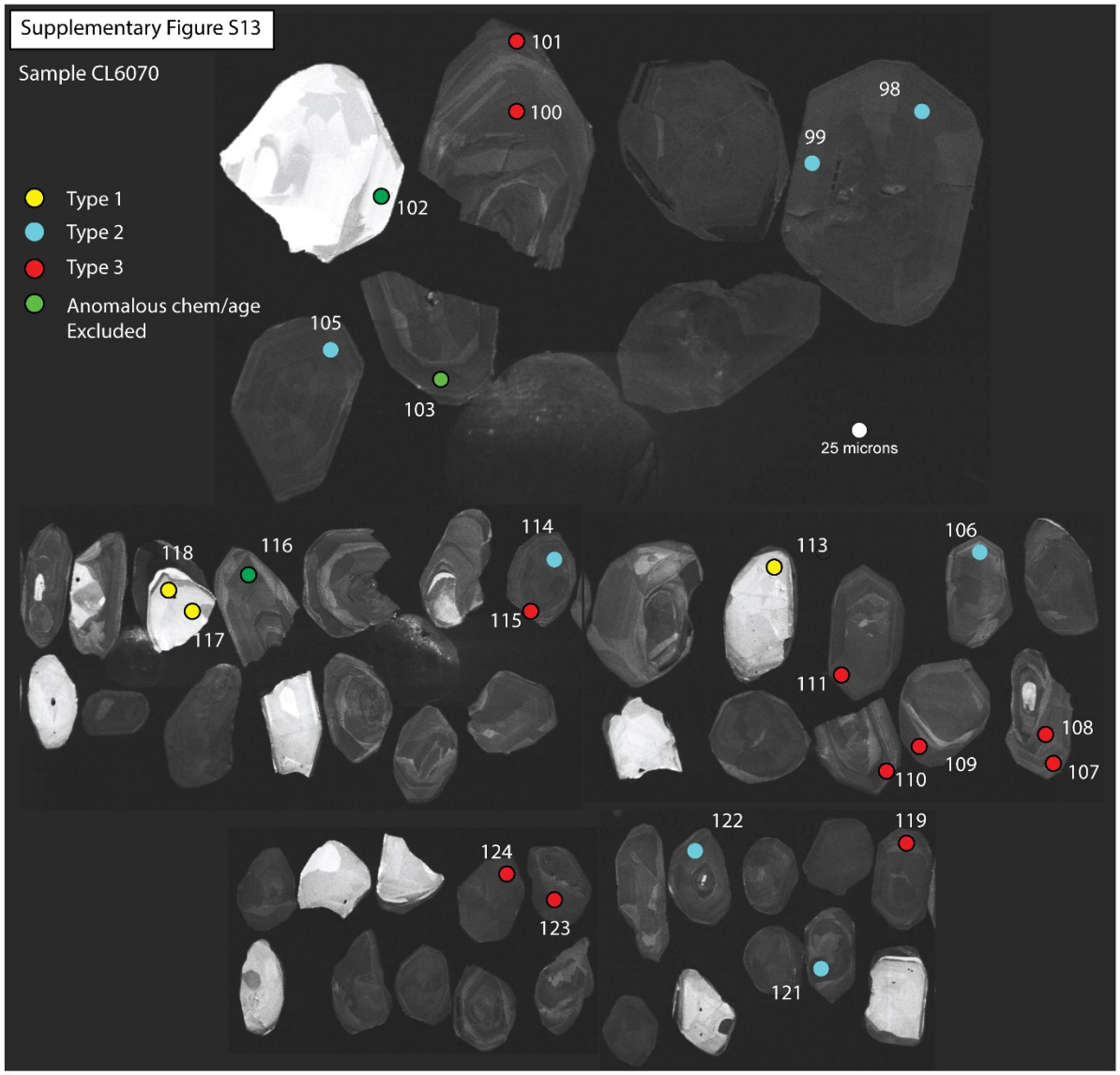

Figure D.13. Cathodoluminescence images of all zircons separated from sample CL6070.

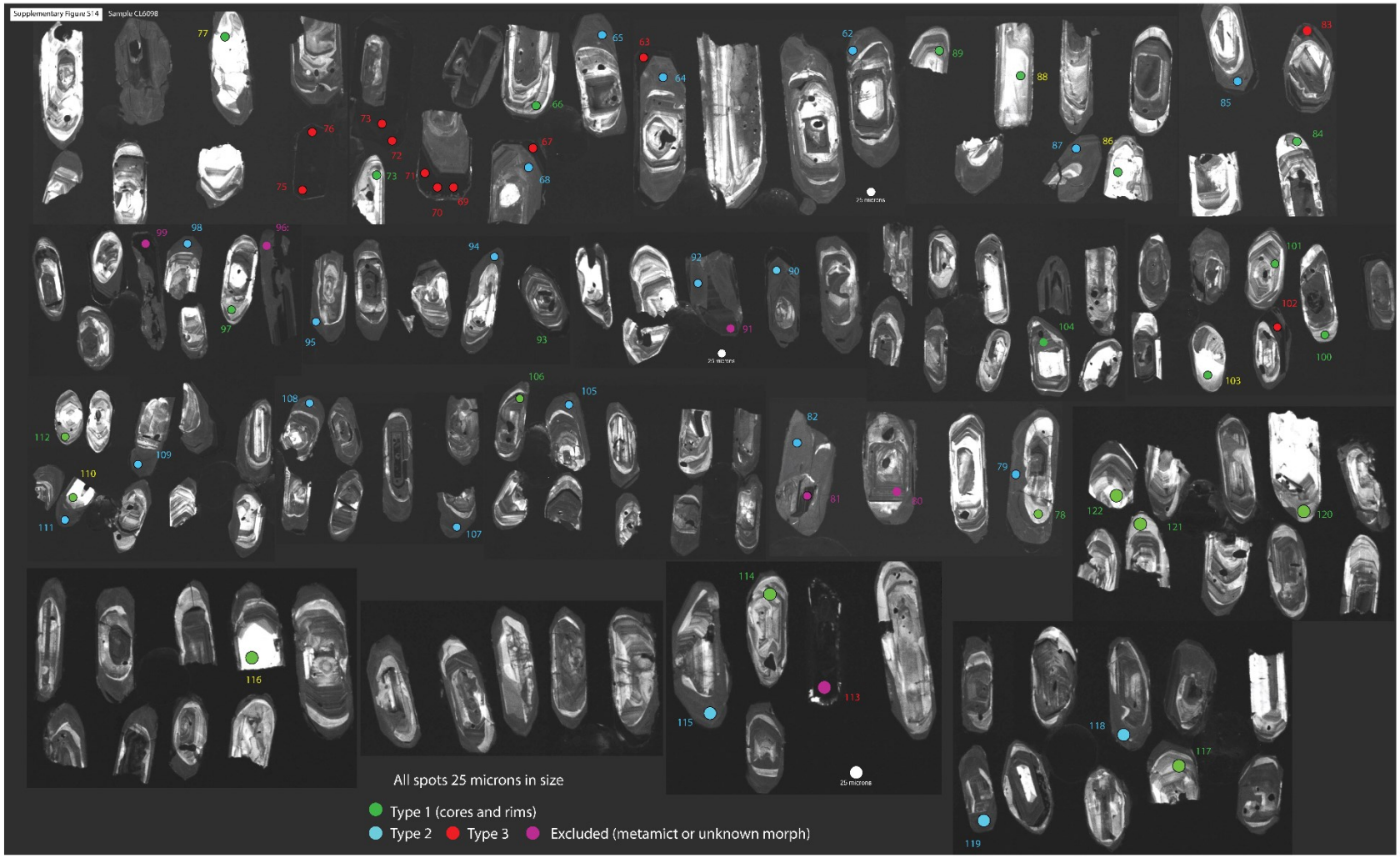

Figure D.14. Cathodoluminescence images of all zircons separated from sample CL6098.

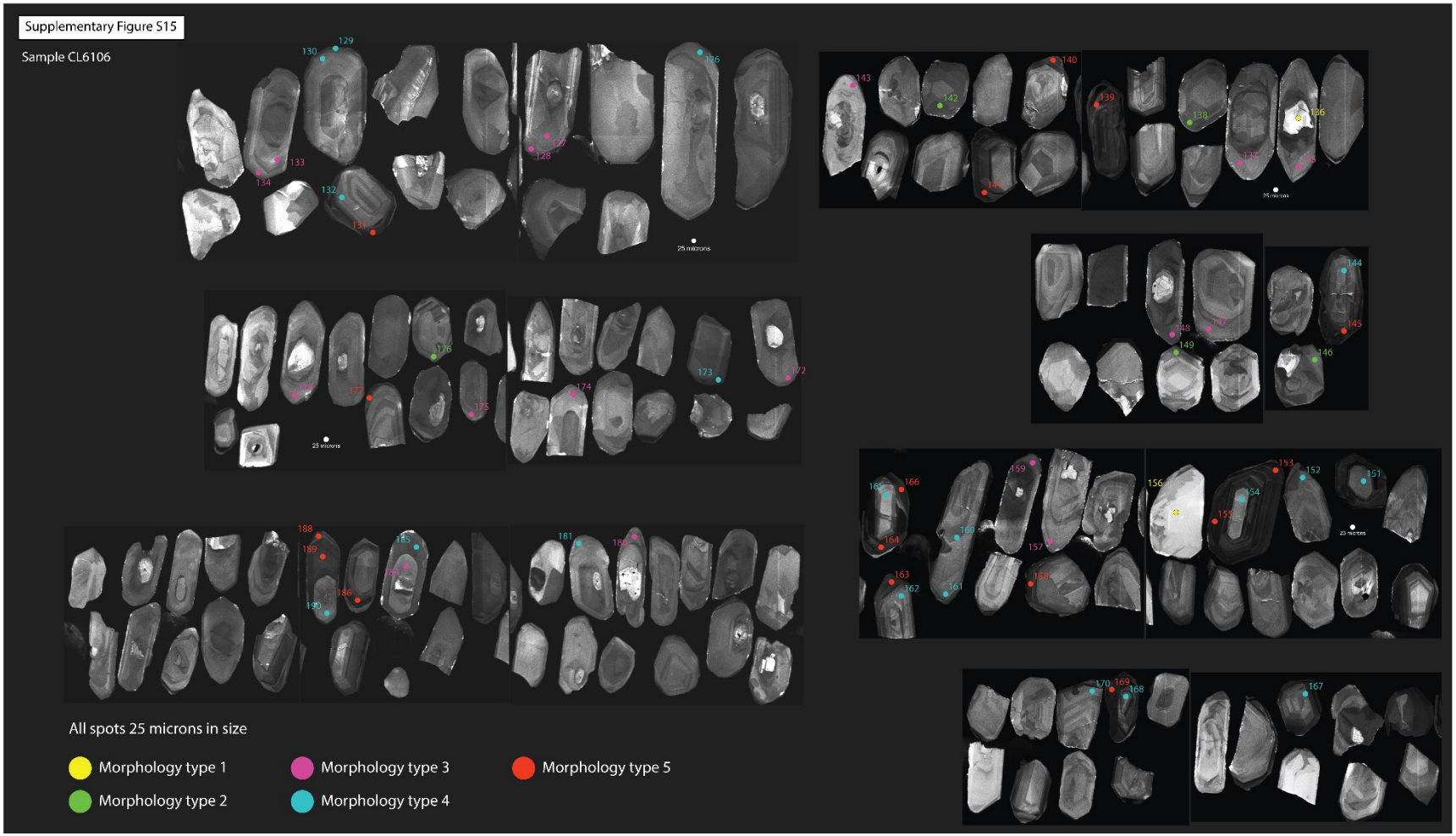

Figure D.15.Cathodoluminescence images of all zircons separated from sample CL6106.

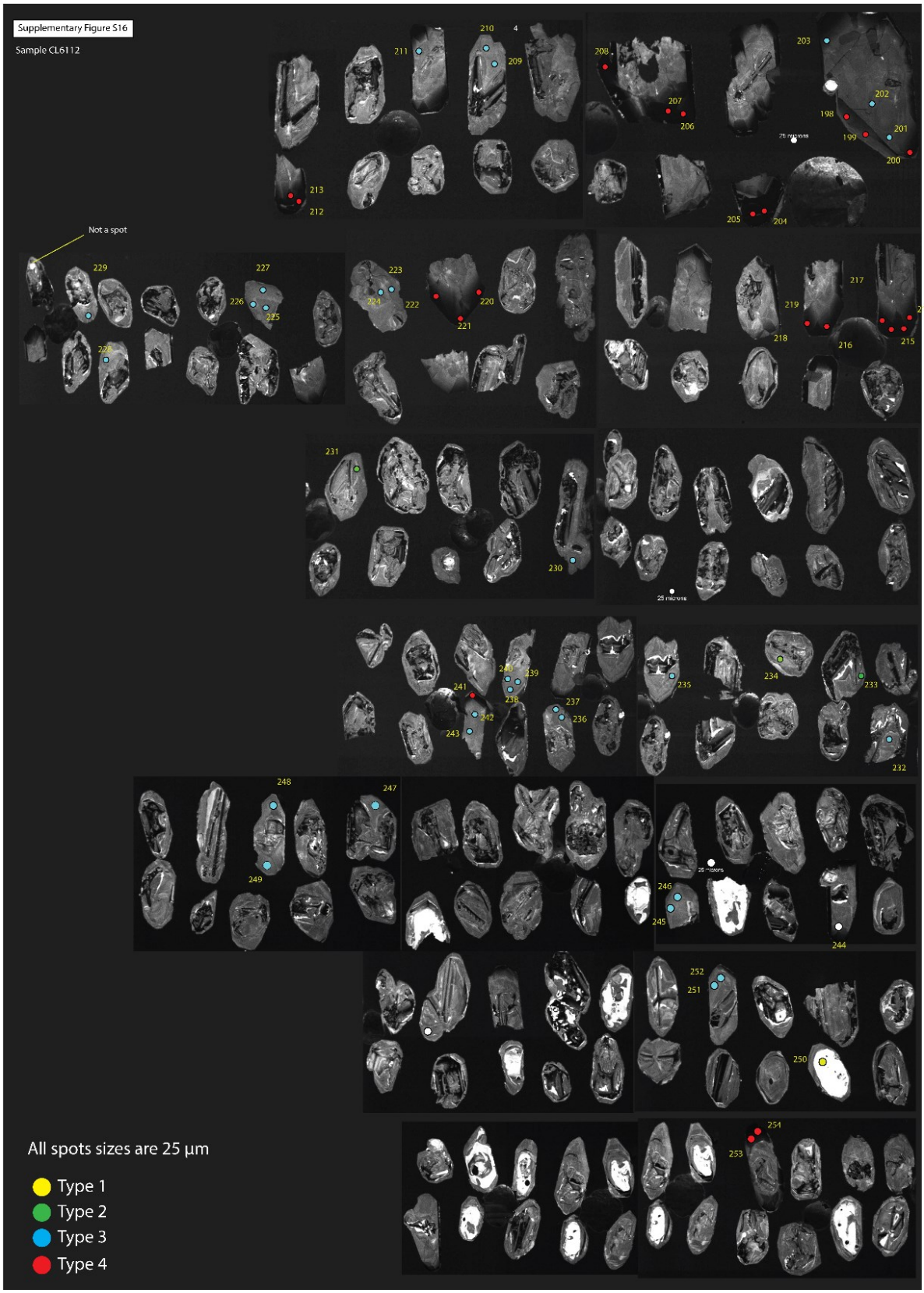

Figure D.16. Cathodoluminescence images of all zircons separated from sample CL6112.

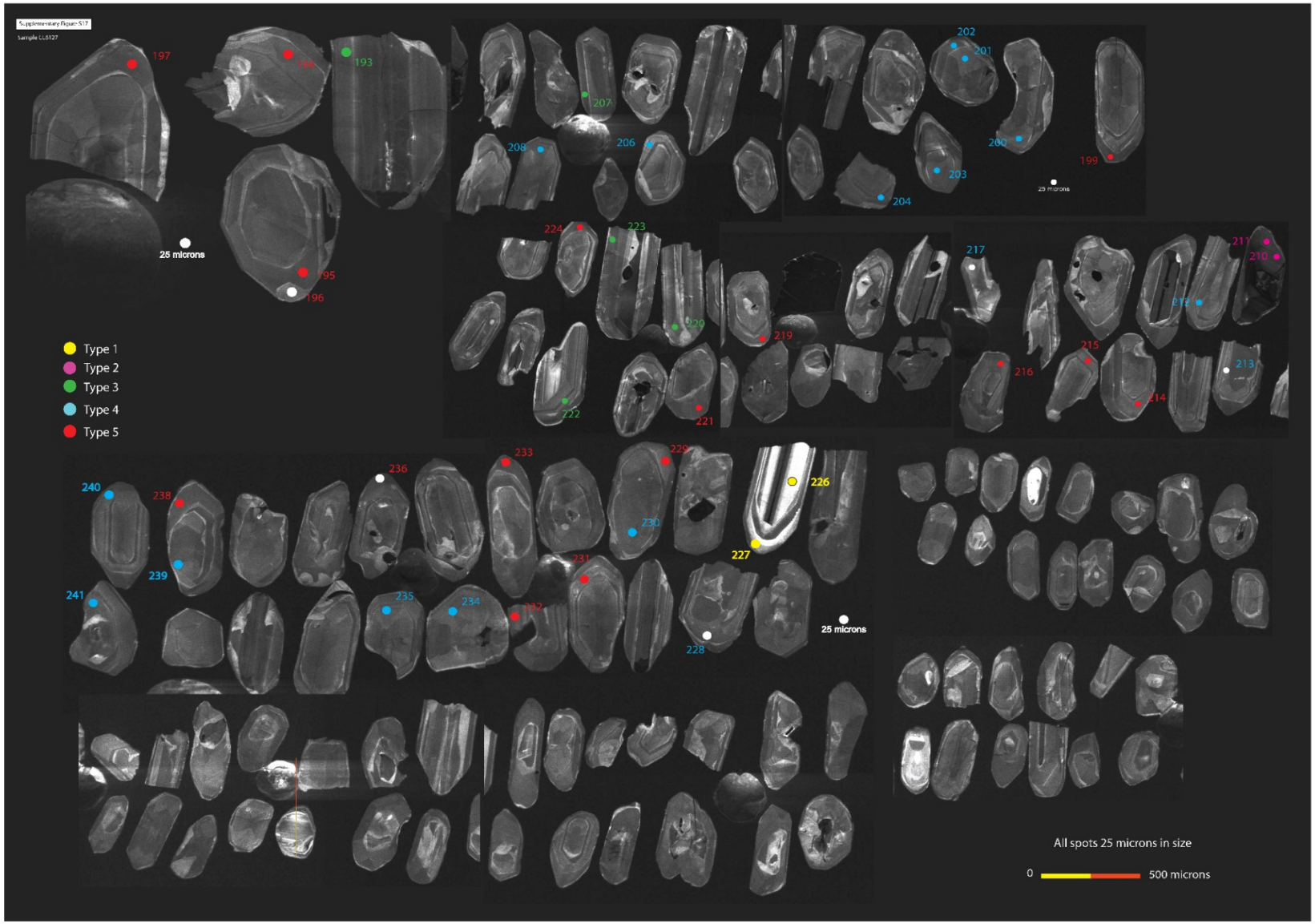

Figure D.17. Cathodoluminescence images of all zircons separated from sample CL6127.

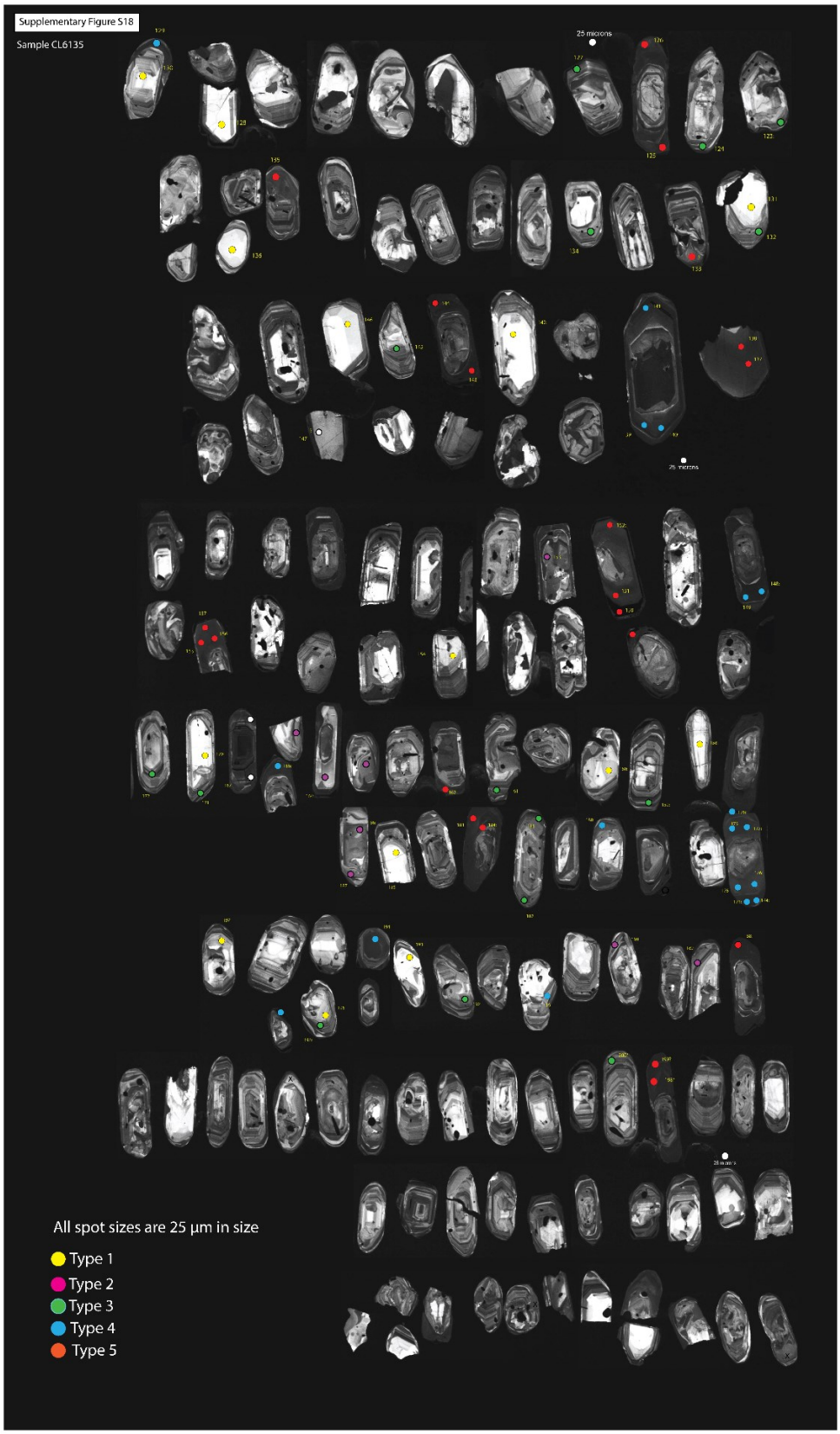

Figure D.18. Cathodoluminescence images of all zircons separated from sample CL6135.

Table D. 1. (Above left and right) Metadata for LA-ICP-MS U-(Th-)Pb analyses and (below) summary of standard materials and analytical errors for each sample.

Laboratory and Sample Preparation	
Laboratory name	Boise State University Isotope Geology Laboratory
Sample type/mineral	Zircon
Sample preparation	Conventional mineral separation, 1 inch resin mount, 0.3 μm polish to finish
Imaging	CL, JEOL T300, 10 nA, 17 mm working distance
Laser ablation system	
Make, Model and type	ESI/New Wave Research, UP213
Ablation cell and volume	Standard ablation cell
Laser wavelength (nm)	213 nm
Pulse width (ns)	4 ns
Fluence (J cm^{-2})	~5 J cm^{-2}
Repetition rate (Hz)	5 Hz
Ablation duration (s)	30 s
Ablation pit depth / ablation rate	15 μm pit depth, measured using an optical microscope, equivalent to 0.05 μm/pulse
Spot diameter (μm)	25 μm
Sampling mode / pattern	Static spot ablation
Carrier gas	100% He in the cell, Ar make-up gas combined using a Y-piece 70 cm from the torch.
Cell carrier gas flow (l min^{-1})	1.15 l min^{-1}
ICP-MS Instrument	
Make, Model and type	ThermoElectron, X-series II, quadrupole
Sample introduction	Ablation aerosol transported through 90 cm long, 1.5 cm dia. tygon tubing coil
RF power (W)	1400 W
Make-up gas flow (l min^{-1})	0.74 l min^{-1} Ar
Detection system	single ion-counting SEM
Masses measured	29, 91 (5); 202–207, 235, 238
Masses measured and dwell times per peak (ms)	29,91(5); 31,89,93,139,140,141,146,147,153,157,159, 163,165,166,169,172,175,177,181(10); 202,204,208,232,238(40); 206(80); 49,207(200)
Total integration time per output data point (s)	~ 0.895 s
'Sensitivity' as useful yield (%, element)	0.01% U ((#ions detected/#atoms sampled)*100; Schaltegger *et al.* 2015)
IC Dead time (ns)	29 ns

Laboratory and Sample Preparation	
Data Processing	
Gas blank	30 s on-peak zero subtracted
Calibration strategy	In session 1, OG1 used as primary reference material and 91500 and FC1 used as secondary reference materials. In session 2, FC1 used as primary reference material and 91500 and Plešovice used as secondary reference material.
Reference Material info	OG1 (3465 Ma; Boise State University, unpublished data) 91500 (1065 Ma; Wiedenbeck et al., 1995) FC1 (1098 Ma; Boise State University, unpublished data) Plešovice (337 Ma; Slama et al., 2008)
Data processing package used / Correction for LIEF	ThermoElectron Plasmalab TRA software for integrated cps acquisition; in-house Microsoft VBA coded spreadsheet for data normalization, concentration calibration, uncertainty propagation and age calculation.
Mass discrimination	$^{207}Pb/^{206}Pb$ and $^{206}Pb/^{238}U$ normalized to reference material
Common-Pb correction, composition and uncertainty	No common Pb correction applied; ablation sweeps with mass 204 signals above background rejected.
Uncertainty level and propagation	Ages are quoted at 2 sigma absolute, propagation is by quadratic addition. Systematic errors based upon reproducibility of reference material are propagated where appropriate: 1.82% (2 sigma) for Pb/U and 0.32% (2 sigma) for Pb/Pb in session 1 and 0.60% (2 sigma) for Pb/U and 0.42% (2 sigma) for Pb/Pb in session 2 .
Quality control / Validation	See accompanying data tables.

Experimental session number	Samples analysed	Primary standard	Published age (207Pb/206Pb)	Secondary reference zircon	Published age (Ma)	Calculated (207Pb/206Pb) age on secondary reference*	±2s (Ma)*	Mean Square of Weighted Deviates and probability of fit	Standard error on 207Pb/206Pb (%)	Standard error on 206Pb/238U (%)
1	CL6013	OG1	3465	Zircon 91500	1065	1043	30	MSWD = 0.9, pof = 0.51	0.18	1.73
	CL6034			FC1	1098	1087	11	MSWD = 0.7, pof = 0.77		
2	CL6070			Zircon 91500	1065	1027	39	MSWD = 0.6, pof = 0.80	0.24	1.5
	CL6106			FC1	1098	1085	12	MSWD = 1.6, pof = 0.10		
3	CL6127			Zircon 91500	1065	1054	28	MSWD = 1.8, pof = 0.06	0.3	1.58
	CL6144			FC1	1098	1086	14	MSWD = 1.5, pof = 0.12		
4	CL6034			Zircon 91500	1065	1072	38	MSWD = 0.7, pof = 0.72	0.32	1.82
	CL6144			FC1	1098	1100	13	MSWD = 1.7, pof = 0.07		
5	CL6098	FC1	1098	Zircon 91500	1065	1081	20	MSWD = 0.9, pof = 0.53	0.32	0.52
	CL6112									
6	CL8025			Zircon 91500	1065	1063	18	MSWD = 1.8, pof = 0.07	0.42	0.6
	CL6135									

***Weighted mean dates with errors that include standard calibration uncertainty.**

Table D. 2. Summary of geochronology analyses for sample CL6070.

Sample No	Spot Number	Type	Apparent Ages (Ma)					Isotope ratios							
			207Pb*/206Pb*	±2s (Ma)	206Pb*/238U*	±2s (Ma)	% disc.	207Pb*/235U*	±2s (%)	206Pb*/238U	±2s (%)	error corr.	207Pb*/206Pb*	±2s (%)	error corr.
CL6070	113	1	2691	41	2554	105	5.1	12.3505	5.5319	0.4862	4.9557	0.8948	0.1842	2.4583	0.0000
	117	1	2703	64	2463	58	8.9	11.9085	4.8204	0.4654	2.8548	0.5901	0.1856	3.8841	0.0000
	118	1	2566	37	2347	73	8.5	10.3437	4.3042	0.4392	3.6956	0.8568	0.1708	2.2065	0.0000
	114	2	1041	47	961	35	7.7	1.6395	4.6028	0.1608	3.9634	0.8595	0.0740	2.3404	0.0000
	121	2	1001	45	1025	27	-2.3	1.7236	3.6082	0.1723	2.8457	0.7858	0.0725	2.2183	0.0000
	122	2	1034	50	982	39	5.0	1.6725	4.9149	0.1645	4.2433	0.8619	0.0737	2.4801	0.0000
	98	2	1001	66	976	25	2.4	1.6351	4.2495	0.1635	2.7105	0.6353	0.0725	3.2728	0.0000
	99	2	991	31	1001	27	-0.9	1.6714	3.3041	0.1679	2.9430	0.8877	0.0722	1.5019	0.0000
	106	2	989	51	1035	40	-4.6	1.7309	4.9020	0.1741	4.2220	0.8599	0.0721	2.4909	0.0000
	105	2	1053	33	1007	36	4.4	1.7354	4.2304	0.1691	3.9027	0.9207	0.0744	1.6327	0.0000
	124	3	1000	46	1012	39	-1.2	1.6999	4.7627	0.1701	4.1898	0.8782	0.0725	2.2648	0.0000
	119	3	999	50	1001	34	-0.2	1.6786	4.3740	0.1680	3.6230	0.8264	0.0725	2.4507	0.0000
	100	3	977	35	1012	39	-3.6	1.6810	4.4877	0.1701	4.1473	0.9226	0.0717	1.7145	0.0000
	101	3	1019	28	965	27	5.3	1.6288	3.3266	0.1614	3.0235	0.9060	0.0732	1.3873	0.0000
	107	3	1030	40	1006	35	2.3	1.7139	4.2220	0.1690	3.7346	0.8827	0.0736	1.9691	0.0000
	108	3	986	50	1003	38	-1.8	1.6721	4.7485	0.1684	4.0508	0.8515	0.0720	2.4777	0.0000
	111	3	984	37	988	33	-0.5	1.6431	4.0179	0.1657	3.5923	0.8920	0.0719	1.7999	0.0000
	115	3	1008	54	993	26	1.4	1.6713	3.8981	0.1666	2.8600	0.7311	0.0728	2.6487	0.0000
	109	3	1056	52	992	34	6.1	1.7104	4.5216	0.1664	3.7186	0.8207	0.0745	2.5722	0.0000

Sample No	Spot Number	Trace element concentrations (ppm)																													
		P	Ti	Y	Zr	Nb	La	Ce	Pr	Nd	Sm	Eu	Gd	Tb	Dy	Ho	Er	Tm	Yb	Lu	Hf	Ta	Th	U	Ce/Ce*	Eu/Eu*	ΣREE	(Gd/Yb)cn	Lu/Hf	Nb/Ta	Th/U
CL6070	113	160.6568	3.7822	413.2635	490681.1792	0.7549		18.2950		0.8915	2.6378	0.2613	7.3390	2.8984	32.4560	12.5116	58.5108	14.5392	152.9211	24.4892	10447.8526	0.4222	42.8731	55.4864		0.1815	327.7509	0.0397	0.0023	1.7880	0.7727
	117	143.8862	7.7863	262.6967	511227.7759	0.5941		13.1145		0.1946	0.6476	0.2770	5.8768	1.9726	20.5932	8.0971	33.6508	8.1928	88.0995	16.1533	11454.7013	0.4001	32.3646	47.6149		0.4341	196.8699	0.0552	0.0014	1.4848	0.6797
	118	95.3200	3.0004	231.1006	530722.5661	0.6297		13.8126		0.2290	0.5584	0.2422	4.3701	1.1971	17.3699	6.3767	36.9903	8.9791	91.3904	19.7512	13055.1656	0.5292	61.2286	102.7866		0.4740	201.2667	0.0396	0.0015	1.1900	0.5957
	114	108.3942	1.3061	347.0195	490151.5503	1.3396		6.2716		0.1456	1.4808	0.3223	11.2556	3.4158	33.8023	11.4812	44.6360	10.6176	96.2726	15.0728	15028.1497	1.0088	127.3663	508.9547		0.2414	234.7743	0.0967	0.0010	1.3278	0.2503
	121	161.6364	1.3561	321.9505	518288.7098	1.2308		5.2930		0.1941	0.5293	0.3311	8.1296	2.5469	24.5302	9.5742	38.0867	8.2466	82.0574	17.1165	18441.1676	1.2455	91.5109	434.5127		0.4880	196.6356	0.0820	0.0009	0.9882	0.2106
	122	130.4119	1.5123	444.4781	514278.8491	1.1276		5.2791	0.0102	0.2801	1.1674	0.7990	10.4485	3.5643	36.9548	14.2574	56.3268	11.9283	107.7622	21.3704	16942.3909	1.0520	98.2961	385.7125	507.4915	0.6994	270.1487	0.0802	0.0013	1.0719	0.2548
	98	179.0072	1.7260	551.4059	513598.7403	1.3932		5.8673	0.0142	0.3780	1.9472	0.7996	15.5432	4.3201	52.0797	16.8877	68.3609	15.3172	136.1295	25.1941	15426.5016	0.8639	102.7092	424.6847	405.7731	0.4444	342.8388	0.0945	0.0016	1.6126	0.2418
	99	157.7376	1.0072	319.9897	513281.4243	1.3447		5.5019		0.4124	0.5448	0.3388	8.4420	2.4326	27.5409	9.2981	41.5776	8.5639	76.4630	14.1445	15426.9690	0.8618	89.2627	369.0409		0.4830	195.2604	0.0913	0.0009	1.5604	0.2419
	106	114.7514	1.2369	253.1026	474014.6086	1.1943		5.7231		0.2104	0.4751	0.5102	6.4336	2.3652	25.3051	8.1101	33.1092	8.4689	72.0339	11.6280	14107.7245	0.7257	97.5539	432.4281		0.8922	174.3728	0.0739	0.0008	1.6458	0.2256
	105	103.7239	1.5487	322.7335	513899.6219	1.2171		5.1986		0.2300	1.1074	0.4263	6.8343	2.7005	27.5835	9.5093	39.6056	8.3569	81.1540	15.9255	16621.5849	0.8830	104.7767	420.3578		0.4738	198.6320	0.0697	0.0010	1.3783	0.2493
	124	160.7988	0.6398	392.2929	518067.9333	0.8272		5.4009		0.4879	1.2954	0.3763	8.1592	2.4925	32.4608	11.7512	49.1875	10.4551	101.9202	20.2420	14952.5803	1.0253	74.2369	589.3525		0.3539	244.2291	0.0662	0.0014	0.8068	0.1260
	119	152.0201	1.7228	221.3672	507845.8503	1.1636		3.9322		0.2592	0.5025	0.3231	5.8973	1.8063	20.2997	6.9470	27.4750	5.9481	56.2578	11.3814	14085.6607	0.7199	34.0740	305.0017		0.5739	141.0298	0.0867	0.0008	1.6165	0.1117
	100	165.8270	1.5431	395.2132	530613.5333	0.9787		5.6745		0.3054	1.1540	0.2537	9.9330	3.0705	32.1548	11.4569	52.1455	11.1448	105.1500	20.7533	16288.9321	1.0571	68.5977	496.4503		0.2291	253.1964	0.0781	0.0013	0.9258	0.1382
	101	77.1098	1.2266	261.2569	513909.1253	0.8869	0.0062	4.5538		0.2776	0.9625	0.2964	5.7841	1.7680	22.7587	7.8687	34.1096	7.3287	71.8928	14.3798	15139.1111	0.8981	46.3500	431.6632	126.2044	0.3841	171.9869	0.0666	0.0009	0.9876	0.1074
	107	177.1327	1.1862	294.3455	489999.3039	1.4544		6.4139		0.4446	1.4641	0.7660	9.2881	2.8902	28.0203	9.3791	39.8966	7.7920	82.6029	11.9695	12100.2387	0.8459	77.3882	367.0375		0.6350	200.9274	0.0930	0.0010	1.7193	0.2108
	108	134.6666	1.6738	426.2717	480287.9865	1.7467		4.7782	0.0172	0.3727	1.3846	0.5003	9.8515	3.2919	39.8657	14.2455	54.5207	12.1598	127.7524	20.0821	11758.9957	0.8191	54.2716	305.8680	272.3125	0.4142	288.8227	0.0638	0.0017	2.1326	0.1774
	111	155.9713	1.7158	432.1515	480142.8381	1.2854		6.2226		0.1178	1.2413	0.4279	11.2528	3.7617	41.8500	14.3760	53.6604	12.1894	117.9908	17.6971	13681.5359	1.0306	120.4960	433.1931		0.3500	280.7877	0.0789	0.0013	1.2473	0.2782
	115	160.4289	1.2799	358.1472	479004.4105	1.5301		5.3518		0.1644	1.2664	0.3484	7.6816	3.0151	32.2803	11.4655	46.5183	10.4047	106.5841	18.0239	13221.5468	1.0668	53.9144	391.1569		0.3415	243.1045	0.0596	0.0014	1.4343	0.1378
	109	100.9132	1.9396	222.6633	468465.8873	1.1186		5.3536			1.1087	0.2213	6.2619	1.6960	21.1132	7.0816	29.0518	7.6485	70.7773	10.5928	11311.7430	0.8600	39.6937	389.9403		0.2568	160.9067	0.0732	0.0009	1.3007	0.1018

Analytical session no: 2
Isotope ratios and ages are NOT corrected for initial common Pb.
Isotope ratio and apparent age errors do NOT include systematic calibration errors of 0.2421% ($^{207}Pb/^{206}Pb$), 1.5088% ($^{206}Pb/^{238}U$) (all 2-sigma).
Isotope ratios and ages corrected using a measured linear secondary standard age bias - ^{206}Pb count rate relationship.
Trace element concentrations in ppm, calculated using mean count rate method.
Sweep-by-sweep downhole fractionation of U/Pb ratios NOT corrected via Si/Zr fractionation factor.
Backgrounds were monitored between sweeps 5 to 20. Sample counts were integrated from sweeps 35 to 60.
Ablation used a laser spot size of 25 microns, and a laser firing repetition rate of 10 Hz.

Table D. 3. Summary of geochronology analyses for sample CL6098.

Sample Number	Spot Number	Type	Apparent Ages (Ma)					Isotope Ratios							
			207Pb*/206Pb*	±2s (Ma)	206Pb*/238U*	±2s (Ma)	% disc.	207Pb*/235U*	±2s (%)	206Pb*/238U	±2s (%)	error corr.	207Pb*/206Pb*	±2s (%)	error corr.
CL6098	77	1	1363	38	1334	32	2.0849	2.7621	3.3012	0.2300	2.6349	0.7982	0.0871	12.0000	0.0000
	116	1	1412	30	1419	29	-0.5221	3.0342	2.7589	0.2463	2.2562	0.8178	0.0894	1.5878	0.0000
	103	1	1488	67	1386	30	6.8097	3.0758	4.2671	0.2399	2.3947	0.5612	0.0930	3.5318	0.0000
	100	1	1374	32	1292	34	5.9997	2.6802	3.3365	0.2219	2.8824	0.8639	0.0876	1.6805	0.0000
	110	1	1397	28	1298	14	7.0341	2.7277	1.8754	0.2231	1.1585	0.6177	0.0887	1.4747	0.0000
	74	1	1447	31	1348	35	6.8719	2.9195	3.3004	0.2326	2.8627	0.8674	0.0910	1.6425	0.0000
	122	1	1402	34	1272	23	9.2922	2.6747	2.6439	0.2182	1.9500	0.7376	0.0889	1.7853	0.0000
	117	1	1387	56	1368	27	1.3740	2.8766	3.6106	0.2365	2.1560	0.5971	0.0882	2.8962	0.0000
	104	1	1454	27	1406	29	3.2571	3.0703	2.6812	0.2438	2.2831	0.8515	0.0913	1.4058	0.0000
	112	1	1445	30	1386	30	4.0921	3.0059	2.9156	0.2398	2.4435	0.8381	0.0909	1.5905	0.0000
	93	1	1437	24	1420	34	1.1856	3.0779	2.9774	0.2465	2.7017	0.9074	0.0906	1.2513	0.0000
	106	1	1440	23	1420	27	1.3846	3.0814	2.4405	0.2464	2.1089	0.8641	0.0907	1.2281	0.0000
	89	1	1458	28	1377	31	5.5667	3.0052	2.9207	0.2381	2.5328	0.8672	0.0915	1.4544	0.0000
	101	1	1413	22	1313	26	7.0831	2.7849	2.4612	0.2259	2.1802	0.8858	0.0894	1.1420	0.0000
	120	1	1426	41	1395	23	2.1787	3.0001	2.8168	0.2417	1.7936	0.6367	0.0900	2.1720	0.0000
	84	1	1443	43	1409	29	2.3277	3.0600	3.2502	0.2444	2.3223	0.7145	0.0908	2.2740	0.0000
	114	1	1441	43	1406	24	2.4503	3.0496	2.9456	0.2437	1.8988	0.6446	0.0907	2.2519	0.0000
	66	1	1442	47	1379	34	4.3794	2.9854	3.6973	0.2385	2.7614	0.7469	0.0908	2.4586	0.0000
	97	1	1430	40	1303	26	8.8784	2.7870	3.0553	0.2240	2.2418	0.7338	0.0902	2.0758	0.0000
	107	2	1020	21	989	18	3.0358	1.6742	2.2153	0.1658	1.9630	0.8861	0.0732	1.0267	0.0000
	115	2	1020	25	974	14	4.5347	1.6464	1.9489	0.1631	1.5177	0.7787	0.0732	1.2226	0.0000
	109	2	966	13	975	20	-0.9106	1.6054	2.2493	0.1633	2.1593	0.9600	0.0713	0.6298	0.0000
	64	2	975	23	995	24	-2.0406	1.6479	2.8032	0.1669	2.5767	0.9192	0.0716	1.1039	0.0000
	90	2	994	19	993	19	0.1292	1.6594	2.2312	0.1665	2.0359	0.9125	0.0723	0.9129	0.0000
	98	2	995	28	987	25	0.8366	1.6504	3.0150	0.1655	2.6906	0.8924	0.0723	1.3605	0.0000
	119	2	1004	31	986	21	1.7811	1.6557	2.7467	0.1653	2.2702	0.8265	0.0726	1.5461	0.0000
	65	2	1006	25	981	20	2.5410	1.6480	2.5438	0.1643	2.2215	0.8733	0.0727	1.2394	0.0000
	111	2	1010	36	987	21	2.2616	1.6621	2.9284	0.1655	2.3112	0.7892	0.0729	1.7983	0.0000
	82	2	1013	33	955	13	5.7442	1.6067	2.1945	0.1597	1.4554	0.6632	0.0730	1.6425	0.0000
	92	2	1017	32	976	20	4.0875	1.6470	2.7432	0.1634	2.2380	0.8158	0.0731	1.5864	0.0000
	94	2	1020	22	983	21	3.6121	1.6629	2.5228	0.1647	2.2803	0.9039	0.0732	1.0793	0.0000
	105	2	1020	24	997	20	2.2969	1.6876	2.4533	0.1672	2.1592	0.8801	0.0732	1.1646	0.0000
	79	2	1022	34	959	27	6.1310	1.6209	3.4344	0.1604	2.9887	0.8702	0.0733	1.6920	0.0000
	87	2	1028	26	966	23	6.0009	1.6385	2.8317	0.1617	2.5154	0.8883	0.0735	1.3003	0.0000
	118	2	1030	30	976	17	5.2481	1.6574	2.3675	0.1634	1.8631	0.7869	0.0736	1.4608	0.0000
	62	2	1032	25	980	17	5.0542	1.6663	2.2807	0.1641	1.9178	0.8409	0.0736	1.2343	0.0000
	95	2	1043	30	959	25	8.0301	1.6377	3.1814	0.1604	2.8224	0.8872	0.0740	1.4679	0.0000
	85	2	1055	19	969	22	8.1951	1.6661	2.6185	0.1622	2.4450	0.9337	0.0745	0.9373	0.0000
	68	2	1056	31	969	25	8.2334	1.6662	3.1761	0.1622	2.7866	0.8774	0.0745	1.5240	0.0000
	108	2	1061	25	982	20	7.4157	1.6951	2.5129	0.1646	2.1846	0.8694	0.0747	1.2418	0.0000
	63	3	1012	14	1037	22	-2.4339	1.7555	2.4372	0.1745	2.3374	0.9591	0.0729	0.6902	0.0000
	67	3	993	13	1009	15	-1.6205	1.6881	1.7185	0.1695	1.5875	0.9238	0.0723	0.6580	0.0000
	71	3	1014	17	1024	14	-0.9971	1.7333	1.7162	0.1722	1.4946	0.8709	0.0730	0.8434	0.0000
	72	3	993	18	1026	24	-3.3195	1.7187	2.6645	0.1725	2.5152	0.9440	0.0723	0.8793	0.0000
	75	3	996	10	1038	16	-4.2338	1.7420	1.7448	0.1746	1.6684	0.9563	0.0723	0.5104	0.0000
	76	3	994	18	1030	12	-3.6853	1.7272	1.5729	0.1733	1.3050	0.8297	0.0723	0.8781	0.0000
	83	3	1004	16	1030	16	-2.5655	1.7354	1.8340	0.1732	1.6549	0.9023	0.0727	0.7905	0.0000
	102	3	1009	27	1028	27	-1.9563	1.7360	3.1409	0.1729	2.8369	0.9032	0.0728	1.3481	0.0000

Table D.3 (cont'd). Summary of geochronology analyses for sample CL6098.

Sample Number	Spot Number	Trace element concentrations (ppm)																												
		P	Ti	Y	Zr	Nb	La	Ce	Pr	Nd	Sm	Eu	Gd	Tb	Dy	Ho	Er	Tm	Yb	Lu	Hf	Ta	Th	U	Ce/Ce*	Eu/Eu*	∑REE	(Gd/Yb)cn	Lu/Hf	Nb/Ta	Th/U
CL6098	77	186.7072	2.7580	1049.3032	400011.9590	1.3702		7.3879	0.1005	2.5418	8.0169	1.2459	30.9862	11.2824	130.2791	43.1937	178.2419	43.7564	496.9671	47.0893	8042.3716	0.4960	78.4513	160.6307	72.1266	0.2417	1001.0891	0.0516	0.0059	2.7625	0.4884
	116	170.6541	3.2605	2375.4977	557115.8863	0.9971	0.0546	7.3336	0.6781	9.9960	17.0377	3.6419	76.1945	24.4033	265.9847	94.4161	370.0321	85.5992	854.5125	#########	10338.0718	0.3340	140.4673	162.7696	9.3425	0.3090	1916.6527	0.0738	0.0103	2.9848	0.8630
	103	189.3181	12.4493	600.3040	425780.4988	3.4328		13.0642	0.0193	1.1752	2.6565	0.1578	13.1001	5.1049	63.3482	22.1314	96.6773	26.0696	306.8119	30.8225	9029.1371	1.4617	34.7612	67.2672	665.5130	0.0818	581.1387	0.0353	0.0034	2.3485	0.5168
	100	186.8066	5.9739	501.1826	389889.3194	4.9991	3.6540	19.7621	0.8798	4.6595	3.8033	0.1902	13.1759	4.6156	64.2660	20.6022	84.0837	22.1940	237.2209	21.5861	10134.2940	3.0745	65.2136	126.9039	2.7024	0.0821	500.6932	0.0459	0.0021	1.6260	0.5139
	110	268.0128	3.9453	1471.5657	521768.2195	3.8132		12.0223	0.1140	3.0391	7.0206	1.2211	31.0867	12.0106	145.4905	54.5107	253.6574	64.4163	718.5023	85.3670	10455.4789	1.4968	118.6260	323.3181	103.4173	0.2527	1388.4585	0.0358	0.0082	2.5475	0.3669
	74	212.8346	3.3133	1256.7751	437667.3482	1.8469		7.3388	0.2022	3.1011	8.5393	0.7265	34.6009	11.5775	139.3561	48.9766	200.5985	55.0499	618.6158	61.6327	8281.3385	0.9310	86.5110	206.2852	35.5886	0.1292	1190.3159	0.0463	0.0074	1.9839	0.4194
	122	259.2896	3.6436	1823.1191	527745.0244	1.5916		10.0087	0.1213	5.3282	9.5907	1.0863	49.4222	17.6848	204.2937	70.3787	297.6555	72.5983	722.3625	85.1136	11313.7535	1.0925	142.7901	213.9755	80.9227	0.1525	1545.6446	0.0566	0.0075	1.4568	0.6673
	117	149.0066	3.9923	954.0795	593368.5493	1.6060		7.3192	0.0660	2.0277	3.4807	0.3636	18.4429	7.2250	90.3841	34.1930	157.0899	36.8258	383.6545	53.8489	12912.1199	0.9353	82.8793	144.7934	108.8153	0.1387	794.9212	0.0398	0.0042	1.7170	0.5724
	104	295.8009	5.1753	1236.1756	419356.9942	2.4337	0.9195	15.7290	0.6423	6.2796	9.6983	1.1527	36.4596	12.1655	143.0528	48.8893	205.4473	51.3955	561.1694	54.9479	7838.8439	1.1951	213.9835	292.5975	5.0183	0.1874	1147.9485	0.0537	0.0070	2.0364	0.7313
	112	210.6496	4.7725	947.5194	520446.9668	1.7108		9.1733	0.0421	2.4291	5.2517	0.3367	24.4371	8.3151	105.0851	37.1407	153.7007	39.7355	427.0835	47.7217	11341.2327	1.1664	81.7088	165.6924	213.4376	0.0909	860.4524	0.0473	0.0042	1.4667	0.4931
	93	173.0215	4.2580	761.6893	417383.8754	3.7307		11.7717		1.2801	3.2481	0.1450	15.8288	6.1995	81.3556	29.2736	129.2284	34.8939	404.0411	40.3063	10625.1635	2.0871	131.3859	384.8889		0.0618	757.5720	0.0324	0.0038	1.7875	0.3414
	106	304.1737	4.5457	1412.1077	455620.6103	4.4733	0.0266	18.2445	0.0498	3.3850	7.2451	0.2923	31.5710	11.7045	150.0465	53.5173	224.9146	57.5200	642.3679	67.3926	9944.9223	2.0178	257.3688	502.8408	122.9666	0.0591	1268.2776	0.0407	0.0068	2.2169	0.5118
	89	201.1702	5.0328	795.6600	442318.9690	2.3541		4.2081	0.0228	0.7595	4.2833	0.1414	19.1666	6.4404	85.1918	31.4242	134.3349	35.3205	401.9105	41.9189	9633.2980	1.3195	65.5884	234.3368	180.7593	0.0477	765.1228	0.0395	0.0044	1.7841	0.2799
	101	250.9831	4.0427	1718.8012	408048.9477	2.8457		12.6782	0.3652	8.6682	13.3486	0.8118	62.2569	19.1428	214.1073	72.3455	283.9977	69.5914	758.4282	70.0623	8247.2167	1.1194	150.6654	279.2276	34.0471	0.0861	1585.8041	0.0679	0.0085	2.5422	0.5396
	120	170.7785	6.0133	595.3950	534953.1654	3.6612		13.1828	0.0236	1.1678	1.9925	0.1253	11.7201	4.7832	64.0712	22.4207	99.3094	24.0133	247.9283	29.5809	14240.0562	1.9063	97.0076	119.6942	547.7852	0.0793	520.3192	0.0391	0.0021	1.9206	0.8105
	84	232.0156	7.3363	865.7548	439417.7720	7.6041		24.2175	0.0485	1.4169	5.1092		21.0406	7.7167	95.3214	32.5620	142.4907	37.9761	402.7448	40.3167	11801.6750	3.6235	71.2998	142.8190	490.1044	#VALUE!	810.9612	0.0432	0.0034	2.0986	0.4992
	114	162.6888	5.7736	815.6353	547825.6537	1.4037	1.9623	9.8161	0.7246	5.7550	6.6731	0.7212	22.2819	7.5910	84.5604	30.8640	132.5271	33.6684	342.7416	44.5448	11446.4833	0.6036	60.7138	112.7273	2.0183	0.1808	724.4314	0.0538	0.0039	2.3253	0.5386
	66	175.4345	4.4817	530.7175	457006.2345	2.9167		8.8915		0.5433	1.2592	0.0923	8.6371	3.7757	43.3785	19.9573	88.0563	26.5455	317.4276	33.0346	11310.7311	1.7893	76.6057	157.4261		0.0856	551.5989	0.0225	0.0029	1.6301	0.4866
	97	171.5380	3.6764	513.1029	397527.1340	1.5585	0.0270	6.4465	0.0302	1.3750	2.6319	0.2361	10.8704	4.1780	54.5785	20.5007	89.4206	23.7544	279.3288	27.0163	8302.6334	0.8550	45.3879	129.1156	55.3532	0.1349	520.3941	0.0322	0.0033	1.8228	0.3515
	107	160.5589	2.8867	534.8559	457580.6749	3.7541	2.5322	8.7059	1.8749	9.6105	4.1438	0.8544	9.8730	3.8297	52.5519	18.4978	87.9878	25.3438	300.0753	34.0000	11645.6705	4.0447	55.0593	1037.8093	0.9796	0.4084	559.8811	0.0272	0.0029	0.9281	0.0531
	115	90.4318	3.3804	467.4823	531570.7903	3.0865	2.6733	5.2590	0.7348	3.9403	2.7668	0.2589	8.4114	3.5808	43.7872	17.0164	78.8644	22.6460	252.0602	35.5842	14796.5664	3.1551	26.0288	602.6097	0.9200	0.1641	477.5836	0.0276	0.0024	0.9783	0.0432
	109	168.3325	2.0290	739.1166	500214.8791	5.0424		1.8467		0.1501	0.8470	0.1834	9.2214	4.4436	59.5478	24.7322	118.9041	34.2961	415.7496	50.8685	13864.8202	6.0514	47.4411	1258.6357		0.2006	720.7906	0.0183	0.0037	0.8333	0.0377
	64	124.3100	2.0741	501.5737	450074.6513	5.0662		1.3820			0.7986	0.1324	7.1046	3.6447	44.0806	17.1898	80.7140	22.5623	273.1353	31.7049	11302.3294	4.9630	16.6785	1001.6307		0.1700	482.4493	0.0215	0.0028	1.0208	0.0167
	90	124.3593	1.2187	321.1635	420869.5216	2.6611		1.3754	0.0225		0.4752	0.0965	4.4020	2.2117	29.9217	12.0661	56.9173	17.3206	212.8291	22.5272	10780.8999	3.5281	24.3393	913.1517	59.9145	0.2040	360.1652	0.0171	0.0021	0.7543	0.0267
	98	111.8076	2.0428	353.8749	395918.1625	2.7927		1.6961		0.2089	0.8193	0.1191	5.3052	2.5581	38.0656	12.8846	65.9349	19.0935	226.3761	23.6971	10034.6663	2.9847	34.6106	871.1409		0.1746	396.7583	0.0194	0.0024	0.9357	0.0397
	119	97.6294	1.8691	508.4951	560769.9761	4.1228		1.3375		0.1034	0.4089	0.1320	5.3094	2.9120	42.1226	17.6696	86.7986	23.5428	260.8575	38.4123	15149.9559	4.2909	26.6405	769.1515		0.2739	479.6066	0.0168	0.0025	0.9608	0.0346
	65	124.4932	1.4856	465.9404	447192.9965	3.0218	0.1875	2.3345	0.1038	1.1202	1.2782	0.1828	7.1493	3.0435	43.5772	17.8805	83.6851	23.2816	276.3741	31.4770	11331.2476	3.3227	29.9594	725.0751	4.1035	0.1849	491.6752	0.0214	0.0028	0.9094	0.0413
	111	153.1137	1.7023	553.2985	523262.8066	3.8481		1.2542		0.1382	0.8643	0.1361	7.3605	3.5554	49.1955	18.7967	91.3336	24.7090	298.5005	38.4212	13745.8199	4.1635	28.3442	800.0273		0.1650	534.2651	0.0204	0.0028	0.9242	0.0354
	82	76.8854	1.5308	344.2397	440492.8433	3.0969		0.7973			0.3979	0.0320	4.8667	1.7751	30.9014	11.7962	54.1950	16.5427	199.6964	22.3588	10954.7775	3.2195	8.5281	617.5859		0.0704	343.3595	0.0202	0.0020	0.9619	0.0138
	92	130.2681	2.0016	622.0160	413768.5730	3.9129		1.9060		0.0505	0.6780	0.2614	8.2130	4.4743	62.6623	23.8297	104.2421	31.4185	376.8583	41.1707	10225.2421	4.9504	45.3802	1098.0596		0.3387	655.7648	0.0180	0.0040	0.7904	0.0413
	94	114.8722	2.3517	380.5523	436799.9428	3.2915		1.5055		0.0564	0.5357	0.1417	5.5960	2.7130	36.7059	14.6429	65.9779	20.1670	243.2463	26.0677	10475.7055	3.2600	33.4692	862.9968		0.2503	417.3559	0.0190	0.0025	1.0097	0.0388
	105	120.9607	1.8143	563.4591	461080.7375	3.4044	0.1351	1.9528	0.1043	0.2043	1.2117	0.2782	7.9954	3.9747	55.0377	20.1064	93.9255	27.2846	342.0085	39.5183	11502.2670	3.0567	38.5201	755.7516	4.0330	0.2733	593.7376	0.0193	0.0034	1.1137	0.0510
	79	150.0885	1.9415	444.0828	425930.1479	4.0417	0.0978	1.3166		0.2641	0.4570	0.0719	5.0804	2.9858	40.0120	15.9784	70.5341	21.5587	264.9984	26.8281	10450.4313	4.0658	12.2975	780.9746	9.4208	0.1443	450.1832	0.0159	0.0026	0.9941	0.0157
	87	147.8650	1.9030	500.4941	435182.9421	3.4965	0.0465	2.5724	0.0501	0.8026	1.1929	0.2991	6.9424	3.5371	46.7042	18.5713	83.0465	24.3644	289.2974	32.1492	11075.4568	3.4116	50.6140	998.6398	13.0734	0.3177	509.5760	0.0199	0.0029	1.0249	0.0507
	118	83.0072	1.6931	552.0988	569513.6460	3.0263	0.1732	1.4113	0.1051	1.0128	1.5444	0.1793	7.3651	3.3891	47.8963	19.0651	89.6555	23.0423	245.3672	35.7479	15212.0316	3.6799	14.7059	629.8631	2.5648	0.1625	475.9546	0.0248	0.0023	0.8224	0.0233
	62	102.7110	2.0466	505.7193	445075.1324	4.3884		1.1008			0.3020	0.1350	5.8667	2.8890	43.8108	17.2706	76.1320	23.7151	281.2841	32.3412	11322.5120	4.6594	15.9091	849.9705		0.3101	484.8474	0.0173	0.0029	0.9418	0.0187
	95	114.3806	1.4812	436.4566	405545.4178	3.1109		1.4638			0.4216	0.2657	5.2169	2.7846	38.9578	15.4502	71.3236	21.7328	270.9510	28.1484	9885.3174	2.9029	20.9996	821.5471		0.5477	456.7164	0.0159	0.0028	1.0717	0.0256
	85	109.9991	2.0818	423.2704	433324.4413	3.4090	0.0534	1.5661	0.0432	0.3883	1.4232	0.1909	5.9821	3.1393	39.8885	15.5704	72.2835	21.3493	265.6395	28.7144	11444.4868	4.2615	33.0750	1056.7221	7.9998	0.2000	456.2320	0.0186	0.0025	0.7999	0.0313
	68	161.2165	1.7913	454.8845	455847.2261	6.4381		0.7551			0.1247	0.0974	4.2782	2.1860	32.8111	16.1459	80.0867	25.0868	327.6884	34.8881	11804.2077	6.5841	6.1802	395.0492		0.4077	524.1482	0.0108	0.0030	0.9778	0.0156
	108	135.4904	1.7256	300.9468	469976.2022	2.7195		1.1830			0.1193	0.0583	3.9745	2.1908	27.5980	10.7051	49.4735	14.5888	181.9939	20.3918	12405.1892	2.9830	24.5532	630.8347		0.2587	312.2770	0.0181	0.0016	0.9117	0.0389
	63	165.0580	1.5471	777.7047	426135.0759	5.4658		2.1244		0.0452	0.7164	0.0666	8.3675	4.6813	66.7362	28.7027	134.4191	42.2324	522.3634	61.6136	11837.7488	8.8793	37.5817	2180.1628		0.0832	872.0688	0.0133	0.0052	0.6156	0.0172
	67	164.7532	1.8944	685.4802	419500.6602	5.4663		1.7310		0.1333	1.0421	0.1210	7.6412	4.0542	56.6681	22.8276	115.2365	37.8745	460.0027	54.6954	13697.4654	14.5998	47.5879	3888.5075		0.1311	762.0274	0.0137	0.0040	0.3744	0.0122
	71	200.9180	1.4295	764.8676	424150.9311	6.0274		2.0606		0.1954	0.5156	0.1064	7.7087	4.5716	62.5449	26.0050	128.9784	41.2718	529.1785	60.4656	13636.3661	17.3377	43.0243	3602.2838		0.1632	863.6026	0.0121	0.0044	0.3476	0.0119
	72	209.6510	1.2702	685.9126	406281.6945	6.0185		1.8565		0.3643	1.1538	0.0659	7.3598	4.0516	58.1776	25.1281	123.8973	36.6838	487.7773	55.7378	13231.3344	13.8570	46.0236	4215.1513		0.0691	802.2537	0.0125	0.0042	0.4343	0.0109
	75	169.3916	2.2082	583.3069	376292.9160	6.0545		1.6510			0.5533	0.1028	6.1717	3.1188	45.4937	18.7802	98.1816	32.2222	444.6067	49.4807	13230.7907	14.4570	33.0899	3242.4736		0.1700	700.3627	0.0115	0.0037	0.4188	0.0102
	76	169.3677	3.5428	632.6251	384692.8163	5.7331	0.0259	1.6384		0.1880	0.6065	0.1602	6.1118	3.4929	53.2928	21.4757	105.7065	34.9146	464.9946	50.8410	12146.5668	13.3564	36.5226	3929.2106	27.0259	0.2544	743.4487	0.0109	0.0042	0.4292	0.0093
	83	163.0140	3.6916	969.6470	419219.1178	9.1232		2.5478		0.2009	2.2304	0.5502	17.6098	7.8841	106.6680	34.1717	140.1904	36.6479	404.6020	43.7679	10490.2460	6.9794	80.4234	2345.6465		0.2684	797.0711	0.0360	0.0042	1.3072	0.0343
	102	168.7954	3.1350	894.2167	398451.6549	8.3116		2.0096	0.0075		2.3821	0.3801	17.2868	7.9017	98.7138	34.7982	145.4880	41.3071	510.7494	51.6672	9253.6786	6.7513	45.9028	1775.8661	261.9304	0.1811	912.6915	0.0280	0.0056	1.2311	0.0258

Analytical session no: 5
Isotope ratios and ages are NOT corrected for initial common Pb.
Isotope ratio and apparent age errors do NOT include systematic calibration errors of 0.32% ($^{207}Pb/^{206}Pb$), 0.52% ($^{206}Pb/^{238}U$) (all 2-sigma).
Trace element concentrations in ppm, calculated using mean count rate method.
Sweep-by-sweep downhole fractionation of U/Pb ratios NOT corrected via Si/Zr fractionation factor.
Backgrounds were monitored between sweeps 5 to 20. Sample counts were integrated from sweeps 34 to 60.
Ablation used a laser spot size of 25 microns, and a laser firing repetition rate of 10 Hz.

Table D.4. Summary of geochronology analyses for sample CL6106.

Sample Number	Spot Number	Type	Apparent Ages (Ma)							Isotope Ratios									
			207Pb*/206Pb*	±2σ (Ma)	207Pb*/235U	±2σ (Ma)	206Pb*/238U*	±2σ (Ma)	% disc.	207Pb*/235U*	±2σ (%)	206Pb*/238U	±2σ (%)	error corr.	238U/206Pb*	±2σ (%)	207Pb*/206Pb*	±2σ (%)	error corr.
CL6106	136	1	2617	39	2509	42	2377	77	9.2	10.8301	4.5306	0.4459	3.8667	0.8518	2.2426	3.8667	0.1761	2.3611	0.0000
	181	4	972	137	991	51	1000	42	-2.9	1.6539	8.1152	0.1678	4.5260	0.5569	5.9612	4.5260	0.0715	6.7358	0.0000
	154	4	998	61	951	38	931	46	6.7	1.5508	6.0806	0.1553	5.2920	0.8694	6.4383	5.2920	0.0724	2.9947	0.0000
	161	4	1022	105	989	46	974	47	4.8	1.6475	7.3524	0.1630	5.2217	0.7094	6.1342	5.2217	0.0733	5.1761	0.0000
	162	4	985	105	984	43	983	41	0.2	1.6355	6.8105	0.1648	4.4449	0.6517	6.0679	4.4449	0.0720	5.1600	0.0000
	170	4	1057	100	1022	48	1005	52	4.9	1.7348	7.4486	0.1688	5.5388	0.7429	5.9258	5.5388	0.0746	4.9802	0.0000
	165	4	925	110	941	47	947	49	-2.5	1.5251	7.7322	0.1583	5.5783	0.7208	6.3172	5.5783	0.0699	5.3544	0.0000
	130	4	1011	115	994	50	986	51	2.4	1.6611	7.9635	0.1653	5.5900	0.7013	6.0492	5.5900	0.0729	5.6718	0.0000
	129	4	941	62	978	36	994	45	-5.6	1.6189	5.7028	0.1667	4.8429	0.8482	5.9996	4.8429	0.0704	3.0113	0.0000
	173	4	1046	52	1023	34	1013	43	3.2	1.7390	5.2538	0.1701	4.5874	0.8720	5.8794	4.5874	0.0742	2.5608	0.0000
	152	4	1039	59	973	39	944	48	9.1	1.6076	6.1572	0.1578	5.4244	0.8801	6.3379	5.4244	0.0739	2.9132	0.0000
	167	5	960	58	1004	40	1024	53	-6.7	1.6872	6.3059	0.1722	5.6301	0.8920	5.8082	5.6301	0.0711	2.8402	0.0000
	168	5	1009	56	1011	31	1012	37	-0.3	1.7067	4.8307	0.1700	3.9586	0.8179	5.8824	3.9586	0.0728	2.7687	0.0000
	163	5	960	71	977	43	985	54	-2.7	1.6182	6.8163	0.1651	5.8622	0.8593	6.0562	5.8622	0.0711	3.4780	0.0000
	164	5	961	69	988	41	1000	51	-4.1	1.6457	6.4596	0.1678	5.5203	0.8538	5.9584	5.5203	0.0711	3.3544	0.0000
	141	5	969	60	1002	31	1018	36	-5.1	1.6833	4.7930	0.1710	3.8020	0.7916	5.8480	3.8020	0.0714	2.9184	0.0000
	169	5	973	42	1004	37	1018	52	-4.6	1.6875	5.8721	0.1711	5.4921	0.9344	5.8455	5.4921	0.0715	2.0780	0.0000
	158	5	973	68	972	37	971	45	0.3	1.6034	5.9699	0.1625	4.9437	0.8271	6.1529	4.9437	0.0716	3.3466	0.0000
	145	5	985	82	998	47	1004	57	-1.9	1.6725	7.3295	0.1686	6.1227	0.8347	5.9329	6.1227	0.0720	4.0292	0.0000
	166	5	986	70	992	41	994	50	-0.8	1.6554	6.4588	0.1668	5.4672	0.8456	5.9969	5.4672	0.0720	3.4389	0.0000
	186	5	990	33	1003	28	1008	38	-1.9	1.6841	4.4331	0.1693	4.1194	0.9276	5.9065	4.1194	0.0721	1.6380	0.0000
	177	5	993	62	999	39	1001	49	-0.8	1.6743	6.1031	0.1681	5.2750	0.8634	5.9506	5.2750	0.0723	3.0695	0.0000
	153	5	1001	55	959	35	940	43	6.1	1.5711	5.6254	0.1571	4.9319	0.8757	6.3668	4.9319	0.0725	2.7058	0.0000
	188	5	1043	63	1012	34	999	40	4.2	1.7105	5.3368	0.1675	4.3132	0.8069	5.9684	4.3132	0.0740	3.1428	0.0000
	140	5	1054	69	1018	36	1001	40	5.1	1.7244	5.5383	0.1679	4.3328	0.7811	5.9542	4.3328	0.0745	3.4496	0.0000
	189	5	1064	53	1016	37	994	48	6.5	1.7205	5.8145	0.1668	5.1877	0.8912	5.9957	5.1877	0.0748	2.6261	0.0000
	131	5	1065	52	1010	32	984	39	7.6	1.7028	5.0328	0.1649	4.3280	0.8586	6.0635	4.3280	0.0749	2.5686	0.0000
	139	5	1048	60	1015	29	1000	32	4.6	1.7172	4.5585	0.1678	3.4657	0.7584	5.9604	3.4657	0.0742	2.9611	0.0000

Data excluded due to element loss and discordance

CL6106	156	1	725	717	929	223	1016	131	-40	1.4957	36.5680	0.1708	13.8786	0.3795	5.8552	13.8786	0.0635	33.8319	0.0000
	149	2	1044	106	983	42	956	37	8.4	1.6336	6.6983	0.1599	4.1279	0.6152	6.2530	4.1279	0.0741	5.2752	0.0000
	138	2	1715	335	1272	152	1027	97	40	2.5013	20.9014	0.1727	10.2607	0.4908	5.7910	10.2607	0.1051	18.2095	0.0000
	142	2	1272	510	987	195	864	133	32	1.6425	30.9041	0.1433	16.4537	0.5324	6.9760	16.4537	0.0831	26.1598	0.0000
	146	2	1067	235	1030	88	1013	65	5	1.7590	13.5963	0.1702	6.9023	0.5073	5.8747	6.9023	0.0749	11.7140	0.0000
	128	3	1046	76	969	34	935	35	10.6	1.5971	5.4891	0.1561	3.9833	0.7243	6.4045	3.9833	0.0742	3.7766	0.0000
	127	3	1128	201	1025	82	977	71	13	1.7431	12.7467	0.1636	7.7978	0.6115	6.1108	7.7978	0.0773	10.0833	0.0000
	133	3	1087	246	998	92	959	67	12	1.6732	14.4000	0.1603	7.5577	0.5246	6.2374	7.5577	0.0757	12.2573	0.0000
	134	3	1057	151	1022	64	1005	61	5	1.7353	9.9306	0.1687	6.5054	0.6546	5.9266	6.5054	0.0746	7.5031	0.0000
	135	3	1086	266	1034	94	1009	54	7	1.7674	14.4862	0.1694	5.7562	0.3970	5.9021	5.7562	0.0757	13.2934	0.0000
	137	3	824	337	982	109	1053	61	-28	1.6292	17.3182	0.1775	6.2821	0.3625	5.6338	6.2821	0.0666	16.1386	0.0000
	143	3	957	413	912	130	894	64	7	1.4559	21.6195	0.1488	7.6566	0.3540	6.7218	7.6566	0.0710	20.2182	0.0000
	147	3	1241	166	1011	71	909	61	27	1.7076	11.1376	0.1513	7.2275	0.6486	6.6073	7.2275	0.0818	8.4741	0.0000
	148	3	-401	1429	633	268	957	133	339	0.8658	56.7937	0.1600	14.9793	0.2637	6.2485	14.9793	0.0392	54.7827	0.0000
	151	3	1010	164	1031	78	1040	86	-3	1.7597	12.1023	0.1751	8.9939	0.7429	5.7096	8.9939	0.0729	8.0979	0.0000
	157	3	1159	176	997	60	925	29	20	1.6684	9.4719	0.1542	3.3383	0.3515	6.4841	3.3383	0.0785	8.8641	0.0000
	159	3	1218	222	1005	82	910	52	25	1.6916	12.8678	0.1517	6.1460	0.4773	6.5920	6.1460	0.0809	11.3052	0.0000
	172	3	1114	164	1021	71	979	68	12	1.7346	11.0820	0.1639	7.4608	0.6729	6.0998	7.4608	0.0767	8.1944	0.0000
	174	3	967	212	983	73	990	47	-2	1.6325	11.5689	0.1660	5.1022	0.4405	6.0251	5.1022	0.0713	10.3831	0.0000
	180	3	1391	210	1135	90	1005	67	28	2.0572	13.1117	0.1688	7.2024	0.5490	5.9255	7.2024	0.0884	10.9564	0.0000
	185	3	1588	458	1309	222	1145	185	28	2.6284	30.1685	0.1944	17.5911	0.5830	5.1449	17.5911	0.0981	24.5091	0.0000
	160	4	1058	124	982	51	948	46	10.4	1.6300	8.0447	0.1584	5.1760	0.6427	6.3111	5.1760	0.0746	6.1585	0.0000
	144	4	892	164	958	55	986	36	-10.6	1.5677	8.8479	0.1654	3.9061	0.4406	6.0476	3.9061	0.0688	7.9390	0.0000
	126	4	914	174	917	56	918	33	0	1.4669	9.3034	0.1531	3.8710	0.4153	6.5330	3.8710	0.0695	8.4599	0.0000
	171	4	588	340	902	106	1035	80	-76	1.4312	17.7677	0.1742	8.3820	0.4716	5.7400	8.3820	0.0596	15.6663	0.0000
	190	4	953	315	929	106	919	69	4	1.4975	17.3801	0.1533	8.0453	0.4627	6.5229	8.0453	0.0708	15.4059	0.0000
	155	5	1052	55	977	40	944	51	10.2	1.6176	6.4428	0.1578	5.8245	0.9032	6.3391	5.8245	0.0744	2.7542	0.0000

Table D.4 (cont'd). Summary of geochronology analyses for sample CL6106.

Sample Number	Spot Number	Trace element concentrations (ppm)																													
		P	Ti	Y	Zr	Nb	La	Ce	Pr	Nd	Sm	Eu	Gd	Tb	Dy	Ho	Er	Tm	Yb	Lu	Hf	Ta	Th	U	Ce/Ce*	Eu/Eu*	ΣREE	(Gd/Yb)cn	Lu/Hf	Nb/Ta	Th/U
CL6106	136	213.7979	2.4608	930.0541	448380.6340	0.6495		8.1570	0.2383	4.4177	6.3592	1.7162	26.0353	7.7345	92.9083	32.0518	128.4759	30.6972	290.8805	38.9213	7239.7717	0.2359	23.8991	31.0787	33.5656	0.4078	668.5933	0.0740	0.0054	2.7535	0.7690
	181	49.5937	1.1063	116.7395	498973.0425	0.0517		0.1225				0.0713	0.5554	0.4146	6.0705	3.1179	16.5946	4.7688	52.2510	13.9721	13902.2405	0.0731	0.3069	44.5563			97.9387	0.0088	0.0010	0.7078	0.0069
	154	56.7156	0.5521	163.2148	492829.6395	0.3231		1.0720			0.3447	0.0575	2.9086	0.8454	11.5292	4.4455	24.1802	7.0370	82.8075	15.0132	10135.0609	0.0566	2.2482	54.9033		0.1756	150.2408	0.0291	0.0015	5.7057	0.0409
	161	47.9146	1.8589	113.3352	461788.8453	0.2186		1.6286				0.2837	0.9124	0.4420	6.1586	2.7739	15.7618	5.1336	63.3559	11.4408	8626.9883	0.2011	3.8010	58.6111			107.8914	0.0119	0.0013	1.0869	0.0649
	162	112.4377	1.1620	129.4943	459371.3670	0.2852		1.2170			0.1456	0.0716	1.9107	0.5721	8.3966	3.7423	19.3043	5.7417	73.0002	13.4770	8326.7937	0.0294	2.7339	63.0688		0.4152	127.5792	0.0217	0.0016	9.7027	0.0433
	170	105.8854	2.1295	103.7947	474274.3255	0.3200		0.8596				0.1293	1.1878	0.4091	5.2228	2.9061	14.1662	4.0391	58.2056	10.8445	9080.4251	0.2580	1.1203	63.9446			97.9702	0.0169	0.0012	1.2404	0.0175
	165	90.4546	1.6793	135.1061	447548.2181	0.1847		0.7459				0.1544	1.2359	0.6359	8.5736	3.2993	20.7149	5.9883	81.6774	15.5866	9421.7820	0.1522	1.1396	64.4157			138.6123	0.0125	0.0017	1.2133	0.0177
	130	56.1094	2.4264	83.0595	446156.8433	0.3333		1.9233				0.0758	0.7603	0.4387	5.0437	2.6444	13.1628	3.8138	49.2921	8.9281	8234.4263	0.2051	4.8404	88.9936			86.0830	0.0128	0.0011	1.6245	0.0544
	129	66.7633	1.7389	87.1002	447334.5415	0.3393		2.0088				0.0761	1.2488	0.2942	4.7852	2.3688	12.5826	3.6490	54.1858	9.0693	8531.7151	0.3289	5.1203	103.3991			90.2685	0.0191	0.0011	1.0318	0.0495
	173	43.3970	2.6579	206.5608	456115.2052	0.3476		1.9371			0.4549	0.2369	2.4558	1.0896	12.3389	5.4724	32.1149	9.2020	121.5970	25.0861	9515.0634	0.2921	6.2643	122.1266		0.6852	211.9856	0.0167	0.0026	1.1898	0.0513
	152	53.8976	1.5849	73.0538	470404.8943	0.2798		1.8033				0.0669	1.3749	0.4066	3.9051	1.9579	9.7238	2.7742	44.8500	6.9419	10422.2278	0.4330	4.8323	127.6831			73.8046	0.0254	0.0007	0.6461	0.0378
	167	81.1162	1.1276	83.6389	449858.3978	0.3440		1.8401				0.0870	1.3001	0.3343	4.0124	2.1283	12.9856	3.7501	48.0496	9.0401	8976.1933	0.2930	6.7875	158.7892			83.5276	0.0224	0.0010	1.1739	0.0427
	168	74.7296	1.2874	134.1635	465059.0420	0.3509		1.8697			0.1495	0.1642	1.8162	0.5778	7.9270	3.3223	20.3564	5.6136	77.1256	15.8485	10889.5382	0.4029	7.3000	189.6390		0.9638	134.7708	0.0195	0.0015	0.8711	0.0385
	163	78.5068	1.4834	117.6246	460783.7018	0.2182		2.6077				0.1470	1.4968	0.4873	8.2899	3.1558	17.9732	5.7667	65.7280	12.2565	9630.9583	0.3203	11.1642	187.3165			117.9090	0.0188	0.0013	0.6811	0.0596
	164	70.0563	2.4136	251.0528	451569.4299	0.6117		2.5114			0.2591	0.3037	3.8681	1.4782	15.9374	7.0518	34.4526	10.6397	129.8628	25.1533	10514.2312	0.6689	9.8403	265.0376		0.9274	231.5180	0.0246	0.0024	0.9145	0.0371
	141	42.5569	1.7387	170.8734	463666.3276	0.3141		1.9763	0.0082		0.4124	0.0973	2.0874	0.9384	10.6394	4.4631	22.9526	6.4377	82.8609	17.2832	11077.2327	0.2569	8.1167	300.9382	235.2615	0.3208	150.1570	0.0208	0.0016	1.2230	0.0270
	169	105.9025	2.1307	302.1245	456075.9501	0.6770		3.4757		0.2099	0.6318	0.2108	3.6223	1.6377	21.5879	8.9142	44.8819	13.0003	161.1106	30.6284	10245.0913	0.6949	13.5779	246.8734		0.4260	289.9114	0.0186	0.0030	0.9742	0.0550
	158	83.6691	1.4088	144.0722	453549.2595	0.6004		2.2343			0.4443	0.1629	1.6017	0.7138	7.8013	4.2109	20.9847	6.4400	80.1901	16.5755	9294.0080	0.2139	9.6885	200.4897		0.5904	141.3596	0.0165	0.0018	2.8073	0.0483
	145	90.4864	2.4115	111.8163	478212.8417	0.5838		2.1023				0.1850	0.8222	0.4760	7.5126	3.3530	16.8118	4.7699	57.0085	12.9814	10364.7680	0.2990	11.6567	223.5356			106.0227	0.0119	0.0013	1.9524	0.0521
	166	50.1829	1.1266	239.3501	464650.1896	0.5131		3.4891			0.0765	0.1767	3.0213	1.1256	18.1185	6.5860	33.8361	9.8008	123.5854	21.6842	10199.1662	0.6584	10.3362	220.8415		1.1234	221.5002	0.0202	0.0021	0.7793	0.0468
	186	117.6062	2.4254	144.8202	498951.1590	0.4077		2.8370		0.2254		0.2089	1.1936	0.6183	9.4372	3.5451	20.2697	5.7954	72.0613	17.3502	11558.6373	0.1461	12.4110	246.3060			133.5421	0.0137	0.0015	2.7912	0.0504
	177	2.3540	1.3594	115.3906	480435.5086	0.4171		1.7292				0.1000	1.4251	0.4277	5.7361	2.8034	16.7430	4.9580	59.6299	12.7636	10324.5571	0.3502	7.0194	199.4319			106.3160	0.0198	0.0012	1.1910	0.0352
	153	107.0079	1.9135	160.7184	454570.2054	0.2504		2.4523			0.3733	0.2917	2.2317	0.7055	10.3301	4.4530	23.7736	7.2196	91.2489	17.4409	9851.0028	0.3191	10.4722	282.7762		0.9772	160.5206	0.0202	0.0018	0.7848	0.0370
	188	83.3965	1.5002	165.1948	489676.5805	0.5734	0.1611	4.1992	0.2852	1.3786	0.3984	0.3926	2.9584	1.0291	10.1085	4.7528	24.6971	6.6595	85.0262	16.4950	11836.0188	0.4987	12.1710	241.4389	4.8031	1.1056	158.5417	0.0288	0.0014	1.1500	0.0504
	140	12.1263	1.1672	193.6691	456411.5149	0.3433		2.5553			0.3643	0.2269	2.1777	0.6962	11.7307	5.0161	25.6087	8.0281	105.3679	21.7499	10780.0032	0.3657	8.1357	192.8609		0.7787	183.5218	0.0171	0.0020	0.9389	0.0422
	189	121.3763	1.9932	116.4908	481429.9248	0.1667		2.6202				0.1073	1.2270	0.5941	6.9254	3.3364	19.2557	4.7788	62.0937	13.5260	12158.6842	0.1908	12.2547	356.8275			114.4646	0.0163	0.0011	0.8736	0.0343
	131	66.3629	1.9757	122.3791	435011.3948	0.3549		2.4355				0.0975	1.5856	0.5621	8.4364	3.1070	16.9875	5.0897	69.1581	11.7332	8680.5260	0.3076	8.7189	206.8263			119.1927	0.0190	0.0014	1.1537	0.0422
	139	57.5486	2.0003	198.7207	466380.2504	0.3783		2.6541	0.0391	0.7624	0.5573	0.3393	2.8313	0.8772	13.1631	5.1639	28.0275	7.9867	110.5039	21.5476	10626.2025	0.2447	11.9318	225.8858	66.6474	0.8257	194.4535	0.0212	0.0020	1.5458	0.0528
Data excluded due to element loss and discordance																															
	156	30.0632	1.2508	48.0344	476716.0284	0.1351						0.0180	0.2543	0.1489	2.1262	1.2868	8.7877	3.3086	52.8910	10.3350	10323.8209	0.0059	0.0203	2.2790			79.1566	0.0040	0.0010	22.8298	0.0089
	149	114.3648	0.6357	135.1794	517477.7762	0.1411		0.4710				0.1041	1.0047	0.5377	8.8267	3.6847	22.5145	5.3965	63.0707	15.6433	13166.1541	0.1139	1.0078	54.6451			121.2538	0.0132	0.0012	1.2386	0.0184
	138	39.6157	1.0928	14.4451	468971.6161	0.0913								0.0217	0.2680	0.3057	3.0415	0.9628	22.4132	4.3685	9074.5323		0.0026	2.1232			31.3815		0.0005		0.0012
	142	25.4136	1.0323	7.5285	462717.7303	0.0243										0.1298	1.3739	0.6777	11.5057	2.6616	10761.7503		0.0065	1.4174			16.3487		0.0002		0.0046
	146	33.8597	0.9515	22.3800	503154.1206	0.1112								0.0310	0.3064	0.3364	3.5693	1.3029	21.7356	5.3659	10466.9421	0.0454	0.0068	14.1900			32.6474		0.0005	2.4500	0.0005
	128	88.3991	1.8196	76.3939	476191.3857	0.1332		0.4534					0.3482	0.3111	4.0572	2.2839	11.7289	3.2536	44.0726	9.2894	9804.9025	0.1027	0.5749	56.7245			75.7982	0.0065	0.0009	1.2976	0.0101
	127	37.5696	0.6139	25.5047	489104.6253	0.0231								0.0371	1.4157	0.6014	4.5353	1.5243	22.2933	4.8643	9326.3865		0.0150	19.4117			35.2715		0.0005		0.0008
	133	38.9567	1.3597	19.8245	446534.4559	0.1587								0.0686	0.6105	0.4395	3.6029	1.2102	20.7700	3.8334	7893.6781		0.0292	12.4761			30.5350		0.0005		0.0023
	134	94.3376	0.7962	34.4682	430655.3439									0.0538	1.8377	0.7209	6.3084	2.0979	30.8109	6.1467	7817.6021		0.0542	11.2293			47.9761		0.0008		0.0048
	135	30.3948	0.9950	37.8643	455949.1898	0.0851								0.0831	1.3160	1.0697	8.2667	2.5478	40.6655	7.6799	9077.4421	0.0549		8.2519			61.6287		0.0008	1.5516	
	137	92.3362	1.1200	32.8619	458537.1016								0.2200	0.0320	1.5938	0.8443	6.1336	1.9235	27.0057	5.3554	9340.9335			7.1788			43.1083	0.0067	0.0006		
	143	82.1586	1.1941	18.2942	486585.7043									0.0585	0.4207	0.3817	3.3062	1.0318	15.3523	3.3552	9745.1952		0.0129	5.8568			23.9065		0.0003		0.0022
	147	35.6556	1.0727	38.9435	527831.7997	0.1162		0.0265						0.1010	1.9036	0.8389	7.0522	2.0358	31.4945	7.9774	10861.6382		0.0141	8.7151			51.4299		0.0007		0.0016
CL6106	148		0.8331	10.2340	515841.4511	0.0486									0.3106	0.2469	2.4479	0.7927	14.3698	3.7263	13127.7160		0.0279	1.7268			21.8942		0.0003		0.0162
	151	36.8815	1.2065	45.3046	483431.7408	0.0779		0.1468				0.0091	0.1073	0.1042	2.0374	1.4584	5.9215	2.4105	29.3114	5.7501	9396.2090	0.0573	0.1304	26.7940			47.2569	0.0030	0.0006	1.3589	0.0049
	157	68.6411	1.2288	69.5392	480624.9924	0.0773		0.1031			0.0609		0.5136	0.1747	3.7569	1.7663	12.2951	4.0394	56.8214	10.6633	9333.8322		0.0633	11.8273			90.1948	0.0075	0.0011		0.0053
	159	94.4351	0.6590	21.7448	468625.3293	0.0786									0.9842	0.5816	3.6520	1.4204	20.0707	3.9631	9643.1548			10.0727			30.6721		0.0004		
	172	61.8507	1.4627	27.3927	462552.4315								0.1842	0.0625	0.4990	0.5498	4.9702	1.6773	27.2396	5.1991	7870.9227		0.0021	9.4107			40.3818	0.0056	0.0007		0.0002
	174	63.8336	0.4792	30.4090	478936.9171	0.2696									1.5177	0.6253	4.7703	1.8126	20.4712	5.2472	11582.2204		0.0155	14.3130			34.4443		0.0005		0.0011
	180	39.7639	0.9803	17.6303	512643.3761	0.0496									0.7773	0.3830	2.7268	0.9647	15.1465	4.7830	12946.1896	0.0250	0.0454	5.4946			24.7813		0.0004	1.9874	0.0083
	185	35.0120	0.8064	7.9937	526447.5043									0.0193	0.3217	0.1627	1.2245	0.3866	6.6260	2.0493	9559.4936	0.0116		1.4035			10.7902		0.0002	#VALUE!	
	160	26.5384	1.4135	208.7232	474255.7839	0.3587		0.5463				0.1428	2.3790	0.7273	12.0996	5.8463	30.2315	8.7231	115.9031	21.2792	9275.8322	0.0542	1.0772	52.8034			197.8782	0.0170	0.0023	6.6204	0.0204
	144	93.5724	1.3413	135.1379	481313.3376			0.5761				0.1436	0.7675	0.6000	7.8306	3.6295	18.0206	5.6839	69.2007	14.8066	9892.3870	0.0287	0.7666	54.8941			121.2591	0.0092	0.0015		0.0140
	126	70.1061	1.4819	32.9832	496137.1193	0.1178		0.0422					0.0788	0.0440	1.2736	0.9315	5.6362	2.0625	31.9386	6.1906	10174.1591	0.0698	0.0054	17.4675			48.1980	0.0020	0.0006	1.6868	0.0003
	171	51.0219	1.1348	60.2990	476860.7790	0.0314							0.3720	0.1695	2.8266	1.8141	10.7843	3.6924	53.1966	10.7720	8546.4254			11.0235			83.6275	0.0058	0.0013		
	190	60.6817	1.5940	15.8646	521300.3214										0.6290	0.3696	2.8817	1.4038	19.4910	5.1006	10868.4086		0.1936	5.7327			29.8757		0.0005		0.0338
	155	98.9083	2.2880	377.3286	469259.3007	0.2750		3.2673	0.0287	0.3547	2.1184	0.8747	6.4429	2.0603	26.5946	11.2942	51.6179	15.7624	183.8993	34.0828	9401.9234	0.3072	19.6291	301.5285	111.7857	0.7239	338.3982	0.0290	0.0036	0.8952	0.0651

Analytical session no: 2
Isotope ratios and ages are NOT corrected for initial common Pb.
Isotope ratio and date errors do NOT include systematic calibration errors of 0.24% ($^{207}Pb/^{206}Pb$) and 1.50% ($^{206}Pb/^{238}U$) (2 sigma).
Isotope ratios and ages corrected using a measured linear secondary standard age bias - ^{206}Pb count rate relationship.
Trace element concentrations in ppm, calculated using mean count rate method.
Sweep-by-sweep downhole fractionation of U/Pb ratios NOT corrected via Si/Zr fractionation factor.
Backgrounds were monitored between sweeps 5 to 20. Sample counts were integrated from sweeps 35 to 60.
Trace element concentrations from analyses with U<27 ppm and known to have intersected inclusions of other minerals based on P and Ti were not included.
Ablation used a laser spot size of 25 microns, and a laser firing repetition rate of 10 Hz.

Table D.5. Summary of geochronology analyses for sample CL6112.

Sample Number	Spot Number	Type	Apparent Age (Ma)					Isotope ratios						
			207Pb*/206Pb*	±2s (Ma)	206Pb*/238U*	±2s (Ma)	% disc.	207Pb*/235U*	±2s (%)	206Pb*/238U	±2s (%)	error corr.	207Pb*/206Pb*	±2s (%)
CL6112	250	1	1587	54	1442	26	9.09	3.3891	3.5413	0.2508	2.0378	0.5754	0.0980	2.8962
	231	2	1438	23	1456	35	-1.24	3.1659	2.9655	0.2534	2.7194	0.9170	0.0906	1.1829
	234	2	1436	23	1425	26	0.77	3.0877	2.3750	0.2474	2.0326	0.8558	0.0905	1.2285
	233	2	1264	29	1208	20	4.44	2.3512	2.3517	0.2060	1.8128	0.7709	0.0828	1.4980
	232	3	981	31	981	21	0.04	1.6284	2.7122	0.1644	2.2535	0.8309	0.0718	1.5092
	201	3	962	34	979	20	-1.75	1.6093	2.7126	0.1640	2.1537	0.7940	0.0712	1.6491
	209	3	1005	38	948	26	5.69	1.5870	3.4728	0.1584	2.9157	0.8396	0.0727	1.8865
	210	3	970	31	949	19	2.15	1.5623	2.6601	0.1586	2.1762	0.8181	0.0714	1.5297
	223	3	999	24	958	23	4.06	1.6008	2.8915	0.1602	2.6280	0.9089	0.0725	1.2060
	226	3	962	27	958	30	0.46	1.5724	3.6025	0.1602	3.3570	0.9318	0.0712	1.3072
	227	3	974	20	962	22	1.28	1.5884	2.6797	0.1609	2.4885	0.9287	0.0716	0.9940
	228	3	992	34	956	19	3.65	1.5912	2.7047	0.1598	2.1401	0.7912	0.0722	1.6540
	229	3	993	32	950	24	4.34	1.5821	3.1295	0.1588	2.7016	0.8633	0.0723	1.5797
	235	3	966	21	969	22	-0.25	1.5944	2.6663	0.1622	2.4596	0.9225	0.0713	1.0292
	236	3	1004	30	970	22	3.38	1.6260	2.9050	0.1624	2.4869	0.8561	0.0726	1.5014
	237	3	980	30	975	24	0.48	1.6173	3.0529	0.1634	2.6857	0.8797	0.0718	1.4516
	238	3	997	29	968	23	2.86	1.6175	2.8977	0.1621	2.5137	0.8675	0.0724	1.4415
	239	3	983	33	952	16	3.10	1.5779	2.4475	0.1592	1.8156	0.7418	0.0719	1.6413
	240	3	964	33	961	24	0.38	1.5784	3.0988	0.1607	2.6498	0.8551	0.0712	1.6067
	242	3	992	27	975	24	1.67	1.6256	2.9699	0.1633	2.6625	0.8965	0.0722	1.3159
	243	3	994	39	958	24	3.54	1.5975	3.2782	0.1603	2.6482	0.8078	0.0723	1.9322
	246	3	952	23	987	18	-3.68	1.6162	2.2456	0.1655	1.9484	0.8676	0.0708	1.1165
	248	3	1011	27	977	20	3.39	1.6440	2.6183	0.1636	2.2496	0.8592	0.0729	1.3397
	249	3	995	32	969	19	2.69	1.6172	2.6343	0.1621	2.0993	0.7969	0.0723	1.5914
	251	3	972	36	955	25	1.77	1.5737	3.3122	0.1596	2.8113	0.8488	0.0715	1.7513
	252	3	960	25	958	17	0.19	1.5711	2.2636	0.1603	1.9050	0.8416	0.0711	1.2226
	245	3	972	27	966	18	0.64	1.5936	2.3982	0.1616	1.9900	0.8298	0.0715	1.3384
	230	3	944	37	994	21	-5.28	1.6221	2.9361	0.1668	2.3019	0.7840	0.0705	1.8227
	224	3	1016	20	986	24	2.96	1.6647	2.8271	0.1652	2.6528	0.9384	0.0731	0.9773
	200	4	967	21	998	19	-3.20	1.6467	2.2899	0.1674	2.0492	0.8949	0.0713	1.0219
	203	4	970	20	1030	26	-6.19	1.7074	2.8639	0.1733	2.6831	0.9369	0.0714	1.0013
	208	4	966	16	1040	19	-7.70	1.7212	2.1433	0.1751	1.9882	0.9276	0.0713	0.8005
	211	4	976	20	963	32	1.36	1.5920	2.8639	0.1611	3.5825	0.9654	0.0717	0.9672
	212	4	967	21	1010	26	-4.36	1.6679	2.9474	0.1695	2.7548	0.9347	0.0713	1.0480
	213	4	969	19	1005	21	-3.74	1.6612	2.4799	0.1687	2.3056	0.9297	0.0714	0.9134
	214	4	989	17	991	26	-0.13	1.6519	2.9347	0.1661	2.8170	0.9599	0.0721	0.8226
	216	4	977	15	998	24	-2.15	1.6554	2.6692	0.1675	2.5598	0.9590	0.0717	0.7565
	217	4	972	19	991	22	-1.90	1.6386	2.5584	0.1662	2.3791	0.9299	0.0715	0.9408
	218	4	963	17	995	17	-3.36	1.6384	1.9907	0.1669	1.7985	0.9034	0.0712	0.8534
	219	4	971	17	994	19	-2.43	1.6431	2.2458	0.1668	2.0943	0.9325	0.0715	0.8109
	220	4	962	21	1011	20	-5.10	1.6662	2.3811	0.1698	2.1361	0.8971	0.0712	1.0521
	221	4	974	20	1003	18	-2.99	1.6619	2.1833	0.1684	1.9519	0.8940	0.0716	0.9782
	222	4	953	22	1015	21	-6.48	1.6659	2.4446	0.1705	2.2044	0.9017	0.0709	1.0569
	253	4	960	16	1005	20	-4.76	1.6536	2.2963	0.1687	2.1580	0.9398	0.0711	0.7848
	254	4	971	14	1002	19	-3.24	1.6577	2.1657	0.1682	2.0467	0.9450	0.0715	0.7081
	207	4	952	24	1022	19	-7.37	1.6771	2.3643	0.1718	2.0453	0.8651	0.0708	1.1860
	206	4	939	22	1018	18	-8.48	1.6597	2.2054	0.1711	1.9290	0.8747	0.0703	1.0688
	215	4	1000	17	1007	20	-0.68	1.6898	2.2559	0.1690	2.0979	0.9299	0.0725	0.8295
	244	4	932	24	993	20	-6.53	1.6113	2.5036	0.1666	2.2093	0.8825	0.0701	1.1776

Table D.5 (cont'd). Summary of geochronology analyses for sample CL6112.

Sample Number	Trace element concentrations (ppm)																							Ce/Ce*	Eu/Eu*	∑REE	(Gd/Yb)cn	Lu/Hf	Nb/Ta	Th/U
	P	Ti	Y	Zr	Nb	La	Ce	Pr	Nd	Sm	Eu	Gd	Tb	Dy	Ho	Er	Tm	Yb	Lu	Hf	Ta	Th	U							
CL6112	298.0963	8.4286	723.2611	410588.2092	1.4366		29.9152	0.0898	2.5588	6.3023	2.3282	21.6188	7.4861	86.0283	27.7308	112.7548	29.8361	329.5388	32.7455	7087.1801	0.5683	36.3803	40.3302	326.5730	0.6098	688.9335	0.0543	0.0046	2.5277	0.9021
	118.5553	6.0471	231.6163	419997.0804	8.7677	0.5102	5.7088	0.1600	0.5250	0.3713	0.0729	1.6320	0.9796	16.1049	7.1334	40.6015	16.1100	245.0189	35.6012	11173.7526	3.4677	37.4949	816.3440	4.8994	0.2863	370.5297	0.0055	0.0032	2.5284	0.0459
	83.8973	4.1266	267.2737	438286.8657	3.2038		4.3610			0.2451	0.0722	2.0554	1.0254	16.5082	8.0409	49.4018	16.6335	261.9196	35.8378	11273.0746	1.1638	28.2143	471.5147		0.3109	396.1008	0.0065	0.0032	2.7529	0.0598
	175.9549	4.4501	370.5320	429531.1154	12.6862		4.0614			0.4953		2.2779	1.3024	23.9974	11.8650	68.2621	23.5142	349.9659	41.9649	10540.5283	11.2524	27.9484	583.2339			527.7064	0.0054	0.0040	1.1274	0.0479
	92.5913	2.9288	256.8981	423109.2433	2.8275		3.2553		0.0506		0.1081	2.1336	0.9099	17.8565	7.0992	44.6272	15.4036	232.4478	27.8439	10355.4187	2.3580	26.5695	548.8595			351.7357	0.0076	0.0027	1.1991	0.0484
	57.8962	1.8350	302.7076	448230.2926	1.0927		1.0950			0.3696	0.1359	1.1555	0.8377	15.6016	8.1349	56.5822	22.1874	354.1882	60.1101	13208.0718	2.0309	13.0918	984.1821		0.6356	520.3981	0.0027	0.0046	0.5380	0.0133
	86.9802	1.4058	208.9317	441329.5669	0.9009		1.2345			0.2370	0.1117	0.8645	0.6921	10.1878	5.6993	35.9631	14.8978	256.3969	40.9159	11545.4463	0.4618	17.8051	566.0802		0.7544	367.2007	0.0028	0.0035	1.9510	0.0315
	68.1295	1.1692	222.4919	426563.1242	0.6296		1.1532				0.0326	1.1260	0.6371	11.1955	6.6312	39.3248	17.0774	298.3295	47.8856	10626.3395	0.2703	17.5575	657.4126			423.3930		0.0045	2.3292	0.0267
	122.2134	1.8868	269.6425	444026.5422	2.3181	0.1048	3.4889	0.0481	0.1488	0.3118	0.1592	1.5131	1.1689	18.4957	7.6262	46.3339	17.5482	272.7507	38.7769	11283.9482	2.3329	28.9042	639.5232	12.0485	0.7085	408.4750	0.0046	0.0034	0.9936	0.0452
	95.7352	0.9278	234.6272	422091.6656	0.7316		1.6006			0.3059	0.0998	1.3389	0.7375	12.5861	6.6088	44.5426	18.7738	317.8545	49.8365	11197.2169	0.4512	17.6049	657.3003		0.4767	454.2850	0.0035	0.0045	1.6216	0.0268
	102.1852	0.8323	235.0214	436898.4538	0.8684		1.4490				0.0603	1.1661	0.7233	12.3569	6.7384	43.4678	17.8060	302.3636	50.4564	11433.0092	0.3538	18.6302	654.5014			436.5878		0.0044	2.4546	0.0285
	82.0895	1.4831	235.3405	425310.5213	1.2964		1.8719				0.1226	1.1064	0.6796	13.1813	6.5620	39.9383	17.1476	278.3723	43.4042	10847.3028	1.0140	21.3881	604.6614			402.3863		0.0040	1.2785	0.0354
	120.7358	2.0227	176.9396	426714.5982	1.7373	1.3846	6.2061	0.3553	1.4486	0.7159	0.2855	2.1041	0.9954	12.9289	5.6547	32.5144	12.1345	193.9328	32.4149	10796.5340	0.4369	25.2366	681.9841	2.1695	0.7111	303.0756	0.0090	0.0030	3.9762	0.0370
	79.8230	1.2115	222.1986	426219.7330	1.2139		2.1075				0.0620	1.2071	0.6242	11.7492	6.4552	37.7727	15.4484	255.0125	41.0983	11004.3918	0.7180	22.4548	616.6572			371.5370		0.0037	1.6906	0.0364
	62.3410	1.7194	201.0095	420000.3326	1.3338		2.0981			0.1549	0.1216	1.5084	0.4940	11.4766	5.8390	36.2847	15.1588	242.9024	38.1156	10595.9642	0.8549	28.6160	731.2404		0.7694	354.1542	0.0051	0.0036	1.5602	0.0391
	63.7995	1.3920	215.0162	435877.8203	0.8296	0.1657	2.5901	0.0721	0.3568	0.3543	0.1734	1.6603	0.7789	10.6154	5.8869	38.3490	15.6988	256.4260	39.8413	10538.4795	0.5040	25.3859	758.9845	5.8103	0.6911	372.9691	0.0054	0.0038	1.6459	0.0334
	52.1828	0.9918	264.8760	429015.5124	0.8552		1.3756				0.0542	0.9400	0.7955	14.2337	7.7434	47.7761	19.6159	331.6231	53.5580	11831.4053	1.1500	17.0083	930.6560			477.7154		0.0045	0.7436	0.0183
	92.7996	1.4310	249.1488	431754.9625	0.6936		1.2905			0.1645	0.0870	1.3122	0.7434	14.5154	7.1497	48.0563	19.0206	312.8339	53.2916	11108.3264	0.4406	17.0741	742.0346		0.5722	458.4650	0.0035	0.0048	1.5742	0.0230
	78.2886	1.3375	225.3340	432377.7251	0.8209		1.6361				0.2141	0.8507	0.6775	12.6916	6.2744	42.6363	17.0163	279.0722	45.6621	10752.1329	0.4898	19.3220	645.1319			406.7311		0.0042	1.6762	0.0300
	54.0913	1.2213	284.9300	429288.6497	1.0323		1.5044				0.0388	0.8901	0.7261	14.5163	7.8355	51.8887	21.1794	361.8856	56.6582	12039.0650	0.9758	16.9171	929.9902			517.1231		0.0047	1.0580	0.0182
	67.9549	1.3997	217.2211	427706.9412	0.9615	0.0761	1.5427	0.0144			0.0799	1.2931	0.7751	13.9457	6.5030	42.5792	15.4878	263.4857	44.2527	10761.5787	0.4547	15.9881	624.3855	11.4416		390.0354		0.0041	2.1147	0.0256
	63.1075	0.8770	223.3988	420763.0915	0.7800		1.3375				0.1383	1.2699	0.6649	12.7193	6.2585	39.3611	16.9692	286.9898	46.0410	10096.4967	0.4308	17.7016	637.0258			411.7494		0.0046	1.8105	0.0278
	75.6014	1.4743	136.1549	400961.2463	1.0619	0.7434	3.2414	0.1352	0.8344	0.4049	0.1141	0.9764	0.4374	6.7285	3.9604	23.3778	9.7865	165.8627	25.3689	9455.2250	0.5071	17.9176	573.9408	2.5069	0.5550	241.9720	0.0049	0.0027	2.0942	0.0312
	34.6507	1.3247	228.9294	407787.4204	0.8066	0.2068	2.1084	0.0243	0.1691	0.2361	0.0974	1.9685	0.8126	12.5989	6.4814	40.8711	17.6118	294.6241	45.8873	10097.3100	0.4999	18.5966	659.0944	7.2852	0.4366	423.6978	0.0055	0.0045	1.6134	0.0282
	86.1847	1.0296	266.0421	410021.3761	0.8589		1.2832				0.1576	0.5511	0.8065	15.0153	7.5950	51.2940	19.3213	337.6218	52.8823	10856.7475	1.0597	15.7749	930.5074			486.5281		0.0049	0.8105	0.0170
	74.0107	0.3219	234.8695	410659.2795	1.0952		1.4372				0.0893	0.6448	0.6829	12.2562	7.2147	45.1867	17.4223	306.2619	47.2873	10773.2689	0.8969	16.8808	854.0009			438.4833		0.0044	1.2211	0.0198
	84.5574	1.4040	223.3384	408798.9793	0.7834		1.3951		0.1047	0.1780	0.0145	0.6903	0.6993	11.1874	6.3367	42.1395	16.7657	300.0507	46.2595	10237.6598	0.4389	16.6301	632.4062		0.1268	425.8215	0.0019	0.0045	1.7848	0.0263
	68.9133	2.0914	197.6979	439963.9212	0.7895		1.2136				0.1239	0.8492	0.6346	9.5331	5.6082	33.4733	14.4821	235.7737	39.2735	11439.7781	0.3743	17.7657	631.2554			340.9651		0.0034	2.1092	0.0281
	168.2363	3.0038	409.8528	431432.3946	10.1636	0.0533	2.6002	0.0076	0.2426	0.6883	0.1295	2.3202	1.4760	29.6852	13.7939	72.6925	25.1547	328.7198	41.1495	11406.4533	12.0963	14.0310	757.6232	31.7547	0.3134	518.7131	0.0058	0.0036	0.8402	0.0185
	60.1811	1.0277	421.2200	435687.3002	2.3398		1.0112		0.1025	0.2415	0.0907	0.5663	0.9579	20.7437	12.2611	75.1060	30.0680	470.8327	74.4086	14121.5673	3.5435	13.5009	1496.3838		0.7498	686.3901	0.0010	0.0053	0.6603	0.0090
	81.1673	0.8499	496.9880	427418.6486	2.3837		1.2205				0.0879	1.3395	1.1030	25.9035	13.6156	93.3918	38.5511	576.9943	93.4272	17024.0553	4.8767	15.0227	2622.1516			845.6342		0.0055	0.4888	0.0057
	98.4178	0.9112	539.8605	430053.0574	2.8673		1.2512				0.0675	2.2681	1.1827	26.5538	14.3506	99.2816	39.8262	616.8556	100.9085	16974.6127	5.6177	16.6448	2699.8025			902.5458		0.0059	0.5104	0.0062
	107.2970	0.7949	364.9134	395370.1897	1.7270		1.2988				0.0797	1.4694	0.8555	20.2124	10.5530	68.9464	26.4997	439.0962	63.4377	12528.7902	3.1744	13.5101	1682.1748			632.4488		0.0051	0.5441	0.0080
	96.9922	0.9068	407.8209	383950.9740	2.8719		0.8930				0.1041	0.5975	0.9903	19.9067	11.0806	75.7002	31.1266	523.3730	75.5732	14612.7310	5.3008	12.7145	2490.2444			739.3453		0.0052	0.5418	0.0051
	97.3003	1.0624	335.9594	389155.1020	1.7799		1.3210			0.0737	0.0608	1.0081	0.9534	18.8970	9.8866	61.1709	25.1207	393.6501	55.2993	12327.9321	3.2313	15.5645	2053.0507		0.6821	567.4417	0.0021	0.0045	0.5508	0.0076
	116.9886	0.9764	445.9570	388890.0530	3.0698		0.9524				0.0153	1.2956	0.9601	24.2383	13.0042	83.8578	34.6936	563.7468	81.1497	13828.4361	4.9132	13.6214	2587.6020			803.9137		0.0059	0.6248	0.0053
	104.2125	0.4834	450.0283	392879.1259	3.0471		1.1520				0.0998	1.3524	1.0140	22.5770	12.2601	77.7926	33.9847	536.0824	78.7139	15062.8736	5.3100	20.3635	3851.3882			765.0287		0.0052	0.5738	0.0053
	91.2530	0.5386	462.9709	373958.7408	2.5870		1.1972				0.1080	1.4898	1.2673	23.6014	12.0747	82.6469	34.1662	576.1131	80.5585	14671.5155	5.4021	18.0407	3422.9237			813.2231		0.0055	0.4789	0.0053
	110.6908	0.6815	478.9371	408173.2240	2.4453		1.2393		0.1567	0.1184	0.1116	1.6040	1.1185	22.9471	13.6664	90.1180	34.8789	563.0143	81.3812	14502.8616	4.5268	14.9194	2262.5846		0.7829	810.3545	0.0024	0.0056	0.5402	0.0066
	83.2996	0.6621	445.4947	381774.3395	2.4022		1.2838				0.0534	1.2009	1.1978	22.4677	13.3375	86.1371	33.3495	552.5771	76.3614	13573.5686	4.4272	14.1731	2217.2292			787.9663		0.0056	0.5426	0.0064
	67.5124	1.0229	451.4420	427140.8939	2.2708		1.2956			0.1932	0.0910	0.7513	1.2729	22.8804	12.4376	85.4001	32.6466	512.5530	78.5889	14655.9650	4.1398	14.4321	1932.4638		0.7306	748.1107	0.0012	0.0054	0.5485	0.0075
	69.7467	1.6974	418.4047	408854.1638	2.7390		1.3391				0.0239	0.9005	1.0703	20.0396	11.5298	75.7944	31.7752	459.4092	70.7712	14444.7880	4.2355	16.6386	2318.4141			672.6532		0.0049	0.6467	0.0072
	91.3392	1.0489	467.5567	406463.1775	2.9694		1.2256				0.0166	1.7818	1.2220	23.8427	13.0948	87.3502	35.7510	547.1855	82.5852	14223.4777	4.8431	14.8760	2288.3093			794.0553		0.0058	0.6131	0.0065
	132.6211	0.5183	397.5787	420257.5397	2.5669		1.3145			0.2580	0.0759	1.4515	0.9613	20.4323	11.4973	74.8878	29.6998	432.4160	68.9142	14431.2397	4.1458	17.1735	2141.3206		0.3790	641.9086	0.0028	0.0048	0.6192	0.0080
	101.7274	0.7224	404.8230	421605.0214	2.3598		1.2496			0.3616	0.1641	1.6687	1.1880	22.5008	11.2316	76.2735	28.8486	457.3522	71.0445	14741.9170	3.7547	18.9190	2464.2804		0.6458	671.8832	0.0030	0.0048	0.6285	0.0077
	117.9310	0.8678	485.4721	422452.9502	3.3772		1.0889					1.1453	1.1335	23.3473	13.6401	89.6028	35.2570	576.3695	93.0170	17210.0696	6.0499	18.3444	3156.0414			834.6016		0.0054	0.5582	0.0058
	68.7940	0.6643	504.1167	424490.5881	2.8035		1.1631				0.0762	1.2948	1.0734	22.9973	13.4888	94.9332	38.1886	618.1630	100.5733	18063.1324	6.3250	14.3196	2443.9751			891.9518		0.0056	0.4432	0.0059
	81.9045	0.5112	441.2723	392511.9611	2.7798		1.0334				0.0694	1.7891	1.0935	23.3036	12.5907	83.1884	32.9385	533.3778	78.2197	14778.6561	5.9608	21.2456	3832.7667			767.6040		0.0053	0.4663	0.0055
	92.5425	0.8938	315.9659	399893.7241	1.5467		1.4016			0.1116		1.1471	0.6215	16.6946	8.6544	57.3033	21.9540	376.7379	52.6778	12326.0449	2.3288	17.1822	1848.8822			537.3036	0.0025	0.0043	0.6642	0.0093

Analytical information is the same as table D.3
Isotope ratios and ages are NOT corrected for initial common Pb.
Isotope ratio and apparent age errors do NOT include systematic calibration errors of 0.32% ($^{207}Pb/^{206}Pb$), 0.52% ($^{206}Pb/^{238}U$) (all 2-sigma).
Trace element concentrations in ppm, calculated using mean count rate method.
Sweep-by-sweep downhole fractionation of U/Pb ratios NOT corrected via Si/Zr fractionation factor.
Backgrounds were monitored between sweeps 5 to 20. Sample counts were integrated from sweeps 34 to 60.
Ablation used a laser spot size of 25 microns, and a laser firing repetition rate of 10 Hz.

Table D.6. Summary of geochronology analyses for sample CL6127.

Sample Number	Spot Number	Type	Apprent Ages (Ma)					Isotope Ratios							
			207Pb* 206Pb*	±2s (Ma)	206Pb* 238U*	±2s (Ma)	% disc.	207Pb* 235U*	±2s (%)	206Pb* 238U	±2s (%)	error corr.	207Pb* 206Pb*	±2s (%)	error corr.
CL6127	226	1 (core)	2647	51	2687	114	-1.50	12.7877	6.0424	0.5171	5.1952	0.8584	0.1794	3.0857	0.0000
	227	1 (rim)	977	65	1023	34	-4.76	1.7000	4.8345	0.1720	3.6153	0.7454	0.0717	3.2096	0.0000
	210	2	989	36	1011	42	-2.23	1.6879	4.8408	0.1698	4.5085	0.9294	0.0721	1.7626	0.0000
	211	2	1015	24	994	45	2.12	1.6788	5.0546	0.1667	4.9128	0.9702	0.0730	1.1891	0.0000
	222	3	1011	58	982	37	2.80	1.6542	4.9533	0.1646	4.0283	0.8111	0.0729	2.8825	0.0000
	220	3	996	45	1001	40	-0.45	1.6751	4.8263	0.1679	4.2882	0.8865	0.0724	2.2146	0.0000
	223	3	1010	62	1006	32	0.37	1.6966	4.5771	0.1689	3.3866	0.7372	0.0729	3.0790	0.0000
	193	3	992	44	1010	40	-1.85	1.6898	4.8319	0.1697	4.3226	0.8926	0.0722	2.1592	0.0000
	201	4	940	50	952	43	-1.30	1.5455	5.4530	0.1592	4.8770	0.8928	0.0704	2.4393	0.0000
	202	4	979	54	952	46	2.71	1.5746	5.7853	0.1592	5.1531	0.8893	0.0717	2.6297	0.0000
	206	4	1022	24	958	52	6.25	1.6202	6.0094	0.1603	5.8946	0.9797	0.0733	1.1692	0.0000
	212	4	1001	40	972	37	2.90	1.6287	4.5638	0.1628	4.1083	0.8979	0.0725	1.9875	0.0000
	208	4	1019	49	978	47	3.99	1.6530	5.6683	0.1638	5.1244	0.9026	0.0732	2.4229	0.0000
	234	4	1045	55	997	41	4.62	1.7097	5.2092	0.1673	4.4444	0.8514	0.0741	2.7172	0.0000
	235	4	1021	47	1014	39	0.72	1.7197	4.7556	0.1703	4.1428	0.8690	0.0733	2.3352	0.0000
	241	4	972	47	1033	41	-6.19	1.7131	4.8659	0.1737	4.2792	0.8774	0.0715	2.3163	0.0000
	239	4	972	47	1033	41	-6.19	1.7131	4.8659	0.1737	4.2792	0.8774	0.0715	2.3163	0.0000
	240	4	1014	45	1019	41	-0.50	1.7229	4.8581	0.1712	4.3328	0.8899	0.0730	2.1972	0.0000
	231	4	1015	48	1006	40	0.89	1.7010	4.9144	0.1689	4.3045	0.8739	0.0730	2.3713	0.0000
	230	4	1020	49	1015	46	0.42	1.7222	5.4074	0.1706	4.8453	0.8944	0.0732	2.4006	0.0000
	236	4	1024	39	1040	43	-1.56	1.7713	4.8302	0.1751	4.4373	0.9167	0.0734	1.9080	0.0000
	200	4	1028	40	932	45	9.37	1.5765	5.5445	0.1555	5.1740	0.9317	0.0735	1.9928	0.0000
	215	5	1023	35	1019	50	0.42	1.7316	5.5337	0.1712	5.2615	0.9494	0.0733	1.7142	0.0000
	194	5	1030	40	976	36	5.25	1.6594	4.4035	0.1635	3.9408	0.8925	0.0736	1.9648	0.0000
	216	5	989	59	1000	27	-1.08	1.6675	4.1030	0.1677	2.8886	0.7004	0.0721	2.9139	0.0000
	214	5	1008	24	1012	44	-0.38	1.7049	4.8281	0.1699	4.6869	0.9689	0.0728	1.1589	0.0000
	219	5	968	39	1004	38	-3.75	1.6591	4.4886	0.1686	4.0596	0.9021	0.0714	1.9151	0.0000
	229	5	975	59	1014	43	-4.01	1.6818	5.4601	0.1703	4.6192	0.8443	0.0716	2.9113	0.0000
	233	5	1018	44	1036	47	-1.77	1.7586	5.3588	0.1744	4.9031	0.9133	0.0731	2.1626	0.0000
	197	5	1089	81	989	48	9.19	1.7330	6.5950	0.1659	5.1964	0.7867	0.0758	4.0609	0.0000
	195	5	1031	53	1013	47	1.80	1.7270	5.6713	0.1701	5.0400	0.8872	0.0736	2.6004	0.0000
	232	5	1020	47	1009	48	1.11	1.7105	5.6380	0.1694	5.1490	0.9118	0.0732	2.2968	0.0000
	207	5	1048	36	976	49	6.87	1.6726	5.7430	0.1634	5.4529	0.9481	0.0742	1.8022	0.0000
	224	5	1090	42	1018	43	6.63	1.7887	5.0526	0.1711	4.5928	0.9072	0.0758	2.1060	0.0000
	199	5	989	47	949	42	4.02	1.5761	5.3303	0.1586	4.8080	0.9004	0.0721	2.3011	0.0000
	221	5	981	32	1020	41	-3.95	1.6970	4.6019	0.1714	4.3266	0.9380	0.0718	1.5678	0.0000
	238	5	1025	25	1018	33	0.66	1.7318	3.6931	0.1711	3.4757	0.9378	0.0734	1.2484	0.0000

Table D.6. (cont'd). Summary of geochronology analyses for sample CL6127.

Sample Number	Trace element concentrations (ppm)																													
	P	Ti	Y	Zr	Nb	La	Ce	Pr	Nd	Sm	Eu	Gd	Tb	Dy	Ho	Er	Tm	Yb	Lu	Hf	Ta	Th	U	Ce/Ce*	Eu/Eu*	∑REE	(Gd/Yb)cn	Lu/Hf	Nb/Ta	Th/U
CL6127	46.2659	2.2838	77.5597	459793.3938	0.0799		1.1571		0.0996	0.2937	0.2259	2.3660	0.6495	7.0420	2.3840	8.6061	2.0690	19.6780	3.2060	9466.9246	0.1086	2.7432	32.0772	0.0000	0.8285	47.7770	0.0995	0.0003	0.7358	0.0855
	147.4162	1.4548	166.5994	460318.0021	0.5187		6.9309			0.2394	0.1227	3.2108	1.0691	10.7039	5.3272	27.1050	7.7285	88.4576	14.7026	10377.3938	0.4569	46.0869	193.7033	0.0000	0.4280	165.5977	0.0300	0.0014	1.1353	0.2379
	241.4823	3.7914	1055.5267	460069.6234	8.3941		23.1247	0.0488	0.7436	2.5730	0.5478	15.2756	6.2279	77.9563	31.8788	154.7457	43.5021	451.5279	67.9358	10621.9759	4.7441	159.6502	980.4899	465.1090	0.2671	876.0881	0.0280	0.0064	1.7694	0.1628
	270.9796	3.5624	1103.6565	459057.2298	8.8946		24.3385		0.9388	2.6550	0.4483	16.0176	6.9409	85.6277	35.0600	170.5287	46.7266	494.0350	75.6265	10164.8636	4.6178	166.4026	1048.7451	0.0000	0.2102	958.9436	0.0268	0.0074	1.9262	0.1587
	137.6898	2.0016	465.5909	471551.7579	1.0186	0.4601	13.2913	0.2039	3.0571	2.2920	0.7509	8.8727	3.3038	37.1146	16.1464	71.9266	18.6614	204.9176	34.5762	9830.2312	0.9391	151.1323	408.9380	10.6406	0.5090	415.5744	0.0358	0.0035	1.0847	0.3696
	181.3464	2.6429	423.4443	460692.4965	1.0740		13.0295	0.0169	0.4630	1.3008	0.3889	8.2626	2.4599	35.7563	14.6147	70.4187	19.0740	207.1902	34.2062	9417.5499	1.2059	174.8854	498.8875	757.6628	0.3627	407.1818	0.0330	0.0036	0.8906	0.3506
	256.1445	1.9606	609.6003	449247.0794	1.8806		12.4475	0.0341	0.4871	2.4752	0.5028	10.5273	4.0941	51.3370	19.8788	90.2991	25.9464	271.6131	47.5292	10534.9585	1.2152	99.1590	386.0541	358.3024	0.3012	537.1719	0.0321	0.0045	1.5475	0.2569
	175.2598	1.8660	478.5338	437472.8752	1.5720		12.7035	0.0488	0.6189	1.6378	0.4903	9.7696	3.4284	39.3492	15.5762	69.2154	18.8708	210.2405	30.6192	9588.8928	1.0957	82.1493	354.9566	255.4359	0.3747	412.5684	0.0384	0.0032	1.4348	0.2314
	256.5187	2.2787	617.2334	458560.4963	2.3669		12.8619		0.7874	1.9282	0.5405	11.8575	3.7674	50.0701	20.3284	97.8042	26.5640	289.6926	44.9743	9919.4832	1.7936	137.3731	439.1995	0.0000	0.3456	561.1766	0.0339	0.0045	1.3196	0.3128
	161.9077	2.0684	381.0220	474629.3914	1.4317		13.4063		0.6961	0.8842	0.5449	7.6218	2.5259	30.2438	13.1605	59.5809	16.5501	188.9688	31.1931	9878.1851	1.0082	178.4457	478.2349	0.0000	0.6418	365.3763	0.0334	0.0032	1.4200	0.3731
	151.5434	1.4100	428.2093	459014.4873	1.1464		10.0993		0.2560	0.5206	0.5202	6.4055	2.6595	32.3901	14.6647	68.0206	19.1237	220.8545	35.6058	9488.1232	1.0048	122.9862	431.5918		0.8709	411.1202	0.0240	0.0038	1.1409	0.2850
	117.0092	2.0411	401.3114	454957.0117	1.0199	0.1872	12.4761	0.1729	1.8909	1.6248	0.4649	9.0818	2.8872	35.3711	12.6094	60.9343	16.0979	177.2733	28.2031	9166.8990	1.0074	143.6629	394.7719	17.0031	0.3700	359.2749	0.0424	0.0031	1.0125	0.3639
	146.4417	1.7088	393.3904	454946.2346	0.8987		12.9472	0.0171	0.5008	1.0224	0.3701	5.6202	2.5555	31.1926	11.8696	61.4206	16.3626	178.9128	29.4597	9512.5908	0.9926	157.2184	452.8873	742.4478	0.4720	352.2512	0.0260	0.0031	0.9055	0.3471
	160.0672	2.2472	695.5212	451430.0665	2.3027		12.7315	0.0084	0.4247	1.8138	0.5632	11.1570	4.0756	52.8707	22.0954	103.0942	27.7113	301.0495	48.0018	9698.5271	1.5501	116.9387	332.2216	1494.3557	0.3828	585.5971	0.0307	0.0049	1.4855	0.3520
	141.2910	2.1655	287.0387	454470.2885	0.9710		11.4276	0.0037	0.3198	0.6640	0.3250	5.4516	1.8261	24.4684	9.6302	44.9841	12.5266	134.4820	23.6150	9598.5707	0.9107	153.7928	420.1033	3053.6872	0.5222	269.7240	0.0335	0.0025	1.0662	0.3661
	198.1102	2.7189	641.8521	468466.1653	1.3480		13.5617	0.0523	0.4670	1.7578	0.5417	10.4186	4.0509	46.3272	20.6938	99.8234	27.4863	303.9706	57.1491	9850.0023	1.3626	183.7312	489.4930	254.0756	0.3870	586.3003	0.0284	0.0058	0.9893	0.3754
	198.1102	2.7189	641.8521	468466.1653	1.3480		13.5617	0.0523	0.4670	1.7578	0.5417	10.4186	4.0509	46.3272	20.6938	99.8234	27.4863	303.9706	57.1491	9850.0023	1.3626	183.7312	489.4930	254.0756	0.3870	586.3003	0.0284	0.0058	0.9893	0.3754
	197.4650	1.8518	412.2051	488970.7337	0.9368	0.2411	13.6320	0.0458	1.5655	1.5457	0.6087	9.6730	2.9065	32.2960	12.3406	61.1353	16.0137	159.2433	31.2760	11500.5707	0.9579	152.5521	434.2518	31.7956	0.4813	342.5232	0.0503	0.0027	0.9780	0.3513
	192.8178	1.9764	524.4194	450641.3142	2.8322		13.0241	0.0025	0.2706	1.7608	0.3527	7.0843	3.1891	40.2504	15.9704	78.5753	21.1418	237.1828	37.5272	10376.9813	2.4442	126.9369	597.3650	5011.1410	0.3053	456.3321	0.0247	0.0036	1.1588	0.2125
	165.3001	1.9607	441.0227	446984.2325	1.2646		11.6473	0.0043	0.1641	1.3650	0.4108	7.2014	3.0758	37.1073	14.7196	69.4447	19.6448	211.4967	34.1049	9778.0624	0.9589	130.0171	385.4952	2659.1229	0.4006	410.3865	0.0282	0.0035	1.3188	0.3373
	139.1302	1.8824	490.8792	450860.8709	2.0056		11.9519		0.7805	1.6158	0.2963	8.2565	3.0059	38.6966	15.7235	73.4121	20.0222	216.1027	36.5640	10707.2428	1.6492	128.5265	491.5801	0.0000	0.2480	426.4280	0.0316	0.0034	1.2162	0.2615
	221.3739	1.7611	400.7842	469621.2741	1.5348	0.0403	14.2420	0.0087	0.2650	1.4379	0.4808	6.9165	2.4738	31.5558	13.7972	64.0034	17.4576	194.9953	31.2049	9727.2587	1.1332	157.8818	467.6751	186.5303	0.4661	378.8793	0.0293	0.0032	1.3544	0.3376
	133.3725	2.2590	278.3014	458278.9845	1.1026		12.4051		0.4501	1.3235	0.4253	5.8987	2.0240	22.5045	9.5613	43.0881	12.3615	130.8586	21.4709	9685.4000	0.9757	164.0343	486.7043	0.0000	0.4654	262.3715	0.0373	0.0022	1.1301	0.3370
	137.4567	1.6076	288.9926	433820.6265	1.2462		11.3514		0.2255	0.9560	0.3978	5.8311	2.0483	24.2161	9.4568	42.4769	12.2884	147.4974	21.9750	8575.4390	0.8568	138.3296	436.7643	0.0000	0.5151	278.7209	0.0327	0.0026	1.4545	0.3167
	135.1988	2.1756	334.8142	438867.2212	1.0033	0.2158	11.5486	0.2008	1.8373	1.3771	0.5949	6.4684	2.3289	28.5321	10.6646	50.9608	15.4651	151.6312	24.7694	8636.4023	0.9167	144.4824	416.6135	13.6025	0.6093	306.5950	0.0353	0.0029	1.0944	0.3468
	176.8870	1.5701	351.8025	453491.0345	1.0462		11.5433	0.0158	0.3011	0.9340	0.4224	7.4612	2.3449	25.3548	11.4613	52.1086	14.7332	156.5472	24.4801	9994.6525	0.9589	134.3298	432.2383	716.8447	0.4892	307.7078	0.0394	0.0024	1.0911	0.3108
	187.0762	1.8127	361.6740	466487.8962	0.9206		12.4026		0.1617	1.4644	0.3598	6.1017	2.2794	27.6014	11.4027	52.4543	14.9947	159.5339	26.5258	10285.6879	1.1073	135.2954	438.7701	0.0000	0.3680	315.2825	0.0316	0.0026	0.8314	0.3084
	135.7739	2.3816	375.1169	452115.7432	0.8031		11.0519		0.5296	1.0379	0.3899	7.3365	2.2380	28.6537	12.0277	58.1746	16.5386	175.8606	28.6149	9992.5568	1.1084	101.9890	337.6288	0.0000	0.4320	342.4540	0.0345	0.0029	0.7245	0.3021
	116.8682	2.5491	430.3559	462219.5214	2.1476	0.1358	11.9902	0.0567	0.7708	1.5759	0.2797	7.0284	2.3392	31.1798	13.2325	63.1480	16.3746	187.6829	31.6654	9943.5671	1.7603	104.2877	442.7935	33.5039	0.2569	367.4599	0.0310	0.0032	1.2200	0.2355
	132.3448	2.3535	389.3757	443306.2927	1.1785		13.9160	0.0174	0.4787	1.3250	0.3552	5.7945	2.6535	31.5622	12.5883	58.3919	16.9965	194.4376	29.4449	8610.8194	1.1581	174.7477	524.4360	782.6514	0.3918	367.9616	0.0247	0.0034	1.0176	0.3332
	150.7267	1.9955	430.2249	428660.2799	0.8234	0.1147	11.2033	0.0687	0.6470	1.1115	0.3799	7.8828	2.7499	37.6802	14.8723	68.3403	18.9172	212.3580	34.1016	8389.0162	0.9463	139.9377	391.6442	30.9484	0.3924	410.4273	0.0307	0.0041	0.8702	0.3573
	185.0193	1.8988	454.1351	444546.3526	1.0718		9.5838		0.6475	1.2926	0.2777	7.9931	2.7934	32.9398	14.5004	69.4276	18.8303	225.0815	36.4133	10186.9961	1.1495	109.7093	417.6796	0.0000	0.2642	419.7809	0.0294	0.0036	0.9324	0.2627
	215.0413	1.5366	591.1316	462445.5697	1.6350		12.1623		0.5735	2.0333	0.4573	7.9119	3.1643	45.3689	18.8079	93.5261	25.8655	291.3170	49.6220	9721.5668	1.0017	138.7525	452.6718	0.0000	0.3486	550.8101	0.0225	0.0051	1.6323	0.3065
	175.3302	2.5647	726.2438	477229.8911	3.9325	0.2173	16.0168	0.1983	1.6630	2.6750	0.6008	13.1810	4.2996	56.2888	23.1694	109.3313	28.7477	307.9094	52.6494	10395.3355	3.1310	102.1353	648.7928	18.9176	0.3093	616.9477	0.0354	0.0051	1.2560	0.1574
	186.4511	3.3225	786.8580	475521.0323	3.6667		15.1575	0.0133	0.3255	1.8696	0.6871	11.6475	4.4050	60.6792	25.8939	118.4811	33.2593	348.3743	53.7178	10155.9987	2.9488	94.2030	597.1674	1114.4875	0.4501	674.5113	0.0277	0.0053	1.2434	0.1577
	180.5884	2.3810	757.1812	453002.5848	3.9814		15.4493		0.1551	1.4047	0.3301	13.5907	4.6597	62.2601	24.9265	114.4642	32.5230	348.4219	57.1058	10336.9063	3.4761	103.1053	620.4352	0.0000	0.2310	675.2911	0.0323	0.0055	1.1454	0.1662
	229.5369	2.2853	869.2838	465744.1880	4.2899		12.5294		0.3592	1.7553	0.5649	11.9199	5.0459	60.4470	26.4024	126.3106	33.6813	345.5524	62.0255	10381.6952	2.8030	93.4813	470.0646	0.0000	0.3775	686.5937	0.0285	0.0060	1.5305	0.1989

Analytical session no: 3
Isotope ratio and date errors do not include systematic calibration errors of 0.30% ($^{207}Pb/^{206}Pb$) and 1.58% ($^{206}Pb/^{238}U$) (2 sigma).
Isotope ratios and ages corrected using a measured linear secondary standard age bias - ^{206}Pb count rate relationship.
Trace element concentrations in ppm, calculated using mean count rate method.
Sweep-by-sweep downhole fractionation of U/Pb ratios NOT corrected via Si/Zr fractionation factor.
Backgrounds were monitored between sweeps 5 to 20. Sample counts were integrated from sweeps 35 to 60.
Ablation used a laser spot size of 25 microns, and a laser firing repetition rate of 10 Hz.

Table D.7. Summary of geochronology analyses for sample CL6135.

Sample Number	Spot Number	Type	Apparent Ages (Ma)					Isotope Ratios						
			207Pb*/206Pb*	±2s (Ma)	206Pb*/238U*	±2s (Ma)	% disc.	207Pb*/235U*	±2s (%)	206Pb*/238U	±2s (%)	207Pb*/206Pb*	±2s (%)	error corr.
CL6135	160	1	1714	55	1621	33	5.43	4.1360	3.7547	0.2858	2.3050	0.1050	2.9640	0.0000
	142	1	1658	57	1637	29	1.23	4.0592	3.6435	0.2891	1.9832	0.1018	3.0565	0.0000
	146	1	1630	74	1614	46	1.01	3.9355	5.1411	0.2845	3.2445	0.1003	3.9880	0.0000
	154	1	1693	39	1631	48	3.64	4.1206	3.9368	0.2879	3.3287	0.1038	2.1020	0.0000
	158	1	1630	56	1662	25	-1.98	4.0698	3.4557	0.2942	1.7326	0.1003	2.9900	0.0000
	170	1	1662	46	1639	30	1.40	4.0728	3.2140	0.2894	2.0404	0.1021	2.4833	0.0000
	185	1	1615	63	1579	61	2.24	3.8091	5.5105	0.2776	4.3311	0.0995	3.4070	0.0000
	193	1	1613	76	1563	32	3.12	3.7603	4.6891	0.2743	2.3213	0.0994	4.0742	0.0000
	131	1	1573	58	1506	42	4.26	3.5300	4.4093	0.2631	3.1404	0.0973	3.0951	0.0000
	195	1	1652	55	1625	37	1.68	4.0129	3.9570	0.2866	2.5944	0.1015	2.9878	0.0000
	197	1	1622	47	1600	46	1.38	3.8796	4.1347	0.2817	3.2631	0.0999	2.5393	0.0000
	136	1	1542	108	1501	57	2.66	3.4607	7.1616	0.2622	4.2811	0.0957	5.7412	0.0000
	130	1	1661	32	1610	40	3.09	3.9898	3.3067	0.2837	2.8177	0.1020	1.7306	0.0000
	169	2	1672	41	1657	34	0.87	4.1472	3.1982	0.2931	2.2979	0.1026	2.2245	0.0000
	171	2	1631	28	1645	24	-0.86	4.0246	2.2292	0.2908	1.6254	0.1004	1.5256	0.0000
	132	2	1667	33	1643	40	1.43	4.0983	3.2597	0.2904	2.7234	0.1024	1.7912	0.0000
	145	2	1683	40	1680	43	0.17	4.2393	3.6413	0.2978	2.9250	0.1032	2.1688	0.0000
	159	2	1631	27	1630	36	0.04	3.9825	2.8843	0.2878	2.5020	0.1004	1.4350	0.0000
	172	2	1669	33	1647	34	1.27	4.1124	2.9673	0.2912	2.3583	0.1024	1.8009	0.0000
	123	2	1661	39	1697	28	-2.18	4.2371	2.8145	0.3012	1.8610	0.1020	2.1115	0.0000
	196	2	1654	37	1655	39	-0.04	4.0999	3.3330	0.2926	2.6881	0.1016	1.9706	0.0000
	134	2	1676	39	1583	48	5.52	3.9458	4.0119	0.2783	3.4088	0.1028	2.1156	0.0000
	181	2	1703	26	1637	34	3.88	4.1593	2.7463	0.2891	2.3662	0.1044	1.3939	0.0000
	182	2	1628	34	1695	36	-4.09	4.1560	3.0268	0.3007	2.3912	0.1002	1.8556	0.0000
	161	2	1636	28	1539	35	5.91	3.7413	2.9440	0.2696	2.5260	0.1006	1.5120	0.0000
	192	2	1713	24	1621	40	5.40	4.1366	3.0618	0.2859	2.7789	0.1049	1.2855	0.0000
	124	2	1510	32	1426	72	5.61	3.2113	5.8893	0.2475	5.6363	0.0941	1.7074	0.0000
	186	3	1703	23	1582	37	7.12	4.0030	2.8842	0.2782	2.6068	0.1044	1.2342	0.0000
	189	3	1662	26	1631	28	1.82	4.0517	2.4053	0.2880	1.9593	0.1020	1.3952	0.0000
	153	3	1653	27	1629	31	1.44	4.0259	2.5728	0.2875	2.1372	0.1016	1.4323	0.0000
	165	3	1675	36	1646	30	1.73	4.1224	2.8577	0.2909	2.0706	0.1028	1.9696	0.0000
	187	3	1659	36	1665	35	-0.38	4.1406	3.0895	0.2947	2.3839	0.1019	1.9652	0.0000
	163	3	1777	33	1655	37	6.88	4.3837	3.1213	0.2926	2.5530	0.1086	1.7957	0.0000
	190	3	1276	63	1195	27	6.32	2.3395	4.0916	0.2037	2.5133	0.0833	3.2287	0.0000
	139	4	1157	68	1149	61	0.69	2.1084	6.7553	0.1951	5.8157	0.0784	3.4369	0.0000
	174	4	1418	25	1464	23	-3.26	3.1525	2.2107	0.2550	1.7874	0.0897	1.3010	0.0000
	148	4	1452	29	1426	35	1.77	3.1167	3.1230	0.2477	2.7273	0.0913	1.5215	0.0000
	149	4	1438	31	1431	36	0.53	3.1038	3.2575	0.2485	2.8087	0.0906	1.6500	0.0000
	173	4	1431	20	1456	30	-1.73	3.1551	2.5218	0.2535	2.2886	0.0903	1.0592	0.0000
	175	4	1450	35	1426	31	1.64	3.1130	3.0478	0.2477	2.4312	0.0912	1.8379	0.0000
	176	4	1428	33	1450	37	-1.55	3.1360	3.3096	0.2523	2.8202	0.0901	1.7320	0.0000
	177	4	1422	35	1423	22	-0.05	3.0580	2.5292	0.2469	1.7176	0.0898	1.8566	0.0000
	178	4	1454	19	1435	29	1.29	3.1417	2.4938	0.2494	2.2799	0.0914	1.0106	0.0000
	179	4	1437	27	1445	33	-0.53	3.1373	2.9219	0.2513	2.5455	0.0906	1.4346	0.0000
	180	4	1453	35	1453	41	0.00	3.1829	3.6670	0.2528	3.1578	0.0913	1.8642	0.0000
	194	4	1475	34	1428	35	3.22	3.1571	3.2821	0.2479	2.7556	0.0924	1.7830	0.0000
	191	4	1445	54	1361	35	5.80	2.9479	4.0332	0.2351	2.8472	0.0909	2.8566	0.0000
	129	4	1466	19	1434	30	2.23	3.1574	2.5387	0.2491	2.3233	0.0919	1.0235	0.0000
	140	4	1414	24	1446	31	-2.27	3.1035	2.7353	0.2516	2.4240	0.0895	1.2672	0.0000
	166	4	1459	24	1413	30	3.14	3.0951	2.6894	0.2451	2.3632	0.0916	1.2838	0.0000
	141	4	1469	23	1444	31	1.65	3.1880	2.7063	0.2511	2.4146	0.0921	1.2222	0.0000
	157	5	1040	29	1011	20	2.77	1.7312	2.5353	0.1698	2.0894	0.0739	1.4360	0.0000
	133	5	1011	54	987	20	2.37	1.6632	3.4566	0.1655	2.1880	0.0729	2.6759	0.0000
	126	5	982	23	979	23	0.30	1.6240	2.7819	0.1639	2.5427	0.0718	1.1285	0.0000
	137	5	1012	41	1017	23	-0.55	1.7191	3.1591	0.1710	2.4239	0.0729	2.0259	0.0000
	138	5	1061	51	1005	22	5.21	1.7388	3.4923	0.1688	2.3854	0.0747	2.5506	0.0000
	151	5	1002	31	1014	25	-1.19	1.7046	3.1202	0.1703	2.7132	0.0726	1.5409	0.0000
	152	5	1004	45	1000	28	0.41	1.6817	3.7213	0.1679	2.9980	0.0727	2.2044	0.0000
	155	5	1016	41	998	23	1.78	1.6877	3.2060	0.1675	2.4865	0.0731	2.0238	0.0000
	156	5	1022	40	998	20	2.32	1.6925	2.9565	0.1675	2.2015	0.0733	1.9734	0.0000
	135	5	1016	27	994	23	2.15	1.6792	2.8446	0.1667	2.5136	0.0731	1.3318	0.0000
	183	5	1007	29	1006	22	0.13	1.6940	2.7769	0.1689	2.3952	0.0728	1.4051	0.0000
	184	5	1007	22	1002	21	0.47	1.6870	2.5181	0.1682	2.2674	0.0727	1.0953	0.0000
	188	5	1014	27	993	19	2.07	1.6775	2.4298	0.1666	2.0204	0.0730	1.3498	0.0000
	144	5	983	28	1035	14	-5.30	1.7276	1.9967	0.1742	1.4682	0.0719	1.3533	0.0000
	125	5	1014	29	1065	20	-5.01	1.8077	2.4896	0.1796	2.0519	0.0730	1.4098	0.0000
	162	5	988	22	1030	20	-4.31	1.7217	2.3224	0.1733	2.0562	0.0721	1.0795	0.0000
	150	5	1026	19	1102	32	-7.40	1.8888	3.3048	0.1865	3.1645	0.0735	0.9526	0.0000

Table D.7.(cont'd). Summary of geochronology analyses for sample CL6135.

Sample Number	Spot Number	Trace element concentrations (ppm)																												
		P	Ti	Y	Zr	Nb	La	Ce	Pr	Nd	Sm	Eu	Gd	Tb	Dy	Ho	Er	Tm	Yb	Lu	Hf	Ta	Th	U	Ce/Ce*	Eu/Eu*	∑REE	(Gd/Yb)cn	Lu/Hf	Nb/Ta	Th/U
CL6135	160	386.5945	5.4931	1024.6305	414362.6718	3.5479		42.9683	0.0511	1.7189	4.2365	0.8620	18.9825	7.5938	105.8443	40.4350	162.5425	45.6037	521.3067	51.9884	7343.4284	1.3658	27.9742	50.8544	824.5313	0.2939	1004.1338	0.0301	0.0071	2.5977	0.5501
	142	242.9729	2.2950	1119.2093	435720.4769	1.9906		20.2135	0.1299	2.8440	8.1485	1.4161	25.0762	9.9284	121.3791	44.0152	188.5195	49.4014	564.1139	57.7357	7546.8987	0.6614	36.8353	59.5561	152.6565	0.3029	1092.9212	0.0368	0.0077	3.0097	0.6185
	146	270.3862	10.3040	517.4734	423463.5261	0.6722		11.9941	0.0418	0.8206	2.0239	0.9538	9.3521	3.7189	49.4563	18.2843	85.1031	25.3215	305.3822	35.6886	7666.2521	0.3463	22.3547	35.7194	281.5733	0.6702	548.1411	0.0253	0.0047	1.9410	0.6258
	154	262.6726	2.5611	1105.4905	444175.8539	3.1024		24.0562	0.1258	3.3973	5.5483	0.9734	24.4480	9.7432	115.8728	41.1450	187.2160	51.5279	591.4986	64.4192	8045.8839	0.7991	44.4753	82.2984	187.5278	0.2555	1119.9716	0.0342	0.0080	3.8822	0.5404
	158	241.0960	3.3332	1667.1965	421346.6025	1.7927		25.8368	0.2197	6.6892	12.1880	2.1611	44.2786	15.4129	192.1449	65.6638	266.8813	71.0850	760.2346	78.1899	7191.8630	0.4901	67.1640	89.8455	115.3421	0.2844	1540.9858	0.0482	0.0109	3.6580	0.7475
	170	228.2256	2.4037	1341.4249	398669.8209	1.4858		25.1260	0.0981	3.6042	8.3683	1.5602	34.5888	12.9067	155.5871	54.2518	222.1381	60.1913	646.2859	65.7308	7041.2959	0.5055	53.0182	78.0730	251.2050	0.2804	1290.4374	0.0443	0.0093	2.9393	0.6791
	185	248.7343	6.5712	724.3974	456171.0945	1.5139		17.9560	0.1325	3.0306	3.7598	0.9668	16.2734	6.7140	76.6109	27.6114	118.6073	30.5011	348.0159	36.1714	7440.5508	0.3815	20.8145	30.1933	132.8801	0.3779	686.3513	0.0387	0.0049	3.9686	0.6894
	193	220.6888	3.5119	847.7282	496957.5049	1.7646		24.7876	0.0737	1.4202	5.0213	1.5235	18.4743	6.9595	83.3173	29.8123	135.0091	36.8992	396.5491	48.0425	8666.6463	0.6105	26.8439	37.2561	329.6393	0.4836	787.8895	0.0385	0.0055	2.8903	0.7205
	131	211.6471	2.9364	580.5168	437662.3589	0.9066		16.5830	0.0958	1.2296	4.3476	0.4780	13.6115	5.2116	60.3983	21.8782	96.1507	26.6410	305.1232	32.6819	7432.8858	0.3936	17.3983	28.6455	169.8027	0.1900	584.4306	0.0369	0.0044	2.3034	0.6074
	195	252.4242	3.5847	1062.8443	517725.9374	5.6782		50.4746	0.0191	1.0914	2.6311	0.6348	15.7274	7.3883	100.6492	38.8154	175.1206	46.3539	488.5037	59.8225	10190.6033	1.8651	44.0798	59.4336	2596.9911	0.3017	987.2320	0.0266	0.0059	3.0444	0.7417
	197	364.5651	4.6094	1732.7149	531666.1009	6.3763		81.2551	0.0824	3.1561	8.5793	1.5616	34.9049	12.6665	166.6094	60.9295	265.5445	68.5608	680.1261	84.1378	10023.4852	2.0936	93.1624	86.7883	967.6597	0.2759	1468.1140	0.0425	0.0084	3.0456	1.0734
	136	252.1122	9.6323	545.5811	470304.3973	0.2787		9.3093	0.0486	1.7986	3.0311	1.3518	11.0546	4.2454	53.4303	20.0737	91.3293	25.9945	302.9589	35.2086	8158.5838	0.2206	14.7471	21.0718	187.6903	0.7139	559.8346	0.0302	0.0043	1.2635	0.6998
	130	355.2546	4.6482	1204.5827	438183.3953	5.3929		72.3345	0.1404	1.7902	5.7572	1.3685	23.9327	9.7980	128.0687	44.4405	193.1704	52.1317	579.4528	58.5565	7595.1395	1.4400	68.5799	79.3471	505.1966	0.3564	1170.9422	0.0342	0.0077	3.7451	0.8643
	169	205.8665	7.1398	824.6403	407322.3926	5.0190		43.1963	0.0345	1.2164	2.8195	0.4429	12.9496	6.0400	79.1401	30.0619	139.8110	43.1962	531.9002	57.5218	9101.7810	1.6783	119.1473	208.4480	1229.6162	0.2241	948.3304	0.0201	0.0063	2.9905	0.5716
	171	195.6863	6.2718	676.7032	396185.4569	12.4370		33.3723	0.0369	0.5110	1.3898	0.2865	6.3286	3.9570	56.0664	22.2032	113.4553	37.5466	513.1740	54.4244	9913.9442	6.1197	132.4920	419.4647	888.0907	0.2954	842.7520	0.0102	0.0055	2.0323	0.3159
	132	226.8651	6.2117	679.4978	430824.7966	3.7509	0.1937	35.9158	0.0812	1.1732	2.1698	0.3890	11.0956	4.2313	63.6497	23.6796	114.6061	33.4603	456.0961	48.2428	9533.6071	1.4839	81.1547	142.7567	70.2000	0.2424	794.9842	0.0201	0.0051	2.5277	0.5685
	145	227.7901	5.0561	1052.7944	433484.3268	3.2279		37.1965	0.1279	2.2736	5.8594	0.4735	24.4309	8.5102	110.3998	39.5196	172.8265	47.5133	526.8034	56.4598	8427.0345	0.9687	80.9257	120.9473	285.2188	0.1210	1032.3944	0.0384	0.0067	3.3323	0.6691
	159	212.8926	6.1313	664.2123	403551.0181	8.0517	0.2821	31.5194	0.2347	2.2336	2.7117	0.2596	9.0581	3.8311	53.8639	21.8061	108.8374	36.9859	478.2249	50.2032	10764.9001	4.1773	111.3309	332.1372	30.0382	0.1602	800.0517	0.0157	0.0047	1.9275	0.3352
	172	217.7354	4.4338	814.0148	418332.1492	5.1023		48.9529	0.0701	2.2168	4.7154	0.7507	15.9356	5.9761	76.9414	30.4213	136.2792	37.5904	472.8469	48.5527	8514.4496	1.3499	95.9818	157.5254	685.0887	0.2648	881.2495	0.0279	0.0057	3.7797	0.6093
	123	204.0650	6.1845	567.9649	445192.7405	3.3741		32.2465	0.0074	0.5697	2.2724	0.3037	9.2023	3.5486	52.5595	20.7219	99.4069	28.5404	353.0050	39.4488	9768.4134	1.2199	54.4143	103.3605	4276.2842	0.2031	641.8330	0.0216	0.0040	2.7659	0.5265
	196	146.6854	3.7862	252.8844	518895.5431	1.2564		11.9562		0.1488	0.1169	0.0826	2.5581	1.1412	19.0452	8.6431	44.6194	14.0789	189.4358	28.5548	14296.6753	0.6716	55.8146	189.3131		0.4620	320.3811	0.0112	0.0020	1.8707	0.2948
	134	265.7065	5.5904	766.0696	448661.7664	3.6343		37.0980	0.0395	0.7808	2.7140	0.4337	13.7846	5.1474	73.7561	27.6991	132.8013	38.9732	484.5157	54.2801	9527.4581	1.6019	80.5753	129.8842	920.2983	0.2168	872.0236	0.0235	0.0057	2.2688	0.6204
	181	204.7857	4.1848	686.3500	429159.5175	4.5959		31.0319	0.0259	0.6940	1.6359	0.2226	8.7401	4.0452	57.9642	24.4921	118.9200	36.9197	452.5239	50.1056	9873.6496	2.4242	70.4249	142.1998	1172.8825	0.1800	787.3211	0.0160	0.0051	1.8959	0.4953
	182	241.2754	7.4624	834.6091	426836.7541	3.8452		42.7224	0.0271	1.4452	3.6588	0.5410	12.7786	5.5974	77.8136	28.0840	134.9365	39.4649	483.7261	54.0414	9161.6840	1.5668	108.1573	158.8697	1546.0911	0.2419	884.8371	0.0219	0.0059	2.4541	0.6808
	161	169.3603	4.6084	453.8165	414517.5851	6.7543		25.5471		0.3209	1.0488	0.0322	4.9651	2.1068	39.4756	15.8482	79.1876	26.1018	336.0048	37.4476	10137.9262	2.9529	66.1860	190.2681		0.0431	568.0865	0.0122	0.0037	2.2873	0.3479
	192	298.1839	7.1448	1343.2298	494657.7546	8.0541		64.0391	0.0500	2.0979	5.1171	0.7822	22.6435	9.5295	127.1618	48.1407	220.2792	58.4101	642.4277	74.1229	10622.2342	2.2807	120.0231	144.3269	1257.2871	0.2222	1274.8017	0.0292	0.0070	3.5314	0.8316
	124	146.1860	3.7899	265.0616	428797.9985	3.4091		10.8028			0.1983	0.0544	2.1453	1.0344	17.2423	8.7218	46.9998	16.2951	229.8803	28.7550	11141.8230	1.6070	28.9426	229.1659		0.2548	362.1295	0.0077	0.0026	2.1215	0.1263
	186	148.1014	3.1422	358.3482	442262.6966	2.9014		19.5747	0.0267	0.1582	0.7170	0.1549	4.9186	1.7549	29.9697	12.6499	66.8108	20.2914	269.0457	32.7289	10836.4467	1.2238	40.0987	98.3943	720.2010	0.2521	458.8013	0.0151	0.0030	2.3708	0.4075
	189	189.0863	7.1037	586.3368	459227.4043	5.2948	0.0502	24.8739	0.0421	0.9018	1.1650	0.2254	6.7262	3.1425	45.6150	19.3889	100.7778	33.3192	431.5120	52.2551	11878.1030	2.8465	80.9235	203.5684	132.6114	0.2461	719.9951	0.0129	0.0044	1.8601	0.3975
	153	144.3064	5.1575	430.8494	426958.0995	4.4190		20.7002		0.2697	1.1124		4.3563	2.5395	37.4318	15.3786	78.6031	24.6747	325.0283	37.0262	11666.2487	2.2831	64.5155	201.9640		0.0000	547.1208	0.0111	0.0032	1.9355	0.3194
	165	153.2649	3.6014	361.2622	392081.5008	2.9952		20.0736		0.1724	0.3757	0.1418	4.0389	1.6371	30.2964	12.3464	65.7709	21.7080	277.3643	31.5562	9235.9423	1.7787	34.6055	96.0969		0.3521	465.4818	0.0120	0.0034	1.6840	0.3601
	187	122.3946	3.8903	170.5640	452188.6193	1.4160		14.1812			0.1869	0.0565	1.0373	0.9253	11.1691	5.3050	32.0840	10.7333	171.5012	27.3647	11860.7076	0.4377	55.3152	175.5642		0.3920	274.5445	0.0050	0.0023	3.2351	0.3151
	163	94.9621	5.3327	194.8291	414063.8035	1.9973	1.8206	14.9243	0.9607	4.9335	2.0483	0.2958	2.8152	1.0182	13.7851	6.1428	32.7721	12.0092	179.6093	24.0957	10515.2030	0.5792	37.3938	136.4629	2.7668	0.3766	297.2308	0.0130	0.0023	3.4483	0.2740
	190	137.0125	3.8986	443.8295	474994.2004	3.9537		11.1991	0.0081	0.2595	0.8834	0.4755	7.1470	3.0823	40.7039	16.1199	71.6679	20.9129	245.7814	29.2970	9931.5388	1.4627	12.9782	166.0107	1358.6949	0.5786	447.5378	0.0241	0.0029	2.7030	0.0782
	139	173.7399	4.1645	531.1497	434505.0269	5.5686	0.7328	14.2154	0.6213	4.4159	5.4967	1.1867	10.3282	4.2045	52.3687	17.8230	88.9118	28.1864	370.1725	46.0783	10866.7157	5.5513	38.8077	381.1027	5.1652	0.4815	644.7420	0.0231	0.0042	1.0031	0.1018
	174	219.4923	4.6261	626.9893	407053.5476	8.4091		36.4484		0.2123	1.2633	0.1954	7.2501	3.6075	54.6453	21.8123	110.4519	36.3557	462.1153	52.5885	9605.3248	4.8209	119.8039	507.8402		0.1973	786.9461	0.0130	0.0055	1.7443	0.2359
	148	209.2696	4.4304	586.5634	407257.5258	7.1482		35.8341	0.0067	0.4005	2.4769	0.3803	9.3019	3.7717	48.4165	19.0568	98.8975	33.1570	469.0392	55.2397	8973.5572	4.9670	173.2853	600.1010	5271.6570	0.2422	775.9788	0.0164	0.0062	1.4391	0.2888
	149	172.4238	5.2075	575.2287	407829.5419	6.8471		33.3439	0.0447	0.4256	1.5048	0.3235	5.8618	3.2964	45.2685	19.0907	96.5883	33.7744	490.0884	60.7436	9129.0572	4.4062	146.3295	479.1730	731.7108	0.3350	790.3340	0.0099	0.0067	1.5940	0.3054
	173	234.5525	3.8609	665.4346	402475.1204	9.2216		38.4857	0.0243	0.5946	1.3378	0.2021	9.2547	4.2309	60.4682	23.1779	115.9441	39.1932	503.7934	55.8647	9828.8239	4.8922	129.8918	602.4940	1553.9357	0.1756	852.5715	0.0152	0.0057	1.8850	0.2156
	175	213.2023	4.9684	635.5969	420239.7475	6.6930		43.1003		0.3146	2.0825	0.3348	8.2905	4.1145	56.6060	22.7556	110.8011	34.3898	436.7578	50.0688	9076.1099	3.1295	92.0490	285.0170		0.2464	769.6162	0.0157	0.0055	2.1387	0.3230
	176	215.8798	3.9559	628.8034	413690.5908	5.7016		36.3485		0.7378	2.0671	0.2892	7.4792	3.8787	56.7848	22.4016	114.8682	34.0570	467.4189	51.6781	8506.1616	2.5863	61.2037	215.1367		0.2249	798.0090	0.0132	0.0061	2.2045	0.2845
	177	197.5071	5.1854	643.8645	418227.5118	7.8271		45.1998	0.0787	0.8639	1.3999	0.3032	7.7378	3.9379	59.6712	22.0532	109.9923	35.0383	459.1033	49.6952	10075.0782	4.6641	151.5922	372.8248	563.0549	0.2816	795.0748	0.0139	0.0049	1.6782	0.4066
	178	211.8491	4.7156	748.3284	410492.7038	7.6234		45.0572	0.0329	0.6333	1.7028	0.3353	9.4628	4.0011	62.8042	25.1689	125.5198	41.0347	528.6838	57.6063	9066.3108	3.9235	134.6148	329.6216	1343.6466	0.2554	902.0431	0.0148	0.0064	1.9430	0.4084
	179	218.1606	4.7926	687.5258	397952.4987	7.6750	0.0445	45.1130	0.0336	0.4667	1.5255	0.3510	8.0021	4.0221	59.7033	23.7679	116.2989	35.9109	477.0356	52.9651	9774.1179	4.5242	137.1028	429.3254	286.1470	0.3071	825.2400	0.0139	0.0054	1.6964	0.3193
	180	136.7976	4.3316	366.9584	416011.2073	4.2985		27.9322		0.2169	0.5750	0.1409	3.8717	2.2053	30.7882	13.3649	68.4033	21.2419	290.5164	33.8659	9962.1578	2.7614	61.2032	207.0119		0.2887	493.1226	0.0110	0.0034	1.5566	0.2957
	194	322.4843	4.3630	1167.2414	512731.7311	9.6340		44.4047	0.0336	1.2653	2.5083	0.4303	17.7414	7.4870	106.1470	40.7695	201.8775	58.6800	711.8053	91.5791	11112.3825	4.9778	112.4290	226.6515	1294.5590	0.1972	1284.7291	0.0206	0.0082	1.9354	0.4960
	191	90.3518	3.0493	254.5775	487988.2358	2.1209		2.5817			0.2429	0.0446	1.0758	0.6775	16.7431	8.1867	46.6631	15.4991	233.3567	34.5624	12491.0895	0.9541	4.7110	105.0652		0.2670	359.6338	0.0038	0.0028	2.2229	0.0448
	129	137.9927	3.7471	425.2754	414359.2028	5.7718	0.1163	12.8807	0.0791	0.4656	1.1513	0.2177	5.8485	2.0051	32.8198	14.4116	74.0919	24.7212	332.3825	38.4697	9660.4436	3.4080	32.1739	672.4501	32.9155	0.2565	539.6611	0.0146	0.0040	1.6936	0.0478
	140	82.0844	2.7368	298.9468	416722.3661	2.6787		0.7301				0.1970	1.1181	0.7205	14.5996	8.3616	60.2620	25.8639	445.0113	72.8677	11409.0984	0.9486	2.2829	440.2318			629.7319		0.0064	2.8239	0.0052
	166	103.6274	3.2596	351.9853	400166.3853	3.5281	0.0157	1.4496				0.1552	1.5595	1.1519	21.6034	11.0167	61.8297	23.2980	344.3193	48.3876	10104.1459	1.4286	2.7792	712.9800			514.7867		0.0048	2.4696	0.0039
	141	108.1807	3.0701	364.5361	421298.2089	4.1856		1.2504				0.1303	1.1726	0.9272	16.8611	10.8196	71.4814	27.9470	447.1316	71.4912	11788.7619	2.7191	5.1692	654.5794			649.2125		0.0061	1.5393	0.0079
	157	323.6625	3.9470	1162.9097	433636.9088	15.5368		23.2168	0.0234	0.2006	2.2162	0.3130	13.7968	6.6870	100.5326	43.3943	200.7860	64.0807	792.1880	87.7767	12420.7703	11.6614	108.3249	456.2855	971.5673	0.1730	1335.2120	0.0144	0.0071	1.3323	0.2374
	133	259.5910	3.1946	659.5560	445570.6706	8.5741		14.7961	0.0242	1.1635	1.5229	0.1435	6.4274	3.7272	53.3992	21.9173	122.6126	40.2758	543.9297	60.9758	14083.4222	10.5404	79.4410	213.5973	600.7367	0.1403	870.9151	0.0098	0.0043	0.8135	0.3719
	126	243.9112	2.8291	526.6547	424475.1842	8.7922	0.0136	8.7421	0.0446	0.3820	0.8117	0.2122	5.4698	2.6414	38.1729	18.6162	94.9152	31.0019	432.6316	50.9550	11978.6017	8.2627	58.1254	447.1362	86.8424	0.3078	684.6064	0.0105	0.0043	1.0641	0.1300
	137	280.6110	3.8520	1111.4398	436902.6430	9.7144		21.1212	0.0427	0.7116	1.6982	0.4313	13.6321	5.8500	98.9984	39.8142	197.5202	60.5070	723.4821	80.6607	10957.7370	5.6277	66.0280	223.1071	485.1323	0.2740	1244.4697	0.0156	0.0074	1.7262	0.2959
	138	280.6053	3.9026	1054.2998	427719.9366	8.3962		20.7303		0.3976	2.2939	0.3823	13.9852	6.9447	99.0863	37.5590	190.0416	56.5822	682.5130	77.3672	10311.1588	4.5524	47.8632	166.6988		0.2064	1187.8832	0.0170	0.0075	1.8443	0.2871
	151	295.3145	3.7572	919.1726	414071.2965	12.2950		18.0873		0.1801	1.3267	0.2501	8.1757	4.8639	71.5959	30.7171	166.7947	56.7929	732.3383	86.1554	10545.7246	6.1820	50.5905	315.4030		0.2321	1177.2781	0.0092	0.0082	1.9888	0.1604
	152	237.2869	3.5932	815.1656	424183.8477	12.0928		16.1435		0.1316	1.2603	0.2336	8.9277	4.0816	66.2602	25.9761	142.6170	47.6394	659.9447	77.1050	11257.0745	9.2970	53.1708	387.3689		0.2129	1050.3206	0.0112	0.0068	1.3007	0.1373
	155	357.5766	3.8255	1149.2834	432754.2116	15.0003		21.3177		0.5486	1.9984	0.2846	11.2524	5.9604	94.0604	38.9558	204.8453	61.7324	807.5468	92.1880	12156.7012	11.3453	85.0125	377.6248		0.1835	1340.6908	0.0115	0.0076	1.3222	0.2251
	156	337.5889	3.5218	1140.5169	429239.5973	15.7915		21.1500		0.3765	2.8308	0.2614	11.6661	6.7818	99.0913	38.9622	196.2031	61.3743	768.3207	86.0680	11627.8349	10.0358	101.7459	465.4087		0.1391	1293.0862	0.0126	0.0074	1.5735	0.2186
	135	295.9527	3.2419	1134.7344	463468.1754	12.4713		23.1852	0.0129	0.2895	2.4332	0.1952	10.9705	6.2654	97.4013	39.1542	198.0632	62.8967	779.5869	93.9531	14779.5828	12.5749	140.9328	337.4883	1764.6462	0.1155	1314.4072	0.0116	0.0064	0.9918	0.4176
	183	215.0326	1.9511	768.8288	425272.8527	12.7515		11.1834		0.1019	1.0985	0.2725	5.9772	3.6004	61.9168	25.7905	138.7198	47.4406	667.7329	80.0001	12616.2346	13.2827	104.2850	821.3447		0.3251	1043.8346	0.0074	0.0063	0.9600	0.1270
	184	240.3820	2.4082	841.1168	431608.2378	13.8801		12.6508		0.1640	1.1768	0.2919	10.0031	3.7680	66.7202	26.8061	146.8158	48.1817	651.3076	85.3516	12171.1559	12.1590	134.0633	976.8929		0.2601	1053.2377	0.0127	0.0070	1.1415	0.1372
	188	318.5134	2.9562	1066.5648	453497.6697	16.6672		15.9024		0.1958	2.0557	0.4214	10.1189	6.0048	87.0877	38.2020	187.7556	62.5886	813.2389	98.0806	13086.5991	15.0271	118.7324	862.8144		0.2825	1321.6524	0.0103	0.0075	1.1091	0.1376
	144	230.1389	2.1040	741.9466	425120.9397	11.8711		11.5398			0.6341	0.2615	7.2682	3.8675	59.7152	25.2373	135.4700	43.2090	598.5432	71.0776	12439.4632	11.6343	110.1296	775.4524		0.3723	956.8235	0.0100	0.0057	1.0204	0.1420
	125	260.3759	2.7050	622.6494	410331.8000	11.7867		9.8061		0.5364	0.4965	0.2302	5.9007	3.0955	50.7047	20.9793	109.6100	34.7754	487.2608	59.9647	11726.6253	10.2859	78.1458	578.4909		0.4111	783.3603	0.0100	0.0051	1.1459	0.1351
	162	227.5073	3.2677	551.3305	405976.8598	9.1498	1.3512	15.5947	1.3880	9.2528	6.8084	0.9371	14.3530	4.4890	53.3303	19.5667	93.0647	31.2190	440.5422	49.5818	11681.4458	9.4403	55.5303	559.1768	2.7919	0.2898	741.4789	0.0270	0.0042	0.9692	0.0993
	150	446.0378	3.6541	1889.4540	396042.7237	26.2693		17.0695		0.3062	2.9040	0.4966	16.6239	9.8146	142.4400	64.3149	331.7473	########	1470.5032	184.1749	17281.3643	38.3651	345.8485	3449.7400		0.2185	2352.4999	0.0094	0.0107	0.6847	0.1003

Analytical session: 6
Isotope ratio and date errors do not include systematic calibration errors of 0.42% ($^{207}Pb/^{206}Pb$) and 0.60% ($^{206}Pb/^{238}U$) (2 sigma).
Trace element concentrations in ppm, calculated using mean count rate method.
Sweep-by-sweep downhole fractionation of U/Pb ratios NOT corrected via Si/Zr fractionation factor.
Backgrounds were monitored between sweeps 5 to 20. Sample counts were integrated from sweeps 35 to 60.
Trace element concentrations from analyses with U<27 ppm and known to have intersected inclusions of other minerals based on P and Ti were not included.
Ablation used a laser spot size of 25 microns, and a laser firing repetition rate of 10 Hz.

Table D.8. Comparison of $^{207}Pb/^{206}Pb$ vs $^{206}Pb/^{238}U$ weighted mean ages and individual dates for each population in the zircons from the various samples.

Sample	Zircon age population	207Pb/206Pb	206Pb/238U
CL6070	1	2703 ± 64 Ma	NA
	1	2691 ± 41 Ma	NA
	1	2566 ± 37 Ma	NA
	2	1017 ± (16) 27 Ma (MSWD = 1.85, PF = 0.086, n = 7/7)	997 ± 27 (MSWD = 2.6, PF = 0.015, n=7/7)
	3	1005 ± (14) 19 Ma (MSWD = 1.40, PF = 0.20, n= 9/9)	994 ± 17 (MSWD = 0.95, PF = 0.28, n= 9/9)
	Combined 2&3	1010 ± (10) 14 (MSWD = 1.6, PF = 0.08, n= 16/16)	996 ± 17 (MSWD = 1.6, PF = 0.076, n= 16/16)
CL6098	1	1428 ± (7) 14 Ma (MSWD = 2.4, PF = 0.01, n = 18/19)	1353 ± 26 Ma (MSWD = 16, PF = 0, n = 19/19)
	2	1020 ± (6) 13 Ma (MSWD = 3.40, PF = 0, n = 20/21)	980 ± 6 Ma (MSWD = 0.98, PF = 0.48, n = 20/21)
	3	1001 ± (6) 10 Ma (MSWD = 1.35, PF = 0.02, n= 8/8)	1027 ± 9 Ma (MSWD = 1.3, PF = 0.25, n = 8/8)
CL6106	1	2617 ± 39 Ma	NA
	2	1044 ± 106 Ma	956 ± 37 Ma
	3	none	none
	4	1000 ± (21) 27 Ma (MSWD = 1.30, PF = 0.23, n = 12/12)	986 ± 23 Ma (MSWD = 1.7, PF = 0.074, n = 12/12)
	5	1003 ± (14) 21 Ma (MSWD = 1.8, PF = 0.036, n = 15/15)	995 ± 18 Ma (MSWD = 0.81, PF = 0.66, n = 15/15)
	Combined 4&5	1002 ± (11) 16 Ma (MSWD = 1.5 , PF = 0.05, n = 27/27)	991 ± 17 Ma (MSWD = 1.19, PF = 0.23, n = 27/27)
CL6112	1	1587 ± 54 Ma	NA
	2	1438 ± 23 Ma	1456 ± 35 Ma
	2	1436 ± 23 Ma	1425 ± 26 Ma
	2	1264 ± 29 Ma	1208 ± 20 Ma
	3	979 ± (6) 11 Ma (MSWD = 1.52, PF = 0.05, n = 24/25)	966 ± 7 Ma (MSWD = 1.5, PF = 0.055, n = 25/25)
	4	968 ± (4) 10 Ma (MSWD = 1.31, PF = 0.17, n= 18/20)	1005 ± 7 Ma (MSWD = 1.08, PF = 0.36, n= 20/20)
CL6127	1 (core)	2467 ± 51 Ma	NA
	1 (rim)	977 ± 65 Ma	1023 ± 34 Ma
	2	989 ± 36 Ma	1011 ± 42 Ma
	2	1015 ± 24 Ma	994 ± 45 Ma
	3	1000 ± (25) 26 Ma (MSWD = 0.13, PF = 0.94, n= 4/4)	1000 ± 23 Ma (MSWD = 0.45, PF = 0.72, n = 4/4)
	4	1013 ± (11) 13 Ma (MSWD = 0.93, PF = 0.51, n = 13/14)	996 ± 25 Ma (MSWD = 2 .6, PF = 0.001 n= 14/14)
	5	1011 ± (10) 16 Ma (MSWD = 1.75, PF = 0.045, n = 14/15)	1003 ± 18 Ma (MSWD = 1.11, PF = 0.34, n = 15/15)
	Combined 3,4,5	1011 ± 10 Ma (MSWD = 1.15, PF = 0.26, n = 32/34)	1002 ± 17 Ma (MSWD = 1.37, PF = 0.077, n = 33/34)
CL6135	1	1648 ± (14) 24 Ma (MSWD = 2.2, PF = 0.01, n = 13/13:	NA
	2	1665 ± (9) 18 Ma (MSWD = 4, PF = 0, n = 13/14)	NA
	3	1673 ± (12) 29 Ma (MSWD = 2.7, PF = 0.030; n =5/6)	NA
	4	1445 ± (7) 10 Ma (MSWD = 2.06, PF = 0.01, n = 16/16)	1438 ± 11 Ma (MSWD = 1.2, PF = 0.27, n = 16/16)
	4	1157 ± 68 Ma	1152 ± 47 Ma
	5	1008 ± (7) 10 Ma (MSWD = 1.64, PF = 0.52; n=17/17)	1000 ± 8 Ma (MSWD = 0.94, PF = 0.50, n = 13/17)
CL6144	1	1019 ± (8) 13 Ma (MSWD = 1.81, PF = 0.01, n= 27/28)	1019 ± 19 Ma (MSWD = 0.84, PF = 0.70, n= 28/28)
	2	1015 ± (7) 10 Ma (MSWD = 1.15, PF = 0.25, n = 40/43)	1013 ± 18 Ma (MSWD = 1.18, PF = 0.20, n = 42/43)
	Combined 1&2	1016 ± (5) 9 Ma (MSWD = 1.4, PF = 0.018, n= 67/71)	1016 ± 18 Ma (MSWD = 0.92, PF = 0.67, n = 70/71)
CL8025	1	1047 ± (12) 14 Ma (MSWD = 0.08, PF = 0.995, n=6/6)	991 ± 21 Ma (MSWD 2.3, PF = 0.04, n= 6/6)
	2	1037 ± (8) 13 Ma (MSWD = 1.5, PF = 0.08, n = 17/18)	988 ± 8 Ma (MSWD = 1.7, PF = 0.05, n = 17/18)
	Combined 1&2	1041 ± (7) 10 Ma (MSWD 1.2, PF = 0.23, n = 23/24)	989 ± 8 Ma (MSWD 1.8, PF = 0.16, n = 23/24)
	3	1040 ± (12) 14 Ma (MSWD = 0.97, PF = 0.47, n = 13/13)	989 ± 10 Ma (MSWD 1.3, PF = 0.22, n = 12/13)

Table D.9. Ti-in-zircon temperatures (°C) calculated for each population over a range of pressures using the geothermometer of Hofmann *et al.* (2014). The aSiO2 = 1 and the aTiO2 = 0.5 following Schiller and Finger (2019). Results reported in the text are 3rd quartile estimates following recommendations of Tomkins *et al.* (2007).

Sample Number	Zircon Type	Quartile range	Ti (ppm)	Pressures (bar)								
				2500	3500	4500	5500	6500	7500	8500	9500	10000
CL6070	1	min	3.0004	672	683	695	707	718	730	742	754	759
		1st quartile	3.3913	681	693	705	717	728	740	752	764	770
		median	3.7822	690	702	713	725	737	749	761	773	779
		3rd quartile	**5.7843**	**724**	**736**	**749**	**761**	**773**	**786**	**798**	**810**	**817**
		max	7.7863	750	762	775	788	800	813	826	838	845
	2	min	0.2880	523	532	542	552	562	572	582	591	596
		1st quartile	0.7912	581	591	602	612	623	633	644	655	660
		median	0.9228	590	601	612	622	633	644	654	665	670
		3rd quartile	**1.7679**	**633**	**645**	**656**	**667**	**678**	**689**	**701**	**712**	**717**
		max	4.6427	706	718	730	742	754	766	779	791	797
	3	min	0.6368	568	578	588	599	609	619	630	640	645
		1st quartile	0.8869	588	598	609	620	630	641	652	662	668
		median	1.2521	610	621	632	643	654	665	676	686	692
		3rd quartile	**1.5906**	**626**	**637**	**648**	**659**	**671**	**682**	**693**	**704**	**709**
		max	2.0536	644	655	667	678	689	701	712	723	729

Table D.9. (cont'd)

Sample Number	Zircon Type	Quartile range	Ti (ppm)	Pressures (bar)								
				2500	3500	4500	5500	6500	7500	8500	9500	10000
CL6098	1	min	2.7580	665	677	689	700	712	723	735	747	752
		1st quartile	3.8109	690	702	714	726	738	750	762	774	780
		median	4.4817	703	715	727	739	751	763	776	788	794
		3rd quartile	**5.4745**	**720**	**732**	**744**	**756**	**769**	**781**	**793**	**805**	**812**
		max	12.4493	793	806	820	833	846	859	872	885	892
	2	min	1.2187	608	619	630	641	652	663	674	685	690
		1st quartile	1.7023	631	642	653	664	675	687	698	709	715
		median	1.9030	639	650	661	672	684	695	706	717	723
		3rd quartile	**2.0466**	**644**	**655**	**666**	**678**	**689**	**700**	**712**	**723**	**729**
		max	3.3804	681	693	704	716	728	740	752	763	769
	3	min	1.2702	611	622	633	644	655	666	677	687	693
		1st quartile	1.5177	623	634	645	656	667	678	689	700	706
		median	2.0513	644	655	667	678	689	701	712	723	729
		3rd quartile	**3.2369**	**678**	**689**	**701**	**713**	**725**	**736**	**748**	**760**	**766**
		max	3.6916	688	700	711	723	735	747	759	771	777

Table D.9. (cont'd)

Sample Number	Zircon Type	Quartile range	Ti (ppm)	Pressures (bar)								
				2500	3500	4500	5500	6500	7500	8500	9500	10000
CL6106	1	min	2.4608	657	669	680	692	703	715	726	738	743
		1st quartile	2.4608	657	669	680	692	703	715	726	738	743
		median	2.4608	657	669	680	692	703	715	726	738	743
		3rd quartile	**2.4608**	**657**	**669**	**680**	**692**	**703**	**715**	**726**	**738**	**743**
		max	2.4608	657	669	680	692	703	715	726	738	743
	2	single zone	0.6357	567	578	588	599	609	619	630	640	645
	4	min	0.5521	559	569	580	590	600	611	621	631	636
		1st quartile	1.1534	605	615	626	637	648	659	670	681	686
		median	1.6321	628	639	650	661	672	684	695	706	711
		3rd quartile	**1.9265**	**639**	**651**	**662**	**673**	**685**	**696**	**707**	**718**	**724**
		max	2.6579	663	674	686	697	709	721	732	744	749
	5	min	1.1266	603	614	625	636	646	657	668	679	684
		1st quartile	1.4461	620	631	642	653	664	675	686	697	702
		median	1.9135	639	650	662	673	684	695	707	718	724
		3rd quartile	**2.0655**	**644**	**656**	**667**	**678**	**690**	**701**	**712**	**724**	**729**
		max	2.4254	656	667	679	690	702	713	725	736	742

Table D.9. (cont'd)

Sample Number	Zircon Type	Quartile range	Ti (ppm)	Pressures (bar)								
				2500	3500	4500	5500	6500	7500	8500	9500	10000
CL6112	1	single zone	8.4286	757	770	782	795	808	821	833	846	852
	2	min	4.1266	696	708	720	732	744	756	768	780	786
		1st quartile	4.2883	700	712	724	736	748	760	772	784	790
		median	4.4501	703	715	727	739	751	763	775	787	793
		3rd quartile	**5.2486**	**716**	**728**	**740**	**753**	**765**	**777**	**789**	**802**	**808**
		max	6.0471	728	740	753	765	777	790	802	815	821
	3	min	0.3219	529	539	548	558	568	578	588	598	603
		1st quartile	1.1692	606	616	627	638	649	660	671	682	687
		median	1.3997	617	628	639	650	661	672	684	695	700
		3rd quartile	**1.7194**	**631**	**643**	**654**	**665**	**676**	**687**	**699**	**710**	**715**
		max	3.0038	672	684	695	707	719	730	742	754	759
	4	min	0.4834	551	562	572	582	592	602	613	623	628
		1st quartile	0.6638	570	580	591	601	612	622	633	643	648
		median	0.8589	586	596	607	618	628	639	650	660	665
		3rd quartile	**0.9880**	**595**	**605**	**616**	**627**	**638**	**648**	**659**	**670**	**675**
		max	1.6974	631	642	653	664	675	686	698	709	714

Table D.9. (cont'd)

Sample Number	Zircon Type	Quartile range	Ti (ppm)	Pressures (bar)								
				2500	3500	4500	5500	6500	7500	8500	9500	10000
CL6127	1	single zone	2.2838	652	663	674	686	697	709	720	732	737
	2	min	3.5624	685	697	709	720	732	744	756	768	774
		1st quartile	3.6197	686	698	710	722	734	745	757	769	775
		median	3.6769	687	699	711	723	735	747	759	771	776
		3rd quartile	**3.7342**	**689**	**700**	**712**	**724**	**736**	**748**	**760**	**772**	**778**
		max	3.7914	690	702	714	726	737	749	761	773	779
	3	min	1.8660	637	648	660	671	682	693	705	716	722
		1st quartile	1.9370	640	651	662	674	685	696	708	719	724
		median	1.9811	641	653	664	675	687	698	709	721	726
		3rd quartile	**2.1620**	**648**	**659**	**670**	**682**	**693**	**705**	**716**	**727**	**733**
		max	2.6429	662	674	685	697	709	720	732	743	749
	4	min	1.4100	618	629	640	651	662	673	684	695	701
		1st quartile	1.8594	637	648	659	671	682	693	704	716	721
		median	2.0087	642	654	665	676	688	699	710	722	727
		3rd quartile	**2.2268**	**650**	**661**	**673**	**684**	**695**	**707**	**718**	**730**	**735**
		max	2.7189	664	676	688	699	711	722	734	746	751
	5	min	1.5366	624	635	646	657	668	679	690	701	707
		1st quartile	1.8557	637	648	659	671	682	693	704	716	721
		median	2.2590	651	662	674	685	696	708	719	731	736
		3rd quartile	**2.3813**	**655**	**666**	**678**	**689**	**700**	**712**	**723**	**735**	**741**
		max	3.3225	680	691	703	715	727	738	750	762	768

Table D.9. (cont'd)

Sample Number	Zircon Type	Quartile range	Ti (ppm)	Pressures (bar)								
				2500	3500	4500	5500	6500	7500	8500	9500	10000
CL6135	1	min	2.2950	652	663	675	686	698	709	721	732	738
		quart1	2.9364	670	682	693	705	717	728	740	752	758
		median	3.5847	685	697	709	721	733	745	757	768	774
		quart3	**5.4931**	**720**	**732**	**744**	**757**	**769**	**781**	**793**	**806**	**812**
		max	10.3040	775	788	801	814	827	840	853	866	872
	2	min	3.7862	690	702	713	725	737	749	761	773	779
		quart1	4.6084	705	717	730	742	754	766	778	790	796
		median	6.1313	729	741	754	766	779	791	803	816	822
		quart3	**6.2718**	**731**	**743**	**756**	**768**	**781**	**793**	**805**	**818**	**824**
		max	7.4624	746	759	771	784	796	809	822	834	841
	3	min	3.1422	675	687	699	710	722	734	746	757	763
		quart1	3.6736	687	699	711	723	735	747	759	770	776
		median	4.5239	704	716	728	740	752	764	776	788	794
		quart3	**5.2889**	**717**	**729**	**741**	**753**	**766**	**778**	**790**	**802**	**808**
		max	7.1037	742	754	767	779	792	804	817	830	836
	4	min	2.7368	665	676	688	700	711	723	734	746	752
		quart1	3.6253	686	698	710	722	734	746	757	769	775
		median	4.3473	701	713	725	737	749	761	773	785	791
		quart3	**4.7349**	**708**	**720**	**732**	**744**	**756**	**768**	**780**	**792**	**798**
		max	5.2075	715	728	740	752	764	776	789	801	807
	5	min	1.9511	640	652	663	674	685	697	708	719	725
		quart1	2.8291	667	679	691	702	714	725	737	749	755
		median	3.2677	678	690	702	714	725	737	749	761	766
		quart3	**3.7572**	**689**	**701**	**713**	**725**	**737**	**749**	**760**	**772**	**778**
		max	3.9470	693	705	717	729	741	753	765	777	783